Life In Motion:

Visualizing Biomacromolecules By Time-Resolved Serial Femtosecond Crystallography

by

Jesse David Coe

A Dissertation Presented in Partial Fulfillment
of the Requirements for the Degree
Doctor of Philosophy

Approved April 2018 by the
Graduate Supervisory Committee:

Petra Fromme, Co-chair
Scott Sayres, Co-chair
Kevin Redding
Vladimiro Mujica

ARIZONA STATE UNIVERSITY

May 2018

ABSTRACT

Time-resolved serial femtosecond crystallography is an emerging method that allows for structural discovery to be performed on biomacromolecules during their dynamic trajectory through a reaction pathway after activation. This is performed by triggering a reaction on an ensemble of molecules in nano- or microcrystals and then using femtosecond X-ray laser pulses produced by an X-ray free electron laser to collect near-instantaneous data on the crystal. A full data set can be collected by merging a sufficient number of these patterns together and multiple data sets can be collected at different points along the reaction pathway by manipulating the delay time between reaction initiation and the probing X-rays. In this way, these 'snapshot' structures can be viewed in series to make a molecular movie, allowing for atomic visualization of a molecule in action and, thereby, a structural basis for the mechanism and function of a given biomacromolecule.

This dissertation presents results towards this end, including the successful implementations of the first diffusive mixing chemoactivated reactions and ultrafast dynamics in the femtosecond regime. The primary focus is on photosynthetic membrane proteins and enzymatic drug targets, in pursuit of strategies for sustainable energy and medical advancement by gaining understanding of the structure-function relationships evolved in nature. In particular, photosystem I, photosystem II, the complex of photosystem I and ferredoxin, and 3-deoxy-D-manno-2-octulosonate-8-phosphate synthase are reported on, from purification and isolation, to crystallogenesis, to experimental design and data collection and subsequent interpretation of results and novel insights gained.

DEDICATION

I dedicate this dissertation to my brothers Steven and Kevin and my parents, Mary Ellen and Mark. I couldn't have done this without their support and encouragement.

ACKNOWLEDGMENTS

I would like to first acknowledge and thank my PhD supervisor, Dr. Petra Fromme, for her encouragement and support throughout my graduate career. Her thirst for knowledge and willingness to push forward into scientifically unknown territory is truly inspiring. Without her ability to take calculated risks and bring the right multidisciplinary brilliances together, none of this would have been possible. Thank you for always pushing and challenging me!

Next, I would like to thank my co-advisor Dr. Scott Sayres for his support, mentorship and incredible ability to transfer knowledge. I benefited much from the brief time I was able to work with him and gained both a large practical knowledge and a great friend in the process. I will think of you every time I'm stuck trying to maneuver a ridiculously long B-Line through a crowded machine shop and I'll miss representing the Sayres lab by jamming out on the Ruben's tube. I will also never forget that Sheetz > Wawa.

To my committee, Dr.'s Kevin Redding and Vladimiro Mujica, I would like to extend my heartfelt thanks to all of the knowledge and advice over past years. Dr. Redding has been immensely helpful in understanding and thinking about my work with photosynthesis and is also quite inspiring with his vast curiosity and knowledge. I ended up taking half of my graduate level classes with Dr. Mujica due to his fantastic teaching style that allowed me to truly understand some of the most complicated areas in physics and chemistry without feeling discouraged. His ability to keep it fun and interesting, including valuable life advice, is something that I will forever value.

Thank you to my undergrad advisor and former supervisory, Hilairy Hartnett and the grad/undergrad students I worked with in my time there. She was a huge inspiration in my eventual decision to pursue a Ph.D. and I learned so much in my time as a volunteer and lab manager in her lab. I'll never forget rocking out and muffling with Zach Smith, Maggie Bowman and Marissa Raleigh or learning the basis for my lab technique and experimental design from Jessie Shipp, Alex Hamilton and Katie Noonan.

A special thanks to Chelsie Conrad (Smith) with whom I spent a majority of my time in grad school working closely with. Through thick and thin, it was a pleasure to grow both professionally

and personally with you over the stresses of countless beamtimes and projects and I'm happy to count you as a friend.

A further special thanks to Shatabdi Roy-Chowdhury who has also been with me through a myriad of protein preps and beamtimes. You have always been a good friend and I will miss our dark lab conversations and shared frustrations. Boba forever!

Thank you to Michael Vaughn, whom I consider my primary mentor within the wet lab realm. I am a much better scientist for the few years we were able to spend working together, you were always able to put things clearly and concisely. I look forward to the next time we can get some Dickey's or throw back some Bulleit.

Thanks to Jay-How Yang, the unsung hero of the lab. I could always count on you to help solve a problem or share a good laugh and I'll forever wonder what you were hiding in your SSRL apartment. Thanks to Natalie Vaughn for your insight, leadership and friendship, you kept all us plebs in line 😉. Thanks to Alex Schaffer for always being a good homie and lab mate, you have a bright future my friend.

Thank you to Jim Zook, despite your coffee thefts I think I came out on top with all the knowledge I gained through our water cooler chats. I owe the majority of my HPLC knowledge to you and I think I can finally stop calling you when something goes wrong.

Thank you to José Martin-Garcia for your mentorship in addition to your help in keeping me sane, I'll miss your patient guidance, friendly encouragement and knowing looks, till the next trip to APS!

Thank you to Chris Kupitz for the introduction into crystallogenesis and protein purification in addition to your friendship. Please don't stab me with a spoon. Thank you as well to all of my other past and present Fromme group lab mates as well, you have all helped me grow with your critical advice, shared experiences and encouragement. In particular: Thank you to my fellow 2013 freshman grad student Bobby Baravati, it's been awesome hanging out, jamming and chatting about the advanced topics make me envious of your brilliance. Kabul tango for days man. Thanks to Zach "The Dob" "pair of Lisa's" Dobson, you've been a great friend and lab mate. Wings and Heady Topper will not be the same. Also, tell Yuval there are 5 or 6. Shout outs to Caraline Sepich,

possibly the most talented undergraduate researcher I have witnessed. Looking forward to seeing what you do in the future. To Erin Discianno, thanks for your friendship, support and commiseration over the past year, welcome to the *cough* show! Thanks to Alex Jones, my disc-rippin' mentor and culture boss extraordinaire. I'll miss your humor and forever admire your stoic sanity and professionalism in the face of malarkey. Thank you to Nirupa Nagaratnam for being an incredibly considerate and kind lab mate, you were an inspiration and I owe you any sharpies I have left over.

Thank you to Mark Holl for your shear brilliance that overcame so many challenges that I am likely only aware of a fraction. Your patience and mentorship were appreciated by anyone wise enough to seek or accept it. Thank you to Tina Esquerra for all of your (mostly) behind the scenes efforts in keeping the lab together both administratively and interpersonally. To Geronimo Campanile, thank you for your friendship and willingness to go above and beyond your job duties to keep the lab running smoothly. I can imagine that without you, I may still be waiting for edits ☺ I'll always remember our early afternoon lunches at Postino's and the enthralling conversations that accompanied them.

Nadia Zatsepin, I can't thank you enough. I owe almost the entirety of my theoretical understanding to you and I will deeply miss our talks about scattering, coding, career and life. You have been a profound mentor and wonderful friend throughout the past 5 years, I wish you all the personal and professional success you deserve, and I hope we continue to stay in touch.

I also owe a huge thanks to Shibom Basu and Natasha Stander who both patiently helped me become more familiar with writing scripts and processing data in addition to selflessly crunching data for me at times when it was beyond my abilities. Thank you to Ganesh Subramanian, I will cherish our discussionos on both a personal and professional level, Ozymandias!

Thank you to Chad Simmons for all your help in my initial learning of crystallography and your willingness to lend a hand in our beamtime preparations, it was a pleasure to learn from you. Thank you to Dan James and Garret Nelson for spending time teaching me all things injection, your expertise was a boon for every beamtime I had the pleasure to work with either of you. A huge thank you to the too often underappreciated Stella Lisova, you saved our butts more times than I can remember with our crazy last minute beamtime requests for nozzles. You rock!

Thank you to Bobby Abdallah and Austin Echelmeier (AKA Baustin 😉) for all of the collaborative work and individually special friendships, the absence of which I would have suffered much more in my graduate tenure. Bobby, we will have to catch up over some Don Q sooner than later. Austin, you're one of the most kind-hearted and genuine people I've ever met and the next time I sing Queen, you know I (and the crowd) will need you there to save me from myself.

I would like to extend my thanks to my Sayres lab mates as well, especially Jake Garcia, Lauren Heald, Nancy Fujikado and Lennon Quiroz. It's been awesome learning all things optics and high vacuum with you guys, I look forward to seeing what the future holds for you all.

For the sake of brevity (lol), I would like to thank all of my international collaborators as well as all the folks at the various beamlines that have made all of the work I have been involved in possible. In particular, a glühwein mit schuß to Henry Chapman, Dominik Oberthuer, Ken Bayerlein, Oleksandr Yefanov, Tom White, Anton Barty, Anja Burkhardt, Katerina Doerner, Iosifina Sarrou, Max Weidorn, Juraj Knoska, and Salah Awel for all of their help and friendship both in Germany and at LCLS, and a round at the goose for Sebastien Boutet, Mark Hunter, Ray Sierra, Menging Liang, Andy (Dr)Aquila  , Hasan Demirci, Marius Schmidt, Jason Tenboer, Kanupriya (KP) Pande and Tom "T-Grizzle" "nobody calls me that" Grant for all the support, scientific expertise and patience over the course of many stressful but fruitful beamtimes. Extra special thanks to Cornelius Gati for not only being a fantastic collaborator, teacher and friend but for taking a chance on me as my future boss. Looking forward to the unstoppable J bear-Corn dog combo.

I want to thank my friends for their support and encouragement through not only my graduate studies but the run up to it as well, especially Eric and Katie Krueger, Jordan Stickleman, Mike Pomo, Tom Wardman, Tim Baxter and Tara MacCulloch. Eric and Katie, I appreciate how much you two have been there for me for this whole journey. I will miss the late nights and long talks about any and everything, you guys are basically family. Sticky, you remain the most positive and optimistic guy I know. Through the years and crazy shenanigans ("did someone say shenanigans?!"), I'm fortunate to be able to call you a friend. Olive juice buddy! Mike, thanks for being a solid, reliable friend and putting up with my complaints, crazy schedule, and keeping me

sane. You're one of the most compassionate and considerate dudes I have ever met, KCCO bro. Tommy, since the early days in Lakeshore you've always been there for me and can always cheer me up. I'll miss the jams, Sundays at Native and backyard grilling my dude. To Tim and Tara, you two have been awesome and supportive housemates and friends for the past few years. I'm quite sure that you have both prevented me from a nervous breakdown as I was finishing up my graduate career. I expect to see you both at the friendship village and of course, roomies 4 lyfe!

To my girlfriend Claire, thank you for being there through thick and thin. I can't express how much I appreciate you and how you have not only put up with my stress (especially during the writing of this) and crazy hours but have been there to talk me down and encourage me through lows as well as enhancing the joys of the highs. From our garage nights to road trips to the quiet binge-watching nights in, you mean the world to me.

To my mom and dad, what can I even say except thank you both for everything! You have both shaped me to be who I am today, cultivated my early love for math and science through unconditional love and support. You are both such an inspiration and I feel so lucky to have such amazing and loving parents. I love you both!

To my brother Kevin, I still want to be like you when and if I someday grow up. You have been an absolute role model and positive influence on me since the first time we talked. From introducing me to all the bands I didn't yet know I love to late nights at just the tip to our deep talks about life, love and future, you have shown me how to embrace the joy in life and what it means to be a man of principle, insight and compassion. I am so excited to see what the future brings for you and Allison and I love you man.

To my brother Steven, Coe-brah's for life man! Even without bringing me snack packs, you are the coolest. I can't explain in words how much it has meant to me to have such a smart, talented and fun brother to take on the world with. From the bunk-bed talks about life to riding bikes and skating to operation golden glove in the backyard to video games in the loft to parties and chasing girls to the current journey through career paths and settling into our own, I love you man and you have and always will be my best friend.

This work was supported by the STC Program of the National Science Foundation through BioXFEL under Agreement No. 1231306, the National Institutes of Health Femtosecond Nano-crystallography of Membrane Proteins Award 617095583, the Center for Applied Structure Discovery.

Experiments described here were carried out at the Linac Coherent Light Source (LCLS), a national user facility operated by Stanford University on behalf of the US Department of Energy (DOE), Office of Basic Energy Sciences (OBES). This research used resources of the Advanced Photon Source, a U.S. Department of Energy (DOE) Office of Science User Facility operated for the DOE Office of Science by Argonne National Laboratory under Contract No. DE-AC02-06CH11357. Parts of this research were carried out at the light source PETRA III at DESY, a member of the Helmholtz Association (HGF).

TABLE OF CONTENTS

Page

LIST OF TABLES

LIST OF FIGURES

Figure Page

Figure Page

Figure Page

1 INTRODUCTION

Introduction to X-ray Crystallography

Structural Biology and the Fundamentals of Crystallography

Structural biology as a field concerns itself with understanding how nature works though exploration of the relationship between structure and function of the complex molecules that allow life itself to exist and propagate. Probing these complex molecules through various techniques allows the inference of their shape and structure, down to the atomic details in a certain few. The largest and most complex of these biomolecules are DNA and RNA, made up of nucleic acids, and proteins, based on amino acids variations of these. These biomacromolecules and their larger assemblies are the most crucial elements to understanding life and the most difficult to probe and understand. High resolution biomacromolecular structures have only been attainable by a few techniques so far, namely X-ray crystallography, nuclear magnetic resonance imaging (NMR) and electron microscopy. Out of these techniques, X-ray crystallography has been the main "workhorse" and is responsible for over 89.5% of structures deposited at the Protein Data Bank (depository for macromolecular structures), highlighted in figure 1.1.

Since the discovery of X-rays in 1895 by Wilhelm Röntgen, X-ray sources have been an invaluable tool in probing the world around us with applications in medicine, physics, chemistry and biology. 17 years later, the first use of X-rays in a diffraction experiment was achieved d after Max von Laue theorized that the wavelength of X-rays could be on the scale of interatomic distances and proceeded to apply them to a copper sulfate pentahydrate crystal resulting in the first diffraction images (Friedrich, Knipping et al. 1913). Extending upon this, the father and son team of Sirs William Henry Bragg and William Lawrence Bragg began to explore diffraction as a tool for structure determination in crystals and arrived at the first crystal structures ever reported (being that of diamond and a few ionic salts) (Bragg and Bragg 1913, WL Bragg 1913). Thus, the field of crystallography was born.

Over the years, more and more powerful X-ray sources began to extend X-ray crystallography towards biological molecules, starting when Dorothy Hodgkin first solved the

structures of cholesterol in 1937, insulin in 1945 and later vitamin B_{12} in 1955, leading to her Nobel Prize. Soon following, the first protein structure was published after John Kendrew developed multiple isomorphous replacement in order to deconvolute the phase problem and solve the structure of myoglobin in 1957 at 6 Å (Kendrew, Bodo et al. 1958), followed shortly by a 2 Å near atomic resolution structure 1959 (Kendrew, Dickerson et al. 1960). Kendrew would also go on to win the Nobel Prize due to this remarkable achievement.

Crystallography as a technique is well understood and will not be covered in depth here. For a detailed treatment of the subject, the reader is referred to texts regarding the subject (e.g. Rupp (2009), Hammond and Hammond (2001), Giacovazzo (2002), Drenth (2007)).

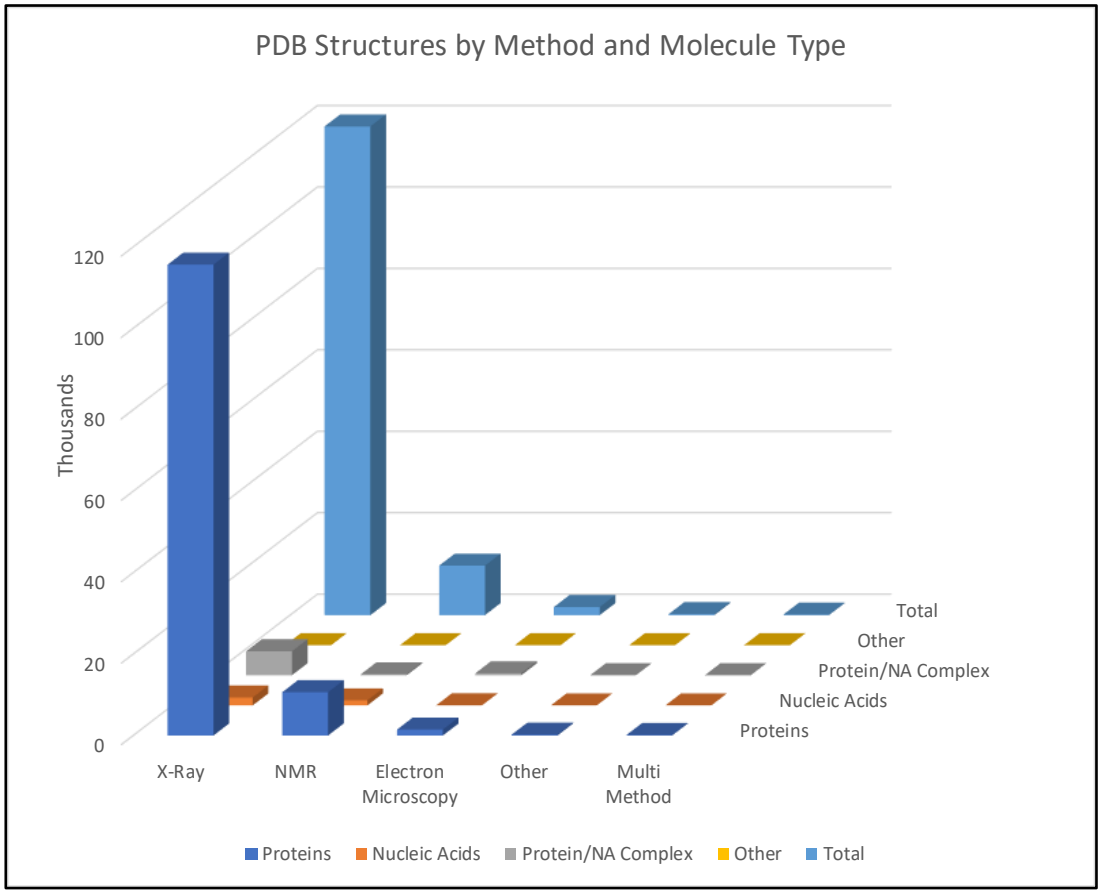

Figure 1.1 PDB Statistics by Method

Shows number of depositions (by thousands) according to experimental method and molecular type. This illustrates the domination by X-ray crystallography as a method for biomacromolecular structure determination. Statistics retrieved on 22 February, 2018 from http://www.rcsb.org (Berman, Westbrook et al. 2006).

Crystallography allows the structure determination by manipulating the interactions between light and matter. In particular, this is achieved through use of a translationally ordered solid in which a repeating element, the asymmetric unit, is organized in multiple copies that possess a conserved distance, angle, and orientation to the surrounding asymmetric units. This repeated relationship between the asymmetric units forms a lattice composed of unit cells that are identical to each other and contain one or more copies of the asymmetric unit in a conserved structure. When crystals are subjected to electromagnetic radiation, they are able to elastically scatter that radiation coherently, i.e. in waves with a defined phase relationship that is dependent upon the wavelength of the light, the geometry of the crystal with respect to the propagating photonic wave, and the electronic structural composition of the asymmetric unit. As with any wave, the product of scattered radiation from these centers results in combining of their amplitudes, called interference. There are two types of interference, destructive and constructive which describe when the waves cancel each other out or add together respectively. In a crystal, the constructive interference will manifest as focused waves in specific geometric orientations governed by the orientation of the lattice planes within a crystal relative to the propagating X-rays. The peaks created by this ordered wave interference can be described mathematically by the Bragg equation (named after the younger of the aforementioned Braggs):

$$2d\sin(\theta) = n\lambda$$

where d is the lattice spacing, θ is the angle between the scattering angle of a particular crystallographic plane and the incident radiation, n is an integer and λ is the wavelength of the X-rays. This manifests as 'Bragg spots' or reflections whose intensities are governed by the cumulative electronic structure of the molecules within the crystal (modulated by the symmetry of how the molecule packs in the crystal unit cell). This also results in a huge boost of the signal to noise ratio (SNR), as the intensity scales quadratically with the number of unit cells in a particular direction. The patterns these Bragg spots form are related to the unit cell with the intensity being related to the electron density, and subsequently the structure, of the molecule through a Fourier transform, allowing structure visualization to be inferred (though phase information is lost and must be elucidated, discussed later). Diffraction from crystals con be observed with any wave such as

electrons or visible light but X-rays are used since they possess wavelengths in the angstrom and below regime in which atomic structure resides and can penetrate large crystal volumes, without significant secondary scattering events.

Limitations in Traditional Crystallography

The scattering power and resultant intensity is proportional to the electron density with high Z atoms possessing a stronger scattering cross section. Macromolecules such as proteins, whose composition is predominantly made up of H, C, N and O atoms, are relatively weak scatterers. This is further compounded by the high solvent content typical in crystals of biomacromolecules, often between 30% and 70% (Matthews 1968), resulting in a low number of crystal contacts and weak scattering intensity per unit cell.

To understand the difficulty in obtaining macromolecular structures, it is important to consider the dependence of reflection intensities on the size of a crystal which can be described with the Darwin equation. This equation relates the integrated intensity, I, to the inherent structure factor, F:

$$I = I_0 r_e^2 \frac{V_{crystal}}{V_{cell}} * \frac{\lambda^3 L}{\omega V_{cell}} * P * A * |F|^2$$

The requirement for large crystals becomes apparent when one considers that the intensity of a reflection is proportional to the crystal volume and is inversely proportional to the square of the unit cell volume. This necessitates large, well-ordered crystals to obtain a usable signal to noise ratio (SNR) for high angle (high resolution) reflections and subsequent structural elucidation.

Due in part to the fragility of macromolecular crystals, their sensitivity to X-ray induced structural damage (see below), and the need for large crystals, crystallogenesis remains a large bottleneck in protein structural discovery. The process in creating suitable protein crystals for traditional crystallography can span decades, being particularly difficult for membrane proteins and large complexes. This is exemplified in the case of photosystem I which spanned 13 years from the first reporting crystallization conditions in 1988 (Witt, Witt et al. 1988) till 2001 when a 2.5 Å resolution structure was reported (Jordan, Fromme et al. 2001). During this time, it took dozens of

researchers' dedicated efforts to develop large, well-ordered crystals and proper handling and preparation techniques.

In addition to the formation of suitable crystals, another challenge facing macromolecular crystallographers is that of radiation damage caused by the ionizing X-rays necessary for achieving atomic resolution. The high brilliances of modern X-ray sources are easily able to damage crystals to the point where artifacts from damage, such as in disulfide bridges (Helliwell 1988) will significantly affect the data and, after a certain dose, the crystals will stop exhibiting diffraction all together. The damage comes in the from of stages where the primary damage is the ionization caused by photoelectric absorption or Compton scattering and secondary damage that follows from this once the ejected (primary) electron can lead to a cascade of lower energy electrons (Garman 2010). These electrons reduce further atoms within the crystal leading to further ionization events, the formation of radicals and generating excitation events, changing the electronic structure of the molecule that alter and break chemical bonds. As this process proceeds, homogeneity and crystalline order become disrupted, leading to significantly decreasing signal and eventual termination. In addition, as this occurs the structures can be altered in a way that experimentally induced artifacts are created that have no biological relevance.

The first breakthrough in addressing this was the development of methods that allowed for cryocooling crystals to temperatures below 100 K, becoming widely used in the early 1990's (Robinson 2015). Cryo-cooling and data collection at cryogenic temperatures became generally accessible after the developments of the loop-mounting method, where the crystal is suspended in a film of cryo-protectant buffer held in a loop by surface tension (Teng 1990), where it can be fast frozen either directly in the cryostream, or by plunge freezing in liquid nitrogen. The sample are kept at cryogenic temperatures during data collection by use of a focused stream of 77 K gaseous nitrogen (Cosier and Glazer 1986). Cryo-crystallography has been estimated to allow for a 70-fold increase in the dose tolerance compared to collection at room temperature (Nave and Garman 2005). However, it only slows down the secondary radiation damage by limiting the diffusion time of the radicals and cannot mitigate the primary damage caused by photoelectron ejection.

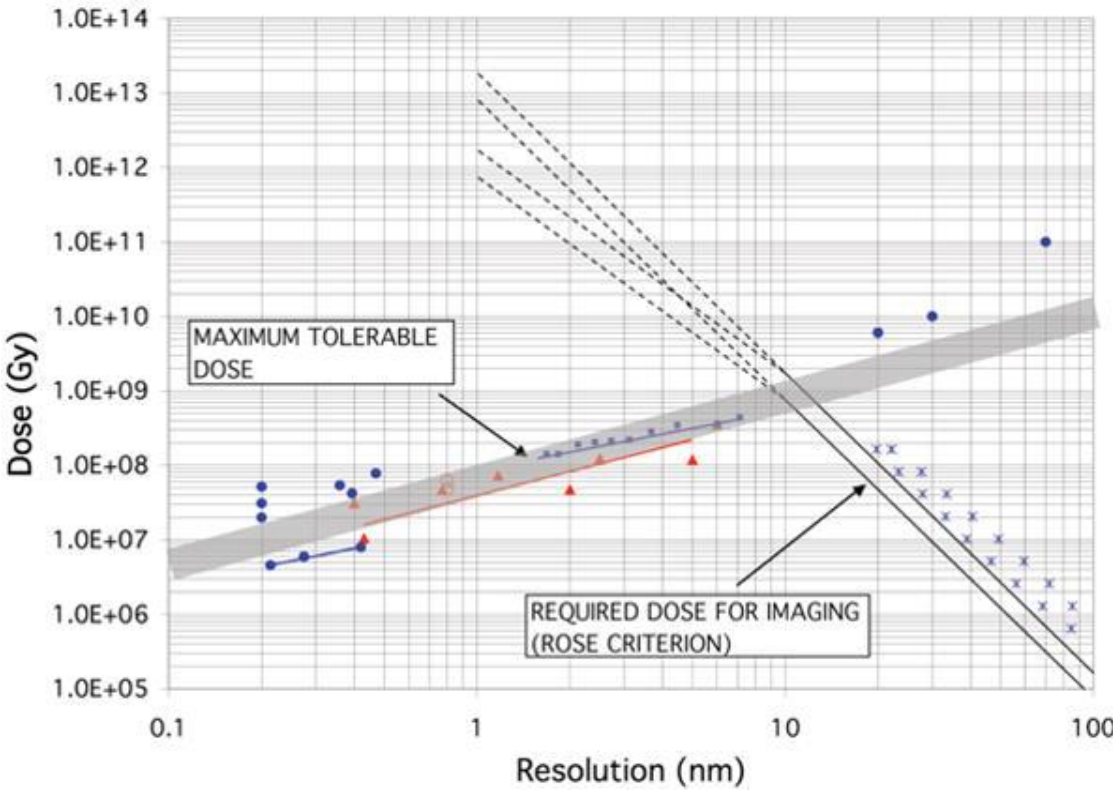

Figure 1.2 Graph Summarizing Required Dose for Imaging and Maximum Tolerable Dose of Radiation

The required dose for imaging is calculated for protein of empirical formula $H_{50}C_{30}N_9O_{10}S_1$ and density 1.35 gm/cm^3 against a background of water for x-ray energies of 1 keV (lower continuous line) and 10 keV (upper continuous line). The dashed continuations of these lines refer to the transition region from coherent (d^{-4}scaling) to incoherent (d^{-3} scaling) behavior, both of which are shown down to 1 nm resolution. Some of our measurements of the required dose for imaging are plotted as crosses. The maximum tolerable dose is obtained from a variety of experiments reported in Howells, Beetz et al. (2009) and from literature. The types of data from the literature are identified by the symbols as follows: filled circles: standard X-ray crystallography, filled triangles: electron crystallography, open circles: single-particle reconstruction, open triangles: electron tomography, diamonds: soft X-ray microscopy (including XDM), filled squares: ribosome experiment. Figure and caption modified from Howells, Beetz et al. (2009)

While cryocooling has allowed for significant advancement in reducing the damage caused by radiation, there remains a limit before damage overcomes the crystal. The manifestation of radiation damage can be divided into global damage and local damage. While global damage becomes strongly apparent in loss of total scattering intensity or increased unit cell parameters (Meents, Gutmann et al. 2010), local damage is more insidious since it occurs much faster in heterogeneously more susceptible localities (e.g. high-Z metallocenters, disulfide bridges) and is more often found only once an obtained electron density map is scrutinized (Holton 2009). For

cryocrystallography, global damage has been shown empirically to be dependent only upon accumulated dose rather than dose rate, possibly due to slower diffusion rates of secondary damage sources (Holton 2009). The dose limit will vary depending on the exact composition of the sample but a conventional limit for resolution-dependent damage was reported as $D_{1/2} = 10*d$ MGy ($D_{1/2}$ is the point at which total diffraction intensity is halved, d is the resolution in Å) (Howells, Beetz et al. 2009). It should be noted that this can vary significantly and macromolecules containing many high-Z centers (such as the photosystems) are susceptible to damage at a much lower dose.

In order to obtain quality and reliable data from diffraction experiments, enough intensity must be gained to deconvolute signal from noise. This is limited by the amount of radiation a crystal can experience before damage becomes a significant factor and a balance must be found see figure 1.2) which requires a certain size crystal (as Gy is a measurement of radiation per mass) in order to achieve a desired resolution (Holton and Frankel 2010). This is compounded by the fact that from the incident beam, most of the X-rays don't scatter elastically. For example, a 100 μm thick crystal being subjected to a 12.4 keV (1 Å) beam will only elastically scatter 0.15% of those X-rays, with 1.85% leading to inelastic scattering and photoelectric ejection (the remaining 98% don't interact at all) (Garman 2010). While this can be mitigated in theory by larger crystals to spread out the dose more evenly (optimally, the crystal and beam size are matched (Zeldin, Gerstel et al. 2013)), there is a practical limitation to the size that macromolecular crystals can actually be grown to.

X-ray Free Electron Lasers (XFELs)

Progression of X-ray Sources

The power of X-ray sources for use in structural biology has progressed exponentially since the early days of Laue and Bragg and has, along with the proliferation of available sources, allowed for an amazing progression in understanding how life works at a molecular level. Perhaps the most stark jump in the timeline of available X-ray sources was the discovery that synchrotrons, originally devoted solely to high energy particle physics, produced X-ray radiation orders of magnitude more brilliant than that of the highest powered rotating anode (Dauter, Jaskolski et al. 2010). While

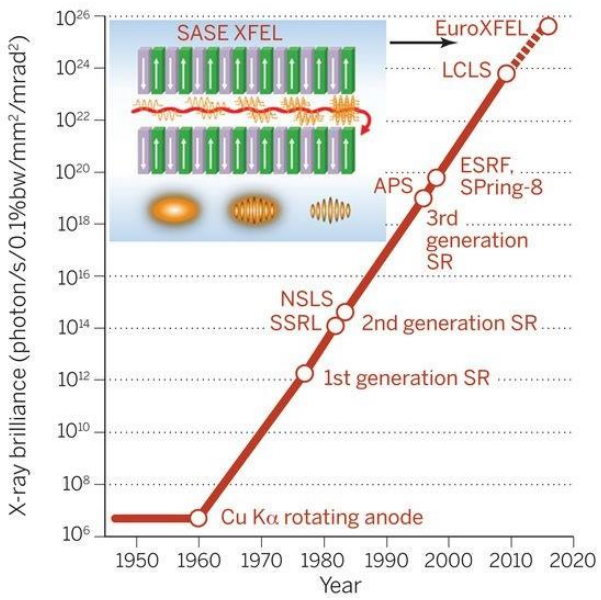

Figure 1.3 Progression of X-ray Source Brilliance

Shows the increase in brilliance increasing in orders of magnitude since the rotating anode. XFELs represent a completely new regime by using the SASE process (inset) to achieve ultrashort, intense pulses. Figure originally from Miao, Ishikawa et al. (2015).

crystallographers were essentially parasitic at the first-generation synchrotrons in the 1970's, using what was essentially viewed as unfortunate energy loss, the potential for synchrotron radiation in diffractive techniques became soon apparent (Rosenbaum, Holmes et al. 1971, Phillips, Wlodawer et al. 1976). The modest gains made in this time period lead to the development of a second generation of synchrotrons dedicated mainly to producing radiation (Dauter, Jaskolski et al. 2010). At this point, the time it took to collect a complete data set for a macromolecular crystal had been brought down from months to hours, allowing for crystallography to become a much more accessible field, attracting more and more researchers and leading to methodical improvements in the way that data were collected.

During the prime of second generation sources, a couple developments stand out that ultimately paved the way for the modern third generation of synchrotrons. The first was the increase of brilliance achieved with the design of a new lattice structure for storage rings, termed the double-bend achromat or Chasman-Green lattice being named after the designers (Chasman, Green et al. 1975). The developers implemented this during the design of NSLS (see figure 1.3) in response to the desire for intense, focused, monochromatic beams and most of todays synchrotrons are based on variations of this system (Robinson 2015).

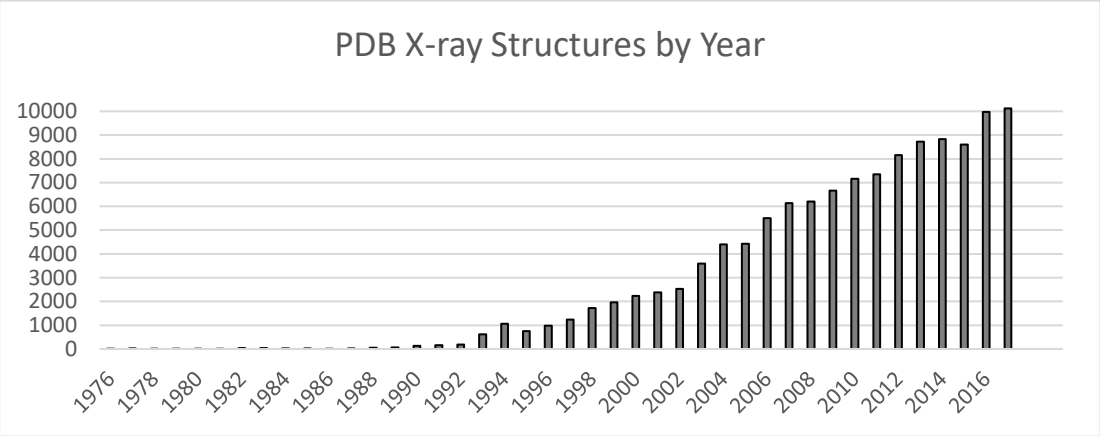

Figure 1.4 Macromolecular Structures Deposited by Year

Before 1990, most years saw two or three dozen structures with no year over 100. After the introduction of more powerful third generation synchrotrons with dedicated beamlines and matured tools for data analysis, an explosive growth occurred and set the stage for the thousands of solved structures per year that we enjoy today.

Another significant advancement made in this era was the introduction of insertion devices, namely wigglers and undulators. These both work on similar principles by which an alternating magnetic field is used to oscillate the electrons responsible for synchrotron radiation. In doing so, a constructive interference arises between radiation emitted due to the changes in momentum experienced by the electrons. This interference allows for higher energies to be obtained as opposed to a bend magnet and can be engineered to peak at specific frequencies, further increasing brilliance (Brown, Halbach et al. 1983).

The incorporation of these developments led to a third generation of light sources to be developed with a higher degree of specialization for particular beamlines and a jump in the optimization of beam characteristics. The resulting jump in brilliance and versatility has allowed for an explosive growth both the size of the community and the amount of knowledge gained, highlighted by the increasing number of structures deposited per year shown in figure 1.4 after 3rd generation sources began to come online in the early 1990's. Of note, this also marks when cryogenic cooling began to be implemented on a mass scale (Garman 2010).

The most recent large jump in X-ray source development occurred in the form of X-ray free electron lasers (XFELs), sometimes dubbed the 4th generation of sources and marking the first time since the parasitic use of 1st generation synchrotrons that the method and characteristics of the

source has fundamentally differed from that of its predecessors. The first hard X-ray XFEL is the Linac Coherent Light Source (LCLS) which saw first light in 2009, housed at the U.S. DOE SLAC laboratory near Stanford (Pellegrini 2012). Both the average and peak brilliance achieved are orders of magnitude higher than even the most powerful beamline at any synchrotron. There are currently 5 hard XFELs around the world, namely LCLS (California, USA), Spring-8 (Hyōgo Prefecture, Japan), European XFEL (Hamburg, Germany), Pohang Accelerator Laboratory ((PAL) Pohang, South Korea), and SwissFEL (Würenlingen, Switzerland) in the operation or commissioning phase.

In contrast to synchrotron light sources where electrons are accelerated over multiple passes to achieve the desired energy, XFELs are based on a linear accelerator and experience a high gain over a single pass like a railgun for electrons. In contrast to their synchrotron counterparts, light produced at XFELs possess' coherence in 2 dimensions and can achieve pulses in the tens of femtoseconds or below, setting the stage for exploring completely new areas and regimes within physics and chemistry. This has particular implications for crystallography which will be explored in the next few sections.

Principles of an XFEL

To understand how an XFEL benefits structural biology (and the inherent limitations), it is i mportant to understand some of the principles behind how it works. As was previously mentioned, an XFEL can produce highly brilliant pulses of X-rays, femtoseconds in duration that possess full coherence. In contrast to a synchrotron, this is done using a single linear accelerator and the basis for these unique characteristics lies in the use of the self amplified spontaneous emission (SASE) principle. Simply put, this is the interaction between light emitted from an oscillating electron beam with the electron beam itself, allowing an exponential gain in emission due to an increasingly strong coupling between the two.

This happens by carefully matching oscillations experienced by electrons in an undulator with the wavelength of their emitted radiation. The electromagnetic field caused by this radiation in turn interacts with the upstream electrons (as light travels faster than the relativistic electrons).

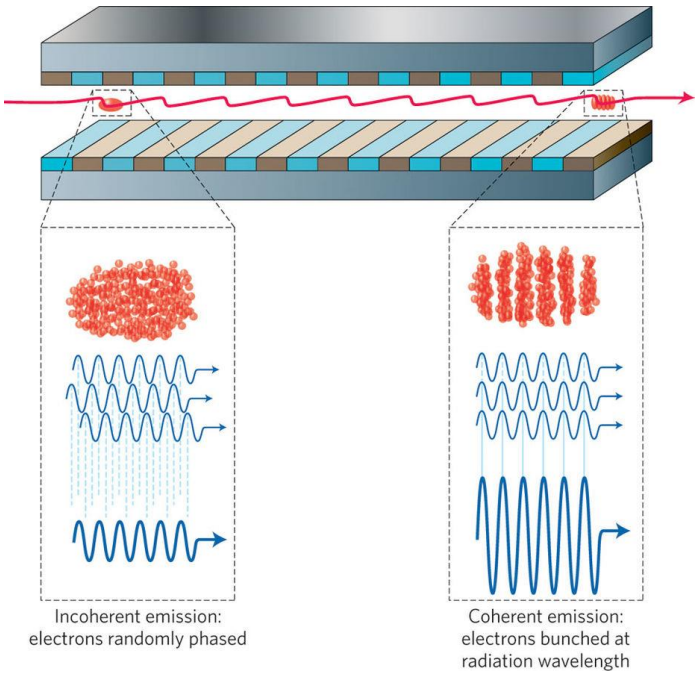

Figure 1.5 XFEL SASE in an Undulator

When electrons enter the undulator, their initially random phases ensure that mostly incoherent radiation is emitted at the resonant radiation wavelength (left). Because the electrons interact collectively with the radiation they emit, small coherent fluctuations in the radiation field grow and simultaneously begin to bunch the electrons at the resonant wavelength. This collective process continues until the electrons are strongly bunched towards the end of the undulator (right), where the process saturates and the electrons begin to de-bunch. Figure and caption from McNeil and Thompson (2010).

The undulator radiation acts as a series of resonant periodic potential wells which can exchange energy with the electrons, either absorbing (slowing of the electron) or transferring (speeding up the electron). This is the cause behind the electrons starting to bunch towards a mean phase which is exactly that of the field caused by the radiation. As this bunching occurs, the coupling increases and thereby so does the electric field which causes the bunching, creating a positive feedback loop that increases the amplitude of the emitted radiation due in part to the phase matching (i.e. coherence) experienced as the emitting electrons are bunched (see figure 1.5). The outcome of this electron bunching and subsequent exponential gain is a beam that possesses full coherence, is temporally constricted in ultrashort pulses, and has extremely high brilliance. For a more in depth, readily accessible mathematical treatment, the reviews contained in McNeil and Thompson (2010) and Pellegrini (2012) are suggested.

Diffract before Destroy: Serial Femtosecond Crystallography (SFX)

With the advent of the XFEL, a new method of data collection has been developed for macromolecular crystallography called serial femtosecond crystallography (SFX). The femtosecond pulse duration offered by XFELs is on the same timescale as the processes that initiate radiation damage. Primary damage and excitation events occur on the scale of 100's of attoseconds to tens of femtoseconds whereas secondary damage occurs in the tens of femtoseconds and longer. The damage mechanisms in SFX are fundamentally different from

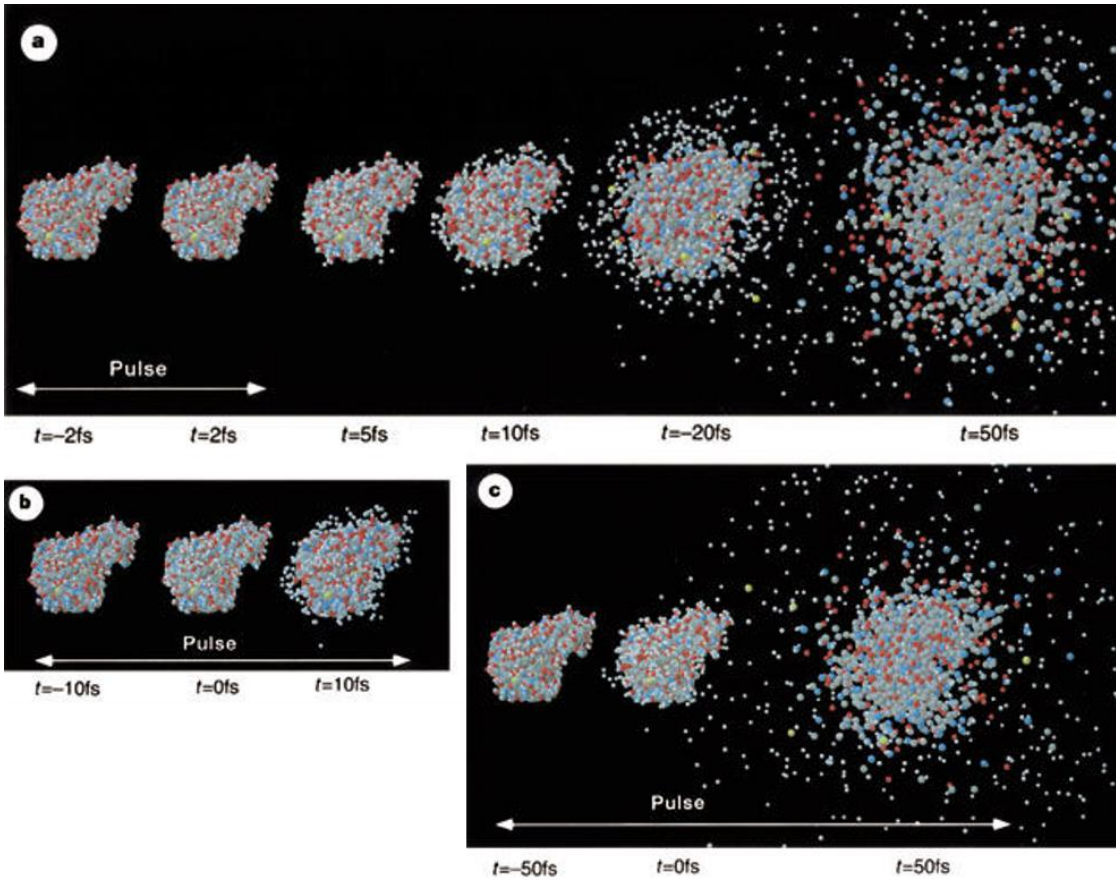

Figure 1.6 Diffract Before Destroy

The integrated X-ray intensity was 3 × 1012 (12 keV) photons per 100-nm diameter spot (3.8 × 106 photons per Å2) in all cases. a, A protein exposed to an X-ray pulse with an FWHM of 2 fs, and disintegration followed in time. Atomic positions in the first two structures (before and after the pulse) are practically identical at this pulse length because of an inertial delay in the explosion. Rnucl = 3%, Relec = 11% b, Lysozyme exposed to the same number of photons as in a, but the FWHM of the pulse was 10 fs. Images show the structure at the beginning, in the middle and near the end of the X-ray pulse. Rnucl = 7%, Relec = 12% c, Behavior of the protein during an X-ray pulse with an FWHM of 50 fs. Rnucl = 26%, Relec = 30%. Figure and caption from Neutze, Wouts et al. (2000).

conventional X-ray crystallography as the molecule is completely destroyed before any secondary damage occurs. The XFEL pulse leads to photoionization of the inner electrons of the atoms, creating “hollow atoms” (Hau-Riege, London et al. 2004). These atoms are now all positively charged and repel each other leading to a Coulomb explosion of the molecules in tens of fs. The pulse duration at current XFEL coherent imaging beamlines is 20 to 50 fs, in the range to obtain structural diffraction data before the molecule is destroyed and in essence outrunning the radiation damage. This has been termed the ‘diffract before destroy’ principle as the energy from the pulse results in a complete disintegration of the molecules and the crystal after diffraction is obtained.

The phrase was coined in after a seminal paper published in 2000 (Neutze, Wouts et al. (2000)) modeling the effects of femtosecond pulses on lysozyme in the gas phase and how imaging information could be obtained before the ensuing Coulomb explosion (see figure 1.6). At this time though, it was unclear whether this would work in practice and, additionally, whether pulses longer than 5-10 fs would cause any artifacts in the data or additional problems. It would be a decade before LCLS was operational for the first users to explore this at a hard X-ray source. In the meantime, FLASH, a soft X-ray FEL in Hamburg, Germany, became operational and marked the first XFEL of any kind (Ackermann, Asova et al. 2007). One of the milestones at FLASH was an experiment that first showed imaging done of an object using femtosecond pulses, outrunning the destruction of the object. This is highlighted in figure 1.7 and acted as a proof of principle for femtosecond FEL imaging.

A few years later in 2009, the first user experiments were conducted at LCLS, enabled by the development of Nanocrystallization and novel sample delivery techniques that allowed for delivery of crystals at room temperature to the XFEL beam. In the first experiment at the AMO beamline operating at soft X-ray energy of 2 keV, photosystem I nanocrystals were delivered to the XFEL beam in a room temperature liquid jet whereby individual diffraction ‘snapshots’ were recorded serially on individual nanocrystals. This proved to be a remarkable success and, as reported in Chapman, Fromme et al. (2011), a damage free structure was determined based on tens of thousands of patterns. The solution and, consequently, method were then validated with

comparison to the previously solved structure obtained from traditional crystallography (Jordan, Fromme et al. 2001). Thus, the field of serial femtosecond crystallography (SFX) was born.

While there are constantly evolving methods and experimental setups regarding SFX experiments, many of which are covered more extensively in following chapters, the principle behind SFX remains the same. A multitude of nano- or micro- crystals are sequentially subjected to an XFEL beam whereby snapshot diffraction patterns are accumulated. This allows for room temperature collection on fully hydrated macromolecular crystals with a low as tens of unit cells in a given direction and without detrimental artifacts caused by secondary radiation damage. This removes the restriction on the crystal size needed to solve a structure and also has significant implications for dynamics as explored in the following section. Due to the partiality of the reflections, variations in the diffracted volume of the the crystals, shot-to-shot beam variations in profile and intensity and the uncorrelated orientations of the crystal lattices, a Monte Carlo method is applied to the data, requiring thousands to hundreds of thousands of individual snapshots to be individually indexed and finally merged to compile a complete data set. The ability to image nanocrystals in a serial fashion with ultrashort femtosecond pulses allows for novel and interesting experimental design which is explored throughout the remainder of this dissertation.

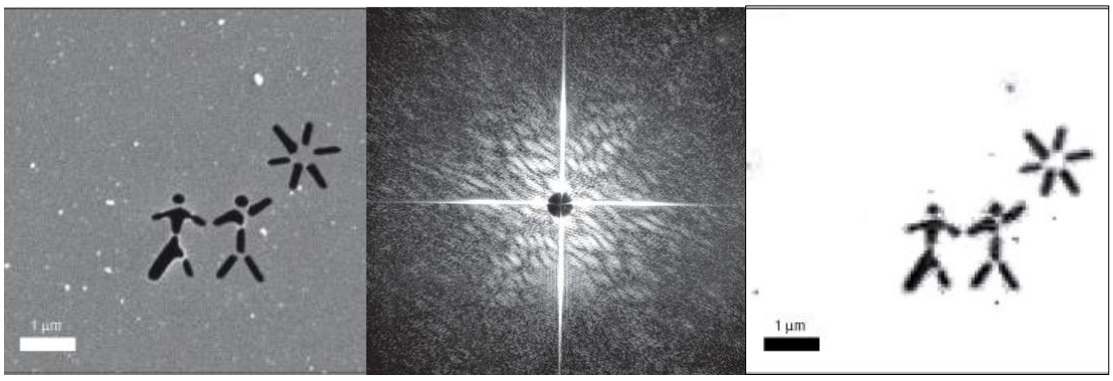

Figure 1.7 First Imaging Using an FEL (FLASH)

Left: An SEM image of the sample prior to FEL beam exposure. The sample is 20 nm thick and was held in a 20 µm wide square support window. Center: Diffraction measured from the FEL pulse off of the image. Subsequent diffraction and SEM imaging showed that the sample was completely destroyed with only a mostly empty window remaining (not pictured). Right: The reconstructed image obtained after phase retrieval and a Fourier transform were performed, showing an impressive match between SEM and FEL diffractive imaging. Figure modified and reprinted from Chapman, Barty et al. (2006).

Time-resolved Crystallography

Many proteins possess conformational dynamics that allow them to perform their functions and so in the search to gain knowledge on their structure-function relationship, it becomes at some point necessary to visualize them in their different confirmations in order to progress our understanding of their function. Time-resolved crystallography is the field concerning itself with elucidating structures along a reaction trajectory to enable the visualization of the dynamics of the reaction along it. In practice, this is done by triggering a reaction, which synchronizes the conformational transitions in the crystals and collecting data sets at different time points in the pursuit of a 'molecular movie' where the frames are now structures and the movie shows a macromolecular machine in action. One of the most promising avenues the advent of the XFEL has brought to structural biology is within time resolved studies, opening new temporal regimes and access to entirely new areas of investigating the dynamic macromolecules.

Traditional Time-resolved Methods

It is important to consider how time-resolved crystallography was (and is) done at conventional light sources to give context to the case at XFELs. At synchrotrons, the use of cryogenic temperatures largely precludes reactions from proceeding at biologically relevant speeds if at all. Due to this, a method called Laue diffraction is usually employed. It is based on using a so-called 'pink beam' which has a polychromatic energy spread. Referring back to the Bragg condition for constructive interference we can see that it is wavelength dependent. In fact, the solution for this at a given angle and fixed wavelength can be represented as a sphere in the mathematical dual space to the crystal lattice (i.e. the reciprocal lattice) with the condition being met at the intersection of a point on the reciprocal lattice with this sphere, named the Ewald sphere. As the energy increases, so too does this radius and this construct can highlight the theoretical resolution limit for a particular wavelength.

With a pink beam, this energy spread results in the ability to measure a solid angle caused by a continuous range of Ewald spheres rather than the thin shell that would be probed with monochromatic light. This increases the ability for the Bragg condition to be met and can be thought

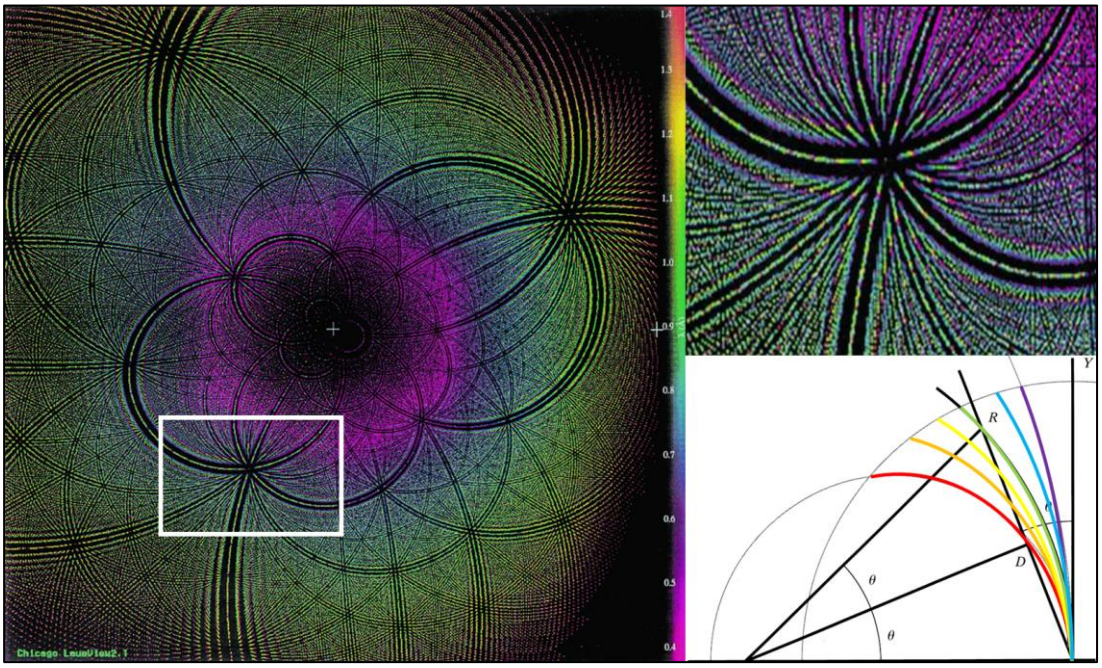

Figure 1.8 Simulated Laue Diffraction and Ewald Representation of a Pink Beam

Left is a simulated diffraction image of a Flock House virus crystal (Fisher, McKinney et al. 1992) using Laue diffraction with an energy spread of 0.4-1.4 Å. The heat map coordinates reflections with the photon energy that stimulates them. Top right is a zoomed in view showing the area highlighted on the left image and shows the local variation in spot-stimulating energies. Bottom right depicts the Ewald slice that arises from a pink beam, showing higher energies (blue, purple) leading to a larger sphere in reciprocal space while lower energies (red, orange) result in a smaller swath. Figure modified from Ren, Bourgeois et al. (1999).

of as groups of crystal planes self-selecting the correct wavelength for diffraction at that particular angle, resulting in diffraction patterns that have many more spots arising from different energies. In other words, rather than rotating the crystal to vary θ, the Bragg condition is met through a range of λ. An example of what this looks like as well as the cause of this 'solid angle' in reciprocal space are highlighted in figure 1.7.

Synchrotrons are naturally suited to perform Laue diffraction due to their natural polychromaticity and pulsed structure (Helliwell 1997), with the use of insertion devices permitting sub-μs time points (Ren, Bourgeois et al. 1999). However, there are many limitations to the power of this method as time points are constrained by the shortest pulse duration to the 100 ps and longer time regime (Bourgeois, Ursby et al. 1996). On top of this, the intensity needed to collect a data set, even on large crystals, means that many pulses are needed to obtain a usable SNR, limiting this method to reversible reactions only (Moffat 1998, Moffat 1998). Furthermore,

chemoactivated reactions have in practiced been limited to either very long lived, stable intermediates or the use of engineered 'caged' substrates which utilize photoactivation to release substrate near the active site in order to overcome the need for diffusion through the crystal (Schlichting, Rapp et al. 1989, Duke, Wakatsuki et al. 1994, Stoddard, Cohen et al. 1998, Schlichting, Berendzen et al. 2000). Even with photoactivation, the size of the crystal poses a limitation on reaction initiation yields due to the balance between sufficient laser power to overcome attenuation as it propagates through the crystal versus the amount of flux before photodamage or bleaching occurs. This causes transient intermediate populations to remain low with reaction initiations typically between 10-15% (Schmidt, Srajer et al. 2013).

Time-resolved SFX

Time-resolved SFX (TR-SFX) is perhaps the biggest breakthrough in structural biology with the introduction of XFELs. It has improved upon previous methods for visualizing time-resolved intermediates of macromolecules in almost every way, having the ability to probe shorter time points, access to irreversible reactions, and avoiding local radiation damage to high-Z atoms common in reaction centers all in a fully hydrated environment at biologically relevant temperatures. Because of the ultrashort pulses used in SFX, the temporal resolution along a reaction timeline is now orders of magnitude better than anything available at a synchrotron (100's of fs at an XFEL (Pande, Hutchinson et al. 2015, Coquelle, Sliwa et al. 2018) vs 100 ps using Laue methods (Schotte, Lim et al. 2003, Schotte, Cho et al. 2012, Jung, Lee et al. 2013, Schotte, Cho et al. 2013)). Furthermore, the intense brilliance and subsequent ability to image nanocrystals lends itself to tighter reaction initiation homogeneity.

TR-SFX can be split into two types of experiments, photoactivated, which uses a pump-probe style setup as shown in figure 1.9a, and chemoactivated, which uses an on the fly diffusive mixing scheme as illustrated in figure 1.9b. In both setups, the principle idea is to collect structural data sets at different points along a reaction timeline, all being 'static' in and of themselves but once they are combined in sequence, the visualization of the macromolecular machine in action can be achieved, similar to how a movie works (imagined in figure 1.9c). Also of note, the serial nature of

SFX lends itself to irreversible reactions since the sample is constantly replenished as has already been successfully shown (Aquila, Hunter et al. 2012). The reaction timepoints that are targeted for a particular data set can be controlled by manipulating the geometry of the setup as well as flow rates and, especially in the case of diffusive mixing, the crystal size.

For pump probe experiments, the time regime has been extended to the fs second regime being limited at present only by the beam jitter (~150 fs) and improving upon the fastest available time resolution from Laue methods by three orders of magnitude. The use of smaller crystals allows

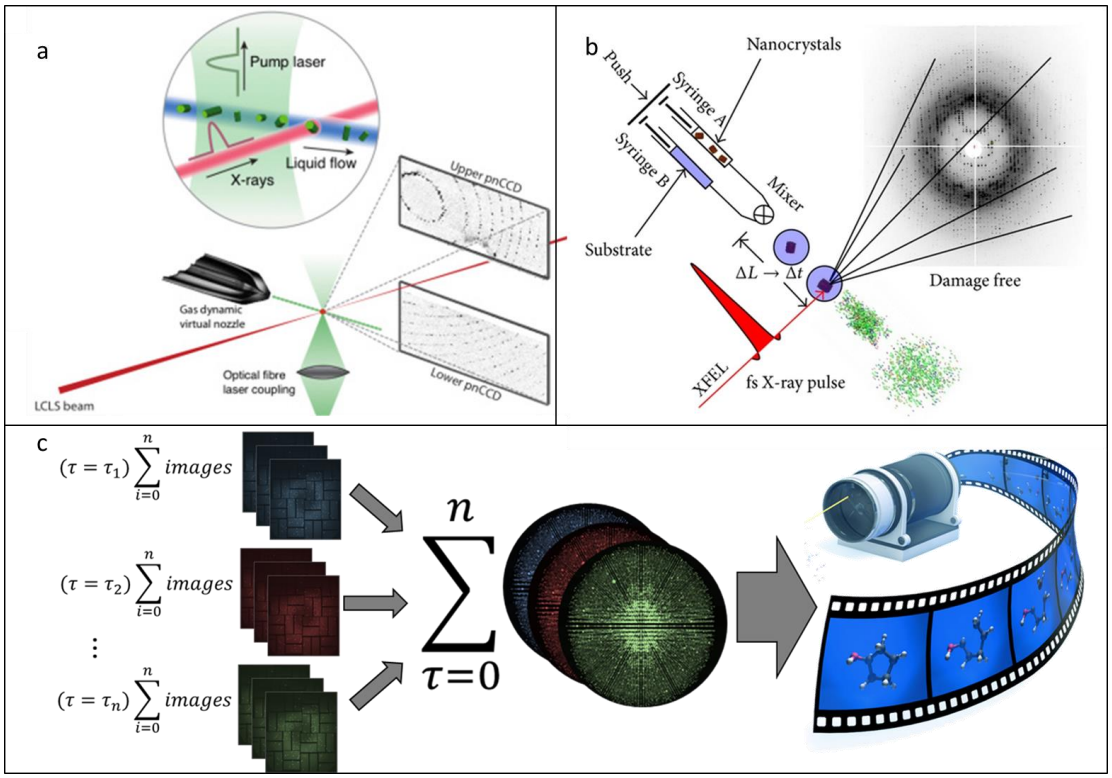

Figure 1.9 Making Molecular Movies: TR-SFX

a. Setup for a pump probe TR-SFX experiment. In this setup, photoactivatable protein crystals are illuminated or 'pumped' with an optical laser to initiate a reaction in the proteins. Delay times can be calculated and adjusted by the placement of the laser (can be in the nozzle to extend range) and flow rate of the jet. b. Depiction of a diffusive mixing TR-SFX setup. Though there are multiple ways this can be achieved, the principle is that a chemically activated reaction is initiated by mixing substrate or chemical trigger with macromolecular crystals. The delay in this case is highly dependent upon crystal size and composition of the mother liquor. In addition, the delay times can be manipulated by crystal size, method and geometry of mixing, as well as jet speed. c. Illustration highlighting how serial data from different reaction time points (τ) are binned into separate structure profiles that can reveal how a macromolecules changes structurally throughout the reaction. Images from **a** and **b** are modified from Aquila, Hunter et al. (2012) and Schmidt (2013) respectively.

for a less intense pump laser for activation due to the decreased attenuation as the light passes through the crystal with respect to molecules farthest downstream in the direction of pump propagation. In addition to tighter reaction homogeneity (it takes over 150 fs for the laser to cross 100 µm crystal), this allows for a minimization of potential photodamage or bleaching.

In the context of chemoactivated experiments, perhaps the biggest boon is the use of nanometer sized crystals. For any kind of diffusive mixing of a chemical trigger (e.g. substrate), both reaction initiation time and homogeneity are highly sensitive to crystal size. For example, a 200 µm crystal versus a 2 µm crystal with a typical small molecule ligand around the size of glucose have been calculated to have mixing times of 2.7 seconds and 600 *micro*seconds respectively (Schmidt 2013). This shows a thousands-fold increase in time resolution, opening up a completely new temporal regime in structural biology that contains many biologically and medically important receptors and enzymes.

Motivation for this dissertation: Energy, Health and the Importance of the Structure-Function Relationship in Dynamic Proteins

Much of the content contained in this dissertation revolves around using serial crystallographic methods, especially TR-SFX, in the pursuit of structure-function relationships in dynamic proteins and method development in the continuing expansion to a broader range of systems. The particular systems focused on herein involve photosynthetic membrane proteins and enzymatic targets implicated in disease that possess both medical relevance and kinetics that allow for expansion of TR-SFX methods.

One of the most powerful and promising techniques that has arisen out of the advent of the XFEL is that of time-resolved methods. The combination of access to the ultrafast temporal regime and the high fluence and energies needed for imaging at an atomic level have already allowed for significant advancements in visualizing macromolecules in motion. The driving motivation behind visualizing these is to understand how they work so that we may be able to, in essence, reverse engineer the result of billions of years of nature's evolution. With the growing population and inherent challenges a global society presents, sustainability is of the utmost

importance and two of the largest issues currently facing us are that of sustainable energy and medical health.

One of the biggest burdens modern medicine is faced with is the ability of disease causing organisms to constantly evolve and develop resistance to established therapeutics. This is further complicated by the need to be organism specific so as to avoid detrimental complications in the afflicted patients. Certainly, understanding the mechanisms behind not only pathogenesis but how the offending organisms sustain themselves and proliferate at a molecular level is key to addressing this issue. Within this context, it is no surprise that proteins represent most of the drug targets today as they exhibit specificity at every level of the taxonomic classifications of life. For rational drug design, the knowledge of the structure of a particular protein is essential. But, in the common case of a dynamic protein, knowledge of its multiple intermediates allows for mechanistic insight in which a protein can be leveraged with a higher degree of control and specificity. Ideally one would be able to obtain a molecular movie of the structural transitions that drive catalysis including the transition state where chemical bonds are formed or cleaved. Drugs that are specifically targeted to these transition state could bring a revolution in rational drug design. TR-SFX has allowed for an unprecedented opportunity to observe enzymes in motion in biologically relevant conditions and holds the promise to provide an advantage in the ever-present struggle against disease.

With regards to alternative energy, we have already made large advancements from biofuels to solar panels to progress towards an artificial leaf. All of this has been inspired by observing nature and how life is sustained, particularly with solar energy. Photosynthesis is at the heart of this and there remain mysteries unsolved, from the ability of photosystem II to exergonically oxidize water to the high efficiency of photosystem I acting as nature's battery in its reduction of ferredoxin. By looking at the large protein complexes that are responsible for oxygenic photosynthesis at a molecular level as they proceed to convert light into energy, one cannot help to be not only in awe but motivated and inspired to unravel the 'how it works' of one of the oldest and most fundamental processes behind life itself.

As the field of structural biology using XFELs has come out of it's infancy, the opportunities and potential of what is now scientifically possible and where this field is heading are starting to

emerge. At the heart of this endeavor are time-resolved studies and the quest for molecular movies to better understand and respond to the dynamic world around us. The particular motivations for this dissertation are primarily the study of photosynthetic processes and antibiotic targets but this represents only a portion (albeit a significant portion) of what can be achieved going forward in terms of learning about the world around us. Through the use of TR-SFX in particular, the opportunity now exists to study these processes in greater detail than has been possible before and it is this that drives me to push forward and stand on the shoulders of giants in the pursuit of new knowledge and greater understanding of the world around us.

References

Ackermann, W. a., G. Asova, V. Ayvazyan, A. Azima, N. Baboi, J. Bähr, V. Balandin, B. Beutner, A. Brandt and A. Bolzmann (2007). "Operation of a free-electron laser from the extreme ultraviolet to the water window." Nature photonics **1**(6): 336-342.

Aquila, A., M. S. Hunter, R. B. Doak, R. A. Kirian, P. Fromme, T. A. White, J. Andreasson, D. Arnlund, S. Bajt and T. R. Barends (2012). "Time-resolved protein nanocrystallography using an X-ray free-electron laser." Optics express **20**(3): 2706-2716.

Berman, H. M., J. Westbrook, Z. Feng, G. Gilliland, T. N. Bhat, H. Weissig, I. N. Shindyalov and P. E. Bourne (2006). The protein data bank, 1999–. International Tables for Crystallography Volume F: Crystallography of biological macromolecules, Springer**:** 675-684.

Bourgeois, D., T. Ursby, M. Wulff, C. Pradervand, A. Legrand, W. Schildkamp, S. Labouré, V. Srajer, T. Teng and M. Roth (1996). "Feasibility and realization of single-pulse Laue diffraction on macromolecular crystals at ESRF." Journal of synchrotron radiation **3**(2): 65-74.

Bragg, W. H. and W. L. Bragg (1913). The structure of the diamond. Proc. R. Soc. Lond. A, The Royal Society.

Brown, G., K. Halbach, J. Harris and H. Winick (1983). "Wiggler and undulator magnets—A review." Nuclear Instruments and Methods in Physics Research **208**(1-3): 65-77.

Chapman, H. N., A. Barty, M. J. Bogan, S. Boutet, M. Frank, S. P. Hau-Riege, S. Marchesini, B. W. Woods, S. Bajt and W. H. Benner (2006). "Femtosecond diffractive imaging with a soft-X-ray free-electron laser." Nature Physics **2**(12): 839-843.

Chapman, H. N., P. Fromme, A. Barty, T. A. White, R. A. Kirian, A. Aquila, M. S. Hunter, J. Schulz, D. P. DePonte, U. Weierstall, R. B. Doak, F. R. Maia, A. V. Martin, I. Schlichting, L. Lomb, N. Coppola, R. L. Shoeman, S. W. Epp, R. Hartmann, D. Rolles, A. Rudenko, L. Foucar, N. Kimmel, G. Weidenspointner, P. Holl, M. Liang, M. Barthelmess, C. Caleman, S. Boutet, M. J. Bogan, J. Krzywinski, C. Bostedt, S. Bajt, L. Gumprecht, B. Rudek, B. Erk, C. Schmidt, A. Homke, C. Reich, D. Pietschner, L. Struder, G. Hauser, H. Gorke, J. Ullrich, S. Herrmann, G. Schaller, F. Schopper, H. Soltau, K. U. Kuhnel, M. Messerschmidt, J. D. Bozek, S. P. Hau-Riege, M. Frank, C. Y. Hampton, R. G. Sierra, D. Starodub, G. J. Williams, J. Hajdu, N. Timneanu, M. M. Seibert, J. Andreasson, A. Rocker, O. Jonsson, M. Svenda, S. Stern, K. Nass, R. Andritschke, C. D. Schroter, F. Krasniqi, M. Bott, K. E. Schmidt, X. Wang, I. Grotjohann, J. M. Holton, T. R. Barends, R. Neutze, S. Marchesini, R. Fromme, S. Schorb, D. Rupp, M. Adolph, T. Gorkhover, I. Andersson, H. Hirsemann, G. Potdevin, H. Graafsma, B. Nilsson and J. C. Spence (2011). "Femtosecond X-ray protein nanocrystallography." Nature **470**(7332): 73-77.

Chasman, R., G. K. Green and E. Rowe (1975). "Preliminary design of a dedicated synchrotron radiation facility." IEEE Transactions on Nuclear Science **22**(3): 1765-1767.

Coquelle, N., M. Sliwa, J. Woodhouse, G. Schirò, V. Adam, A. Aquila, T. R. Barends, S. Boutet, M. Byrdin and S. Carbajo (2018). "Chromophore twisting in the excited state of a photoswitchable fluorescent protein captured by time-resolved serial femtosecond crystallography." Nature chemistry **10**(1): 31.

Cosier, J. t. and A. Glazer (1986). "A nitrogen-gas-stream cryostat for general X-ray diffraction studies." Journal of Applied Crystallography **19**(2): 105-107.

Dauter, Z., M. Jaskolski and A. Wlodawer (2010). "Impact of synchrotron radiation on macromolecular crystallography: a personal view." Journal of synchrotron radiation **17**(4): 433-444.

Drenth, J. (2007). Principles of protein X-ray crystallography, Springer Science & Business Media.

Duke, E., S. Wakatsuki, A. Hadfield and L. Johnson (1994). "Laue and monochromatic diffraction studies on catalysis in phosphorylase b crystals." Protein Science **3**(8): 1178-1196.

Fisher, A., B. McKinney, J.-P. Wery and J. Johnson (1992). "Crystallization and preliminary data analysis of Flock House virus." Acta Crystallographica Section B: Structural Science **48**(4): 515-520.

Friedrich, W., P. Knipping and M. Laue (1913). "Interferenzerscheinungen bei roentgenstrahlen." Annalen der Physik **346**(10): 971-988.

Garman, E. F. (2010). "Radiation damage in macromolecular crystallography: what is it and why should we care?" Acta Crystallographica Section D: Biological Crystallography **66**(4): 339-351.

Giacovazzo, C. (2002). Fundamentals of crystallography, Oxford university press, USA.

Hammond, C. and C. Hammond (2001). The Basics of Cristallography and Diffraction, Oxford.

Hau-Riege, S. P., R. A. London and A. Szoke (2004). "Dynamics of biological molecules irradiated by short x-ray pulses." Phys Rev E Stat Nonlin Soft Matter Phys **69**(5 Pt 1): 051906.

Helliwell, J. (1988). "Protein crystal perfection and the nature of radiation damage." Journal of Crystal Growth **90**(1-3): 259-272.

Helliwell, J. R. (1997). [14] Overview of synchrotron radiation and macromolecular crystallography. Methods in enzymology, Elsevier. **276:** 203-217.

Holton, J. M. (2009). "A beginner's guide to radiation damage." J Synchrotron Radiat **16**(Pt 2): 133-142.

Holton, J. M. and K. A. Frankel (2010). "The minimum crystal size needed for a complete diffraction data set." Acta Crystallographica Section D: Biological Crystallography **66**(4): 393-408.

Howells, M. R., T. Beetz, H. N. Chapman, C. Cui, J. Holton, C. Jacobsen, J. Kirz, E. Lima, S. Marchesini and H. Miao (2009). "An assessment of the resolution limitation due to radiation-damage in X-ray diffraction microscopy." Journal of electron spectroscopy and related phenomena **170**(1-3): 4-12.

Howells, M. R., T. Beetz, H. N. Chapman, C. Cui, J. M. Holton, C. J. Jacobsen, J. Kirz, E. Lima, S. Marchesini, H. Miao, D. Sayre, D. A. Shapiro, J. C. Spence and D. Starodub (2009). "An assessment of the resolution limitation due to radiation-damage in x-ray diffraction microscopy." J Electron Spectros Relat Phenomena **170**(1-3): 4-12.

Jordan, P., P. Fromme, H. T. Witt, O. Klukas, W. Saenger and N. Krauß (2001). "Three-dimensional structure of cyanobacterial photosystem I at 2.5 Å resolution." Nature **411**(6840): 909-917.

Jung, Y. O., J. H. Lee, J. Kim, M. Schmidt, K. Moffat, V. Šrajer and H. Ihee (2013). "Volume-conserving trans–cis isomerization pathways in photoactive yellow protein visualized by picosecond X-ray crystallography." Nature chemistry **5**(3): 212.

Kendrew, J., R. Dickerson, B. Strandberg, R. Hart, D. Davies, D. Phillips and V. Shore (1960). "Structure of myoglobin." Nature **185**(422): 427-1960.

Kendrew, J. C., G. Bodo, H. M. Dintzis, R. Parrish, H. Wyckoff and D. C. Phillips (1958). "A three-dimensional model of the myoglobin molecule obtained by x-ray analysis." Nature **181**(4610): 662-666.

Matthews, B. W. (1968). "Solvent content of protein crystals." Journal of molecular biology **33**(2): 491-497.

McNeil, B. W. and N. R. Thompson (2010). "X-ray free-electron lasers." Nature photonics **4**(12): 814.

Meents, A., S. Gutmann, A. Wagner and C. Schulze-Briese (2010). "Origin and temperature dependence of radiation damage in biological samples at cryogenic temperatures." Proceedings of the National Academy of Sciences **107**(3): 1094-1099.

Miao, J., T. Ishikawa, I. K. Robinson and M. M. Murnane (2015). "Beyond crystallography: Diffractive imaging using coherent x-ray light sources." Science **348**(6234): 530-535.

Moffat, K. (1998). "Time-resolved crystallography." Acta Crystallographica Section A: Foundations of Crystallography **54**(6): 833-841.

Moffat, K. (1998). "Ultrafast time-resolved crystallography." Nature Structural and Molecular Biology **5**(8s): 641.

Nave, C. and E. F. Garman (2005). "Towards an understanding of radiation damage in cryocooled macromolecular crystals." Journal of synchrotron radiation **12**(3): 257-260.

Neutze, R., R. Wouts, D. van der Spoel, E. Weckert and J. Hajdu (2000). "Potential for biomolecular imaging with femtosecond X-ray pulses." Nature **406**(6797): 752-757.

Pande, K., C. D. M. Hutchinson, G. Groenhof, A. Aquila, J. S. Robinson, J. Tenboer, S. Basu, S. Boutet, D. Deponte, M. Liang, T. White, N. Zatsepin, O. Yefanov, D. Morozov, D. Oberthuer, C. Gati, G. Subramanian, D. James, Y. Zhao, J. Koralek, J. Brayshaw, C. Kupitz, C. Conrad, S. Roy-Chowdhury, J. Coe, M. Metz, X. Paulraj Lourdu, T. Grant, J. Koglin, G. Ketawala, R. Fromme, V. Srajer, R. Henning, J. Spence, A. Ourmazd, P. Schwander, U. Weierstall, M. Frank, P. Fromme, A. Barty, H. Chapman, K. Moffat, J. J. Van Thor and M. Schmidt (2015). "Femtosecond Structural Dynamics Drives the Trans/Cis Isomerization in Photoactive Yellow Protein." in submission.

Pellegrini, C. (2012). "The history of X-ray free-electron lasers." The European Physical Journal H **37**(5): 659-708.

Phillips, J. C., A. Wlodawer, M. M. Yevitz and K. O. Hodgson (1976). "Applications of synchrotron radiation to protein crystallography: preliminary results." Proceedings of the National Academy of Sciences **73**(1): 128-132.

Ren, Z., D. Bourgeois, J. R. Helliwell, K. Moffat, V. Srajer and B. L. Stoddard (1999). "Laue crystallography: coming of age." Journal of Synchrotron Radiation **6**(4): 891-917.

Robinson, A. L. (2015). "History of synchrotron radiation." Synchrotron Radiation News **28**(4): 4-9.

Rosenbaum, G., K. C. Holmes and J. Witz (1971). "Synchrotron radiation as a source for X-ray diffraction." Nature **230**(5294): 434.

Rupp, B. (2009). Biomolecular crystallography: principles, practice, and application to structural biology, Garland Science.

Schlichting, I., G. Rapp, J. John, A. Wittinghofer, E. F. Pai and R. S. Goody (1989). "Biochemical and crystallographic characterization of a complex of c-Ha-ras p21 and caged GTP with flash photolysis." Proceedings of the National Academy of Sciences **86**(20): 7687-7690.

Schlichting, I., J. Berendzen, K. Chu, A. M. Stock, S. A. Maves, D. E. Benson, R. M. Sweet, D. Ringe, G. A. Petsko and S. G. Sligar (2000). "The catalytic pathway of cytochrome P450cam at atomic resolution." Science **287**(5458): 1615-1622.

Schmidt, M. (2013). "Mix and inject: reaction initiation by diffusion for time-resolved macromolecular crystallography." Advances in Condensed Matter Physics **2013**.

Schmidt, M., V. Srajer, R. Henning, H. Ihee, N. Purwar, J. Tenboer and S. Tripathi (2013). "Protein energy landscapes determined by five-dimensional crystallography." Acta Crystallographica Section D: Biological Crystallography **69**(12): 2534-2542.

Schotte, F., M. Lim, T. A. Jackson, A. V. Smirnov, J. Soman, J. S. Olson, G. N. Phillips, M. Wulff and P. A. Anfinrud (2003). "Watching a protein as it functions with 150-ps time-resolved X-ray crystallography." Science **300**(5627): 1944-1947.

Schotte, F., H. S. Cho, V. R. Kaila, H. Kamikubo, N. Dashdorj, E. R. Henry, T. J. Graber, R. Henning, M. Wulff and G. Hummer (2012). "Watching a signaling protein function in real time via 100-ps time-resolved Laue crystallography." Proceedings of the National Academy of Sciences **109**(47): 19256-19261.

Schotte, F., H. S. Cho, J. Soman, M. Wulff, J. S. Olson and P. A. Anfinrud (2013). "Real-time tracking of CO migration and binding in the α and β subunits of human hemoglobin via 150-ps time-resolved Laue crystallography." Chemical physics **422**: 98-106.

Stoddard, B. L., B. E. Cohen, M. Brubaker, A. D. Mesecar and D. E. Koshland (1998). "Millisecond Laue structures of an enzyme–product complex using photocaged substrate analogs." Nature Structural & Molecular Biology **5**(10): 891-897.

Teng, T.-Y. (1990). "Mounting of crystals for macromolecular crystallography in a free-standing thin film." Journal of Applied Crystallography **23**(5): 387-391.

Witt, I., H. Witt, D. Di Fiore, M. Rögner, W. Hinrichs, W. Saenger, J. Granzin, C. Betzel and Z. Dauter (1988). "X-Ray Characterization of Single Crystals of the Reaction Center I of Water Splitting Photosynthesis." Berichte der Bunsengesellschaft für physikalische Chemie **92**(12): 1503-1506.

WL Bragg, B. (1913). The structure of some crystals as indicated by their diffraction of X-rays. Proc. R. Soc. Lond. A, The Royal Society.

Zeldin, O. B., M. Gerstel and E. F. Garman (2013). "Optimizing the spatial distribution of dose in X-ray macromolecular crystallography." Journal of synchrotron radiation **20**(1): 49-57.

,

2 SERIAL FEMTOSECOND CRYSTALLOGRAPHY: A REVOLUTION IN STRUCTURAL BIOLOGY

Jose M. Martin-Garcia, Chelsie E. Conrad, Jesse Coe, Shatabdi Roy-Chowdhury, Petra Fromme*

School of Molecular Sciences, Arizona State University, Tempe, AZ, 85287-1604, USA
Center for Applied Structural Discovery, The Biodesign Institute, Arizona State University, Tempe, AZ, 85287-7401, USA.

This chapter is a published review on serial femtosecond crystallography. I wrote the abstract, introduction, most of the crystallization and characterization section, parts of the sample delivery methods section and all of the structural dynamics section with the exception of data acquisition and processing, of which I wrote parts. I did the majority of editing and performed all tasks related to all three rounds of revisions and rebuttals to reviewer comments. I obtained all permissions and performed all submissions as well.

Abstract

Macromolecular crystallography at synchrotron sources has proven to be the most influential method within structural biology, producing thousands of structures since its inception. While its utility has been instrumental in progressing our knowledge of structures of molecules, it suffers from limitations such as the need for large, well-diffracting crystals, and radiation damage that can hamper native structural determination. The recent advent of X-ray free electron lasers (XFELs) and their implementation in the emerging field of serial femtosecond crystallography (SFX) has given rise to a remarkable expansion upon existing crystallographic constraints, allowing structural biologists access to previously restricted scientific territory. SFX relies on exceptionally brilliant, micro-focused X-ray pulses, which are femtoseconds in duration, to probe nano/micrometer sized crystals in a serial fashion. This results in data sets comprised of individual snapshots, each capturing Bragg diffraction of single crystals in random orientations prior to their subsequent destruction. Thus structural elucidation while avoiding radiation damage, even at room temperature, can now be achieved. This emerging field has cultivated new methods for nanocrystallogenesis, sample delivery, and data processing. Opportunities and challenges within SFX are reviewed herein.

Introduction

Since the invention of the first light bulb by Thomas Alva Edison in 1879, light sources have been the primary tools for the investigation of matter. But it was the discovery of X-rays in 1895 by Wilhelm Conrad Röentgen which catalyzed a revolutionary change in our understanding of the physical world. The ability of X-rays to reveal the invisible has made them one of the most important

research and diagnostic tools in medicine, chemistry, and physics in the last century. One of the most powerful sources of X-rays in modern research are synchrotrons, in which electrons are accelerated by radiofrequency cavities to extremely high energies (typically ≥ 3 GeV) and transferred to a storage ring in which they can be maintained at high current in stable 'bunches' for hours. The electrons are then subsequently perturbed in an undulating electromagnetic field to induce X-ray emission. The first synchrotron facility was built in the early 1970's and due to the increasing demand from both the scientific community and private research sector; the number of synchrotron facilities has grown quickly since. In the last three decades, synchrotrons have been built or are in the construction phase in 24 countries. APS at the Argonne National Laboratory (Chicago, USA), the ESRF (Grenoble, France), PETRA III (Hamburg, Germany), Spring-8 (Harima Science Park City, Japan), and DIAMOND (Oxfordshire, England) are currently the largest and most powerful synchrotron light sources. X-ray methods have also played an increasingly more important role in the life sciences as evidenced by medical X-ray imaging, X-ray scattering, and highlighted here, X-ray crystallography. The latter typically makes use of X-rays from 3.5 keV to 20 keV (3.5 Å to 0.6 Å) to enable the determination of the atomic structure of matter. The most difficult and challenging biomolecules, such as large complexes and membrane proteins, are almost exclusively solved with synchrotron radiation. However, in spite of the usefulness and power of these facilities, there are two important areas in which synchrotron facilities are limited in addressing the full range of current scientific challenges. The main limitations are primary and secondary X-ray damage which cannot be outrun by pulse durations currently available at synchrotron sources (tens of ps). Secondary damage can be minimized by freezing but primary damage is unavoidable.

To overcome these limitations a new light source has emerged in the form of the X-ray free electron laser (XFEL) which has improved upon many of the properties of synchrotron radiation sources, in some cases by orders of magnitude. Free electron lasers (FELs) have been used over many years since their conception by John Madey in the early 70's(Madey 1971), initially operating at infrared wavelengths. More recently, visible and near ultraviolet wavelengths were achieved(Pellegrini 2012). Since its discovery, the idea of extending FELs to shorter wavelengths,

in particular to the X-ray regime, have been considered and explored by many scientists (see (Pellegrini 2012) for a review on the development of FELs). After many years of theoretical and experimental work along with new technological advances, three XFELs are currently operational. Namely, they are the Deutsches Elektronen-Synchrotron's (DESY) Free-electron LASer in Hamburg (FLASH), SLAC's Linac Coherent Light Source (LCLS), and RIKEN's Spring-8 Angstrom Compact free electron LAser (SACLA). At its core, an XFEL consists of an electron source, a linear accelerator, and undulator magnets spaced to produce X-ray wavelengths (typically ranging from 0.01 to 10 nm) (Madey 1971, Dattoli and Renieri 1985, Saldin, Schneidmiller et al. 2013). Briefly, a relativistic electron beam is accelerated to almost the speed of light in a linear accelerator prior to interaction with the undulator. Upon interaction with the undulator, the electrons move in curved paths via the magnets. The long length of an XFEL undulator allows the relativistic electrons to interact with their emitted radiation which causes bunching of the electrons with spacing equal to the wavelength of the emitted X-rays. As the electrons bunch, their emission becomes more coherent and allows for a stronger interaction between the two. This results in beam with highly coherent pulses with femtosecond duration. The coherence causes radiative emission proportional to the number of electrons squared in contrast to a synchrotron (incoherent) in which the radiative emission scales proportional to the number of electrons due to cancelation effects from the out of phase generated electromagnetic fields (Pellegrini and Stöhr 2003). Because the number of electrons in a bunch is on the order of a billion, this causes a massive increase in flux compared to synchrotron sources. Furthermore, the high longitudinal coherence (and thus, ultrashort duration) of the pulses pushes the peak brilliance orders of magnitude higher than that achievable at a modulating the electron energy and magnetic field strength. Figure 2.1 illustrates this principle. XFELs generate high gain, ultrashort pulsed X-rays with only a single undulator pass(Pellegrini and Reiche 2004), accomplished by the interaction between oscillating electrons, moving at relativistic speeds, with their emitted electromagnetic waves (for a more detailed synchrotron. The output wavelength can by tuned by overview of XFEL physics please refer to Ackermann, Asova et al. (2007) and McNeil, et al. (McNeil and Thompson 2010)). The interaction between the electrons and

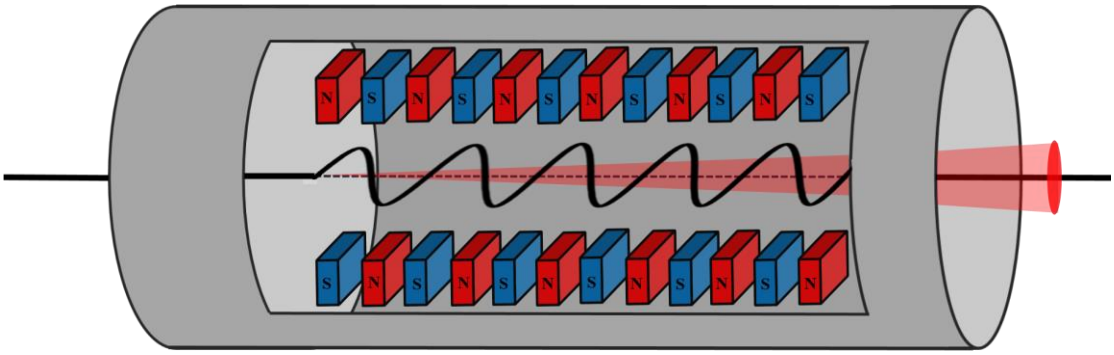

Figure 2.1 U**ndulator Segment**

A relativistic electron beam (solid line) is brought to high energy in a linear accelerator (not pictured) prior to interaction with the undulator. The electrons then travel on a sinusoidal path, induced by a special arrangement of magnets called an undulator, a periodic array of magnetic dipoles shown as red and blue boxes. Because the electrons move in curved paths via the magnets, the change in momentum causes the emission of monochromatic radiation the same way a synchrotron does (depicted as a red cone).

their radiation causes spatial redistribution of the electrons into compact bunches perpendicular to their direction of motion. This generates coherent X-ray pulses with durations of tens of femtoseconds. The first hard XFEL, LCLS, was built at the SLAC National Accelerator Laboratory in California and has been in operation since April 2009(Emma, Akre et al. 2010). It produces X-ray pulses of approximately 3 mJ energy at 120 Hz. Each pulse has a duration that ranges from around 300 fs down to a few femtoseconds with up to 1013 coherent photons per pulse. Thus, the LCLS instrument has set a new standard, with a peak X-ray brilliance over ten orders of magnitude higher than that of the most powerful synchrotron radiation sources(Altarelli 2010). XFELs are unique light sources that can be used to explore matter at atomic length and femtosecond time scales. The increase in brightness along with ultra-short pulses has facilitated the appearance of a new application of XFEL technology in the field of structural biology via serial femtosecond crystallography (SFX) (Chapman, Fromme et al. 2011, Spence, Weierstall et al. 2012). A typical setup for SFX data collection is illustrated in Figure 2.2.

The technique of macromolecular X-ray crystallography and its historical success in determining the structure of biological macromolecules has always suffered from a major bottleneck, namely the production of well diffracting crystals. This problem is especially prevalent in the structure determination of membrane proteins, which are notorious for their difficulty in

forming high diffraction quality crystals. In some cases, years have been devoted to determining crystallization conditions for a membrane protein and it is not uncommon that only showers of nanocrystals (crystals between 200 nm to 10 μm) are observed while attempts to grow larger crystals remain unsuccessful. These nanocrystals were once seen as only a possible intermediate towards achieving useable crystals(Cusack, Belrhali et al. 1998). Modern microfocus beamlines have expanded the usefulness of these nanocrystals but even they experience constraints on what is achievable mainly due to severe X-ray damage by long exposure times, often requiring cryo-cooling and necessitating crystals larger than 10 μm, which must be even larger in the case of large unit cells (common in membrane proteins and large complexes)(Smith, Fischetti et al. 2012). With the advent of XFELs, crystals which would have previously been too small for use have been shown to be suitable for structure determination(Chapman, Fromme et al. 2011). Generally, these small crystals are easier to produce and possess significantly less long-range disorder. Furthermore, nanocrystals are ideal for time-resolved studies as a greater percentage of molecules in the crystal can be activated homogeneously by light or rapid mixing. For light activated reactions, time domains ranging from the femtosecond to microsecond regimes can be probed and temporal resolution of reactions induced by mixing can range from seconds down to microseconds (Schmidt, Srajer et al. 2013, Kupitz, Basu et al. 2014, Tenboer, Basu et al. 2014, Wang, Weierstall et al. 2014, Barends, Foucar et al. 2015).

In addition to the challenges of sample preparation, the problem of X-ray induced radiation damage has hindered progress in structure determination even in well-diffracting crystals. Traditionally, cryogenic cooling of crystals has been the most successful way to minimize damage, increasing the radiation dose tolerance by a factor between 30 and 50(Owen, Rudiño-Piñera et al. 2006, Holton 2009, Howells, Beetz et al. 2009). Cryo-cooling works by slowing the dispersion of radiation-induced reactive products that occur during the X-ray exposure. Upon exposure to X-rays, photoionization and processes related to Auger decay take place, leading to heat as well as the production of radicals and photo-ions. These diffuse within the crystal at rates dependent on available kinetic energy. This can lead to subsequent chemical reactions that result in the breaking

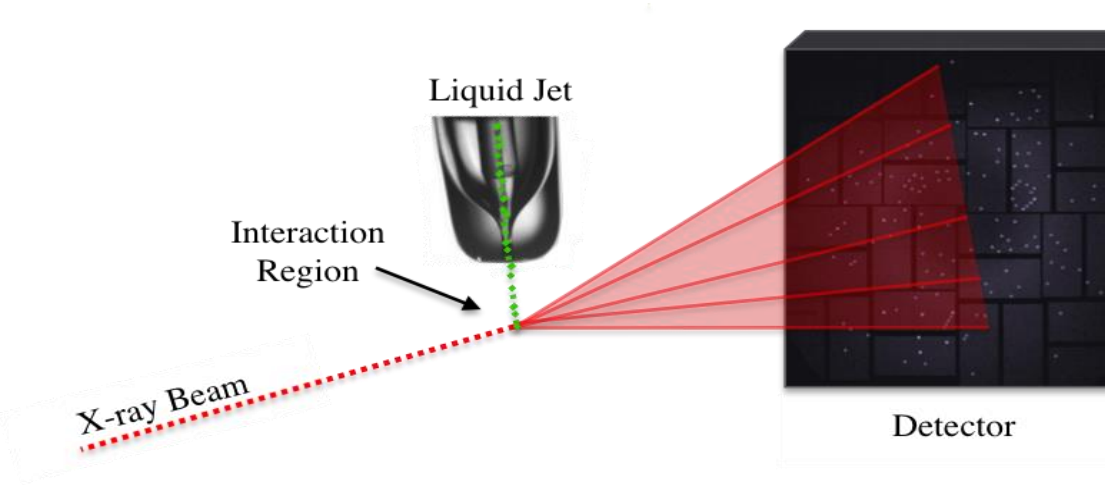

Figure 2.2 Schematic of a Typical SFX Experiment at LCLS.

Randomly oriented nanocrystals (green) in their mother liquor are delivered into the focus of X-ray beam by a gas-focused liquid injector. The X-ray beam, which is transverse to the jet, hits the crystals in the interaction region. Diffraction snapshots of single crystals are recorded using a Cornell-SLAC pixel array detector (CSPAD) located in the forward-scattering region.

of chemical bonds and thus a reduction in the diffraction quality of the crystal. While cryo-cooling does not influence the primary X-ray damage (i.e. photoionization and Auger decay), it slows down diffusion of the secondary processes of X-ray induced damage, radicals and heat progression. This method thus allows crystals to tolerate longer exposure times, improving the signal to noise ratio. Nonetheless, even at cryogenic temperatures site-specific radiation damage remains a problem, in which rapid photo-damage by the X-ray beam in areas with high X-ray cross-sections can occur, decreasing diffraction until it ultimately terminates. In such cases, partial data sets from many crystals must be merged in order to obtain a structural model. Furthermore, these models can exhibit significant artifacts from damage which can be substantially different from the native structure(Carugo and Carugo 2005). Examples of radiation damage include the breakage of disulfide bonds and salt bridges, tyrosine residues becoming hydrolyzed, decarboxylation of glutamate and aspartate residues, B-factor increase, and loss of diffraction progressing from high to low resolution(Burmeister 2000, Ravelli and McSweeney 2000, Garman and Owen 2006, Liu, Wacker et al. 2013). Radiation damage is particularly troublesome in limiting resolution of high-Z catalytic centers, causing metalloproteins to be the most prone to local radiation damage. For example, spectroscopy has shown that X-ray radiation exposure to cryo-cooled, photosystem II

crystals leads to the metal center becoming photo-reduced below the native oxidation state. This effect was still seen at 4% of average doses used for crystallography(Yano, Kern et al. 2005).

In 2000 Neutze et al.(Neutze, Wouts et al. 2000) conducted molecular dynamic simulations on the time course of the Coulomb explosion of T4 lysozyme at a total flux of 3.8 x 10^6 12 keV photons per $Å^2$ over pulse durations of 2, 10, and 50 fs (the presumed theoretical flux achievable by an XFEL) in vacuum. At this time, XFELs were still in the planning phases. They predicted that the onset of the Coulomb explosion would occur at 5-10 fs and predicted that if the pulses are short, diffraction of the molecule could be collected before it is destroyed referred to as “diffraction before destruction”. This principle relies on an XFELs ability to deliver a sufficient number of photons (~10^{13} photons/pulse, orders of magnitude greater than that required to form a plasma) for structure determination on time scales competing with primary radiation damage events. The first experimental demonstration of this principle was carried out using the soft XFEL, FLASH, located at DESY(Ayvazyan, Baboi et al. 2006). In this experiment an intense 25 fs, 4 x 10^3 W/cm^2 pulse, containing 10^{12} photons, produced a coherent diffraction pattern from a non-periodic object before destruction occurred(Chapman, Barty et al. 2006). Thus, XFELs have the potential to minimize the effects of radiation damage and reduce the size restrictions on crystals suitable for X-ray structure determination. SFX requires new data processing and handling as the determination of crystallographic structures is based on thousands of snapshot diffraction patterns at room temperature by continuous delivery of orientationally unrelated nanocrystals in their mother liquor(Chapman, Fromme et al. 2011, Boutet, Lomb et al. 2012, Sierra, Laksmono et al. 2012, Weierstall, Spence et al. 2012, Weierstall 2014, Weierstall, James et al. 2014).

In December 2009 the first SFX experiment was carried out at LCLS, using nanocrystals of photosystem I (PSI) as the first sample. PSI mediates the conversion of light energy from the sun to chemical energy in plants, green algae, and cyanobacteria, is one of the most complex membrane proteins crystalized so far, the entire complex consisting of 36 proteins and 381 cofactors(Jordan, Fromme et al. 2001). Tens of thousands of diffraction patterns were collected, which allowed for the determination of the PSI structure, providing a proof of concept for SFX(Chapman, Fromme et al. 2011). Furthermore, this study resolved interference fringes between

the Bragg peaks which were originally suggested by Sayre in 1952(Sayre 1952). He proposed that diffraction from crystals with a countable number of unit cells, would show the Fourier transforms of the crystals in the diffraction pattern leading to fringes between the Bragg peaks directly related to the number of unit cells (n-1)(Sayre 1952). This theory came to fruition in the first SFX experiments when these fringes were detected in the diffraction patterns. In the future, with higher spatial resolution detectors, these shape transforms can be used for direct phasing(Spence, Kirian et al. 2011).

Six years after the first SFX experiments were carried out (Chapman, Fromme et al. 2011), evidence has continued to mount that XFELs make overcoming radiation damage in protein crystallography an attainable realization(Lomb, Barends et al. 2011, Aquila, Hunter et al. 2012, Barty, Caleman et al. 2012, Boutet, Lomb et al. 2012, Johansson, Arnlund et al. 2012, Koopmann, Cupelli et al. 2012, Sierra, Laksmono et al. 2012, Johansson, Arnlund et al. 2013, Liu, Wacker et al. 2013, Redecke, Nass et al. 2013, Barends, Foucar et al. 2014, Hunter, Segelke et al. 2014, Sawaya, Cascio et al. 2014, Fenalti, Zatsepin et al. 2015, Kang, Zhou et al. 2015). In addition, SFX not only mitigates radiation damage but is suitable for crystals with as little as a few hundred unit cells. Thereby, data can be collected from nanocrystals eliminating the need to grow large crystals. Experimental evidence is emerging that nanocrystals may show significantly less long-range disorder than their larger counterparts, making them ideal candidates for the structure determination of challenging proteins.

Nanocrystallization and Characterization

Because nanocrystals were previously seen as merely a stepping stone for the desired growth of large crystals, nanocrystal growth methods have remained largely unexplored. Due to the serial nature of SFX, a few unique characteristics must be considered for the development of nanocrystallization techniques. First, a different crystal in a random orientation is used for each diffraction pattern, with patterns being captured in a serial fashion(Chapman, Fromme et al. 2011). Thus, to constantly replenish the sample between X-ray pulses, crystals are delivered to the X-ray interaction region by a liquid jet (in a typical SFX experiment) composed of crystals in their mother

liquor at room temperature(Chapman, Fromme et al. 2011). The delivery of the crystals to the X-ray region is much more rapid than the X-ray repetition rate. Consequently, most crystals do not interact with the X-rays(Weierstall, James et al. 2014). Additionally, since diffraction patterns represent “still frame” slices through the Ewald sphere, only partial reflections can be recorded (i.e. there is no goniometer and therefore no rotation to record full profiles of reflections). In order to measure accurate structure factors of the Miller indices (h, k, l), high redundancy of the data sets (> 50) are required via Monte Carlo data analysis methods(Kirian, Wang et al. 2010). Due to approximately one in every ten thousand crystals resulting in a diffraction pattern and the necessity for high multiplicity of the data, tens to hundreds of milligrams of sample may be needed for successful SFX data sets, where samples are delivered in a liquid jet. The hit rate (percentage of pulses that result in crystal diffraction) is largely a function of crystal density and as such, must be considered in growth methods and characterization of the crystals.

Since data from many crystals must be merged in analysis of SFX data, it is also important to consider crystal homogeneity. For example, if there is a large size distribution in the sample, then the data set will be composed of diffraction patterns with varying relative Bragg peak intensities (directly related to the number of unit cells and hence, the size). This can lead to scaling issues which become problematic in subsequent analysis. Furthermore, the presence of some outlying (e.g. larger) crystals may necessitate attenuation of the beam to prevent damage to the detector. This in turn would limit resolution on images obtained from the more plentiful smaller crystals. Size inhomogeneity can also lead to instabilities or clogging in the liquid jet(Kupitz, Grotjohann et al. 2014). Therefore, it is imperative to consider and monitor crystal size distribution while screening conditions for nanocrystallization. These considerations become even more pronounced in time-resolved experiments where the crystal size is the primary parameter in reaction initiation homogeneity(Tenboer, Basu et al. 2014, Ibrahim, Chatterjee et al. 2015). To meet the need for large sample volumes, optimized crystal density and crystal size homogeneity, in addition to the traditional optimization of crystal diffraction quality, nanocrystallization techniques are rapidly emerging to address the unique challenges present in SFX.

Nanocrystallogenesis

As is the case in the growth of macroscopic crystals, knowledge of a proteins phase space is highly beneficial for the optimization of crystallization conditions. Driven by thermodynamics, the formation of protein crystals requires a controlled decrease in solubility of the protein that ideally avoids the formation of non-ordered precipitation. Traditionally, the supersaturated area of phase space is typically reached by gradually increasing the precipitant concentration, allowing for few nucleation sites to form that grow by addition of the free protein to the nuclei over time, resulting in a few large crystals(McPherson 1999). In contrast to this approach, nanocrystallization is best achieved by inducing a high number of nucleation sites, whereby the free protein concentration is rapidly decreased by the formation of a plethora of nuclei followed by their growth into a multitude of small crystals(Kupitz, Grotjohann et al. 2014, McPherson and Cudney 2014). Typically this is achieved by increase of the concentration of protein, precipitating agents, or both as compared to optimized conditions for large crystal growth for the same protein(Kupitz, Grotjohann et al. 2014). While the approaches for each size regime differ, they both rely fundamentally on the knowledge of the proteins phase space and may be even more important for growth of well-ordered nanocrystals as formation of amorphous precipitate is best avoided.

Many of the existing methods for macro-crystallogenesis are also applicable for nanocrystallization with modification necessary to occupy a different area of phase space(Hunter, Segelke et al. 2014, Kupitz, Grotjohann et al. 2014, Bublitz, Nass et al. 2015, Sugahara, Mizohata et al. 2015, Wu, Nogly et al. 2015, Yamashita, Pan et al. 2015). Batch methods, in which the protein and precipitating conditions are mixed to homogeneity initially, provide a good example of well-established methodology that needs little modification for suitability in SFX (outside of parameter values). This is illustrated in Figure 2.3 where a batch approach for macro- and nanocrystals differs only by starting point within the phase space(Schlichting 2015). It has been reported in some cases that large crystals grown by traditional methods can also be mechanically crushed to obtain the smaller crystals needed for SFX(Redecke, Nass et al. 2013, Stevenson, Makhov et al. 2014). This is, however, not generally applicable and may lead to loss of quality or destruction of fragile crystals, such as those common amongst membrane proteins. Nanocrystalline showers with traditional

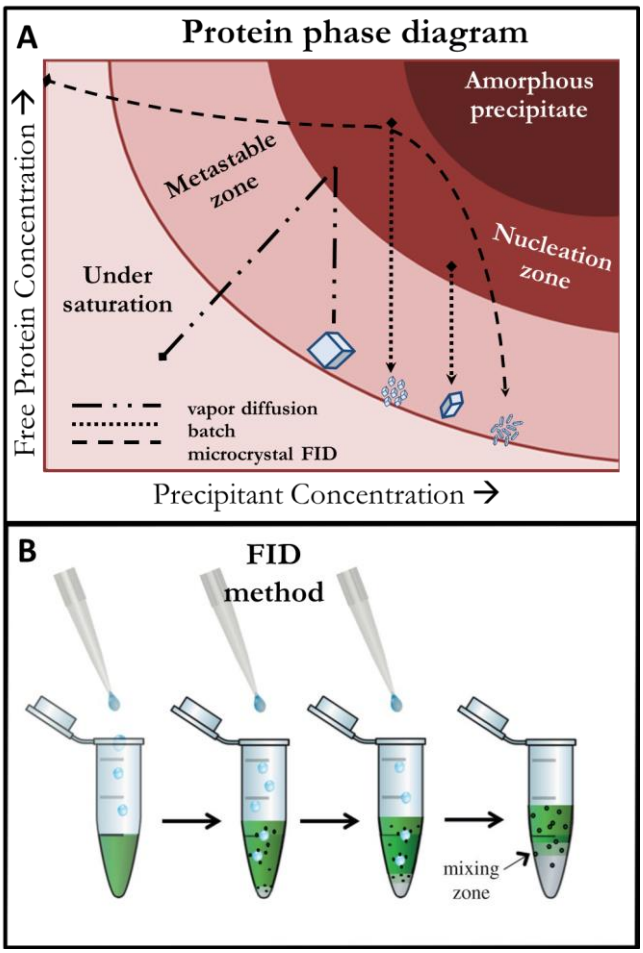

Figure 2.3. **Methods Phase Diagram and FID**

A) 2-dimensional slice of a typical free protein phase diagram with selected crystallogenesis methods exemplifying the general relationship between phase space occupation and resultant crystalline protein. B) Depiction of the microcrystalline FID method in the case of a denser precipitant being dropped through a protein solution and the subsequent interface resulting in microcrystal pelleting (B reproduced with permission from (Kupitz, Basu et al. 2014)).

methods such as vapor diffusion have been obtained, using a brute force approach with many individual setups to scale for SFX experiments(Lawrence, Conrad et al. 2015). While this poses no theoretical issue, the concern for this type of nanocrystal preparation is due to the tedious nature of sample preparation involved to obtain enough material for full data set collection. While this can in part be alleviated with sample conserving delivery systems(Conrad, Basu et al. 2015, Fromme, Ishchenko et al. 2015, Sugahara, Mizohata et al. 2015) (assuming they are compatible), sample density and homogeneity remain challenging and necessitate specific consideration.

The nanocrystalline free interface diffusion (FID) method is an example of a technique that has been developed from an existing method for SFX applications(Kupitz, Grotjohann et al. 2014). In this method, one solution (either the protein or precipitant solution) is added drop wise to the other. The less dense of the two (typically the protein/buffer solution) is first placed in a vessel, typically a microcentrifuge tube. The denser solution (typically precipitants such as high concentration salts, polyethylene glycol, etc.) is then added drop wise, thereby allowing for a high

nucleation rate at the protein/precipitant interface of the two solutions but still inducing some mixing immediately. Nanocrystals will form at the interface, owing to the access of areas of phase space that typically results in high nucleation rates (i.e. high concentrations of both protein and precipitants). Additional benefits arise in the common scenario where the denser solution is the precipitant since this allows crystals that form at the interface to settle due to gravity into the precipitant rich layer. This provides a way to effectively quench crystal growth as well as accumulate a high density of nanocrystals, allowing practical optimization of crystal density by resuspension to a desired concentration. Gentle centrifugation of the setup has also been shown to expedite crystal formation (e.g. photosystem II forming nanocrystals in as little as 30 minutes with centrifugation in contrast to 1 day without centrifugation(Kupitz, Grotjohann et al. 2014)) and has led to improvement of crystal size and homogeneity due to the tendency for crystals to spend less time in relatively high concentrations of free protein after nuclei formation, resulting in more uniform growth throughout the sample. It is important to note that over time, full mixing of the two layers will occur (rate proportional to miscibility). This could lead to the dissolution of the crystals if the mixture represents an undersaturated portion of phase space. Oswald ripening and decreased size homogeneity can also occur if there is high mobility or an appreciable amount of free protein left over after complete mixing has occurred. This can be avoided by harvesting the crystal pellet or removal of the free protein layer before considerable mixing occurs.

In-vivo crystallization

Crystallization *in vivo* using insect and mammalian cells is a highly innovative approach towards nanocrystallography that has been recently discovered(Koopmann, Cupelli et al. 2012, Redecke, Nass et al. 2013, Gallat, Matsugaki et al. 2014, Ginn, Messerschmidt et al. 2015). This technique was first applied in SFX in 2012 after nanocrystals were identified by electron microscopy inside insect cells when cathepsin B from *Trypanosoma brucei* was overexpressed using the recombinant baculovirus system(Koopmann, Cupelli et al. 2012). Redecke and co-workers observed needle shaped nanocrystals protruding out of the cell after 70 hours but were still surrounded by the cell membrane(Redecke, Nass et al. 2013). The crystals were 10-15 μm in length and about 0.5-1 μm in width. These crystals were isolated and used for SFX

analysis(Redecke, Nass et al. 2013). It has been proposed that this spontaneous crystallization may occur due to accumulation of the protein in a specific organelle such as the endoplasmic reticulum, peroxisomes, or secretory granules(Doye and Poon 2006, Koopmann, Cupelli et al. 2012). In vivo crystallization is not limited to the Sf9 insect cells and has been demonstrated for multiple proteins in cockroaches, seeds, and bacterial cells(Doye and Poon 2006, Gallat, Matsugaki et al. 2014, Sawaya, Cascio et al. 2014). However, little is understood about the mechanism of *in-vivo* crystallization as it was initially hypothesized to be a rare occurrence. Additionally, the crystals were not probed when they were first found as they were too small for macro-crystallography(Doye and Poon 2006, Koopmann, Cupelli et al. 2012). With the advent of XFELs, in vivo crystallization could potentially become a major method for crystallization, thus removing the bottleneck of determining crystallization conditions for applicable proteins. Before *in vivo* crystallization comes to fruition as a more general method, further research needs to be done towards understanding the necessary mechanistic components involved.

Growing crystals using LCP

Lipidic cubic phase (LCP), a bicontinuous mesophase that acts as a membrane-mimetic, has been used to crystallize a variety of membrane proteins, notably G coupled-protein receptors, ion channels, and transporters(Liao, Li et al. 2012, Caffrey 2015). Unlike membrane protein crystals grown *in surfo* (in partial or full detergent micelles), which usually exhibit type II micelle crystal packing and often have a high solvent content, crystals grown in LCP feature type I crystal packing(Katona, Andreasson et al. 2003). This packing allows for hydrophilic protein-protein and hydrophobic protein-lipid-protein interactions and thus, often leads to tighter and more rigid packing, in turn possibly leading to a lower solvent content and better diffraction(Liu, Ishchenko et al. 2014). To crystallize membrane proteins in LCP, purified protein at high concentration (usually > 20 mg/mL) is mixed with molten monoolein in Hamilton gas-tight syringes using a syringe-mixer(Cheng, Hummel et al. 1998). For standard crystallography, special robots (e.g. Flexus Crystal IMP, Gryphon LCP, NT8-LCP, Mosquito LCP, ProCrys Meso) can be used to dispense the LCP and precipitant and crystals are often grown in micro-batch assays of <1 nL to 100 nL. Cherezov and colleagues have had notable success in adapting the LCP crystallization method for

SFX(Liu, Wacker et al. 2013, Liu, Ishchenko et al. 2014, Liu, Wacker et al. 2014, Fenalti, Zatsepin et al. 2015, Zhang, Unal et al. 2015). In this method, protein laden LCP is injected in another syringe containing precipitate solution and incubated for 24 hours to two weeks to permit crystallization(Liu, Wacker et al. 2013, Liu, Wacker et al. 2014). Excess precipitate solution is removed and the crystals embedded in the LCP are delivered using a high-viscosity-injector(Weierstall, James et al. 2014).

Crystal Detection and Characterization

Some SFX experiments have been carried out with crystals that are > 5 μm and can therefore be identified by established methods such as polarized light microscopy in combination with UV-fluorescence microscopy. Nanocrystals are very difficult to identify and differentiate from amorphous precipitate, particularly if the crystal size is on the order or smaller than 1 μm, nearing the limit of resolution for optical microscopy methods. Techniques such as tryptophan fluorescence and birefringence may also be limited since the signal for each is proportional to crystal size. Alternative methods for detecting small crystals have proven to overcome the aforementioned difficulties. One of the most useful methods for rapid feedback during initial and optimization stages of crystallogenesis is the use of second-order harmonic generation (SHG) spectroscopy, in particular the SONICC (second order non-linear imaging of chiral crystals) instrument invented by G. Simpson(Wampler, Kissick et al. 2008). SONICC can identify nanocrystals of chiral molecules as small as 100 nm(Wampler, Kissick et al. 2008). When a chiral crystal is exposed to two 1024 nm photons in a strong field, frequency doubling occurs due to inherent polarization anisotropy, allowing a detector to measure the 512 nm photon output. Constructive interference arising from crystalline translational symmetry increases the probability of this occurring, allowing for practical measurements to be taken. It should be cautioned that the signal strength depends on the space group (with higher symmetry leading to decreased signal in general) and also the specific molecular polarization susceptibility (higher SHG is typical in molecules with a chromophore)(Newman, Scarborough et al. 2015). While truly centrosymmetric space groups are impossible in natural protein crystals, many of the high symmetry space groups can still lead to attenuation of signal below detection, resulting in false negatives. Furthermore, some precipitants are chiral (e.g.

sugars, chiral salts) and can crystallize in space groups that can be active in SHG (i.e. false positives) so care must be taken when interpreting results.

The most trustworthy method to verify the existence of diffracting crystals is X-ray powder diffraction, which can be carried out at either cryogenic or ambient temperatures. For room temperature powder diffraction measurements, a high density pellet of crystals is transferred to an X-ray transparent capillary(Steitz, Richmond et al. 1974, Balbirnie, Grothe et al. 2001, Von Dreele 2007). In contrast with cryogenic powder diffraction, room temperature powder diffraction measurements are ideal for optimizing relative resolution for an XFEL since this ensures that there are not artifacts arising from the freezing process. It is also important to include buffer in the capillary to avoid drying out of the small crystals which can affect diffraction quality. While powder diffraction data can be collected from nanocrystals at low flux X-ray home sources, it requires several microliters of dense crystal sample which is more than is produced from commercial screens(Stevenson, Makhov et al. 2014). It also depends highly on the sample quality and density so establishing conditions for powder diffraction typically requires synchrotron radiation to produce measurable diffraction for un-optimized samples(Stevenson, DePonte et al. 2014).

Transmission electron microscopy (TEM) is another reliable method to monitor nanocrystal quality and requires low sample volumes. Strong correlations exist between crystals that have highly ordered lattices visible through TEM and crystals that feature better X-ray diffraction quality(Stevenson, DePonte et al. 2014). While this technique can provide insightful characterization, it requires elaborate sample preparation and often involves negative staining which can affect electron diffraction and is only suitable for very thin nanocrystals (< 200 nm)(Stevenson, DePonte et al. 2014, Wen 2014). Large crystals can be mechanically crushed in order to achieve dimensions suitable for TEM(Stevenson, Makhov et al. 2014).

In protein crystallography, dynamic light scattering (DLS) is commonly used to analyze protein homogeneity since a monodisperse (i.e. homogenous and non-aggregated) sample is ideal for crystallization(Proteau, Shi et al. 2010). In addition, DLS is also used in SFX experiments to determine nanocrystal size distribution and homogeneity across multiple conditions(Schubert, Meyer et al. 2015). DLS measures the light scattered by particles in solution. As molecules in

solution undergo Brownian motion, the change in intermolecular distance leads to constructive and destructive interference of the scattered light. Fluctuations in intensity over time are indicative of the particle size and can be derived from the Stokes-Einstein relation. DLS only requires a few microliters of sample for analysis at broad range of concentrations (about 10^8–10^{12} crystals/mL)(Filipe, Hawe et al. 2010). However, large particles such as dust or aggregates can affect the accuracy of size determination(Berne and Pecora 1976). Another important parameter to take into account in SFX experiments is the crystal density. Crystal density can be optimized by using nanoparticle tracking analysis (NTA), which, like DLS, infers the Brownian motion of particles in solution and relates this movement to an equivalent hydrodynamic radius. Unlike DLS, NTA uses video to track the Brownian motion and thus, captures the light scattering signal from individual particles(Carr and Malloy 2006). This not only allows for particle size to be determined on a particle-by-particle basis but also allows for particle concentration to be estimated which is extremely helpful for optimizing crystal density for SFX experiments(Filipe, Hawe et al. 2010). However only particles < 1 μm can be detected and 1 mL of particle concentrations of 10^7 –10^9 crystals/mL(Filipe, Hawe et al. 2010) is required. Therefore, DLS and NTA provide a means to monitor nanocrystal size. Furthermore, microfluidic devices using dielectrophoresis have been invented that can sort nanocrystals according to size(Abdallah, Roy-Chowdhury et al. 2015).

Sample delivery methods

The majority of SFX data has been collected from a jet of small crystals (typically 200 nm - 10 μm) in their mother liquor. This scheme allows the sample to be constantly replenished for each XFEL pulse as the crystals are destroyed with each shot. While this has shown great success and breadth, limitations of this method have trigged multiple strategies to deliver crystals to the X-ray interaction region to be born over the last 6 years. In this section the current crystal delivery methods used at XFELs are reviewed (summarized in Table 1).

Gas-focused liquid injectors:

In preparation for the first SFX experiments, the gas dynamic virtual nozzle (GDVN) was invented to continuously deliver crystals to the X-ray pulses(DePonte, Weierstall et al. 2008,

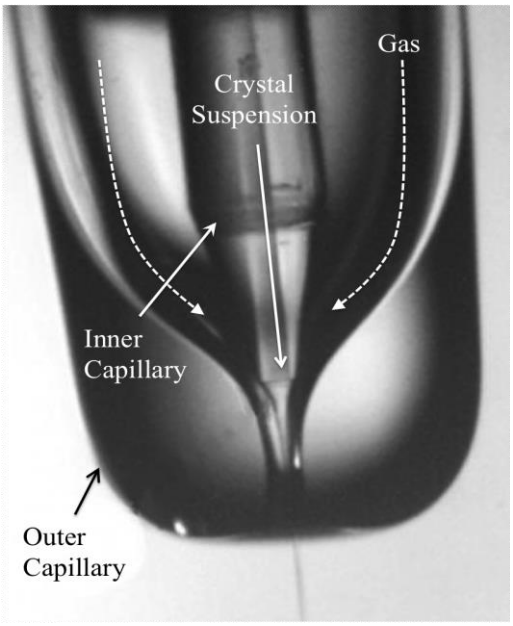

Figure 2.4 Schematic of a GDVN.

The GDVN is assembled by placing a smaller, hollow-core fused silica optical fiber (inner capillary) inside a larger, borosilicate glass capillary (outer capillary). Crystals are passed through the inner capillary while a focusing gas is passed through the outer capillary and thus occupies the space in between the two capillaries. A thin, micrometer jet is produced when the co-flowing gas meets the crystals as they exit the inner capillary. The scale bar is 0.1 mm.

Weierstall, Spence et al. 2012). Based on the principle that flowing gas encompassing a liquid can focus the liquid jet to a smaller diameter (1/10 the original capillary size) the GDVN produces a liquid jet that is only a few microns in diameter(DePonte, Weierstall et al. 2008, Weierstall, Spence et al. 2012). This is achieved by mounting a smaller capillary inside a larger capillary. Crystals in their mother liquor are delivered through the smaller, inner capillary and high-pressured gas flows through the interstitial space between the larger, outer capillary and the inner capillary (see figure 2.4). The GDVN has been used successfully for many SFX experiments (see Table 1) including time-resolved studies(Aquila, Hunter et al. 2012, Redecke, Nass et al. 2013, Kupitz, Basu et al. 2014) and has thus far been the workhorse for the majority of SFX experiments. While the GDVN has experienced much success, several limitations exist. Namely, clogging of the smaller, inner capillary can occur due to blockage from aggregating crystals, the shear forces experienced during jetting have been suspected to damage some fragile crystals(Demirci, Sierra et al. 2013, Stevenson, DePonte et al. 2014), and ice can form on the nozzle by back-spraying of debris from the explosion at the X-ray interaction region (DePonte, Weierstall et al. 2008, Demirci, Sierra et al. 2013). Clogging events can be decreased by filtering the sample prior to sample loading and using in-line filters upstream from the nozzle. However, filtering could result in loss of sample and damage to crystals, thus highlighting the need for knowledge and control over the size distribution(Demirci, Sierra et al. 2013). One challenge when using the GDVN is that the X-ray pulse repetition rates currently available (≤120 Hz) are low

compared to the minimal flow rate of the GDVN at 10 µL/min, thus the majority of crystals never interact with the X-ray beam since they flow through the interaction region between pulses(Weierstall 2014). Therefore, large sample volumes are needed to produce a complete SFX dataset using this method. Data sets using the GDVN can require 10 mL of crystal suspensions, typically containing on the order of 10^9-10^{11} crystals/mL(Chapman, Fromme et al. 2011, Schlichting and Miao 2012, Kupitz, Grotjohann et al. 2014, Galli, Son et al. 2015).

Several strategies have been proposed to reduce the flow rate of the GDVN. First, the GDVN can be operated in a pulsed mode whereby the jet is switched on and off, using a high performance liquid chromatography (HPLC) valve, as to minimize sample loss between pulses. It has been reported that flow times of 300 µs separated by times of 2 ms without flow could reduce the GDVN sample consumption by a factor of four(Weierstall 2014). Similar to a pulsed method, droplets can be used to deliver crystals to the X-ray beam. In acoustic droplet ejection, droplets can be produced by a piezoelectric transducer(Chen and Basaran 2002). To optimally synchronize the crystal filled drops, the droplets would be trigged by the XFEL. However, droplet speeds produced tend to be unstable on the necessary timescales, making synchronization difficult. Additional challenges faced by this method include large droplet size and thus high background(Soares, Engel et al. 2011, Roessler, Kuczewski et al. 2013), crystal settling without the addition of a viscous solution(Weierstall 2014), and compatibility with high vacuum(Weierstall 2014). To date, neither the pulsed liquid jet nor acoustic droplet ejection has been employed at an XFEL successfully.

Electrospinning injectors:

In one method of counteracting the fast consumption of sample by the GDVN, an electrospun liquid microjet, which uses high electric fields instead of gas to focus the liquid, has been implemented(Sierra, Laksmono et al. 2012). Electrospinning allows for a slower moving jet and thus, fewer sample flows between XFEL pulses and the amount of sample needed for a dataset can be reduced(Weierstall, James et al. 2014). The slow speed is also suitable for experiments with long pump-probe delay times as it allows for longer incubation times compared to those

achievable with the GDVN(Sierra, Laksmono et al. 2012). However, to form a continuous jet and prevent crystal settling, the crystals must be suspended in a suitable viscous media (e.g. glycerol, PEG, or sucrose); otherwise the electrospun jet breaks up into highly charged droplets once surface tension is overcome. The embedding media also serves as a cryo-protectant, necessary to prevent jet dehydration due to the length of time spent in vacuum, making this method not universally suitable. Caution of the impact of the electric field and the high charge of the jet and droplets on the sample must also be considered as they are unknown at present(Sierra, Laksmono et al. 2012).

High-viscosity media injectors

LCP has a viscosity similar to vacuum grease, which makes harvesting tens of thousands of small crystals from their sticky, viscous environment impractical. Thus, an alternative method was devised so that the crystal laden LCP could be delivered directly to an X-ray beam. To extrude such a viscous material, the high-viscosity injector (commonly referred to as the “LCP injector”) amplifies the pressure of an HPLC using a hydraulic stage to extrude the viscous media out of a capillary. A co-flowing gas stream ensures that the highly viscous fluid does not curl back onto the nozzle and forms a stable jet(Weierstall, James et al. 2014). Unlike the GDVN, the jet is not focused to a smaller size and maintains the inner diameter of the capillary it is extruded from (10-100 μm). In addition, the high viscosity injector has been shown to work both in vacuum and in air(Nogly, James et al. 2015). To decrease sample consumption for soluble nanocrystals, crystals have been successfully manually mixed post-crystallization with LCP and grease(Fromme, Ishchenko et al. 2015, Sugahara, Mizohata et al. 2015). Recently, agarose-based gels have been shown to be compatible for the sample delivery of both soluble and membrane proteins which are embedded into pre-gelled agarose using a coupled syringe setup as described in Conrad et al(Conrad, Basu et al. 2015). The agarose jet also offers an improved background over grease(Sugahara, Mizohata et al. 2015) or LCP, leading to higher quality data(Conrad, Basu et al. 2015).

Fixed Targets:

For most experiments that use a flowing jet, either liquid, viscous, or electrospun, the optimal crystal hit rate is usually around 10-30%, as higher crystals densities tend to lead to

clogging. Flowing jets remain the ideal method for sample delivery for most SFX experiments as they do not require freezing and are the most practical technique for conducting time-resolved experiments. But for a small subset of experiments, fixed targets may be beneficial since this approach has the potential to decrease the sample quantities necessary for a data set to be collected. Fixed targets vary from traditional goniometers, to windowed sample support wafers/grids (analogous to electron microscopy holders), and to microfluidic chips[45,104,106]. The main advantage of sample support wafers is their compatibility with 2D nanocrystals, which require a scaffolding and thus, cannot be delivered in a flowing jet[102]. In order to prevent dehydration, crystals must be immersed in oil before being painted onto the support grid. Microfluidic devices have also been used for fixed target experiments at XFELs and have been designed to trap single crystals[104,112]. These traps can theoretically ensure that the X-ray beam interacts with only one crystal at a time but with current designs, crystal stacking will occur before all the traps are filled. Fixed targets can result in crystal orientation bias[113]. Currently, fixed target approaches are severely limited by slow data acquisition. Data acquisition rates are primarily limited by the velocity of the fixed target stage and the time it takes to replace the sample grid or chip. For example, if the stage motor could operate at 120 Hz and automated scripts aligned the X-rays to each window/trap, a fixed target containing 800 window/traps, the sample holder would need to be replaced every 6.67 minutes. In addition, some fixed targets produce high background due to the support material[103-105].

Recently, data has also been collected at XFELs with a conventional goniometer approach on very large crystals (up to millimeters in size) under cryogenic conditions. This method has been used to determine a dark structure of photosystem II with minimal X-ray damage at 1.95 Å resolution[114]. However, this approach is low throughput and tedious as it can require days or even weeks of very precious data collection time at FELs on hundreds of individually mounted crystals(Suga, Akita et al. 2015). The experiment required freezing, attenuation, and translation of the beam focus by 50 µm at an X-ray spot size of 1 µm to avoid X-ray damage. Furthermore, freezing and the large crystal size prohibits time-resolved experiments from being feasible. Except for cases like photosystem II, where X-ray damage significantly alters the structure of the catalytic

metal complex, it is questionable if this is advantageous compared to standard macromolecular crystallography at synchrotron sources.

Structural dynamics and molecular movies: challenges and opportunities

In addition to broadening the array of macromolecules available to crystallography, SFX also expands upon the information that can be obtained regarding functional dynamics. Macromolecular crystals typically exhibit extremely high solvent content and weak electrostatic contacts in comparison to their smaller molecular counterparts. While this has always presented a challenge to crystallogenesis of well-diffracting crystals, the porous nature of macromolecular crystals lend them to intact catalytic or functional activity in the crystalline phase(Hofbauer, Zouni et al. 2001, Moffat 2001, Fromme, Bottin et al. 2002, Li, Lyons et al. 2013). This is because large solvent channels that are present in the crystals can allow for conformational movement of the proteins or even the diffusion of a substrate to active sites in crystals. This property indicates an exciting opportunity to see intermediate structures over the course of a functional reaction. By achieving time-resolved structure determination (i.e. multiple structures along a reaction pathway), one can begin to directly understand the relationship between structure and function of macromolecules. This has numerous applications such as rational drug design and renewable energy by unraveling the mechanism of biochemical processes. However, some important considerations must be taken into account in order to realize reliable time-resolved structures. Time-resolved crystallography has historically been performed on large single crystals by Laue multi-wavelength crystallography (for a review see (Hajdu and Johnson 1990)) and has exhibited considerable gains over the past twenty years, moving from the millisecond(Genick, Borgstahl et al. 1997) to the picosecond(Schotte, Cho et al. 2012) temporal resolution regimes. This has opened the door to viewing conformationally dynamic proteins in action on an atomic scale. While this technique continues to improve, both within its experimental parameters and subsequent data analysis, it faces some hard limitations due to the nature of large crystals and current synchrotron sources, namely: 1) temporal resolution is limited by pulse length achievable using a synchrotron, 2) irreversible reactions cannot be studied as the induction of a reaction would cause a permanent

Table 2.1 Summary of Sample Delivery Methods Currently Being Deployed

Sample Delivery	Average Flow	Advantages	Limitations	Experimental Environment	Examples of Systems/Proteins Studied
Gas Dynamic Virtual Nozzle(DePonte, Weierstall et al. 2008)	10-25 µL/min(Schlichting 2015)	amenable for TR-SFX(Aquila, Hunter et al. 2012, Kupitz, Basu et al. 2014), compatible with most systems	high sample consumption(Weierstall 2014, Weierstall, James et al. 2014, Sugahara, Mizohata et al. 2015), freezing around nozzle tip(Weierstall 2014), fragile crystals might be damaged during jetting(Demirci, Sierra et al. 2013, Stevenson, DePonte et al. 2014),	vacuum	photosystem I & II(Kern, Alonso-Mori et al. 2013, Kupitz, Basu et al. 2014), photosystem I-ferredoxin(Aquila, Hunter et al. 2012), lysozyme(Boutet, Lomb et al. 2012), cathepsin B(Redecke, Nass et al. 2013), photosynthetic reaction center(Johansson, Arnlund et al. 2013),Cry3A(Sawaya, Cascio et al. 2014), photoactive yellow protein(Tenboer, Basu et al. 2014), P-type ATPase(Bublitz, Nass et al.
Electrospinning(Sierra, Laksmono et al. 2012)	140-3100 nL/min(Sierra, Laksmon	low sample consumption(Sierra, Laksmono et al. 2012), compatible with membrane proteins (Kern,	requires cryoprotectant to prevent the jet from freezing(Sierra, Laksmono et al. 2012), unknown if high electric fields affect crystals(Conrad, Basu et al. 2015)	vacuum	photosystem II(Kern, Alonso-Mori et al. 2012), 30S ribosomal subunit(Demirci, Sierra et al. 2013), thermolysin(Hattne, Echols et al. 2014)
Lipidic Cubic Phase(Weierstall, James et al. 2014)	50-200 nL/min(Liu, Wacker et al. 2013)	low sample consumption(Liu, Wacker et al. 2013), crystals grown in LCP do not need to be harvested(Liu, Wacker et al. 2013), some soluble crystals post-	Debye Sherrer rings(Conrad, Basu et al. 2015), membrane protein crystals cannot be mixed post crystallization(Conrad, Basu et al. 2015), crystals grown in LCP cannot be filtered before injection	both	5-HT2B receptor(Liu, Wacker et al. 2013), smoothened receptor(Weierstall, James et al. 2014), human delta opioid receptor(Fenalti, Zatsepin et al. 2015), human angiotensin receptor(Zhang, Unal et al. 2015), rhodopsin arrestin complex(Kang, Zhou et al. 2015), diacylglycerol kinase(Li, Stansfeld et al. 2015),
Grease(Sugahara, Mizohata et al. 2015)	460-480 nL/min(Sugahara, Mizohata et al. 2015)	low sample consumption(Sugahara, Mizohata et al. 2015)	Debye-Sherrer rings(Conrad, Basu et al. 2015), not shown to be compatible with membrane proteins(Conrad, Basu et al. 2015)	atmosphere	lysozyme(Sugahara, Mizohata et al. 2015), glucose isomerase(Sugahara, Mizohata et al. 2015), thaumatin(Sugahara, Mizohata et al. 2015), fatty acid–binding protein type 3(Sugahara, Mizohata et al. 2015), luciferin-regenerating enzyme(Yamashita, Pan et al.
Agarose(Conrad, Basu et al. 2015)	100-200 nL/min(Conrad, Basu et al. 2015)	low sample consumption(Conrad, Basu et al. 2015), compatible with membrane and soluble proteins(Conrad, Basu et al. 2015), low	requires cryoprotectant to prevent the jet from freezing when operated in vacuum(Conrad, Basu et al. 2015)	both	phycocyanin(Conrad, Basu et al. 2015), photosystem I & II(Conrad, Basu et al. 2015), sindbis virus(Lawrence, Conrad et al. 2015)

Sample Delivery Method	Average Flow Rate	Advantages	Limitations	Experimental Environment	Examples of Systems/Proteins Studied
fixed target: sample supports (wafers(Hunter, Segelke et al. 2014) (Pedrini, Tsai et al. 2014, Feld, Heymann et al. 2015)and chips(Lyubimov, Murray et al. 2015, Mueller, Marx et al. 2015))	NA	low sample consumption(Lyubimov, Murray et al. 2015), compatible with 2D crystals(Pedrini, Tsai et al. 2014), target can be rotated about a fixed angle(Lyubimov, Murray et al. 2015)	commercial wafers/chips material is not X-ray transparent(Feld, Heymann et al. 2015, Lyubimov, Murray et al. 2015), low data collection rates (<10 hz, limited by velocity of sample holder)(Hunter, Segelke et al. 2014), crystal traps can produce crystal orientation biases(Lyubimov, Murray et al. 2015) and fill rate is limited to ~50% to prevent crystal stacking(Mueller, Marx et al. 2015), in vacuum experiments	both	rapid encystment protein 24 kDa(Hunter, Segelke et al. 2014), bacteriorhodopsin(Pedrini, Tsai et al. 2014), anthrax toxin protective antigen(Feld, Heymann et al. 2015), lysozyme(Lyubimov, Murray et al. 2015), sperm whale myoglobin(Mueller, Marx et al. 2015)
Fixed Target: Goniometer (Cohen, Soltis et al. 2014)(Grids/Mesh/ Loops)	NA	amenable to micro- and to macro- crystals(Cohen, Soltis et al. 2014), compatible with standard goniometers(Cohen, Soltis et al. 2014)	requires cryopreservation and freezing(Cohen, Soltis et al. 2014), not amenable for TR-SFX, requires hitting the crystal in a different position each shot to avoid damage	atmosphere	RNA polymerase II(Cohen, Soltis et al. 2014), general transcription factor IIB(Cohen, Soltis et al. 2014), large nucleic acid scaffold(Cohen, Soltis et al. 2014), monomeric iron-containing hydrogenase (Cohen, Soltis et al. 2014), sperm whale myoglobin(Cohen, Soltis et al. 2014), cytochrome c oxidase(Hirata, Shinzawa-Itoh et al. 2014), synaptotagmin-1 SNARE complex(Zhou, Lai et al. 2015), β2-adrenoreceptor/nanobody

modification of the molecules in the crystal, 3) only light activated, pump-probe type experiments are generally feasible at present, with limited light penetration being one of the major obstacles, and 4) homogeneity of reaction initiation must be considered and presents a challenge. SFX presents an opportunity to complement the Laue method by providing access to experiments previously impossible by overcoming the above challenges via its unique experimental characteristics. XFELs have pulse durations on the order of tens of femtoseconds, which, within the framework of time-resolved crystallography, allow access to detect and resolve fast time points in catalytic reaction processes. Thereby, more temporally constrained intermediates can be detected along a reaction pathway. Recent work has pushed temporal resolution to the sub-picosecond regime(Barends, Foucar et al. 2015, Pande, Hutchinson et al. 2015), which is utterly out of reach at existing synchrotron sources. This allows insight into ultrafast intermediates and therefore, the promise of a much finer understanding of catalytic mechanisms.

With irreversible reactions one must consider the way in which data is collected. In traditional crystallography a crystal is rotated during data collection and each diffraction pattern corresponds to a rotational increment of the reciprocal space. If an irreversible reaction is to be probed fully, data collection would require thousands of large crystals for each time point as the crystal would be permanently altered after the induction of the reaction. This would require an oppressively large number of crystals to collect a complete data set from individual crystals. The serial “diffraction before destruction” nature of SFX experiments completely bypasses this constraint, as only one diffraction pattern is collected from each crystal. Since the sample is constantly replenished, there is no constraint on the reversibility of a reaction. The utilization of Monte Carlo merging of an immense number of individual crystals in random orientations leads to accurate structure factors for time-resolved experiments due to implications from the central limit theorem.

Considerations of structural homogeneity and the constraint of Laue to predominantly pump-probe style experiments are highly intertwined due to one parameter: diffusion. Thus far, Laue crystallography has been predominantly limited to photo-activated reactions since chemically activated reactions would necessitate diffusion of a substrate throughout the crystal, limiting

reaction timescales available. While the large solvent channels in crystalline macromolecules often allow for diffusion to take place via soaking with a diffusing substrate(Bolduc, Dyer et al. 1995, Stoddard and Farber 1995, Helliwell, Nieh et al. 2003) (assuming the active site is unobstructed and the substrate is sufficiently small relative to the solvent channels), the size of the crystal limits diffusion times, thereby constraining the time regime of reaction intermediates accessible in an experiment. There have been chemically activated time-resolved experiments performed successfully by incorporating photo-activated caged substrates into the crystal(Schlichting, Rapp et al. 1989, Stoddard, Cohen et al. 1998, Ursby, Weik et al. 2002), thus reducing diffusion times to that of the photo-penetration of the pump laser. However, the incorporation of caged substrates requires extensive knowledge about a given system and is not generally compatible(Schmidt 2013). The small size of the crystals used in SFX theoretically allow for diffusion times on microsecond time scales, allowing access to many reactions on the short millisecond and even microsecond regimes in the absence of caged substrates. For example, a crystal with dimensions of 0.5x0.5x0.5 μm^3 has been modeled to exhibit a diffusion time of 17 µs, while a 3x4x5 μm^3 crystal is estimated to take 1 ms, and a large 300x400x500 μm^3 crystal would take 9.5 s(Schmidt 2013). Many biological reactions occur with intermediates observed in the time range of ms and faster but significantly less occur in the longer regime of seconds. One must also consider reaction homogeneity since Bragg diffraction relies upon translational symmetry of the molecules in the crystal. This means that in order to observe an intermediate structure, a sufficient proportion of the molecules must be in a single conformation during probing in order for a structure to be elucidated.

Photoactivated reactions have one major advantage over substrate or other diffusion based reactions as initiation is homogeneous and rapid. However, the degree of reaction initiation by photoinduction is also limited by the size of the crystal since molecules absorb the light as it travels through the crystal causing a decrease in transmission with increasing path length. When considering faster time points, the reaction homogeneity of the molecules in the crystal is sensitive to the lifetime of the intermediate state as compared to the time difference of reaction initiation from the front and back surfaces of the crystal relative to the pump beam. The distance traveled with respect to the front and back of photo-activated crystals is not the main cause of this temporal offset

(though this is on the order of picoseconds for large crystals); instead, it is the attenuation of the pump intensity as it proceeds through the crystal, undergoing absorption and scattering. Depending on the particular robustness of the sample, one can attempt to address this by increasing the power of the laser but this approach is constrained by photo-damage and heating effects that can occur. Thus, the size of nanocrystals provides an advantage, allowing a much smaller difference of reaction initiation throughout the crystal and requiring decreased pump intensities for maximal reaction initiation. Furthermore, the volume of the crystal itself is so small that in practice, the whole crystal can be illuminated by the pump, minimizing considerations of the intensity profile of the pump laser. Because of these attributes, SFX provides the basis for a much higher reaction initiation yield, a point which as has already been shown in practice(Tenboer, Basu et al. 2014).

Time-Resolved Serial Femtosecond Crystallography

The structure-mechanistic relationship found in biological reactions is rarely explained through resolution of a single, static structure. Instead, the dynamics *between* initial and final states embody the mechanism. TR-SFX permits access to transient intermediates that occur as a reaction is proceeding, providing still snapshots of these states. Snapshots of the initial, intermediate, and final state(s) can be viewed in a quick succession from start to finish to reveal motion of the enzyme and thus a “molecular movie” can be obtained to unravel how these biological molecules proceed in nature.

The first time-resolved SFX (TR-SFX) experiment was carried out on PSI-ferredoxin co-crystals which undergo electron transfer reactions that lead to the subsequent undocking of ferredoxin and dissolution of the crystals upon light excitation, leading to a rapid loss of diffracting quality upon pumping. Large differences have been obtained in the diffraction patterns between the excited and uninitiated reactions as revealed by the Wilson plot. The timing of these differences agrees with the time range previously found by spectroscopic methods for electron transfer(Setif and Bottin 1995, Diaz-Quintana, Leibl et al. 1998). These experiments provided the proof of concept for TR-SFX, (though an electron density map was not obtained due to data limitations)(Aquila, Hunter et al. 2012).

The first successful TR-SFX experiment was performed using photosystem II, the membrane protein responsible for splitting water into its constituent protons, electrons and oxygen. This process provides the electrons for the photosynthetic electron transfer chain in oxygenic photosynthesis. The catalytic oxygen evolving cluster, structurally the most interesting domain in photosystem II, is particularly susceptible to radiation damage due to the presence of 5 Mn atoms. The X-ray photo-damage processes are virtually eliminated by the “diffraction before destruction” nature of SFX. A further concern of time-resolved studies with X-rays is that local photo-damage can be induced by repeated illumination of the crystal by the pump laser in Laue time-resolved experiments. Again, this problem is mitigated by TR-SFX since relatively low pump energy and flux can be applied per crystal due to smaller, more permeable crystals. Indeed, TR-SFX has succeeded in ‘shining the first light’ on the undamaged ground state of PSII using single and multiple laser excitations prior to diffraction, allowing multiple states to be studied along the multiple-excitation reaction pathway. This revealed large conformational changes occurring in the photo-excited “double flash state” of PSII, which includes movement of the protein via its coordination of the oxygen evolving cluster(Kupitz, Basu et al. 2014). Though higher resolution is needed to provide a deeper understanding of the water splitting process, TR-SFX in general provides the most feasible path forward toward obtaining a series of initial, final and intermediate structures during a reaction, i.e. molecular movies of biomolecules at work.

More recently, atomic resolution has been achieved for TR-SFX using PYP(Tenboer, Basu et al. 2014). This experiment also pushed the limits on the time-resolution available at an XFEL, capturing reaction time points down to the sub-picosecond regime(Pande, Hutchinson et al. 2015). These studies improve upon the temporal resolution that has been achieved in Laue crystallography(Schotte, Cho et al. 2012) by orders of magnitude and is only significantly limited by beam characteristics (i.e. time-jitter)(Pande, Hutchinson et al. 2015). As developments continue with future generation sources, temporal resolution will be pushed even further. In addition to ultrafast time resolution, it is notable that the TR-SFX studies on PYP have also shown huge improvement on reaction initiation (40% at XFELs with nanocrystals compared to 10-15% achieved at a synchrotron with larger crystals(Schmidt, Srajer et al. 2013, Tenboer, Basu et al. 2014)),

allowing for stronger signal from transient intermediates to be detected, leading to data that can be easily interpretable. Even more recently, research in this time domain has led to novel observations of global structural changes in myoglobin upon lysis of an Fe-CO bond that occur within a few picoseconds(Barends, Foucar et al. 2015).

Though no mixing TR-SFX work has been published to date, the stage is set for 'on the fly' mixing experiments that take advantage of the nature of SFX. Many enzymes have biologically interesting intermediates that occur on time scales faster than those accessible to soaking experiments of large crystals. Although one could scale down the size of the crystals and thereby, narrow the reaction initiation temporal profile, the tradeoff with decreased diffraction severely limits the range of this method. In theory, the sizes of crystals available for SFX alleviates this concern, decreasing necessary mixing times such that a new regime of reactions is accessible. Delivery methods based on the GDVN have already been developed for time-resolved mixing experiments e.g. a double focused mixing jet(Wang, Weierstall et al. 2014) where a jet containing crystals is mixed within a stream containing the desired substrate prior to discharging from the nozzle . For a more in depth look at substrate mixing techniques, the reader is referred to (2013).

Indeed, the most promising areas for XFELs to push the boundaries within structural biology is the ability to study temporal dynamics with femtosecond pulses, allowing access to ultrafast timescales and thereby, short lived intermediates. Without sacrificing resolution, TR-SFX paves the way for dynamic structural elucidation of biological processes that feature fast (<100 ps) conformational changes, irreversible reactions, non-photo-activated inductions, and to those which are limited by crystal size. TR-SFX can also avoid the local radiation damage often experienced in the active sites of macromolecules and generate a higher fraction of intermediate states(Tenboer, Basu et al. 2014). This has far reaching implications for many fields, notably alternative energy and drug design, which both rely heavily on understanding the relationship between structure and mechanism. The reactions accessible to TR-SFX studies will continue to broaden as 'mix and inject' methods for chemo-activated reactions continue development. With TR-SFX and other time-resolved XFEL methods (such as time-resolved wide angle X-ray scattering, e.g.(Arnlund, Johansson et al. 2014)), it is evident that XFELs provide new ways to

explore a novel regime of time-resolved structural biology, leading towards true movies of dynamic macromolecules in action.

Data acquisition and data processing in SFX

The short duration pulses delivered by XFELs have necessitated the development of new detector technologies capable of integrating all of the photons that arrive within the time duration of a few femtoseconds, while sustaining full-frame readout at the XFEL pulse repetition rate. Although X-ray charge coupled device (CCD) detectors are very common at synchrotrons, few CCD detectors have readout speeds that match the LCLS repetition rate. Two CCD's were used at LCLS for the first experiments (at 2 keV), the pnCCD and the fCCD(Strüder, Epp et al. 2010, Doering, Chuang et al. 2011). Due to their very low noise and high quantum efficiency over a large range of energies, they have been used for imaging and spectroscopy experiments. However, a larger dynamic range then the CCDs can currently cover (a few hundred thousands of photons) is necessary for SFX experiments at atomic resolution (energies >6 keV). The first detector specifically designed for higher energies presently used for SFX experiments at LCLS was the Cornell-SLAC pixel array detector (CSPAD)(Koerner, Philipp et al. 2009, Philipp, Koerner et al. 2010, Philipp, Hromalik et al. 2011, Hart, Boutet et al. 2012). Today the CSPAD is the principal detector used for SFX experiments at LCLS. It consists of 64 separate modules (194x185 pixels each), allowing cost-effective replacement and experimental flexibility. The CSPAD is tiled to produce a 2.3 megapixel detector, with readout speeds matching the repetition rate of 120 Hz(Hart, Boutet et al. 2012). The panel distribution leaves an adjustable sized hole in the middle to allow for adjustable incident beam focuses, preventing the beam from damaging the detector (the beam is powerful enough to melt through a conventional beam stop)(White, Barty et al. 2013).

The use of detectors composed of multiple modules introduces unique concerns, namely the exact location of each module must be known in order to correctly assess the data. While the experimental geometry may be known to low precision prior to an experiment, it can be subsequently refined using the collected data. In this case, assembling a physically correct image during initial processing is futile and a known calibration sample is used to refine the experimental

geometry. The detector geometry is specified in a pixel location map containing the coordinates of each detector pixel in a suitably defined coordinate system. All constraints for an experimental geometry description are saved in a single text file which can be implemented within any of the available SFX software(White, Barty et al. 2013, Barty, Kirian et al. 2014, Hattne, Echols et al. 2014). The success of indexing, predicting spot locations using a crystal orientation matrix and integrating reflection intensities depends upon the precise knowledge of the location of these sensors in three-dimensional space. This means that an accurate calibration and refinement of the tile metrology is critical.

Data analysis in SFX has unique challenges with respect to data sets collected at synchrotrons. This is due to the serial nature from snapshot diffraction patterns of randomly oriented crystals with unknown partiality and shot to shot variation in the beam characteristics. Furthermore, the images collected during an experiment consist not only of single crystal hits (one crystal in the beam) but also blank patterns (no crystal in the beam) and multi-hits (multiple crystals in the beam). The XFELs at LCLS and SACLA operate up to 120 Hz and 60 Hz, respectively, resulting in hundreds of thousands of patterns collected per hour, thus creating terabytes of data. Due to these challenges, conventional crystallographic data processing methods cannot be efficiently used for SFX data collection. Thus, new data analysis tools for SFX have been developed. In order to optimize efficiency during data collection it is important to have rapid feedback during data collection. First, data is reduced by eliminating blank and multi-hit patterns which is implemented within the programs Cheetah(Barty, Kirian et al. 2014) and CASS(Foucar, Barty et al. 2012). They perform the data pre-processing steps, evaluate the quality of each data frame, and reject all those frames that are not suitable for further analysis. Once the data size is reduced, detector artifacts are removed and background subtraction is performed. Each frame is then subjected to Bragg peak location analysis (so called ‘peak finding’) in which Bragg peaks are identified by searching for clusters of connected pixels based on a series of parameters including minimum numbers of pixels per peak, the number of peaks in a frame, intensity thresholds, and signal to noise ratio. A minimum number of Bragg peaks must be identified in the diffraction pattern as a further constraint, so that patterns with too few peaks (i.e. impossible to index) are rejected.

The background corrected and sorted diffraction patterns identified during the hit finding process are subjected to indexing and integration by programs such as CrysFEL(White, Barty et al. 2013), cctbx.xfel(Hattne, Echols et al. 2014), and nXDS(Kabsch 2010). The purpose of these programs is to identify Bragg peaks in the hits and then to perform indexing. Determining the unit cell parameters and the orientation of a crystal is carried out by the widely used algorithms such as MOSFLM(Powell 1999, Rossmann and van Beek 1999, Powell, Johnson et al. 2013), DIRAX(Duisenberg 1992), LABELIT(Sauter, Grosse-Kunstleve et al. 2004), and XDS(Kabsch 2010), based on the Bragg peak locations in a diffraction pattern. Once each pattern has been successfully indexed, the intensities are merged and integrated using the Monte Carlo method(Kirian, Wang et al. 2010, Kirian, White et al. 2011). One of the largest problems in SFX data analysis is the indexing ambiguity which occurs when the Bravais symmetry is higher than the space group symmetry. An indexing ambiguity arises in some polar space groups (like P63) where each pattern has multiple ways it can be indexed. In standard crystallography this indexing ambiguity is solved by exploration of the data set with both indexing options, where only one option leads to a correct X-ray structure. However, since many individual patterns are merged in SFX, the ambiguity must be solved before any additional processing to avoid artificial twinning. In order to overcome the indexing ambiguity problem, CrystFEL has implemented an algorithm based on the expectation maximization approach(Liu and Spence 2014) which has been successfully applied and validated using both simulated and experimental diffraction(Liu and Spence 2014). As with conventional crystallography, the “phase problem” has to be solved in order to reconstruct a real-space electron density map from the measured SFX intensities. Indeed, this presents itself as a primary challenge in serial crystallography data analysis. Until recently, all crystallographic structures so far determined by XFEL have been phased by molecular replacement, using phases from known or related structures(Chapman, Fromme et al. 2011, Boutet, Lomb et al. 2012, Johansson, Arnlund et al. 2012, Sierra, Laksmono et al. 2012, Redecke, Nass et al. 2013). This method limits the target protein molecules to be investigated by SFX since the protein of interest must have a known homologous structure. Even if it does, there is risk that phase bias can be introduced. However, some conventional phasing methods have also been suggested to be applied

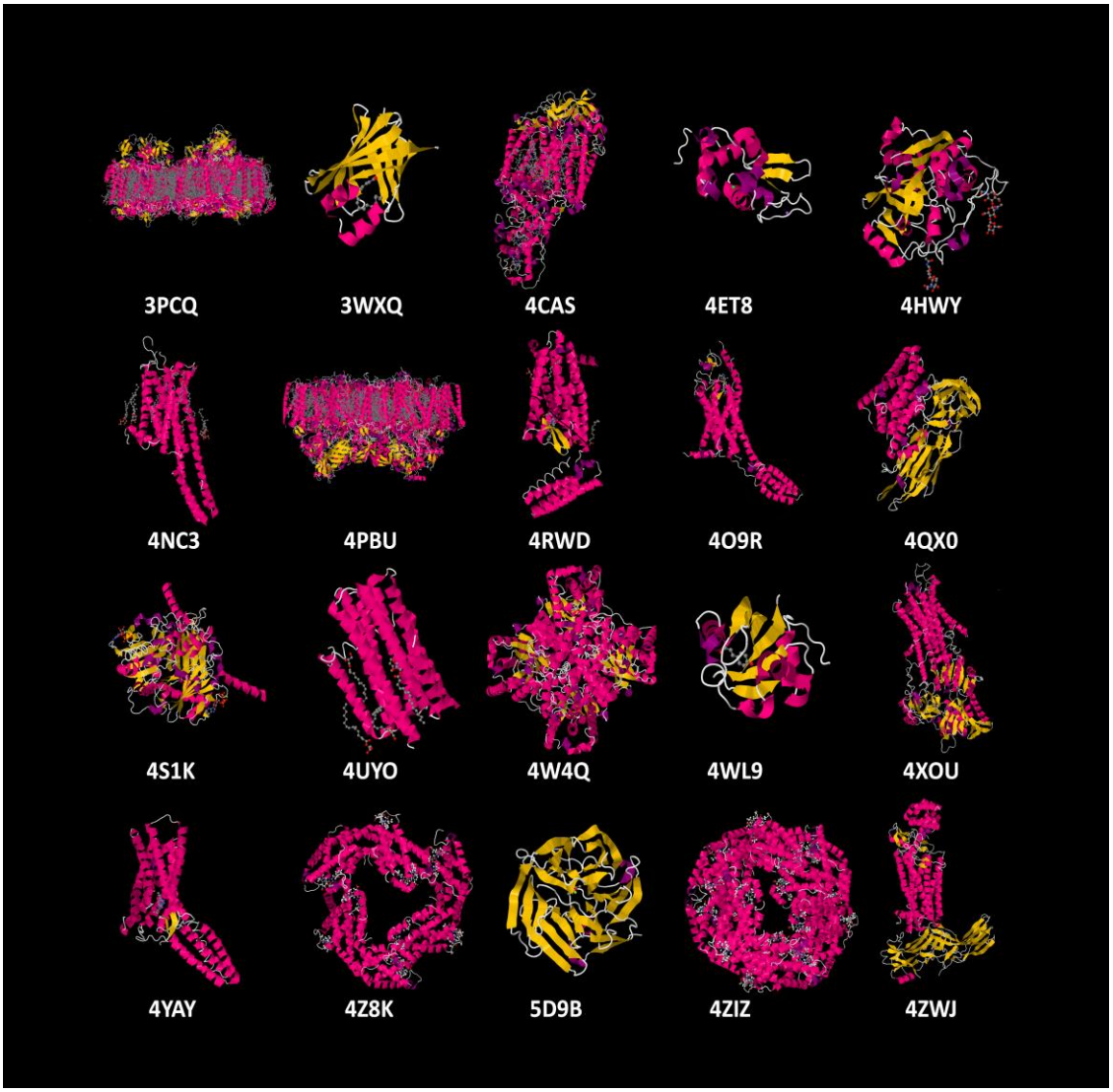

Figure 2.5. **Select Structures Solved Using XFELs by PDB Code.**

From top left: photosystem I (3PCQ(Chapman, Fromme et al. 2011)), FABP3 (3WXQ(Sugahara, Mizohata et al. 2015)), purple bacterial reaction center (4CAS(Johansson, Arnlund et al. 2013)), lysozyme (4ET8(Boutet, Lomb et al. 2012)), cathepsin B (4HWY(Redecke, Nass et al. 2013)), 5-HT2B (4NC3(Liu, Wacker et al. 2013)), photosystem II(Kupitz, Basu et al. 2014)), δ-opiod receptor (4RWD(Fenalti, Zatsepin et al. 2015)), smoothened receptor ((Weierstall, James et al. 2014)), Cry3A (4QX0(Sawaya, Cascio et al. 2014)), CPV17 polyhedron (4S1K(Ginn, Messerschmidt et al. 2015)), diacylglycerol kinase (4UYO(Li, Stansfeld et al. 2015)), xylose isomerase (4W4Q(Sugahara, Mizohata et al. 2015)), photoactive yellow protein (4WL9(Tenboer, Basu et al. 2014)), SR Ca^{2+}-ATPase (4XOU(Bublitz, Nass et al. 2015)), angiotensin II receptor (4YAY(Zhang, Unal et al. 2015)), phycocyanin (4Z8K(Conrad, Basu et al. 2015)), luciferin-regenerating enzyme (5D9B(Yamashita, Pan et al. 2015)), C-phycocyanin (4ZIZ(Fromme, Ishchenko et al. 2015)), rhodopsin-arrestin complex (4ZWJ(Kang, Zhou et al. 2015))

to SFX data such as multiple isomorphous replacement or multi/single-wavelength anomalous dispersion (MIR, MAD, SAD)(Son, Chapman et al. 2011, Son, Chapman et al. 2013, Barends,

Foucar et al. 2014, Barends, Foucar et al. 2015). Barends(Barends, Foucar et al. 2014) and co-workers have demonstrated for the first time that the conventional phasing method of SAD can also be successfully used for SFX experiments(Barends, Foucar et al. 2014). In this experiment they collected and solved the structure to 2.1 Å resolution of a lysozyme heavy atom derivative that gives a strong anomalous signal from two gadolinium atoms per asymmetric unit. The MAD phasing method has also been recently adapted to SFX by using modified Karle-Hendrickson equations(Son, Chapman et al. 2011, Son, Chapman et al. 2013). This proposed generalized version of MAD phasing method offers another potential for experimental phasing for structural determination in SFX.

In addition to the classical methods, new phasing techniques have been proposed for SFX data analysis. Methods such as *ab initio* phasing by the evaluation of the shape transforms (or the oversampling method)(Chapman, Fromme et al. 2011, Spence, Kirian et al. 2011, Liu, Poon et al. 2013, Kirian, Bean et al. 2014) and the "high-intensity radiation induced phasing" (HI-RIP)(Galli, Son et al. 2015) have been proposed. The phase transform method exploits the intensity scattered between neighboring Bragg peaks (or fringes) from crystals that contain less than 20 unit cells in each crystal direction. This phenomenon has historically been obscured by noise in large crystals due to inverse scaling of inter-Bragg intensity with the number of unit cells. Each recorded Bragg peak represents a particular portion of the Ewald sphere and phasing is achieved by oversampling between the Bragg peaks. The HI-RIP method takes advantage of the ionization process of the atoms that occur within the femtosecond timescale of the pulse in SFX experiments(Hau-Riege, London et al. 2004). The change in the electronic configuration of atoms leads to the modification of the atomic scattering factors during diffraction(Son, Chapman et al. 2011). In the case of SFX this would introduce the possibility of determining phases by varying the scattering factors of the heavy atoms. This new approach, which has been already tested with Trypanosoma brucei cathepsin B protein, would represent a powerful method of experimental phasing without the need to modify the protein crystals assuming sulfur atoms are present in the native structure(Galli, Son et al. 2015).

Challenges and outlook

Nearly six years after the first SFX data were collected using an XFEL at LCLS and four years after the proof of principle of SFX was published(Chapman, Fromme et al. 2011), a new era in structural biology has emerged. Figure 2.5 shows a gallery illustrating the breadth of protein structures successfully solved with XFELs to date. The unique properties of XFELs (ultrashort, extremely intense pulses with high frequency and coherence) have attracted considerable attention of a wide community of scientists in fields ranging from material science, to chemistry, to structural biology, and to high energy physics. This has led to ground breaking discoveries but new science brings new challenges and access to experimental time at XFELs is presently one of the major limitations. Currently, there are only two high energy XFELs in operation in the world (i.e. only two experiments can take place in the world at the same time). It is exceedingly unfortunate that due to this, beamtime is so scarce, thus becoming a major limiting factor as the field progresses out of its initial stages. Fortunately, three new XFELs are currently under construction, in South Korea (PAL), in Switzerland (SwissFEL), and in Germany (European XFEL), which are expected to enter the commissioning phase in 2016 (PAL) and 2017 (European XFEL and SwissFEL). Furthermore, XFEL facilities are planned or are under initial stages of construction in Italy and China.

Along with the unprecedented new scientific opportunities, the successes of LCLS and SACLA have opened the eyes of the community for the need for further novel instrumentation developments in the field of XFELs. One challenge is the production of coherent photons of higher energies (50 keV or more). Another is the production of single spike pulses that are shorter than 1 fs. In addition, optics, diagnostics, detectors, sample delivery, and data acquisition must continue to be developed to keep up with the new development in data acquisition speed and X-ray pulse duration and intensity. Lower noise and higher dynamic range detectors are needed to take full advantage of these scientific opportunities. In this sense, a second generation of XFEL-capable detectors, the ePix family, is being developed at SLAC for this purpose. In parallel with the development of second generation XFELs, a new generation of detectors are being developed to meet the technical specifications required (such as the AGIPD(Allahgholi, Becker et al. 2015) at European XFEL or the Jungfrou at SwissFEL)(Denes and Schmitt 2014).

Research in the field of structural biology can now collect nearly damage-free X-ray data on biomacromolecular nanocrystals and continues to greatly impact the field by addressing many limitations faced by traditional crystallography. Going beyond SFX, computational simulations using rubisco have shown that a serial femtosecond imaging technique on individual molecules, in combination with the oversampling phasing method, could open a new horizon of structural elucidation of macromolecules without the need to first crystallize them (Miao, Chapman et al. 2004). However, with the photon flux of current XFELs, the ultimate goal of collecting atomic resolution data on a solution of individual, non-crystallized molecules remains currently out of reach. As the technique progresses, single particle imaging to atomic resolution may become feasible with future development of XFELs and data processing. In order to obtain high resolution 3D structural information of single large protein complexes, there are several challenges that need to be overcome. First, the pulse fluence of XFELs is not yet high enough to allow the measurement of high resolution diffraction signal from a single large protein complex. This can, in principle, be overcome by improving the XFEL peak intensity and using better focusing optics. Second, the dynamic range of the detectors presently used for single-particle imaging with XFELs is ~10^3. This has to be increased by at least 1 – 2 orders of magnitude. Finally, background free sample delivery is critical for single particle imaging with XFELs. New future XFEL facilities such as the European XFEL will increase the repetition rate from 120 Hz to 27 kHz due to its superconducting linear accelerator(Altarelli and Mancuso 2014). This will represent a significant increase of the pulse repetition rate available today. However, the pulses will not be evenly distributed over the time of 1 second but are delivered in form of ten 600 µs pulse trains(Allahgholi, Becker et al. 2015). This poses further challenges for sample injection as jets have to run very fast during the duration of the pulse train, whereas sample would run without interception with the X-rays in the time between the arrivals of the pulse trains. Sample delivery systems that could match these increased repetition rates are challenging. Neither current fixed target options nor viscous jets can match the increased data collection rates. At SLAC a new XFEL, LCLS II, is under development, which will operate in the low to medium energy regime (current planning includes a maximum energy of 5 keV), which will allow for data to be collected at repetition rates up to 1 M Hz. Faster sample delivery injectors

are presently under development to meet the needs of second-generation XFEL sources. Additionally, efficient diffraction-pattern screening algorithms and parallelized execution will be necessary to reduce the raw data stream into a more manageable set of data frames containing only diffraction patterns which have a high likelihood of being usable for indexing and intensity integration. This means that saving each and every frame for post analysis will no longer be practical and data reduction will have to be performed in real time. Developing programs further like Cheetah(Barty, Kirian et al. 2014) and CASS(Foucar, Barty et al. 2012) to do both faster on-the-fly analysis would allow researchers to pass this information directly to indexing programs for auto-indexing on-the-fly without the need to save any intermediate data. Due to their effectiveness and high speed, Cheetah(Barty, Kirian et al. 2014) and CASS(Foucar, Barty et al. 2012), have been demonstrated to be essential in the first stages of SFX data treatment.

To support next generation XFEL facilities, new features are continually under development to meet the constantly evolving needs of new experiments. In fact, while originally designed for implementation at LCLS, Cheetah has undergone several updates in the last year and a half and has now been implemented in serial millisecond crystallography experiments at synchrotron sources (https://github.com/antonbarty/cheetah(Nogly, James et al. 2015)) and for SFX data collected at SACLA (https://github.com/biochem-fan/cheetah/commits/online). In addition to Cheetah and CASS software, a new software system called Karabo is currently under development at the European XFEL. European users will have access to CrystFEL through Karabo to enable fast data analysis required by the immense data acquisition challenge.

With proof of principle experiments already displaying the breadth of the technique, it is clear that the future is not just bright but brilliant. As SFX emerges from its infancy, it is apparent that molecular movies will provide a bedrock for new advances and discoveries from structural biology, to medicine, to energy conversion.

Table 2.2 Details of the Structures Depicted in Figure 2.5.

[1] denotes experiments done at LCLS; [2] denotes experiments done at SACLA

Protein Name	Organism	DB Code	Protein Classification	Resolution	Space Group	Unit cell	R_{work}, R_{free}	Year	Reference
photosystem I	*Thermosynechococcus elongatus*	3PCQ	membrane	8.98 Å	$P6_3$	281.0, 281.0, 165.2 90, 90, 120	0.25, 0.23	2010[1]	(Chapman et al., 2011)
FABP3	*Homo sapiens*	3WXQ	soluble	1.6 Å	$P2_12_12_1$	133.25, 226.26, 307.09 90, 90, 90	0.178, 0.222	2014[2]	(Sugahara et al., 2015)
purple bacterial reaction center	*Blastochloris viridis*	4CAS	membrane	3.5 Å	$P2_12_12_1$	104.8, 104.8, 104.8 90, 90, 90	0.295, 0.329	2013[1]	(Johansson et al., 2013)
lysozyme	*Gallus gallus*	4ET8	soluble	1.9 Å	$P4_32_12$	33.71, 54.85, 70,66 90, 90, 90	0.196, 0.229	2012[1]	(Boutet et al., 2012)
cathepsin B	*Trypanosoma brucei*	4HWY	soluble	2.1 Å	$P4_22_12$	57.90, 84.80, 384.30 90, 90, 90	0.182, 0.213	2012[1]	(Redecke et al., 2013)
serotonin receptor 5-HT2B	*Homo sapiens*	4NC3	membrane	2.8 Å	$C222_1$	79.0, 79.0, 38.0 90, 90, 90	0.227, 0.270	2013[1]	(Liu et al., 2013)
photosystem II	*Thermosynechococcus elongatus*	4PBU	membrane	5.0 Å	$P2_12_12_1$	125.40, 125.40, 54.56 90, 90, 90	0.262, 0.261	2014[1]	(Kupitz et al., 2014)
δ-opioid receptor	*Homo sapiens*	4RWD	membrane	2.7 Å	C121	61.50, 122.20, 168.50 90, 90, 90	0.208, 0.238	2014[1]	(Fenalti et al., 2015)
smoothened receptor	*Homo sapiens*	4O9R	membrane	3.2 Å	$P12_11$	40.50, 157.30, 52.40 90, 97, 90	0.232, 0.278	2014[1]	(Weierstall et al., 2014)
Cry3A	*Bacillus thuringiensis*	QX0	soluble	2.8 Å	$C222_1$	116.88, 134.81, 105.15 90, 90, 90	0.165, 0.192	2014[1]	(Sawaya et al., 2014)
CPV17 polyhedrin	*Uranotaenia sapphirina cypovirus*	4S1K	soluble	2.2 Å	I23	156.23, 89.29, 96.42 90, 92.30, 90	0.14, 0.19	2015[1]	(Ginn et al., 2015)
diacylglycerol kinase	*Escherichia coli*	4UYO	membrane	2.18 Å	$P2_12_12_1$	75.30, 91.80, 141.70 90, 90, 90	0.208, 0.236	2014[1]	(Li et al., 2015)
xylose isomerase	*Streptomyces rubiginosus*	4W4Q	soluble	2.0 Å	I222	94.00, 100.00, 103.00 90, 90, 90	0.159, 0.196	2014[2]	(Sugahara et al., 2015)
photoactive yellow protein	*Halorhodospira halophila*	4WL9	soluble	1.6 Å	$P6_3$	66.90, 66.90, 40.80 90, 90, 90	0.198, 0.231	2014[1]	(Tenboer et al., 2014)
SR Ca^{2+}-ATPase	*Oryctolagus cuniculus*	4XOU	membrane	2.8 Å	C121	162.00, 76.30, 151.10 90, 109, 90	0.304, 0.343	2015[1]	(Bublitz et al., 2015)
angiotensin II receptor	*Homo sapiens*	4YAY	membrane	2.9 Å	C121	72.80, 41.00, 167.70 90, 99.40, 90	0.228, 0.274	2015[1]	(Zhang et al., 2015)
phycocyanin	*Thermosynechococcus elongatus*	4Z8K	soluble	2.5 Å	$P6_3$	153.40, 153.40, 39.64 90, 90, 120	0.187, 0.255	2015[1]	(Conrad et al., 2015)
luciferin regenerating enzyme	*Photinus pyralis*	5D9B	soluble	1.5 Å	$P2_12_12_1$	186.38, 186.38, 60.34 90, 90, 120	0.184, 0.232	2015[2]	(Yamashita et al., 2015)
C-phycocyanin	*Thermosynechococcus elongatus*	4ZIZ	soluble	1.75 Å	H32	109.24, 109.24, 452.64 90, 90, 90	0.204, 0.254	2015[1]	(Fromme et al., 2015)
rhodopsin-arrestin complex	*Homo sapiens*	4ZWJ	membrane, soluble	3.3 Å	$P2_12_12_1$	48.21, 77.59, 84.76 90, 90, 90	0.252, 0.293	2015[1]	(Kang et al., 2015)

References

Abdallah, B. G., S. Roy-Chowdhury, J. Coe, P. Fromme and A. Ros (2015). "High Throughput Protein Nanocrystal Fractionation in a Microfluidic Sorter." Analytical chemistry **87**(8): 4159-4167.

Ackermann, W., G. Asova, V. Ayvazyan, A. Azima, N. Baboi, J. Bähr, V. Balandin, B. Beutner, A. Brandt and A. Bolzmann (2007). "Operation of a free-electron laser from the extreme ultraviolet to the water window." Nature photonics **1**(6): 336-342.

Allahgholi, A., J. Becker, L. Bianco, A. Delfs, R. Dinapoli, P. Goettlicher, H. Graafsma, D. Greiffenberg, H. Hirsemann and S. Jack (2015). "AGIPD, a high dynamic range fast detector for the European XFEL." Journal of Instrumentation **10**(01): C01023.

Altarelli, M. (2010). "From 3rd-to 4th-generation light sources: Free-electron lasers in the X-ray range." Crystallography Reports **55**(7): 1145-1151.

Altarelli, M. and A. P. Mancuso (2014). "Structural biology at the European X-ray free-electron laser facility." Philosophical Transactions of the Royal Society of London B: Biological Sciences **369**(1647): 20130311.

Aquila, A., M. S. Hunter, R. B. Doak, R. A. Kirian, P. Fromme, T. A. White, J. Andreasson, D. Arnlund, S. Bajt and T. R. Barends (2012). "Time-resolved protein nanocrystallography using an X-ray free-electron laser." Optics express **20**(3): 2706-2716.

Arnlund, D., L. C. Johansson, C. Wickstrand, A. Barty, G. J. Williams, E. Malmerberg, J. Davidsson, D. Milathianaki, D. P. DePonte and R. L. Shoeman (2014). "Visualizing a protein quake with time-resolved X-ray scattering at a free-electron laser." Nature methods **11**(9): 923-926.

Ayvazyan, V., N. Baboi, J. Bähr, V. Balandin, B. Beutner, A. Brandt, I. Bohnet, A. Bolzmann, R. Brinkmann and O. Brovko (2006). "First operation of a free-electron laser generating GW power radiation at 32 nm wavelength." The European Physical Journal D-Atomic, Molecular, Optical and Plasma Physics **37**(2): 297-303.

Balbirnie, M., R. Grothe and D. S. Eisenberg (2001). "An amyloid-forming peptide from the yeast prion Sup35 reveals a dehydrated β-sheet structure for amyloid." Proceedings of the National Academy of Sciences **98**(5): 2375-2380.

Barends, T. R., L. Foucar, A. Ardevol, K. Nass, A. Aquila, S. Botha, R. B. Doak, K. Falahati, E. Hartmann and M. Hilpert (2015). "Direct observation of ultrafast collective motions in CO myoglobin upon ligand dissociation." Science **350**(6259): 445-450.

Barends, T. R., L. Foucar, A. Ardevol, K. Nass, A. Aquila, S. Botha, R. B. Doak, K. Falahati, E. Hartmann and M. Hilpert (2015). "Direct observation of ultrafast collective motions in CO myoglobin upon ligand dissociation." Science: aac5492.

Barends, T. R., L. Foucar, S. Botha, R. B. Doak, R. L. Shoeman, K. Nass, J. E. Koglin, G. J. Williams, S. Boutet and M. Messerschmidt (2014). "De novo protein crystal structure determination from X-ray free-electron laser data." Nature **505**(7482): 244-247.

Barty, A., C. Caleman, A. Aquila, N. Timneanu, L. Lomb, T. A. White, J. Andreasson, D. Arnlund, S. Bajt and T. R. Barends (2012). "Self-terminating diffraction gates femtosecond X-ray nanocrystallography measurements." Nature Photonics **6**(1): 35-40.

Barty, A., R. A. Kirian, F. R. Maia, M. Hantke, C. H. Yoon, T. A. White and H. Chapman (2014). "Cheetah: software for high-throughput reduction and analysis of serial femtosecond X-ray diffraction data." Journal of Applied Crystallography **47**(3): 1118-1131.

Berne, B. J. and R. Pecora (1976). Dynamic light scattering: with applications to chemistry, biology, and physics, Courier Corporation.

Bolduc, J. M., D. H. Dyer, W. G. Scott, P. Singer, R. M. Sweet, D. Koshland and B. L. Stoddard (1995). "Mutagenesis and Laue structures of enzyme intermediates: isocitrate dehydrogenase." Science **268**(5215): 1312-1318.

Boutet, S., L. Lomb, G. J. Williams, T. R. Barends, A. Aquila, R. B. Doak, U. Weierstall, D. P. DePonte, J. Steinbrener and R. L. Shoeman (2012). "High-resolution protein structure determination by serial femtosecond crystallography." Science **337**(6092): 362-364.

Boutet, S., L. Lomb, G. J. Williams, T. R. Barends, A. Aquila, R. B. Doak, U. Weierstall, D. P. DePonte, J. Steinbrener, R. L. Shoeman, M. Messerschmidt, A. Barty, T. A. White, S. Kassemeyer, R. A. Kirian, M. M. Seibert, P. A. Montanez, C. Kenney, R. Herbst, P. Hart, J. Pines, G. Haller, S. M. Gruner, H. T. Philipp, M. W. Tate, M. Hromalik, L. J. Koerner, N. van Bakel, J. Morse, W. Ghonsalves, D. Arnlund, M. J. Bogan, C. Caleman, R. Fromme, C. Y. Hampton, M. S. Hunter, L. C. Johansson, G. Katona, C. Kupitz, M. Liang, A. V. Martin, K. Nass, L. Redecke, F. Stellato, N. Timneanu, D. Wang, N. A. Zatsepin, D. Schafer, J. Defever, R. Neutze, P. Fromme, J. C. Spence, H. N. Chapman and I. Schlichting (2012). "High-resolution protein structure determination by serial femtosecond crystallography." Science **337**(6092): 362-364.

Bublitz, M., K. Nass, N. D. Drachmann, A. J. Markvardsen, M. J. Gutmann, T. R. Barends, D. Mattle, R. L. Shoeman, R. B. Doak and S. Boutet (2015). "Structural studies of P-type ATPase–ligand complexes using an X-ray free-electron laser." IUCrJ **2**(4): 409-420.

Burmeister, W. P. (2000). "Structural changes in a cryo-cooled protein crystal owing to radiation damage." Acta Crystallographica Section D: Biological Crystallography **56**(3): 328-341.

Caffrey, M. (2015). "A comprehensive review of the lipid cubic phase or in meso method for crystallizing membrane and soluble proteins and complexes." Acta Crystallographica Section F: Structural Biology Communications **71**(1): 3-18.

Carr, B. and A. Malloy (2006). NanoParticle Tracking Analysis–The NANOSIGHT system.

Carugo, O. and K. D. Carugo (2005). "When X-rays modify the protein structure: radiation damage at work." Trends in Biochemical Sciences **30**(4): 213-219.

Chapman, H. N., A. Barty, S. Marchesini, A. Noy, S. P. Hau-Riege, C. Cui, M. R. Howells, R. Rosen, H. He and J. C. Spence (2006). "High-resolution ab initio three-dimensional x-ray diffraction microscopy." JOSA A **23**(5): 1179-1200.

Chapman, H. N., P. Fromme, A. Barty, T. A. White, R. A. Kirian, A. Aquila, M. S. Hunter, J. Schulz, D. P. DePonte and U. Weierstall (2011). "Femtosecond X-ray protein nanocrystallography." Nature **470**(7332): 73-77.

Chen, A. U. and O. A. Basaran (2002). "A new method for significantly reducing drop radius without reducing nozzle radius in drop-on-demand drop production." Physics of fluids **14**: L1-L4.

Cheng, A., B. Hummel, H. Qiu and M. Caffrey (1998). "A simple mechanical mixer for small viscous lipid-containing samples." Chemistry and Physics of Lipids **95**(1): 11-21.

Cohen, A. E., S. M. Soltis, A. Gonzalez, L. Aguila, R. Alonso-Mori, C. O. Barnes, E. L. Baxter, W. Brehmer, A. S. Brewster, A. T. Brunger, G. Calero, J. F. Chang, M. Chollet, P. Ehrensberger, T. L. Eriksson, Y. Feng, J. Hattne, B. Hedman, M. Hollenbeck, J. M. Holton, S. Keable, B. K. Kobilka, E. G. Kovaleva, A. C. Kruse, H. T. Lemke, G. Lin, A. Y. Lyubimov, A. Manglik, Mathews, II, S. E. McPhillips, S. Nelson, J. W. Peters, N. K. Sauter,

C. A. Smith, J. Song, H. P. Stevenson, Y. Tsai, M. Uervirojnangkoorn, V. Vinetsky, S. Wakatsuki, W. I. Weis, O. A. Zadvornyy, O. B. Zeldin, D. Zhu and K. O. Hodgson (2014). "Goniometer-based femtosecond crystallography with X-ray free electron lasers." Proc Natl Acad Sci U S A **111**(48): 17122-17127.

Conrad, C. E., S. Basu, D. James, D. Wang, A. Schaffer, S. Roy-Chowdhury, N. A. Zatsepin, A. Aquila, J. Coe and C. Gati (2015). "A novel inert crystal delivery medium for serial femtosecond crystallography." IUCrJ **2**(4): 421-430.

Conrad, C. E., S. Basu, D. James, D. Wang, A. Schaffer, S. Roy-Chowdhury, N. A. Zatsepin, A. Aquila, J. Coe, C. Gati, M. S. Hunter, J. E. Koglin, C. Kupitz, G. Nelson, G. Subramanian, T. A. White, Y. Zhao, J. Zook, S. Boutet, V. Cherezov, J. C. Spence, R. Fromme, U. Weierstall and P. Fromme (2015). "A novel inert crystal delivery medium for serial femtosecond crystallography." IUCrJ **2**(Pt 4): 421-430.

Cusack, S., H. Belrhali, A. Bram, M. Burghammer, A. Perrakis and C. Riekel (1998). "Small is beautiful: protein micro-crystallography." Nature Structural & Molecular Biology **5**: 634-637.

Dattoli, G. and A. Renieri (1985). Experimental and theoretical aspects of the free-electron laser. Laser handbook. Vol. 4.

Demirci, H., R. G. Sierra, H. Laksmono, R. L. Shoeman, S. Botha, T. R. Barends, K. Nass, I. Schlichting, R. B. Doak and C. Gati (2013). "Serial femtosecond X-ray diffraction of 30S ribosomal subunit microcrystals in liquid suspension at ambient temperature using an X-ray free-electron laser." Acta Crystallographica Section F: Structural Biology and Crystallization Communications **69**(9): 1066-1069.

Demirci, H., R. G. Sierra, H. Laksmono, R. L. Shoeman, S. Botha, T. R. M. Barends, K. Nass, I. Schlichting, R. B. Doak, C. Gati, G. J. Williams, S. Boutet, M. Messerschmidt, G. Jogl, A. E. Dahlberg, S. T. Gregory and M. J. Bogan (2013). "Serial femtosecond X-ray diffraction of 30S ribosomal subunit microcrystals in liquid suspension at ambient temperature using an X-ray free-electron laser." Acta Crystallographica Section F **69**(9): 1066-1069.

Denes, P. and B. Schmitt (2014). "Pixel detectors for diffraction-limited storage rings." Journal of synchrotron radiation **21**(5): 1006-1010.

DePonte, D., U. Weierstall, K. Schmidt, J. Warner, D. Starodub, J. Spence and R. Doak (2008). "Gas dynamic virtual nozzle for generation of microscopic droplet streams." Journal of Physics D: Applied Physics **41**(19): 195505.

DePonte, D. P., U. Weierstall, K. Schmidt, J. Warner, D. Starodub, J. C. H. Spence and R. B. Doak (2008). "Gas dynamic virtual nozzle for generation of microscopic droplet streams." Journal of Physics D: Applied Physics **41**(19): 195505.

Diaz-Quintana, A., W. Leibl, H. Bottin and P. Sétif (1998). "Electron transfer in photosystem I reaction centers follows a linear pathway in which iron-sulfur cluster FB is the immediate electron donor to soluble ferredoxin." Biochemistry **37**(10): 3429-3439.

Doering, D., Y.-D. Chuang, N. Andresen, K. Chow, D. Contarato, C. Cummings, E. Domning, J. Joseph, J. Pepper and B. Smith (2011). "Development of a compact fast CCD camera and resonant soft x-ray scattering endstation for time-resolved pump-probe experiments." Review of Scientific Instruments **82**(7): 073303.

Doye, J. P. and W. C. Poon (2006). "Protein crystallization in vivo." Current opinion in colloid & interface science **11**(1): 40-46.

Duisenberg, A. J. (1992). "Indexing in single-crystal diffractometry with an obstinate list of reflections." Journal of applied crystallography **25**(2): 92-96.

Emma, P., R. Akre, J. Arthur, R. Bionta, C. Bostedt, J. Bozek, A. Brachmann, P. Bucksbaum, R. Coffee and F.-J. Decker (2010). "First lasing and operation of an ångstrom-wavelength free-electron laser." nature photonics **4**(9): 641-647.

Feld, G. K., M. Heymann, W. H. Benner, T. Pardini, C.-J. Tsai, S. Boutet, M. A. Coleman, M. S. Hunter, X. Li, M. Messerschmidt, A. Opathalage, B. Pedrini, G. J. Williams, B. A. Krantz, S. Fraden, S. Hau-Riege, J. E. Evans, B. W. Segelke and M. Frank (2015). "Low-Z polymer sample supports for fixed-target serial femtosecond X-ray crystallography." Journal of Applied Crystallography **48**(4): 1072-1079.

Fenalti, G., N. A. Zatsepin, C. Betti, P. Giguere, G. W. Han, A. Ishchenko, W. Liu, K. Guillemyn, H. Zhang and D. James (2015). "Structural basis for bifunctional peptide recognition at human δ-opioid receptor." Nature structural & molecular biology.

Fenalti, G., N. A. Zatsepin, C. Betti, P. Giguere, G. W. Han, A. Ishchenko, W. Liu, K. Guillemyn, H. Zhang, D. James, D. Wang, U. Weierstall, J. C. Spence, S. Boutet, M. Messerschmidt, G. J. Williams, C. Gati, O. M. Yefanov, T. A. White, D. Oberthuer, M. Metz, C. H. Yoon, A. Barty, H. N. Chapman, S. Basu, J. Coe, C. E. Conrad, R. Fromme, P. Fromme, D. Tourwe, P. W. Schiller, B. L. Roth, S. Ballet, V. Katritch, R. C. Stevens and V. Cherezov (2015). "Structural basis for bifunctional peptide recognition at human delta-opioid receptor." Nat Struct Mol Biol **22**(3): 265-268.

Filipe, V., A. Hawe and W. Jiskoot (2010). "Critical evaluation of Nanoparticle Tracking Analysis (NTA) by NanoSight for the measurement of nanoparticles and protein aggregates." Pharmaceutical research **27**(5): 796-810.

Foucar, L., A. Barty, N. Coppola, R. Hartmann, P. Holl, U. Hoppe, S. Kassemeyer, N. Kimmel, J. Küpper and M. Scholz (2012). "CASS—CFEL-ASG software suite." Computer Physics Communications **183**(10): 2207-2213.

Fromme, P., H. Bottin, N. Krauss and P. Sétif (2002). "Crystallization and electron paramagnetic resonance characterization of the complex of photosystem I with its natural electron acceptor ferredoxin." Biophysical journal **83**(4): 1760-1773.

Fromme, R., A. Ishchenko, M. Metz, S. R. Chowdhury, S. Basu, S. Boutet, P. Fromme, T. A. White, A. Barty and J. C. Spence (2015). "Serial femtosecond crystallography of soluble proteins in lipidic cubic phase." IUCrJ **2**(5): 545-551.

Gallat, F.-X., N. Matsugaki, N. P. Coussens, K. J. Yagi, M. Boudes, T. Higashi, D. Tsuji, Y. Tatano, M. Suzuki and E. Mizohata (2014). "In vivo crystallography at X-ray free-electron lasers: the next generation of structural biology?" Philosophical Transactions of the Royal Society of London B: Biological Sciences **369**(1647): 20130497.

Galli, L., S.-K. Son, T. A. White, R. Santra, H. N. Chapman and M. H. Nanao (2015). "Towards RIP using free-electron laser SFX data." Journal of synchrotron radiation **22**(2): 249-255.

Garman, E. F. and R. L. Owen (2006). "Cryocooling and radiation damage in macromolecular crystallography." Acta Crystallographica Section D: Biological Crystallography **62**(1): 32-47.

Genick, U. K., G. E. Borgstahl, K. Ng, Z. Ren, C. Pradervand, P. M. Burke, V. Šrajer, T.-Y. Teng, W. Schildkamp and D. E. McRee (1997). "Structure of a protein photocycle intermediate by millisecond time-resolved crystallography." Science **275**(5305): 1471-1475.

Ginn, H. M., M. Messerschmidt, X. Ji, H. Zhang, D. Axford, R. J. Gildea, G. Winter, A. S. Brewster, J. Hattne and A. Wagner (2015). "Structure of CPV17 polyhedrin determined by the improved analysis of serial femtosecond crystallographic data." Nature communications **6**.

Hajdu, J. and L. N. Johnson (1990). "Progress with Laue diffraction studies on protein and virus crystals." Biochemistry **29**(7): 1669-1678.

Hart, P., S. Boutet, G. Carini, M. Dubrovin, B. Duda, D. Fritz, G. Haller, R. Herbst, S. Herrmann and C. Kenney (2012). The CSPAD megapixel x-ray camera at LCLS. SPIE Optical Engineering+ Applications, International Society for Optics and Photonics.

Hattne, J., N. Echols, R. Tran, J. Kern, R. J. Gildea, A. S. Brewster, R. Alonso-Mori, C. Glöckner, J. Hellmich and H. Laksmono (2014). "Accurate macromolecular structures using minimal measurements from X-ray free-electron lasers." Nature methods **11**(5): 545.

Hattne, J., N. Echols, R. Tran, J. Kern, R. J. Gildea, A. S. Brewster, R. Alonso-Mori, C. Glockner, J. Hellmich, H. Laksmono, R. G. Sierra, B. Lassalle-Kaiser, A. Lampe, G. Han, S. Gul, D. DiFiore, D. Milathianaki, A. R. Fry, A. Miahnahri, W. E. White, D. W. Schafer, M. M. Seibert, J. E. Koglin, D. Sokaras, T. C. Weng, J. Sellberg, M. J. Latimer, P. Glatzel, P. H. Zwart, R. W. Grosse-Kunstleve, M. J. Bogan, M. Messerschmidt, G. J. Williams, S. Boutet, J. Messinger, A. Zouni, J. Yano, U. Bergmann, V. K. Yachandra, P. D. Adams and N. K. Sauter (2014). "Accurate macromolecular structures using minimal measurements from X-ray free-electron lasers." Nat Methods **11**(5): 545-548.

Hau-Riege, S. P., R. A. London and A. Szoke (2004). "Dynamics of biological molecules irradiated by short X-ray pulses." Physical Review E **69**(5): 051906.

Helliwell, J. R., Y. P. Nieh, J. Habash, P. F. Faulder, J. Raftery, M. Cianci, M. Wulff and A. Hädener (2003). "Time-resolved and static-ensemble structural chemistry of hydroxymethylbilane synthase." Faraday discussions **122**: 131-144.

Hirata, K., K. Shinzawa-Itoh, N. Yano, S. Takemura, K. Kato, M. Hatanaka, K. Muramoto, T. Kawahara, T. Tsukihara and E. Yamashita (2014). "Determination of damage-free crystal structure of an X-ray-sensitive protein using an XFEL." Nature Methods **11**(7): 734-736.

Hofbauer, W., A. Zouni, R. Bittl, J. Kern, P. Orth, F. Lendzian, P. Fromme, H. Witt and W. Lubitz (2001). "Photosystem II single crystals studied by EPR spectroscopy at 94 GHz: The tyrosine radical Y." Proceedings of the National Academy of Sciences **98**(12): 6623-6628.

Holton, J. M. (2009). "A beginner's guide to radiation damage." Journal of synchrotron radiation **16**(2): 133-142.

Howells, M. R., T. Beetz, H. N. Chapman, C. Cui, J. Holton, C. Jacobsen, J. Kirz, E. Lima, S. Marchesini and H. Miao (2009). "An assessment of the resolution limitation due to radiation-damage in X-ray diffraction microscopy." Journal of electron spectroscopy and related phenomena **170**(1-3): 4-12.

Hunter, M. S., B. Segelke, M. Messerschmidt, G. J. Williams, N. A. Zatsepin, A. Barty, W. H. Benner, D. B. Carlson, M. Coleman and A. Graf (2014). "Fixed-target protein serial microcrystallography with an x-ray free electron laser." Scientific reports **4**.

Ibrahim, M., R. Chatterjee, J. Hellmich, R. Tran, M. Bommer, V. K. Yachandra, J. Yano, J. Kern and A. Zouni (2015). "Improvements in serial femtosecond crystallography of photosystem II by optimizing crystal uniformity using microseeding procedures." Structural Dynamics **2**(4): 041705.

Johansson, L. C., D. Arnlund, G. Katona, T. A. White, A. Barty, D. P. DePonte, R. L. Shoeman, C. Wickstrand, A. Sharma and G. J. Williams (2013). "Structure of a photosynthetic reaction centre determined by serial femtosecond crystallography." Nature communications **4**.

Johansson, L. C., D. Arnlund, G. Katona, T. A. White, A. Barty, D. P. DePonte, R. L. Shoeman, C. Wickstrand, A. Sharma, G. J. Williams, A. Aquila, M. J. Bogan, C. Caleman, J. Davidsson, R. B. Doak, M. Frank, R. Fromme,

L. Galli, I. Grotjohann, M. S. Hunter, S. Kassemeyer, R. A. Kirian, C. Kupitz, M. Liang, L. Lomb, E. Malmerberg, A. V. Martin, M. Messerschmidt, K. Nass, L. Redecke, M. M. Seibert, J. Sjohamn, J. Steinbrener, F. Stellato, D. Wang, W. Y. Wahlgren, U. Weierstall, S. Westenhoff, N. A. Zatsepin, S. Boutet, J. C. Spence, I. Schlichting, H. N. Chapman, P. Fromme and R. Neutze (2013). "Structure of a photosynthetic reaction centre determined by serial femtosecond crystallography." Nat Commun **4**: 2911.

Johansson, L. C., D. Arnlund, T. A. White, G. Katona, D. P. DePonte, U. Weierstall, R. B. Doak, R. L. Shoeman, L. Lomb and E. Malmerberg (2012). "Lipidic phase membrane protein serial femtosecond crystallography." Nature Methods **9**(3): 263-265.

Jordan, P., P. Fromme, H. T. Witt, O. Klukas, W. Saenger and N. Krauß (2001). "Three-dimensional structure of cyanobacterial photosystem I at 2.5 Å resolution." Nature **411**(6840): 909-917.

Kabsch, W. (2010). "Xds." Acta Crystallographica Section D: Biological Crystallography **66**(2): 125-132.

Kang, Y., X. E. Zhou, X. Gao, Y. He, W. Liu, A. Ishchenko, A. Barty, T. A. White, O. Yefanov and G. W. Han (2015). "Crystal structure of rhodopsin bound to arrestin by femtosecond X-ray laser." Nature **523**(7562): 561-567.

Katona, G., U. Andreasson, E. M. Landau, L.-E. Andreasson and R. Neutze (2003). "Lipidic cubic phase crystal structure of the photosynthetic reaction centre from Rhodobacter sphaeroides at 2.35 Å resolution." Journal of molecular biology **331**(3): 681-692.

Keedy, D. A., L. R. Kenner, M. Warkentin, R. A. Woldeyes, J. B. Hopkins, M. C. Thompson, A. S. Brewster, A. H. Van Benschoten, E. L. Baxter, M. Uervirojnangkoorn, S. E. McPhillips, J. Song, R. Alonso-Mori, J. M. Holton, W. I. Weis, A. T. Brunger, S. M. Soltis, H. Lemke, A. Gonzalez, N. K. Sauter, A. E. Cohen, H. van den Bedem, R. E. Thorne and J. S. Fraser (2015). "Mapping the conformational landscape of a dynamic enzyme by multitemperature and XFEL crystallography." eLife **4**: e07574.

Kern, J., R. Alonso-Mori, J. Hellmich, R. Tran, J. Hattne, H. Laksmono, C. Glöckner, N. Echols, R. G. Sierra, J. Sellberg, B. Lassalle-Kaiser, R. J. Gildea, P. Glatzel, R. W. Grosse-Kunstleve, M. J. Latimer, T. A. McQueen, D. DiFiore, A. R. Fry, M. Messerschmidt, A. Miahnahri, D. W. Schafer, M. M. Seibert, D. Sokaras, T.-C. Weng, P. H. Zwart, W. E. White, P. D. Adams, M. J. Bogan, S. Boutet, G. J. Williams, J. Messinger, N. K. Sauter, A. Zouni, U. Bergmann, J. Yano and V. K. Yachandra (2012). "Room temperature femtosecond X-ray diffraction of photosystem II microcrystals." Proceedings of the National Academy of Sciences of the United States of America **109**(25): 9721-9726.

Kern, J., R. Alonso-Mori, R. Tran, J. Hattne, R. J. Gildea, N. Echols, C. Glöckner, J. Hellmich, H. Laksmono and R. G. Sierra (2013). "Simultaneous femtosecond X-ray spectroscopy and diffraction of photosystem II at room temperature." Science **340**(6131): 491-495.

Kirian, R. A., R. J. Bean, K. R. Beyerlein, O. M. Yefanov, T. A. White, A. Barty and H. N. Chapman (2014). "Phasing coherently illuminated nanocrystals bounded by partial unit cells." Philosophical Transactions of the Royal Society of London B: Biological Sciences **369**(1647): 20130331.

Kirian, R. A., X. Wang, U. Weierstall, K. E. Schmidt, J. C. Spence, M. Hunter, P. Fromme, T. White, H. N. Chapman and J. Holton (2010). "Femtosecond protein nanocrystallography—data analysis methods." Optics express **18**(6): 5713-5723.

Kirian, R. A., T. A. White, J. M. Holton, H. N. Chapman, P. Fromme, A. Barty, L. Lomb, A. Aquila, F. R. Maia and A. V. Martin (2011). "Structure-factor analysis of femtosecond microdiffraction patterns from protein nanocrystals." Acta Crystallographica Section A: Foundations of Crystallography **67**(2): 131-140.

Koerner, L. J., H. T. Philipp, M. S. Hromalik, M. W. Tate and S. M. Gruner (2009). "X-ray tests of a Pixel Array Detector for coherent x-ray imaging at the Linac Coherent Light Source." Journal of Instrumentation **4**(03): P03001.

Koopmann, R., K. Cupelli, L. Redecke, K. Nass, D. P. DePonte, T. A. White, F. Stellato, D. Rehders, M. Liang and J. Andreasson (2012). "In vivo protein crystallization opens new routes in structural biology." Nature methods **9**(3): 259-262.

Kupitz, C., S. Basu, I. Grotjohann, R. Fromme, N. A. Zatsepin, K. N. Rendek, M. S. Hunter, R. L. Shoeman, T. A. White and D. Wang (2014). "Serial time-resolved crystallography of photosystem II using a femtosecond X-ray laser." Nature **513**(7517): 261-265.

Kupitz, C., I. Grotjohann, C. E. Conrad, S. Roy-Chowdhury, R. Fromme and P. Fromme (2014). "Microcrystallization techniques for serial femtosecond crystallography using photosystem II from Thermosynechococcus elongatus as a model system." Philosophical Transactions of the Royal Society of London B: Biological Sciences **369**(1647): 20130316.

Lawrence, R. M., C. E. Conrad, N. A. Zatsepin, T. D. Grant, H. Liu, D. James, G. Nelson, G. Subramanian, A. Aquila and M. S. Hunter (2015). "Serial femtosecond X-ray diffraction of enveloped virus microcrystals." Structural Dynamics **2**(4): 041720.

Lawrence, R. M., C. E. Conrad, N. A. Zatsepin, T. D. Grant, H. Liu, D. James, G. Nelson, G. Subramanian, A. Aquila, M. S. Hunter, M. Liang, S. Boutet, J. Coe, J. C. H. Spence, U. Weierstall, W. Liu, P. Fromme, V. Cherezov and B. G. Hogue (2015). "Serial femtosecond X-ray diffraction of enveloped virus microcrystals." Structural Dynamics **2**(4): 041720.

Lee, H. H., I. Cherni, H. Yu, R. Fromme, J. D. Doran, I. Grotjohann, M. Mittman, S. Basu, A. Deb, K. Dorner, A. Aquila, A. Barty, S. Boutet, H. N. Chapman, R. B. Doak, M. S. Hunter, D. James, R. A. Kirian, C. Kupitz, R. M. Lawrence, H. Liu, K. Nass, I. Schlichting, K. E. Schmidt, M. M. Seibert, R. L. Shoeman, J. C. Spence, F. Stellato, U. Weierstall, G. J. Williams, C. Yoon, D. Wang, N. A. Zatsepin, B. G. Hogue, N. Matoba, P. Fromme and T. S. Mor (2014). "Expression, purification and crystallization of CTB-MPR, a candidate mucosal vaccine component against HIV-1." IUCrJ **1**(Pt 5): 305-317.

Li, D., J. A. Lyons, V. E. Pye, L. Vogeley, D. Aragão, C. P. Kenyon, S. T. Shah, C. Doherty, M. Aherne and M. Caffrey (2013). "Crystal structure of the integral membrane diacylglycerol kinase." Nature **497**(7450): 521-524.

Li, D., P. J. Stansfeld, M. S. Sansom, A. Keogh, L. Vogeley, N. Howe, J. A. Lyons, D. Aragao, P. Fromme and R. Fromme (2015). "Ternary structure reveals mechanism of a membrane diacylglycerol kinase." Nature communications **6**.

Li, D., P. J. Stansfeld, M. S. Sansom, A. Keogh, L. Vogeley, N. Howe, J. A. Lyons, D. Aragao, P. Fromme, R. Fromme, S. Basu, I. Grotjohann, C. Kupitz, K. Rendek, U. Weierstall, N. A. Zatsepin, V. Cherezov, W. Liu, S. Bandaru, N. J. English, C. Gati, A. Barty, O. Yefanov, H. N. Chapman, K. Diederichs, M. Messerschmidt, S. Boutet, G. J. Williams, M. Marvin Seibert and M. Caffrey (2015). "Ternary structure reveals mechanism of a membrane diacylglycerol kinase." Nat Commun **6**: 10140.

Liao, J., H. Li, W. Zeng, D. B. Sauer, R. Belmares and Y. Jiang (2012). "Structural insight into the ion-exchange mechanism of the sodium/calcium exchanger." Science **335**(6069): 686-690.

Liu, H., B. K. Poon, D. K. Saldin, J. C. Spence and P. H. Zwart (2013). "Three-dimensional single-particle imaging using angular correlations from X-ray laser data." Acta Crystallographica Section A: Foundations of Crystallography **69**(4): 365-373.

Liu, H. and J. C. Spence (2014). "The indexing ambiguity in serial femtosecond crystallography (SFX) resolved using an expectation maximization algorithm." IUCrJ **1**(6): 393-401.

Liu, W., A. Ishchenko and V. Cherezov (2014). "Preparation of microcrystals in lipidic cubic phase for serial femtosecond crystallography." Nature protocols **9**(9): 2123-2134.

Liu, W., D. Wacker, C. Gati, G. W. Han, D. James, D. Wang, G. Nelson, U. Weierstall, V. Katritch and A. Barty (2013). "Serial femtosecond crystallography of G protein–coupled receptors." Science **342**(6165): 1521-1524.

Liu, W., D. Wacker, C. Gati, G. W. Han, D. James, D. Wang, G. Nelson, U. Weierstall, V. Katritch, A. Barty, N. A. Zatsepin, D. Li, M. Messerschmidt, S. Boutet, G. J. Williams, J. E. Koglin, M. M. Seibert, C. Wang, S. T. Shah, S. Basu, R. Fromme, C. Kupitz, K. N. Rendek, I. Grotjohann, P. Fromme, R. A. Kirian, K. R. Beyerlein, T. A. White, H. N. Chapman, M. Caffrey, J. C. Spence, R. C. Stevens and V. Cherezov (2013). "Serial femtosecond crystallography of G protein-coupled receptors." Science **342**(6165): 1521-1524.

Liu, W., D. Wacker, C. Wang, E. Abola and V. Cherezov (2014). "Femtosecond crystallography of membrane proteins in the lipidic cubic phase." Philosophical Transactions of the Royal Society of London B: Biological Sciences **369**(1647): 20130314.

Lomb, L., T. R. Barends, S. Kassemeyer, A. Aquila, S. W. Epp, B. Erk, L. Foucar, R. Hartmann, B. Rudek and D. Rolles (2011). "Radiation damage in protein serial femtosecond crystallography using an x-ray free-electron laser." Physical Review B **84**(21): 214111.

Lyubimov, A. Y., T. D. Murray, A. Koehl, I. E. Araci, M. Uervirojnangkoorn, O. B. Zeldin, A. E. Cohen, S. M. Soltis, E. L. Baxter, A. S. Brewster, N. K. Sauter, A. T. Brunger and J. M. Berger (2015). "Capture and X-ray diffraction studies of protein microcrystals in a microfluidic trap array." Acta Crystallogr D Biol Crystallogr **71**(Pt 4): 928-940.

Madey, J. M. (1971). "Stimulated emission of bremsstrahlung in a periodic magnetic field." Journal of Applied Physics **42**(5): 1906-1913.

McNeil, B. W. and N. R. Thompson (2010). "X-ray free-electron lasers." Nature photonics **4**(12): 814.

McPherson, A. (1999). Crystallization of biological macromolecules, Cold Spring Harbor Laboratory Press.

McPherson, A. and B. Cudney (2014). "Optimization of crystallization conditions for biological macromolecules." Acta Crystallographica Section F: Structural Biology Communications **70**(11): 1445-1467.

Miao, J., H. N. Chapman, J. Kirz, D. Sayre and K. O. Hodgson (2004). "Taking X-Ray Diffraction to the Limit: Macromolecular Structures from Femtosecond X-Ray Pulses and Diffraction Microscopy of Cells with Synchrotron Radiation*." Annu. Rev. Biophys. Biomol. Struct. **33**: 157-176.

Moffat, K. (2001). "Time-resolved biochemical crystallography: a mechanistic perspective." Chemical reviews **101**(6): 1569-1582.

Mueller, C., A. Marx, S. W. Epp, Y. Zhong, A. Kuo, A. R. Balo, J. Soman, F. Schotte, H. T. Lemke, R. L. Owen, E. F. Pai, A. R. Pearson, J. S. Olson, P. A. Anfinrud, O. P. Ernst and R. J. Dwayne Miller (2015). "Fixed target matrix for femtosecond time-resolved and in situ serial micro-crystallography." Structural Dynamics **2**(5): 054302.

Neutze, R., R. Wouts, D. van der Spoel, E. Weckert and J. Hajdu (2000). "Potential for biomolecular imaging with femtosecond X-ray pulses." Nature **406**(6797): 752-757.

Newman, J. A., N. M. Scarborough, N. R. Pogranichniy, R. K. Shrestha, R. G. Closser, C. Das and G. J. Simpson (2015). "Intercalating dyes for enhanced contrast in second-harmonic generation imaging of protein crystals." Acta Crystallographica Section D: Biological Crystallography **71**(7): 1471-1477.

Nogly, P., D. James, D. Wang, T. A. White, N. Zatsepin, A. Shilova, G. Nelson, H. Liu, L. Johansson and M. Heymann (2015). "Lipidic cubic phase serial millisecond crystallography using synchrotron radiation." IUCrJ **2**(2): 168-176.

Owen, R. L., E. Rudiño-Piñera and E. F. Garman (2006). "Experimental determination of the radiation dose limit for cryocooled protein crystals." Proceedings of the National Academy of Sciences of the United States of America **103**(13): 4912-4917.

Pande, K., C. D. M. Hutchinson, G. Groenhof, A. Aquila, J. S. Robinson, J. Tenboer, S. Basu, S. Boutet, D. Deponte, M. Liang, T. White, N. Zatsepin, O. Yefanov, D. Morozov, D. Oberthuer, C. Gati, G. Subramanian, D. James, Y. Zhao, J. Koralek, J. Brayshaw, C. Kupitz, C. Conrad, S. Roy-Chowdhury, J. Coe, M. Metz, X. Paulraj Lourdu, T. Grant, J. Koglin, G. Ketawala, R. Fromme, V. Srajer, R. Henning, J. Spence, A. Ourmazd, P. Schwander, U. Weierstall, M. Frank, P. Fromme, A. Barty, H. Chapman, K. Moffat, J. J. Van Thor and M. Schmidt (2015). "Femtosecond Structural Dynamics Drives the Trans/Cis Isomerization in Photoactive Yellow Protein." in submission.

Pedrini, B., C. J. Tsai, G. Capitani, C. Padeste, M. S. Hunter, N. A. Zatsepin, A. Barty, W. H. Benner, S. Boutet, G. K. Feld, S. P. Hau-Riege, R. A. Kirian, C. Kupitz, M. Messerschmitt, J. I. Ogren, T. Pardini, B. Segelke, G. J. Williams, J. C. Spence, R. Abela, M. Coleman, J. E. Evans, G. F. Schertler, M. Frank and X. D. Li (2014). "7 A resolution in protein two-dimensional-crystal X-ray diffraction at Linac Coherent Light Source." Philos Trans R Soc Lond B Biol Sci **369**(1647): 20130500.

Pellegrini, C. (2012). "The history of X-ray free-electron lasers." The European Physical Journal H **37**(5): 659-708.

Pellegrini, C. and S. Reiche (2004). "The development of X-ray free-electron lasers." Selected Topics in Quantum Electronics, IEEE Journal of **10**(6): 1393-1404.

Pellegrini, C. and J. Stöhr (2003). "X-ray free-electron lasers—principles, properties and applications." Nuclear Instruments and Methods in Physics Research Section A: Accelerators, Spectrometers, Detectors and Associated Equipment **500**(1): 33-40.

Philipp, H. T., M. Hromalik, M. Tate, L. Koerner and S. M. Gruner (2011). "Pixel array detector for X-ray free electron laser experiments." Nuclear Instruments and Methods in Physics Research Section A: Accelerators, Spectrometers, Detectors and Associated Equipment **649**(1): 67-69.

Philipp, H. T., L. J. Koerner, M. S. Hromalik, M. W. Tate and S. M. Gruner (2010). "Femtosecond radiation experiment detector for x-ray free-electron laser (XFEL) coherent x-ray imaging." Nuclear Science, IEEE Transactions on **57**(6): 3795-3799.

Powell, H. R. (1999). "The Rossmann Fourier autoindexing algorithm in MOSFLM." Acta Crystallographica Section D: Biological Crystallography **55**(10): 1690-1695.

Powell, H. R., O. Johnson and A. G. Leslie (2013). "Autoindexing diffraction images with iMosflm." Acta Crystallographica Section D: Biological Crystallography **69**(7): 1195-1203.

Proteau, A., R. Shi and M. Cygler (2010). "Application of dynamic light scattering in protein crystallization." Current protocols in protein science: 17.10. 11-17.10. 19.

Ravelli, R. B. and S. M. McSweeney (2000). "The 'fingerprint'that X-rays can leave on structures." Structure **8**(3): 315-328.

Redecke, L., K. Nass, D. P. DePonte, T. A. White, D. Rehders, A. Barty, F. Stellato, M. Liang, T. R. Barends and S. Boutet (2013). "Natively inhibited Trypanosoma brucei cathepsin B structure determined by using an X-ray laser." Science **339**(6116): 227-230.

Redecke, L., K. Nass, D. P. DePonte, T. A. White, D. Rehders, A. Barty, F. Stellato, M. Liang, T. R. Barends, S. Boutet, G. J. Williams, M. Messerschmidt, M. M. Seibert, A. Aquila, D. Arnlund, S. Bajt, T. Barth, M. J. Bogan, C. Caleman, T. C. Chao, R. B. Doak, H. Fleckenstein, M. Frank, R. Fromme, L. Galli, I. Grotjohann, M. S. Hunter, L. C. Johansson, S. Kassemeyer, G. Katona, R. A. Kirian, R. Koopmann, C. Kupitz, L. Lomb, A. V. Martin, S. Mogk, R. Neutze, R. L. Shoeman, J. Steinbrener, N. Timneanu, D. Wang, U. Weierstall, N. A. Zatsepin, J. C. Spence, P. Fromme, I. Schlichting, M. Duszenko, C. Betzel and H. N. Chapman (2013). "Natively inhibited Trypanosoma brucei cathepsin B structure determined by using an X-ray laser." Science **339**(6116): 227-230.

Roessler, C. G., A. Kuczewski, R. Stearns, R. Ellson, J. Olechno, A. M. Orville, M. Allaire, A. S. Soares and A. Héroux (2013). "Acoustic methods for high-throughput protein crystal mounting at next-generation macromolecular crystallographic beamlines." Journal of synchrotron radiation **20**(5): 805-808.

Rossmann, M. G. and C. G. van Beek (1999). "Data processing." Acta Crystallographica Section D: Biological Crystallography **55**(10): 1631-1640.

Saldin, E., E. Schneidmiller and M. V. Yurkov (2013). The physics of free electron lasers, Springer Science & Business Media.

Sauter, N. K., R. W. Grosse-Kunstleve and P. D. Adams (2004). "Robust indexing for automatic data collection." Journal of applied crystallography **37**(3): 399-409.

Sawaya, M. R., D. Cascio, M. Gingery, J. Rodriguez, L. Goldschmidt, J.-P. Colletier, M. M. Messerschmidt, S. Boutet, J. E. Koglin and G. J. Williams (2014). "Protein crystal structure obtained at 2.9 Å resolution from injecting bacterial cells into an X-ray free-electron laser beam." Proceedings of the National Academy of Sciences **111**(35): 12769-12774.

Sawaya, M. R., D. Cascio, M. Gingery, J. Rodriguez, L. Goldschmidt, J. P. Colletier, M. M. Messerschmidt, S. Boutet, J. E. Koglin, G. J. Williams, A. S. Brewster, K. Nass, J. Hattne, S. Botha, R. B. Doak, R. L. Shoeman, D. P. DePonte, H. W. Park, B. A. Federici, N. K. Sauter, I. Schlichting and D. S. Eisenberg (2014). "Protein crystal structure obtained at 2.9 A resolution from injecting bacterial cells into an X-ray free-electron laser beam." Proc Natl Acad Sci U S A **111**(35): 12769-12774.

Sayre, D. (1952). "Some implications of a theorem due to Shannon." Acta Crystallographica **5**(6): 843-843.

Sayre, D. (1952). "The squaring method: a new method for phase determination." Acta Crystallographica **5**(1): 60-65.

Schlichting, I. (2015). "Serial femtosecond crystallography: the first five years." IUCrJ **2**(2): 0-0.

Schlichting, I. (2015). "Serial femtosecond crystallography: the first five years." IUCrJ **2**(2): 246-255.

Schlichting, I. and J. Miao (2012). "Emerging opportunities in structural biology with X-ray free-electron lasers." Current opinion in structural biology **22**(5): 613-626.

Schlichting, I., G. Rapp, J. John, A. Wittinghofer, E. F. Pai and R. S. Goody (1989). "Biochemical and crystallographic characterization of a complex of c-Ha-ras p21 and caged GTP with flash photolysis." Proceedings of the National Academy of Sciences **86**(20): 7687-7690.

Schmidt, M. (2013). "Mix and inject: reaction initiation by diffusion for time-resolved macromolecular crystallography." Advances in Condensed Matter Physics **2013**.

Schmidt, M., V. Srajer, R. Henning, H. Ihee, N. Purwar, J. Tenboer and S. Tripathi (2013). "Protein energy landscapes determined by five-dimensional crystallography." Acta Crystallographica Section D: Biological Crystallography **69**(12): 2534-2542.

Schotte, F., H. S. Cho, V. R. Kaila, H. Kamikubo, N. Dashdorj, E. R. Henry, T. J. Graber, R. Henning, M. Wulff and G. Hummer (2012). "Watching a signaling protein function in real time via 100-ps time-resolved Laue crystallography." Proceedings of the National Academy of Sciences **109**(47): 19256-19261.

Schubert, R., A. Meyer, K. Dierks, S. Kapis, R. Reimer, H. Einspahr, M. Perbandt and C. Betzel (2015). "Reliably distinguishing protein nanocrystals from amorphous precipitate by means of depolarized dynamic light scattering." Journal of Applied Crystallography **48**(5): 1476-1484.

Setif, P. Q. and H. Bottin (1995). "Laser flash absorption spectroscopy study of ferredoxin reduction by photosystem I: spectral and kinetic evidence for the existence of several photosystem I-ferredoxin complexes." Biochemistry **34**(28): 9059-9070.

Sierra, R. G., H. Laksmono, J. Kern, R. Tran, J. Hattne, R. Alonso-Mori, B. Lassalle-Kaiser, C. Glöckner, J. Hellmich and D. W. Schafer (2012). "Nanoflow electrospinning serial femtosecond crystallography." Acta Crystallographica Section D: Biological Crystallography **68**(11): 1584-1587.

Sierra, R. G., H. Laksmono, J. Kern, R. Tran, J. Hattne, R. Alonso-Mori, B. Lassalle-Kaiser, C. Glockner, J. Hellmich, D. W. Schafer, N. Echols, R. J. Gildea, R. W. Grosse-Kunstleve, J. Sellberg, T. A. McQueen, A. R. Fry, M. M. Messerschmidt, A. Miahnahri, M. M. Seibert, C. Y. Hampton, D. Starodub, N. D. Loh, D. Sokaras, T. C. Weng, P. H. Zwart, P. Glatzel, D. Milathianaki, W. E. White, P. D. Adams, G. J. Williams, S. Boutet, A. Zouni, J. Messinger, N. K. Sauter, U. Bergmann, J. Yano, V. K. Yachandra and M. J. Bogan (2012). "Nanoflow electrospinning serial femtosecond crystallography." Acta Crystallogr D Biol Crystallogr **68**(Pt 11): 1584-1587.

Smith, J. L., R. F. Fischetti and M. Yamamoto (2012). "Micro-crystallography comes of age." Current opinion in structural biology **22**(5): 602-612.

Soares, A. S., M. A. Engel, R. Stearns, S. Datwani, J. Olechno, R. Ellson, J. M. Skinner, M. Allaire and A. M. Orville (2011). "Acoustically mounted microcrystals yield high-resolution X-ray structures." Biochemistry **50**(21): 4399-4401.

Son, S.-K., H. N. Chapman and R. Santra (2011). "Multiwavelength anomalous diffraction at high x-ray intensity." Physical review letters **107**(21): 218102.

Son, S.-K., H. N. Chapman and R. Santra (2013). "Determination of multiwavelength anomalous diffraction coefficients at high X-ray intensity." Journal of Physics B: Atomic, Molecular and Optical Physics **46**(16): 164015.

Spence, J., U. Weierstall and H. Chapman (2012). "X-ray lasers for structural and dynamic biology." Reports on Progress in Physics **75**(10): 102601.

Spence, J. C., R. A. Kirian, X. Wang, U. Weierstall, K. E. Schmidt, T. White, A. Barty, H. N. Chapman, S. Marchesini and J. Holton (2011). "Phasing of coherent femtosecond X-ray diffraction from size-varying nanocrystals." Optics express **19**(4): 2866-2873.

Steitz, T. A., T. J. Richmond, D. Wise and D. Engelman (1974). "The lac repressor protein: molecular shape, subunit structure, and proposed model for operator interaction based on structural studies of microcrystals." Proceedings of the National Academy of Sciences **71**(3): 593-597.

Stevenson, H., D. DePonte, A. Makhov, J. F. Conway, O. Zeldin, S. Boutet, G. Calero and A. Cohen (2014). "Transmission electron microscopy as a tool for nanocrystal characterization pre-and post-injector." Philosophical Transactions of the Royal Society of London B: Biological Sciences **369**(1647): 20130322.

Stevenson, H., D. DePonte, A. Makhov, J. F. Conway, O. Zeldin, S. Boutet, G. Calero and A. Cohen (2014). "Transmission electron microscopy as a tool for nanocrystal characterization pre-and post-injector." Philosophical Transactions of the Royal Society B: Biological Sciences **369**(1647): 20130322.

Stevenson, H. P., A. M. Makhov, M. Calero, A. L. Edwards, O. B. Zeldin, Mathews, II, G. Lin, C. O. Barnes, H. Santamaria, T. M. Ross, S. M. Soltis, C. Khosla, V. Nagarajan, J. F. Conway, A. E. Cohen and G. Calero (2014). "Use of transmission electron microscopy to identify nanocrystals of challenging protein targets." Proc Natl Acad Sci U S A **111**(23): 8470-8475.

Stevenson, H. P., A. M. Makhov, M. Calero, A. L. Edwards, O. B. Zeldin, I. I. Mathews, G. Lin, C. O. Barnes, H. Santamaria and T. M. Ross (2014). "Use of transmission electron microscopy to identify nanocrystals of challenging protein targets." Proceedings of the National Academy of Sciences **111**(23): 8470-8475.

Stoddard, B. L., B. E. Cohen, M. Brubaker, A. D. Mesecar and D. E. Koshland (1998). "Millisecond Laue structures of an enzyme–product complex using photocaged substrate analogs." Nature Structural & Molecular Biology **5**(10): 891-897.

Stoddard, B. L. and G. K. Farber (1995). "Direct measurement of reactivity in the protein crystal by steady-state kinetic studies." Structure **3**(10): 991-996.

Strüder, L., S. Epp, D. Rolles, R. Hartmann, P. Holl, G. Lutz, H. Soltau, R. Eckart, C. Reich and K. Heinzinger (2010). "Large-format, high-speed, X-ray pnCCDs combined with electron and ion imaging spectrometers in a multipurpose chamber for experiments at 4th generation light sources." Nuclear Instruments and Methods in Physics Research Section A: Accelerators, Spectrometers, Detectors and Associated Equipment **614**(3): 483-496.

Suga, M., F. Akita, K. Hirata, G. Ueno, H. Murakami, Y. Nakajima, T. Shimizu, K. Yamashita, M. Yamamoto and H. Ago (2015). "Native structure of photosystem II at 1.95 A resolution viewed by femtosecond X-ray pulses." Nature **517**(7532): 99-103.

Sugahara, M., E. Mizohata, E. Nango, M. Suzuki, T. Tanaka, T. Masuda, R. Tanaka, T. Shimamura, Y. Tanaka and C. Suno (2015). "Grease matrix as a versatile carrier of proteins for serial crystallography." Nature methods **12**(1): 61-63.

Sugahara, M., E. Mizohata, E. Nango, M. Suzuki, T. Tanaka, T. Masuda, R. Tanaka, T. Shimamura, Y. Tanaka, C. Suno, K. Ihara, D. Pan, K. Kakinouchi, S. Sugiyama, M. Murata, T. Inoue, K. Tono, C. Song, J. Park, T. Kameshima, T. Hatsui, Y. Joti, M. Yabashi and S. Iwata (2015). "Grease matrix as a versatile carrier of proteins for serial crystallography." Nat Meth **12**(1): 61-63.

Tenboer, J., S. Basu, N. Zatsepin, K. Pande, D. Milathianaki, M. Frank, M. Hunter, S. Boutet, G. J. Williams and J. E. Koglin (2014). "Time-resolved serial crystallography captures high-resolution intermediates of photoactive yellow protein." Science **346**(6214): 1242-1246.

Ursby, T., M. Weik, E. Fioravanti, M. Delarue, M. Goeldner and D. Bourgeois (2002). "Cryophotolysis of caged compounds: a technique for trapping intermediate states in protein crystals." Acta Crystallographica Section D: Biological Crystallography **58**(4): 607-614.

Von Dreele, R. B. (2007). "Multipattern Rietveld refinement of protein powder data: an approach to higher resolution." Journal of Applied Crystallography **40**(1): 133-143.

Wampler, R. D., D. J. Kissick, C. J. Dehen, E. J. Gualtieri, J. L. Grey, H.-F. Wang, D. H. Thompson, J.-X. Cheng and G. J. Simpson (2008). "Selective detection of protein crystals by second harmonic microscopy." Journal of the American Chemical Society **130**(43): 14076-14077.

Wang, D., U. Weierstall, L. Pollack and J. Spence (2014). "Double-focusing mixing jet for XFEL study of chemical kinetics." Journal of synchrotron radiation **21**(6): 1364-1366.

Weierstall, U. (2014). "Liquid sample delivery techniques for serial femtosecond crystallography." Philosophical Transactions of the Royal Society of London B: Biological Sciences **369**(1647): 20130337.

Weierstall, U. (2014). "Liquid sample delivery techniques for serial femtosecond crystallography." Philos Trans R Soc Lond B Biol Sci **369**(1647): 20130337.

Weierstall, U., D. James, C. Wang, T. A. White, D. Wang, W. Liu, J. C. Spence, R. B. Doak, G. Nelson and P. Fromme (2014). "Lipidic cubic phase injector facilitates membrane protein serial femtosecond crystallography." Nature communications **5**.

Weierstall, U., J. Spence and R. Doak (2012). "Injector for scattering measurements on fully solvated biospecies." Review of Scientific Instruments **83**(3): 035108.

Wen, J. G. (2014). Transmission electron microscopy. Practical Materials Characterization, Springer**:** 189-229.

White, T. A., A. Barty, F. Stellato, J. M. Holton, R. A. Kirian, N. A. Zatsepin and H. N. Chapman (2013). "Crystallographic data processing for free-electron laser sources." Acta Crystallographica Section D: Biological Crystallography **69**(7): 1231-1240.

Wu, W., P. Nogly, J. Rheinberger, L. M. Kick, C. Gati, G. Nelson, X. Deupi, J. Standfuss, G. Schertler and V. Panneels (2015). "Batch crystallization of rhodopsin for structural dynamics using an X-ray free-electron laser." Acta Crystallographica Section F: Structural Biology Communications **71**(7): 856-860.

Yamashita, K., D. Pan, T. Okuda, M. Sugahara, A. Kodan, T. Yamaguchi, T. Murai, K. Gomi, N. Kajiyama and E. Mizohata (2015). "An isomorphous replacement method for efficient de novo phasing for serial femtosecond crystallography." Scientific reports **5**.

Yano, J., J. Kern, K.-D. Irrgang, M. J. Latimer, U. Bergmann, P. Glatzel, Y. Pushkar, J. Biesiadka, B. Loll and K. Sauer (2005). "X-ray damage to the Mn4Ca complex in single crystals of photosystem II: a case study for metalloprotein crystallography." Proceedings of the National Academy of Sciences of the United States of America **102**(34): 12047-12052.

Zhang, H., H. Unal, C. Gati, G. W. Han, W. Liu, N. A. Zatsepin, D. James, D. Wang, G. Nelson and U. Weierstall (2015). "Structure of the angiotensin receptor revealed by serial femtosecond crystallography." Cell **161**(4): 833-844.

Zhang, H., H. Unal, C. Gati, G. W. Han, W. Liu, N. A. Zatsepin, D. James, D. Wang, G. Nelson, U. Weierstall, M. R. Sawaya, Q. Xu, M. Messerschmidt, G. J. Williams, S. Boutet, O. M. Yefanov, T. A. White, C. Wang, A. Ishchenko, K. C. Tirupula, R. Desnoyer, J. Coe, C. E. Conrad, P. Fromme, R. C. Stevens, V. Katritch, S. S. Karnik and V. Cherezov (2015). "Structure of the Angiotensin receptor revealed by serial femtosecond crystallography." Cell **161**(4): 833-844.

Zhou, Q., Y. Lai, T. Bacaj, M. Zhao, A. Y. Lyubimov, M. Uervirojnangkoorn, O. B. Zeldin, A. S. Brewster, N. K. Sauter, A. E. Cohen, S. M. Soltis, R. Alonso-Mori, M. Chollet, H. T. Lemke, R. A. Pfuetzner, U. B. Choi, W. I.

Weis, J. Diao, T. C. Sudhof and A. T. Brunger (2015). "Architecture of the synaptotagmin-SNARE machinery for neuronal exocytosis." Nature **525**(7567): 62-67.

3 LARGE SCALE SAMPLE PRODUCTION: ISOLATION AND PURIFICATION OF PROTEINS FOR SERIAL CRYSTALLOGRAPHY

The Necessity for an Abundance of Sample in Serial Crystallography

In contrast to traditional crystallography where 10's of mg of a protein are usually sufficient for screening of conditions, optimization and structural determination, serial crystallography by nature often demands one or more orders of magnitude more sample with some single experiments necessitating over a gram of the biomacromolecule in question (though this has been about the limit in the authors experience). With protein production, isolation and purification procedures often taking multiple days to complete, maximization of absolute yields is essential.

One of the main perpetrators in the need for sample is the common form of sample introduction using a liquid jet. In order to maintain a stable jet, flow rates are often in the of µL/min. While this may not seem obtrusive at first, it is important to remember that a typical experiment can take over a day to collect a full data set. With concentrated slurries up to 10% v/v nanocrystals, this translates to 10's to 100's of mg's of protein for a data set. Most of this material is actually not even used for X-ray diffraction, passing through the interaction region between XFEL pulses, without interaction with the X-rays, but high flow rates are required in order to maintain a stable jet. In the following section, sample production for targets is discussed. It should be stated that each of these protein preparations were multiday events and that it took a team of people to sustain multiple protein preparations per week so as to obtain enough sample for a single experiment. Thankfully, it should be noted that at the time of writing of this document, significant efforts have been made to limit the 'wasted' sample such as use of viscous jets and fixed target approaches mentioned previously or the generation of synchronized droplets that will be discussed in chapter 5.

Photosynthesis Overview

Oxygenic Photosynthesis

Photosynthesis is arguably the most important biological process on the planet, fueling our planet with "bio" usable energy that has ultimately, in its oxygenic form, shaped our atmosphere and subsequently allowed for higher life as we know it to exist. Photosynthesis is the process by

which solar energy is converted into chemical energy, used to provide energy for the life functions of the organism performing it. This process is performed by plants, algae and cyanobacteria by converting energy from light into chemical energy through electron transfer pathways and ensuing chemical reactions. Photosynthesis can be divided into two types, oxygenic and anoxygenic. Bacteria that perform anoxygenic photosynthesis are the oldest photosynthetic organisms on the planet. They are sensitive to oxygen and possess simpler photosynthetic reaction centers, which perform the key step in Photosynthesis, the light induced charge separation. These anoxygenic reaction centers are thought to be the evolutionary ancestors of photosystem I and II found in oxygenic photosynthetic organisms (Blankenship and Hartman 1998). The focus of this research is centered on oxygenic photosynthesis.

Oxygenic photosynthesis first began about 2.5 billion years ago, driving the oxygenation of Earth's atmosphere and paving the way for advanced eukaryotes to develop. The reactions involved in oxygenic photosynthesis begin with membrane proteins embedded in thylakoid membranes, compartments that exist within cyanobacteria and the chloroplasts of plants and algae. Figure 3.1 shows a depiction of the major protein complexes in a thylakoid membrane along with a scheme showing a general path for electron transfer in these so-called "light reactions". The depictions of these protein complexes are derived from electron density maps which are determined using X-ray crystallography. Many other proteins and cofactors are necessary for the complex photosynthetic pathway to function, many of which are discussed below.

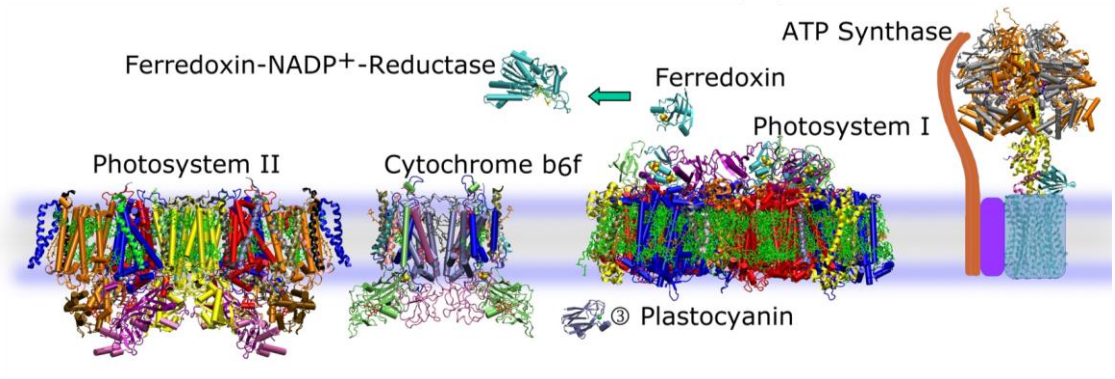

Figure 3.1 The Photosynthetic Membrane Pathway

Image showing X-ray structures of the major proteins involved in the light reactions of oxygenic photosynthesis including the electron and proton transport. Membrane is oriented with the lumen below and the stroma above. Figure originally from Fromme and Grotjohann (2008).

Electron Transfer in Oxygenic Photosynthesis

The pathway of electron transfer as a whole in photosynthesis is driven by light and essentially powered through a long redox pathway through various proteins and cofactors, gaining the potential energy from light absorption events in the photosystems. This is illustrated in the so-called 'Z-scheme' energetic representation of the pathway, shown in figure 3.2. Electron transport begins when PSII uses internal and external antenna system to capture light and induce a charge separation at the reaction center of the complex. This charge separation fuels the water spitting reaction in a five-step reaction cycle that oxidizes two water molecules and nets four electrons, four protons and a molecule of molecular oxygen per cycle. The oxidation of water occurs in the oxygen-evolving complex (OEC) of PSII and will be discussed in detail below. At the acceptor site the liberated electrons allow for a mobile plastoquinone (PQ) to be doubly reduced while taking up two protons to form plastoquinole (PQH_2) which subsequently diffuses from PSII into the thylakoid membrane. As PQH_2 is produced and released from its binding pocket in PSII, it is constantly replenished with PQ for further cycles.

PQH_2 traverses the membrane until it binds to the cytochrome b_6f complex whereby it transfers two electrons and two protons to the complex. The b_6f complex then releases the protons into the interior (lumen) of the thylakoid which, and an additional proton is pumped across the membrane in the Q-cycle. Together with the four protons released in the oxidation of water, this results in an electrochemical proton gradient across the membrane that powers ATP synthase (ATPase) through proton motive force and synthesize ATP. The electronic charge allows the b_6f complex subsequently reduces two molecules of either copper-containing plastocyanin (PC) or iron containing cytochrome c_6 (cyt c_6). Both PC and cytochrome c_6 are soluble, single-electron carriers that, upon reduction, undock and diffuse through the lumenal space before binding to and reducing PSI. The identity of the carrier varies between organisms, with plants only using PC while some cyanobacteria are able to use both, producing cyt c_6 upon only under conditions with high iron concentration in the growth media (Fromme, Melkozernov et al. 2003) conditions (Fromme, Melkozernov et al. 2003). PSI captures light by an external antenna and transfers the energy through its internal antenna system into the center of the complex, where charge separation takes

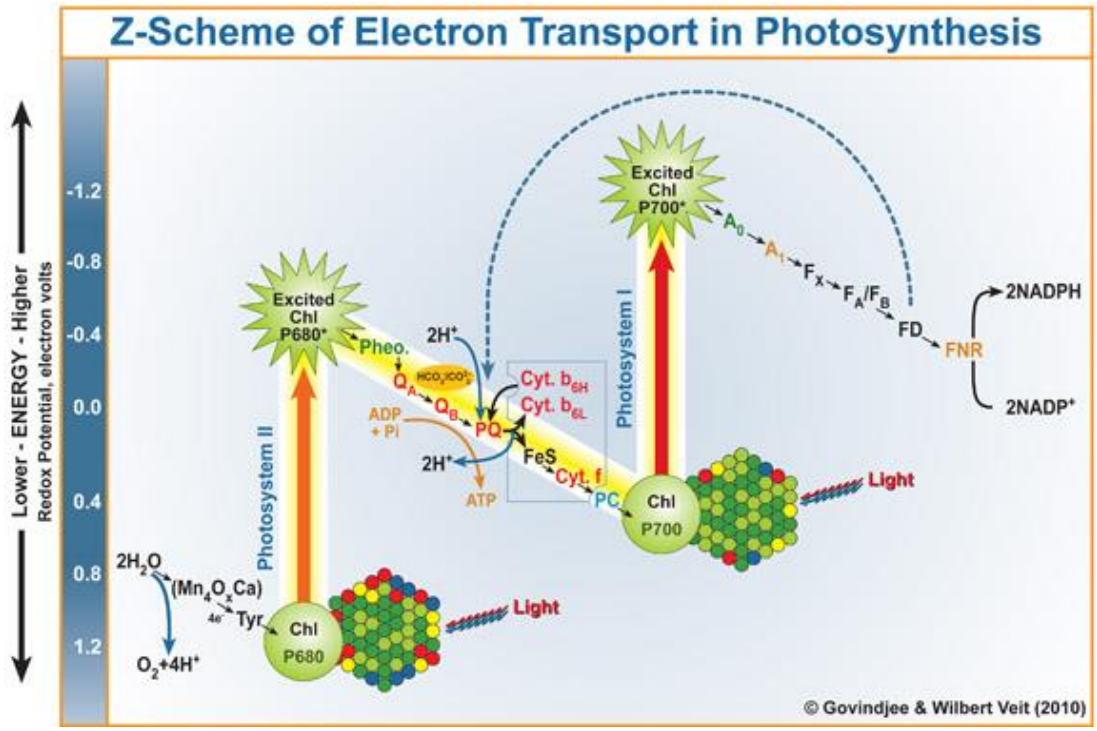

Figure 3.2 Z-Scheme of Photosynthesis

Energetic representation of the light powered energy transfer through the thylakoid membrane in oxygenic photosynthesis. From water oxidation through reduction of $NADP^+$, the pathways is an energetically downhill pathway through a series of proteins and cofactors powered by photon absorption events at the reaction centers P680 (PSII) and P700 (PSI). Figure reproduced with permission.

place. When P700 is excited it initiates light-driven charge separation transferring an electron across the membrane. PSI is thereby powered by a second solar energy absorption event. The electron is transferred at the acceptor site from the terminal FeS clusters to the soluble protein ferredoxin (Fd) which proceeds to undock from PSI and diffuses into the cytoplasm. Two Fd molecules in sequence then dock and transfer the electrons to the ferredoxin:$NADP^+$ reductase (FNR), thereby providing the electrons for the reduction of $NADP^+$ and H+ to NADPH through two charge separation events (Setif and Bottin 1995).

NADPH along with ATP and CO_2 power the Calvin-Basham-Benson cycle, creating stored energy in the form of carbohydrates, sugars and other macromolecules for the organism in these 'dark reactions' (reactions not directly dependent upon light energy). The work contained herein focuses on PSI, PSII, and ferredoxin in particular. For more general reading on photosynthesis the reader is referred to reviews by Raines (2003) or Mikkelsen, Jørgensen et al. (2010).

Structure of Photosystem I

PSI is a large membrane protein complex that utilizes energy from sunlight to drive light induced charge separation across the photosynthetic membrane. The excitation energy from the light absorption in the antenna is transferred to the primary donor P700 which upon excitation to P700* triggers a charge separation event leading to an effective transmembrane electron transfer from the lumenal to the stromal side of the membrane through a series of cofactors. Electrons from

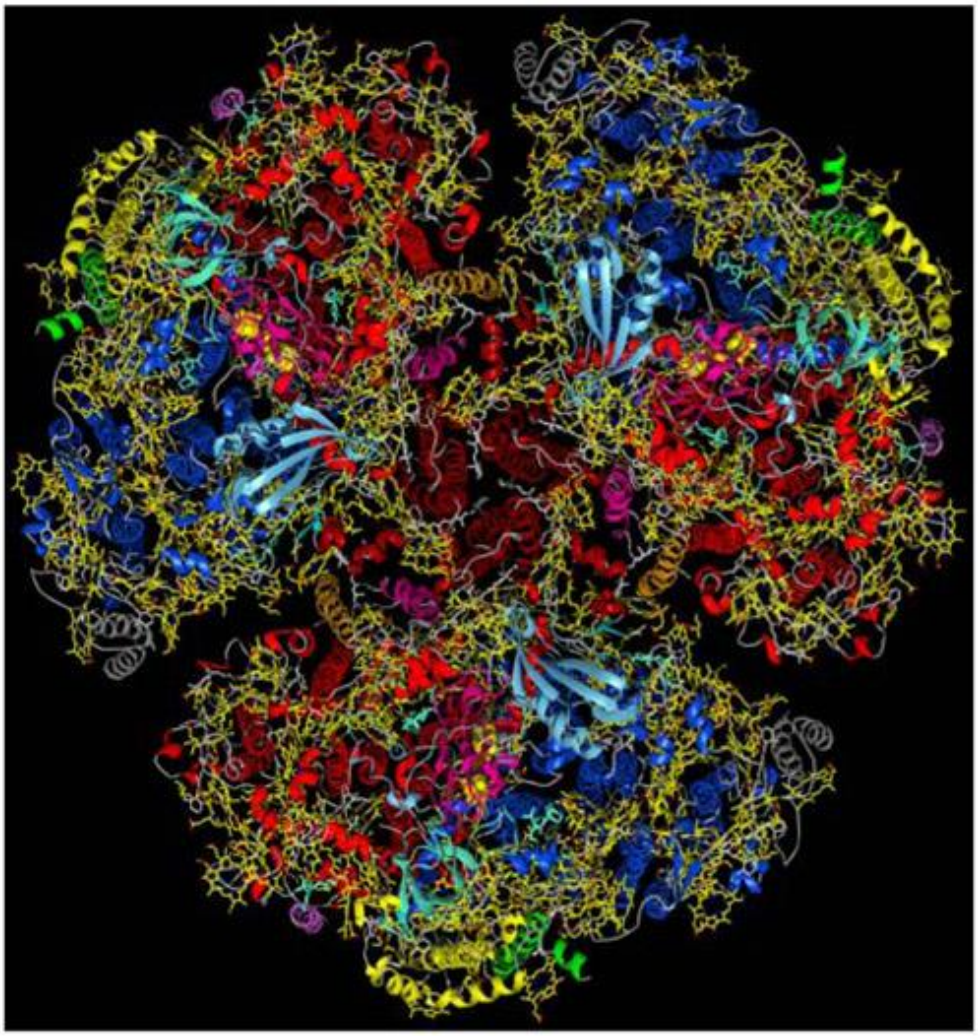

Figure 3.3 Atomic Structure of PSI (*T. elongatus*)

Structure of PSI from T. elongatus cyanobacteria at 2.5 Å (Jordan, Fromme et al. 2001) viewed normal to the membrane from the stromal side. This PSI trimer represents the largest membrane protein complex solved to high resolution. Figure courtesy of Petra Fromme.

this reaction go on to power the carbon fixing 'dark' reactions of the Calvin-Basham-Benson cycle.

PSI appears in multiple oligomeric forms throughout nature. In plants it occurs monomerically, bound to four antennae light harvesting proteins (LHCI-1 to 4). In cyanobacteria, it largely exists in trimeric form, though monomers are found in low light conditions and in *Chroococcidiopsis* sp TS-821 PSI appears to form in tetrameric and dimeric species (Li, Semchonok et al. 2014).

The cyanobacterial PSI trimer is the largest and most complex membrane protein complex that has been crystallized (Fromme and Witt 1998) and for which a structure has been determined (Jordan, Fromme et al. 2001). Shown in figure 3.3, the trimer has a molecular weight over 1 megadalton and consists of 36 protein subunits and 381 cofactors. Each monomer contains 96 chlorophylls (making up a large intrinsic antenna system), 22 carotenoids, three 4Fe-4S iron-sulfur clusters, four lipds, two phylloquinones and a Ca^{2+} ion (Jordan, Fromme et al. 2001). Most of the chlorophylls are coordinated by the two largest subunits PsaA and PsaB, each comprising 11 transmembrane helices each (Jordan, Fromme et al. 2001). Most of the remainder of the chlorophylls are associated with the seven surrounding small membrane integral subunits (PsaF, PsaI, PsaJ, PsaK, PsaL, PsaM and PsaX). These subunits are known to help coordinate many of the cofactors and PsaL and PsaI are also involved in the formation of the trimer. They are also implicated in stabilization of a complex between PSI and IsiA, a protein that forms an extended peripheral antenna under iron stressed conditions (Nield, Morris et al. 2003).

Within the core, PsaA and PsaB form a heterodimer that house 79 of the 96 chlorophylls.

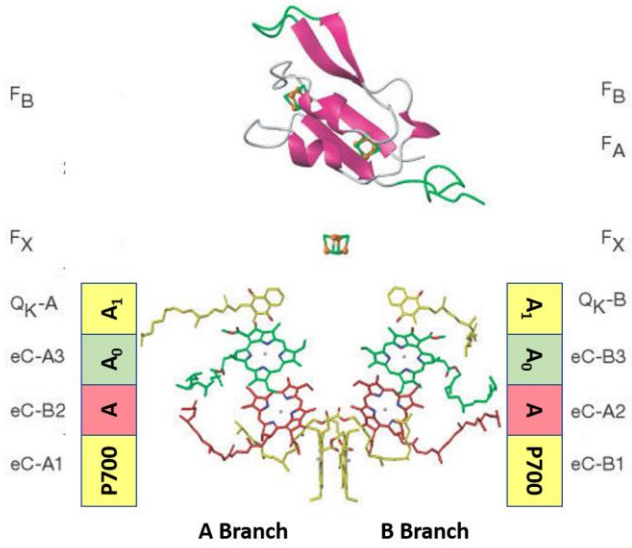

Figure 3.4 Electron Transport Cofactors in PSI

Cofactors involved in electron transport in PSI starting with the four chlorophylls where charge separation occurs (P_{700} and A), moving through another pair of chlorophylls (A_0), two phylloquinones (A_1) and finally the three 4Fe4S clusters (F_X, F_A, F_B). Figure modified from Krauß (2008).

These chlorophylls loosely follow the pseudo-C_2 symmetry exhibited by PsaA/PsaB and have an average center to center distance of 9.9 Å within this network (Jordan, Fromme et al. 2001, Byrdin, Jordan et al. 2002). This allows for strong excitonic coupling and efficient Förster energy transfer and helps explain the extremely high quantum efficiency for the excitation energy transfer and trapping (99%) found in PSI. Upon absorption of light, the energy is funneled from this antenna system to the primary donor in PSI, P_{700}.

Upon solving the structure, P_{700} was found to be a heterodimer of chlorophyll *a* and chlorophyll *a'* (Jordan, Fromme et al. 2001), the so-called special pair, arranged perpendicular to each other with a resulting π-stacked coupling. Once the light energy reaches it, a strongly reducing excited state (P_{700}^*) is formed which initiates charge separation become P_{700}^+. Illustrated in figure 3.4, the electron transfer pathway within PSI can proceed along two different paths, the so-called A- and B- branches corresponding to cofactors mainly bound by PsaA and PsaB respectively. On both sides, these branches consist of two chlorophyll *a* molecules followed by a phylloquinone at which point the paths merge at F_x. F_x is the first of the three iron-sulfur clusters in PSI and it lies along the membrane-normal pseudo-C_2 axis between PsaA and PsaB. It is the only membrane intrinsic iron-sulfur cluster as the two downstream clusters, F_A and F_B, both reside in the stromal hump, coordinated by PsaC.

The chlorophylls most proximal to P_{700}, termed A, partner with P_{700} to form the charge separated state P_{700}^+/A^-. There is even evidence to support the charge separation initiating at A (Müller, Slavov et al. 2010). Consecutive reduction then proceeds to A_0, another chlorophyll, followed by A_1, a phylloquinone. Though both A- and B-branches are active, they have very different rates in electron transfer with the A-branch showing a much slower (~200 ns) electron transfer from A_1 to F_x than in the B-branch (~10 ns) (Guergova-Kuras, Boudreaux et al. 2001). F_x is coordinated by four cysteine residues (very common in natural iron-sulfur clusters) in PsaB that are strictly conserved (Krauß 2008).

The three subunits, PsaC, PsaD and PsaE comprise a membrane extrinsic domain located on the stromal side and known as the 'stromal hump', pictured in figure 3.5. PsaC is very similar in structure to bacterial ferredoxins, possessing two conserved motifs of CXXCXXCXXXCP by

which it binds the two terminal iron-sulfur clusters in the PSI electron transport chain, F_A and F_B (Oh-oka, Takahashi et al. 1988, Golbeck 1994, Jordan, Fromme et al. 2001, Krauß 2008). The pseudo-C_2 axis of symmetry in the core does not extend to F_A and F_B which exhibit a 62 ° angle leading to asymmetry in edge to edge distances between them and F_x of 14.9 Å for F_A and 22.0 Å for F_B (Jordan, Fromme et al. 2001). PsaD is the closest of the three stromal subunits to the C_3 axis of the trimer and has been shown to possess no defined structure in solution (Xia, Broadhurst et al. 1998), thought to fold upon PSI complex assembly (Krauß 2008). PsaE has the weakest interaction with the core of the three subunits, thought to be the last to bind in the proposed sequential assembly of the stromal hump (Antonkine, Jordan et al. 2003). Interestingly, the stromal hump can be removed and reconstituted without significant disruption to electron transfer kinetics (Golbeck 1992, Golbeck 1994). All three stromal subunits are implicated in the binding and electron transfer efficiency between PSI and Fd.

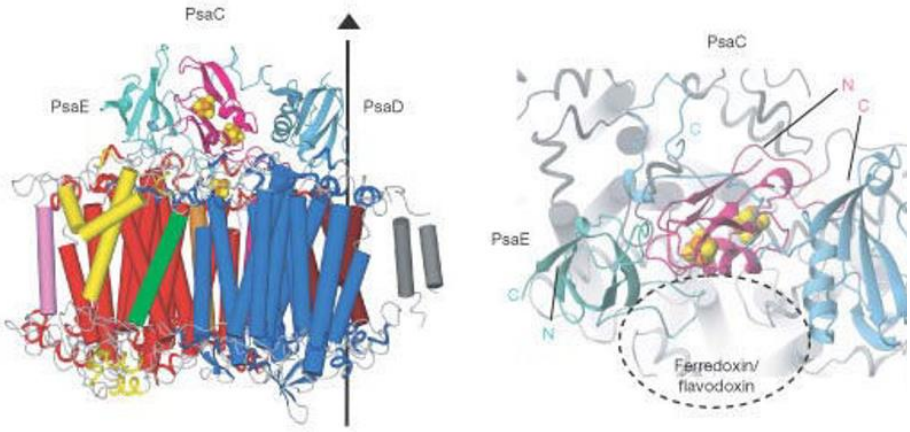

Figure 3.5 Stromal Hump of PSI

Membrane parallel (left) and top down (right) views of PSI highlighting the stromal subunits PsaC, PsaD, and PsaE. PsaC (pink) coordinates the terminal electron acceptors in PSI, F_A and F_B as is shown. Top down view also highlights the proposed binding spot for ferredoxin, supported by both the structure and mutagenic studies. Figure originally pubished in Jordan, Fromme et al. (2001).

Interestingly, the redox potentials from F_A and F_B in spinach were reported at -540 mV and -590 mV respectively. This would suggest that the transfer from F_A to F_B is energetically uphill, in contrast to all other steps along the photosynthetic transport chain (Brettel 1997). This means that

in the absence of an acceptor, the electron is most favorable to localize at F_A. It is well established thought that the transport goes $F_X \rightarrow F_A \rightarrow F_B$ (Golbeck 1999) though so this hints that upon binding Fd, there is a change in the chemical environment surrounding the clusters. Indeed, this iagrees with EPR studies performed on PSI-Fd cocrystals that purported evidence of a change to the physical and chemical properties of F_B upon PSI binding Fd (Fromme, Bottin et al. 2002). The practical purpose for this has been suggested to be a mechanism to reduce creation of reactive superoxide by the Mehler reaction where PSI transfers electrons to oxygen in the absence of electron acceptors (for example when the dark reactions are slowed down and no oxidized Fd is available to accept the electrons). F_B is closer to the solvent exposed surface whereas F_A is buried deeper, towards the membrane, thereby is less prone to react with oxygen (Fromme and Grotjohann 2006). Possibly this perturbation in the local environment could manifest as a conformational change susceptible to study through time-resolved structural studies.

Interaction of Photosystem I and Ferredoxin

Ferredoxin1, commonly just ferredoxin (Fd) is a small (~10 kDa) soluble protein that possess a 2Fe-2S iron sulfur cluster that acts as the electron acceptor to PSI and is thereby the terminal electron acceptor in the photosynthetic electron transport from the thylakoid membrane. It can be replaced in iron-stressed conditions by flavodoxin. The interaction between PSI and Fd has been well characterized, though a bound structure of the PSI-Fd complex remains elusive. It binds to the stromal hump of PSI with the suspected binding site highlighted in figure 3.5 (Jordan, Fromme et al. 2001). Mutagenesis studies initially implicated that all three stromal subunits are involved in binding Fd with varying degrees of influence on the electron transfer efficiency (Rousseau, Setif et al. 1993, Xu, Jung et al. 1994, Fischer, Hippler et al. 1998). Prior to the high resolution structure of PSI, the kinetics of Fd reduction by PSI were well studied using transient absorption spectroscopy (Setif and Bottin 1994, Setif and Bottin 1995). The results of these studies indicated three separate first order phases in the reduction of Fd with $t_{1/2}$'s of ~0.5 μs, ~10 μs and ~100 μs with variations in the actual half-life being dependent upon the sources used for PSI and Fd. The slow phase is dependent upon concentrations suggesting that it may be due to probabilistic collision between the undocked species of Fd to PSI. The two faster phases, however, have been

speculated to correspond to two different binding sites with differing proximities of the Fd iron sulfer cluster to F_A or F_B (Setif and Bottin 1995). Without a structure of the two in complex though, confirmation of these theories remains unavailable.

In this dissertation, crystals of the PSI-Fd co-complex have been grown and were investigated by both traditional and serial crystallographic methods, some details of which will be expanded upon later. Currently though, the resolution is limited, preventing a molecular structure to be determined at present. Large crystals of this complex have shown diffraction up to 3.8 Å resolution (H.Q. Yu and R. Fromme, unpublished) however the occupancy of Fd appears to be too low for a confident electron density to be determined. PSI-Fd nanocrystals were the subject of one of the first SFX experiment, again being resolution limited for a structure but changes in the unit cell at time points of 5 µs and 10 µs are in agreement with the previous spectroscopic studies (Aquila, Hunter et al. 2012).

Structure of Photosystem II

The function of PSII is to catalyze the light driven electron transfer from water, at the luminal side of the membrane to plastoquinone at the stromal side of the membrane. It supplies the electrons for the photosynthetic electron transfer chain and thereby significantly contributes to the conversion of solar energy into chemo-potential energy. It does this by generating a transmembrane charge separation whereby water is used as a substrate that is completely oxidized. This results in a net product of four protons, four electrons and a single molecular oxygen from four photons and 2 molecules of water. PSII is the only system in nature that is able to catalyze light driven water splitting, utilizing one of the highest redox potentials in nature within its reaction center at ~1.25 V(Rappaport, Guergova-Kuras et al. 2002). This process in particular is responsible for oxygenating the planet, allowing for and sustaining our broad and complex biosphere and supplying the energy needed for respiration in all aerobic organisms on the planet.

PSII exists as a dimer of large monomeric functional units of PSII, each containing 20 protein subunits and over 50 cofactors. The structure of PSII was first solved in 2001 to a 3.8 Å resolution(Zouni, Witt et al. 2001) and many improvements have followed with a 1.9 Å high resolution structure being published in 2011(Umena, Kawakami et al. 2011), shown in figure 3.6.

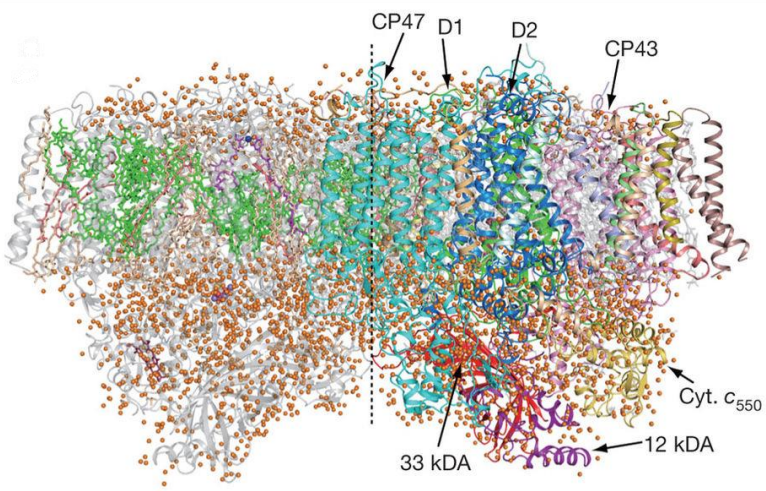

Figure 3.6 Structure of PSII

Ground state structure of PSII at 1.9 Å resolution. Some of the protein subunits are labeled and colored individually in the monomer on the right, of particular the CP47, CP43, D1 and D2 subunits that comprise the core. The monomer on the left has the cofactors highlighted. Figure originally published in Umena, Kawakami et al. (2011).

The center of a PSII monomer consists of the D1 and D2 proteins which form the heterodimeric core and bind the cofactors of the electron transfer chain and the CP43 and CP47 proteins which surround the core and house most of the antenna chlorophylls. D1 and CP43 also coordinate the pentanuclear oxygen-evolving complex (OEC) where the water oxidation occurs. Surrounding this core are 13 smaller membrane-intrinsic protein subunits: PsbH, PsbI, PsbJ, PsbK, PsbL, PsbM, PsbO, PsbT, PsbU, PsbV, PsbY, PsbX and PsbZ. The final three subunits, PsbO, PsbU and PsbV comprise a lumenal membrane-extrinsic domain together with loop regions from the four core proteins (Umena, Kawakami et al. 2011). In addition to the OEC, there are over 70 other cofactors within the PSII complex that include 11 β-carotenes, 14 lipids, a non-heme iron, 35 chlorophylls, 2 mobile plastoquinones and 2 pheophytins (Loll, Kern et al. 2005).

The initial energy used to power PSII is also collected by a light harvesting complex that, in cyanobacteria and red algae, is a phycobilisome consisting of phycocyanin, phycoerythrin and linker protiens (Grossman, Schaefer et al. 1993). This energy is then eventually transferred to chlorophylls bound by CP43 and CP47 which is then subsequently funneled to the reaction center contained in the D!/D2 core of each monomer. The CP43 and CP47 proteins also function to maintain structural stability which has been confirmed by mutagenic deletion studies (Eaton-Rye and Vermaas 1991, Roegner, Chisholm et al. 1991).The initial energy used to power PSII is first

collected by a light harvesting complex that, in cyanobacteria and red algae, is a phycobilisome consisting of phycocyanin, phycoerythrin and linker protiens (Grossman, Schaefer et al. 1993). This energy is then eventually transferred through chlorophylls bound by CP43 and CP47 which is then subsequently funneled to the reaction center contained in the core. The CP43 and CP47 proteins also function to maintain structural stability which has been confirmed by mutagenic deletion studies (Eaton-Rye and Vermaas 1991, Roegner, Chisholm et al. 1991).

The Kok Cycle: Electron Transport and Oxygen Evolution in PSII

Within the D1 and D2 subunits of PSII, an electron transport chain comprised of four chlorophyll *a* molecules, two pheophytins and two plastoquinones (PQs) are coordinated as shown amongst various electron transport cofactors in figure 3.7a. The four chlorophylls are organized in a dimer of chlorophyll 'special pairs', believed to comprise an excitonically coupled tetramer referred to as P_{680}, named so due to its maximum absorption at 680 nm. Charge separation occurs at the P_{680} and allows the ensuing electron transfer to the mobile plastoquinone, PQ_B. Although there are two similar branches for of cofactors between P_{680} and the PQ's, mediated by the D1 and D2 subunits respectively, only the branch primarily along D1 is active.

P_{680} uses light energy to enter an excited state, P_{680}^*, which allows charge separation to occur with the negative charge migrating through a downhill redox pathway, first to the D1 pheophytin, on to PQ_A (coordinated by D2) and finally to PQ_B (coordinated by D1). PQ_B is bound weaker than PQ_A and upon becoming doubly reduced, binds two protons from the stromal side of the membrane and dissociates from its binding pocket before being replaced by a free PQ. The positive charge resides on P_{680}^+, which is reduced through electron transfer from the manganese containing OEC via a tyrosine (D1-161, termed Tyr_Z) residue located in the D1 subunit between the OEC and P_{680}.

A closer look at the OEC (figure 3.7b) reveals a distorted cubane-like structure of four oxygens, three manganese and a calcium with an additional 'dangler' manganese. The OEC catalyzes the water splitting reaction and subsequently the transmembrane electron transport by mitigating the electron hole in P_{680} via a series of oxidation state changes in the manganese-oxygen

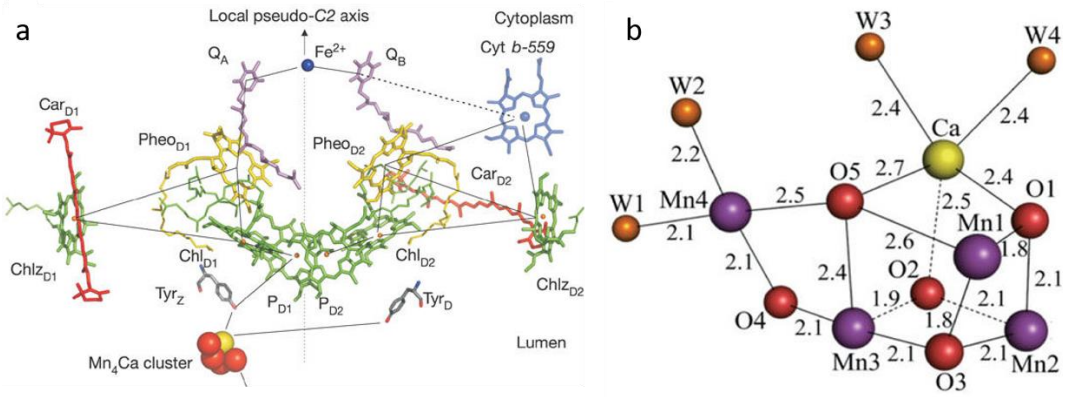

Figure 3.7 Electron Transport Chain and OEC of PSII

a) Membrane planer look at the cofactors involved in the transmembrane electron transfer in PSII. Pseudo-C_2 axis (D1/D2) is indicated by the arrow. b) Structure of the OEC as found in the 1.9 Å structure reported in Umena, Kawakami et al. (2011) showing interatomic distances in angstroms. a) originally published in Loll, Kern et al. (2005), b) originally published in Umena, Kawakami et al. (2011).

-calcium cluster. There are 5 such states, known as the S-states of the Kok cycle, and over the course of these states, the OEC progresses from from S_0 to S_4 state with each progression coupling to a light absorption/charge separation event in the PSII reaction center. Upon reaching the transient S_4 state, a transition occurs whereby a molecular oxygen is released and at least one of the two substrate water molecules bind the metal cluster, resetting the cluster to the S_0 state and beginning a new cycle (Yano and Yachandra 2008).

There is much debate and speculation as to the progression of oxidation states of Mn, the knowledge of which is crucial to understanding the mechanism behind water splitting in PSII. Evidence from spectroscopic studies have indicated that the dark S_1 state has oxidation states for Mn1-4 as (III, III, IV, IV) respectively (Britt, Campbell et al. 2004, Haumann, Müller et al. 2005, Pushkar, Yano et al. 2008, Yeagle, Gilchrist et al. 2008, Yano and Yachandra 2014) which is in agreement with theoretical calculations (Isobe, Shoji et al. 2012, Cox, Retegan et al. 2014). In this model, there is a predicted symmetry reducing Jahn-Teller distortion that should increase distances between the metals in the Mn_3O_4Ca cubane structure (Yamaguchi, Yamanaka et al. 2013). As the OEC progresses from S_1 to S_3, it is then expected that the oxidation progresses to a (IV, IV, IV, IV) oxidation state whereby the cubane shrinks (Dau, Zaharieva et al. 2012). This was supported by

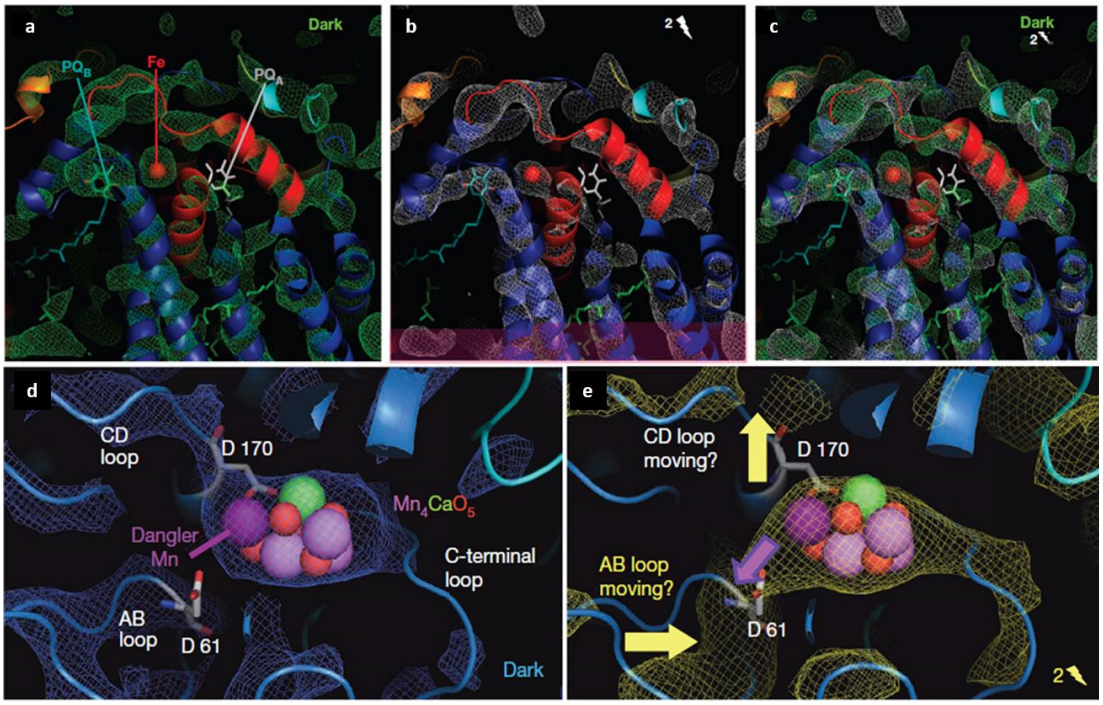

Figure 3.8 Comparison of Electron Density Maps from S_1 and S_3 States

Results from a 2-flash TR-SFX experiment on PSII from *T. elongatus* reported in Kupitz, Basu et al. (2014). (a-c) Electron density omit maps at 1.5 σ of the electron acceptor portion of PSII. (a) the ground state, S_1, (b) the S_3 state, after two flashes, (c) an overlay of the S_1 and S_3 states, showing movement of the non-heme iron. (d,e) Electron density omit maps of the at 1.5 σ of the OEC and surrounding coordination sphere. (d) The S_1 and (e) S_3 states show movement of the A/B and C/D loops in addition to an increase in the atomic distance between the dangler Mn and the cubane-like portion of the OEC. Figures originally published in Kupitz, Basu et al. (2014).

structures solved using 2 flash time-resolved SFX experiments (Kupitz, Basu et al. 2014). In this model, there is a predicted symmetry reducing Jahn-Teller distortion that should increase distances between the metals in the Mn_3O_4Ca cubane structure (Yamaguchi, Yamanaka et al. 2013). As the OEC progresses from S_1 to S_3, it is then expected that the oxidation progresses to a (IV, IV, IV, IV) oxidation state whereby the cubane shrinks (Dau, Zaharieva et al. 2012). This was supported by structures solved using 2 flash time-resolved SFX experiments (Kupitz, Basu et al. 2014).

In addition to apparent bond compression in the cubane, this double flash experiment showed other structural changes in the ligand coordination sphere surrounding the OEC. Figure 3.8 shows a difference density map between measured ground state, S_1 (left), and doubly flashed, S_3 (right), states. As can be seen in the figure, in the transition between states the ligand D170 in

the CD loop appears to move away from the cluster whereas the D61 residue from the AB loop appears to connect. These movements are supported through previous mutagenic experiments that failed to connect D170 with manganese coordination in higher S-states (Debus, Strickler et al. 2005) as well as implicating that D61 might be involved in the $S_2 \rightarrow S_3$ transition (Kupitz, Basu et al. 2014)

Determining Chlorophyll Concentration

Chlorophyll assays were used extensively during extraction, isolation, purification and crystallization of both PSI and PSII. A chlorophyll assay is a spectrophotometric measurement to allow determination of chlorophyll concentration. Chl concentration can then be used as a proxy for the concentration of the photosynthetic proteins in a given solution, specifically for purified PSI (96 chl/monomer) and PSII (35 chl/monomer). An 80% v/v acetone solution is used to extract the chlorophyll from the proteins. To do so, a predetermined mass ofacetone is weighed out (to avoid pipette error due to volatility and low surface tension of acetone) and its density (785 mg/mL) is used to calculate the volume needed for the other 20%. For example, for a 1 mL assay, the mass of acetone needed is:

$$mass_{acetone} = 0.8 * 1mL * 785 \frac{mg}{mL} = 628\ mg$$

The remaining volume is comprised of a mixture of water and sample, the ratio of which depends on the concentration of the protein solution being measured (this usually ranges from a 1:200 to a 1:2000 total dilution). To continue with the example above, a 1 mL total volume assay with a 1:1000 dilution would result in 1 µL protein solution, 199 µL water and 628 mg acetone.

Acetone solutions absent the protein solution were always prepared ahead of time in microcentrifuge tubes and assays were always performed in at least triplicate for chl determination. For a given assay, the determined volume of solution was pipetted into solution and the tip ejected into solution to remove loss from material that could adhere to the inside of the pipette tip. To ensure consistent and reliable results, small aliquots of the protein solution to be tested were first pipetted into a separate container to minimize unintended material adsorbed on the outside of pipette tips as well. Upon addition of the solution, microcentrifuge tubes were sealed, vortexed for

30 seconds and centrifuged for 2 min at 14,000 rcf. The resulting solution was then measured from 660 nm – 710 nm using a spectrophotometer and the absorbances at 664 nm (A_{664}, absorbance maximum) and 700 nm (A_{700}, baseline correction) were used to determine the chlorophyll concentration (C_{chl}) using the formula:

$$C_{chl} = \frac{A_{664} - A_{700}}{l * 76780\ M^{-1}cm^{-1}} * \frac{V_{total}}{V_{sample}}$$

where 76,780 M^{-1} cm^{-1} is the molar extinction coefficient for Chla in 80% acetone,(Porra, Thompson et al. 1989), *l* is the pathlength in cm, V_{total} is the total volume of the assay and V_{sample} is the volume of the protein solution added to the assay. A solution of 80% v/v acetone was used to blank the spectrophotometer prior to sample measurement. The mean value of at least three assays was always used and a new set of assays were performed if the standard deviation was more than 5% of the mean value. For the sake of brevity, the term 'chlorophyll assay' will indicate a set of 3 or more assays going forward.

Photosystem I

Materials for PSI Isolation and Purification

The following are abbreviations and compositions of buffers and solutions that were used during the extraction and purification process for photosystem I:

MCM buffer:	20 mM 2-(N-morpholino)ethanesulfonic acid (MES) pH=6.4, 10 mM $CaCl_2$, 10 mM $MgCl_2$
MMCM buffer:	20 mM (MES) pH=6.4, 10 mM $CaCl_2$, 10 mM $MgCl_2$, 500 mM D-mannitol
PMSF solution:	500 mM phenylmethylsulfonyl fluoride (PMSF) in dimethylsulfoxide
Tocopherol solution:	500 mM α-tocopherol in ethanol
A_x buffer:	20 mM MES pH=6.4, 0.02% w/v n-dodecyl-β-maltopyranoside (β-DDM), x mM $MgSO_4$
G_x buffer:	5 mM MES pH=6.4, 0.02% w/v β-DDM, x mM $MgSO_4$

Lysis of Cells and Preparation of Thylakoid Membranes

All steps of protein production are performed in the dark or dim green light to minimize photodamage. PMSF solution and acetone solution were both made fresh before each prep.

Additionally, tocopherol solution was added to both MCM and MMCM prior to protein preparation. 25-100 g of frozen *T. elongatus* cells were thawed in 250 mL centrifuge bottles containing MCM that had been warmed in a 56 °C water bath (200 mL for under 30 g, 400 mL else). Cells were then vigorously shaken to dissolve pellets and resuspend them. The cells were then centrifuged at 7,000 rcf in a fixed angle rotor at 24 °C for 10 min to effectively wash the cells. The supernatant was then discarded and the pellet(s) was resuspended in ~20 mL cold (0-4 °C) MMCM that had been stored on ice. This and all subsequent resuspensions were performed in centrifuge bottles submerged in loose ice with dedicated paintbrushes to ensure homogeneity and minimize protease degradation. In addition, PMSF solution was added during this and each following resuspension to achieve a final concentration of 500 µM PMSF.

Upon cells being homogeneously resuspended, suspension was then strained through a 16-32 mesh wire sieve and the cells were disrupted by being passed through a microfluidizer (Microfluidics Model M-110L) twice. Prior to introduction of the cell suspension, the microfluidizer lines were washed and primed with MMCM to avoid any contamination with storage solution. Cells were sheared using nitrogen gas at a pressure of ~10 kpsi. The lysate was then centrifuged at 29,000 rcf at 4 °C for 10 min. The supernatant was transferred to new centrifuge bottles and kept on ice will the pellets were resuspended in cold MCM. Both resuspended pellets and supernatants were then centrifuged at 18,000 rcf at 4 °C for 10 min and all supernatant was either discarded or frozen at -20 °C for future phycobilisome purifications. Small pellets were then resuspended in MCM and subsequently combined with and used to resuspend large pellets. These resuspensions were then centrifuged at 18,000 rcf at 4 °C for 10 min followed by another identical resuspension and centrifugation to thoroughly remove soluble components and ‘wash’ thylakoid membranes. After the final wash, pellets were resuspended in a minimal volume (~30-50 mL total) of MCM and combined. During later protein preparations, a Dounce homogenizer was used to increase accuracy in chlorophyll determination and minimize variances in homogeneity introduced through user technique.

Detergent Extraction of PSI from Thylakoid Membranes

A chlorophyll assay was then performed on the combined thylakoid membrane suspension to determine the chlorophyll concentration. The sample was then diluted with MCM to achieve a chl concentration of 1 mM. Prior to dilution, the final volume was calculated and used to further calculate the mass of β-DDM needed to achieve a final concentration of 0.6% w/v β-DDM. This was then dissolved into the MCM prior to the ensuing dilution of the thylakoid membrane suspension with the now detergent containing MCM. The β-DDM containing MCM was then slowly added to the gently stirring thylakoid membrane suspension to avoid high local concentrations of detergent which can be harsh for proteins. This solution was then completely covered and allowed to continue stirring for 60 min during which time the β-DDM extracted membrane proteins from the thylakoid membranes, solubilizing them in detergent micelles.

Following completion of solubilization, the solution was centrifuged in either a Ti-70 rotor at 50,000 rpm (184,000 rcf) for 90 min or a Ti-45 rotor at 45,000 rpm (158,000 rcf) for 2 hours. Selection of rotor was based upon total volume (Ti-70 can accommodate 200 mL, Ti-45 can accommodate 560 mL). The supernatant had a decreasing concentration of PSI toward the top due to the large molecular weight of the PSI trimer in comparison to other proteins present (PSI trimer begins to pellet during this time). Thus, the top portion of the supernatant was discarded (~70%). The 'lower' portion was then combined and a chlorophyll assay was performed. The remaining pellets were covered with 5-10 mL of A100 and set to shake at 4 °C for 90 min in order to loosen and resuspend the PSI contained in the top layer of the pellet. This solution was then pooled as well and a chlorophyll assay was performed.

Purification using Anion-exchange Chromatography

Anion exchange chromatography was used to isolate PSI from other proteins in the detergent extract. This is performed using columns filled with a charged resin, in this case either the quaternary amine containing Q-Sepharose HP (GE Healthcare) or TOYOPEARL DEAE-650M (Tosoh Bioscience) for large columns. Both resins are used to separate proteins by their binding affinity at different ionic conditions. Columns used were either 20 cm in length and 5 cm inner diameter (XK 50/20, GE Heathcare) or 60 cm in length and 5 cm inner diameter (XK 50/60, GE

Healthcare). Void volumes, defined as the effective liquid volume contained in the resin slurry, varied slightly with the bed height but were approximately 340 mL for the XK 50/20 (~15 cm bed height) and 1100 mL for the XK 50/60 (~50 cm bed height). Prior to a given day of purification, columns were connected to FPLCs (AktaPure, GE Healthcare) and packed using A_{150} and double the running flow rates to ensure homogeneous column packing and lack of hardware issues that could arise during the purification.

During ultracentrifugation, the column is equilibrated with A_{100} and a water bath is used to cool columns to 4 °C via a water jacket that surrounds the columns. A superloop (150 mL, GE Healthcare) is also primed with A_{100} (A_0 for DEAE). Following the chlorophyll determinations, the solubilized membrane extract was then aliquoted into a minimum number of 150 mL portions containing ≤ 25 millimoles chlorophyll for XK 50/20 columns or ≤ 80 millimoles chlorophyll for XK 50/60 columns. A 150 mL volume of sample was then manually loaded into the superloop using a 60 mL Luer-Lok syringe coupled with a 0.22 µm syringe filter to remove any particles that could disrupt the column pumping procedure. Upon application, a program with constant flow rate was initiated, the contents of which are described in table 3.1. Fortunately, the PSI trimer has the highest binding affinity to the resin among the proteins left in the detergent extract and this allows a straightforward procedure to isolate it. The essential steps in the program include a wash step to flow through all non-PSI trimer proteins, followed by an elution step to collect the PSI trimers. After elution, the column is then flowed with a high ionic strength in order to remove anything that may still be bound followed by an equilibration step to prime the column for a subsequent run.

% A_{150}	XK 50/20		XK 50/60	
	Vol (mL)	Flow Rate (mL/min)	Vol (mL)	Flow Rate (mL/min)
0/30	300	10	300	25
70/60	300	10	700	25
100	350	10	1000	25
0/30	350	10	700	25

Table 3.1 Elution Gradient for PSI Using XK 50/20 (Q-Sepharose) and XK 50/60 (DEAE)

Of note, for the XK 50/20, A_{100} was used as the equilibration buffer whereas A_0 was used for the XK 50/60.

Crystallization as a Final Purification

As FPLC runs completed elution, fractions containing PSI trimers (third peak in the elution profile, see figure 3.9) were collected and pooled together in ultrafiltration concentrators (Amicon Stirred Cell 400 mL, EMD Millipore). Prior to use, concentrators were fitted with 100 kDa cutoff filters (Biomax 76 mm, EMD Millipore) which had been pre-wetted for at least 2 hours in a solution of G_0, allowing the PSI trimer to be retained while all other contents of the HPLC elution buffer including the beta-DDM detergent micelles (72,000 kDa) flow through the membrane. The concentrators were then sealed, placed in a 4 °C refrigerator and connected to a tank of ultrapure argon, used as a pressure inducing headspace gas. The magnetic stir plates placed below the cells were then set to a gentle stir and the regulator for the argon was adjusted to maintain a headspace pressure of 30-60 psi. The sample was then concentrated to a minimal volume (typically 2-10 mL) with pooled fractions from additional FPLC runs being added upon completion. During concentration, the filtrate was monitored visually to ensure a chlorophyll and, by proxy, PSI was not passing through the membrane). In the occasion that leakage was detected, the flow through was recombined with the solution remaining in the cell and concentration was repeated following inspection of seals on the cell and, if necessary, a new filter membrane being fitted.

Once all fractions had been concentrated to a minimal volume, an amount of G_0 was added to dilute the PSI trimer solution to achieve a concentration of 2-6 mM $MgSO_4$. The selection of this was dependent upon final use of the sample, with lower values (i.e. 2 mM $MgSO_4$) resulting in smaller crystals and larger concentrations resulting in larger. For the sake of brevity, the usual target was 6 mM $MgSO_4$ as this would require a lower dilution and thus a lower volume to subsequently concentrate. Dilutions were calculated from the exact volume left with the knowledge that PSI trimer fractions were eluted at an ionic strength of 135 mM $MgSO_4$.

Following dilution, a subsequent round of protein concentration was performed to reduce the volume until a chlorophyll concentration between 5 and 12 mM was achieved. The pressure used in this second round of concentration had influence on the time and, by proxy, mean size of the crystals formed. The pressure used ranged from 5-40 psi with higher pressures being associated with a smaller final crystal size. Upon arriving at the desired final volume, the valve for

the headspace gas was shut off and the pressure relieved in the concentrator. The magnetic stir plate was also turned off to allow PSI to nucleate and deposit as crystals on the membrane over a period of 8-16 hours.

The following day, crystals were harvested by adding a minimal amount of G_{0-3} (lower salt was used in the pursuit of nanometer sized crystals that had been concentrated with high headspace pressure and concentrations below 3 mM $MgSO_4$) to the membrane (typically 3-10 mL, dependent upon the scale of the prep) and allowing the deposited crystals to "soak" for 1 hour in order to loosen the deposit. The settled crystals and solution were then homogenized by "washing" the membrane. This was achieved by gently pipetting the clear to light straw yellow color was achieved (indicating that minimal retentate over the membrane while holding the concentrator at shallow angle and rotating once the visible portion of the membrane (i.e. not concealed by the crystal layer) became visibly white. Once all protein crystals were visibly suspended in solution i.e. the whole membrane appeared clean, the solution was then transferred to one or more centrifuge tubes, ranging from 1.5 mL microcentrifuge tubes to 50mLcentrifuge tubes (the choice of which was dependent upon volume and intended use).

When necessary, the slurry containing PSI crystals was roughly separated by size by using diffusive settling. This procedure entailed homogenizing the slurry, either through pipette mixing or gentle rocking, and aliquoting it into a series of 1.5 ml microcentrifuge tubes. The crystals in the suspension were allowed to settle for 10 minutes whereby the topmost layer was removed to a fresh set of microcentrifuge tubes. The cutoff for the top layer supernatant was selected by visual examination of transparency, the dark green opaque pellet being left in the tube while the slightly more transparent supernatant containing smaller crystals was removed. This first pellet was then quenched with a volume of fresh G_0, typically filling the microcentrifuge tube to voluminous capacity. This process was repeated as needed, typically resulting in 10, 20, 30 and 40 minute fractions with larger denominations representing longer settling times and subsequently smaller size regimes of crystals.. The temporal label indicates the time of the final settling step, e.g. the 30 minute pellet would have been in the top layer for 10 *plus* 20 minutes in two subsequent settling events before settling in a third set of tubes after an additional 30 minutes post top layer removal. This is

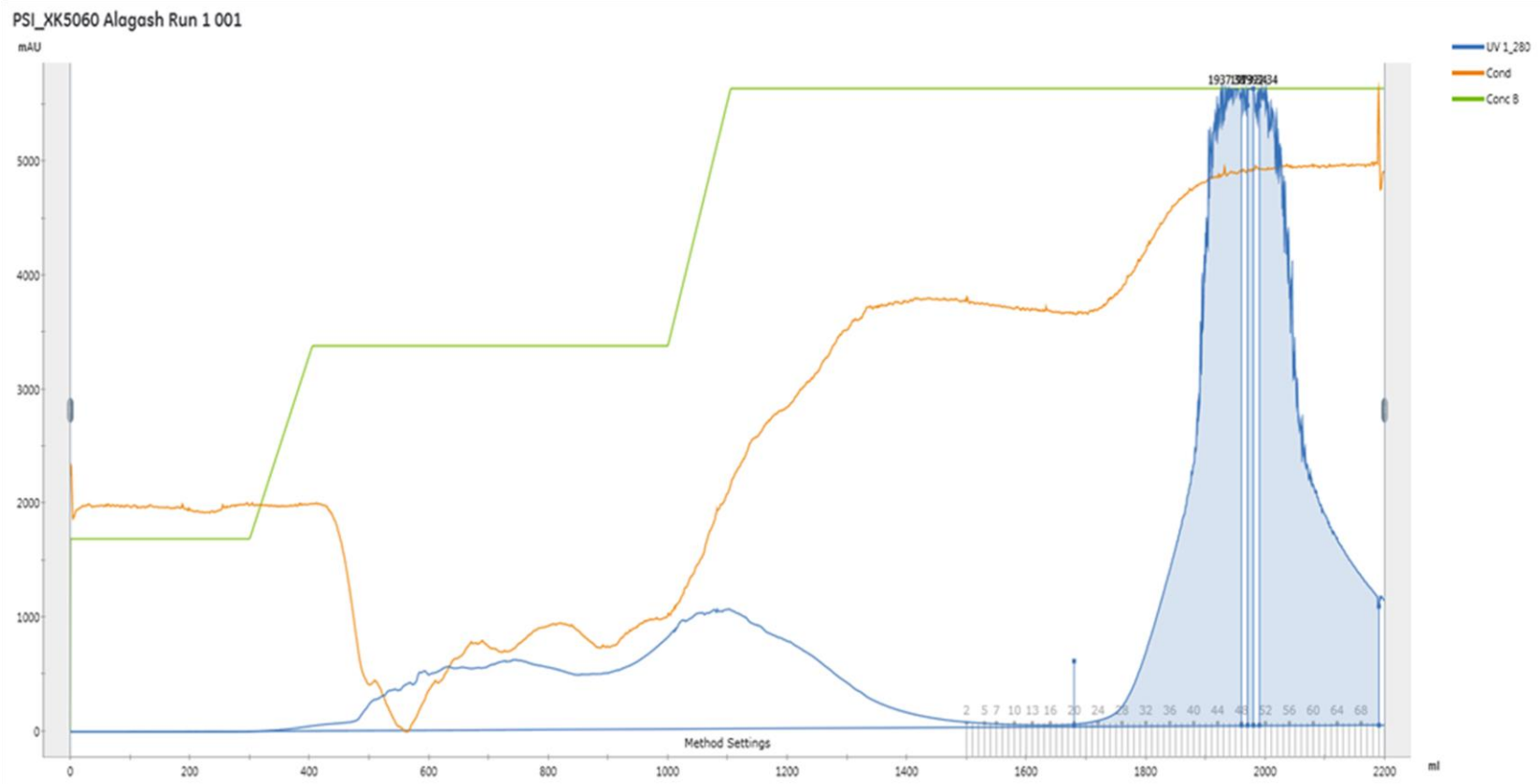

Figure 3.9 Chromatograph of PSI elution on XK 50/60

Elution profile for PSI on XK 50/60 column containing DEAE resin. The first two peaks contain PSII as well as PSI monomer and other proteins present in the washed lysate. Right peak is PSI trimer, showering a large and relatively narrow peak profile eluting at 150 mM $MgSO_4$. Note that the run is cut off after the peak due to there being no need to re-equilibrate the column.

necessary due to a pseudo-homogenization that occurs in the transfer process. The supernatants from the final fraction (e.g. 40 minute samples) were then pooled together in a larger tube (usually a 15 or 50 mL centrifuge tube) and topped off with ~5 fold dilution with G_0. This frequently resulted in another pellet over extended periods of time. The supernanants of non-crystallized PSI could be used for experiments not requiring crystal PSI, such as spectroscopy.

Photosystem II

Materials for PSII Isolation and Purification

The following are abbreviations and compositions of buffers and solutions that were used during the extraction and purification process for photosystem II: (a note the name of the buffers is Prep so Prep 1 refers to a buffer and not protein "preparation 1"

Prep 1:	20 mM MES pH=6.0, 10 mM $CaCl_2$, 10 mM $MgCl_2$
Prep 2:	20 mM MES pH=6.0, 10 mM $CaCl_2$, 10 mM $MgCl_2$, 500 mM D-mannitol
Prep 3:	20% v/v glycerol, 20 mM MES pH=6.0, 10 mM $CaCl_2$, 10 mM $MgCl_2$, 500 mM D-mannitol
PMSF solution:	500 mM PMSF in dimethylsulfoxide
Tocopherol solution:	500 mM α-tocopherol in ethanol
Acetone solution:	80% v/v acetone
A_xG buffer:	20% v/v glycerol, 10 mM $MgCl_2$, 10 mM $CaCl_2$, 20 mM MES pH=6.0, 0.02% w/v n-dodecyl-β-maltopyranoside (β-DDM), x mM $MgSO_4$
D_x buffer:	*X% w/v poly(ethylene glycol), avg. MW=2000 amu (PEG 2K, Sigma), 100 mM piperazine-N, N'-bis (PIPES) pH=7, 5 mM $CaCl_2$*
C buffer	100 mM PIPES pH=7, 5 mM $CaCl_2$, 0.03% β-DDM

Lysis of Cells and Preparation of Thylakoid Membranes

Both PSI and PSII are membrane proteins located in the thylakoid membranes of *TS. elongatus* and, as such, share many similarities in the initial steps of purification. Thus, for brevity, the lysis and thylakoid preparation for PSII was very similar identical to that of PSI (described above) with the following exceptions.

Prep 1 was used in place of MCM in all cases except for the step just prior to solubilization in which case prep 3 was used. During cell lysis, prep 2 was used in place of MMCM. The major difference between the PSI and PSII buffers is the pH. While PSI is isolated at pH 6.6, the buffers for PSII isolation feature a pH of 6.0. The reason is that the oxygen evolving complex (OEC) of PSII is the most sensible part of PSII and it is more stable at a lower pH during isolation and purification. This matters most during the solubilization step where PSII is exposed to high detergent concentration. The pH of the thylakoid lumen, where the OEC is located is close to pH 5.5 under illumination conditions, however the stromal side of PSII is close to pH 8 under illumination conditions and is destabilized releasing the mobile plastoquinone QB at pH 5.5. The pH of 6.0 is ideal for stabilization of PSII during isolation from the membrane and chromatography. The reader may wonder why the pH is increased to 7.5 at the later steps which involve crystallization. At these steps the detergent concentration is low (0.03 % which corresponds to 3x CMC). Under these conditions PSII is stable at a much broader pH range from 5.5 to 8.0. The solubility of PSII increases with the pH, higher PSII concentrations can be reached at pH 7.5 for crystallization without the danger of aggregation. The size of the prep was usually smaller for PSII than for PSI, rather than ranging from 25-100 g of frozen *TS. elongatus* cells used for PSI preps, PSII preps generally ranged between 20-45 g of cells. As PSII is much more prone to photoinduced damage than PSI, the complete PSII prep from breaking of cells to the crystallization steps were performed under dim green light and extra care was taken to ensure no light entered the room and often work was done with even less light than in a PSI prep.

Detergent Extraction and Separation of PSII from Membranes

A chlorophyll assay was then performed on the combined thylakoid membrane suspension to determine chlorophyll concentration. The sample was then diluted with Prep 3 to achieve a chl concentration of 0.75 mM. Prior to dilution, the final volume was calculated and used to further calculate the mass of β-DDM needed to be added to achieve a final concentration of between 0.5 and 1 % w/v β-DDM. After systematic studies to vary the detergent to Chl ration in the solubilization steps, we determined that the quality of PSII was better and better ordered crystals formed at lower detergent concentration, therefore the most recent preps since summer 2016 were decidedly

performed using a detergent concentration of 0.5% as this lead to the largest protein yield with the highest resolution diffraction from crystals observed downstream. The lyophilized detergentwas then dissolved into the Prep 3prior to the ensuing dilution of the thylakoid membrane suspension. This detergent containing Prep 3 was slowly added to the gently stirring thylakoid membrane suspension to avoid high local concentrations of detergent which can be harsh for proteins. PSII is particularly susceptible to damage at this point as compared to PSI so extra care was taken by using a pipette at this step to control dropwise delivery of the detergent solution. This stirred solution was then completely covered and allowed to continue stirring for 45 min during which time the β-DDM extracted membrane proteins from the thylakoid membranes, solubilizing them in detergent micelles.

Following completion of solubilization, the solution was centrifuged in either a Ti-70 rotor at 50,000 rpm (184,000 rcf) for 2 hours or a Ti-45 rotor at 45,000 rpm (158,000 rcf) for 2.5 hours. Selection of rotor was based upon total volume (Ti-70 can accommodate 200 mL, Ti-45 can accommodate 560 mL). The supernatant was then pooled together by gently pouring it off into a beaker and a chlorophyll assay was performed to determine concentration and total yield.

Purification using Anion-exchange Chomatography

Anion exchange chromatography was used to isolate PSII from the lysate pool. Due to the more fragile nature of PSII, a weak tentacle anion exchange resin where there is a spacer between the resin and the charged groups was used to prevent disassembly of the complex. Columns used were either 70 cm in length and 2.6 cm inner diameter (XK 26/70, GE Heathcare) or 60 cm in length and 5 cm inner diameter (XK 50/60, GE Healthcare) and were packed with TOYOPEARL DEAE-650M (Tosoh Bioscience). This resin uses diethylaminoethyl exchange groups which are weaker and, thus, much more gentle than the quaternary amines present in Q-Speharose resin used for PSI isolation. This translated to void volumes of ~200 mL and ~900 mL for the XK 26/70 and XK 50/60 column housings resp. Prior to a given day of purification, columns were connected to FPLCs (AktaPure, GE Healthcare) and packed using $A_{150}G$. Flow rates used to pack were doubled from purification conditions to ensure homogeneous column packing and this was done at least a day prior to troubleshoot any hardware issues that could arise.

During ultracentrifugation, the column is equilibrated with 10% concentration of $A_{150}G$. The HPLC buffers contain 10% glycerol to stabilize PSII during purification. A water bath is used to cool columns to 4 °C via a water jacket that surrounds the columns. A superloop (150 mL, GE Healthcare) is also primed with A_0G.

Once a chlorophyll determination was made, the number of FPLC runs was calculated with each run containing a chlorophyll mass of no more than 20 millimoles for the XK 26/70 columns or 60 millimoles for the XK 50/60 columns. The sample was immediately diluted with A_0G to 150 mL/FPLC run so as to decrease the concentration of β-DDM from the solubilization concentration. Further dilution may be required as the detergent concentration should not exceed 0.12 % w/v for any PSII solution that is not being loaded immediately to avoid damage caused by a high detergent

% $A_{150}G$	XK 26/70		XK 50/60	
	Vol (mL)	Flow Rate (mL/min)	Vol (mL)	Flow Rate (mL/min)
10	465	10	1395	25
13	385	10	1155	25
28	250	10	750	25
100	250	10	750	25
10	350	10	1050	25

Table 3.2 Schedule for PSII FPLC Runs

environment. The 150 mL aliquot was then manually loaded into the superloop using a 60 mL Luer-Lok syringe coupled with a 0.22 µm syringe filter to remove any particles that could disrupt the column pumping procedure (in the case of larger than 150 mL volume, remainder was then loaded after a sufficient volume had been applied to the column). Upon application, a program with constant flow rate was initiated, the contents of which are described in table 3.2. The elution profile is shown in figure 3.10. The column is equilibrated with 15 mM $MgSO_4$ so that most of the contaminant proteins do not bind and are eluted with the flow through, leaving PSII and PSI bound to the column. The second peak containing the PSII dimer is then eluted and collected at an ionic strength of 42 mM $MgSO_4$. The PSI, which remains on the column, was traditionally discarded with a complete high-salt wash at 150 mM $MgSO_4$, as it was thought to be unusable after experiencing the 20% v/v glycerol contained in the A_xG buffers. However, I have now established a protocol

which allows for isolation of high quality PSI to be isolated and subsequently crystallized from the PSII column runs, which is discussed below.

Concentration and Cryogenic Storage of Purified PSII

The eluent fractions contained in the peak that elutes at 42 mM from all FPLC column runs were collected, pooled and concentrated using a 100 kDa cutoff centrifugal filter (Ultracel 100 kDa, Millipore). These PSII dimer containing fractions were continually added to filters which were centrifuged at 3,800 rcf at 4 °C in a swinging bucket rotor. The number of filters depended upon the number of FPLC runs, usually equating to 2 filters per 2 runs (in the case of an odd number of runs, the number of filters was kept at an even number for simplicity in rotor balancing). As the centrifugal filters had 15 mL capacity each, lower than the volume collected in each run which are typically ~150 mL/run for the small columns and ~400 mL/run for the large columns, the filters were continually refilled to capacity as time passed. The volume of pooled fractions that was unable to be contained at a given time was stored in a clean beaker, covered in parafilm and held at 4 °C. Prior to addition into the filtration units, the pooled fractions were homogenized and added in equivalent aliquots to each filter so as to ensure homogeneity of retained masses between all units. Once all dilute PSII fractions were sufficiently concentrated (~ 40 µL/g of initial cells, i.e. 1 mL for a 25 g prep), retentate from the concentrators was pooled together and homogenized. This was then either flash frozen or precipitated a form of further purification, depending on the timeline for the intended use of a particular prep. In either case, a chlorophyll assay is performed to determine concentration and yield.

In the case of the protein being frozen, protein was homogenized with glycerol as a cryoprotectant until a final concentration of 40% v/v glycerol was achieved. Following this, the protein was inserted into cryogenic bull semen tubes in 200 µL aliquots and submerged into liquid nitrogen for flash freezing. Tubes were then grouped into labeled cryogenic sheaths and stored long term in a dedicated dewar under liquid nitrogen.

Crystallization of PSII as the final purification step

The last purification step of PSII was done by crystallization. In the case of immediate precipitation or upon unthawing of cryogenically stored sample, a series of fresh buffer D_x and fresh

buffer C were prepared. The fast thawing of PSII is important for the quality of the PSII crystal preparations. The straws were removed from the liquid nitrogen container and stored in a shallow dewar under liquid N_2. Then each straw was removed individually from the liquid nitrogen, the filter was cut off using scissors and the PSII solution in the straw was fast thawed by moving it fast between gloved fingers above a 1.5 reaction vessels. This is important as slow thawing could hamper the quality of PSII as larger ice crystals may form in a slow thawing process around 0° C. The volume of the PSII was inferred by calculating the mass difference of the 1.5 ml microcentrifuge tube before and after addition of the PSII solution (density was approximated with 1 g/mL, acceptable since the following dilution is made in two steps to accommodate for this). This solution was diluted to a concentration of 1mM chl with buffer C and stirred. Then the exact volume and chl concentration was determined and the solution diluted to 0.75 mM chlorophyll. We have recently systematically varied the chl concentration in this step between 0.5 mM and 0.75 mM and it was determined that best diffraction crystals were observed when the first crystallization step was performed at the slightly lower chl concentration of 0.6 mM. To this solution, a volume of buffer D_{15} was added at 4° C dropwise for a final chlorophyll concentration of half of the previous concentration and a final PEG concentration of 7.5 %. It is important that this step is performed using cool packs equilibrated to 4° C in the fridge. The precipitation is much faster at 0° C and leads to amorphous precipitate instead of crystals. This precipitation step takes at least 40 minutes but this first crystallization step can also be performed overnight. Subsequently, crystals from the pellet are imaged and characterized before being pelleted by centrifugation at 3,500 rcf for 5 min at 4 °C using a swinging bucket centrifuge. The supernatant was then used for a chlorophyll assay to determine the PSII concentration of the supernatant. 1 ml of the supernatant is frozen and later used for determination of the rate of O2 evolution and concentrated to a Chl concentration of 100 µM for SDS gel electrophoresis. The remaining volume of the supernatant is discarded. The pellet was then dissolved into buffer C to gain a chl concentration of nominally 1 mM. Then the chl concentration was determined and the solution further diluted to achieve a chlorophyll concentration of 0.75 mM. 100ul of this sample was frozen at -80 for subsequent O_2 evolution measurements and SDS gel electrophoresis. The subsequent crystallization was performed as

described before though this time D_{13} was used as a precipitant. Again, the crystals were imaged and samples of the supernatant and the dissolved pellet were taken and frozen at -80C for subsequent SDS gel electrophoresis and determination of rate of oxygen evolution. This process was then repeated with D_{11}. These crystals were further characterized with SONICC, DLS and microscopy and stored at 4 °C until use (typical precipitations shown in figure 5.11, chapter 5).

PSI Retention and Viability Post-PSII Elution

During more recent purifications, I explored the idea to isolate PSI and PSII from the same prep. I developed a new protocol where PSI retained on the DEAE column post PSII elution could be recovered and tested for its viability to crystallize. These preps were performed identical to a PSII prep until the 42 mM $MgSO_4$ elution step, at which point the program was held to avoid introducing the high ionic wash step (150 mM $MgSO_4$). The run was then manually ended upon elution of PSII and a manual run begun. The process consisted of first equilibrating the column to A_{42} buffer by flowing through a column volume through, gradually removing the glycerol and adjusting the pH to 6.4. After this equilibration, A_0 and A_{150} were used to elute the PSI off at an ionic strength of 75 mM $MgSO_4$ which was collected upon elution. At this point the collected fractions were pooled and treated as described above for a typical PSI prep. Advantageously, the PSI was eluted at a much lower ionic strength compared to those performed on the strong anion exchange resin (Q-sepharose) used in typical PSI preparations, allowing a generally faster desalting and initial crystallization. Initial viability of PSI recovered in this way was characterized using characterization by SDS PAGE, DLS, SONICC, and microscopy. This was validated after crystals grown using this protein were used as calibration sample at various beamtimes, showing high quality diffraction to better than 3 A resolution and no apparent loss in diffraction quality.

3-deoxy-D-manno-2-octulosonate-8-phosphate synthase (KDO8PS)

Structure and function of KDO8PS

3-deoxy-D-manno-2-octulosonate-8-phosphate synthase (KDO8PS) is a protein that occurs in gram negative bacteria which performs an aldose condensation reaction between arabanose-5-phosphate (A5P) and phosphoenol pyruvate (PEP) to form 3-deoxy-D-manno-2-

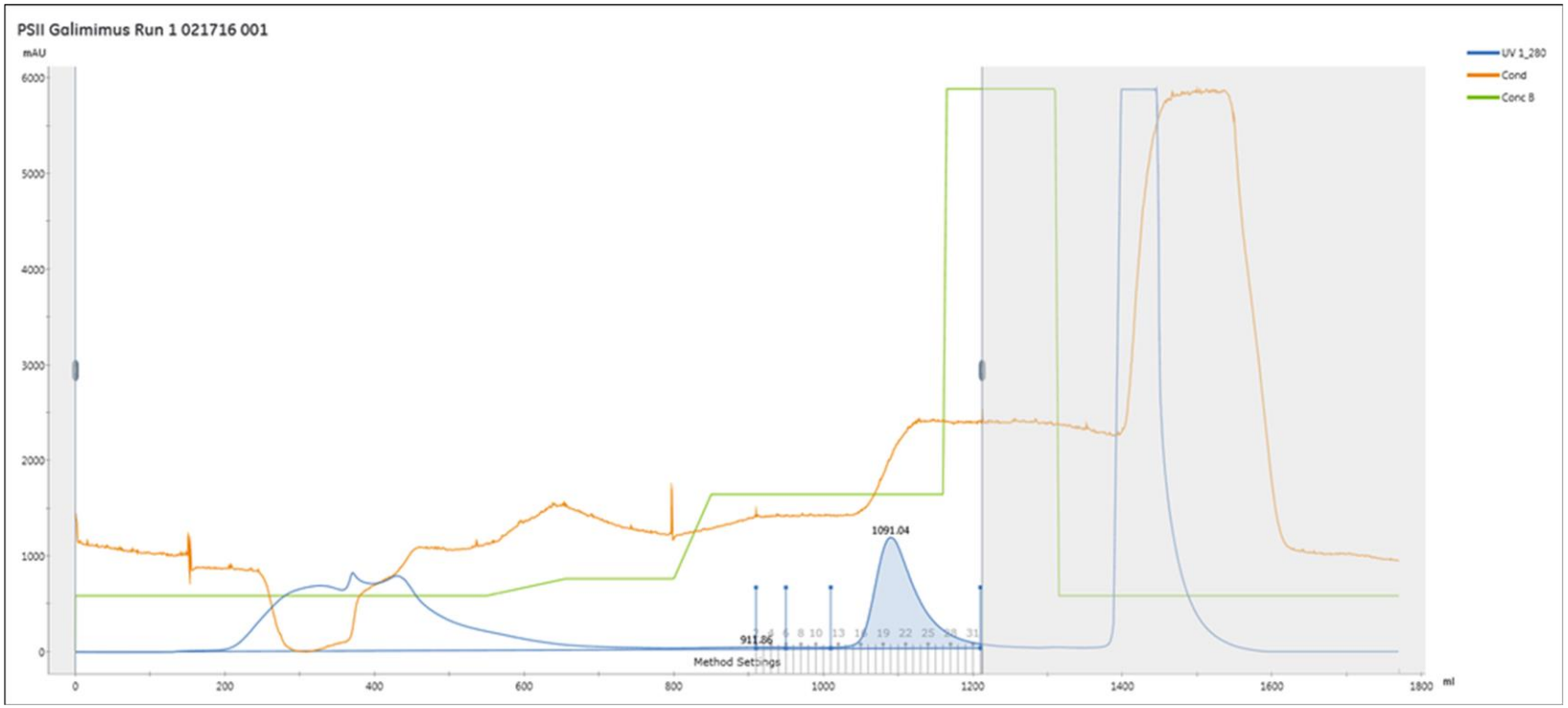

Figure 3.10 Chromatograph of PSII on XK 26/50 Column

Elution profile of PSII on XK 26/50 column containing DEAE resin. Three peaks are present, the earliest being proteins other than PSI and PSII present in the cell lysate after ultracentrifugation, the middle containing PSII dimers and the last (greyed out) comprising of PSI.

octulosonate-8-phosphate (KDO8P) and inorganic phosphate (Pi). After formation, KDO8P is eventually dephosphorylated to KDO which is essential in the formation of lipopolysaccharide, unique to Gram-negative bacteria and essential for growth and virulence (Raetz and Dowhan 1990). Because of the critical role KDO8PS possesses in this process, it is an interesting novel drug target for fighting the increasing antibiotic resistance experienced in Gram-negative bacteria. The family of KDO8PS enzymes can be divided into two branches, those using a divalent metal cation for catalysis and those which are metal-ion independent (Vainer, Belakhov et al. 2005). The work contained herein was performed with KDO8PS from *Escherichia coli*, belonging to the metal independent family, and references to KDO8PS going forward will pertain to this variant of the enzyme.

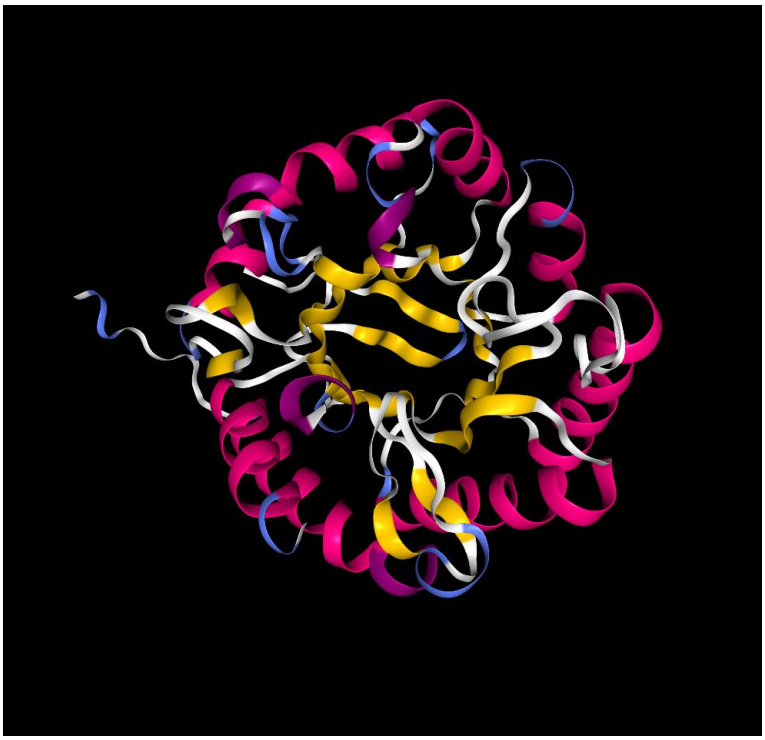

Figure 3.11 Asymmetric Funnel Active Site of KDO8PS

Top down view of the irregular funnel binding site in KDO8PS. The binding site of PEP is towards the bottom of the funnel, while A5P binds in shallower position. Both substrates are coordinated by positively charged His, Lys and Arg residues. Though both substrates can bind independently, the binding of A5P hinders PEP from entering, leading to a sequential binding during enzymatic action. Structural model from PDB entry 1X8F (Vainer, Belakhov et al. 2005).

Shown in figure 3.11, the catalytic site of KDO8PS resembles an irregular funnel, the bottom of which is comprised off a net positive electrostatic potential which serves as an attractive force for the negatively charged phosphate of PEP (Vainer, Belakhov et al. 2005). KDO8PS has been shown to actively produce KDO8P with either A5P or PEP as the initially bound substrate (Liang, Kohen et al. 1997). Natural structures have been solved with KDO8PS

in complex with both PEP and the product KDO8P in addition to its apo form (Vainer, Belakhov et al. 2005) (figure 3.12), though all structures are missing the catalytically necessary L7 loop which closes off the active site upon binding of both substrates (Duewel, Radaev et al. 2001). The structures obtained were determined using soaking procedures with PEP and KDO8P respectively, lacking A5P for progression in the case of PEP and showing KDO8P in a conformation with its phosphate group bound to the PEP binding site rather than the expected A5P site. This shows why the back-reaction with KDO8P and Pi to PEP and A5P does not occur (Vainer, Belakhov et al. 2005) but also suggests that the product bound state visualized may not be the actual intermediate of the forward reaction.

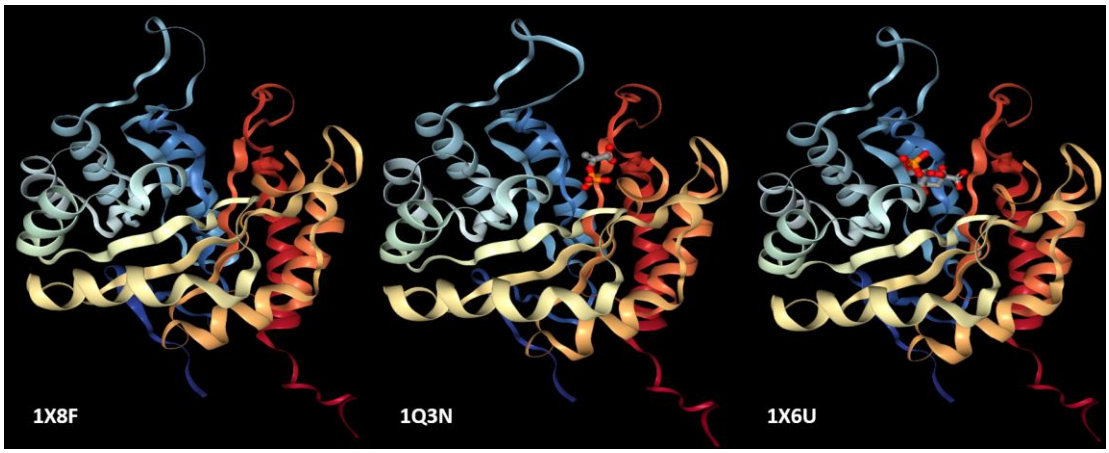

Figure 3.12 Known Structures of *E. coli* KDO8PS

From left to right are the apo-, PEP bound, and KDO8P (product) bound states solved by Vainer, Belakhov et al. (2005).

The enzymatic kinetics of KDO8PS have been investigated using time-resolved electrospray ionization mass spectrometry (TR-ESI-MS) and show the presence of an enzyme bound intermediate that exists on a millisecond time scale (Li, Sau et al. 2005) (see figure 3.13), the identity of which is currently under debate. An acyclic intermediate was initially proposed (Baasov and Kohen 1995, D'Souza, Benenson et al. 1997) which was supported The enzymatic kinetics of KDO8PS have been proved using time-resolved electrospray ionization mass spectrometry (TR-ESI-MS) and show the presence of an enzyme bound intermediate that exists on a millisecond time scale (Li, Sau et al. 2005) (see figure 3.13), the identity of which is currently under debate. An acyclic intermediate was initially proposed (Baasov and Kohen 1995, D'Souza,

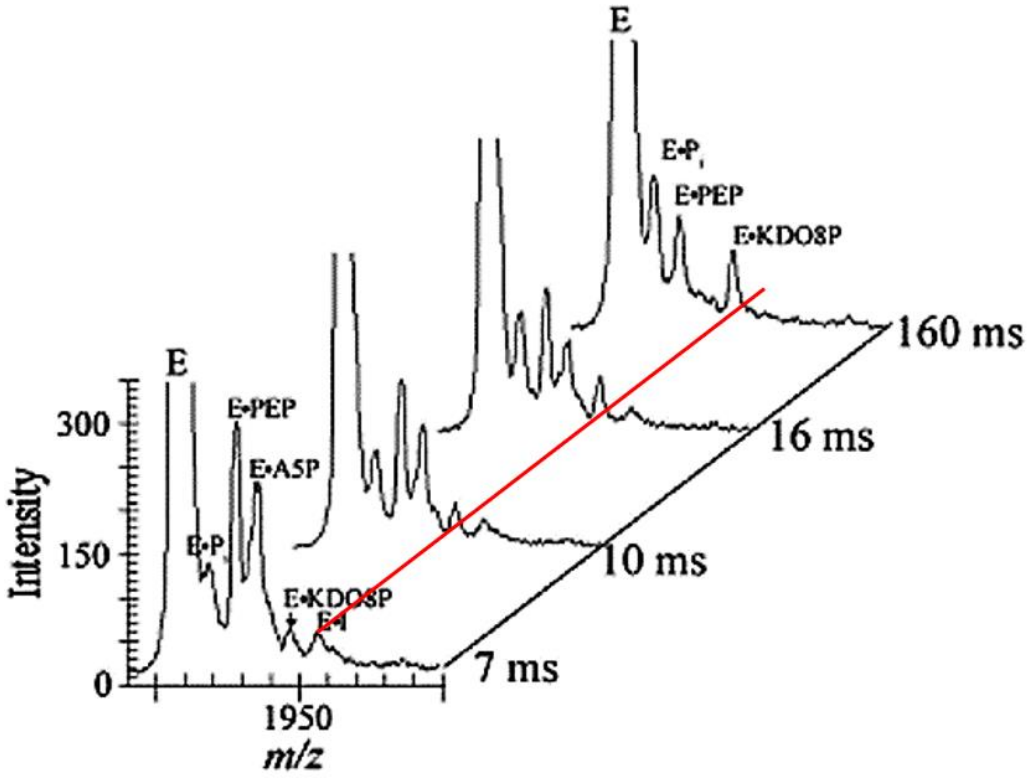

Figure 3.13 Time-Resolved Mass Spectra of KDO8PS

Results from ESI-MS using 80 µM KDO8PS presoaked with PEP and mixed through a T junction with 60 µM A5P. Different time points were measured by varying the flow rate. E is the enzyme (KDO8PS) and E·P_i, E·PEP, E·A5P, E·KDO8P and E·I symbolize complexes between KDO8PS and phosphate, PEP, A5P, KDO8P and the unknown intermediate respectively. The shorter time points show a much more significant contribution from the intermediate state which is almost wholly depleted after 160 ms while the product bound state conversely increases (red line highlights the intermediate). Figure modified from Li, Sau et al. (2005).

Benenson et al. 1997) which was supported by the discovery of an acyclic intermediate in the metal dependent KDO8PS from *Aquifex aeolicus* (Kona, Xu et al. 2007). However, this intermediate has yet to be visualized in a metal independent variant and the mechanism for the formation of an acyclic intermediate is also unknown. The current leading theories are highlighted in figure 3.14 and revolve around the question whether the water molecule performs a nucleophilic attack pre- or post- bond formation between $C3^{PEP}$ and $C1^{A5P}$ (Wang, Duewel et al. 2001). The carbanion intermediate has been proposed for metallo-KDO8PS due to the likely occurrence of a deprotonated metal-bound water which would lead to a hydroxyl attack of PEP (Duewel, Radaev et al. 2001). The oxocarbenium intermediate is proposed for metal free species due to the strong

unstabilized negative charge of the PEP carboxylate, causing an increased nucleophilicity in the surrounding double bond. This would support the formation of an oxocarbenium intermediate via nucleophilic attack on A5P (Asojo, Friedman et al. 2001) However, there is evidence to suggest a carbanion intermediate for the nonmetallo enzyme as well from the absence of one of the two water molecules in electron densities of PEP- and A5P-bound *A aeolicus* KDO8PS that was converted to a non-metallo state through a site mutation (Kona, Xu et al. 2007).

Motivation for KDO8PS as a TR-SFX target

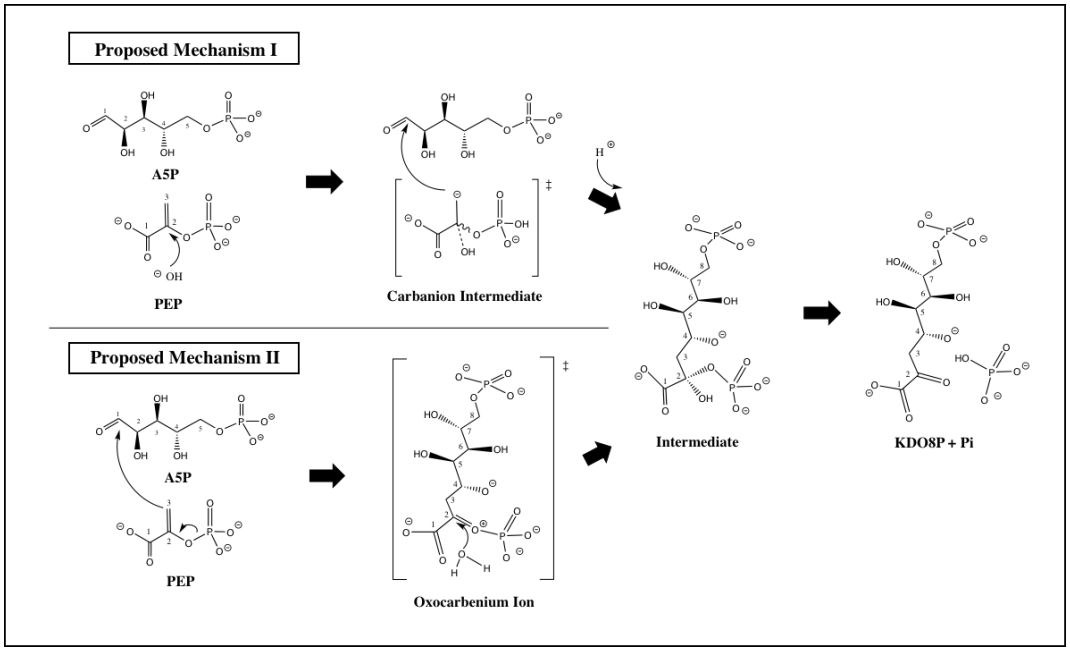

Figure 3.14 Proposed KDO8PS Intermediates

The two most likely candidates for the mechanism behind the aldose-condensation between PEP and A5P. The upper pathway displays a carbanion intermediate while the lower shows an oxocarbenium intermediate. Both pathways converge to a linear phosphorylated KDO8P intermediate.

With the advent of XFELs, phototriggered TR-SFX has allowed the temporal boundaries in structural discovery to truly be pushed into the ultrafast regime. However, many conformationally active proteins are not phototriggered, including many enzymes important to medicine and health. Where there exist limitations such as reversibility and temporal constraints in photoactivated macromolecules, for a protein whose structural changes are triggered through chemical activation there has generally been even more strict limitations in traditional macrocrystallography with regards to the breadth of feasible targets. While there are many clever ways to probe functional

intermediates in enzymes using crystallography such as flash freezing or mutagenic manipulation, many interesting reactions occur on sub-second timescales that are generally unavailable in traditional crystallography. Capturing wild type intermediates using freezing techniques remains challenging and is usually limited to reactions with slow turnover rates below 1 min^{-1}-(Fiedler, Thorell et al. 2002, Karlsson, Parales et al. 2003, Leiros, McSweeney et al. 2004, Theisen, Misra et al. 2004).

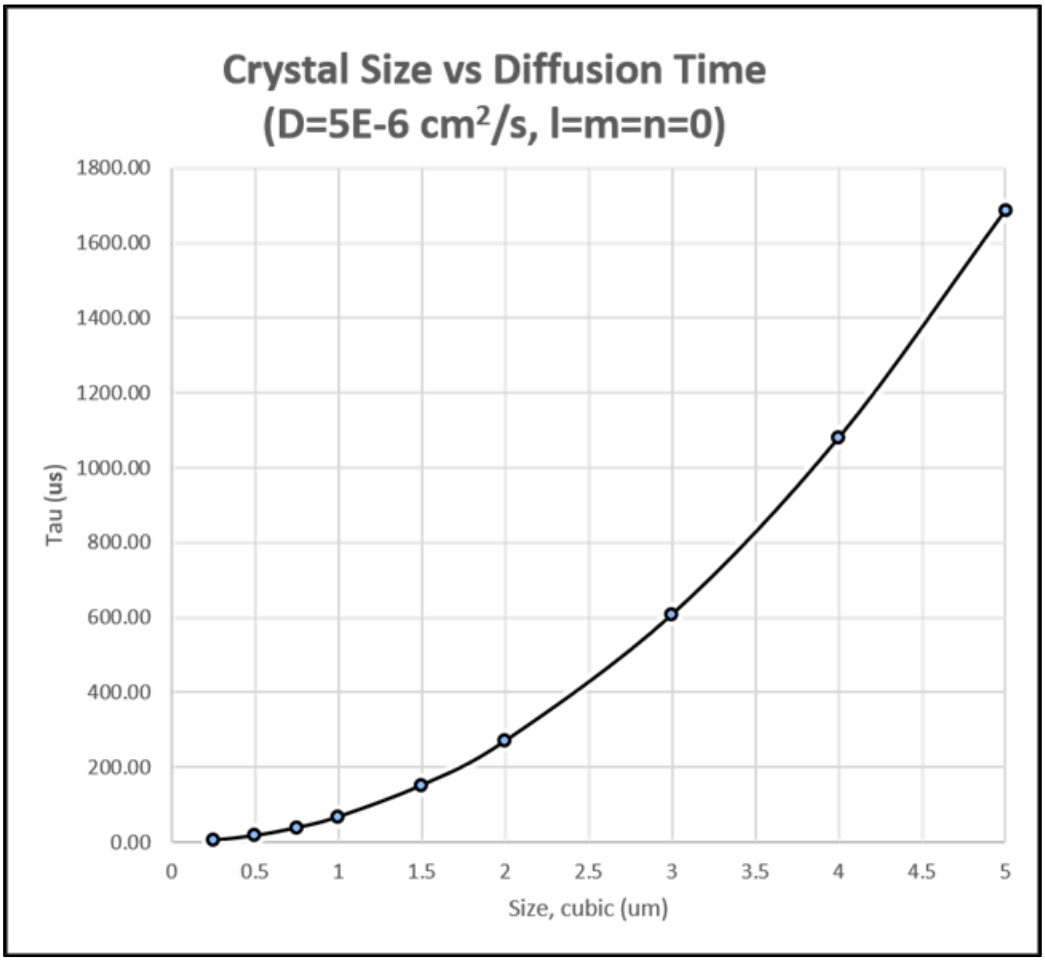

Figure 3.15 Substrate Diffusion as a Function of Crystal Size

Shows the relationship between diffusion time delays for substrate into cubic crystals as a function of crystal size, measured by the crystal face dimension in microns. Sufficiently small crystals can experience complete diffusion around a µs or less. Calculations are based off the solution for Fick's 2nd law with the constraints that mixing is instantaneous and the concentration of substrate is non-limiting. The diffusion coefficient is on the low end for small sugars like PEP which usually range between $5* 10^{-6}$-$10 * 10^{-6}$ cm^2/s (Perry and Chilton 1973). This is calculated from the rate limiting contribution of the slowest element in the Fourier sum, namely l=m=n=0.

The unique characteristics available in SFX mitigate many of the challenges experienced in attempted time-resolved structures for enzymatic intermediates. The serial nature and ultrashort pulses certainly lend themselves toward capturing shorter lived states without introducing possible artifacts from mutagenic alterations of the enzyme or freezing techniques. In addition, the small size of the nano and micro crystals in TR-SFX lends itself to a much shorter diffusion time of substrate within the crystal, allowing as fast as μs diffusion compared to timescales in seconds to minutes (Schmidt 2013) (see figure 3.15). The faster diffusion times also lead to a higher temporal reaction initiation homogeneity, leading to the ability for higher populations of short lived intermediates to be observed that could subsequently lead to more confidence and higher resolution of electron densities from time resolved SFX studies on crystals with an inevitable mixture of states.

KDO8PS stands as a particularly good model system to attempt one of the first time-resolved mixing experiments in SFX. This is exemplified by 3 things in particular, namely: it has unknown intermediate states that are currently controversily discussed, the resolution of which has implications for medical advancement of new antibiotics; it has some known intermediates, allowing for validation of the method of 'mix-and-inject' TR-SFX; past work, both structurally and otherwise, has shown its kinetics to range within the projected millisecond time regime available to this field, including beyond the limit of anything so far achievable in traditional crystallography; it can be prepared in large enough quantities necessary for SFX with relatively low expense and time.

Solutions used in Expression and Purification of KDO8PS

LB broth:	1% w/v bacto-tryptone, 0.5% w/v yeast extract, 18 mM NaCl
Lysis buffer:	20 mM Tris-HCl pH=7.3, 75 mM KCl, 5 mM ethylenediaminetetraacetic acid (EDTA), 2 mM β-mercaptoethanol,
PSB:	2.2% w/v protamine sulfate, 20 mM Tris pH=5, 300 mM KCl, 2 mM β-mercaptoethanol, 1 tablet protease inhibitor cocktail (SIGMAFAST)
Dialysis buffer:	20 mM Tris-HCl pH=7.3, 75 mM KCl, 2 mM β-mercaptoethanol
Buffer A:	20 mM Tris-HCl pH=7.3, 2 mM β-mercaptoethanol
Buffer B:	20 mM Tris-HCl pH=7.3, 500 mM KCl, 2 mM β-mercaptoethanol

Overexpression, Lysis and Purification of KDO8PS in E. Coli

The wild-type KDO8PS gene (GenScript) was cloned into a pET-23d plasmid which was subsequently introduced into Lemo23(DE3) competent *E. coli* (New England Biolabs) during transformation as described in Conrad (2016). The plated culture was introduced to LB media containing ampicillin and chloramphenicol. This was then incubated at 37 °C and shaken at 250 rpm until an O.D. of A_{600}=0.6-0.8 was reached, at which point isopropyl-1-thio-β-D-galactopyranoside (IPTG) was added to a final concentration of 0.2 mM. After a further 4 hour incubation, the cells were harvested by centrifugation at 8,000 rcf for 10 min followed by storage at -80 °C in ~5 g aliquots in 50 mL centrifuge tubes.

50 mg of lysozyme was added to 25 mL of lysis buffer which was then added to a 5 g aliquot of frozen KDO8PS overexpressed *E. coli* cells in centrifuge tubes to thaw the cells. To enable homogenized solubilization of the *E. coli* pellet, a mixture of mechanical mixing with a stir bar and vortexing for 20 s increments were iteratively used until a visual homogenous cell suspension was achieved. At all times with the exception of vortexing the centrifuge tubes containing solution were kept on ice and times between vortexing were no shorter than 1 min. Following homogenization, tubes were allowed to rock gently at room temperature for 30 minutes to allow lysozyme to weaken the cell walls. After the lysozyme incubation, the tubes are cooled in an ice bath in preparation for lysis.

Once cooled, tubes were placed in a secondary containment beaker and surrounded by packed ice. This sample was then sonicated in at 50% power with 5-6 ten second pulses, each separated by a 30 second cooldown to avoid damage from heating. Ice was replenished and repacked as needed to stabilize centrifuge tube. Lysis was confirmed by characteristic changes in

% buffer B / [KCl] mM	Vol (mL)	Flow Rate (mL/min)
15 / 75	315	10
25 / 125	135	10
100 / 500	125	10
15 / 75	165	10

Table 3.3 FPLC Method Parameters for KDO8PS

turbidity. To separate still, intact cells from the suspension, the solution was transferred slowly to a fresh, sterile tube and any highly viscous (unlysed) material was separated, combined and cooled

prior to a second round of lysis. Upon completion of lysis, the suspension was centrifuged at 12,000 rcf, 4 °C for 15 min to pellet and separate any unlysed cells.

The supernatant was then combined into a sterile beaker surrounded by an ice bath contained in a larger beaker. This solution was set to a gentle stir and to this, PSB was added dropwise in a volumetric ratio of 0.134:1 of PSB:lysate. This solution was allowed to stir for 15 min, during which time genetic material was precipitated out. This solution was then centrifuged 12,000 rcf, 4 °C for 30 min to separate solubilized lysate from precipitated genetic material. The cell lysate was then inserted into pre-wetted 3 kDa cutoff dialysis tubing and placed into 4 L beakers containing dialysis buffer (1 L buffer/5 mL lysate) which were stirred at 4 °C for at least 12 hours. Dialysis buffer was changed after 4 hours to ensure equilibration of lysate with 75 mM KCl. This lysate was then centrifuged for 10 min at 7,000 rcf, 4 °C to remove precipitated proteins. The supernatant was filtered through a 0.22 µm syringe filter and divided into aliquots reflecting 2.5 g of starting material (i.e. if 10 g of frozen pellet were lysed, de-salted lysate was divided into 4 aliquots). Each aliquot was then injected on to an anion exchange column (900 mm x 16 mm, DEAE-Sepharose(Toyopearl)) that had been equilibrated with buffers A & B to an ionic strength of of 75 mM KCl. The step gradient HPLC protocol is reflected in table 3.3 with a typical elution profile reflected in figure 3.16. Absorption was measured at 215 nm due to KDO8PS lacking tryptophans and containing only four tyrosines (resulting in an extremely low absorbance at 280 nm). Confirmation of KDO8PS in the elution peak was verified using sodium dodecyl sulfate polyacrylamide gel electrophoresis (SDS-PAGE) and a thiobarbituric acid assay as described in Ray (1980). Pooled fractions of KDO8PS were then concentrated with a 10 kDa cutoff centrifugal filter (Centricon, Millipore) until an absorbance value of A_{205}=0.645 (20 mg/mL) was achieved. This solution was then frozen in 1-2 mL aliquots at -80 °C in cryogenic tubes for storage until crystallization.

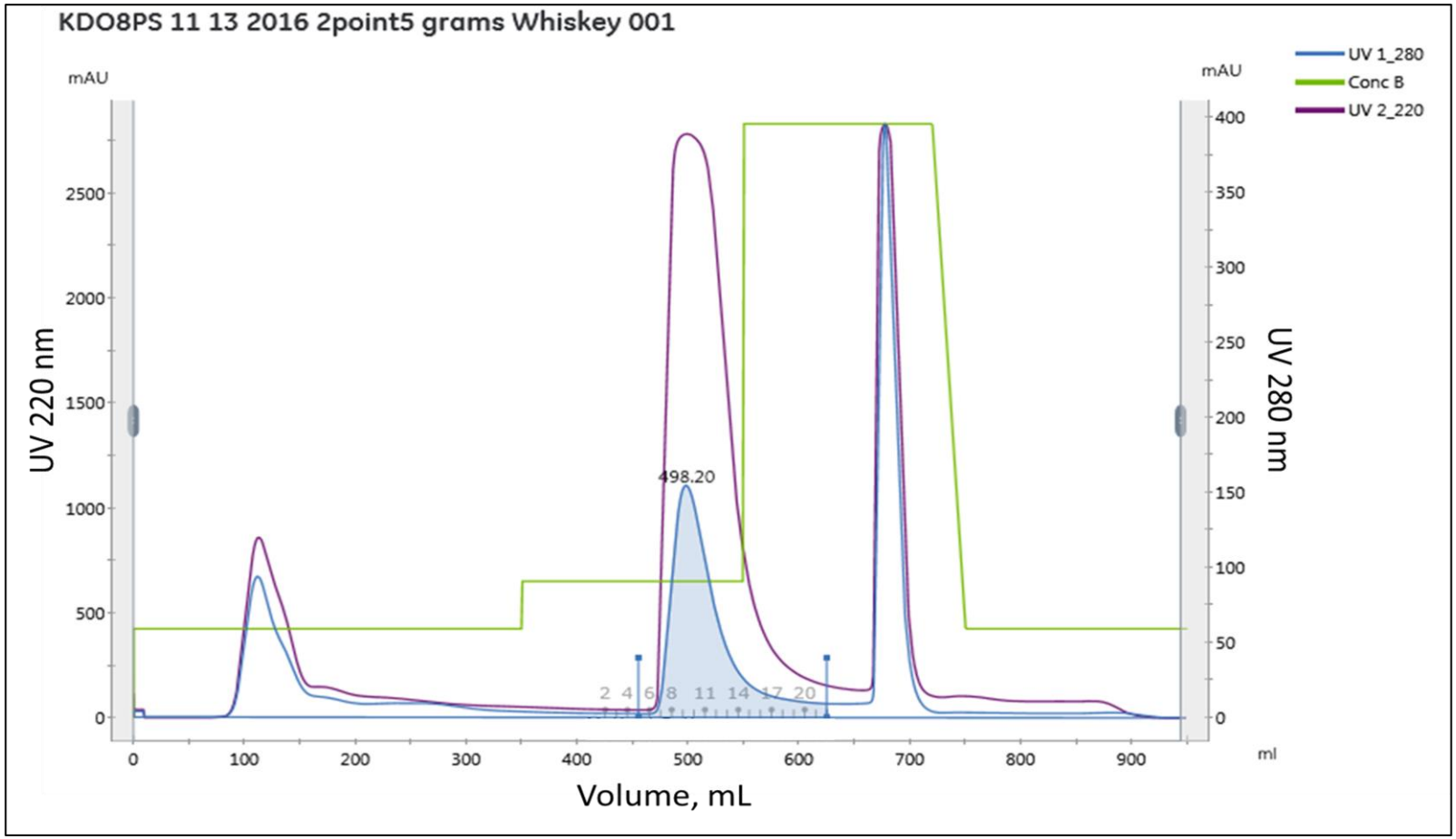

Figure 3.16 Chromatograph for KDO8PS FPLC Run

Typical elution profile for a KDO8PS FPLC run. Note the difference in scaling for the absorbance at 220 nm and 280 nm due to the lack of tyrosine in KDO8PS. The middle (2nd) peak represents the KDO8PS tetramer.

. **References**

Antonkine, M. L., P. Jordan, P. Fromme, N. Krauß, J. H. Golbeck and D. Stehlik (2003). "Assembly of protein subunits within the stromal ridge of photosystem I. Structural changes between unbound and sequentially PS I-bound polypeptides and correlated changes of the magnetic properties of the terminal iron sulfur clusters." Journal of molecular biology **327**(3): 671-697.

Aquila, A., M. S. Hunter, R. B. Doak, R. A. Kirian, P. Fromme, T. A. White, J. Andreasson, D. Arnlund, S. Bajt and T. R. Barends (2012). "Time-resolved protein nanocrystallography using an X-ray free-electron laser." Optics express **20**(3): 2706-2716.

Asojo, O., J. Friedman, N. Adir, V. Belakhov, Y. Shoham and T. Baasov (2001). "Crystal structures of KDOP synthase in its binary complexes with the substrate phosphoenolpyruvate and with a mechanism-based inhibitor." Biochemistry **40**(21): 6326-6334.

Baasov, T. and A. Kohen (1995). "Synthesis, inhibition, and acid-catalyzed hydrolysis studies of model compounds of the proposed intermediate in the KDO8P-synthase-catalyzed reaction." Journal of the American Chemical Society **117**(23): 6165-6174.

Blankenship, R. E. and H. Hartman (1998). "The origin and evolution of oxygenic photosynthesis." Trends in biochemical sciences **23**(3): 94-97.

Brettel, K. (1997). "Electron transfer and arrangement of the redox cofactors in photosystem I." Biochimica et Biophysica Acta (BBA)-Bioenergetics **1318**(3): 322-373.

Britt, R. D., K. A. Campbell, J. M. Peloquin, M. L. Gilchrist, C. P. Aznar, M. M. Dicus, J. Robblee and J. Messinger (2004). "Recent pulsed EPR studies of the photosystem II oxygen-evolving complex: implications as to water oxidation mechanisms." Biochimica et Biophysica Acta (BBA)-Bioenergetics **1655**: 158-171.

Byrdin, M., P. Jordan, N. Krauss, P. Fromme, D. Stehlik and E. Schlodder (2002). "Light harvesting in photosystem I: modeling based on the 2.5-Å structure of photosystem I from Synechococcus elongatus." Biophysical journal **83**(1): 433-457.

Conrad, C. E. (2016). Overcoming Barriers in Structural Biology Through Method Development of Serial Crystallography, Arizona State University.

Cox, N., M. Retegan, F. Neese, D. A. Pantazis, A. Boussac and W. Lubitz (2014). "Electronic structure of the oxygen-evolving complex in photosystem II prior to OO bond formation." Science **345**(6198): 804-808.

D'Souza, F. W., Y. Benenson and T. Baasov (1997). "Catalytic mechanism of KDO8P synthase: synthesis and evaluation of a putative reaction intermediate." Bioorganic & Medicinal Chemistry Letters **7**(19): 2457-2462.

Dau, H., I. Zaharieva and M. Haumann (2012). "Recent developments in research on water oxidation by photosystem II." Current opinion in chemical biology **16**(1-2): 3-10.

Debus, R. J., M. A. Strickler, L. M. Walker and W. Hillier (2005). "No evidence from FTIR difference spectroscopy that aspartate-170 of the D1 polypeptide ligates a manganese ion that undergoes oxidation during the S0 to S1, S1 to S2, or S2 to S3 transitions in photosystem II." Biochemistry **44**(5): 1367-1374.

Duewel, H. S., S. Radaev, J. Wang, R. W. Woodard and D. L. Gatti (2001). "Substrate and Metal Complexes of 3-Deoxy-d-manno-octulosonate-8-phosphate Synthase from Aquifex aeolicus at 1.9-Å Resolution

IMPLICATIONS FOR THE CONDENSATION MECHANISM." Journal of Biological Chemistry **276**(11): 8393-8402.

Eaton-Rye, J. J. and W. F. Vermaas (1991). "Oligonucleotide-directed mutagenesis of psbB, the gene encoding CP47, employing a deletion mutant strain of the cyanobacterium Synechocystis sp. PCC 6803." Plant molecular biology **17**(6): 1165-1177.

Fiedler, E., S. Thorell, T. Sandalova, R. Golbik, S. König and G. Schneider (2002). "Snapshot of a key intermediate in enzymatic thiamin catalysis: Crystal structure of the α-carbanion of (α, β-dihydroxyethyl)-thiamin diphosphate in the active site of transketolase from Saccharomyces cerevisiae." Proceedings of the National Academy of Sciences **99**(2): 591-595.

Fischer, N., M. Hippler, P. Setif, J. P. Jacquot and J. D. Rochaix (1998). "The PsaC subunit of photosystem I provides an essential lysine residue for fast electron transfer to ferredoxin." The EMBO journal **17**(4): 849-858.

Fromme, P. and H. T. Witt (1998). "Improved isolation and crystallization of Photosystem I for structural analysis." Biochimica et Biophysica Acta (BBA)-Bioenergetics **1365**(1): 175-184.

Fromme, P., H. Bottin, N. Krauss and P. Sétif (2002). "Crystallization and electron paramagnetic resonance characterization of the complex of photosystem I with its natural electron acceptor ferredoxin." Biophysical journal **83**(4): 1760-1773.

Fromme, P., A. Melkozernov, P. Jordan and N. Krauss (2003). "Structure and function of photosystem I: interaction with its soluble electron carriers and external antenna systems." FEBS letters **555**(1): 40-44.

Fromme, P. and I. Grotjohann (2006). Structural analysis of cyanobacterial photosystem I. Photosystem I, Springer**:** 47-69.

Fromme, P. and I. Grotjohann (2008). "Overview of photosynthesis." Wiley-VCH Verlag, Weinheim, Germany.

Golbeck, J. H. (1992). "Structure and function of photosystem I." Annual review of plant biology **43**(1): 293-324.

Golbeck, J. H. (1994). Photosystem I in cyanobacteria. The molecular biology of cyanobacteria, Springer**:** 319-360.

Golbeck, J. H. (1999). "A comparative analysis of the spin state distribution of in vitro and in vivo mutants of PsaC. A biochemical argument for the sequence of electron transfer in Photosystem I as FX→ FA→ FB→ ferredoxin/flavodoxin." Photosynthesis research **61**(2): 107-144.

Grossman, A. R., M. R. Schaefer, G. G. Chiang and J. L. Collier (1993). "The phycobilisome, a light-harvesting complex responsive to environmental conditions." Microbiological reviews **57**(3): 725-749.

Guergova-Kuras, M., B. Boudreaux, A. Joliot, P. Joliot and K. Redding (2001). "Evidence for two active branches for electron transfer in photosystem I." Proceedings of the National Academy of Sciences **98**(8): 4437-4442.

Haumann, M., C. Müller, P. Liebisch, L. Iuzzolino, J. Dittmer, M. Grabolle, T. Neisius, W. Meyer-Klaucke and H. Dau (2005). "Structural and oxidation state changes of the photosystem II manganese complex in four transitions of the water oxidation cycle (S0→ S1, S1→ S2, S2→ S3, and S3, 4→ S0) characterized by X-ray absorption spectroscopy at 20 K and room temperature." Biochemistry **44**(6): 1894-1908.

Isobe, H., M. Shoji, S. Yamanaka, Y. Umena, K. Kawakami, N. Kamiya, J.-R. Shen and K. Yamaguchi (2012). "Theoretical illumination of water-inserted structures of the CaMn 4 O 5 cluster in the S 2 and S 3 states of

oxygen-evolving complex of photosystem II: full geometry optimizations by B3LYP hybrid density functional." Dalton transactions **41**(44): 13727-13740.

Jordan, P., P. Fromme, H. T. Witt, O. Klukas, W. Saenger and N. Krauß (2001). "Three-dimensional structure of cyanobacterial photosystem I at 2.5 Å resolution." Nature **411**(6840): 909-917.

Karlsson, A., J. V. Parales, R. E. Parales, D. T. Gibson, H. Eklund and S. Ramaswamy (2003). "Crystal structure of naphthalene dioxygenase: side-on binding of dioxygen to iron." Science **299**(5609): 1039-1042.

Kona, F., X. Xu, P. Martin, P. Kuzmic and D. L. Gatti (2007). "Structural and mechanistic changes along an engineered path from metallo to nonmetallo 3-deoxy-D-manno-octulosonate 8-phosphate synthases." Biochemistry **46**(15): 4532-4544.

Krauß, N. (2008). "Structure and function of cyanobacterial photosystem I." Photosynthetic Protein Complexes: A Structural Approach: 23-64.

Kupitz, C., S. Basu, I. Grotjohann, R. Fromme, N. A. Zatsepin, K. N. Rendek, M. S. Hunter, R. L. Shoeman, T. A. White and D. Wang (2014). "Serial time-resolved crystallography of photosystem II using a femtosecond X-ray laser." Nature **513**(7517): 261-265.

Leiros, I., S. McSweeney and E. Hough (2004). "The reaction mechanism of phospholipase D from Streptomyces sp. strain PMF. Snapshots along the reaction pathway reveal a pentacoordinate reaction intermediate and an unexpected final product." Journal of molecular biology **339**(4): 805-820.

Li, M., D. A. Semchonok, E. J. Boekema and B. D. Bruce (2014). "Characterization and evolution of tetrameric photosystem I from the thermophilic cyanobacterium Chroococcidiopsis sp TS-821." The Plant Cell **26**(3): 1230-1245.

Li, Z., A. K. Sau, C. M. Furdui and K. S. Anderson (2005). "Probing the role of tightly bound phosphoenolpyruvate in Escherichia coli 3-deoxy-D-manno-octulosonate 8-phosphate synthase catalysis using quantitative time-resolved electrospray ionization mass spectrometry in the millisecond time range." Analytical biochemistry **343**(1): 35-47.

Liang, P.-H., A. Kohen, T. Baasov and K. S. Anderson (1997). "Catalytic mechanism of Kdo8P synthase. Pre-steady-state kinetic analysis using rapid chemical quench flow methods." Bioorganic & Medicinal Chemistry Letters **7**(19): 2463-2468.

Loll, B., J. Kern, W. Saenger, A. Zouni and J. Biesiadka (2005). "Towards complete cofactor arrangement in the 3.0 Å resolution structure of photosystem II." Nature **438**(7070): 1040-1044.

Mikkelsen, M., M. Jørgensen and F. C. Krebs (2010). "The teraton challenge. A review of fixation and transformation of carbon dioxide." Energy & Environmental Science **3**(1): 43-81.

Müller, M. G., C. Slavov, R. Luthra, K. E. Redding and A. R. Holzwarth (2010). "Independent initiation of primary electron transfer in the two branches of the photosystem I reaction center." Proceedings of the National Academy of Sciences **107**(9): 4123-4128.

Nield, J., E. P. Morris, T. S. Bibby and J. Barber (2003). "Structural analysis of the photosystem I supercomplex of cyanobacteria induced by iron deficiency." Biochemistry **42**(11): 3180-3188.

Oh-oka, H., Y. Takahashi, K. Kuriyama, K. Saeki and H. Matsubara (1988). "The protein responsible for center A/B in spinach photosystem I: isolation with iron-sulfur cluster (s) and complete sequence analysis." The Journal of Biochemistry **103**(6): 962-968.

Perry, R. H. and C. Chilton (1973). "Chemical engineering's handbook." McGraw-Hill Kogakusha, Ltd: 2-74.

Porra, R., W. Thompson and P. Kriedemann (1989). "Determination of accurate extinction coefficients and simultaneous equations for assaying chlorophylls a and b extracted with four different solvents: verification of the concentration of chlorophyll standards by atomic absorption spectroscopy." Biochimica et Biophysica Acta (BBA)-Bioenergetics **975**(3): 384-394.

Pushkar, Y., J. Yano, K. Sauer, A. Boussac and V. K. Yachandra (2008). "Structural changes in the Mn4Ca cluster and the mechanism of photosynthetic water splitting." Proceedings of the National Academy of Sciences **105**(6): 1879-1884.

Raetz, C. and W. Dowhan (1990). "Biosynthesis and function of phospholipids in Escherichia coli." Journal of Biological Chemistry **265**(3): 1235-1238.

Raines, C. A. (2003). "The Calvin cycle revisited." Photosynthesis research **75**(1): 1-10.

Rappaport, F., M. Guergova-Kuras, P. J. Nixon, B. A. Diner and J. Lavergne (2002). "Kinetics and pathways of charge recombination in photosystem II." Biochemistry **41**(26): 8518-8527.

Ray, P. (1980). "Purification and characterization of 3-deoxy-D-manno-octulosonate 8-phosphate synthetase from Escherichia coli." Journal of bacteriology **141**(2): 635-644.

Roegner, M., D. A. Chisholm and B. A. Diner (1991). "Site-directed mutagenesis of the psbC gene of photosystem II: isolation and functional characterization of CP43-less photosystem II core complexes." Biochemistry **30**(22): 5387-5395.

Rousseau, F., P. Setif and B. Lagoutte (1993). "Evidence for the involvement of PSI-E subunit in the reduction of ferredoxin by photosystem I." The EMBO journal **12**(5): 1755-1765.

Schmidt, M. (2013). "Mix and inject: reaction initiation by diffusion for time-resolved macromolecular crystallography." Advances in Condensed Matter Physics **2013**.

Setif, P. Q. and H. Bottin (1994). "Laser flash absorption spectroscopy study of ferredoxin reduction by photosystem I in Synechocystis sp. PCC 6803: evidence for submicrosecond and microsecond kinetics." Biochemistry **33**(28): 8495-8504.

Setif, P. Q. and H. Bottin (1995). "Laser flash absorption spectroscopy study of ferredoxin reduction by photosystem I: spectral and kinetic evidence for the existence of several photosystem I-ferredoxin complexes." Biochemistry **34**(28): 9059-9070.

Theisen, M. J., I. Misra, D. Saadat, N. Campobasso, H. M. Miziorko and D. H. Harrison (2004). "3-hydroxy-3-methylglutaryl–CoA synthase intermediate complex observed in "real-time"." Proceedings of the National Academy of Sciences of the United States of America **101**(47): 16442-16447.

Umena, Y., K. Kawakami, J.-R. Shen and N. Kamiya (2011). "Crystal structure of oxygen-evolving photosystem II at a resolution of 1.9 Å." Nature **473**(7345): 55-60.

Vainer, R., V. Belakhov, E. Rabkin, T. Baasov and N. Adir (2005). "Crystal structures of Escherichia coli KDO8P synthase complexes reveal the source of catalytic irreversibility." Journal of molecular biology **351**(3): 641-652.

Wang, J., H. S. Duewel, R. W. Woodard and D. L. Gatti (2001). "Structures of Aquifex aeolicus KDO8P synthase in complex with R5P and PEP, and with a bisubstrate inhibitor: role of active site water in catalysis." Biochemistry **40**(51): 15676-15683.

Xia, Z., R. W. Broadhurst, E. D. Laue, D. A. Bryant, J. H. Golbeck and D. S. Bendall (1998). "Structure and properties in solution of PsaD, an extrinsic polypeptide of photosystem I." The FEBS Journal **255**(1): 309-316.

Xu, Q., Y.-S. Jung, V. P. Chitnis, J. A. Guikema, J. H. Golbeck and P. R. Chitnis (1994). "Mutational analysis of photosystem I polypeptides in Synechocystis sp. PCC 6803. Subunit requirements for reduction of NADP+ mediated by ferredoxin and flavodoxin." Journal of Biological Chemistry **269**(34): 21512-21518.

Yamaguchi, K., S. Yamanaka, H. Isobe, T. Saito, K. Kanda, Y. Umena, K. Kawakami, J. R. Shen, N. Kamiya and M. Okumura (2013). "The nature of chemical bonds of the CaMn4O5 cluster in oxygen evolving complex of photosystem II: Jahn-Teller distortion and its suppression by Ca doping in cubane structures." International Journal of Quantum Chemistry **113**(4): 453-473.

Yano, J. and V. K. Yachandra (2008). "Where water is oxidized to dioxygen: structure of the photosynthetic Mn4Ca cluster from X-ray spectroscopy." Inorganic chemistry **47**(6): 1711-1726.

Yano, J. and V. Yachandra (2014). "Mn4Ca cluster in photosynthesis: where and how water is oxidized to dioxygen." Chemical reviews **114**(8): 4175-4205.

Yeagle, G. J., M. L. Gilchrist, L. M. Walker, R. J. Debus and R. D. Britt (2008). "Multifrequency electron spin-echo envelope modulation studies of nitrogen ligation to the manganese cluster of photosystem II." Philosophical Transactions of the Royal Society B: Biological Sciences **363**(1494): 1157-1166.

Zouni, A., H.-T. Witt, J. Kern, P. Fromme, N. Krauss, W. Saenger and P. Orth (2001). "Crystal structure of photosystem II from Synechococcus elongatus at 3.8 Å resolution." Nature **409**(6821): 739.

4 SMALL IS BEAUTIFUL: GROWTH AND DETECTION OF NANOCRYSTALS

Jesse Coe and Alexandra Ros

Forward

This chapter is a book chapter on nanocrystallogenesis that is part of a text that will be published later this year (2018) by Springer. I co-wrote this with Dr. Alexandra Ros and my contributions include writing of introduction, nanocrystallogenesis and conclusion sections. I also wrote half of the characterization section, created figures 4.1-4.4, and lead the editing and revision process.

Introduction

With the advent of X-ray free electron lasers (FELs), the field of serial femtosecond crystallography (SFX) was borne, allowing a stream of nanocrystals to be measured individually and diffraction data to be collected and merged to form a complete crystallographic data set. This allows submicron to micron crystals to be utilized in an experiment when they were once, at best, only an intermediate result toward larger, usable crystals. SFX and its variants have opened new possibilities in structural biology, including studies with increased temporal resolution, extending to systems with irreversible reactions, and minimizing artifacts related to local radiation damage. Perhaps the most profound aspect of this newly established field is that 'molecular movies', in which the dynamics and kinetics of biomolecules are studied as a function of time, are now an attainable commodity for a broad variety of systems, as discussed in Chapters 12-13. However, one of the historic challenges in crystallography has always been crystallogenesis and this is no exception when preparing samples for serial crystallography methods. In the following chapter, we focus on some of the specific characteristics and considerations inherent in preparing a suitable sample for successful serial crystallographic approaches.

While this chapter's title directly refers to "nano-"crystals, the following is also applicable to small crystals that may not be strictly sub-micron. Synchrotron serial crystallography at a micro-focused beamline is also a highly effective technique that is very similar to nano-crystallography at X-ray FELs but requires larger crystals than the minimum needed for SFX. Furthermore, depending

on specifics of a given experiment, larger crystals may also be preferable at an X-ray FEL, sometimes up to a few tens of microns in the largest dimension, which is common for membrane proteins as discussed in Chapter 5. Other times, growth of crystals larger than a couple microns tends to be elusive at best, a challenge common with G-protein coupled receptors (covered in depth in Chapter 11). In any case, it is common within the field for the terms “nanocrystal” and “microcrystal” to be somewhat synonymous, with “nanocrystal” appearing for a broad size regime in the literature. For the sake of brevity, we will refer to all small crystals suitable for serial crystallography as “nanocrystals” hereto forth.

Nanocrystallogenesis

When approaching nanocrystallogenesis, the parameters governing growth remain largely the same from macrocrystallography, namely thermodynamics, kinetics, and solubility. The notable difference is that the objective occupies a different region of the phase space. To additionally optimize diffraction quality, one must also consider and control crystal size and size homogeneity. These parameters have an impact upon data collection in serial crystallography and failure to optimize can cause malfunction of sample introduction and/or an increase in time and sample needed to complete a data set. It is also very important to consider and prioritize characteristics for a given experiment, especially in the case of a serial experiment aimed at something more complex than a single static structure.

In general, crystallogenesis can be thought about as a multidimensional phase space consisting of any and all conditions experienced by the protein in solution. A simplified depiction of this can be seen in **Figure 1** where a 2-D slice is shown between protein concentration and a generic precipitant. However, in practice a comprehensive phase space is highly complicated and can be sensitive to multiple additives, temperature, protein homogeneity, time, pH, etc., essentially anything that comprises part of the crystallization environment. While each protein will have its own unique phase space, there are generalities that can help guide optimization and avoid a brute force approach past initial screening (even this is not strictly brute force as most commercial screens rely on empirical successes). It should also be noted that all the traditional pre-screening optimizations (e.g. purification, configurational and oligomeric homogeneity,

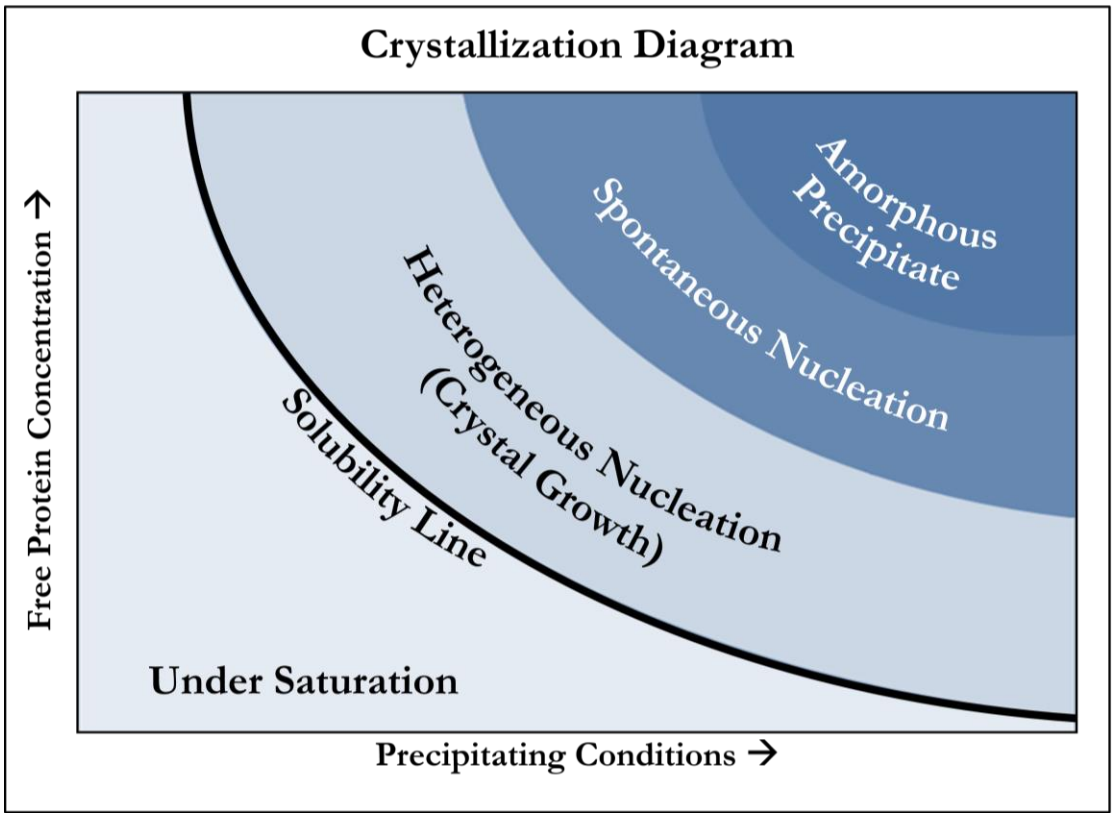

Figure 4.1: Generalized Solubility Phase Diagram for Crystallization.

Illustrates the typical qualitative relationship between solubility and concentrations of protein and precipitating conditions (e.g. salt concentration, pH, temperature). As one or both of these concentrations are increased, the solubility tends to decrease until a supersaturated state is achieved where nucleation is able to occur. The segmented regions in the supersaturated phase qualitatively increase in their propensity for nuclei to form as they move away from the solubility curve. Once supersaturation becomes very large, disordered (non-crystalline) nuclei tend to be favored, illustrated by the amorphous precipitate region in the top right.

detergent screening, mutagenic engineering, etc.) will still play an immense role in the ability to obtain quality samples. We will not go into detail about these here but would refer you to texts by Scopes(Scopes 2013) or Doublie(Doublié 2007) for additional reading on the topic.

Thermodynamics of solubility and nucleation

In its most fundamental sense, the formation of crystals is nothing more than a controlled precipitation of a molecule or molecular system such that translational symmetry is achieved through free energy minima. The process is driven by thermodynamics through solubility and intermolecular forces. This pertains to any size of crystal and just like macrocrystallogenesis of macromolecules, the first step is to find a foothold within the broad parameter phase space

governing a particular sample of interest. This typically involves trying many conditions in a broad screen to look for trends and patterns in solubility by sparsely sampling phase space(Jancarik and Kim 1991). It is important to remember that in order to find precipitating conditions, one must consider a plethora of variables including not only the concentration and composition of protein and mother liquor but also the pH, temperature, time and method among others. While **Figure 1** is an example of a generic crystallization diagram, a useful tool in visualizing phase space, it should be stressed that this is simplified and, as mentioned above, many variables govern the actual phase space, making it n-dimensional. The 'precipitating condition' represented on the x-axis can either be thought of as representing the entire suite of precipitating variables other than the concentration of the protein itself, or as a single variable, equating to simply a 'slice' of the n-dimensional phase space.

In contrast to macrocrystallogenesis, where a single or few large crystals are desired, the main goal for a serial crystallography sample is to obtain *many* crystals that are *small* in size. That is to say, the objective is to reach a completely different area in phase space. Highly oversaturating conditions are the crux of this, allowing the formation of many nuclei and rapid depletion of protein concentration. In **Figure 1** this equates to nearing the border between the nucleation and amorphous precipitate regions. To achieve this and guide crystallogenic optimization, we must first consider how nucleation and crystallization are driven.

For the favorability of spontaneous nucleation and crystal growth to occur, the free energy of the system must decrease from the process. From a physiochemical perspective, the formation of nuclei is a stochastic function of concentration. As the concentration increases, so too does the chance for the macromolecules to collide and, subsequently, collide with a favorable orientation that can lower the local energy (but collisions also lead to unfavorable orientations that eventually dissipate). This can be written in terms of the free energy of crystallization as

$$\Delta G_{crystal} = \Delta H_{crystal} - T(\Delta S_{crystal} + \Delta S_{solvent}) \qquad \text{eq. 1}$$

Since a crystal is inherently ordered, the entropy from the macromolecular crystal will always be negative (equating to a positive contribution to the free energy). Thereby, the loss of degrees of freedom for the protein needs to be compensated with an entropic gain from disrupted

solvent shells (there may also be an enthalpic contribution but it has generally been shown to be minimal in comparison(Vekilov, Feeling-Taylor et al. 2002)). Even upon such an event, the solution is still dynamic and subsequent collisions can cause the nuclei to increase in size or disperse. General phase transitions, *e.g.* nanocrystallization, intrinsically are a competition between the destabilizing interfacial (surface area) free energy components and the stabilizing bulk (volume) free energy components. For simplicity, consider an ideal case where the surface energy doesn't vary with orientation (i.e. a spherical nucleus). This leads to a free energy for the nucleus being the Gibbs-Thomson equation for a condensed droplet as a function of radius, namely

$$\Delta G_{nucleation} = \frac{4}{3}\pi r^3 \nu k_B T \ln(S) + 4\pi r^2 \gamma \qquad \text{eq. 2}$$

where k_B, T and S are the Boltzmann constant, temperature and entropy, respectively, the ν term represents a molar volume element for an additional molecule with respect to the packing, r is the radius of the droplet, and the γ term representing the specific energy of the surface (Garcıa-Ruiz 2003). Certainly, in the real nucleation case, the γ term will have an anisotropic dependence upon facet composition but the fundamental form of the equation remains a competition between a positive surface component (acting similar to an activation barrier) and a negative (stabilizing) volumetric component that dominates as r becomes larger. This means that a critical radius occurs when we set the derivative of equation 2 to zero:

$$\frac{d\Delta G_{nucleation}}{dr} = 4\pi r^2 \nu k_B T \ln(S) + 8\pi r\gamma = 0 \qquad \text{eq. 3}$$

$$\therefore \qquad r_{critical} = -\frac{2\gamma}{\nu k_B T \ln(S)} \qquad \text{eq. 4}$$

In essence, a critical sized nucleus is formed when the contribution to the overall energy from the nucleus volume overcomes the surface energy increase as an additional molecule is added(Garcıa-Ruiz 2003). However, in order to get to this point, growth of smaller, quasi-stable nuclei must continue to grow against an uphill energy barrier until a critical size is reached.

For any amount of supersaturation, critical nuclei are possible given enough time but at low levels of supersaturation, deterioration of the sub-critical nuclei dominates. This region is typically represented as the heterogeneous nucleation or growth zone (see **Figure 1**). As can be qualitatively understood, higher degrees of supersaturation lead to more collision events and

shorter, more feasible time scales for critical nuclei to occur. This is represented as the spontaneous nucleation zone. In extremely elevated levels of supersaturation through increased protein concentration, collisions will be so frequent as to overcome the preference for energetically favorable orientations necessary for quasi-stable nuclei, as the unstable nuclei lifetimes are outcompeted by collisions. Alternatively, increasingly precipitating conditions also lead to higher levels of supersaturation that change the potential energy surface of collisions, allowing slower relaxation times. Both of these can lead to critical radii being achieved without the molecules exhibiting translational symmetry, resulting in an amorphous precipitate. It should be noted that other than the solubility line, the zone separations represented in crystallization phase diagrams are not well defined and are, without a conventional metric, somewhat arbitrary. This does not exclude their usefulness, especially in conveying and differentiating phase space trajectories experienced in different methods. For any set of sample characteristics, fine screening solution content and physical parameters is crucial. One of the most impactful factors in attaining your goal lies in the chosen method, for which the following section is dedicated.

Methods

It has been almost 60 years since the first protein crystal structure was published(Perutz, Rossmann et al. 1960) and even longer since the first protein crystals were observed in 1840(Giegé 2013). In the time since, many ways to produce macromolecular crystals have been devised. Vapor diffusion, batch, free interface diffusion and dialysis methods are amongst the most historically popular ways to make macrocrystals, each having their own benefits and challenges (these and other methods have been covered extensively elsewhere(Rupp 2009, McPherson 2017), the reader is referred to these publications for detailed review of these and other methods). Again, when aiming for nanocrystals, we are simply trying to access a different area of phase space and so, in most cases, we can just adapt these techniques to suit our purpose. Another pervading theme in sample production for serial crystallography is the sheer mass needed for a successful data set, sometimes requiring hundreds of milligrams of protein! This is certainly something to consider and, when possible, increasing crystallization setup volumes should be considered as it

can lead to consistency throughout data collection on top of reducing tediousness of sample preparation.

It is important to remember that crystals are not grown statically and the method and implementation will largely affect experimental crystallogenesis results. Once a foothold condition is found, fine screening around it should be done with multiple methods. This is especially important for nanocrystals due to the multitude of parameters that need to be simultaneously optimized. While one method may give the best diffraction, this must sometimes be weighed against size or yield or even growth time. It's important to keep in mind the specifics of the experiment at hand. If it is the case that the goal is simply to obtain a novel structure from a protein that resists the formation of large, well-ordered crystals then diffraction quality will of course take precedence. However, this is not always the case. For example, in a kinetic study with substrate mixing there are multiple variables to simultaneously optimize. In this type of experiment, as reaction time regimes become short, size and size homogeneity become increasingly important to maintain temporally homogeneous data sets along a reaction timeline. Of course, enhancing resolution is still very important but so long as the resolution is sufficient to see conformational changes in a particular system, the other parameters may become more beneficial to focus ones efforts.

Adaptation of existing conditions

While obtaining structures on samples that only seem to form small crystals is certainly a benefit of SFX, this represents only a fraction of targets. The ability to "outrun" radiation damage, the high temporal resolving power and the extreme brilliance found at an X-ray FEL lend it to completely new areas of study and the ability to overcome some of the shortcomings of other light sources. For example, the structures of metalloproteins can be determined without site specific radiation damage(Cohen, Soltis et al. 2014, Hirata, Shinzawa-Itoh et al. 2014), irreversible reactions and conformational homogeneity in transient states can be probed(Aquila, Hunter et al. 2012, Kupitz, Basu et al. 2014), and ultrafast time regimes (sub ps) are now accessible to study dynamics(Tenboer, Basu et al. 2014, Pande, Hutchinson et al. 2015). This opens many avenues for progression on proteins that already have a static crystal structure and, subsequently, already have well-established crystallization conditions. With this in mind, a primary goal of this chapter is

to guide the translation of existing macrocrystallogenic conditions into those suitable for SFX and initial conditions are assumed.

By far the most common and effective way to get a foothold on possible crystallization conditions is mass sparse-matrix screening and this remains true for nanocrystallization. Interpreting the results differs as one searches for conditions giving nanocrystals but most times the large crystal “hit” in a screen can be optimized into nanocrystal conditions in the same way that a shower of crystals can lead to macrocrystal conditions. It should also be noted that most large-scale screening is done with vapor diffusion and while this can still lead to nanocrystals, it is a method that moves through phase space because of evaporative concentration and can be a generally “slow” method with respect to inducing nucleation. In its traditional form, it is also an extremely tedious method to obtain the milligrams of sample generally necessary for a serial crystallography experiment. That is not to say that it could not be used and one can certainly imagine a volumetrically upscaled sitting drop setup, but it is rarely the most convenient or optimal technique. It is important to keep in mind that, in general, increased concentration of precipitating condition leads to smaller crystals. While this is certainly true for chemical precipitants (e.g. salt, polyethylene glycol (PEG)), it is worthwhile to think about the kinetics or time as well. For example, in a vapor diffusion experiment, the volume and concentration of the well solution controls how fast the sample cocktail concentrates via evaporation. Parameters such as temperature or viscosity can also have a large effect on the thermodynamic rate of nucleus formation. For example, a highly viscous precipitant (e.g. PEG) can slow down the process by which the protein molecules collide in solution versus a lower viscosity precipitant, which will favor a much faster diffusion rate. Or in the case of temperature, crystallogenesis at a higher temperature will increase the available energy in solution, giving faster diffusion and thus tending to favor more nuclei and smaller crystals (of course caution must be taken when varying the temperature too much to avoid possibly unwanted effects such as denaturation or expansive freezing of water). The speed of a method will depend on its crystallization diagram; the time spent in each region of phase space will dictate the overall results of a given setup.

Free interface diffusion

One method that has been adapted from a traditional method is that of nanocrystalline free interface diffusion (FID), originally described by Kupitz et al. 2014(Kupitz, Grotjohann et al. 2014) and shown in **Figure 2**. The difference lies in the need for larger volumes and high nucleation rates. Typically, the less dense of the two solutions—which is typically the protein solution--is first aliquoted into a vessel, often a microcentrifuge tube because the sloped sides have the potential to act as a parameter by influencing the mixing region volume and concentration profile. A quick centrifugation can be helpful to remove any bubbles and create a flat interface before addition of

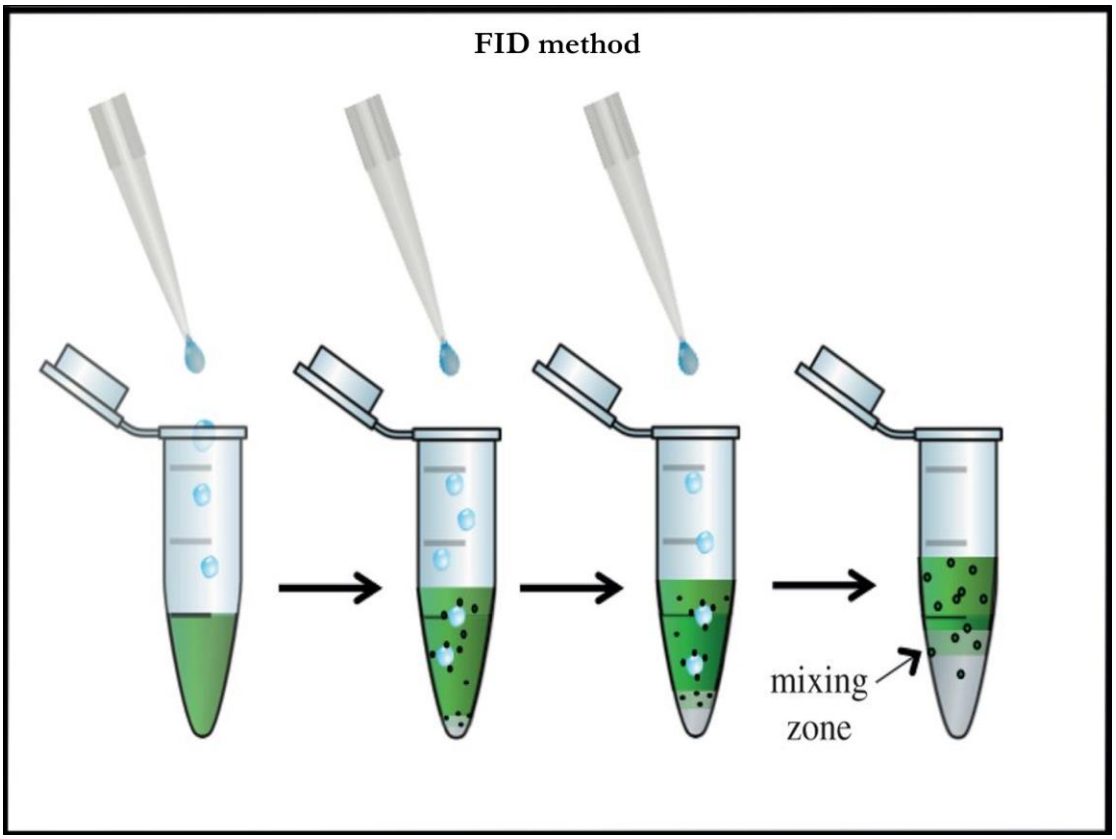

Figure 4.2: Schematic of Nanocrystal Free Interface Diffusion (FID) Setup.

As the denser solution (either protein or precipitant) is dropwise added to the center of the other and a layered setup with a mixing region between occurs. The mixing region acts as an interface with high local concentrations of both protein and precipitating conditions, allowing diffusive mixing. The concentrations and volume of this will depend upon the container geometry, droplet size and viscosities of the two solutions. The sloped sides of a microcentrifuge tube (pictured here) can allow for easily varying the surface area to volume ratio, though this should be taken into account when attempting to upscale a setup. (adapted from Kupitz et al.(Kupitz, Grotjohann et al. 2014))

the second solution. Once a flat interface is obtained, the denser solution is added through the center of the surface dropwise. It will form a bottom layer and some perturbation at the interface, giving a small volume mixing zone. This allows for very high concentrations of each solution at the interface, higher than can be achieved with thorough mixing (most other methods involve the need for mixing of a protein containing solution and a precipitant containing solution, leading to a necessary dilution of both upon mixing). The perturbation from dropping one solution through the other tends to speed up the process, The access to high nucleation regions of phase space experienced at this interface can cause nanocrystals to form and, as they grow larger, tend to settle towards the bottom layer. In the case that the precipitant is denser, as is common with many precipitants containing high salt or PEG, this serves as a sort of auto-quenching effect as the

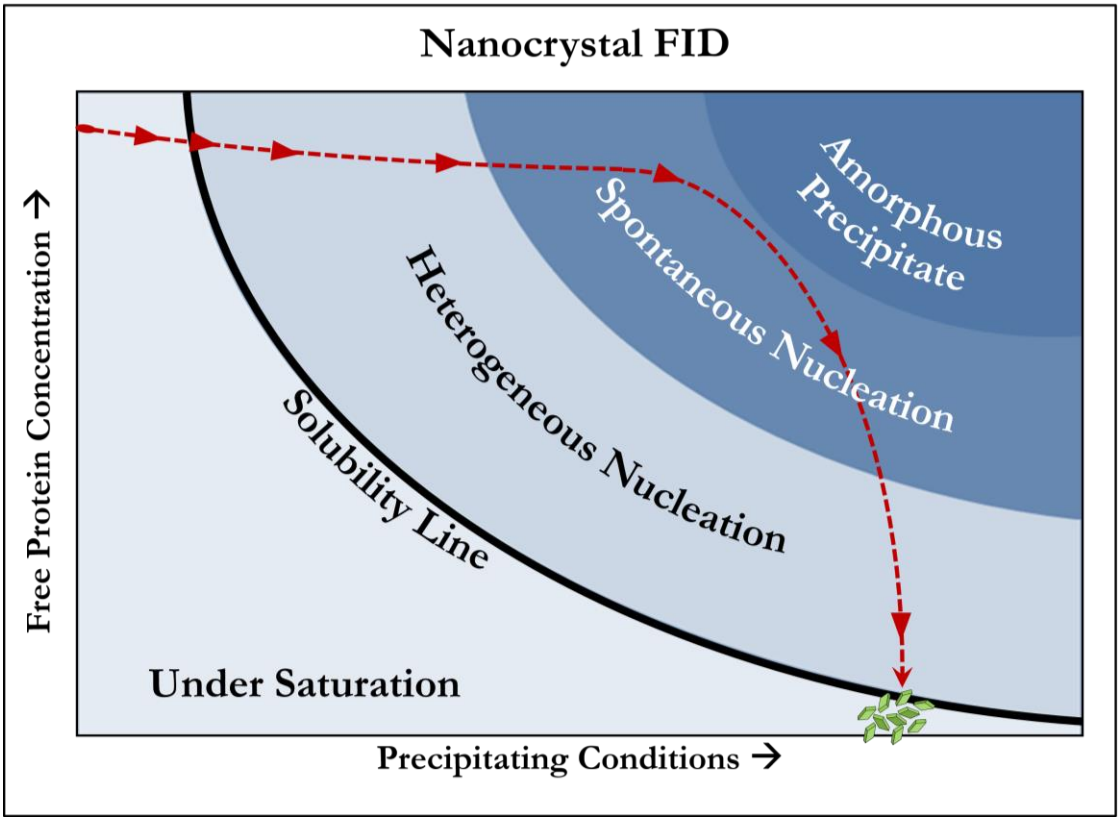

Figure 4.3: Nanocrystal FID Phase Diagram.

The red line shows a conceptual path experienced by proteins moving through the interface into the mixing region and finally depositing as part of a crystal. The spacing of the arrows denote a likely temporal trajectory as diffusion slowly allows it to enter the mixing region and then more rapidly adsorb onto a nucleus before settling as crystal growth is achieved.

crystals settle away from the free protein layer and into the precipitant rich layer. Different volumetric ratios, total volume and even droplet radius can have a profound effect on results from this method and volumetrically conserved upscaling tends to eventually break down reproducibility and quality. The limit of this is highly specific to a given protein/mother liquor and is likely a function of the mixing region profile which depends upon surface area and volume ratios, viscosities and perturbation. Gentle centrifugation is a way to enhance gravitational settling and can also expedite crystal favoring nucleation formation and uniform growth. As can be expected, over extended periods full mixing of the two layers can occur and to prevent any loss of quality or even dissolution, crystals should be harvested and/or quenched prior to complete diffusion (the time sensitivity of this will be a function of miscibility between the layers as well as volume-interfacial surface area ratio). This method can be particularly useful when either or both precipitant and protein concentrations are constrained by solubility in other methods and a smaller crystal size is desired. This is due to the ability to have saturated concentrations at the interface. It should by be noted, however, that reproducibility is sensitive to even minor differences in the setup of this method due to the many affecting variables involved such as volume, ratio, drop size, position of the perturbation in the interface and containerinducing a minimal but necessary mixing region.

Batch nanocrystallization

Batch crystallization is a “cocktail” approach where the protein and precipitating conditions are homogenized. This is particularly useful in making the large volumes often necessary for SFX experiments due to its ease and simplicity. This has the added benefits of decreasing sensitivity to user technique and volumetric scaling, though caution should be taken to ensure scaling does not interfere with homogeneity. It can be seen in **Figure 4** that there is no movement through phase space prior to nucleation (or lack thereof). Protein stock and precipitating mother liquor are typically added to a vial or microcentrifuge tube and either homogenized by pipette mixing or using a magnetic stir rod. The stir rod allows homogeneity to be retained as protein begins to precipitate out and can allow either the protein or precipitant to be added slowly, avoiding high concentration interfaces with significant contact time. Analogously, when pipette mixing, multiple aliquots can be serially pipette mixed to allow a more gradual introduction of precipitating conditions. This is

perhaps the most convenient method as it is a short, simple setup that can usually be upscaled to complete experimental volumes suitable for consistent data collection. While this method can theoretically be done in any size vessel, experimental demand usually requires a few milliliters of sample for a full data set. Fine screening with a dilution gradient using a crystallization robot can help explore specific batch conditions prior to upscaling. It is also worth noting that recently, microfluidic approaches have also been successful at fine screening batch conditions with minimal volume constraints (Abdallah, Roy-Chowdhury et al. 2016).

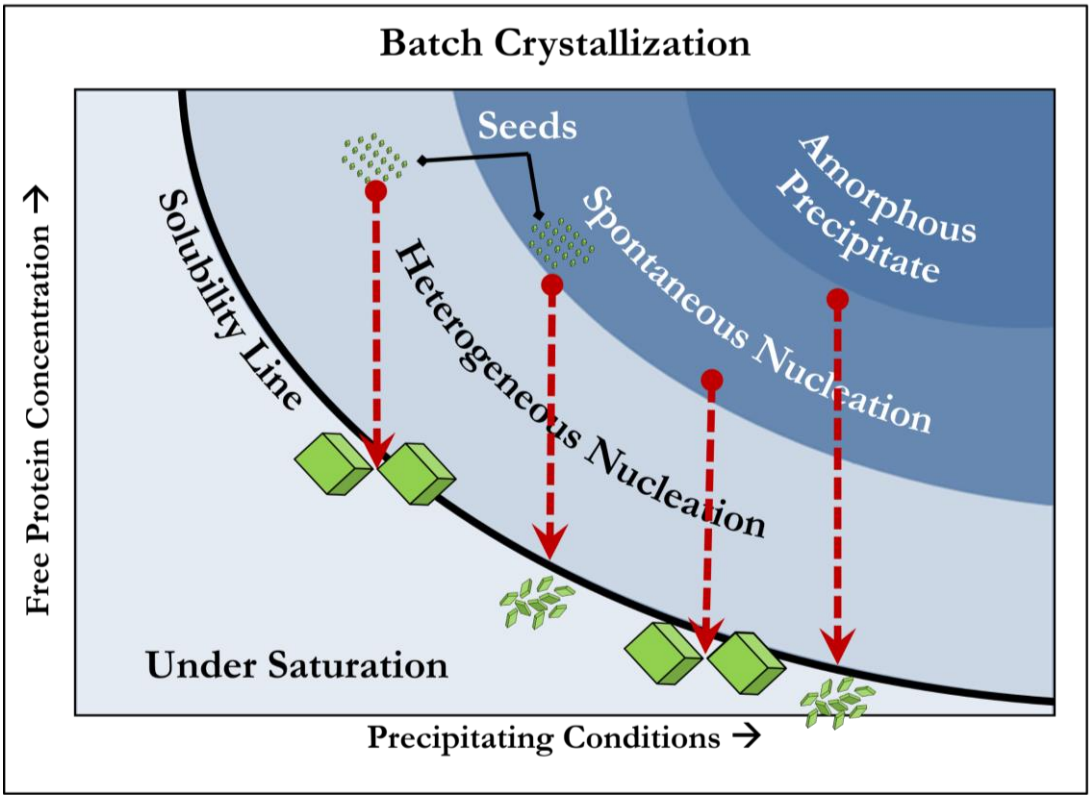

Figure 4.4: Batch Crystallization Phase Diagram.

Illustration of the "cocktail" method where a protein and precipitant are homogenized, essentially picking a supersaturated point in phase space and letting it evolve with equilibration. As can be seen, the crystal size (among other parameters) is highly sensitive to these conditions and will tend to smaller crystals further away from the solubility curve. The use of seeding is also highlighted here as it often allows milder conditions to result in a similar result. Seeding can also encourage homogeneity and accelerate crystallogenesis.

Other methods and sample delivery considerations

There are many other methods that have been successfully used to grow macromolecular nanocrystals that are thus far a little less general. Almost any method that has been used for

microcrystal growth can be adapted to nanocrystal generation, the key is using parameters to enter a different region of phase space. In fact, even methods to create nanocrystals such as mechanically crushing macrocrystals have had success(Kupitz, Olmos Jr et al.), although caution should be taken with this as homogeneity and quality can be severely impacted, the degree of which is very dependent on the crystal contacts within the crystal.

A particularly interesting method of crystallization that should be mentioned is that of *in vivo* over-expression. Using baculovirus-Sf9 cells, multiple proteins have now been shown to crystallize *in vivo*(Redecke, Nass et al.) with successful injecting of the un-lysed cells in one case(Sawaya, Cascio et al.). While the mechanism behind i*n vivo* crystallization and its general applicability is currently unclear, it is certainly worth monitoring the progress behind this phenomenon.

One method of crystallization that has been extremely successful with membrane proteins, particularly G-coupled protein receptors, is the use of the lipidic cubic phase (LCP) as both a crystallization and delivery media. LCP is a bi-continuous mesophase that can allow type I crystal packing (i.e. stacked membrane embedded planar 2D crystals lacking detergent micelles(Ostermeier and Michel 1997)) due to its membrane mimetic properties, typically leading to tighter packing and often higher resolution than obtainable with crystals grown in detergents or other surfactants (*in surfo*). **Chapter 5** is dedicated to this method as it has been so successful when approaching some of the most challenging proteins.

One of the clear advantages of an LCP capable system for serial crystallography is the ability to create a much slower moving viscous jet, which reduces sample consumption by orders of magnitude. The reduction of sample requirements has driven the development of alternative viscous carriers in which pre-grown crystals can be embedded into a viscous media, allowing 1-2 orders of magnitude less material(Weierstall, James et al. 2014, Fromme, Ishchenko et al. 2015, Martin-Garcia, Conrad et al. 2017).

A useful tool that can be implemented with any method is seeding, the use of pre-grown crystals to ‘seed’ nucleation. These seeds are of course obtained by some initial crystallization method but the addition to a subsequent crystallization attempt can have a profound effect.

Thinking back to the crystallization phase diagrams, different areas of phase space can now be approached. Using seeds also tends to encourage homogeneity among crystal size(Ibrahim, Chatterjee et al.) and across different batches. The most convenient side effect is that while pursuing nanocrystallogenic optimization, any sample made along the way can be used for subsequent trials and can be doped into any method easily.

Stability and storage

Since serial crystallography avoids radiation damage via constantly replenishing sample during data collection, freezing techniques and optimization therein are, in general, unnecessary. Instead, one must consider how the sample is stored and handled prior to sample introduction to best preserve diffraction quality and physical characteristics that are optimized during crystallogenesis.

Crystal size is one of the most sensitive characteristics to the storage method and technique. Ideally, crystals are kept in a solution of their mother liquor or a variant thereof. This has the benefit of needing only to resuspend the sample prior to introduction and data collection (once an optimal crystal density has been determined and achieved). It is not uncommon, however, that the precipitating conditions used in initial crystallogenesis allow further growth over time, since many crystallization experiments have a slow growth phase due to supersaturated conditions in the mother liquor. This can occur from any free protein continuing to adsorb to crystal surfaces. It is therefore highly advisable to either remove uncrystallized protein as soon as the desired crystals are obtained or to further decrease solubility, though the impact is highly dependent upon the amount of time the sample must be stored and specific conditions. While in some cases an optimized method will have little remaining protein in solution, this can still be necessary. Fortunately, this can usually be achieved by allowing crystals to settle, carefully removing the supernatant and replacing with fresh mother liquor, effectively “washing” the crystals. It should be noted that this does have the effect of shifting the solution out of equilibrium and will cause the surface molecules to fall back into solution until equilibrium is obtained. For a larger size crystal this can be negligible, but for a smaller crystal it may be significant and may be advisable to try to find a minimal concentration that keeps stability or to shift to higher precipitating conditions, effectively decreasing equilibrium concentration of free protein.

Ostwald ripening, the process by which larger crystals tend to grow while smaller ones tend to dissolve due to thermodynamic favorability, may also disturb the size, homogeneity and number of individual crystals. This occurs because even though crystals have been formed, the solution is effectively in a dynamic equilibrium with solubility being low but not strictly absent. Because of the lower number of interactions with the bulk crystal for the molecules on the surface of a crystal, they tend to detach and go into solution periodically before stochastically recombining with a crystal. Due to the difference in surface area, this process favors large crystals in the long run. Certainly, the more size homogenous the sample, the slower this process will occur but absolute size homogeneity is impossible to achieve practically. One way to avoid Ostwald ripening is to further decrease the solubility of the protein, effectively quenching the exchange. Simply by "washing" the sample as described above with a higher precipitating condition can achieve this, although a dramatic change in solubility can sometimes damage the crystals and sometimes a stepwise approach is preferable. Temperature can also be used to decrease solubility, though again care must be taken to monitor unwanted effects on crystal quality.

As data are usually collected at or near biological temperatures, stability during transportation can also be a concern. Fortunately, due to the high nucleating conditions needed for a plethora of small crystals, nanocrystallogenesis is typically a fast process and oftentimes samples can be grown on site within a matter of hours or days prior to an experiment. However, if this is not the case, it is imperative to ensure the integrity of the sample is not compromised during transport by anticipating environmental perturbations such as handling or temperature variance. As automation and remote data collection in serial experiments is almost certainly inevitable, this will likely become more and more general of a consideration. Temperature secure containers, eliminating gas from sample head space, shock absorption or even embedding crystals into a viscous media (if viable) are among the approaches that can ameliorate shipping concerns. As always, testing and characterizing to optimize results and protect precious sample is vital.

Considerations and characterization for SFX optimization

Characteristics – what is optimal?

There are some unique characteristics that apply in serial crystallography that must be controlled and optimized for a given sample. Size homogeneity and sample density are always general concerns, affecting data collection efficiency and quality. Of course, size itself plays a vital role and sometimes bigger is better. But there are many circumstances where it is not and thoughtful selection is crucial to a successful experiment, *e.g.* for time-resolved studies. In fact, for time resolved studies, it can be important for both size and size distribution to be minimized. Size governs reaction homogeneity upon probing since the activation trigger (e.g. light, substrate) will have a different distribution to the different molecules in the crystal dependent upon volume. In the case of a chemical trigger, molecules towards the center would on average experience a delayed reaction initiation due to reactant diffusion within the crystal. For optically triggered reactions, molecules downstream in the direction of the pump laser propagation would experience increasing attenuation in pump power, leading to lower yields of reaction initiation. There will also be a temporal range of reaction initiation similar to the chemical trigger case but the range would be in the 10s-100s of femtoseconds for micrometer sized crystals. This still must be taken into account when exploring dynamics on these timescales and, like the diffusive case, smaller crystals are preferable with respect to homogeneous initiation. Reaction timeline homogeneity itself is of course important as the serial snapshots are merged into a data set and large distributions will broaden conformational heterogeneity. This will be covered in more detail in the later **chapters 12-13**.

Sample density, i.e. the concentration of crystals in a suspension, is another key factor. Depending on X-ray source size, crystal size and jet size, the optimal sample density can be calculated by approximating a Poisson distribution for the hit rate versus concentration (usually falling in the 10^9-10^{11} crystals/mL range), though a Poisson approximation will become less accurate as the crystal size becomes much larger than the beam focal spot. It is important to verify that the protein-rich phase is in fact crystalline and, especially in the sub-micron range, this is not always straightforward. In fact, many times small crystals may be mistaken for amorphous

precipitate to even the trained eye. Techniques in microscopy and diffraction that can be used to verify crystallinity are covered in section 3.2.

Data analysis considerations

In serial crystallography, data are collected as a series of diffraction “snapshots” from different crystals that are merged together to form a complete data set. As opposed to a rotation series on a goniometer, only partial reflections are measured and thus structure factors must be elucidated using Monte Carlo methods. The high multiplicities of measured reflections needed necessitate a large amount of sample even in an ideal case, where each crystal is the exact same size, morphology, quality, etc. Changes in sample homogeneity signify that even more measurements, i.e. single snapshot diffraction patterns, are needed for the data to converge to reliable and comparable intensities.

In early SFX studies, $>10^5$ diffraction patterns were thought to be necessary to determine structures(Kirian, Wang et al. 2010). This has considerably decreased in the past few years and full data sets have now been obtained with under 10,000 (in some cases, under 1000!(Uervirojnangkoorn, Zeldin et al. 2015)) images needed(Fromme, Ishchenko et al. 2015, Ginn, Brewster et al. 2015, Ginn, Messerschmidt et al. 2015). A narrower size distribution of protein nanocrystals, however, might greatly reduce the number of diffraction patterns required for successful merging and integration. In addition, the peak intensity of Bragg reflections in the individual diffraction patterns scales with the crystal size quadratically, which may lead to significant variation in peak intensities. This means that a high size inhomogeneity not only introduces another parameter that needs to be addressed using Monte Carlo methods, practical considerations may necessitate attenuation of the beam to avoid detector damage. This can lead to a decreased signal-to-noise ratio (SNR) for patterns representing the smaller sized crystals in a sample since the beam intensity used is often determined from the strongest scattering crystals.

Another consideration for data analysis related to crystal size is experimental solutions to the phase problem, *i.e.* phasing. There is a huge interest to improve SFX data analysis for *de novo* structure determination. Crystal size homogeneity may play a crucial role in this approach. For example, Spence *et al.* have proposed that coherent diffraction intensities between Bragg

reflections of sufficiently small crystals may be used for novel phasing approaches(Spence, Weierstall et al. 2012). These coherent shape-transformed Bragg reflections allow for two-dimensional projection images of the entire nanocrystal, which could be used to solve the crystallographic phase problem in SFX without prior information, crystal modifications, or resolution restrictions. It is expected that this novel approach works best for a specific crystal size range. When crystals become too small (containing too few unit cells), the inter-Bragg diffraction intensities reduce, thus an optimal intermediate size is desired(Brehms and Diederichs 2014). The details of methods involving these properties will be discussed in **Chapter 9**. Whether exploiting nanocrystals discreteness for novel phasing approaches or minimizing the time and amount of sample needed for a complete data set, there is a clear motivation to obtain control over crystallogenic parameters in order to improve data quality.

Practicality: Sample and hardware

There are some practical concerns that arise from the hardware used for SFX experiments, which must also be considered. From the sample delivery point of view, most experiments have been performed using some type of gas focused jet (sample delivery is covered in detail in **chapter 5**) and to minimize wasted sample, constrictions in the hardware are often very small (nozzles usually contain a capillary with 30 – 100 µm inner diameter). Minimum flow rates for a stable jet (equating to minimal sample consumption) can vary depending on buffer composition, especially viscosity. With polyalcohols, such as polyethylene glycol, being a common precipitating agent, this can be a frequent concern and it is worth experimenting to try minimizing viscosity during final sample preparation. Setting up small aliquots of different concentrations and monitoring crystal integrity over time can save later frustration over hindrance of data collection due to a clogged nozzle or inconsistent jet.

Another issue that arises due to the small nature of sample delivery hardware is clogging due to the crystals themselves or other particles. Certainly, one must select a nozzle size appropriate for the employed crystals (a good rule of thumb is *at least twice the size* of the largest crystals in the batch) but many times even a sample with relatively good size homogeneity will have a few large outliers. It should be kept in mind that optimal sample densities are on the order of 10^{9}-

10^{11} crystals/mL and it only takes one crystal to clog the nozzle. It is therefore in a user's best interest to have filtering systems in place prior to the injection hardware to avoid time loss for fixing/replacing the hardware. In-line filtering is almost always a necessity but it is oftentimes advisable to 'pre-filter' the sample prior to containment in a sample delivery reservoir. Many commercially available plumbing and filter setups can be adapted to this purpose, for example standard liquid chromatography hardware. It should be noted that not all filters are created equal and different types and quoted porosities can have detrimental effects on a crystalline sample such as shearing crystals apart. It is advisable to test the effect of filtration on the sample prior to a beamtime in order to know which filter will work best for a given crystal suspension. The density at which a crystal suspension is filitered can also have an effect and, in general, it is prudent to filter at low concentrations and allow a sample to settle before removing supernatant for concentration. Filtering can also serve to improve size homogeneity during sample preparation should you experience a bimodal or multimodal distribution.

Even when a particular sample is not strongly constrained by quantity or another method of sample introduction is used that can sidestep the above-mentioned concerns, size heterogeneity can cause other concerns. In addition to data quality and efficiency concerns addressed in the previous section, saturation or even destruction of the detector must be considered. Especially with the extremely brilliant X-ray FELs, a well diffracting crystal can easily exceed the intensity at which a detector can be damaged. Even when not damaged, saturation can occur, obscuring values for structure factors (i.e. intensities above the saturation threshold will be measured incorrectly as the threshold value). To avoid this, the beam is usually attenuated to a level that certainly avoids damage and minimizes saturation. Remembering that peak scattered intensity scales quadratically with respect to the number of unit cells illuminated by the beam, it becomes clear how attenuating to the largest crystals that are introduced to the beam can quickly limit the lower size limit for useful data collection.

Control of homogeneity through post growth methods:

Once crystals are obtained in suitable concentrations, it is important to characterize crystal size homogeneity. This can be accomplished with the methods described in section 3.3. However, we emphasize that dynamic processes may play a significant role, requiring stringent analysis of crystals prior to crystallographic measurements. Crystals may grow, aggregate or dissolve after production and these processes need to carefully be accounted for. To reduce the amount of unwanted larger crystals, a straight forward approach of filtering may be employed. While this approach is suitable for sufficiently large amounts of crystals available, it might not be applicable when the concentration of smaller crystals is low or when the crystals are prone to decomposition through mechanical filtering approaches. In addition, as discussed above, novel phasing approaches may require specific size ranges and narrow size distributions, which require more sophisticated approaches for post growth crystal sizing.

One approach to fractionate crystals by size has recently proposed by Abdallah *et al.*(Abdallah, Zatsepin et al. 2015) In this novel microfluidic method, crystals are deviated in their migration path while flowing through a micrometer-sized constriction and collected in various outlet reservoirs of a microfluidic device. The method relies on dielectrophoresis, where the applied dielectrophoretic force scales with the radius of the crystals to the power of three(Abdallah, Zatsepin et al. 2015). In the application demonstrated by Abdallah *et al.*, crystals experienced negative dielectrophoresis, repulsing large objects into a center stream, while smaller particles deviate to side channels. Smaller crystals can thus be recovered in the side channels. The first realization of this dielectrophoretic crystal sorting was demonstrated with photosystem I (PSI crystals, as demonstrated in **Figure 5**). The sorted crystals were characterized with various techniques, demonstrating that they were not decomposed during the sorting process and that they retained excellent diffraction quality even after sorting(Abdallah, Chao et al. 2013). This continuous crystal sorting method was further developed for higher throughput to account for the mL volumes of crystal suspension needed in liquid jet based injection methods for SFX with X-ray FELs(Abdallah, Chao et al. 2013).

Characterization

During the crystal screening and growth process, one needs to continually characterize the crystallogenic results to guide optimization. Compared to macrocrystals, this can be a significantly more complex task due to the necessity for high density, homogeneous crystal suspensions typical in serial crystallography, which are also generally harder or sometimes impossible to visualize with routine microscopy. This is not to say that the task is necessarily always difficult, just that it requires a thoughtful approach with a larger arsenal of tools than is traditionally necessary.

Optical Detection – visualizing your crystals

While it is still a good idea to first look at potential crystals under an optical microscope, it can be difficult to score results, especially as crystals approach one micron or smaller. Using a polarized filter to look for birefringence can be particularly useful to look for crystals whose sizes are near this threshold. In practice, the intensity from birefringence scales with the size of the crystals and so its usefulness does have a lower limit. Nonetheless, it can certainly enhance the ability to differentiate crystals from amorphous precipitate and can often provide enough contrast to indicate crystals below a micron. It should be noted that birefringence requires optical anisotropy and will therefore be absent or diminished in space groups with high symmetry (e.g. cubic). However, this does allow most salt crystals to be ruled out, which can be a concern with the high concentrations that can arise in nanocrystal creation.

One of the most useful ways to identify crystallinity is that of second harmonic generation (SHG) microscopy. There has been considerable effort developing this technique, specifically for identification of nanocrystals, and commercial instruments, such as Formulatrix's SONICC (second order nonlinear imaging of chiral crystals), have enjoyed success within the community. SHG works on the principle that under very intense illumination with light, two photon processes become significant and subsequent frequency doubling occurs over the fundamental wavelength. In our case, this is dependent on the polarizability of both the molecule and the crystal as a whole, constructively interfering with additional unit cells. In practice, this means that it is only observable from crystals (or other periodic objects) and will differentiate between them and amorphous material, often down to ~100 nm or smaller. It is also very sensitive to anisotropy and complete

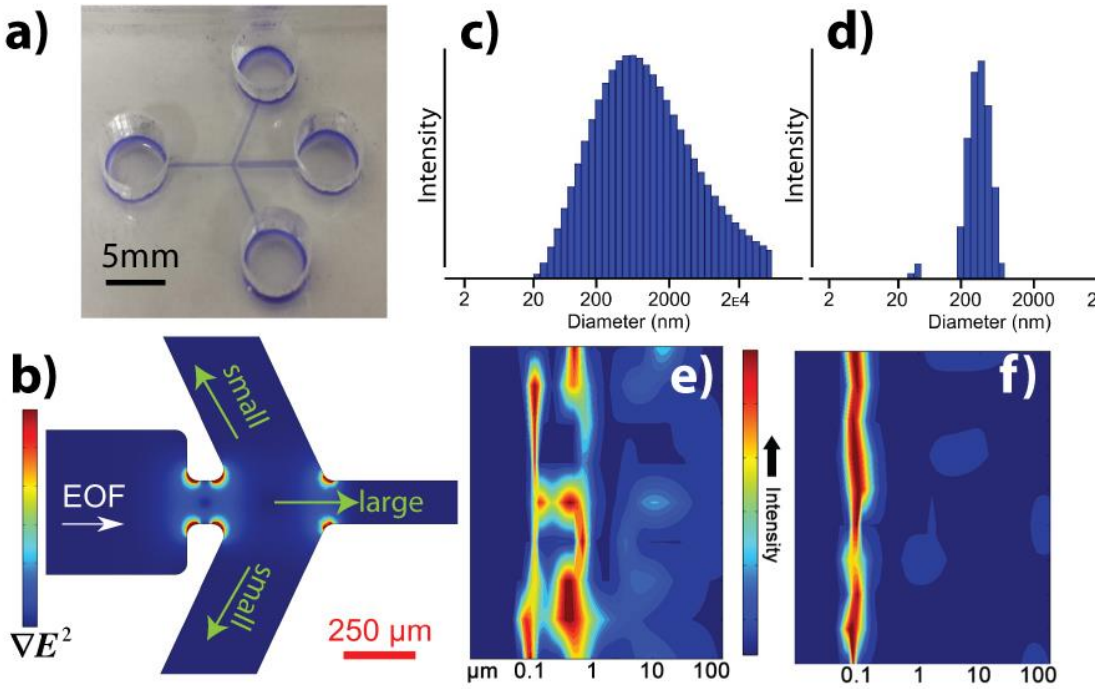

Figure 4.5 Microfluidic Sorting:

a) Image of the microfluidic sorter used for high throughput crystal sorting. b) Mechanism of crystal sorting in the microfluidic device near the constriction region. Electroosmotic flow (EOF) is used to deliver sample to the constriction region. The green arrows indicate the flow of large and small particles after the constriction regions, where sorting occurs. c) Dynamic light scattering (DLS) analysis of PSI crystal suspension prior to sorting. d) DLS analysis of PSI crystal suspension after sorting with the dielectrophoretic sorter indicating crystals <600nm). e) PSI crystal suspension prior to dielectrophoretic sorting and f) after sorting in the low throughput version (adapted from: Abdallah *et al*.(Abdallah, Zatsepin et al. 2015)) A homogeneous size

destructive interference will occur in any centrosymmetric space group. Like birefringence, this also rules out cubic space groups but prevents false positives from most salts. In addition, other space groups of high symmetry may suffer from diminished signal, albeit not strictly zero(Haupert and Simpson). The signal also has an inherent dependence on the polarizability of the protein itself and this can lead to varying size limits or even feasibility. Commercial dyes have been developed that can intercalate through the crystal and enhance signal, a noteworthy aid for one aiming for the smaller end of the size regime. A good cross validation for potential nanocrystals observed in either SHG or polarized microscopy is UV-microscopy, which can easily highlight protein from salt by way of tryptophan fluorescence. In fact, the SONICC instrument couples an ultraviolet two-photon excitation fluorescence (UV-TPEF) method with SHG imaging, allowing overlapping images of a

drop for secondary characterization. This is a great cross validation for proteins with any aromatic residues that either have a SONICC prohibitive space group (false negatives) or a precipitant that can form chiral (non-protein) crystals (false positives). The use of a multiphoton process is inherently confocal in nature and allows a decreased background and narrower depth of field, particularly important with the smallest size regime or unoptimized conditions. Excellent reviews on the principles of SHG and UV-TPEF imaging can be found in Kissick et al.(Kissick, Wanapun et al.) and Madden et al.(2011), respectively.

Light Scattering Techniques for size determination

Light scattering methods are traditionally used to characterize particle sizes in suspension. Among those, dynamic light scattering (DLS) and nanoparticle tracking analysis (NTA) have been primarily applied for the characterization of crystal suspensions. NTA has only become recently available commercially but has found immediate application in crystallography. DLS is a well-established method used routinely in nano- and microparticle analysis.

DLS takes advantage of the scattering characteristics of suspended particles in solution. It is thus not surprising that DLS has also been employed for the characterization of suspensions of small crystals required for crystallography and in particular the smaller crystals needed for SFX. In DLS, a laser is directed into the crystal suspension and the scattered light is measured at some fixed angle. Since the particles in the solution exhibit Brownian motion, the measured scattered light intensity will also vary randomly over time, typically in the microsecond time regime. If the particles are large, the time variations at the detector are slow, whereas for small particles the time variations are faster. The time fluctuations of this scattering are recorded in DLS and related to the particle size distribution in solution using suitable correlation analysis.

We may write the autocorrelation function of the scattered light intensity as(Pecora 2000):

$$C(t) = \frac{\langle I(t)I(0)\rangle}{\langle I(0)I(0)\rangle} = 1 + g(t)^2 \qquad \text{eq. 5}$$

where t is the time and $g(t)$ is the normalized first order time autocorrelation function. For monodiperse particles, $g(t)$ constitutes an exponential function with a time decay governed by the particle diffusion coefficient, D, and the scattering vector, q:

$$g(t) = exp(-q^2 Dt) \quad \text{eq. 6}$$

The scattering vector is given by:

$$q = \frac{4\pi}{\lambda} \sin \frac{\theta}{2} \quad \text{eq. 7}$$

with λ the wavelength and θ the scattering angle. From eq. 6 we notice the direct relation of $g(t)$ to the diffusion coefficient and thus the size of a particle. The latter is obtained through the Stokes-Einstein relation:

$$D = \frac{k_B T}{6\pi\eta r} \quad \text{eq. 8}$$

Here, k_B is the Boltzmann constant, T is the temperature, η is the viscosity and r is the radius of a sphere. In a DLS measurement, we thus determine the diffusion coefficient of a particle corresponding to a sphere. Therefore r is replaced with the hydrodynamic diameter ($d_h = 2r$) for non-spherical particles. Suitable mathematical corrections need to be applied to obtain the size of non-spherical particles in DLS measurements.

Most particle and specifically crystal suspensions are not monodisperse. To account for polydispersity in DLS measurements, one introduces the methods of 'cumulants'. The decay function $g(t)$ is then assumed to consist of the sum of decay functions, where each summand accounts for a specific subset of particles. Analyzing polydispersity in DLS measurements requires suitable software, which is included in most commercial DLS instrumentation. It is also interesting to note that while DLS typically cannot distinguish between crystal and amorphous particles, a technique in which depolarized light from the scattered light is ascribed to birefringence has been developed, indicating crystallinity(Schubert, Meyer et al. 2015). For a more detailed description of the DLS theoretical framework we refer the interested reader to the literature, for example a review by Pecora(Pecora 2000) or a book by Schmitz(Schmitz 1990).

The size range suitable for a DLS analysis spans from as low as 1 nm well into the micron regime where optical characterization becomes available. However, a sample needs to be carefully characterized in order to avoid gravitational settling, which may compete with Brownian motion in µm-sized crystals. Moreover, the scattered intensity scales with the particle diameter to the 6th power, which signifies that a 10 times larger particle scatters a million times more intensely. This

relation needs to be critically viewed in DLS as the scattering of larger particles can easily overtake the much weaker scatting of smaller particles and bias the data analysis. Small crystals can thus be easily overlooked in suspension containing larger particles, such that the potentially more useful particle sizes for SFX may not be recognized.

However, DLS has become a routine tool in size characterization and it is powerful when 1) different crystallization batches are compared, 2) rapid analysis is necessary – such as at a beam time prior to injection, 3) the amount of crystal suspension is limited and not compatible with sample cell size for NTA (see below) or dilution of the sample cannot be performed for NTA and 4) if a broad size range from several tens of nanometers up to micrometers is to be characterized.

DLS instruments offer a variety of cuvettes and thus variation in the sample volume to be analyzed. Standard measurements can be routinely carried out in volumes from 1 mL down to 50 µL. For crystallization trials, performed in small volumes, such as the hanging droplet method or even miniaturized on microfluidic platforms(Pecora 2000), it becomes important to perform DLS analysis in volumes below 50 µL. This can be accomplished with instruments exhibiting specialized optics, such that the DLS laser can be directed into a hanging droplet or microfluidic channel.

Alternative to DLS, particle tracking has been applied for the characterization of crystal size distributions. In particle tracking methods, the scattering or fluorescence of small objects below 1 µm is recorded by video microscopy; hence, the method is often referred to as nanoparticle tracking analysis, or NTA. A laser of certain wavelength is directed in a sample chamber and the displacement of individual particles from frame to frame is recorded. The mean square displacement of a particle, $\bar{x}$, is related to the diffusion coefficient, D, in the 2-dimensional case via:

$$\bar{x} = \sqrt{4Dt} \qquad \text{eq. 9}$$

where t is the time. Once D is determined it can be related to the particle size, or more precisely its hydrodynamic radius, r_H, via the Stokes-Einstein relation shown in eq. 8. Be aware that D is a function of both temperature and viscosity in addition to the particle size so a new calibration must be performed whenever one or both of these variables are modified.

Suitable algorithms can track the particle motions and displacement and determine their size. In NTA, since it is a direct visualization process, particles can be counted and thus particle

concentrations can be determined. This is an important additional data point for SFX experiments and the particle concentration can be adjusted to optimize hit rates. Since NTA tracks single particles, it also allows a more detailed analysis of multimodal distributions compared to DLS, an ensemble process, and is less prone to masking of smaller particles due to the augmented scattering properties of larger particles as apparent in DLS (Schmitz 1990).

Particle tracking analysis *per se* is not a novel method and can be easily implemented via suitable imaging instrumentation and free software packages(Abdallah, Roy-Chowdhury et al. 2016), such as available for ImageJ(Rasband 1997). NTA has recently become available commercially and thus facilitated greatly for crystallography applications. The NanoSight instrument from Malvern (UK) has suitable measurement cells that allow size distribution analysis for proteins and protein crystals in the range from ~30 nm to 2 µm. Clearly, this size range shows that crystal suspensions with larger expected particle size distributions should be analyzed by DLS. Another consideration in particle tracking analysis is the size of the measurement chamber, requiring several hundred microliters to fill the entire chamber. If crystal suspensions are limited in amount, recovery needs to be attempted or in the worst case, this analysis cannot be performed.

Transmission Electron Microscopy

Transmission electron microscopy (TEM) is a useful tool in crystallography, and has provided valuable information on the quality of micro- and nanocrystals prior to serial crystallography. TEM represents a vacuum technique, where an electron beam is directed through a thin specimen. Micro- and nanocrystals are typically mounted on a thin grid for TEM imaging with use of a negative stain for increased contrast. The electron beam interacts with both the electron cloud and nuclei of the atoms in the crystals leading to electron scattering. Scattered electrons pass through an objective lens, which upon focusing creates the primary image. Additional optical components are used to form a highly magnified final image of the primary image.

Obviously, as an imaging technique for nm-sized particles, a strength of TEM is to provide unequivocal information of the size of nano- and microcrystals. It is the most direct visualization method of assessing the size of crystals, but is not suited for fast analysis. Analyzing the size-

distribution of protein crystals with TEM is a time-consuming process, and requires the sophisticated and expensive TEM instrument as well as specialized training for the experimenter. However, provided enough crystalline material is at hand, this analysis could be automated to provide size and heterogeneity information of a particular crystallization trial. But this analysis is typically not performed in favor of faster and less cumbersome techniques such as NTA and DLS related to size-based analysis.

The major strength of TEM relates to revealing information about crystallinity. TEM can provide information about the existence of nanocrystals including variations in the crystal forms or the evaluation of diffraction quality. TEM allows direct visualization of the crystal lattices and the Fourier transform of TEM images from protein crystals reveals their electron diffraction patterns or 'Bragg' spots. The higher the order of these spot, the better (in general) the diffraction quality of protein crystals.

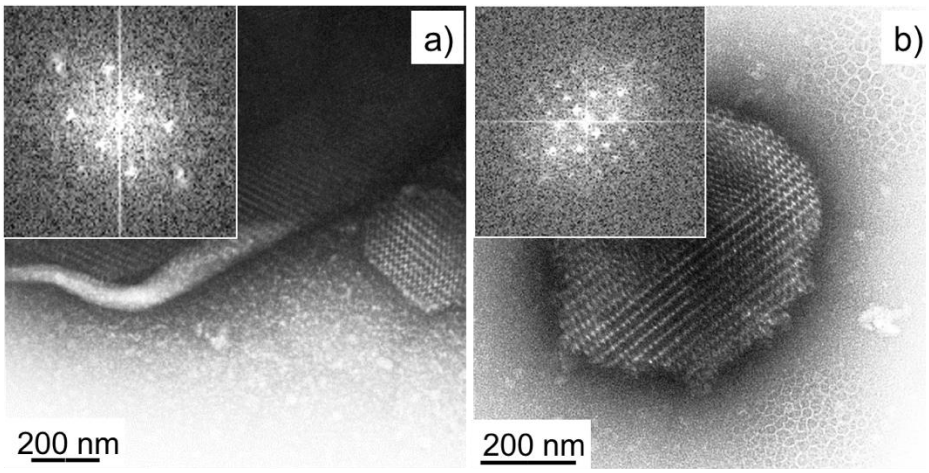

Figure 4.6 TEM Imaging of Nanocrystals

a) TEM image of PSI crystals prior to microfluidic size fractionation and corresponding Bragg spots after Fourier transformation (inset); b) TEM image obtained using negative uranyl acetate staining image of PSI crystals after microfluidic size fractionation and corresponding Bragg spots after Fourier transformation (inset). TEM analysis confirms excellent crystallinity of PSI crystals after fractionation (adapted from Abdallah *et al.*(Stevenson, Lin et al. 2016))

Stevenson *et al.* demonstrated, that Bragg spots obtained from TEM analysis of several analyzed protein crystals are indicative of crystal quality(Bai, Barnett et al. 2017). The information gained with TEM analysis of crystals includes information related to crystal lattice variations

between different crystallization methods as well as crystal pathology including lattice defects, anisotropic diffraction and nanocrystal nuclei contamination by heavy protein aggregates.

TEM thus constitutes a useful tool to identify nanocrystals for challenging protein targets(Regtmeier, Eichhorn et al. 2007) and for the evaluation and optimization of crystal growth(Stevenson, Lin et al. 2016). TEM has also been used to characterize the crystal quality after the fractionation of protein crystals by size using microfluidic tools. Abdallah *et al.* used a negative stain TEM (following a procedure previously published by Stevenson *et al.*(Stevenson, Makhov et al. 2014)) to show that PSI crystals subjected to size-based sorting showed excellent lattice resolution and highly ordered Bragg spots, as demonstrated in **Figure 6**. Indeed, SFX at an X-ray FEL was successful with these sorted crystals (Stevenson, Makhov et al. 2014).

Powder diffraction

As anyone who has grown aesthetically beautiful crystals only to find that they have less than stellar diffraction can attest, you never know until you shoot them! While the size of the samples generally prohibits any single crystal diffraction at home X-ray sources, nanocrystals are perfectly suited for powder diffraction at more accessible X-ray sources. If possible, this should be attempted before a serial crystallography experiment. While the low comparative flux can prevent knowledge of the actual diffraction limit that might be attainable at a more powerful source, powder diffraction is the best way to test for a diffracting sample and can differentiate between batches or conditions by comparative resolution limits. It is also very easy to prepare for since typically nanocrystals solutions are already a 'powder'. However, at higher resolutions the powder rings become more frequent and faint, eventually causing them to be indiscernible from background, providing a limit on resolution. The powder diffraction rings can be evaluated to get a rough estimate of the crystal size contributing to the powder rings, though resolution of a reliable size estimate is likely limited to a very small size regime (less than a few hundred nm). One can also obtain other information such as using the spacing of the rings to obtain information about the lattice spacing in the crystal.

The easiest way to do this is to harvest an aliquot of the sample (about 10 µL of pelleted nanocrystals usually works well) and put them into an X-ray transparent mountable

capillary (e.g. MiTeGen MicroRT). This should be centrifuged to create a dense powder pellet from which the liquid should be removed to ensure density. In practice, some of the mother liquor should be implemented elsewhere in the tube to avoid drying of the pellet, which can affect resolution. Then the sealed capillary can be mounted and data collected on the dense nanocrystalline pellet. Be sure to mimic the conditions as close as possible to your actual experiment (e.g. lighting for light sensitive proteins, temperature, mother liquor composition).

Conclusion

Experimental beamtime at X-ray FELs are currently much more limited than at other light sources. The careful development and characterization of crystal samples for SFX experiments with X-ray FELs is thus extremely important. There are unique characteristics that must be considered for each specific experiment, having a profound effect upon the quality of data that can be obtained. Generally, as many characterization methods as possible should be performed and this chapter summarized the most important and currently applied methods. The primary factor to consider for initial nanocrystallization trials are the higher concentrations generally key to converting macrocrystal conditions into nanocrystal conditions. Obtained nanocrystals need to be carefully characterized by size, size homogeneity, density, quantity and quality, which will all play a critical role in a successful experiment. It is always helpful to carry out cross validation whenever possible while characterizing results with nanocrystals. With the further development and improvement of facilities at the existing X-ray FEL instruments and the next generation of X-ray FELs either coming online or in the planning stages, the available characterization facilities are expected to be considerably more abundant and state of the art. This will certainly facilitate crystal characterization prior to SFX with X-ray FELs for any future experiment. In addition, as Chapter 9 will explore, the movement towards smaller size regimes accessible in crystallography has led to the ability to access interesting characteristics inherent to truly discrete crystals, resulting in new modes of data collection and analysis.

References

Abdallah, B. G., T. C. Chao, C. Kupitz, P. Fromme and A. Ros. (2013, Oct 22). "Dielectrophoretic sorting of membrane protein nanocrystals." ACS nano Retrieved 10, 7, from http://www.ncbi.nlm.nih.gov/pmc/articles/PMC3894612/pdf/nihms523135.pdf.

Abdallah, B. G., N. A. Zatsepin, S. Roy-Chowdhury, J. Coe, C. E. Conrad, K. Dörner, R. G. Sierra, H. P. Stevenson, T. D. Grant, G. Nelson, D. R. James, G. Calero, R. M. Wachter, J. C. H. Spence, U. Weierstall, P. Fromme and A. Ros (2015). "Microfluidic sorting of protein nanocrystals by size for XFEL diffraction." Structural Dynamics **2**: 041719.

Abdallah, B. G., S. Roy-Chowdhury, R. Fromme, P. Fromme and A. Ros (2016). "Protein Crystallization in an Actuated Microfluidic Nanowell Device." Crystal Growth & Design **16**: 2074-2082.

Aquila, A., M. S. Hunter, R. B. Doak, R. A. Kirian, P. Fromme, T. A. White, J. Andreasson, D. Arnlund, S. Bajt and T. R. Barends (2012). "Time-resolved protein nanocrystallography using an X-ray free-electron laser." Optics express **20**(3): 2706-2716.

Bai, K., G. V. Barnett, S. R. Kar and T. K. Das (2017). "Interference from Proteins and Surfactants on Particle Size Distributions Measured by Nanoparticle Tracking Analysis (NTA)." Pharmaceutical Research **34**(4): 800-808.

Brehms, W. and K. Diederichs (2014). "Breaking the indexing ambiguity in serial crystallography." Acta Crystallographica Section D **D70**: 101-109.

Cohen, A. E., S. M. Soltis, A. Gonzalez, L. Aguila, R. Alonso-Mori, C. O. Barnes, E. L. Baxter, W. Brehmer, A. S. Brewster, A. T. Brunger, G. Calero, J. F. Chang, M. Chollet, P. Ehrensberger, T. L. Eriksson, Y. Feng, J. Hattne, B. Hedman, M. Hollenbeck, J. M. Holton, S. Keable, B. K. Kobilka, E. G. Kovaleva, A. C. Kruse, H. T. Lemke, G. Lin, A. Y. Lyubimov, A. Manglik, Mathews, II, S. E. McPhillips, S. Nelson, J. W. Peters, N. K. Sauter, C. A. Smith, J. Song, H. P. Stevenson, Y. Tsai, M. Uervirojnangkoorn, V. Vinetsky, S. Wakatsuki, W. I. Weis, O. A. Zadvornyy, O. B. Zeldin, D. Zhu and K. O. Hodgson (2014). "Goniometer-based femtosecond crystallography with X-ray free electron lasers." Proc Natl Acad Sci U S A **111**(48): 17122-17127.

Doublié, S. (2007). Macromolecular crystallography protocols, Springer.

Fromme, R., A. Ishchenko, M. Metz, S. R. Chowdhury, S. Basu, S. Boutet, P. Fromme, T. A. White, A. Barty and J. C. Spence (2015). "Serial femtosecond crystallography of soluble proteins in lipidic cubic phase." IUCrJ **2**(5): 545-551.

Garcıa-Ruiz, J. M. (2003). "Nucleation of protein crystals." Journal of structural biology **142**(1): 22-31.

Giegé, R. (2013). "A historical perspective on protein crystallization from 1840 to the present day." The FEBS journal **280**(24): 6456-6497.

Ginn, H. M., A. S. Brewster, J. Hattne, G. Evans, A. Wagner, J. M. Grimes, N. K. Sauter, G. Sutton and D. Stuart (2015). "A revised partiality model and post-refinement algorithm for X-ray free-electron laser data." Acta Crystallographica Section D: Biological Crystallography **71**(6): 1400-1410.

Ginn, H. M., M. Messerschmidt, X. Ji, H. Zhang, D. Axford, R. J. Gildea, G. Winter, A. S. Brewster, J. Hattne and A. Wagner (2015). "Structure of CPV17 polyhedrin determined by the improved analysis of serial femtosecond crystallographic data." Nature communications **6**.

Haupert, L. M. and G. J. Simpson (2011). "Screening of protein crystallization trials by second order nonlinear optical imaging of chiral crystals (SONICC)." Methods **55**(4): 379-386.

Hirata, K., K. Shinzawa-Itoh, N. Yano, S. Takemura, K. Kato, M. Hatanaka, K. Muramoto, T. Kawahara, T. Tsukihara and E. Yamashita (2014). "Determination of damage-free crystal structure of an X-ray-sensitive protein using an XFEL." Nature Methods **11**(7): 734-736.

Ibrahim, M., R. Chatterjee, J. Hellmich, R. Tran, M. Bommer, V. K. Yachandra, J. Yano, J. Kern and A. Zouni (2015). "Improvements in serial femtosecond crystallography of photosystem II by optimizing crystal uniformity using microseeding procedures." Structural Dynamics **2**(4): 041705.

Jancarik, J. and S.-H. Kim (1991). "Sparse matrix sampling: a screening method for crystallization of proteins." Journal of applied crystallography **24**(4): 409-411.

Kirian, R. A., X. Wang, U. Weierstall, K. E. Schmidt, J. C. Spence, M. Hunter, P. Fromme, T. White, H. N. Chapman and J. Holton (2010). "Femtosecond protein nanocrystallography—data analysis methods." Optics express **18**(6): 5713-5723.

Kissick, D. J., D. Wanapun and G. J. Simpson (2011). "Second-order nonlinear optical imaging of chiral crystals." Annual review of analytical chemistry (Palo Alto, Calif.) **4**: 419.

Kupitz, C., S. Basu, I. Grotjohann, R. Fromme, N. A. Zatsepin, K. N. Rendek, M. S. Hunter, R. L. Shoeman, T. A. White and D. Wang (2014). "Serial time-resolved crystallography of photosystem II using a femtosecond X-ray laser." Nature **513**(7517): 261-265.

Kupitz, C., I. Grotjohann, C. E. Conrad, S. Roy-Chowdhury, R. Fromme and P. Fromme (2014). "Microcrystallization techniques for serial femtosecond crystallography using photosystem II from Thermosynechococcus elongatus as a model system." Philosophical Transactions of the Royal Society B: Biological Sciences **369**(1647): 20130316.

Kupitz, C., J. L. Olmos Jr, M. Holl, L. Tremblay, K. Pande, S. Pandey, D. Oberthür, M. Hunter, M. Liang and A. Aquila (2017). "Structural enzymology using X-ray free electron lasers." Structural Dynamics **4**(4): 044003.

Madden, J. T., E. L. DeWalt and G. J. Simpson (2011). "Two-photon excited UV fluorescence for protein crystal detection." Acta Crystallographica Section D: Biological Crystallography **67**(10): 839-846.

Martin-Garcia, J. M., C. E. Conrad, G. Nelson, N. Stander, N. A. Zatsepin, J. Zook, L. Zhu, J. Geiger, E. Chun and D. Kissick (2017). "Serial millisecond crystallography of membrane and soluble protein microcrystals using synchrotron radiation." IUCrJ **4**(4).

McPherson, A. (2017). "Protein crystallization." Protein Crystallography: Methods and Protocols: 17-50.

Ostermeier, C. and H. Michel (1997). "Crystallization of membrane proteins." Current opinion in structural biology **7**(5): 697-701.

Pande, K., C. D. M. Hutchinson, G. Groenhof, A. Aquila, J. S. Robinson, J. Tenboer, S. Basu, S. Boutet, D. Deponte, M. Liang, T. White, N. Zatsepin, O. Yefanov, D. Morozov, D. Oberthuer, C. Gati, G. Subramanian, D. James, Y. Zhao, J. Koralek, J. Brayshaw, C. Kupitz, C. Conrad, S. Roy-Chowdhury, J. Coe, M. Metz, X. Paulraj Lourdu, T. Grant, J. Koglin, G. Ketawala, R. Fromme, V. Srajer, R. Henning, J. Spence, A. Ourmazd, P. Schwander, U. Weierstall, M. Frank, P. Fromme, A. Barty, H. Chapman, K. Moffat, J. J. Van Thor and M. Schmidt (2015). "Femtosecond Structural Dynamics Drives the Trans/Cis Isomerization in Photoactive Yellow Protein." in submission.

Pecora, R. (2000). "Dynamic Light Scattering Measurement of Nanometer Particles in Liquids." Journal of Nanoparticle Research **2**(2): 123-131.

Perutz, M. F., M. G. Rossmann, A. F. Cullis, H. Muirhead, G. Will and A. North (1960). "Structure of hæmoglobin: a three-dimensional Fourier synthesis at 5.5-Å. resolution, obtained by X-ray analysis." Nature **185**(4711): 416-422.

Rasband, W. (1997). ImageJ. US National Institutes of Health, Bethesda, MD.

Redecke, L., K. Nass, D. P. DePonte, T. A. White, D. Rehders, A. Barty, F. Stellato, M. Liang, T. R. Barends, S. Boutet, G. J. Williams, M. Messerschmidt, M. M. Seibert, A. Aquila, D. Arnlund, S. Bajt, T. Barth, M. J. Bogan, C. Caleman, T. C. Chao, R. B. Doak, H. Fleckenstein, M. Frank, R. Fromme, L. Galli, I. Grotjohann, M. S. Hunter, L. C. Johansson, S. Kassemeyer, G. Katona, R. A. Kirian, R. Koopmann, C. Kupitz, L. Lomb, A. V. Martin, S. Mogk, R. Neutze, R. L. Shoeman, J. Steinbrener, N. Timneanu, D. Wang, U. Weierstall, N. A. Zatsepin, J. C. Spence, P. Fromme, I. Schlichting, M. Duszenko, C. Betzel and H. N. Chapman (2013). "Natively inhibited Trypanosoma brucei cathepsin B structure determined by using an X-ray laser." Science **339**(6116): 227-230.

Regtmeier, J., R. Eichhorn, T. T. Duong, D. Anselmetti and A. Ros (2007). "Dielectrophoretic Manipulation of DNA: Separation and Polarizability." Anal.Chem. **79**: 3925-3932.

Rupp, B. (2009). Biomolecular crystallography: principles, practice, and application to structural biology, Garland Science.

Sawaya, M. R., D. Cascio, M. Gingery, J. Rodriguez, L. Goldschmidt, J. P. Colletier, M. M. Messerschmidt, S. Boutet, J. E. Koglin, G. J. Williams, A. S. Brewster, K. Nass, J. Hattne, S. Botha, R. B. Doak, R. L. Shoeman, D. P. DePonte, H. W. Park, B. A. Federici, N. K. Sauter, I. Schlichting and D. S. Eisenberg (2014). "Protein crystal structure obtained at 2.9 A resolution from injecting bacterial cells into an X-ray free-electron laser beam." Proc Natl Acad Sci U S A **111**(35): 12769-12774.

Schmitz, K. S. (1990). An introduction to dynamic light scattering of macromolecules. United States.

Schubert, R., A. Meyer, K. Dierks, S. Kapis, R. Reimer, H. Einspahr, M. Perbandt and C. Betzel (2015). "Reliably distinguishing protein nanocrystals from amorphous precipitate by means of depolarized dynamic light scattering." Journal of Applied Crystallography **48**(5): 1476-1484.

Scopes, R. K. (2013). Protein purification: principles and practice, Springer Science & Business Media.

Spence, J. C. H., U. Weierstall and H. N. Chapman (2012). "X-ray lasers for structural and dynamic biology." Reports on Progress in Physics **75**(10).

Stevenson, H. P., A. M. Makhov, M. Calero, A. L. Edwards, O. B. Zeldin, Mathews, II, G. Lin, C. O. Barnes, H. Santamaria, T. M. Ross, S. M. Soltis, C. Khosla, V. Nagarajan, J. F. Conway, A. E. Cohen and G. Calero (2014). "Use of transmission electron microscopy to identify nanocrystals of challenging protein targets." Proc Natl Acad Sci U S A **111**(23): 8470-8475.

Stevenson, H. P., A. M. Makhov, M. Calero, A. L. Edwards, O. B. Zeldin, I. I. Methews, G. Lin, C. O. Barnes, H. Santomaria, T. M. Ross, S. M. Soltis, C. Khosla, V. Nagarajan, J. F. Conway, A. E. Cohen and G. Calero (2014). "Use of transmission electron microscopy to identify nanocrystals of challenging protein targets." Proc. Natl Acad. Sci. USA **111**: 8470–8475.

Stevenson, H. P., G. W. Lin, C. O. Barnes, I. Sutkeviciute, T. Krzysiak, S. C. Weiss, S. Reynolds, Y. Wu, V. Nagarajan, A. M. Makhov, R. Lawrence, E. Lamm, L. Clark, T. J. Gardella, B. G. Hogue, C. M. Ogata, J. Ahn, A. M. Gronenborn, J. F. Conway, J. P. Vilardaga, A. E. Cohen and G. Calero (2016). "Transmission electron

microscopy for the evaluation and optimization of crystal growth." Acta Crystallographica Section D-Structural Biology **72**: 603-615.

Tenboer, J., S. Basu, N. Zatsepin, K. Pande, D. Milathianaki, M. Frank, M. Hunter, S. Boutet, G. J. Williams and J. E. Koglin (2014). "Time-resolved serial crystallography captures high-resolution intermediates of photoactive yellow protein." Science **346**(6214): 1242-1246.

Uervirojnangkoorn, M., O. B. Zeldin, A. Y. Lyubimov, J. Hattne, A. S. Brewster, N. K. Sauter, A. T. Brunger and W. I. Weis (2015). "Enabling X-ray free electron laser crystallography for challenging biological systems from a limited number of crystals." Elife **4**: e05421.

Vekilov, P. G., A. Feeling-Taylor, S.-T. Yau and D. Petsev (2002). "Solvent entropy contribution to the free energy of protein crystallization." Acta Crystallographica Section D: Biological Crystallography **58**(10): 1611-1616.

Weierstall, U., D. James, C. Wang, T. A. White, D. Wang, W. Liu, J. C. Spence, R. B. Doak, G. Nelson and P. Fromme (2014). "Lipidic cubic phase injector facilitates membrane protein serial femtosecond crystallography." Nature communications **5**.

5 RESULTS FROM SERIAL FEMTOSECOND CRYSTALLOGRAPHY

Introduction

The following chapter's focus centers on the experimental design and results of over a dozen beamtimes using serial crystallography. SFX experiments are in general highly interdisciplinary and multifaceted with many distinct aspects that are crucial to a successful result. Among these aspects are sample purity, crystallization and crystal quality, sample selection, sample handling, sample delivery, data acquisition, data reduction, analysis and interpretation for a *general* SFX experiment. It is rarely even this simple with time resolved approaches adding not only complications to many of those elements but new elements as well such as a laser for pump-probe experiments or microfluidic devices and diffusive modeling for on-the-fly mixing experiments. With this in mind, each beamtime often takes a massive team of people contributing countless hours before, during and subsequent to an experiment. While many of the results discussed herein are published, the author is unable to list every person that contributed to the following experiments but wishes to acknowledge and express gratitude to everyone who made all of this possible.

SFX of Photosynthetic Membrane Proteins

This section addresses experiments directed toward understanding the processes and mechanisms behind photosynthesis, particularly PSI and PSII as they are the protein complexes responsible for the first step of the conversion of solar energy into chemical energy. As a reminder, PSI is the terminal complex involved in the photosynthetic membrane electron transfer pathway and essentially acts as natures battery, effectively transferring a negative charge across the thylakoid membrane to its ultimate acceptor, Fd. PSII is the initial complex in the pathway and possesses one of the highest redox potentials ever seen in nature which enables it to oxidize water molecules into their constituent oxygen, protons and electrons, initiating the photosynthetic electron transport chain. Understanding these processes is exceedingly valuable in the pursuit of alternative energy strategies, addressing a massive issue in modern society.

Nanocrystallogenesis of PSI

As mentioned in chapter 3, the final step in purification and storage of PSI is crystallization using a pressure filtration concentrator. One of the key steps in the crystallization of PSI is the desalting of the PSI solution after elution of the anion exchange column. PSI is uncommon in that rather than increased salt concentration being the general method of precipitation (salting out), it has an increased solubility as the concentration of salt goes up (salting in). This means that a phase diagram for PSI would look similar to that in figure 5.1. Some control in crystal size can be established during this final purification step both by control of the concentration of $MgSO_4$ and the rate of concentration of the solution by manipulating the headspace gas pressure. The concentration of $MgSO_4$ can be determined by the dilution ratio with G_0 against the remaining solution (salt concentration dependent upon elution method, usually 135 mM for Q-sepharose column, ~ 90 mM for DEAE). Final concentrations range from 1-8 mM $MgSO_4$ with the larger concentration resulting in larger crystals and lower concentrations resulting in smaller crystals (in general). The head space pressure can range anywhere up to 75 psi (limited by the specification for the concentrator/filtration membrane). Higher pressure results in a faster increase of protein concentration and subsequently a faster travel into the spontaneous nucleation region of phase space. This exhibits large control over the crystal size as a rapid nuclei formation results in a high number of nuclei and subsequent rapid decrease in free protein, inhibiting further growth and resulting in the ability for homogeneous, sub-micron crystals to be formed. The exact resultant size will be dependent upon the mass of PSI present as well as filtration efficiency which varies between filters and over time. When made fresh, these crystals have the potential to be used immediately for SFX experiments or for seeding (if larger crystals are desired) with no further recrystallization necessary, however resolution has anecdotally decreased after a week or so with an estimated rate of ~ 1 Å / week (P. Fromme, personal communication).

Recrystallization methods used for PSI nano- and micro- crystals are largely batch methods as this is generally simple to perform reproducibly for the large quantities necessary for SFX and allows in general for high size homogeneity. For recrystallization, a suspension containing microcrystals is first centrifuged to pellet the crystals in a pre-weighed vessel. The supernatant is

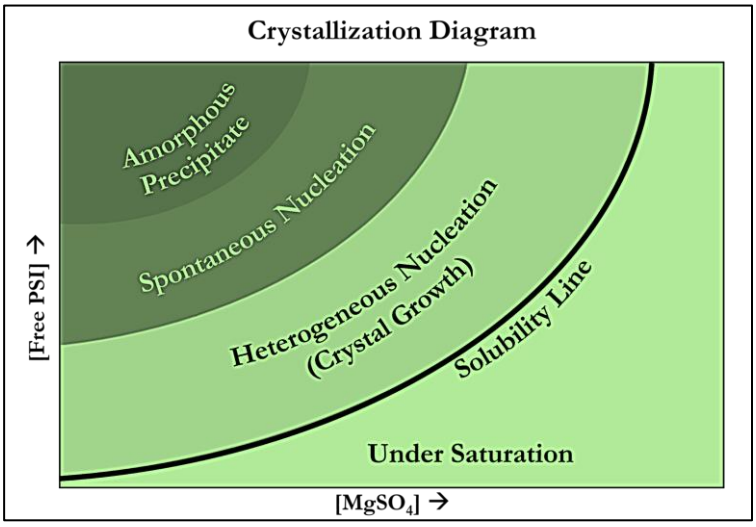

Figure 5.1 Depiction of Salting In of PSI

General form of PSI phase space compared to concentration of magnesium sulfate. Note that the solubility of PSI increases with salt concentration so that PSI 'salts in' to solution.

then removed (it is crucial for reproducibility to remove *all* supernatant, usually requiring multiple centrifugations) and a volume to mass equivalent of G_{100} (i.e. 50 µL of G_{100} would be added to a 50 mg pellet) is added and pipette mixed with the crystals to dissolve the crystals by salting them back into solution. A chlorophyll assay is then performed and this solution is diluted with G_{50} to obtain a concentration of 25 mM chlorophyll (~ 260 µM PSI). This solution is then rapidly mixed with a low salt solution to obtain a final chl concentration of 460 µM. This can be, and has been, performed multiple ways including pipette mixing, through use of a stirred solution and, perhaps most interestingly, by putting the protein in the bottom of a large beaker or pitcher in distinct droplets and then pouring in the precipitant while swirling the solution mechanically by hand (great for very large, >50 mL, batches). Batch variations usually require prep to prep testing using various salt concentration solutions (usually 1-4 mM $MgSO_4$, i.e. G_1-G_4) in small batches to obtain optimal conditions for a particular size regime. It should be noted that the inclusion of seeds was highly beneficial to size homogeneity. Seeds are included in these tests by 'doping' the precipitating solution just prior to batch mixing. Seeds were from consistent batches for both testing and final crystallogenesis and seed batches were also screened as seed quality and homogeneity has a significant effect upon crystal quality.

Novel Effects from Discrete Unit Cells and Post Growth Size Homogeneity Sorting

One of the largest challenges presented in structure determination with crystallography is the loss of phase information in diffraction (i.e. only intensities are collected). New solutions to the

crystallographic phase problem have historically had a huge impact on structural biology, including the widely used methods of anomalous diffraction (Hendrickson and Teeter 1981, Kahn, Fourme et al. 1985, Guss, Merritt et al. 1988), isomorphous replacement (Green, Ingram et al. 1954, Blow and Crick 1959), and molecular replacement (Rossmann and Blow 1962, Rossmann and Blow 1963, Rossmann 1972). This is partly due to limitations each method possesses such as the need for atomic resolution diffraction, a solved homologous model, or the ability to chemically modify the sample, meaning that the more tools are available to address the phase problem, the broader becomes the range of suitable macromolecular crystals available for crystallographic structure determination. One idea that has long been appreciated but has yet to come to fruition is the use of diffraction between Bragg reflections, the inclusion of which would allow for the determination of the electron density autocorrelation function and subsequently experimental measurement of the phases, removing the restrictions on resolution needed for a unique structural solution (Sayre 1952).

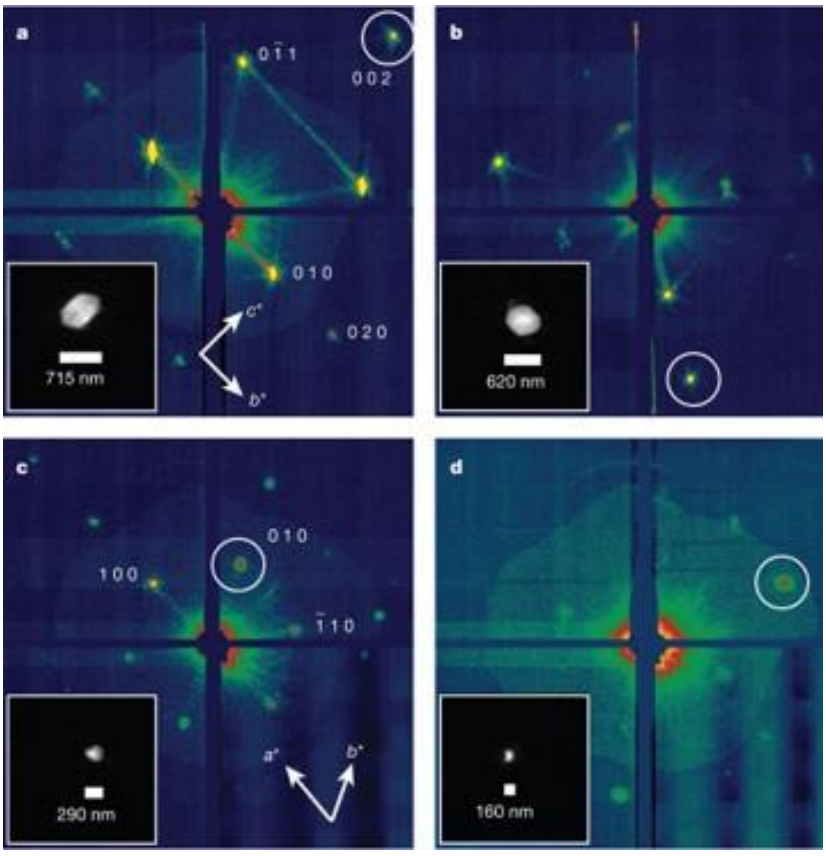

Figure 5.2 Shape Transforms and Inter-Bragg Sampling

Diffraction images obtained from sub-micron PSI crystals, showing coherent diffraction effects from discrete crystals. Note the inter-Bragg fringes arising from discrete and coherently diffracting nanocrystals and non-uniform Bragg peak profiles due to the shape transform convolution. The insets show reconstructed crystal shapes determined from the shape transform function of the circled peaks using the Shrinkwrap algorithm (Marchesini, He et al. 2003). Image

Part of the reason that this idea remained largely unexplored was due to

the need for finite unit cells, in contrast to the need for large crystals needed in traditional crystallography. This requirement comes from the convolution of the shape transform of the crystal with the sharp Bragg peaks which is further modulated by the molecular transform (Laue 1936). For large crystals, the Bragg condition dominates the convolution and resolving the shape transform, which provides the inter-Bragg sampling, is generally limited by the SNR. The development of SFX and its use of finite nanocrystals has been shown to access the size regime needed to observe and measure these discrete effects, first reported using PSI nanocrystals as shown in figure 5.2 (Chapman, Fromme et al. 2011). While this experiment, conducted in 2009, showed proof of principle for measuring inter-Bragg scattering, the focus was on Bragg peak

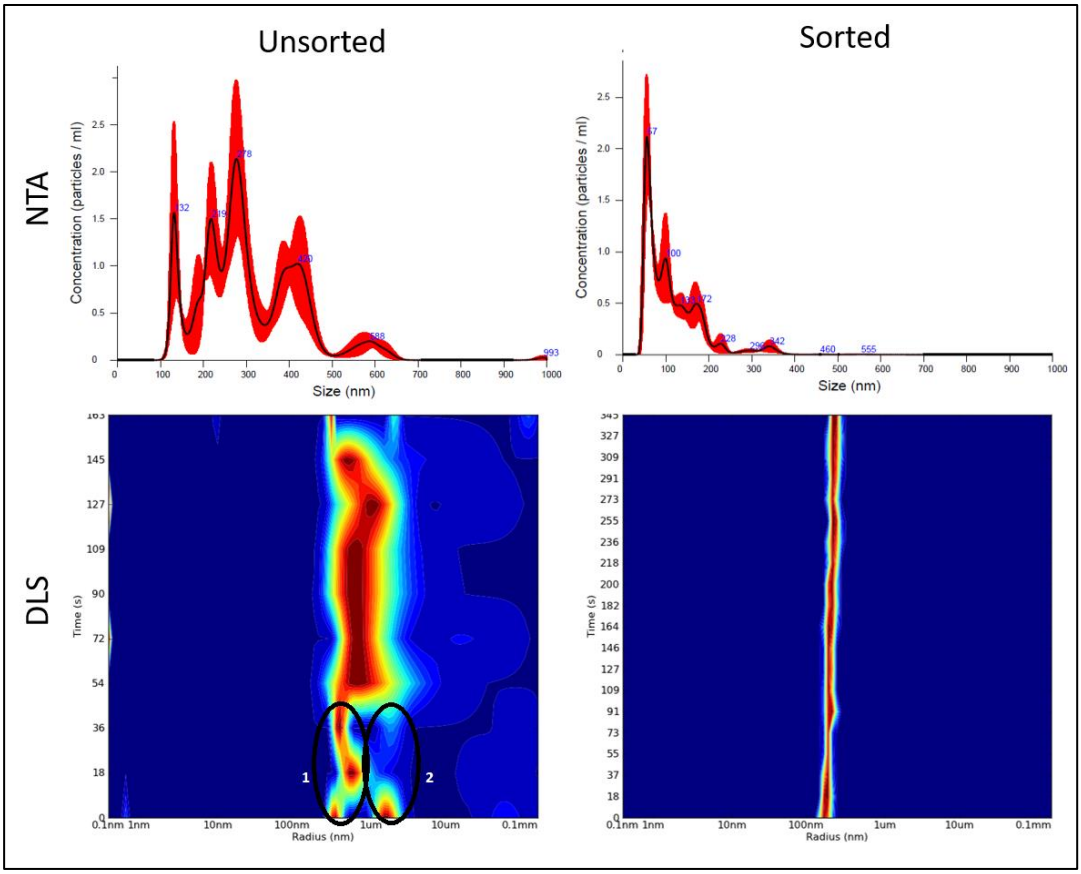

Figure 5.3 Improvement of Size Distribution by Microfluidic Sorting

Size homogeneity and minimization was achieved through microfluidic sorting as described in Abdallah, Zatsepin et al. (2015). Left images show pre-sorted size determination as measured with nanoparticle tracking analysis (NTA, top) and dynamic light scattering (DLS, bottom, exhibiting indicated multimodal distribution) as compared with the right two images showing increased size homogeneity in the sorted fractions.

detection and the data that were collected were low in number, relatively weak due to probabilistic crystal-beam geometry within the comparatively large liquid jet focus (10um) and a high variability in crystal size that led to detector saturations and signal bleeding.

Some challenges with using SFX lie in the serial nature of the method as well as some of the beam characteristics inherent in current XFEL sources. The use of many crystal diffraction snapshots in building a data set means that the non-uniformity of the beam and shot-to-shot variation as well as partiality of reflections must be taken into consideration. A solution to many of these issues is the use of averaging through Monte Carlo methods as shown at a recent experiment at a soft-XFEL (Kirian, Bean et al. 2015), though for size distribution and beam characteristics, higher homogeneity lowers the restriction for the minimum amount of data needed to provide a reliable data set. For this purpose, the use of a microfluidic sorter based off of the model described in Abdallah, Zatsepin et al. (2015) was proposed to be coupled with the experiment, allowing improvement of PSI nanocrystal size distribution (see figure 5.3). In addition to decreasing the need for Monte Carlo summing, the homogeneous crystal size decreases the probability of saturated pixels and signal bleed-through to pixels surrounding an oversaturated peak.

In June 2016 at the AMO beamline at LCLS, PSI nanocrystals, SFX data sets on both sorted and unsorted PSI nanocrystals were collected in the pursuit to obtain enough high-quality data to resolve a *de novo* structure of PSI through use of the shape and molecular transform effects

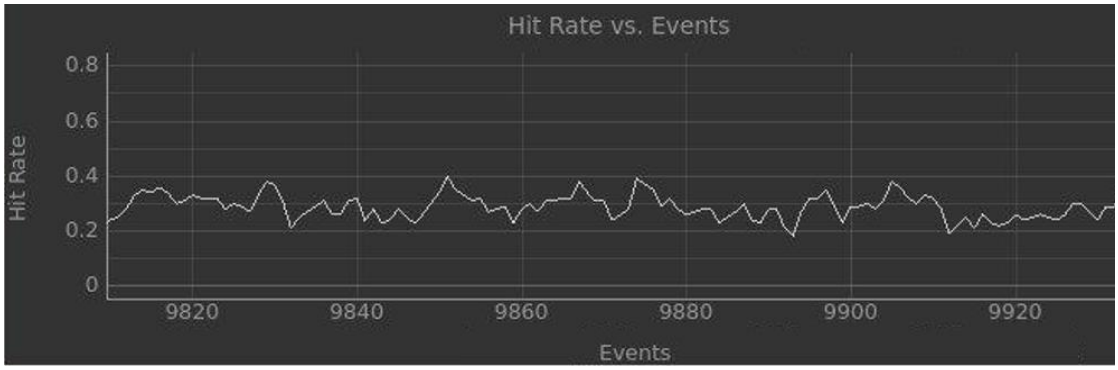

Figure 5.4 Typical Hit Rate of PSI Nanocrystals at AMO

Graph of hit rate achieved with approximately 10^{10} nanocrystals/mL during discrete phasing beamtime at the AMO instrument at LCLS. Hit rate is measured live as a decimal fraction (y axis) against fs pulse events (x axis) using ONDA (Mariani, Morgan et al. 2016), a live data monitoring suite for XFEL experiments.

inherent with discrete nanocrystals. The experiment was performed with a liquid-liquid focused GDVN (Oberthuer, Knoška et al. 2017) at an energy of 1.8 keV with a FWHM of ~ 1 µm imaged on a pnCCD detector with a maximum resolution of 7 Å. Pulse duration was 50 fs with an average pulse energy of 2.3 mJ.

Crystals were prepared in two protein preparations as described above, each using ~70 g of dried, frozen *T. elongatus* cells, the XK 50/60 column with DEAE resin and two Amicon concentrators pressurized at 70 psi and desalting accomplished with the addition of G_0 to obtain a final concentration of 1 mM $MgSO_4$. This resulted in ~ 20 mL of submicron crystals with densities ranging between 1 * 10^{10} and 5 * 10^{11} crystals/mL. These crystals were then separated by size through diffusive settling. The final sample used for the experiment consisted of over 50 mL of PSI nanocrystals with a size distribution of 395 +/- 31 nm at a density of 2 * 10^{10} crystals/mL as measured using DLS and NTA were prepared for 72 hours of data collection. Over 10 mL of this

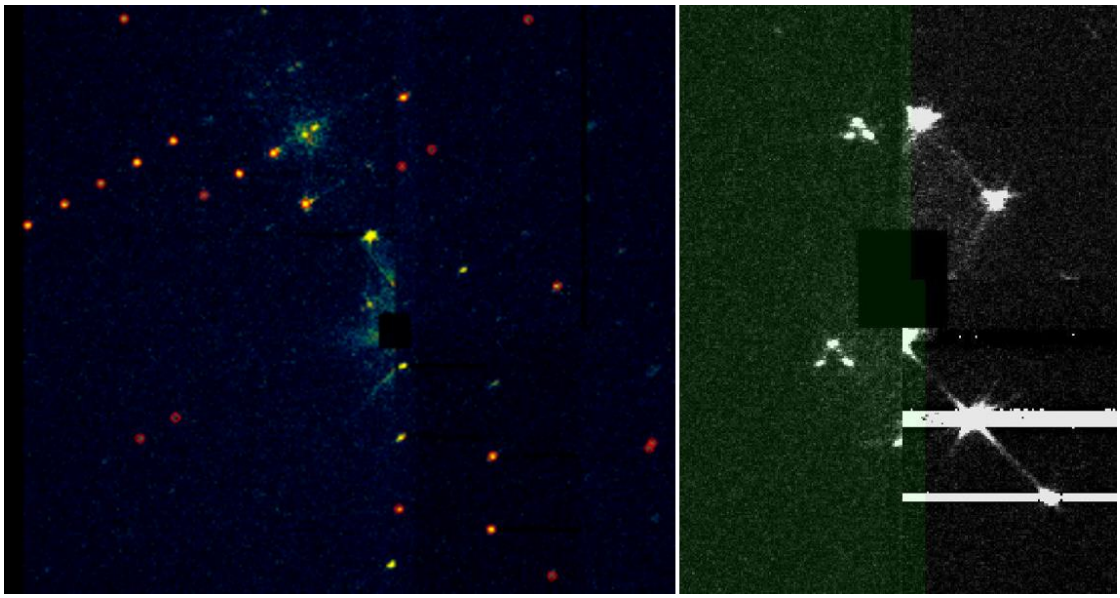

Figure 5.5 Diffraction Patterns of PSI at AMO

Raw diffraction patterns from the front (right) and back (left) detectors. Both detectors exhibit shape transform convolution of the Bragg peaks and the back detector shows strong inter-Bragg coherent scattering. Note that white bars are saturated portions of the panels and are artifacts unindicative of characteristics of the crystal that are masked out upon further processing.

solution was subjected to microfluidic sorting, increasing size homogeneity as shown in figure 5.3.

During the experiment, over a million diffraction patterns were collected over the course of three 12-hour shifts. Hit rates were initially approaching 80% leading to a dilution of the sample to optimize for single crystal diffraction (as opposed to multiple hits) and resulting in hit rates of approximately 20-40%, as can be seen in figure 5.4. Sample selection was optimized on the fly by use of online data monitoring for real-time hit rates (ONDA, (Mariani, Morgan et al. 2016)) and by

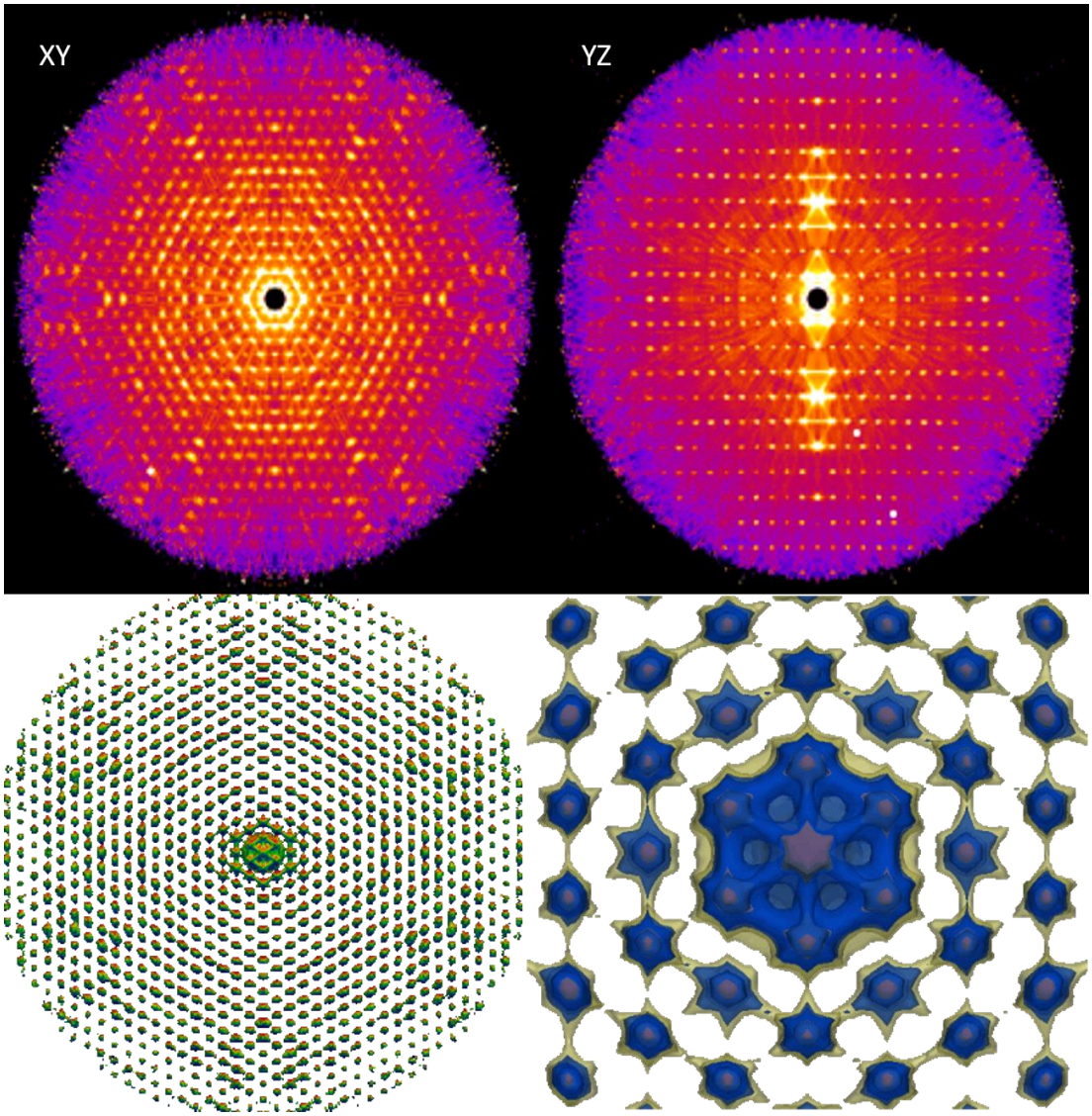

Figure 5.6 XY Slice of 3-D Merged Patterns from PSI Nanocrystals

Top images show initial, on-the-fly merged data from ~28,000 patterns from a sorted batch of PSI nanocrystals from two slices of reciprocal space. Inter-Bragg intensities are highly apparent, indicating coherent diffraction and suitably discrete nanocrystals. On-the-fly analysis was crucial to optimizing sample selectionBottom images show final merged data from ~300,000 merged indexed PSI diffraction patterns to the 14 Å resolution limit (left) and zoomed in on the lowest order reflections (right). The presence of both inter-Bragg diffraction and shape

merging compiled data from sample grouped by protein batch and post crystallization method in order to ascertain which characteristics exhibited maximized inter-Bragg scattering. Strong coherent inter-Bragg scattering and non-spherical Bragg peak profiles indicative of shape transform convolution were apparent in the raw data as shown in figure 5.5.

In summary, over 300,000 indexed patterns were identified to be suitable for further data analysis and were used to obtain a merged 3-D profile in reciprocal space. Both the final merged data and a grouped merge used for sample selection are highlighted in figure 5.6, showing strong features of coherent diffraction from discrete nanocrystals. The resolution limit for the data is 14 Å, constrained by the chosen metrology for the experiment and well within what is needed to find the experimental autocorrelation. Further data processing is still ongoing including optimization of background subtraction, necessary for accurate measurement of inter-Bragg scattering, and pattern selection criteria, the optimal parameters of which is as-of-yet unresolved. It is a boon that this particular PSI structure is already known to 2.5 Å resolution (Jordan, Fromme et al. 2001) as this will allow for validation for the *de novo* phasing being attempted. Should this prove successful, this novel phasing method will be a breakthrough in structure elucidation, serving as an unrestrained direct phasing method for nanocrystallography.

TR-SFX of PSI

The specifics of electron transfer in photosynthesis is one of the most outstanding problems in nature, having strong implications for renewable energy. Among the as yet elusive aspects of this are the details of electron transfer in PSI, specifically with its coupling to its soluble electron acceptor, Fd. While crystals of the PSI-Fd co-complex have been achieved, the structure remains elusive due primarily to resolution limitations (Fromme, Bottin et al. 2002). Though experiments are described in a later section toward this goal directly, one possible way to gain insight is to perform pump-probe time-resolved crystallography on PSI by itself in order to explore any inherent conformational changes that may occur in either the luminal donor or stromal acceptor sites upon charge separation.

The time regime for initial probing of conformational change should be on the time scale that electron transfer to Fd has been shown to occur on or faster, namely ≤ 15 μs (Setif and Bottin

1994, Setif and Bottin 1995). As this avenue has not been largely explored, the newly commissioned European XFEL (EU-XFEL) presents a uniquely advantageous beam structure for preliminary investigation. This is due to the deliverable XFEL beam at EU-XFEL consisting of a pulse-train structure in which 'trains' of 30+ pulses are delivered at 10 Hz with equal temporal spacing existing between both the pulses in each train as well as between the trains. The idea was to use the pulsed structure of the train to obtain multiple time points simultaneously in addition to the dark state for calibration, validation and control/comparison reasons.

In November 2017, four 12-hour shifts were allotted to perform TR-SFX on PSI at the SPB/SFX beamline at EU-XFEL. These were the first time resolved pump-probe experiments at

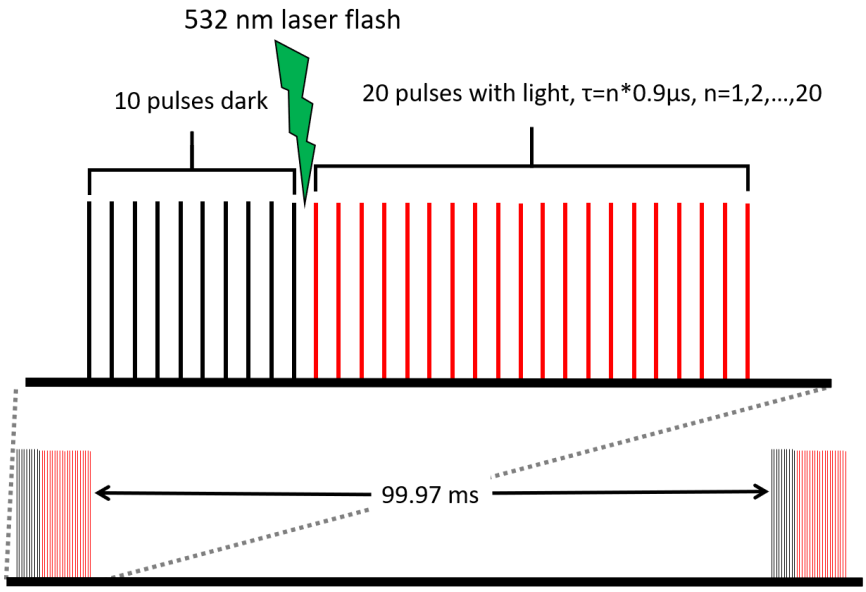

Figure 5.7 Schematic of PSI TR-SFX Pulse Structure at EU-XFEL

Depiction of the pulse train structure of the EU-XFEL beam and how it is utilized for pump-probe TR-SFX of PSI. The trains operate at 10 Hz with each train being composed of thirty ~50 fs pulses spaced by 900 ns within the train. The laser flash was matched with the pulse train to occur after the first 10 pulses, allowing for rapid dark state structure resolution at 10 * 10 = 100 Hz. The further 20 pulses in each train represent simultaneous collection of 20 equally spaced time points between 900 ns and 18 μs that can be utilized individually or binned in groups to increase usable diffraction patterns in a data set.

the EuXFEL which started user based commissioned operation in September 2017. The pump-probe setup implemented is partially described in figure 5.7 and utilized the first 10 pulses for the

dark state structure followed by 20 pulses representing 20 individual time points ranging from 900 ns to 18 µs, each spaced by 900 ns. The spacing of the pulses within each pulse train were extremely fortunate in their temporal spacing as this matched the µs time regime anticipated for the structural changes during electron transfer reactions in PSI. The temporal sampling spanned from the sub-microsecond time regime where the first spectroscopic changes occur in the PSI-Fd complex through the ~10 µs times associated with the second order electron transfer and subsequent undocking between PSI and Fd (Setif and Bottin 1994, Setif and Bottin 1995). As conformational changes involved in this process may occur even in the absence of Fd, this presented us with an exciting and challenging opportunity. This experiment also marked the first TR-SFX experiment performed at the EU-XFEL and the forth user experiment overall at the EU-XFEL SPB/SFX beamline.

Among the challenges that were faced were the 900 ns pulse spacing, the large beam diameter, uncertainties in energy and geometry characteristics, and an unmatured data acquisition pipeline that was still in the testing and commissioning phase. The 900 ns spacing between the pulses is in stark contrast with the 8.3 ms used at the 120 Hz LCLS, leading to a need for a calculated liquid jet speed of ~44 m/s in order to pass 40 µm between shots. This is actually less distance between shots than the 50 µm damage radius previously measured experimentally at LCLS (unpublished), though that was with a much smaller beam diameter (~ 1 µm at LCLS vs. ~20 µm at EU-XFEL) and a presumably lower pulse energy (energy at interaction region unknown at EU-XFEL at time of experiment). Thankfully, Stella Lisova was able to handcraft high quality nozzles that were able to maintain stable focused jets approximately 3.5 µm in diameter, leading to sustainable flow rates around 25 µL/min.

As this experiment fell within the first cycle of user experiments, the EU-XFEL beam was still in the process of being optimized, a continual process which can take years before improvements begin to level out. Consequently, the focus of the beam had not yet been fully optimized. The somewhat wide beam (estimated to be 15 µm x 20 µm) led to a low energy density and necessitated larger crystals to match the beam size for sufficient diffraction. While not insurmountable, this presents a challenge in multiple fronts. As has been discussed, one of the

main advantages in TR-SFX is the ability to use small crystals to decrease reaction inhomogeneities, though for pump probe experiments with expected microsecond kinetics this should provide a minimal barrier. The necessity for larger crystals, however, impacts collection hit rates indirectly as a crystal slurry of larger crystals is generally harder to jet at the same protein concentration. In addition, the larger size of the crystals means that for the same protein concentration, there will be a 1000 fold decrease in crystals/mL, though this is offset to an extent by the fact that crystals approaching the beam size start to deviate from Poisson statistics and the hit rate should approach volumetric ratios.

Another challenge of being early users during the user supported commissioning phase of the EU-XFEL is that new data acquisition and processing infrastructure is being explored and inherently troubleshot. This means that data were collected in new and uncommon file formats which were still in the process of evolving. Data storage and need for user interfaces that have been developed over years at other facilities had to be developed and/or integrated into the particular infrastructure used at EU-XFEL. Driving the need for novel infrastructure is the unique characteristics involved in data acquisition with the pulsed train beam structure which is expected in its full form to have thousands of pulses/train (Altarelli, Brinkmann et al. 2006, Geloni, Saldin et al. 2010). Furthermore, a completely new detector called the Adaptive Gain Integrated Pixel Detector (AGIPD), was developed in a feat of modern engineering. In the AGIPD, each pixel has three gain settings, all possessing a dark current offset value and measured value as well an indicator for the gain setting per pulse setting, of which each pixel possesses 500 sets (in essence each pixel has 500 ‘time’ dimensions to save values for up to 500 images per pulse train before subsequent inter-train readout). This is in order to accommodate the large amounts of data anticipated for operation with higher number of pulses per train (up to 2,700(Allahgholi, Becker et al. 2015)), with the ability to on-the-fly reject or save data according to algorithmic hitfinding such that up to 500 patterns will be able to be stored over the course of a pulse train before being read out in the milliseconds interim. This means that it basically acts as a completely new detector with individual gain settings for each pulse within a train. This complexity has incredible promise for rapid data collection in the future but the complexity means that completely novel ways of dealing

with the output must be created and as some of the first users attempting to do so, troubleshooting is inevitably part of data acquisition, handling, and processing.

Over 1 gram of PSI was produced for this beamtime due to the need for high flow rates, large crystals, and the plan to collect 20 + 1 (dark) timepoints, effectively limiting data collection to 10 Hz for each time point and necessitating optimized hit rate. PSI crystals were grown to ~ 20 µm in the largest dimension, being approximately the largest size that could still be prefiltered with commercial fritted stainless steel filters available so as to avoid clogging problems during injection. These were grown in batch using seeding and a G_3 bulk precipitation as described in a previous section. Figure 5.8 shows an example of the crystals grown and their typical density.

A crystal slurry containing an approximately 10% volumetric composition of 5 x 5 x 20 µm PSI microcrystals was delivered using a GDVN with a glass nozzle and 50 µm inner diameter

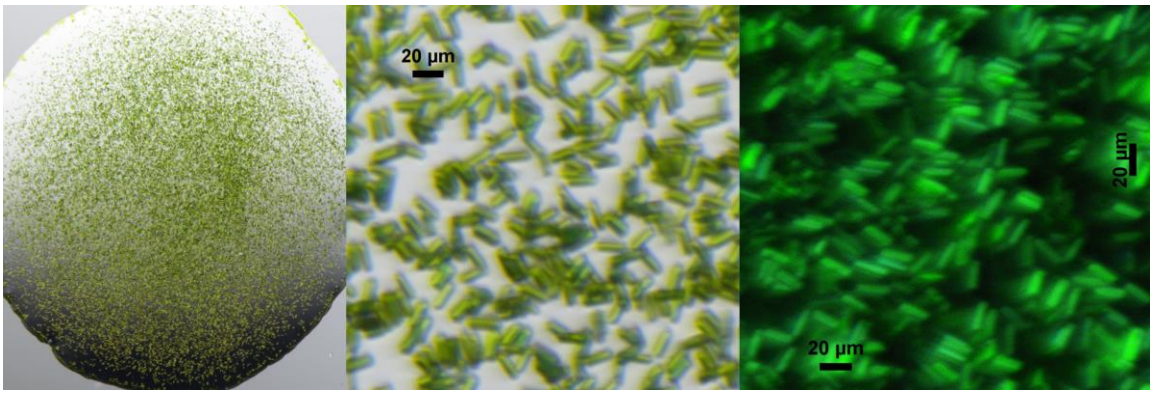

Figure 5.8 20 µm PSI Crystals

PSI microcrystals used in pump-probe TR-SFX experiment at EU-XFEL. Images of a 1 µL drop (left), and zoomed in brightfield (center) and exhibiting birefringence under polarized light (right). Zoomed in pictures highlight relatively large 20 µm size in the longest dimension, necessary for the low (≥ 15µm x 20 µm) beam focus.

capillary. The nozzles were covered with a black polymer except for the last 500 µm to avoid any premature photoactivation upstream of the immediate sample. The incoming X-ray pulse train signal was used to trigger a green picosecond laser 9.27 µs after the initial XFEL pulse so that the first ten pulses were prior to laser excitation followed by 20 snapshots of the PSI after laser triggering induced the electron transfer reactions. The X-ray pulses were approximately at an energy of 9.15 keV and approximately 100 fs in duration (there is still some post-data collection debate about the exact energy and pulse width).

In spite of the challenges present, over 60,000 hits were obtained with comparable resolution to that found at LCLS for the dark PSI crystals, being near 3-3.5 Å visually as can be seen in a typical diffraction pattern shown in figure 5.9. Of note, these were the first TR-SFX experiments ever conducted on PSI. Data were collected over four 12-hour shifts with approximately 25 hours of data collection, a marked improvement over the previous couple experiments performed at the EU-XFEL SPB/SFX beamline.

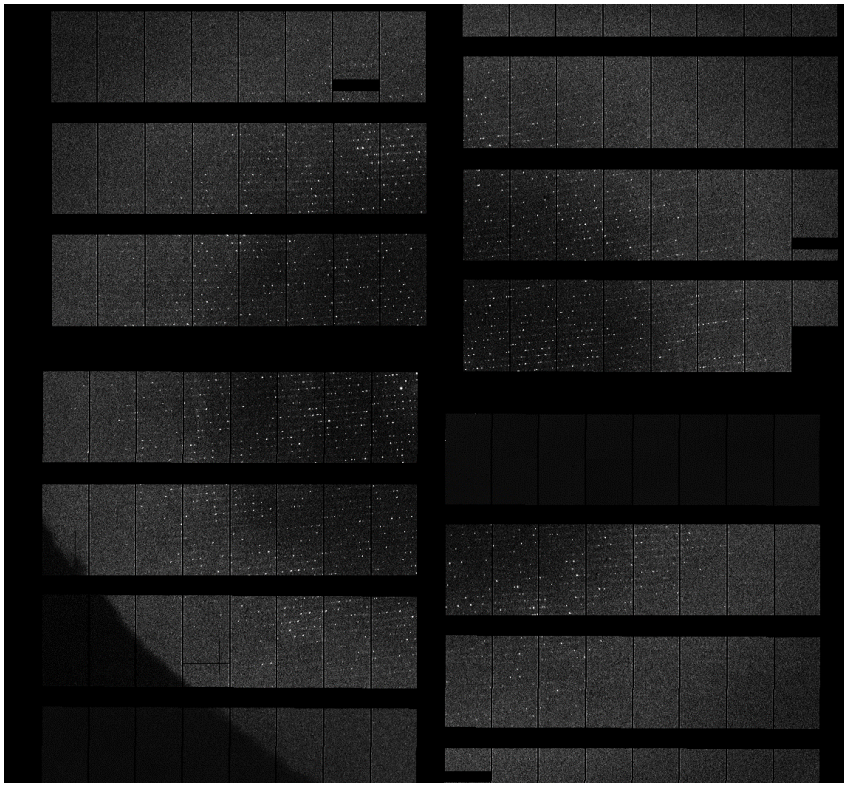

Figure 5.9 PSI Diffraction Pattern at SPB/SFX, EU-XFEL

Shows a typical diffraction pattern observed during TR-SFX of PSI at the SPB/SFX beamline, EU-XFEL. Well separated spots are visible by eye well into the solvent ring indicate suitable resolution. Resolution is approximately 2.55 Å at the bottom and top edges and 3.1 Å on the

At present, we have been able to index 31,142 patterns out of 60,690 total 'hits' resulting in an indexing rate of 51.31%, though there are likely still some false hits included within the total number. Due to some of the challenges with incorporating masks, darks, and other calibrations, final hitfinding and merging are still being optimized. In addition to the need for optimized data reduction, indexing is very challenging as it is influenced by discrepancies in metrology and exact photon energy, though this indicates that large improvements in the indexing rate will likely be achieved with further data evaluation. Promisingly, analysis of hits as a function of their placement within the pulse train showed that there was no variance with respect to hit rates, diffraction resolution and indexability, indicating that the jet was replenished

sufficiently between pulses to outrun upstream damage (see figure 5.10). Current efforts are on refining the geometry and incorporating CHEETAH software (Barty, Kirian et al. 2014) in order to optimize data correction and hitfinding parameters. There are likely not enough patterns to visualize all 20 time points (though post refinement methods will be explored) however binning them into groups may prove fruitful and allow enough patterns to complete a few binned data sets.

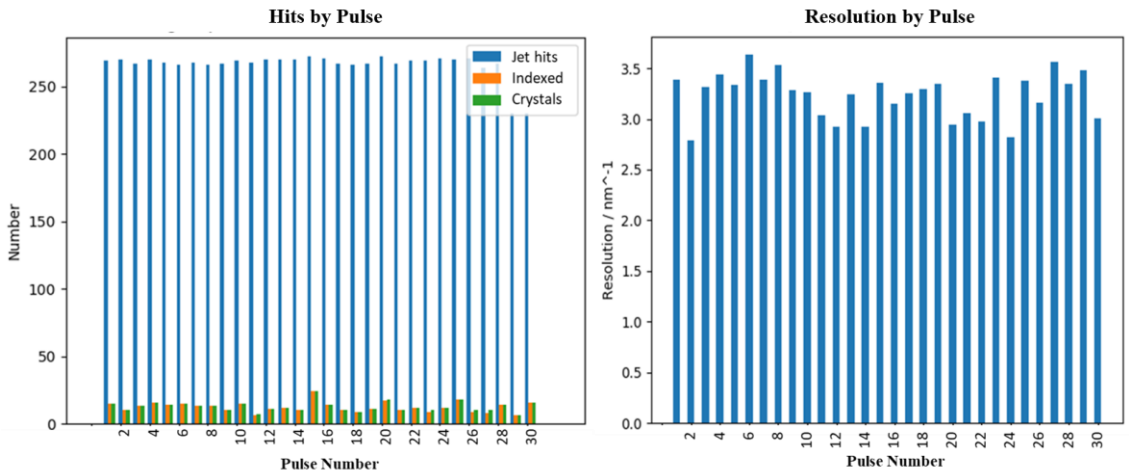

Figure 5.10 EU-XFEL PSI Data Acquisition by Pulse Number

Graphs showing hit rates and resolution as a function of pulse number, averaged over all the trains in a run for resolution and summed over all trains in a run for the hits. The invariance in hit rate for the jet indicates the flow rate is fast enough to reform a jet within the 900 ns spacing between shots, whereas the invariance in crystal and indexed hits by pulse shows that upstream damage is being avoided. This is further supported by the approximately even distribution in highest resolution peaks found, displayed in reciprocal space units, nm^{-1}.

Crystallization of PSII

The PSII crystallization performed varied slightly by batch but was generally performed as previously reported in Chapter 3 and elsewhere (Kupitz, Basu et al. 2014). During crystallization of PSII, there are multiple factors that have a significant effect on the final obtained crystal quality, including cell growth conditions, chemical environment during and after solubilization, column purification efficiency, and rate and method of crystallization. One of the primary indicators for optimal PSII cell growth conditions is the maximum absorbance wavelength in the range of 670 – 685. The light intensity during growth is critical for the ability to isolate high quality PSI and PSII from the cells. A balance must be obtained with the amount of light provided to cyanobacteria, as light fuels photosynthesis and the subsequent growth but light can also cause photoinhibition by

which photodamage occurs to PSII. Photosystem II has a high turnover rate and is constantly replaced in a cell, even under moderate light conditions. However, when cells are exposed to excess light radicals are formed as well as singlet oxygen which suppress the synthesis of repair proteins, leaving much of the PSII in a damaged state (Prasil 1992, Aro, Virgin et al. 1993, Murata, Takahashi et al. 2007). Environmental stresses, such as limited CO_2 or unmoderated temperature, can also contribute to the formation of radicals. As such, optimization of lighting conditions has proven to be one of the more crucial elements to optimization of cell growth for crystallization-suitable PSII, with increasing intensities of red and white light as the cell density increases (20-163 µE and 10-50 µE respectively).

Optimization of the PSII solubilization

The detergent solubilization is another critical step in the PSII isolation procedure. Improvements within the isolation and purification were introduced by systematic studies where cell

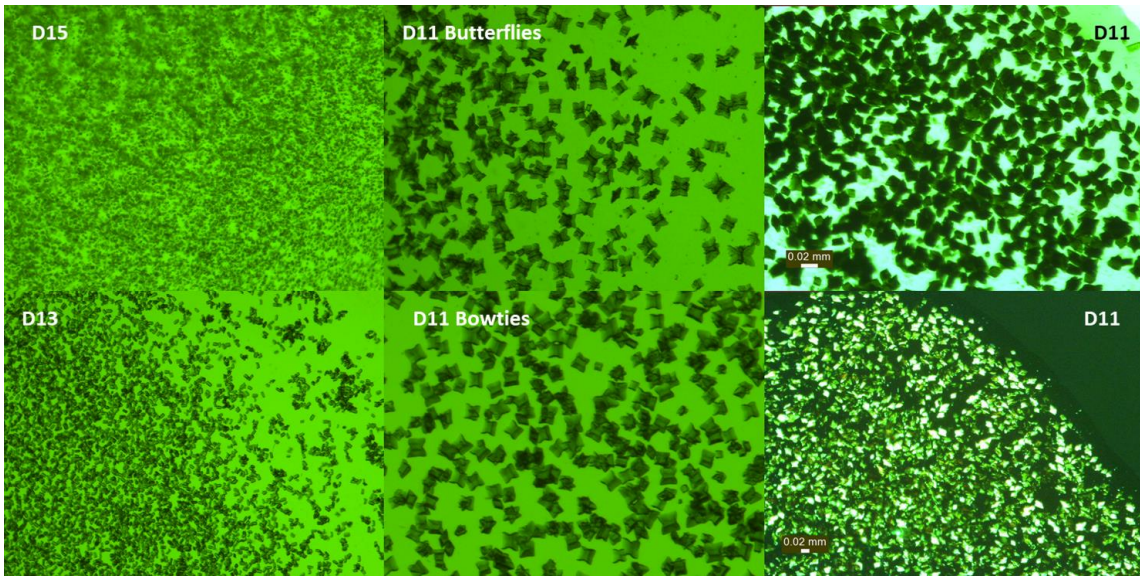

Figure 5.11 PSII Morphology and Size Control from Precipitations

PSII is sensitive to protein quality and concentrations of precipitant during crystallogenesis. Initial precipitations are performed at higher concentrations of 15% (top left) and 13% (bottom left) PEG 2000, harsher conditions that generally result in smaller crystals with higher PEG concentrations. Decreased protein quality as well as too rapid or inhomogeneous addition of the precipitant can lead to visually mosaic macromorphologies such as 'butterflies' (top middle) or 'bowties' (bottom middle). Fortunately, subsequent precipitations can be applied to further purify homogeneous PSII dimers or correct artifacts caused by suboptimal crystallization technique as seen in the sharp, homogeneous crystals pictured in brightfield (top right) and exhibiting birefringence under polarized light (bottom right).

batches of *T elongatus* cells were divided into identical fractions so as to minimize variables. Tests were performed by varying the solubilization concentration of β-DDM between 0.5-1.0 % w/v, the thylakoid/protein concentration between 750 µM and 1 mM chlorophyll, and the incubation time under stirring between 45-60 min. Macrocrystallography at the home X-ray source was then used to compare protein quality of different PSII preparations. The results showed that a 0.75% w/v [β-DDM], 750 µM [chlorophyll] and 1 hour were the optimal conditions during out screening.

Finally, for crystallization the microcrystal FID technique (described in chapter 2) previously used (Kupitz, Basu et al. 2014) has been largely eschewed for a batch method by which the precipitating D_x (x=11-15 w/v % PEG 2000) solution was added to a stirred solution of PSII in buffer C. This appears to have a positive effect on homogeneity of both crystal size and micromorphology, though both characteristics are still highly batch dependent and sensitive to even slight variations in buffer composition (e.g. different stocks, chemical source). For onsite and most offsite crystallization, PSII frozen in high glycerol was first thawed as described in Chapter 3. Initial precipitations were performed as described in Chapter 3 whereby serial precipitations with $D_{15} \rightarrow D_{13} \rightarrow D_{11}$ were performed. We have recently explored a broader range of precipitation conditions using D_x with x ranging from 11-17% w/v PEG 2000 in addition to avoiding the freezing step altogether (i.e. crystallizing immediately following column purification) to obtain optimal size and micromorphology of the PSII crystals. Figure 5.11 shows some of the various macromorphologies common with PSII precipitations and crystals.

Continuous Diffraction

In the pursuit of unlocking the molecular mechanism behind water splitting in PSII, significant progress has been made including an impressive effort by which the S_3 state was visualized using TR-SFX as reported in Kupitz, Basu et al. (2014). This allowed novel insight into the structural changes associated with the transition of the oxygen evolving complex (OEC) through the Kok cycle, however more detailed insight was precluded by a resolution cutoff at 5.0 Å for the dark structure and 5.5 Å for the illuminated state. During subsequent beamtimes at LCLS aimed at investigating this further, it became apparent that while Bragg diffraction was cutoff in this

medium to low resolution range, the diffraction patterns feature coherent diffusive scattering extending to higher angle scattering beyond the Bragg cutoff, as highlighted in figure 5.12. While diffuse scattering was previously deemed unsuitable for structure determination, the idea was born that this diffuse scattering contained useful structural information that could allow resolution to be extended beyond the truncation experienced with Bragg peaks.

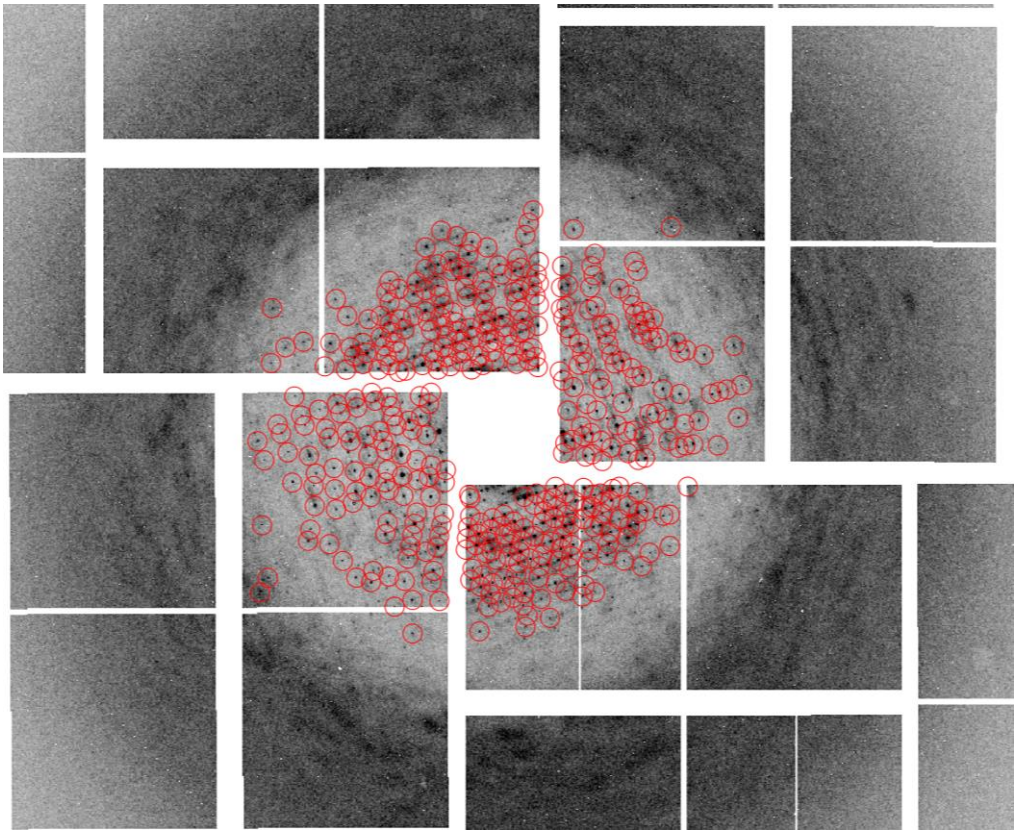

Figure 5.12 PSII Diffraction Pattern Showing Diffuse Scattering

SFX diffraction snapshot of PSII microcrystals exhibiting strong diffuse scattering both within and beyond the Bragg cutoff. Bragg peaks are marked with red circles. Note the visible incoherent scattering into and beyond the solvent ring.

As a structural unit, e.g. the asymmetric unit, is displaced from the ideal lattice the phase is shifted from the diffracted wave by $2\pi\Delta x/d$ at the scattering angle 2θ that corresponds to resolution d with Δx being the displacement. Bragg intensities will begin to diminish by $e^{-4\pi^2 q^2 \sigma^2}$ (the Debye-Waller factor), q being the resolution 1/d, for a root-mean-square value of displacement, σ, for all contributing scattering units (Borie 1965). While this disorder has long been used as an aid for scaling and inferring the temperature factor through a Wilson plot, it also leads to an

increasing incoherent sum of molecular Fraunhofer diffraction of the individual subunits coinciding with the quadratically diminishing Bragg peaks as a function of q. This effect is illustrated in figure 5.13. Incoherent scattering experiences a relative increase in scattering intensity after $q=1/2\pi\sigma$ due to the loss of elastically scattered photons contributing to Bragg peaks.

The observation of this phenomenon has profound implications as it gives access to the single molecule diffraction pattern modulated by the space group packing of the molecules in the unit cell. The continuous diffraction of an object allows high sampling of reciprocal space, avoiding the phase problem experienced in Bragg diffraction when reconstructing an image. In real space, the Bragg intensities represent a pair correlation, or Patterson, function of the crystal. Ambiguities can arise when more than one asymmetric unit occupies a unit cell and the correlation could be between molecules in different unit cells or in the same unit cell (why there is no phase problem for P1 crystals). This ambiguity arises from translational symmetry, therefore being removed in the highly sampled single molecular transform. This would allow for an unambiguous solution to the Fourier transform using iterative phasing algorithms (Fienup 1987, Miao, Charalambous et al. 1999, Robinson, Vartanyants et al. 2001, Elser 2003, Chapman, Barty et al. 2006). Other than the multiplicity inherent with the space group, this is highly reminiscent of diffraction from a single molecule.

The combination of collecting diffuse scattering data simultaneously with Bragg diffraction provides incredible advantages over the single molecule case though, as some of the problems that have limited single particle diffraction are overcome. First of these is the difficulty in matching orientation as indexed Bragg peaks provide an orientation basis for the snapshot images, a large challenge in imaging of single particles with XFELs (Aquila, Barty et al. 2015). Though there are algorithms that have been developed for incoherent X-ray sources (e.g. Huldt, Szőke et al. (2003), Loh and Elser (2009)), the flux is more limited at these sources compared to an XFEL, significantly limiting the SNR needed for successful imaging. The other outstanding advantage gained from collecting Bragg and continuous scattering together comes from the use of a crystal itself as the N molecules in a crystal that contribute to the measured Fraunhofer diffraction, resulting in a significant N-fold boost in signal.

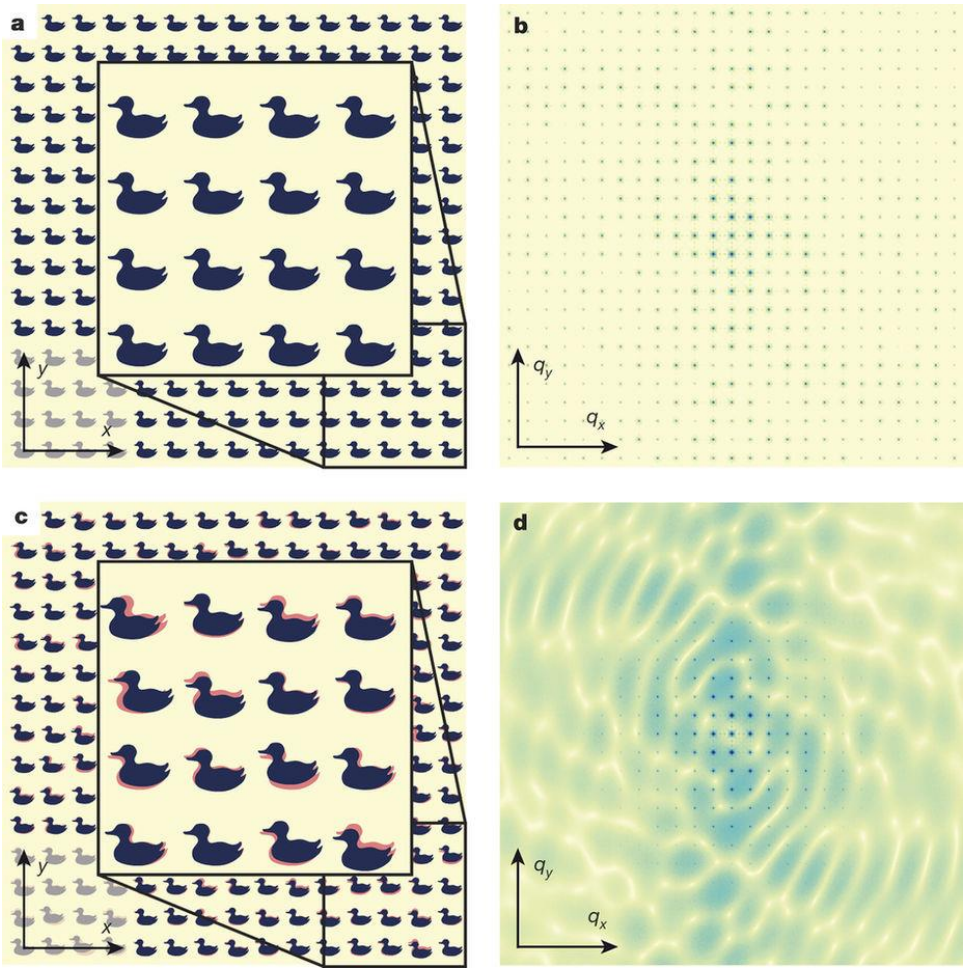

Figure 5.13 Random Translational Disorder Gives Rise to the Molecular Transform

Diffraction of an array of objects in a perfect lattice (a) results in constructive interference and therefore Bragg peaks, as depicted in (b). Diffraction of an array of objects that deviates from the perfect lattice by a root-mean-square value of σ (c) results in increasing destructive interference resulting in loss of Bragg diffraction quadratically with past q=1/2πσ (d). The elastically scattered photons begin to contribute to incoherent Fraunhofer diffraction as the decrease in Bragg diffraction begins to emerge. Figure originally published in Ayyer, Yefanov

If these principles are applied to the 5 Å resolution limited data from PSI TR-SFX experiments, an r.m.s. of 5 Å / 2π = 0.8 Å in each dimension (or $\sqrt{3 * (0.8\,\text{Å})^2} = 1.39\,\text{Å}$ in 3-D) is the upper bound that would account for the Bragg cutoff at this point if this is ascribed purely to translational disorder. This led to the investigation of previous data by applying mathematical treatment (a full description of which can be found in Ayyer, Yefanov et al. (2016)) to the non-Bragg scattering profile. It should be noted that this technique only works if the lattice imperfections are

translational as rotational disorder and other forms of disorder remove the orientational pseudo-homogeneity by the discrete orientations contained in a given space group. The XFEL data possesses an advantage in this circumstance as large time-integration prevents distinguishing between static and dynamic disorder which is avoided by the essentially static snapshot diffraction obtained in SFX experiments.

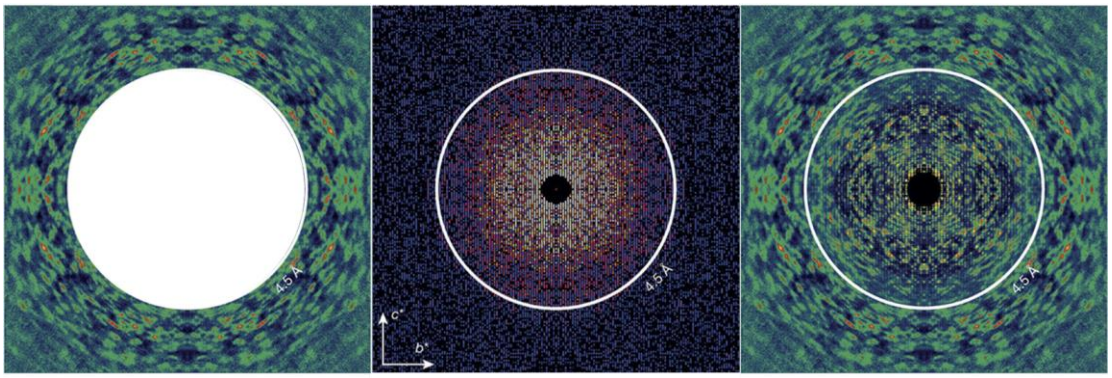

Figure 5.14 Separate Treatment of Bragg and Diffuse Scattering Data

Slices of collected merged data from PSII SFX diffraction patterns. Diffuse scattering was merged (left) and kept separate from the merged Bragg peaks (middle). The low-resolution structure gained from the Bragg data was then used to model the unit cell symmetry applied molecular transform to compliment the reciprocal space shell of experimentally collected diffuse scattering resulting in a completed spherical diffraction volume. A slice of this volume is shown (right) with the white ring indicating the q = 4.5 Å value where the Bragg model and experimental diffuse scattering were merged. Figure modified from Ayyer, Yefanov et al. (2016).

It became apparent when looking at the data that some of the challenges with attempting this revolved around the challenge of background correction related to SNR. The background subtraction needs to be highly accurate as the diffuse signal was often orders of magnitude weaker than average solvent background values. This is compounded by shot to shot variation and variances with jet size over time. However, the solvent background is generally featureless and both the beam and jet variations can be addressed simultaneously by inferring intensity from global and q-dependent intensity values. Initially this was done by development of an algorithm that related these values directly for each individual image, though new algorithms have been developed that take non-linear and local variances into account (unpublished).

It was also observed that diffuse scattering within the Bragg region was difficult to reliably measure with some ambiguity occurring near Bragg peaks as their profile is elusive due to, among

other things, partiality. This was addressed by essentially splitting the data into two data sets, whereby a low resolution was separated and treated per the usual crystallographic pipeline to obtain a low-resolution. The continuous diffraction data past the Bragg cutoff was merged separately such that it comprised a spherical shell in reciprocal space. The inner sphere of

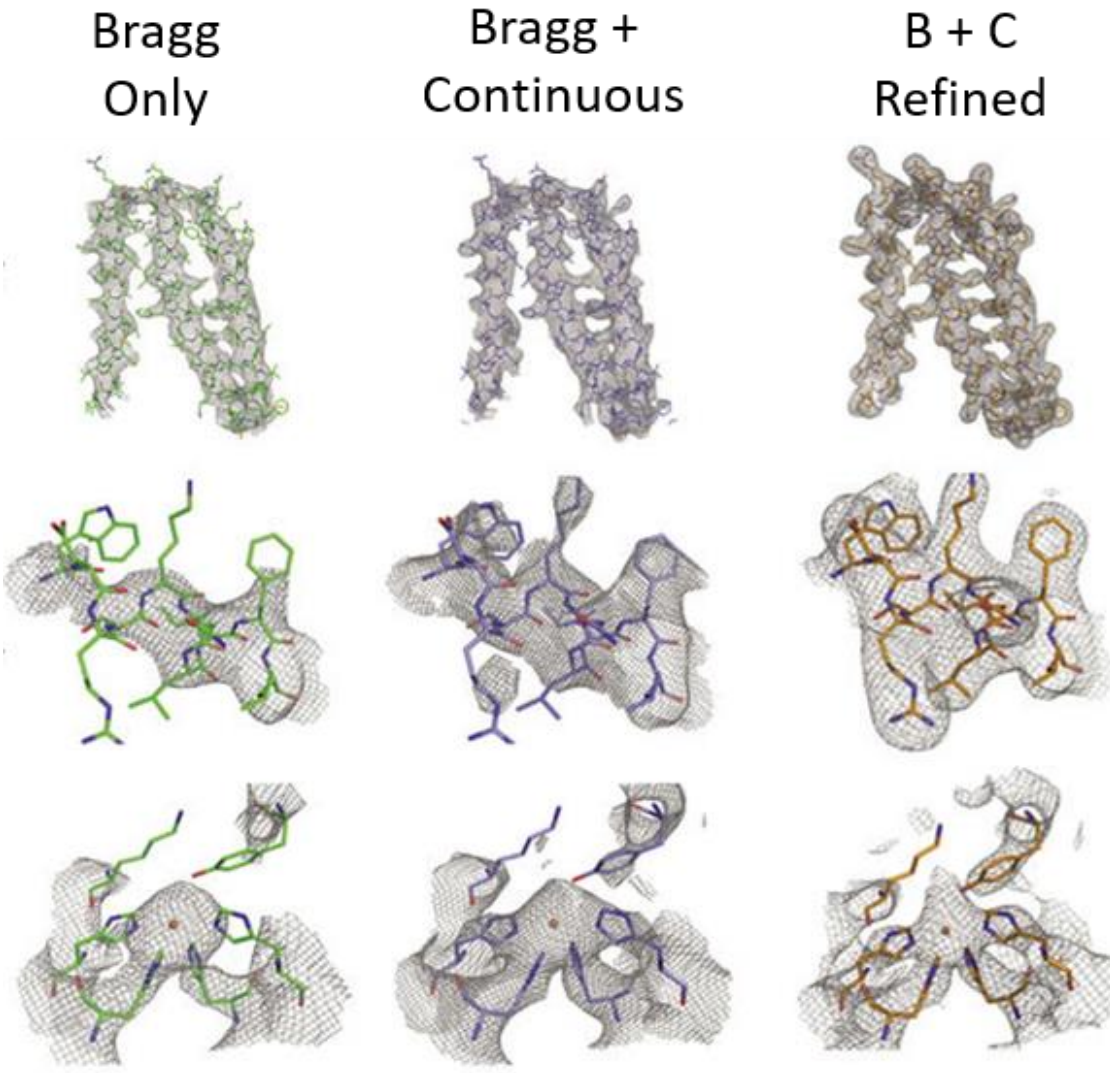

Figure 5.15 Improvements to Electron Density from Continuous Diffraction

Shows selections showing improvement between structures derived from Bragg data only (green, left), from the diffraction sphere including continuous diffraction and the Bragg derived scaffolding (blue, center) and post pseudo-crystallographic refinement (orange, right). The top row pictures helices from the PsbY and PsbZ chains, the middle row shows a closeup of a section from PsbZ showing the emergence of electron density around Trp, Lys and Arg sidechains, and the bottom row highlights the coordination environment around the non-heme iron. Top and bottom row densities are contoured at 1.5 σ, middle row densities at 1.25 σ. All densities are contoured against the 1.9 Å resolution structure reported in Umena, Kawakami et

continuous diffraction was then modeled by applying the orientational incoherent summing of the molecular transform of the four related PSII orientations imposed by the $P2_12_12_1$ space group to obtain calculated values for the missing inner sphere within the continuous diffraction volume. Slices from the reciprocal space data in this process are highlighted in figure 5.14

Using a previously determined model of PSII, a 4.5 Å smoothened molecular envelope support was generated to provide a real-space constraint for the continuous diffraction data. Iterative phasing of the continuous diffraction data shell ranging from 4.5 – 3.3 Å was then performed on the collected continuous diffraction data using the difference-map algorithm (Elser 2003, Elser and Millane 2008) and constrained by the 4.5 Å support. Once the phasing converged, the phases and amplitudes from the entire combined diffraction sphere were Fourier transformed to produce a 3.3 Å resolution structure. Through averaging of multiple random starts, a self-consistent electron density to 3.5 Å was achieved and validated by Fourier shell correlation and the phase retrieval transfer function (Shapiro, Thibault et al. 2005). Refinement of this structure was performed using a pseudo-crystallographic method developed for single-particle cryo-EM (Fischer, Neumann et al. 2015).

The successful result of this work led to the improvement in resolution from 4.5 Å to the 3.5 Å resolution model achieved after incorporation of the continuous diffraction data. This allowed

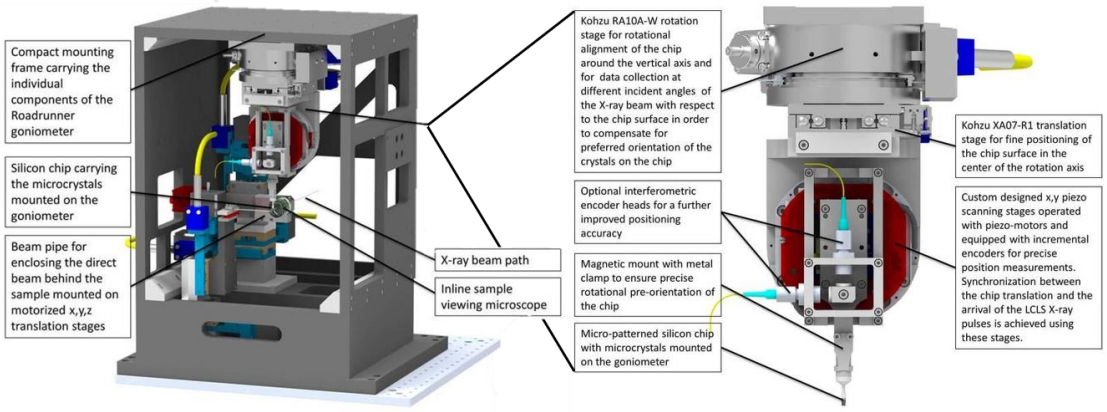

Figure 5.16 Schematic of the Roadrunner Fixed Target Setup

Shows the setup of the initial version of the goniometer-based Roadrunner fixed target setup which utilizes a porous fabricated chip that crystals can be applied to prior to being mechanically rastered in sync with the XFEL beam at LCLS using an XFEL coupled trigger. The manufactured silicon chips are able to hold crystals with between 20,000 and 60,000 pores allowing for rapid data collection with extremely high hit rates. Figure modified from Roedig, Gisriel et al. (2017)

marked improvements in electron densities. Visualization of side chains and cofactor coordination was markedly improved, examples of which are depicted in figure 5.15.

Minimizing Sample Consumption through a Fixed Target Approach

Over the course of multiple TR-SFX experiments, variations in crystal quality from different batches have been notably significant, with crystal quality being highly sensitive to a large number of variables ranging from starting cell quality to purification details through minute differences in crystallogenesis. An issue with this is that a data set typically requires tens of thousands of patterns equivalent to many crystal batches and so the resolution of a data set is subject not to the most well diffracting batch but often the lowest of a large set of crystal batches needed to collect sufficient data for a complete data set. This is further compounded when attempting to collect multiple data sets, inherently necessary for structural characterization of multiple time points along a reaction pathway (e.g. S-states of the Kok cycle).

This is not to say that there aren't tens of thousands of crystals per batch, indeed there are often billions or even trillions. It has been estimated that one crystal in every 10,000-100,000 actually interacts with the beam though, so the large majority of the crystals produced for a beamtime never interact with the X-ray pulses and instead flow past the interaction region in between pulses. Most of the efforts to address this problem have stemmed from the way in which

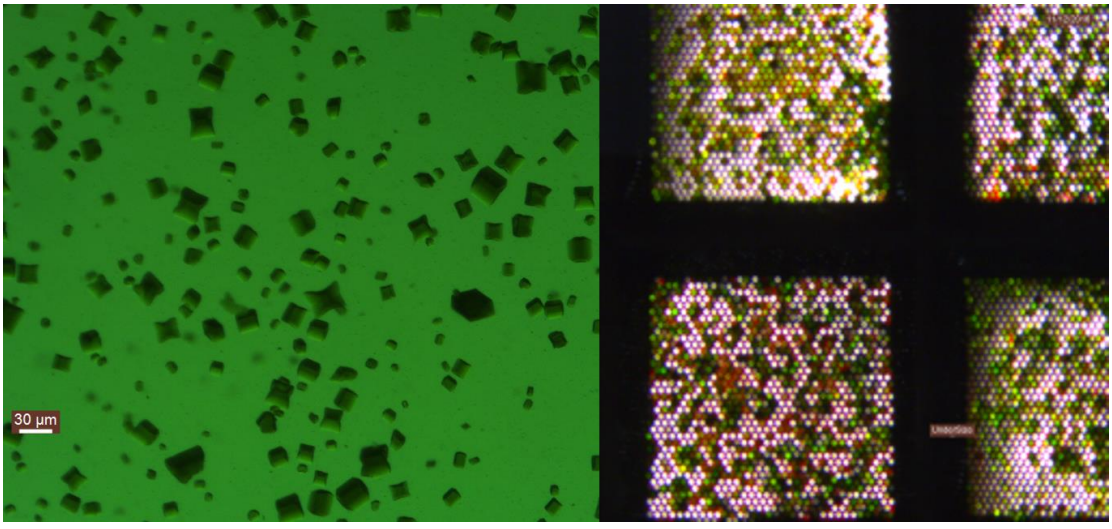

Figure 5.17 Larger PSII Crystals for Fixed Target Chip Loading

Micrograph images of 10-30 µm crystals (left) and the result of a loading test using the blotting procedure (right).

sample delivery is conducted by looking for alternatives to a liquid jet, such as the viscous jets and fixed target approaches discussed in Chapter 2. Fixed target approaches possess the additional benefits of reducing solvent background, the ability to use larger crystals (hence larger signal), and avoiding the need for mechanical shaking to prevent settling. In an attempt to increase the hit rate and reduce sample consumption as well as address the issue presented with batch variance, three beamtimes have been conducted to perform TR-SFX on a chip by using the Roadrunner high-speed goniometer based system developed by Alke Meents, initially described in Roedig, Ginn et al. (2017) and depicted in figure 5.16.

The windows in the chips used in these experiments can be matched to the size of the crystals that are optimal for the TR-SFX experiments. This allows the use of larger sized microcrystals leading to a stronger signal since there is no concern of the clogging issues associated with injection using a GDVN. However, the crystals must be still small enough to allow for full excitation of all PSII molecules in the crystal for time resolved experiments. The PSII crystals are loaded using a blotting method by which a volume of crystal slurry is carefully applied to the face of the chip containing through-hole wells sized between 5 and 20 µm (this can be varied, and the crystal and well sizes should roughly match). Excess solvent is then removed by blotting with a lint-free paper wipe from the other side, drawing crystals into the translationally symmetric pores. Particulars such as crystal size, density and volume applied must be tested for a particular batch of chips in order to achieve a maximum number of single crystals per hole. In addition, great care must be taken while loading as the chips are composed of a thin membrane only microns thick (we have used 25 µm and 35 µm silicon chips) and can easily be damaged during the loading and blotting processes. This is exacerbated by the need to do the loading in a humidified chamber with only dim green light to avoid photoexcitation of PSII. Figure 5.17 shows an example of larger PSII crystals grown for chip loading and a test for sample loading density optimization.

The initial experiments, where the roadrunner system was first tested at an XFEL were conducted in November 2016 at the MFX beamline at LCLS and at this point the goal was to show the proof of concept for on the chip XFEL data collection with 120Hz. The goal for PSII was to visualize the ground state and test viability of the method for PSII, among other samples for which

data were collected at this beamtime. We had planned to evaluate the PSII data based on Bragg peaks and continuous diffraction. This LCLS end station (MFX) differs from the CXI end station and most other SFX beamlines in that it operates at atmospheric pressure. This has the disadvantage of increased background due to scattering from the gas used to sustain pressure (typically air or helium) but allows for novel experimental design options to be implemented. For data collection on a chip (which takes approximately 20min/chip) the sample environment, e.g. ability to humidify the crystals on the chip, is crucial since the solvent normally present in a liquid jet is absent. Over the course of four 12-hour shifts, data on PSII crystals were collected on 33 chips with an average hitrate of 25.12% resulting in 744,404 hits, remarkable feat considering the total collection time was under 8 hours. Of these hits, the final indexing rate was 83 % leading to 621,303 indexed diffraction patterns.

After comparing the data, it was noticed that the unit cell distribution was broader than usual and upon closer inspection, it was apparent that there was a correlation with the raster scanning of the chip. Oscillations were observed in both the unit cell parameters and the resolution of diffraction, shown in figure 5.18. This was attributed to issues with humidity as the chamber was humidified with a wet gas stream that was coming in on one side of the chip, possibly affecting hydration of the crystals as a function of geometry. Follow up experiments have been performed

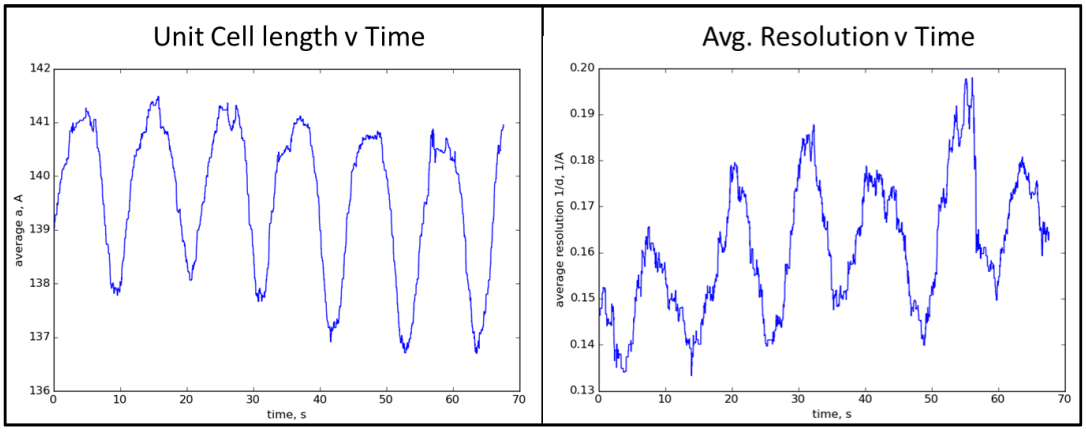

Figure 5.18 Apparent Oscillations in PSII Unit Cell and Resolution During Raster Scanning

Data from a single run of PSII on a chip using the Roadrunner setup. Shows the periodic shift in unit cell length in the *a* direction (left) and maximum resolution of Bragg spots on each image (right).

since, dedicated to TR-SFX of PSII on a chip with newer designs and improved humidity control, again at the MFX beamline (experiments performed in September 2017 and March 2018). Current analysis from these beamtimes is still ongoing but Bragg resolution has seen a marked increase. The Bragg resolution was increased to 3.3 Å resolution and a preliminary structure determined based on the Bragg data only (unpublished). The background correction (as discussed above) is the major challenge for the data evaluation of the continuous diffraction and is currently in progress.

At the beamtime in September 2017 TR-SFX of PSII was attempted for the first time on a chip. The aim was to probe the S_4 state and this proved to be quite challenging as the crystals were excited by triple laser excitation on the moving chip before their structure was probed by the XFEL. The most recent beamtime in March 2018 combined TR-SFX with XES spectroscopy on the chip. Data evaluation of these first TR-SFX fixed target beamtimes is still in progress and will likely take several months or longer. The fact that time-resolved data sets can be collected using the roadrunner system highlights the great potential of this fixed target method to allow molecular movies to be made with minimal sample consumption and optimal batch selection. The humidity issue seems to have been largely addressed with the resolution being less strongly correlated with

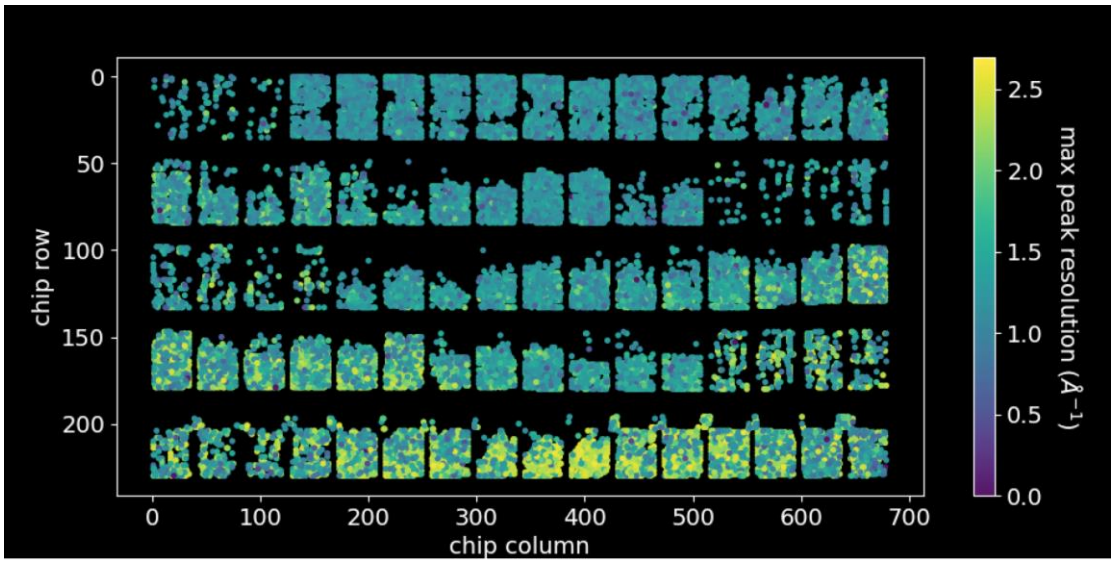

Figure 5.19 Resolution by Location on the Chip

Profile of crystals imaged on a single chip by their max resolution in Å^{-1}, indicated by the heat map. Note the higher q scattering (yellow) favors the bottom of the chip suggesting larger, more intensely diffracting crystals may be mobile during the course of imaging.

the rastering periods. However, it seems that over the course of raster scanning of a chip, the larger crystals tend to slide to the bottom, leading to an asymmetric profile of diffraction resolution weighted to the bottom of the chip (indicated in figure 5.19). Regardless of challenges experienced during these investigations, the Roadrunner method holds high promise towards future elucidation of the mechanistic splitting of water by PSII.

Co-crystallization of PSI-Fd

Though initial conditions have been established for over a decade (Fromme, Bottin et al. 2002), the co-crystallization of PSI and Fd presents many challenges. The first of which is the incredible efficiency by which PSI absorbs photons and transfers charge to a bound Fd which subsequently undocks. As with any crystallogenesis, conformational homogeneity of the macromolecular complex is crucial to obtaining not only well-diffracting crystals, but precipitation with crystallinity at all. This is further compounded by the need for sufficiently high occupancy of the ferredoxin in the crystal to allow for visualization of the complex. Both advantageous and challenging, Fd is suspected of involvement crystal contacts, resulting in dissolution of crystals upon exposure to light though this is also indicative of functionality (e.g. no steric hinderance), necessary for impactful structure-function interpretation. Figure 5.20 shows an example of the dissolution of microcrystals

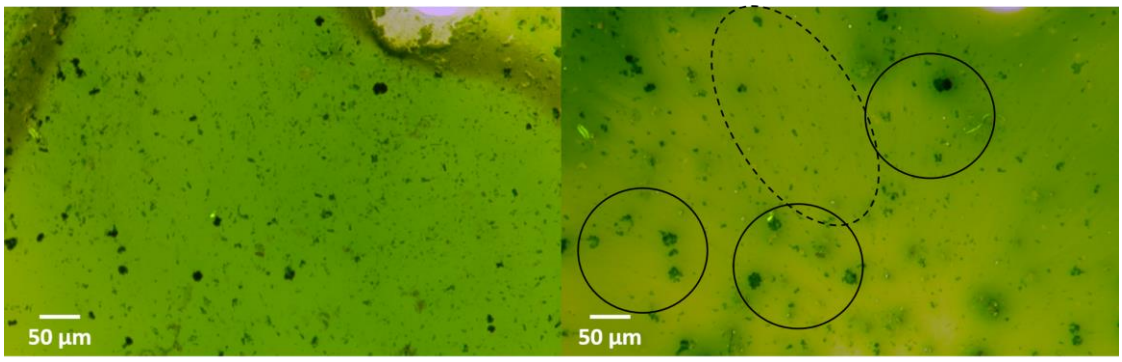

Figure 5.20 Dissolution of PSI-Fd Co-crystals in White Light

PSI-Fd co-crystals seconds after exposure to the white light from a microscope (left) and 2 minutes later (right). Note the loss of sharp features in larger crystals (solid, circled) and complete dissolution of the smaller crystals (oval, dashed). The areas surrounding some of the larger crystals show areas of darker green surrounding them, indicative of the high local concentrations of freshly dissolved PSI-Fd cocrystals. In order to maintain crystal integrity, crystals must be maintained in complete darkness. Crystals pictured were grown with FID method during initial trials and were dropped into a 5 uL drop of mother liquor to avoid effects from evaporation.

under white light. Due to these concerns, from the initial incubation of PSI and Fd through the crystallization and experimentation, the co-complex must be kept in complete darkness. Microcrystals are particularly susceptible to the fast dissolution upon light excitation due to the comparable lack of attenuation (large PSI-Fd co-crystals are extremely opaque due to the large density of chromophores). Furthermore, the nature of SFX precludes the use of cryogenic temperatures for data collection. Under cryogenic temperatures the undocking of ferredoxin may be hindered or slowed down as the solvent is frozen and thereby not mobile. SFX data, however, are collected at RT, which allows for the undocking to take place in the crystals.

Prior to crystallization, stored PSI crystals were centrifuged and dissolved as described in the previous section with the modification of being dissolved in F4 buffer (200 mM HEPES pH=7.5, 300 mM $CaCl_2$, 0.004% w/v β-DDM). To this solution, both F5 buffer (100 mM HEPES pH=7.5,150 mM $CaCl_2$, 0.012% w/v β-DDM) and Fd were added in complete darkness to final concentrations of 60-120 µM PSI and 75-150 µM Fd with a PSI:Fd =1:1.25. The PSI-Fd complex was then allowed to incubate at room temperature for no less than 1 hour and no longer than 6 hours prior to crystallization. During initiation of incubation between PSI and Fd through crystallization and loading of sample for an experiment, the solutions and the formed crystals were necessarily kept in complete darkness and manipulated through use of IR-active night vision goggles (model PVS7-HPT, American Technologies Network, San Francisco).

Nanocrystallogenesis had previously been done using PEG 400 as a precipitant as reported in Aquila, Hunter et al. (2012). These crystals showed a size distribution between 500 nm and 2 µm. The TR_SFX experiments on the PSI-ferr complex were the first TR-SFX experiments on protein crystals ever preformed at an XFEL during the first runs of LCLS where only the soft X-ray beamline AMO was operational and the energy was limited to 2 keV. These experimental constraints limited the resolution to 10 Å (Aquila, Hunter et al. 2012).

For this to be improved upon, in increase in both crystal quality and size were targeted for optimization. In the course of this optimization, three different sources of Fd were used for crystallogenesis in anticipation that the different binding efficiencies from the varied Fd sources may show increased crystal quality and allow for maximization of occupancy and subsequently crystal quality. Furthermore, the different kinetics between the Fd sources with PSI could be used as a parameter for reaction homogeneity during time-resolved studies. Three ferredoxin sources

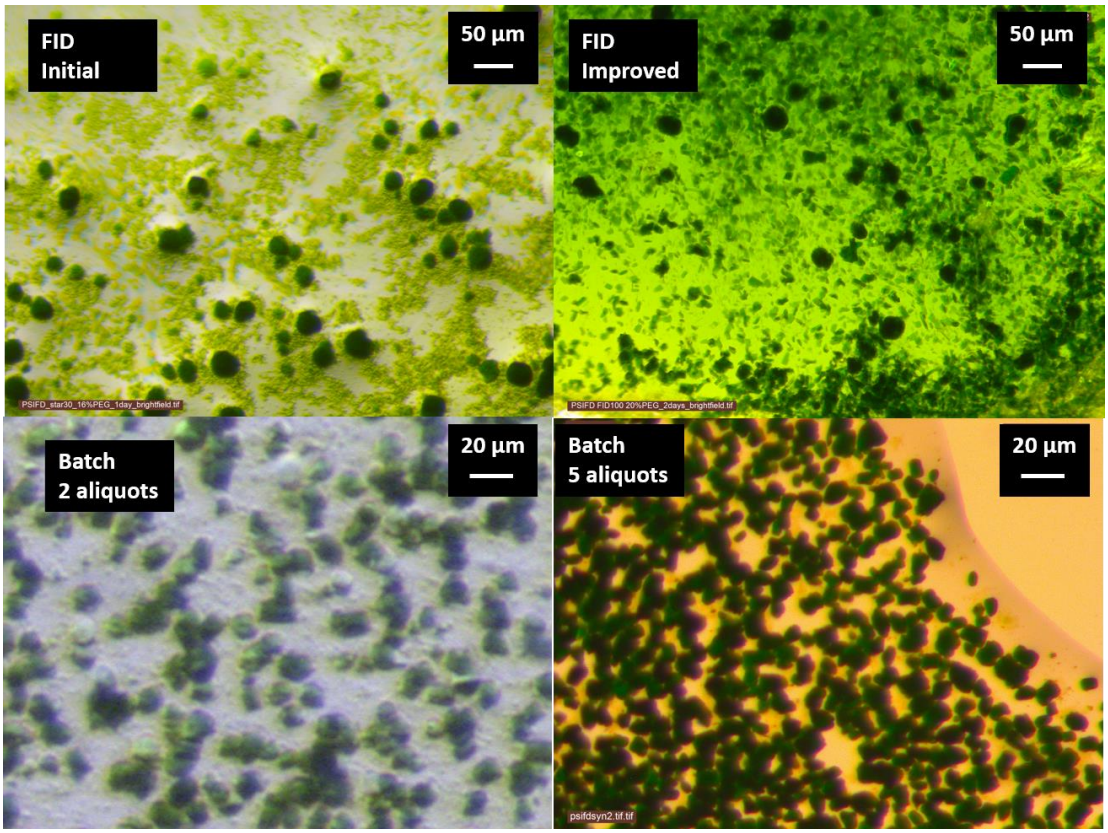

Figure 5.21 Improvement of PSI-Fd Crystals

Shows serial improvement in PSI-Fd microcrystallogenesis starting from initial experiments using the FID method (top left), optimized FID methods (top right), batch experiments using three equal volumentric increments of precipitant with pipette mixing (bottom left), and batch experiments using five precipitant additions with incrementally decreasing volumes (bottom right). Note the difference in PSI still in solution between FID (top) and batch (bottom) methods. Size homogeneity also showed marked improvement after increasing the number and varying the volume of aliquots that were applied to batch methods, likely due to a decrease in local concentration variances of chemical composition during pipette mixing.

were used, namely, *Chlamydomonas reinhardtii* (Cr-Fd), *Synechocystis sp. PCC 6803* (Sy-Fd) and spinach (Sp-Fd). *T. elongatus* Fd was not included due to its anecdotal inability to co-crystallize

with PSI (P. Fromme, personal communication), thought to be from an inhomologous flexible loop motif in the TS. elongatus ferredoxin that hinders the formation of crystal contacts

Initial trials for improved microcrystals of PSI-Fd were performed using the FID method with moderate success. Ultimately, the procedure was optimized to allow for larger crystals, with a size of 5-15 µm to be grown. This was achieved by using a 1:1 volumetric ratio of PSI:PEG 400 **(==3**0% w/v PEG and 80-100 mM PSI) with total volumes ranging from 50-1000 µL. Though relatively successful, problems with size inhomogeneity were present, particularly most procedures leading to growth of larger crystals that would necessitate sample prefiltration, costly in practice to perform in complete darkness. These initial results led to attempts to implement a batch method using rapid pipette mixing with final concentrations of 17-20% PEG 400 and 45-50 µM PSI. Batch method crystallization showed a marked improvement in both yield and size homogeneity, with further improvement arising from the use of a higher number of aliquots (five as opposed to two previously) used during pipette mixing. In addition to the higher number, the volumes used for each aliquot was adjusted to bring the solution to a point just under supersaturation before the final aliquot as was inferred by the opacity of the solution as viewed through the IR night vision goggles. The gradual improvement of crystal macromophology is depicted in figure 5.21.

TR-SFX of PSI-Fd

As previously mentioned, the co-crystal structure between PSI and Fd has yet to be determined in spite of both protein structures having been solved independently and many biophysical characterization studies having been performed. PSI-Fd has been shown through spectroscopic studies to likely possess biphasic kinetics in the electron transfer between them, with a fast kinetics occurring at 500 ns and a slower kinetics where ostensibly the electron is transferred between 5 – 10 µs (Setif and Bottin 1994, Setif and Bottin 1995). Though the first TR-SFX experiment ever performed was on the PSI-Fd co-complex (reported in Aquila, Hunter et al. (2012)), the limited amount of data as well as the limited resolution prohibited any structure, dark or time-resolved, from being elucidated. However, one interesting finding that was observed was that a strong difference signal was observed between the dark ground state and the single flash excited

state with time delays of 5 µs and 10 µs. This was indicative of a possible conformational change (5 µs) and undocking (10 µs) as can be seen in figure 5.22. If this hypothesis is confirmed, this would indicate that the 5 µs time point would present a very interesting target for capturing an intermediate structure of the co-complex prior to undocking but after electron transfer had occurred.

Successful efforts were made in improving control of crystal size during crystallogenesis of PSI-Fd as described in the previous section, allowing for larger micro-crystals to be grown than those explored in the previous study (~500 nm) in hopes of increasing observable resolution for structural studies. For these studies, Fd from *Chlamydomonas reinhardtii* (Cr-Fd), *Synechocystis sp. PCC 6803* (Sy-Fd) and spinach (Sp-Fd) were overexpressed in competent *E. coli* and purified with anion exchange chromatography in order to screen the different Fd's for co-crystallization experiments, possibly leading to resolution improvements since Fd is known to be involved in crystal contacts (Fromme, Bottin et al. 2002). The varied Fd sources also possesses the benefit of allowing for modulation of reaction kinetics as indicated by the aforementioned spectroscopic studies (Setif and Bottin 1994, Setif and Bottin 1995).

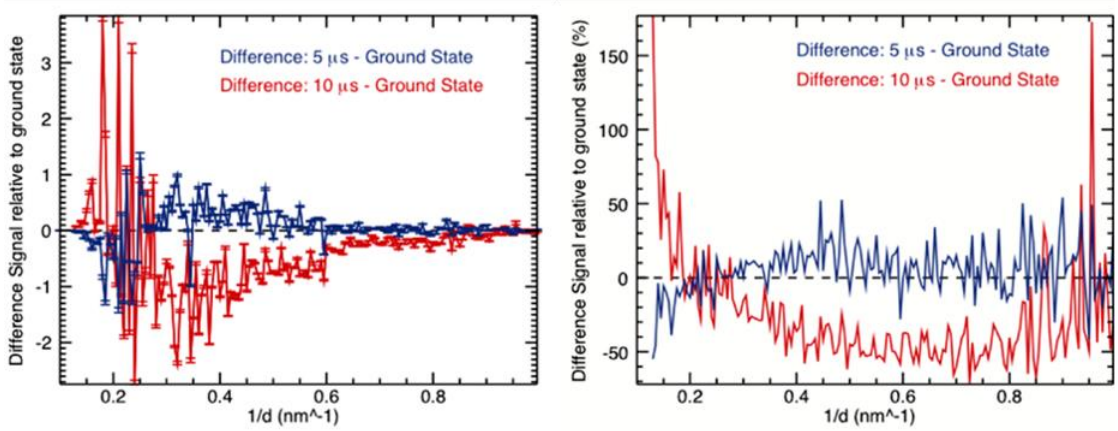

Figure 5.22 Difference Signal Observed in Previous PSI-Fd TR-SFX

Shows difference signal between positive time-points and ground state measurements of photoactivated PSI-Fd nanocrystals as a function of reciprocal space resolution (1/d, nm^{-1}). Depicted as quantitative relative signal (left) and as a percentage of ground state signal (right). Note the decreased intensities for the 10 µs time point, the magnitude of which appears to increase with higher q, possibly indicating an undocking of Fd from PSI. Figure modified from Aquila, Hunter et al. (2012).

In preparation for TR-SFX investigations of PSI-Fd, over 5 grams of PSI were isolated and purified in addition to over 200 mg each of the three Fd sources. Screening of crystallization

conditions was performed by systematically varying the three Fd sources, PSI and precipitant concentrations, method (FID, FIDC and variations on batch methods), and additives including the detergent additives Cymal-(2,3,4,6) and the Calixar additive kit (Molecular Dimensions). Large crystals were also grown by the method of vapor diffusion based off the most promising candidates from these screening results and probed for X-ray diffraction at the Advance Light Source synchrotron in Berkeley, CA in an attempt to differentiate the effect of the individual parameters on crystal quality. Unfortunately, the crystals showed very low resolution (< 12 Å), suspected of being caused by novice looping and freezing technique, and were unable to allow any new insights to be gained towards optimal conditions. However, microcrystal screening allowed for improved micromorphology as described in the previous section (see figure 5.21) and no significant difference was observed with regards to additive composition or Fd source.

In preparation for a TR-SFX pump probe experiment, calculations were made for optimal pump characteristics. In general, a wavelength with sufficient energy to trigger the reaction but sufficiently far removed from the absorbance maximum is preferred for crystallographic experiments. This is due to the need for homogenous reaction initiation throughout the crystal. A wavelength near the absorbance maximum suffers due to attenuated excitiation as the pump laser propagates through the crystal. As such, a wavelength in the green light region is optimal for photosynthetic membrane proteins (which is at 10% of the absorption maximum of PSI at 680nm) and so a 527 nm laser was used in the calculations of optimal light excitation. Extinction coefficient values for chlorophyll at this wavelength were experimentally probed using spectrophotometry and the value was found to be 3,800 L mol^{-1} cm^{-1}. Using this value, the fluence calculation was made to determine the laser power needed in order to have at least one photon per chlorophyll at the back of a crystal 5 µm in a given dimension (i.e. after the pump had propagated through 5 µm of crystalline PSI-Fd) and the ideal fluence was found to be 300 nJ.

In March of 2015, a beamtime was allocated to investigate the structure and dynamics of PSI-Fd using pump-probe TR-SFX at the CXI beamline at LCLS, SLAC. Over the course of five

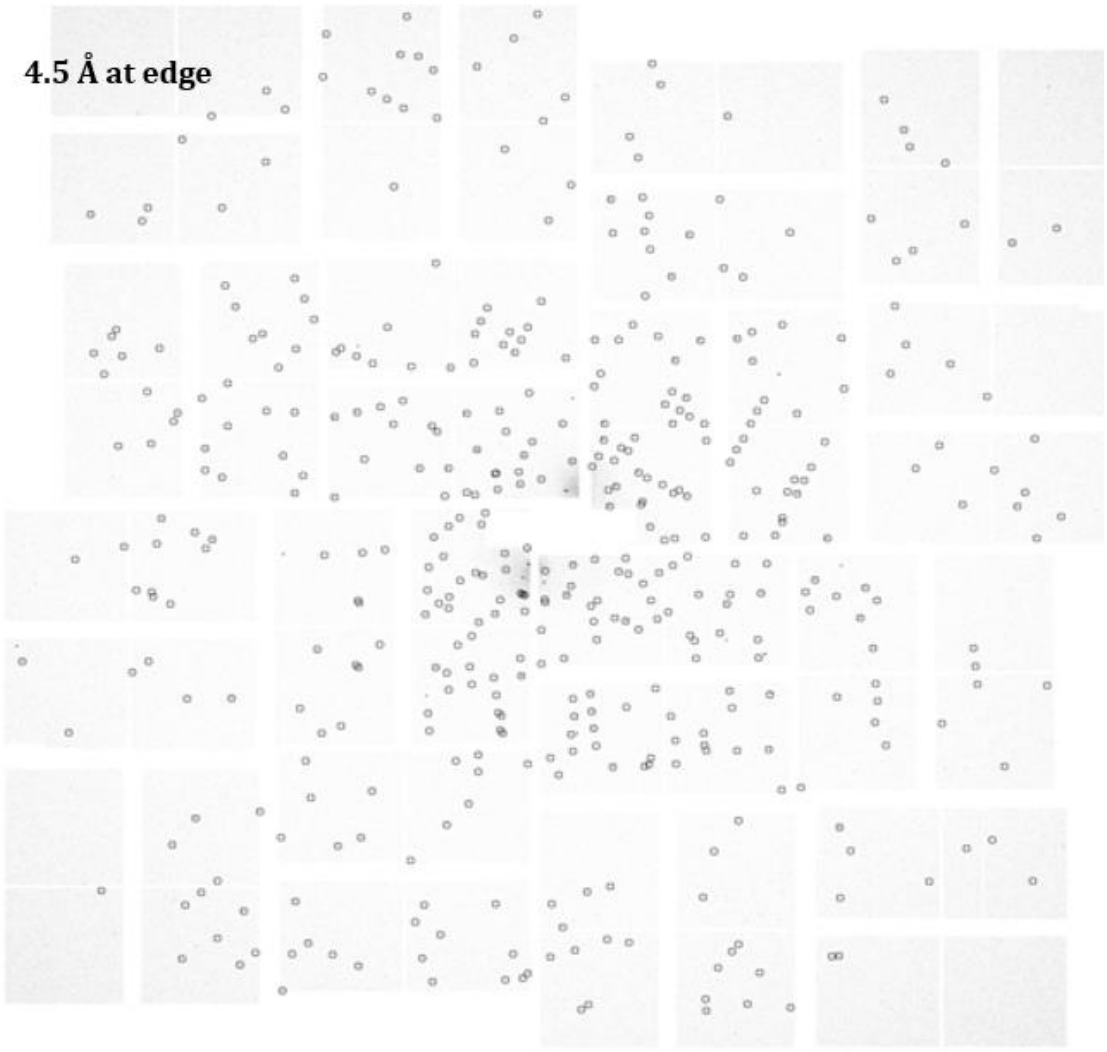

Figure 5.23 Improved Diffraction of PSI-Fd Microcrystals at LCLS

Maximum resolution of PSI-Fd microcrystal diffraction reached 4.5 Å, a marked improvement over previously collected microcrystal diffraction. Over 700,000 crystal diffraction patterns were measured during the course of the experiment.

12-hours shifts time points of 500 ns and 5 µs were probed, interleaved in an alternating 60/60 Hz scheme with non-illuminated dark patterns. The pump laser used to illuminate the crystals was chosen to be a ns pulse laser at 527 nm with a fluence of 4.53 mJ/cm^2 in a top hat focal spot of 530 µm in diameter. The pump laser was emitted with 100 ns pulses at 60 Hz, triggered upstream by the XFEL pulses. The XFEL beam was ~1 µm^2 with 8.7 keV Xrays and 30-35 fs pulses with total pulse energies averaging between 1.69-2.03 mJ. Data was collected using a 50 µm inner diameter GDVN (DePonte, Weierstall et al. 2008) with an inline 20 µm stainless steel fritted filter (IDEX) at

flow rates of 16 +/- 5 µL/min. Over 40 mL of sample with various compositions as mentioned above were injected. All sample preparation, handling, and loading was performed in complete darkness using night vision goggles as described previously followed by injection in a darkened hutch with all high vacuum windows of the interaction chamber being sealed from light to avoid premature electron transfer initiation within the crystals.

In total over 700,000 crystal hits were recorded with ~250,000 being indexed leading to an average hit rate of approximately 4% and indexing rate of 35% over all conditions and time points. The resolution observed during the experiment marked an improvement upon previous measurements with microcrystals, showing spots up to 4.5 Å as highlighted in figure 5.23. However, the average resolution observed varied only slightly between the different Fd sources and additive conditions, falling around 8 Å as shown by the typical diffraction pattern and virtual powder pattern in figure 5.24. The space group and unit cell were found to be within good agreement of that reported previously (Fromme, Bottin et al. 2002) and a very narrow distribution of parameters. Preliminary data quality assessment showed that all three time points (dark, 500 ns, and 5 µs) showed similar quality and intensity distribution, indicating that crystal quality was not

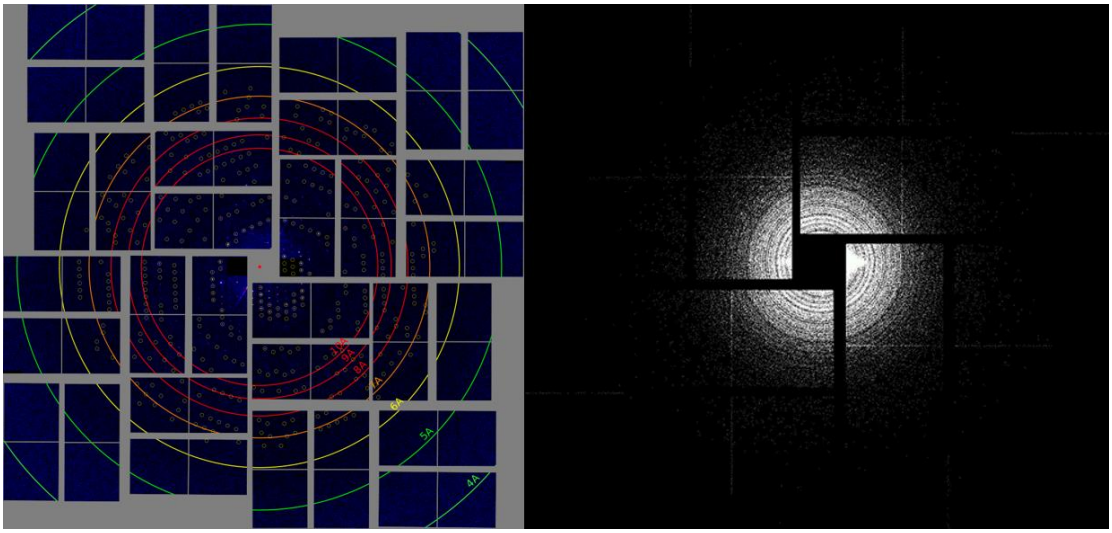

Figure 5.24 PSI-Fd TR-SFX Data Diffraction Limited

Images of a typical diffraction pattern (left) and a virtual powder pattern from a run (right). Virtual powder is constructed by summing peaks from all frames collected over the course of a run, effectively creating a powder pattern from the collective snapshots similar to that found by powder diffraction. Both images indicate the observed Bragg cutoff in the 7-9 Å range found throughout the collected data.

compromised by laser pumping at this resolution. The unit cell parameters, $CC_{1/2}$ and resolution dependent spot intensity are displayed in figure 5.25. Initially the phasing of the low-resolution data sets as well as the cumulative data set were attempted but unfortunately none of these attempts converged.

With many developments in the data reduction and processing pipeline since this experiment, it may be possible that reanalyzing the data in the future could prove fruitful for structure

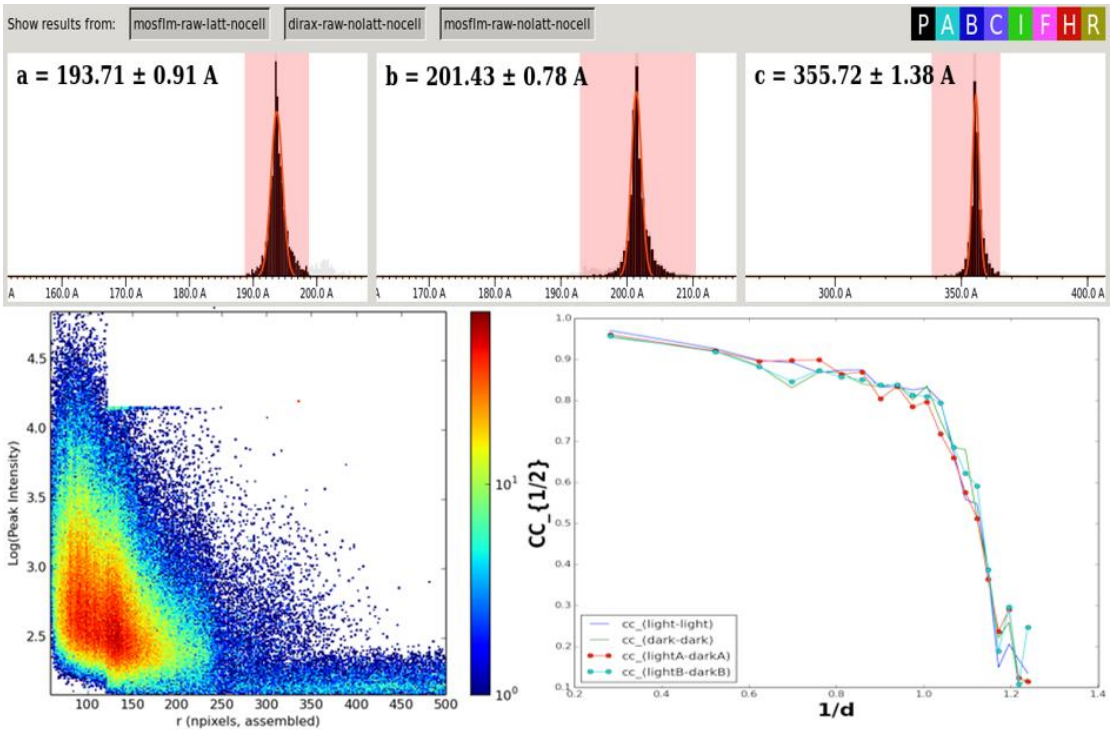

Figure 5.25 Unit Cell Parameters and Resolution Statistics from PSI-Fd TR-SFX

Unit cell parameters (top) for $P2_12_12_1$ space group observed in 2015 PSI-Fd TR-SFX experiment are in good agreement with previously reported values (Fromme, Bottin et al. 2002). Logarithmic comparison of intensity as a function of q (bottom left) shows a strong cutoff at low resolution (~8-9 Å), though peaks are seen out to the 4.5 Å edge of the detector (values in pixels with 500 pixels being equivalent to 4.5 Å). $CC_{1/2}$ values (bottom right) show the same resolution cutoff with $CC_{1/2}$=0.5 occurring at ~8.5 Å. Notably all comparisons (light-light, light-dark, dark-dark) show the same general trend and cutoff, indicating that illumination did not have a detrimental effect on data quality at the time points measured.

determination. In addition, many of the patterns exhibited strong continuous diffraction as shown in figure 5.26, showing continuous scattering up to 3.5 Å. This has also been observed at microfocused synchrotron beamlines (discussed in a following section) and current work is focused on analyzing the data by a combination of evaluation of continuous diffraction and Bragg diffraction.

If this could be leveraged, this could provide a breakthrough in the understanding of photosynthetic electron transfer between PSI and Fd

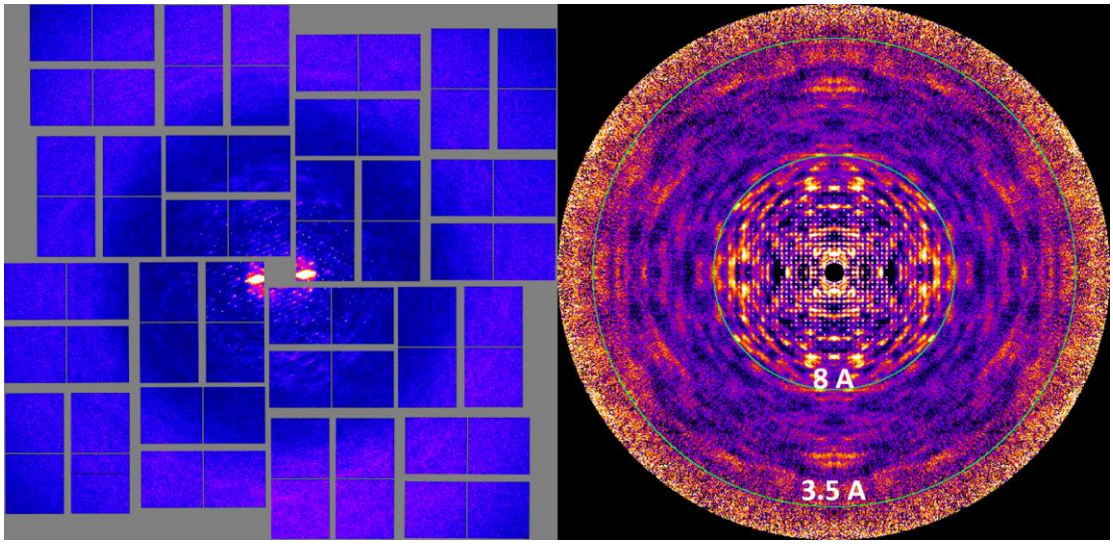

Figure 5.26 PSI-Fd Continuous Diffraction from Microcrystals

A typical pattern showing strong diffuse scattering well into the solvent ring (left) and the XY slice from a merged data set from 2,974 selected patterns showing the strongest diffuse scattering (right).

Improving Resolution with Additives

A screening beamtime was awarded to test improvements in Bragg diffraction resolution anticipated upon improved micromorphology with the use of additives during the crystallization process. Screening of detergents and further additions including amino acids were performed. Cymol's 2-4 (detergents) additives were screened in an attempt to create mixed micelles that might allow tighter crystal packing. Amino acid additives were tested based off anecdotal observations in the crystallization of other photosynthetic membrane proteins (Y. Mazor, personal communication, February 2016). During screening, there was a notable visual improvement in the micromorphology of PSI-Fd crystals grown in the presence of some amino acids, particularly glycine as shown in figure 5.27. However, results from detergent screening were inconclusive as batch variance hindered reliable comparison. Typical of a screening beamtime, only 6 hours was awarded for data collection at LCLS leading to the need to focus on few conditions. Because of this restriction, only data from the top three amino acid candidates (glycine, histidine and lysine,

based on visual screening of the crystals prior to data collection) were collected in addition to a combination of the three as well as a control sample prepared without any additives for comparison.

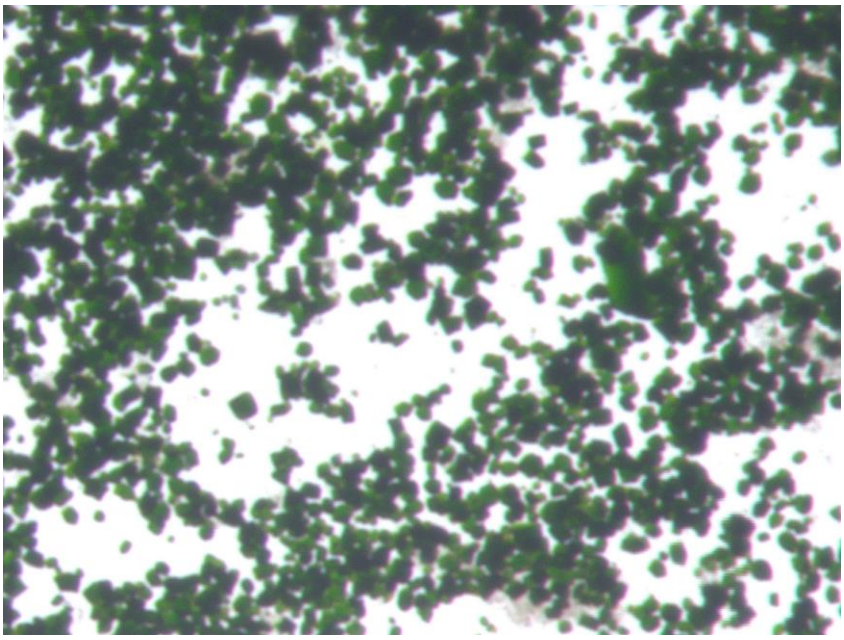

Figure 5.27 Sharper PSI-Fd Crystals by Use of Amino Acid Additives

Further improvement was made on the micromorphology of PSI-Fd co-crystals by use of amino acid additives. The most improvement found was with 5 µM glycine, pictured above. Visible improvement was observed with histidine and lysine as well, with additives being homogenized into the precipitating solution.

During the 6-hour shift, almost 4 hours of data collection was achieved with an average hit rate of 8.43% resulting in a total of 128,883 hits. Resolution was limited to above 7 Å for all samples, limiting indexing rate to 12.4% and resulting in just under 16,000 indexed patterns. While this low resolution again precluded a structural model, there was a statistically significant improvement in resolution between glycine doped co-crystals with respect to the additive free crystals. The fact that the condition specific maximum resolution observed was significantly improved for all samples when compared with the previous experiment indicates that the protein quality may have differed or may have been due to the larger sized crystals used for screening.

Continuous diffraction with PSI-Fd macrocrystals

In an attempt to determine the first structure of PSI with Ferredoxin bound in the dark state of the PSI-Fd complex , large crystals were grown with the vapor diffusion technique similar to previously described (Fromme, Bottin et al. 2002) with final PEG 400 concentrations ranging between 6% and 8% w/v. The crystals were then gradually transferred from the drop into a 40%

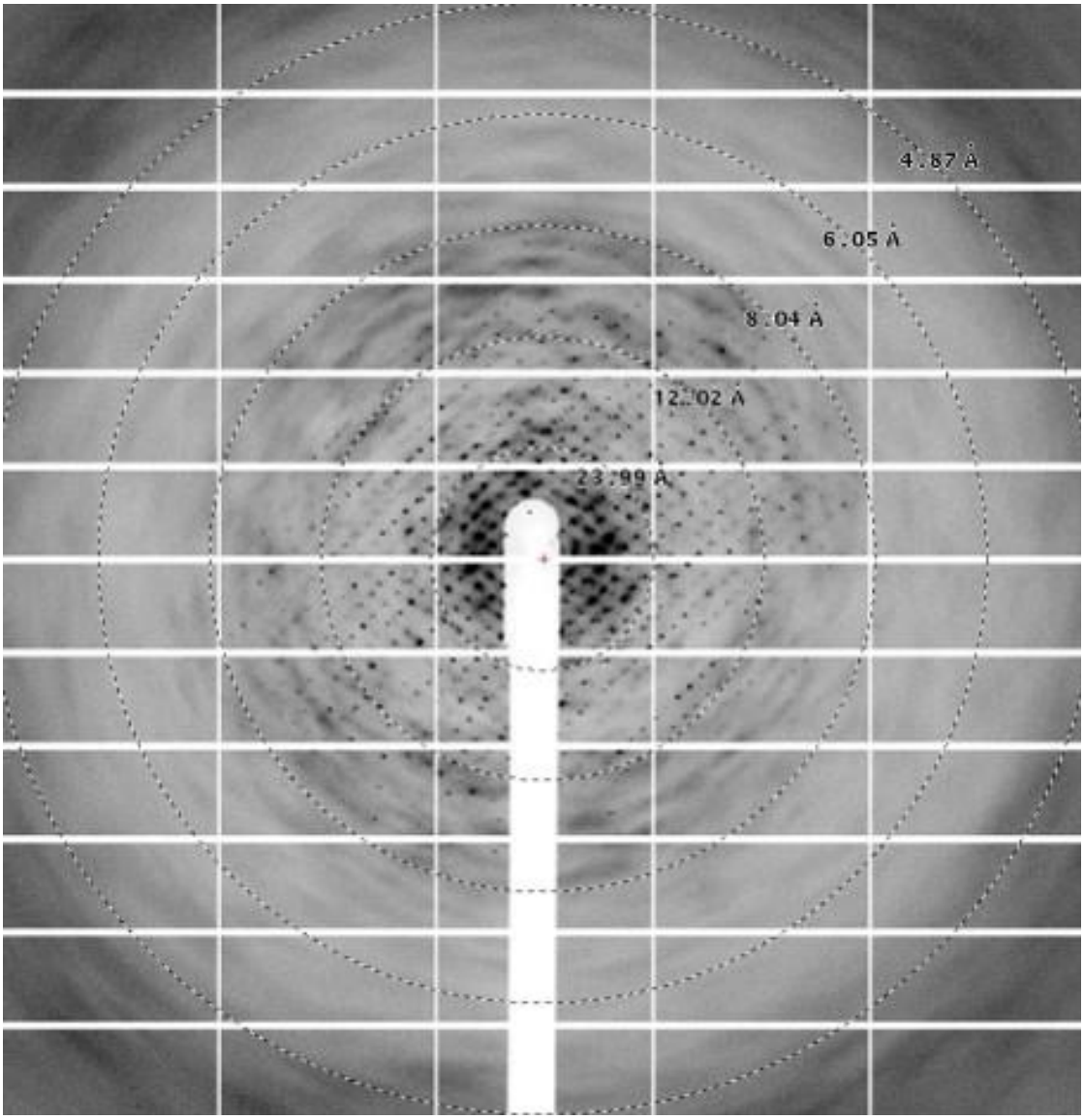

Figure 5.28 Intense Continuous Diffraction of PSI-Fd Measured at the P14 Beamline, PETRA-III

100 ms capture with 12.4 keV X-Rays of a 400 µm PSI-Fd co-crystal, collected at cryogenic temperature during a helical raster scanning method. Note the sharp Bragg peak kutoff around 8 Å and intense diffuse scattering to the edge of the detector. This is indicative that random translational disorder may be a primary constraint in resolution of Bragg diffraction.

PEG 400 w/v solution for cryoprotection by serial equilibrations into PEG solutions ranging between the % PEG content of the drop through 40% with no incremental increases being larger than 4%. For example, a crystal grown with 8% w/v PEG 400 final drop concentration would be transferred into a 12% solution, followed by a 16%, 20% etc. until a final incubation in 40% PEG concentration

was achieved. Each incubation step was performed for no less than 5 minutes to avoid the detrimental effects possible from a stark and rapid change in local chemical environment. Upon incubation in a 40% PEG solution, the crystals were then procured with a commercial crystallization loop and flash frozen in liquid nitrogen before being stored in a puck until beamtime. Crystals ranged in size, with the average being 250 µm and the largest being 500 µm.

Traditional cryo-crystallography was then performed with these crystals at the P-14 microfocus beamline at the PETRA-III synchrotron in Hamburg, Germany. Crystals were mounted and an ultra-cooled nitrogen cryostream was used to keep crystals at 100 K during data collection. X-ray diffraction data collection was performed using helical raster scanning with 100 ms pulse duration per image at a rotation angle of 0.1 degrees per image. Similar to previous experiments at XFELs, the resolution seemed to cutoff right around 8 Å with strong diffraction prior to the abrupt cutoff. Interestingly, there was evidence for incredibly strong diffuse scattering to high resolution, similar in resolution to what was observed at the LCLS TR-SFX experiment described above but much more pronounced as can be seen in figure 5.28. Unfortunately, only one day of beamtime was committed to this experiment and so the focus was on Bragg diffraction. This led to multiple adjustments in detector distance to optimize Bragg peak quality and rendered the data sets to be in too small of bins to allow for evaluation of the diffuse scattering data following the route developed for PSII experiments at LCLS (Ayyer, Yefanov et al. 2016). This is highly encouraging though, as more data collection with dedication to continuous diffraction data under optimized conditions could pose the most likely way forward in the quest for a ground state structure for the PSI-Fd complex.

Towards Structural Enzymology: KDO8PS

Crystallization from Known Conditions and Yield Improvement

Previous work on crystallization and purification of KDO8PS from *E. coli* has been performed using large crystals as described in Vainer, Belakhov et al. (2005) and it was from these conditions that initial trials for microcrystallization were performed. Initial microcrystallization efforts were initiated by a previous Ph.D. student, Chelsie Conrad, whereby successful microcrystallogenesis was performed using the FID method. These crystals, shown in figure 5.29,

were grown by dropping a 20% poly(ethylene glycol) methyl ether, MW=5,000 AMU (PEGME 5K) solution into an equivalent volume of 21 mg/mL KDO8PS with volumes not exceeding 50 µL each.

In order to optimize reaction homogeneity for diffusive mixing imduced TR-SFX, both the size of the crystals and their size homogeneity are crucial for this type of experiments. In pursuit of this goal with KDO8PS, batch methods using a slow addition of the precipitant to a stirring solution were tested in addition to the previously established FID methods, as this batch method has had large success in microcrystallization for other successful SFX experiments (e.g. lysozyme used as a calibration for multiple experiments, PSII, PYP (Tenboer, Basu et al. 2014, Pande, Hutchinson et al. 2015)). Systematic screening was performed across

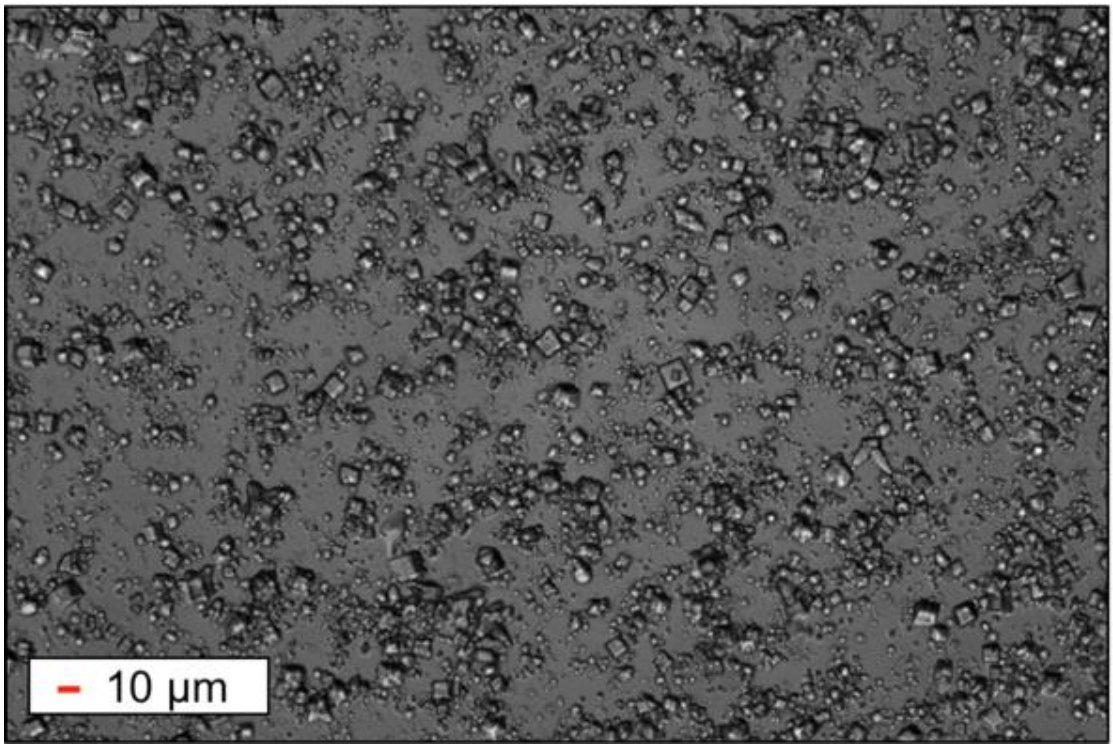

Figure 5.29 KDO8PS Microcrystals Grown with the FID Method

Darkfield micrograph of KDO8PS microcrystals grown according to the microcrystal FID protocol as described in Kupitz, Grotjohann et al. (2014) and adapted for crystallization of KDO8. While showing dominantly sharp cubic micromorphology, the size ranges between 1-10 µm, showing size inhomogeneity that is detrimental to diffusive mixing experiments. Image courtesy of Chelsie Conrad.

protein and precipitant concentrations as well as volumetric ratios between them. While improvements were made, it was noticed that a higher homogeneity was achieved with larger

volumes with all other variables being held constant It was hypothesized that the discrepancy between total batch size may be attributed to the volumetric ratio between the drop size and the total batch size, which would explain the difference in batch size as the drop size was held nearly invariant due to the similar drop size achieved when using 10 µL and 200 µL pipette tips. The path through phase space for batch methods are usually depicted as a straight line with a constant velocity but this is not pedantically correct in the case of discrete dropwise addition. This can be thought of as a series of steps, the size of which is directly related to the incremental increase of the precipitant concentration in each step vs the final precipitant concentration reached. Indeed, this was shown in the previous section when crystallization of PSI-Fd was largely improved by increasing the number of aliquoted additions during pipette mixing, e.g the use of smaller step sizes in the path through phase space. Using the best conditions established during the aforementioned rounds of fine screening, the batch methods were performed again using a thin inner diameter needled syringe to deliver minimal volume drops. In addition, the solution was stirred as rapidly as possible without creating turbulent flow so as to rapidly homogenize the solution after each precipitant addition. The small drops and rapid mixing decrease both the magnitude and lifetime of local pockets of inhomogeneous concentration that are suspected to be the primary cause of inhomogeneity. Indeed, this technique supported the initial hypothesis, providing both control of the mean size and decrease in the standard deviation from it as exemplified in figure 5.30. Interestingly, the protein concentration did not appear to have a strong effect on the morphological properties (though it of course has a strong effect on yield), which responded dominantly to the concentration of PEGME 5K to tenths of a w/v percentage. Typical concentrations for the final solutions ranged between 8.75-12 mg/mL KDO8PS and 6-8% w/v PEG-ME 5K.

Serial Millisecond Crystallography of KDO8PS

Since KDO8PS structures have been determined using classical cryo-X-ray crystallograohy for the PEP bound and KDO8P bound states as well as the apo form, a mixture of states is less prohibitive for structural determination as they can be deconvoluted during data processing using the known states. The lifetimes of the intermediates have been studied by time-resolved mass spectrometry and it has been determined that the time range for the individual steps

ranges from tens to hundreds of milliseconds (Li, Sau et al. 2005). This makes KDO8PS a good candidate for serial millisecond crystallography (SMX), developed as a synchrotron analogue of SFX. This makes use of high powered microfocus beamlines that allow for data collection with millisecond exposure times, where data can be collected in a serial fashion on sufficiently sized microcrystals (typically >10 µm) (Nogly, James et al. 2015, Martin-Garcia, Conrad et al. 2017, Weinert, Olieric et al. 2017). This benefits from the ability to use ambient temperatures and a solvated environment established for SFX combined with the generally more available experimental time at synchrotrons and has proven to be a successful technique (Stellato, Oberthur et al. 2014, Nogly, James et al. 2015, Nogly, Panneels et al. 2016, Martin-Garcia, Conrad et al. 2017, Weinert, Olieric et al. 2017). In addition, the beam of synchrotrons has a larger bandwidth,

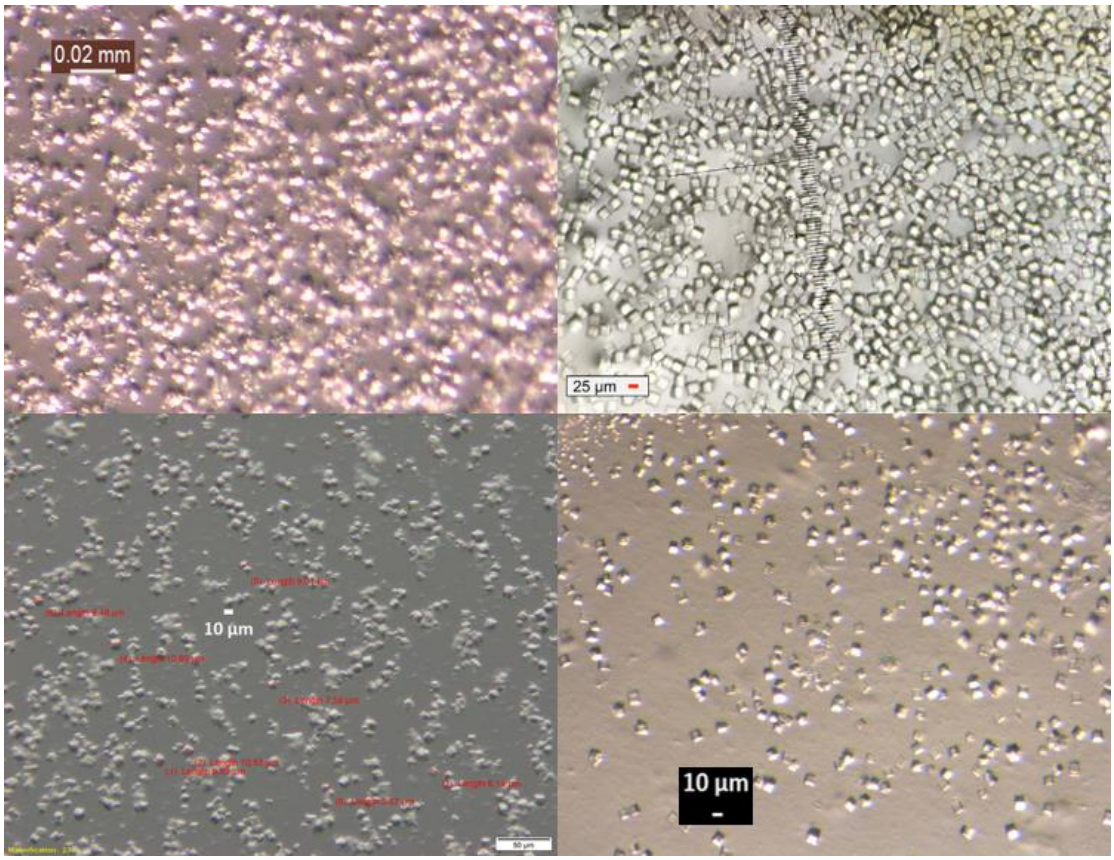

Figure 5.30 Improved Homogeneity of KDO8PS Microcrystals from Batch Methods

The decrease of droplet volume to total volume ratio had a significant effect on KDO8PS crystal growth using a stirred batch solution. Micrographs show various sizes of crystals achievable with this method, all possessing high size homogeneity.

decreasing the partiality of measured reflections and subsequently requiring a lower multiplicity for accurate structure factor determination.

To date, all published SMX work has been done by using a viscous jet using the lipidic cubic phase injector (Weierstall, James et al. 2014), including the first SMX experiments performed on KDO8PS crystals reported in Martin-Garcia, Conrad et al. (2017). In particular, a new method developed by Chelsie Conrad was promising, as it allows for embedding of crystals post-crystallization in an extremely viscous solution of poly(ethylene oxide), MW=1 million (PEO) similar to the use of agarose (Conrad, Basu et al. 2015) but more suited for ambient temperature injection (in contrast to the vacuum friendly agarose).

Viscous medium	PEO
Crystal size (µm)	10 - 15
Crystal-to-detector distance (mm)	550
Duration (h)	~3
Protein/carrier volume (µL)	10.1
Wavelength (Å)	1.03
Maximum Resolution observed (Å)	3.0
Resolution (Å)	60-3.8
Space group	I23
a b, c (Å)	118.6 ,118.6, 118.6
α,β, γ (°)	90, 90, 90
No. of collected images	100,282
No. of hits/indexed patterns	1698/382
I/δ(I)	
Multiplicity	25.1 (9.0)
Completeness (%)	100
CC* (%)	0.932 (0.397)
R_{split} (%)	37.3 (135.7)

Table 5.1 Data Statistics for KDO8PS in PEO at APS

MFX was performed on PEO embedded KDO8PS crystals at the ID23 beamline at the Advance Photon Source, Argonne National Laboratory at 10 Hz with 10 ms exposure time to a 12 keV, 10 µm beam. Crystals were made using FID and ranged from 5-15 µm and 11 µL of settled crystal pellet was embedded into PEO using the syringe mixing method described in Conrad, Basu et al. (2015). Data was collected for 3 hours, resulting in a 1.7% hit rate giving 1,698 hits. Unfortunately, only 382 of these could be indexed, possibly due to detrimental effects from the embedding of crystals in PEO in the form of mechanical damage or dehydration (PEO is highly hygroscopic). I is currently hypothesized that the indexable patterns may have arisen from larger crystals that may be more resistant to these effects due to the higher volume to surface ratio. The data collected matched the unit cell and space group parameters found in larger crystals.

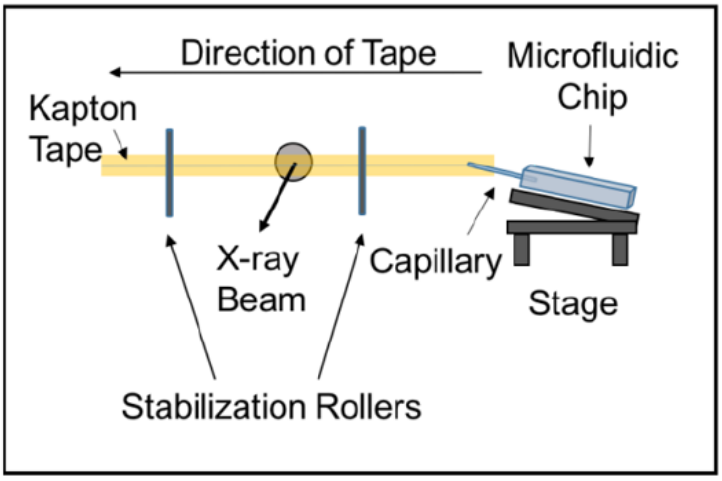

Figure 5.31 Illustration of Tape Drive Setup at P11 beamline, Petra III

Shows the tape drive setup for MFX at PETRA III for diffusive mixing TR-SFX of KDO8PS. Presoaked KDO8PS with PEP is mixed through a microfluidic mixing device prior to being 'painted' on a conveyor style belt of X-ray transparent Kapton tape. Surface tension then holds the mixed sample on the tape as it is translated across the 100 ms X-ray pulses, resulting in serial diffraction patterns. The time delay can be adjusted by geometry of the setup and the speed of the tape drive.

The next attempt at SMX with KDO8PS was by use of a tape drive whereby a capillary was used to deliver liquid sample to an X-ray transparent Kapton tape which was mechanically screened across the interaction region, as depicted in figure 5.31. This has the similar benefit that larger crystals can be utilized without the increased need for sample consumption a nozzle with a larger capillary would require. Time points are determined by the speed of the Kapton tape, the internal mixing capabilities of the mixer, the length of the capillary, flow rate, and geometry of the capillary from the interaction region.

Crystals were grown to an edge length of 25 µm and prepared for both the apo and PEP bound forms. The PEP bound crystals were prepared by first removing the supernatant from settled crystals. The volume removed was then replaced with a mother liquor containing 2.5 mM PEP and gently pipette mixed to allow the crystals to incubate with the PEP substrate. The plan was to collect data first from the apo form, followed by data collection on the PEP bound form and then by mixing with a mother liquor solution containing 10 mM PEP and 10 mM A5P to image crystals in a steady state form. Unfortunately, during this beamtime we were unable to measure even lysozyme due to what we later found out to be issues with the beam being inadvertently attenuated upstream but this type of experiment has potential going forward as well diffracting conditions have been identified for future experiments.

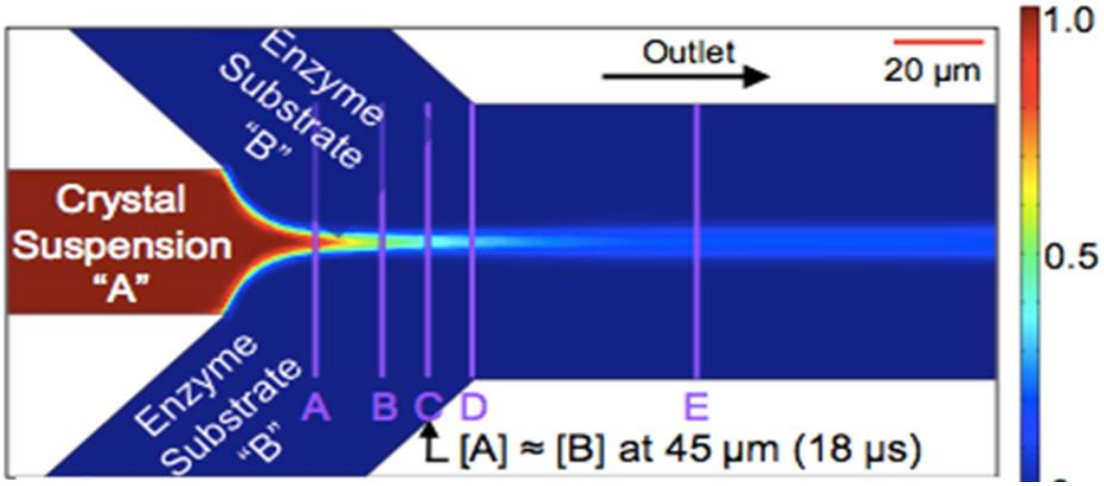

Figure 5.32 Microfluidic Substrate Mixing for TR-SFX

Shows a model for diffusive mixing of a KDO8PS crystal slurry hydrodynamically mixed with substrate in a microfluidic device. The model shows that complete solution mixing should occur within 18 µs which, coupled with the diffusion times into the crystal, determines the reaction homogeneity.

SFX of KDO8PS: Towards Mix and Inject TR-SFX

In the pursuit of capturing the unknown intermediate in the aldose condensation of PEP and A5P by KDO8PS, small crystals with rapid (sub 10 ms) time points are essential. Current efforts are aimed at using microfluidic mixing within the nozzle to allow for the delay times to approach single and sub ms time delays, like the approach described in Calvey, Katz et al. (2016). For the proof of principle and validation, however, longer time points offer the opportunity to compare to the known structures. For this purpose, an inline mixing device prior to the nozzle is sufficient as the steady state product formation has been measured to be 3.5 s-1 (Li, Sau et al. 2005). This mixing device was developed by the group of Dr. Alexandra Ros and has been successfully tested to achieve a stable jet using KDO8PS crystals through a GDVN coupled microfluidic device with flow rates as low as 3 µL/min. The devices built are improved versions based off those described in Abdallah, Chao et al. (2013), Abdallah, Roy-Chowdhury et al. (2015), and Abdallah, Zatsepin et al. (2015) and a model of mixing times achievable, calculated by COMSOL (Multiphysics) is depicted in figure 5.32.

In the fall of 2017, two beamtimes were awarded to investigate KDO8PS with TR-SFX. The first beamtime was performed at the MFX beamline at LCLS using 3.3 mJ, 45 fs pulses of 9.5

keV X-rays at 10 Hz. 2-5 µm crystals were made using the stirred-batch method with a final concentration of 10.5 mg/mL KDO8PS and 7.2% PEGME 5K. Diffraction of the apo KDO8PS form was observed with visible resolution out to the water ring, as highlighted in figure 5.33. Unfortunately, only 43 minutes of data collection were performed and this, combined with a decreased hit rate inherent in dilution from mixing, led to only tens of hits before the focus of the beamtime was shifted towards other goals.

The following experiment again focused on work towards TR-SFX of KDO8PS and was performed at the European XFEL. For this beamtime the mixing device was coupled with a droplet generator to mitigate the large amount of sample wasted in between pulses. This is particularly an issue at the newly commissioned EU-XFEL. With only 900 ns spacing between pulses within a pulse train (described previously), jet speeds must travel upwards of 44 m/s to replenish the sample between pulses due to jet disruption and upstream damage of the crystals due to energy released

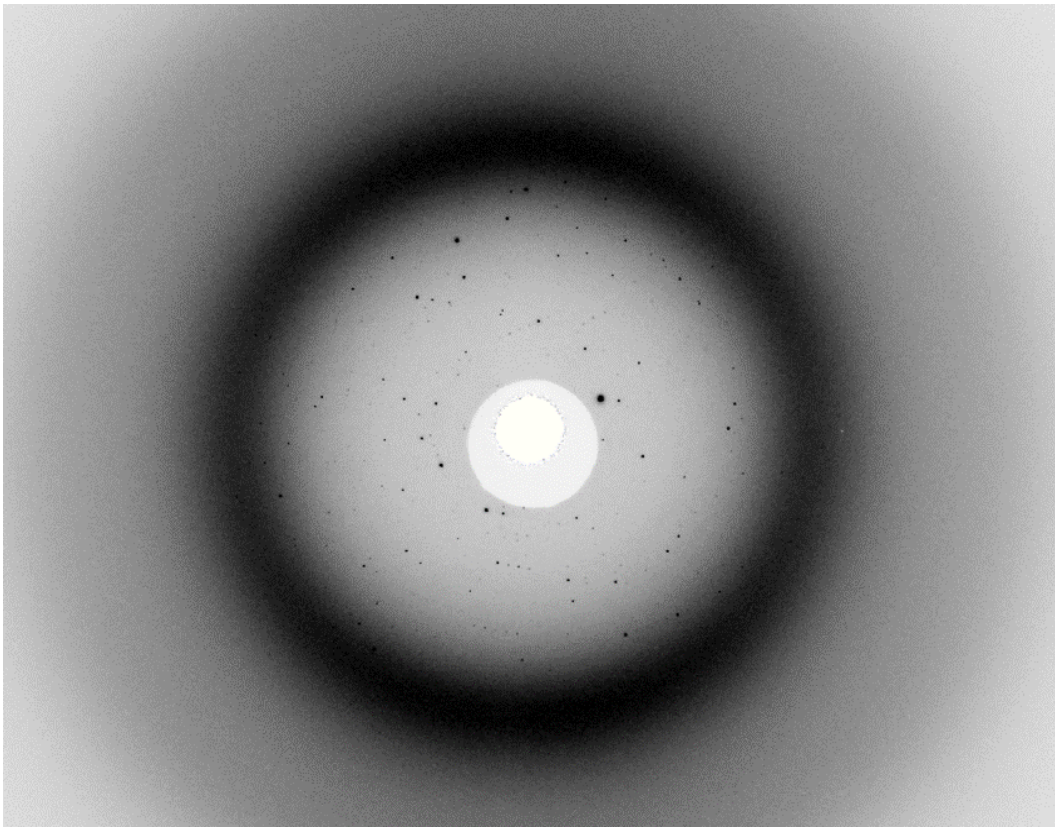

Figure 5.33 Diffraction from KDO8PS at MFX

Shows measured diffraction at the MFX beamline from KDO8PS crystals to the solvent ring.

during the jet explosion. In order to avoid the loss of sample between these pulses, in this case especially during the 99.7 ms separating pulse trains, oil was co-flowed with the sample. The final goal of these experiments was aimed at synchronizing droplets to the pulses spaced by oil sections to maintain a stable jet.

The experiment was performed at the SPB/SFX beamline at EU-XFEL with photon energies of 9.15-9.3 keV and 32 pulses/pulse train with pulse trains at 10 Hz (total 320 Hz) for five

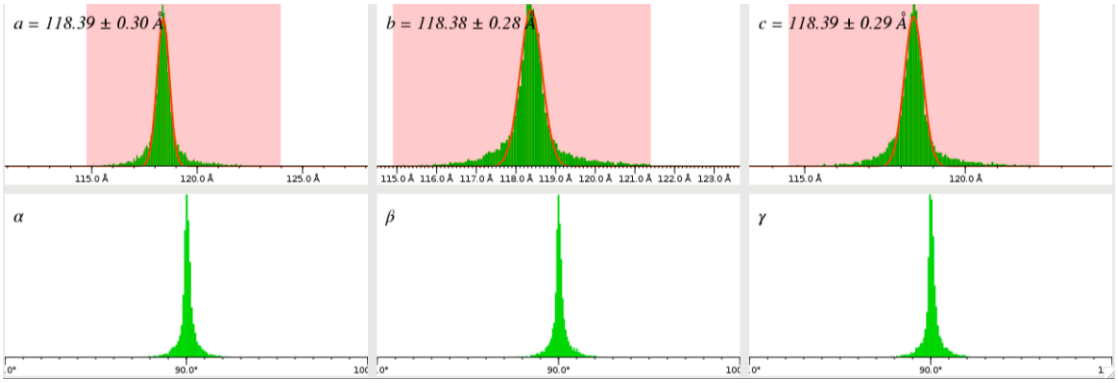

Figure 5.34 Unit Cell Parameters of KDO8PS EU-XFEL Data

KDO8PS data from 10,000 indexed patterns collected at the SPB/SFX beamline at EU-XFEL show an I32 with a=b=c=118.39, α=β=γ=90.0 °. Note the tight distributions. This is in agreement with data collected at APS and from macrocrystallographic structures previously published (Vainer, Belakhov et al. 2005).

12-hour shifts. This marked the second user beamtime to ever be conducted at this beamline (even earlier than the PSI beamtime described earlier in this chapter). Over the course of this beamtime, we obtained 4.1 million images including 37,000 crystal hits. Due to time constraints and both hardware and software issues, only data on the apo state in stochastically mixed oil droplets was collected.

Currently, 10,000 of the hits have been indexed leading to an indexing rate of 27% with well restrained unit cell parameters in the I32 space group, in agreement with previously measured data and literature values. The unit cell distribution is illustrated in figure 5.34. The resolution for the data set is currently estimated to be ~2.2 Å, as is indicated by the typical diffraction pattern shown in figure 5.35. This is even higher than the highest resolution reported for data collection at synchrotrons in the PDB (2.4 A). The data processing is still ongoing. It is very complex as the new AGIPD detector with three gain settings has not been fully commissioned yet and data formats as

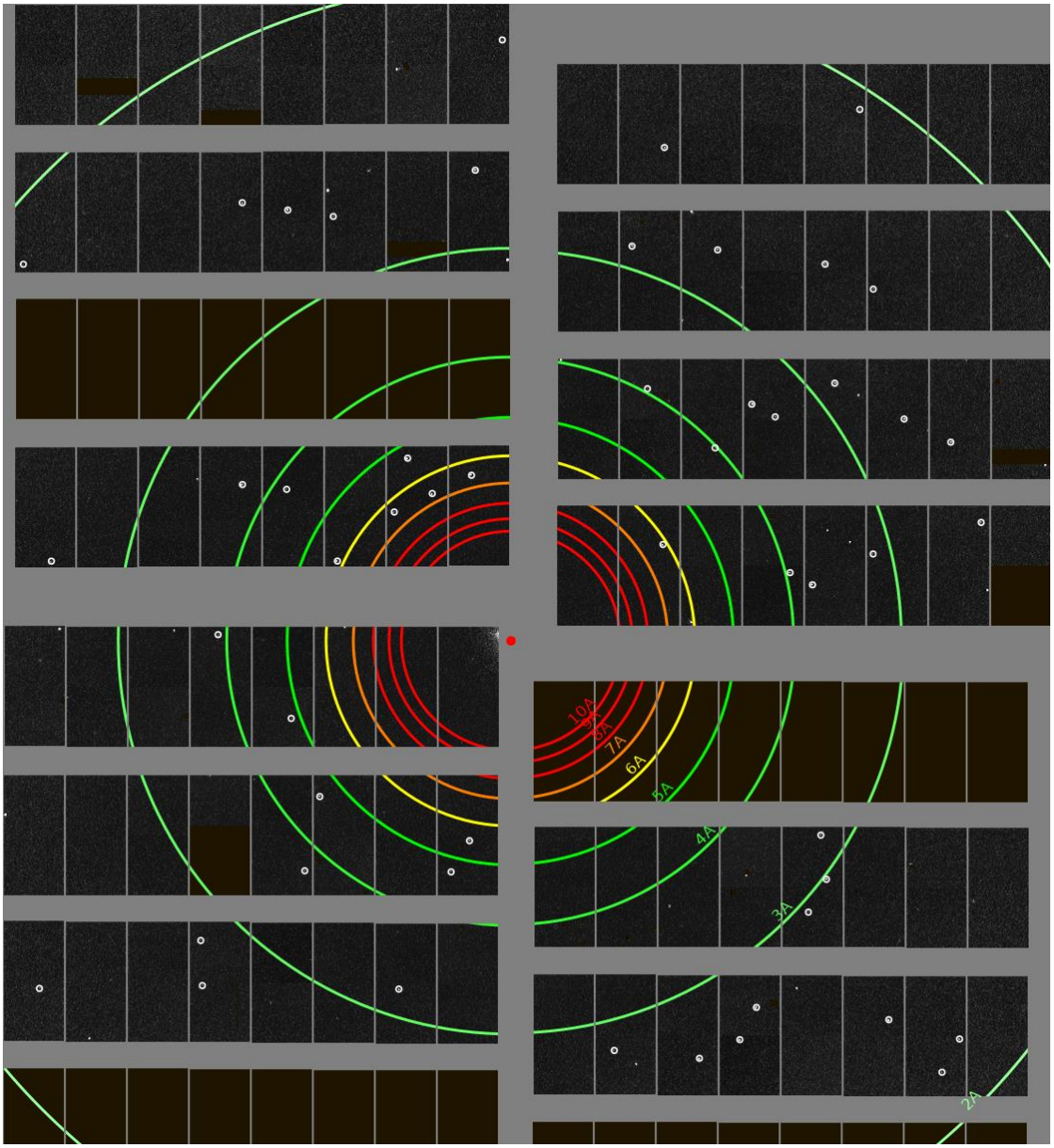

Figure 5.35 High Resolution Diffraction of KDO8PS at EU-XFEL

Typical diffraction pattern of KDO8PS from the SPB/SFX beamline at EU-XFEL. Outermost resolution ring indicates 2 Å with diffraction seen just short of it. Identified peaks are circled by version of CHEETAH software recently modified for EU-XFEL data (Barty, Kirian et al. 2014).

well as detector calibration parameters are constantly being upgraded. With the ongoing resolution of file compatibility and data processing issues, the hit rate, indexing rate and resolution are all expected to improve. In addition, recent progress has been made towards integrating masks and dark calibrations that will allow for accurate structure factor measurement from the intensities, one of the primary issues currently hindering a structural model from being constructed.

References

Abdallah, B. G., T.-C. Chao, C. Kupitz, P. Fromme and A. Ros (2013). "Dielectrophoretic sorting of membrane protein nanocrystals." ACS nano **7**(10): 9129-9137.

Abdallah, B. G., S. Roy-Chowdhury, J. Coe, P. Fromme and A. Ros (2015). "High throughput protein nanocrystal fractionation in a microfluidic sorter." Anal Chem **87**(8): 4159-4167.

Abdallah, B. G., N. A. Zatsepin, S. Roy-Chowdhury, J. Coe, C. E. Conrad, K. Dörner, R. G. Sierra, H. P. Stevenson, F. Camacho-Alanis and T. D. Grant (2015). "Microfluidic sorting of protein nanocrystals by size for X-ray free-electron laser diffraction." Structural Dynamics **2**(4): 041719.

Allahgholi, A., J. Becker, L. Bianco, A. Delfs, R. Dinapoli, P. Goettlicher, H. Graafsma, D. Greiffenberg, H. Hirsemann and S. Jack (2015). "AGIPD, a high dynamic range fast detector for the European XFEL." Journal of Instrumentation **10**(01): C01023.

Altarelli, M., R. Brinkmann, M. Chergui, W. Decking, B. Dobson, S. Düsterer, G. Grübel, W. Graeff, H. Graafsma and J. Hajdu (2006). "The European x-ray free-electron laser." Technical design report, DESY **97**: 1-26.

Aquila, A., M. S. Hunter, R. B. Doak, R. A. Kirian, P. Fromme, T. A. White, J. Andreasson, D. Arnlund, S. Bajt and T. R. Barends (2012). "Time-resolved protein nanocrystallography using an X-ray free-electron laser." Optics express **20**(3): 2706-2716.

Aquila, A., A. Barty, C. Bostedt, S. Boutet, G. Carini, D. DePonte, P. Drell, S. Doniach, K. Downing and T. Earnest (2015). "The linac coherent light source single particle imaging road map." Structural Dynamics **2**(4): 041701.

Aro, E.-M., I. Virgin and B. Andersson (1993). "Photoinhibition of photosystem II. Inactivation, protein damage and turnover." Biochimica et Biophysica Acta (BBA)-Bioenergetics **1143**(2): 113-134.

Ayyer, K., O. Yefanov, D. Oberthuer, S. Roy-Chowdhury, L. Galli, V. Mariani, S. Basu, J. Coe, C. Conrad, R. Fromme, A. Schaffer, K. Doerner, D. James, C. Kupitz, M. Metz, G. Nelson, P. L. Xavier, K. R. Beyerlein, M. Schmidt, I. Sarrou, J. Spence, U. Weierstall, T. White, J. H. Yang, Y. Zhao, M. Liang, A. Aquila, M. Hunter, J. S. Robinson, J. Koglin, S. Boutet, P. Fromme, A. Barty and H. Chapman (2016). "Macromolecular diffractive imaging using imperfect crystals." Nature **Accepted**.

Barty, A., R. A. Kirian, F. R. Maia, M. Hantke, C. H. Yoon, T. A. White and H. Chapman (2014). "Cheetah: software for high-throughput reduction and analysis of serial femtosecond X-ray diffraction data." Journal of Applied Crystallography **47**(3): 1118-1131.

Blow, D. and F. Crick (1959). "The treatment of errors in the isomorphous replacement method." Acta Crystallographica **12**(10): 794-802.

Borie, B. (1965). "X-Ray Diffraction in Crystals, Imperfect Crystals, and Amorphous Bodies." Journal of the American Chemical Society **87**(1): 140-141.

Calvey, G. D., A. M. Katz, C. B. Schaffer and L. Pollack (2016). "Mixing injector enables time-resolved crystallography with high hit rate at X-ray free electron lasers." Structural Dynamics **3**(5): 054301.

Chapman, H. N., A. Barty, S. Marchesini, A. Noy, S. P. Hau-Riege, C. Cui, M. R. Howells, R. Rosen, H. He, J. C. Spence, U. Weierstall, T. Beetz, C. Jacobsen and D. Shapiro (2006). "High-resolution ab initio three-dimensional x-ray diffraction microscopy." J Opt Soc Am A Opt Image Sci Vis **23**(5): 1179-1200.

Chapman, H. N., P. Fromme, A. Barty, T. A. White, R. A. Kirian, A. Aquila, M. S. Hunter, J. Schulz, D. P. DePonte, U. Weierstall, R. B. Doak, F. R. Maia, A. V. Martin, I. Schlichting, L. Lomb, N. Coppola, R. L. Shoeman, S. W. Epp, R. Hartmann, D. Rolles, A. Rudenko, L. Foucar, N. Kimmel, G. Weidenspointner, P. Holl, M. Liang, M. Barthelmess, C. Caleman, S. Boutet, M. J. Bogan, J. Krzywinski, C. Bostedt, S. Bajt, L. Gumprecht, B. Rudek, B. Erk, C. Schmidt, A. Homke, C. Reich, D. Pietschner, L. Struder, G. Hauser, H. Gorke, J. Ullrich, S. Herrmann, G. Schaller, F. Schopper, H. Soltau, K. U. Kuhnel, M. Messerschmidt, J. D. Bozek, S. P. Hau-Riege, M. Frank, C. Y. Hampton, R. G. Sierra, D. Starodub, G. J. Williams, J. Hajdu, N. Timneanu, M. M. Seibert, J. Andreasson, A. Rocker, O. Jonsson, M. Svenda, S. Stern, K. Nass, R. Andritschke, C. D. Schroter, F. Krasniqi, M. Bott, K. E. Schmidt, X. Wang, I. Grotjohann, J. M. Holton, T. R. Barends, R. Neutze, S. Marchesini, R. Fromme, S. Schorb, D. Rupp, M. Adolph, T. Gorkhover, I. Andersson, H. Hirsemann, G. Potdevin, H. Graafsma, B. Nilsson and J. C. Spence (2011). "Femtosecond X-ray protein nanocrystallography." Nature **470**(7332): 73-77.

Conrad, C. E., S. Basu, D. James, D. Wang, A. Schaffer, S. Roy-Chowdhury, N. A. Zatsepin, A. Aquila, J. Coe, C. Gati, M. S. Hunter, J. E. Koglin, C. Kupitz, G. Nelson, G. Subramanian, T. A. White, Y. Zhao, J. Zook, S. Boutet, V. Cherezov, J. C. Spence, R. Fromme, U. Weierstall and P. Fromme (2015). "A novel inert crystal delivery medium for serial femtosecond crystallography." IUCrJ **2**(Pt 4): 421-430.

DePonte, D. P., U. Weierstall, K. Schmidt, J. Warner, D. Starodub, J. C. H. Spence and R. B. Doak (2008). "Gas dynamic virtual nozzle for generation of microscopic droplet streams." Journal of Physics D-Applied Physics **41**(19).

Elser, V. (2003). "Phase retrieval by iterated projections." JOSA A **20**(1): 40-55.

Elser, V. and R. Millane (2008). "Reconstruction of an object from its symmetry-averaged diffraction pattern." Acta Crystallographica Section A: Foundations of Crystallography **64**(2): 273-279.

Fienup, J. R. (1987). "Reconstruction of a complex-valued object from the modulus of its Fourier transform using a support constraint." JOSA A **4**(1): 118-123.

Fischer, N., P. Neumann, A. L. Konevega, L. V. Bock, R. Ficner, M. V. Rodnina and H. Stark (2015). "Structure of the E. coli ribosome–EF-Tu complex at< 3 Å resolution by C s-corrected cryo-EM." Nature **520**(7548): 567.

Fromme, P., H. Bottin, N. Krauss and P. Sétif (2002). "Crystallization and electron paramagnetic resonance characterization of the complex of photosystem I with its natural electron acceptor ferredoxin." Biophysical journal **83**(4): 1760-1773.

Geloni, G., E. Saldin, L. Samoylova, E. Schneidmiller, H. Sinn, T. Tschentscher and M. Yurkov (2010). "Coherence properties of the European XFEL." New Journal of Physics **12**(3): 035021.

Green, D., V. Ingram and M. Perutz (1954). The structure of haemoglobin-IV. Sign determination by the isomorphous replacement method. Proc. R. Soc. Lond. A, The Royal Society.

Guss, J. M., E. A. Merritt, R. P. Phizackerley, B. Hedman, M. Murata, K. O. Hodgson and H. C. Freeman (1988). "Phase determination by multiple-wavelength x-ray diffraction: crystal structure of a basic" blue" copper protein from cucumbers." Science **241**(4867): 806-811.

Hendrickson, W. A. and M. M. Teeter (1981). "Structure of the hydrophobic protein crambin determined directly from the anomalous scattering of sulphur." Nature **290**(5802): 107.

Huldt, G., A. Szőke and J. Hajdu (2003). "Diffraction imaging of single particles and biomolecules." Journal of structural biology **144**(1-2): 219-227.

Jordan, P., P. Fromme, H. T. Witt, O. Klukas, W. Saenger and N. Krauß (2001). "Three-dimensional structure of cyanobacterial photosystem I at 2.5 Å resolution." Nature **411**(6840): 909-917.

Kahn, R., R. Fourme, R. Bosshard, M. Chiadmi, J. Risler, O. Dideberg and J. Wery (1985). "Crystal structure study of Opsanus tau parvalbumin by multiwavelength anomalous diffraction." FEBS letters **179**(1): 133-137.

Kirian, R. A., R. J. Bean, K. R. Beyerlein, M. Barthelmess, C. H. Yoon, F. Wang, F. Capotondi, E. Pedersoli, A. Barty and H. N. Chapman (2015). "Direct phasing of finite crystals illuminated with a free-electron laser." Physical Review X **5**(1): 011015.

Kupitz, C., S. Basu, I. Grotjohann, R. Fromme, N. A. Zatsepin, K. N. Rendek, M. S. Hunter, R. L. Shoeman, T. A. White and D. Wang (2014). "Serial time-resolved crystallography of photosystem II using a femtosecond X-ray laser." Nature **513**(7517): 261-265.

Kupitz, C., I. Grotjohann, C. E. Conrad, S. Roy-Chowdhury, R. Fromme and P. Fromme (2014). "Microcrystallization techniques for serial femtosecond crystallography using photosystem II from Thermosynechococcus elongatus as a model system." Philosophical Transactions of the Royal Society B: Biological Sciences **369**(1647): 20130316.

Laue, M. (1936). "The external shape of crystals and its influence on interference phenomena in crystalline lattices." Ann. Phys **26**: 55.

Li, Z., A. K. Sau, C. M. Furdui and K. S. Anderson (2005). "Probing the role of tightly bound phosphoenolpyruvate in Escherichia coli 3-deoxy-D-manno-octulosonate 8-phosphate synthase catalysis using quantitative time-resolved electrospray ionization mass spectrometry in the millisecond time range." Analytical biochemistry **343**(1): 35-47.

Loh, N.-T. D. and V. Elser (2009). "Reconstruction algorithm for single-particle diffraction imaging experiments." Physical Review E **80**(2): 026705.

Marchesini, S., H. He, H. N. Chapman, S. P. Hau-Riege, A. Noy, M. R. Howells, U. Weierstall and J. C. Spence (2003). "X-ray image reconstruction from a diffraction pattern alone." Physical Review B **68**(14): 140101.

Mariani, V., A. Morgan, C. H. Yoon, T. J. Lane, T. A. White, C. O'Grady, M. Kuhn, S. Aplin, J. Koglin and A. Barty (2016). "OnDA: online data analysis and feedback for serial X-ray imaging." Journal of applied crystallography **49**(3): 1073-1080.

Martin-Garcia, J. M., C. E. Conrad, G. Nelson, N. Stander, N. A. Zatsepin, J. Zook, L. Zhu, J. Geiger, E. Chun and D. Kissick (2017). "Serial millisecond crystallography of membrane and soluble protein microcrystals using synchrotron radiation." IUCrJ **4**(4).

Miao, J., P. Charalambous, J. Kirz and D. Sayre (1999). "Extending the methodology of X-ray crystallography to allow imaging of micrometre-sized non-crystalline specimens." Nature **400**(6742): 342.

Multiphysics, C. "2013, Version 4.4, COMSOL." Inc., Burlington, MA, USA.

Murata, N., S. Takahashi, Y. Nishiyama and S. I. Allakhverdiev (2007). "Photoinhibition of photosystem II under environmental stress." Biochimica et Biophysica Acta (BBA)-Bioenergetics **1767**(6): 414-421.

Nogly, P., D. James, D. Wang, T. A. White, N. Zatsepin, A. Shilova, G. Nelson, H. Liu, L. Johansson and M. Heymann (2015). "Lipidic cubic phase serial millisecond crystallography using synchrotron radiation." IUCrJ **2**(2): 0-0.

Nogly, P., V. Panneels, G. Nelson, C. Gati, T. Kimura, C. Milne, D. Milathianaki, M. Kubo, W. Wu and C. Conrad (2016). "Lipidic cubic phase injector is a viable crystal delivery system for time-resolved serial crystallography." Nature communications **7**: 12314.

Oberthuer, D., J. Knoška, M. O. Wiedorn, K. R. Beyerlein, D. A. Bushnell, E. G. Kovaleva, M. Heymann, L. Gumprecht, R. A. Kirian and A. Barty (2017). "Double-flow focused liquid injector for efficient serial femtosecond crystallography." Scientific reports **7**: 44628.

Pande, K., C. D. M. Hutchinson, G. Groenhof, A. Aquila, J. S. Robinson, J. Tenboer, S. Basu, S. Boutet, D. Deponte, M. Liang, T. White, N. Zatsepin, O. Yefanov, D. Morozov, D. Oberthuer, C. Gati, G. Subramanian, D. James, Y. Zhao, J. Koralek, J. Brayshaw, C. Kupitz, C. Conrad, S. Roy-Chowdhury, J. Coe, M. Metz, X. Paulraj Lourdu, T. Grant, J. Koglin, G. Ketawala, R. Fromme, V. Srajer, R. Henning, J. Spence, A. Ourmazd, P. Schwander, U. Weierstall, M. Frank, P. Fromme, A. Barty, H. Chapman, K. Moffat, J. J. Van Thor and M. Schmidt (2015). "Femtosecond Structural Dynamics Drives the Trans/Cis Isomerization in Photoactive Yellow Protein." in submission.

Prasil, O. (1992). "Dynamics of photosystem II: mechanism of photoinhibition and recovery process." Topics in Photosynthesis: The Photosystem Structure, Function and Molecular Biology.

Robinson, I. K., I. A. Vartanyants, G. Williams, M. Pfeifer and J. Pitney (2001). "Reconstruction of the shapes of gold nanocrystals using coherent x-ray diffraction." Physical review letters **87**(19): 195505.

Roedig, P., H. M. Ginn, T. Pakendorf, G. Sutton, K. Harlos, T. S. Walter, J. Meyer, P. Fischer, R. Duman and I. Vartiainen (2017). "High-speed fixed-target serial virus crystallography." nAture methods **14**(8): 805.

Rossmann, M. and D. Blow (1963). "Determination of phases by the conditions of non-crystallographic symmetry." Acta Crystallographica **16**(1): 39-45.

Rossmann, M. G. and D. M. Blow (1962). "The detection of sub-units within the crystallographic asymmetric unit." Acta Crystallographica **15**(1): 24-31.

Rossmann, M. G. (1972). The molecular replacement method: a collection of papers on the use of non-crystallographic symmetry, Routledge.

Sayre, D. (1952). "SOME IMPLICATIONS OF A THEOREM DUE TO SHANNON." Acta Crystallographica **5**(6): 843-843.

Setif, P. Q. and H. Bottin (1994). "Laser flash absorption spectroscopy study of ferredoxin reduction by photosystem I in Synechocystis sp. PCC 6803: evidence for submicrosecond and microsecond kinetics." Biochemistry **33**(28): 8495-8504.

Setif, P. Q. and H. Bottin (1995). "Laser flash absorption spectroscopy study of ferredoxin reduction by photosystem I: spectral and kinetic evidence for the existence of several photosystem I-ferredoxin complexes." Biochemistry **34**(28): 9059-9070.

Shapiro, D., P. Thibault, T. Beetz, V. Elser, M. Howells, C. Jacobsen, J. Kirz, E. Lima, H. Miao and A. M. Neiman (2005). "Biological imaging by soft x-ray diffraction microscopy." Proceedings of the National Academy of Sciences **102**(43): 15343-15346.

Stellato, F., D. Oberthur, M. Liang, R. Bean, C. Gati, O. Yefanov, A. Barty, A. Burkhardt, P. Fischer and L. Galli (2014). "Room-temperature macromolecular serial crystallography using synchrotron radiation." IUCrJ **1**(4): 0-0.

Tenboer, J., S. Basu, N. Zatsepin, K. Pande, D. Milathianaki, M. Frank, M. Hunter, S. Boutet, G. J. Williams and J. E. Koglin (2014). "Time-resolved serial crystallography captures high-resolution intermediates of photoactive yellow protein." Science **346**(6214): 1242-1246.

Umena, Y., K. Kawakami, J.-R. Shen and N. Kamiya (2011). "Crystal structure of oxygen-evolving photosystem II at a resolution of 1.9 Å." Nature **473**(7345): 55-60.

Vainer, R., V. Belakhov, E. Rabkin, T. Baasov and N. Adir (2005). "Crystal structures of Escherichia coli KDO8P synthase complexes reveal the source of catalytic irreversibility." Journal of molecular biology **351**(3): 641-652.

Weierstall, U., D. James, C. Wang, T. A. White, D. Wang, W. Liu, J. C. Spence, R. B. Doak, G. Nelson and P. Fromme (2014). "Lipidic cubic phase injector facilitates membrane protein serial femtosecond crystallography." Nature communications **5**.

Weinert, T., N. Olieric, R. Cheng, S. Brünle, D. James, D. Ozerov, D. Gashi, L. Vera, M. Marsh and K. Jaeger (2017). "Serial millisecond crystallography for routine room-temperature structure determination at synchrotrons." Nature communications **8**(1): 542.

6 OTHER PUBLICATIONS AND CONTRIBUTIONS

Introduction

This chapter will address the various projects I was involved in that resulted in publication or are at least in submission at the time of this writing that are not addressed elsewhere in this dissertation. For each publication the abstract is provided followed by a brief description of the work and my contribution to it. They are roughly ordered by date of publication from earliest to most recent.

Time-Resolved Serial Crystallography Captures High-Resolution Intermediates of Photoactive Yellow Protein

Science 346.6214 (2014): 1242-1246. (Tenboer, Basu et al. 2014)

Jason Tenboer[1], Shibom Basu[2], Nadia Zatsepin[3], Kanupriya Pande[1], Despina Milathianaki[4], Matthias Frank[5], Mark Hunter[5] , Sébastien Boutet[4], Garth J. Williams[4], Jason E. Koglin[4], Dominik Oberthuer[6], Michael Heymann[7], Christopher Kupitz[2],Chelsie Conrad[2], Jesse Coe[2], Shatabdi Roy-Chowdhury[2], Uwe Weierstall[3], Daniel James[3], Dingjie Wang[3], Thomas Grant[8], Anton Barty[7], Oleksandr Yefanov[7], Jennifer Scales[1], Cornelius Gati[6,7], Carolin Seuring[6], Vukica Srajer[9], Robert Henning[9], Peter Schwander[1], Raimund Fromme[2], Abbas Ourmazd[1], Keith Moffat[9,10], Jasper J. Van Thor[11], John C. H. Spence[3], Petra Fromme[2], Henry N. Chapman[6,7], Marius Schmidt[1]

[1]*Physics Department, University of Wisconsin, Milwaukee, WI 53211, USA.*
[2]*Department of Chemistry and Biochemistry, Arizona State University, Tempe, AZ 85287, USA.*
[3]*Department of Physics, Arizona State University, Tempe, AZ 85287, USA.*
[4]*Linac Coherent Light Source, SLAC National Accelerator Laboratory, Sand Hill Road, Menlo Park, CA 94025, USA.*
[5]*Lawrence Livermore National Laboratory, Livermore, CA 94550, USA.*
[6]*Centre for Ultrafast Imaging, University of Hamburg, 22761 Hamburg, Germany.*
[7]*Center for Free Electron Laser Science, Deutsches Elektronen Synchrotron DESY, Notkestrasse 85, 22607 Hamburg, Germany.*
[8]*Hauptman-Woodward Institute, State University of New York at Buffalo, 700 Ellicott Street, Buffalo, NY 14203, USA.*
[9]*Center for Advanced Radiation Sources, University of Chicago, Chicago, IL 60637, USA.*
[10]*Department of Biochemistry and Molecular Biology and Institute for Biophysical Dynamics, University of Chicago, Chicago, IL 60637, USA.*
[11]*Faculty of Natural Sciences, Life Sciences, Imperial College, London SW7 2AZ, UK.*

Abstract

Serial femtosecond crystallography using ultrashort pulses from x-ray free electron lasers (XFELs) enables studies of the light-triggered dynamics of biomolecules. We used microcrystals of photoactive yellow protein (a bacterial blue light photoreceptor) as a model system and obtained high-resolution, time-

resolved difference electron density maps of excellent quality with strong features; these allowed the determination of structures of reaction intermediates to a resolution of 1.6 angstroms. Our results open the way to the study of reversible and nonreversible biological reactions on time scales as short as femtoseconds under conditions that maximize the extent of reaction initiation throughout the crystal.

In these experiments, pump-probe TR-SFX was performed on the photoactive yellow protein (PYP), marking the first high resolution TR-SFX structures reported with 1.6 Å resolution at time points of 10 ns and 1 µs in addition to the dark state. This allowed for a proof of principle to be made for pump-probe TR-SFX as the I_T, I_{CT}, pR_1 and pR_2 states of the PYP photocycle represented within these time points have been previously elucidated using the Laue method at 32 ns and 1 µs photoactivation time delays respectively (Ihee, Rajagopal et al. 2005, Jung, Lee et al. 2013, Schmidt, Srajer et al. 2013). Figure 6.1 shows a comparison of the structures obtained from

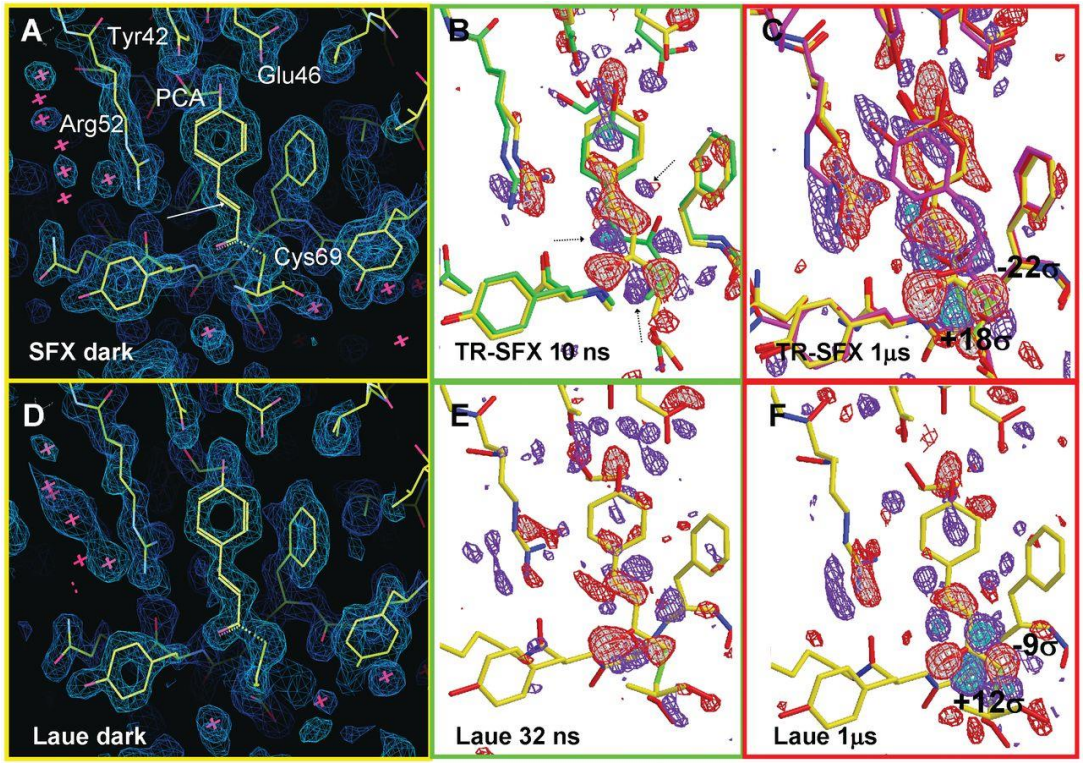

Figure 6.1 Comparison of PYP Chromophore Electron Density from TR-SFX and Laue Data

Comparison of electron densities obtained for dark state, ns, and µs delay times between TR-SFX and Laue data sets. (A-C) are modeled from SFX data sets while (D-F) are from Laue. (A) and (D) show dark state structures with the p-coumaric acid (PCA) chromophore and coordinating side chains labeled in (A). Difference electron density maps are show for ns time points (B,E) and 1 µs time points (C,F) with contour levels of -3σ/-4σ/+3σ/+5σ indicated with red/white/blue/cyan respectively. (B) shows arrows indicating the double bond about which isomerization occurs. Figure originally published in Tenboer, Basu et al. (2014).

the dark, ns and µs time points from both XFEL and Laue data. Not only did this successfully show comparable structures but confirmed the increase in reaction initiation yield percent expected from the smaller microcrystals suitable for TR-SFX with a calculated 40% reaction initiation in the TR-SFX data sets vs the 10-15% typical in synchrotron studies (Schmidt, Srajer et al. 2013). This is in part due to the relatively lower laser power needed for a high multiplicity of photons per reaction center, allowing for multiple excitations for a given reaction center to partially mitigate stochastic backreaction to the ground state. In addition to method validation, new structural changes were found after refinement of the 1 µs TR-SFX time point as the higher populations allowed much stronger features in the difference electron density maps, lending to more readily interpretable data. My contributions toward this project were development of initial crystallization conditions, sample characterization and handling and logging during the experiments.

Crystallization of Photosystem II for Time-Resolved Structural Studies Using an X-ray Free Electron Laser

Methods in enzymology. Vol. 557. Academic Press, 2015. 459-482.(Coe, Kupitz et al. 2015)

Jesse Coe, Christopher Kupitz, Shibom Basu, Chelsie E. Conrad, Shatabdi Roy-Chowdhury, Raimund Fromme, and Petra Fromme

Department of Chemistry and Biochemistry, Arizona State University, Tempe, Arizona, USA

Abstract

Photosystem II (PSII) is a membrane protein supercomplex that executes the initial reaction of photosynthesis in higher plants, algae, and cyanobacteria. It captures the light from the sun to catalyze a transmembrane charge separation. In a series of four charge separation events, utilizing the energy from four photons, PSII oxidizes two water molecules to obtain dioxygen, four protons, and four electrons. The light reactions of photosystems I and II (PSI and PSII) result in the formation of an electrochemical transmembrane proton gradient that is used for the production of ATP. Electrons that are subsequently transferred from PSI via the soluble protein ferredoxin to ferredoxin-$NADP^+$ reductase that reduces $NADP^+$ to NADPH. The products of photosynthesis and the elemental oxygen evolved sustain all higher life on Earth. All oxygen in the atmosphere is produced by the oxygen-evolving complex in PSII, a process that changed our planet from an anoxygenic to an oxygenic atmosphere 2.5 billion years ago. In this chapter, we provide recent insight into the mechanisms of this process and methods used in probing this question.

In this book chapter, an in-depth review, progress was summarized towards the progress to date in understanding the mechanism behind water splitting in PSII based on time-resolved X-ray diffraction studies using XFELS. The primary focus was based off of recent work exploring the S_3 state through TR-SFX performed in Kupitz, Basu et al. (2014). This article reviewed and discussed every step from purification and crystallization to experimental design and interpretation of TR-SFX data collected on PSII crystals. Highlights of this article were focused on the preparation of nanocrystals through new techniques and the use of a synthetic plastoquinone to validate quinone exchange and progression through the Kok cycle. The articles also summarizes the results with observed changes in the OEC coordination sphere electron density and conclusions drawn from it for the mechanism of water splitting in PSII. My contributions included writing the manuscript of this review book chapter, much of the literature research and leading multiple rounds of editing and submission tasks.

Structural basis for bifunctional peptide recognition at human δ-opioid receptor

Nature Structural and Molecular Biology 22.3 (2015): 265.(Fenalti, Zatsepin et al. 2015)

Gustavo Fenalti[1], Nadia A. Zatsepin[2], Cecilia Betti[3,4], Patrick Giguere[5,6,7], Gye Won Han[1], Andrii Ishchenko[1], Wei Liu[1], Karel Guillemyn[3,4], Haitao Zhang[1], Daniel James[2], Dingjie Wang[2], Uwe Weierstall[2], John C.H. Spence[2], Sébastien Boutet[8], Marc Messerschmidt[8], Garth J. Williams[8], Cornelius Gati[9], Oleksandr M. Yefanov[9], Thomas A. White[9], Dominik Oberthuer[9,10], Markus Metz[9,11], Chun Hong Yoon[9,12], Anton Barty[9], Henry N. Chapman[9,11], Shibom Basu[13,14], **Jesse Coe**[13,14], Chelsie E. Conrad[13,14], Raimund Fromme[13,14], Petra Fromme[13,14], Dirk Tourwé[3,4], Peter W. Schiller[15], Bryan L. Roth[5,6,7], Steven Ballet[3,4], Vsevolod Katritch[1], Raymond C. Stevens[1] and Vadim Cherezov[1]

1 Department of Integrative Structural and Computational Biology, The Scripps Research Institute, La Jolla, California, USA
2 Department of Physics, Arizona State University, Tempe, Arizona, USA
3 Department of Chemistry, Vrije Universiteit Brussel, Brussels, Belgium
4 Department of Bioengineering Sciences, Vrije Universiteit Brussel, Brussels, Belgium
5 National Institute of Mental Health Psychoactive Drug Screening Program, University of North Carolina Chapel Hill Medical School, Chapel Hill, North Carolina, USA
6 Department of Pharmacology, University of North Carolina Chapel Hill Medical School, Chapel Hill, North Carolina, USA
7 Division of Chemical Biology and Medicinal Chemistry, University of North Carolina Chapel Hill Medical School, Chapel Hill, North Carolina, USA
8 Linac Coherent Light Source, SLAC National Accelerator Laboratory, Menlo Park, California, USA
9 Center for Free Electron Laser Science, Deutsches Elektronen-Synchrotron (DESY), Hamburg, Germany
10 Institute of Biochemistry and Molecular Biology, University of Hamburg, Hamburg, Germany
11 Department of Physics, University of Hamburg, Hamburg, Germany
12 European XFEL GmbH, Hamburg, Germany

[13] Department of Chemistry and Biochemistry, Arizona State University, Tempe, Arizona, USA
[14] Center for Applied Structural Discovery at the Biodesign Institute, Arizona State University, Tempe, Arizona, USA
[15] Laboratory of Chemical Biology and Peptide Research, Clinical Research Institute of Montreal, Montreal, Quebec, Canada

Abstract

Bi-functional μ- and δ- opioid receptor (OR) ligands are potential therapeutic alternatives to alkaloid opiate analgesics with diminished side effects. We solved the structure of human δ-OR bound to the bi-functional δ-OR antagonist and μ-OR agonist tetrapeptide H-Dmt(1)-Tic(2)-Phe(3)-Phe(4)-NH_2 (DIPP-NH_2) by serial femtosecond crystallography, revealing a *cis*-peptide bond between H-Dmt(1) and Tic(2). The observed receptor-peptide interactions are critical to understand the pharmacological profiles of opioid peptides, and to develop improved analgesics. The management of pain, mood states and other human neurophysiological processes is regulated by the release of classical endogenous opioid peptides, like endomorphins, enkephalins and dynorphins, that selectively bind to and activate their respective μ-, δ- and κ-opioid receptor (OR) subtypes(Pasternak 2014). Alkaloid opiates like morphine, targeting μ-OR, are the most widely used analgesics for the treatment of moderate to severe pain, but chronic administration produces side effects such as tolerance, dependence and addiction, therefore complicating their clinical use. Co-administration of the δ-OR antagonist naltrindole has been shown to prevent the development of morphine-induced tolerance and dependence(Abdelhamid, Sultana et al. 1991), thus prompting the design of compounds with a mixed δ-OR antagonist and μ-OR agonist function. This bi-functional pharmacological profile has been achieved with both morphinan-based small molecules and opioid peptide analogues, leading to compounds with reduced liability for tolerance and dependence *in vivo*, thus suggesting their high therapeutic potential(Schiller 2010, Healy, Bezawada et al. 2013).

This paper describes structure elucidation of the δ-opioid receptor (OR) with the tetrapeptidic ligand H-Dmt(1)-Tic(2)-Phe(3)-Phe(4)-NH_2 (DIPP-NH_2) which has been shown to act as both a δ-OR antagonist and a μ-OR agonist. Many alkaloid opiates, such as morphine, target the μ-OR in the treatment of pain but possess the detrimental side effects of tolerance and dependence which can lead to addiction. These have been shown to be mitigated by co-administration of a δ-OR antagonist (Abdelhamid, Sultana et al. 1991). Thus, the bifunctionality of DIPP-NH_2 is pharmacologically interesting since it supports DIPP-NH_2 and similarly functional analogues as a non-addictive alternative to existing alkaloid opiates. A construct was engineered and crystalized of the δ-OR and DIPP-NH_2 fused with an N-terminal linked apocytochrome b_{562}RIL (δ-OR-DIPP-NH_2). Crystal structures of the δ-OR-DIPP-NH_2 construct obtained at both a synchrotron at cryogenic temperatures and an XFEL at room temperature showed important details regarding DIPP-NH_2's pharmacological bifunctionality. A comparison with the inactive state

structure of the μ-OR (Manglik, Kruse et al. 2012) bound to an antagonist with the δ-OR-DIPP-NH_2 structure (shown in figure 6.2) showed a clash with two non-conserved residues in the side chain, implicating this site's role in differentiation of agonist versus antagonist properties of opioid peptide ligands. The solved SFX structure also elucidated

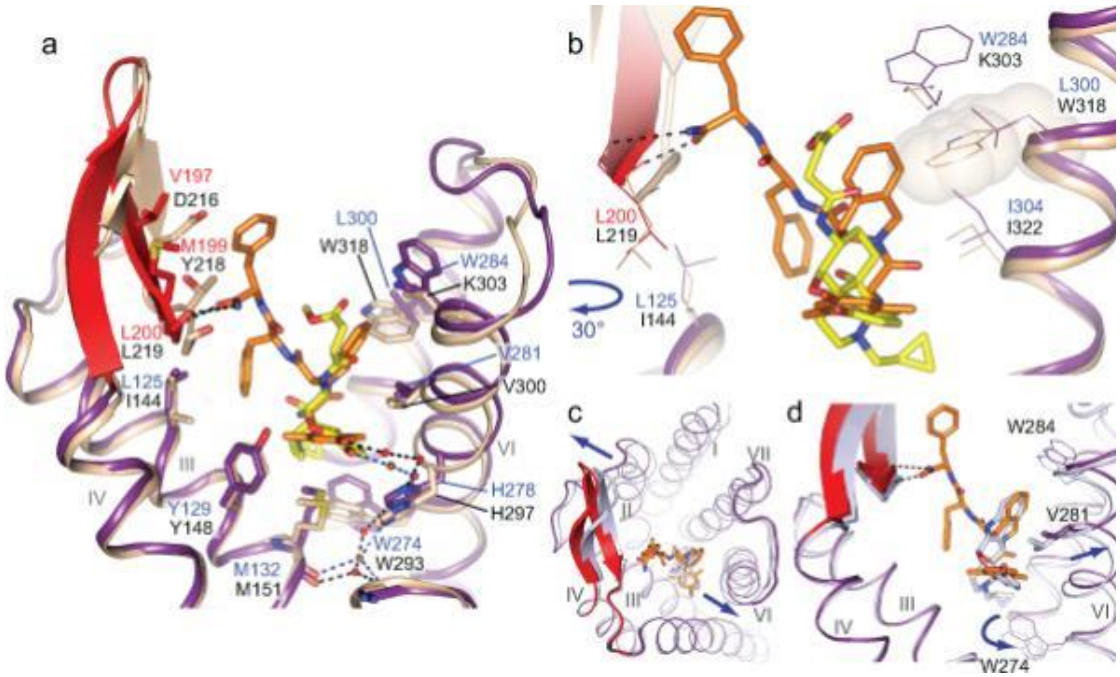

Figure 6.2 Structural Basis for the Recognition of DIPP-NH2 by δ-OR

a) Superposition of the δ-OR structure (purple cartoon with red ECL2) bound to the bifunctional peptide DIPP-NH2 (orange sticks), and the μ-OR structure (beige cartoon) bound to β-FNA (yellow sticks). b) Superposition indicates that the Tic(2) group on DIPP-NH2 would clash with Trp318 (transparent beige sphere) on μ-OR. c) Superposition of BRILΔ36δ-OR–DIPP-NH2 (purple) and naltrindole-bound δ-OR (light blue) showing helix movements (indicated by arrows) observed upon DIPPNH2binding. d) Close-up view of conformational changes occurring upon DIPP-NH2 binding compared to naltrindole bound receptor, including the shift of the Val2816.55 side chain. The change in orientation of the Trp2746.58 side chain in the naltrindole bound δ-OR structure is caused by the positioning of the cyclopentene group of naltrindole deeper into the receptor core. (originally published in Fenalti, Zatsepin et al. (2015))

characteristics of the peptide recognition site in the δ-OR beyond what was previously found with non-peptide antagonists (Granier, Manglik et al. 2012, Fenalti, Giguere et al. 2014). The structure solved in this study was determined using nanocrystals embedded in lipidic cubic phase (LCP), a viscous membrane mimetic that has shown high success in allowing crystallization of many GPCR's. My contributions involved characterization of crystalline samples using both microscopy and SHG spectroscopy, sample delivery preparation, SFX data collection at beamline CXI at LCLS

including logging each experimental step in the data collection electronic logbook of LCLS as well as our electronic logbook to record all data for each 5-10 min run of the experimental data collection conditions. This is a very elaborative task that is critical for the complex data collection at XFELs. For each run more than 35 parameters had to be recorded and entered, including all info on sample (including concentration, volume, crystallization conditions, pre-filtering conditions, crystal density), info on X-rays (including pulse length, X-ray energy, detector distance, flux, transmission) sample delivery (nozzles ID, sample flow rate, gas flow rate, pressure on sample) as well as careful recording of any problems observed (for example instability of the X-ray beam, clogging of nozzle, jittering of the jet, switch to water to remove debris on nozzle etc.).

High throughput protein nanocrystal fractionation in a microfluidic sorter

Analytical chemistry 87.8 (2015): 4159-4167.(Abdallah, Roy-Chowdhury et al. 2015)

Bahige G. Abdallah, Shatabdi Roy-Chowdhury, **Jesse Coe**, Petra Fromme, and Alexandra Ros

Department of Chemistry and Biochemistry, Arizona State University, Tempe, Arizona 85287, United States
Center for Applied Structural Discovery, Biodesign Institute, Arizona State University, Tempe, Arizona 85287, United States

Abstract

Protein crystallography is transitioning into a new generation with the introduction of the X-ray free electron laser, which can be used to solve the structures of complex proteins via serial femtosecond crystallography. Sample characteristics play a critical role in successful implementation of this new technology, whereby a small, narrow protein crystal size distribution is desired to provide high quality diffraction data. To provide such a sample, we developed a microfluidic device that facilitates dielectrophoretic sorting of heterogeneous particle mixtures into various size fractions. The first-generation device demonstrated great potential and success toward this endeavor; thus, in this work, we present a comprehensive optimization study to improve throughput and control over sorting outcomes. First, device geometry was designed considering a variety of criteria, and applied potentials were modeled to determine the scheme achieving the largest sorting efficiency for isolating nanoparticles from microparticles. Further, to investigate sorting efficiency within the nanoparticle regime, critical geometrical dimensions and input parameters were optimized to achieve high sorting efficiencies. Experiments revealed fractionation of nanobeads from microbeads in the optimized device with high sorting efficiencies, and protein crystals were sorted into sub-micrometer size fractions as desired for future serial femtosecond crystallography experiments.

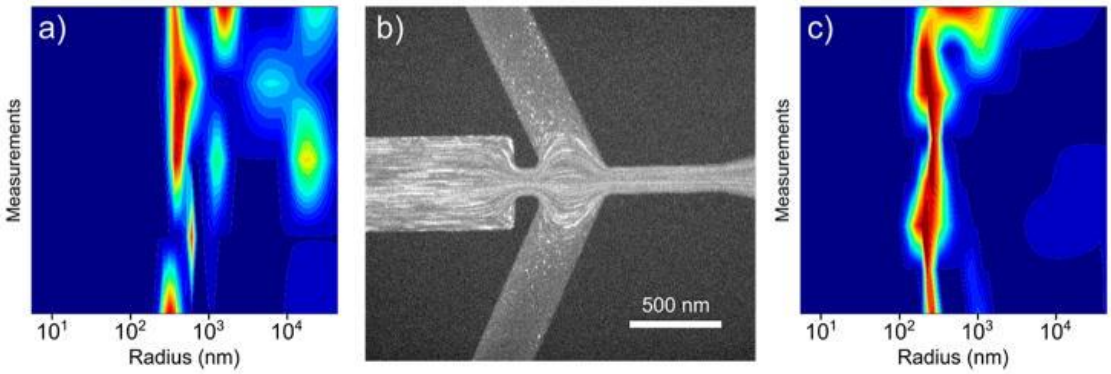

Figure 6.3 PSI Crystal Sorting in the Optimized Design

a) DLS signal heat map illustrating the broad size distribution (~200 nm to ~20 μm) of a bulk PSI crystal suspension. b) Fluorescence microscopy image of PSI crystals being sorted in the device where large crystals are focusing and small crystals deflect into "S". c) DLS signal heat map of the "S" fraction showing a submicrometer size distribution is isolated from the bulk. (originally published in Abdallah, Roy-Chowdhury et al. (2015))

This article reports on the development, characterization and testing of a novel microfluidic device designed to sort nanocrystals. The importance of size homogeneity and interesting properties of discrete crystals were described in previous chapters. The device described has the aim of allowing optimization of the homogeneity of the nanocrystal size post-crystallogenesis through a fractionation technique. The method used for crystal size segregation is based upon dielectrophoretic separation, utilizing inhomogeneities in an induced electric field within microfluidic channels that creates a flow profile that is particle size sensitive. Initial design of the electronic and mechanical profile was performed by modeling with COMSOL (Multiphysics) and well-characterized polystyrene beads, known to behave similar to PSI nanocrystals (Abdallah, Chao et al. 2013). Upon fabrication of the device, the experimental proof of concept and optimization of the system were performed using both polystyrene beads and slurries of nano-micrometer sized PSI crystals (shown in figure 6.3). The modelled separation of nanocrystals was then validated, showing sorting efficiencies of 91.6% and 93.8% for particle sizes of 500 nm and 2.5 µm respectively, characterized by DLS and NTA. My contribution to this research was production of PSI nanocrystal sample as well as size characterization using DLS and NTA. I also contributed to the experiments conducted together with B. Abdallah and edited the manuscript.

Structure of the angiotensin receptor revealed by serial femtosecond crystallography

Cell 161.4 (2015): 833-844.(Zhang, Unal et al. 2015)

Haitao Zhang[1], Hamiyet Unal[2], Cornelius Gati[3], Gye Won Han[4], Wei Liu[5], Nadia A. Zatsepin[6], Daniel James[6], Dingjie Wang[6], Garrett Nelson[6], Uwe Weierstall[6], Michael R. Sawaya[7], Qingping Xu[8], Marc Messerschmidt[9], Garth J. Williams[10], Sebastien Boutet[10], Oleksandr M. Yefanov[3], Thomas A. White[3], Chong Wang[11], Andrii Ishchenko[4], Kalyan C. Tirupula[2], Russell Desnoyer[2], **Jesse Coe**[5], Chelsie E. Conrad[5], Petra Fromme[5], Raymond C. Stevens[1,4,12], Vsevolod Katritch[2], Sadashiva S. Karnik[2], and Vadim Cherezov[4]

1Department of Biological Sciences, Bridge Institute, University of Southern California, Los Angeles, CA 90089, USA
2Department of Molecular Cardiology, Lerner Research Institute, Cleveland Clinic, Cleveland, OH 44195, USA
3Center for Free Electron Laser Science, Deutsches Elektronen-Synchrotron DESY, 22607 Hamburg, Germany
4Department of Chemistry, Bridge Institute, University of Southern California, Los Angeles, CA 90089 USA
5Department of Chemistry and Biochemistry, Center for Applied Structural Discovery at the Biodesign Institute, Arizona State University, Tempe, AZ 85287, USA
6Department of Physics, Arizona State University, Tempe, AZ 85287, USA
7Department of Chemistry and Biochemistry, the UCLA-DOE Institute for Genomics and Proteomics, University of California, Los Angeles, CA 90095, USA
8Joint Center for Structural Genomics, Stanford Synchrotron Radiation Light Source, SLAC National Accelerator Laboratory, Menlo Park, CA 94025, USA
9BioXFEL Science and Technology Center, Buffalo, NY 14203, USA
10Linac Coherent Light Source, SLAC National Accelerator Laboratory, Menlo Park, CA 94025, USA
11Department of Chemistry and Chemical Biology, Harvard University, Cambridge, MA 02138, USA
12iHuman Institute, ShanghaiTech University, Shanghai, 201210 China

Abstract

Angiotensin II type 1 receptor (AT_1R) is a G protein coupled receptor that serves as a primary regulator for blood pressure maintenance. Although several anti-hypertensive drugs have been developed as AT_1R blockers (ARBs), the structural basis for AT_1R ligand-binding and regulation has remained elusive, mostly due to the difficulties of growing high-quality crystals for structure determination using synchrotron radiation. By applying the recently developed method of serial femtosecond crystallography at an X-ray free-electron laser, we successfully determined the room-temperature crystal structure of the human AT_1R in complex with its selective antagonist ZD7155 at 2.9-A° resolution. The AT_1R-ZD7155 complex structure revealed key structural features of AT_1R and critical interactions for ZD7155 binding. Docking simulations of the clinically used ARBs into the AT_1R structure further elucidated both the common and distinct binding modes for these antihypertensive drugs. Our results thereby provide fundamental insights into AT_1R structure-function relationship and structure-based drug design.

This article reported the first structure of the human angiotensin II type 1 receptor (AT_1R), a GPCR that controls blood pressure, in complex with a selective antagonist ZD7155. AT_1R possesses high pharmacological relevance in diagnosis and therapeutics targeting cardiovascular

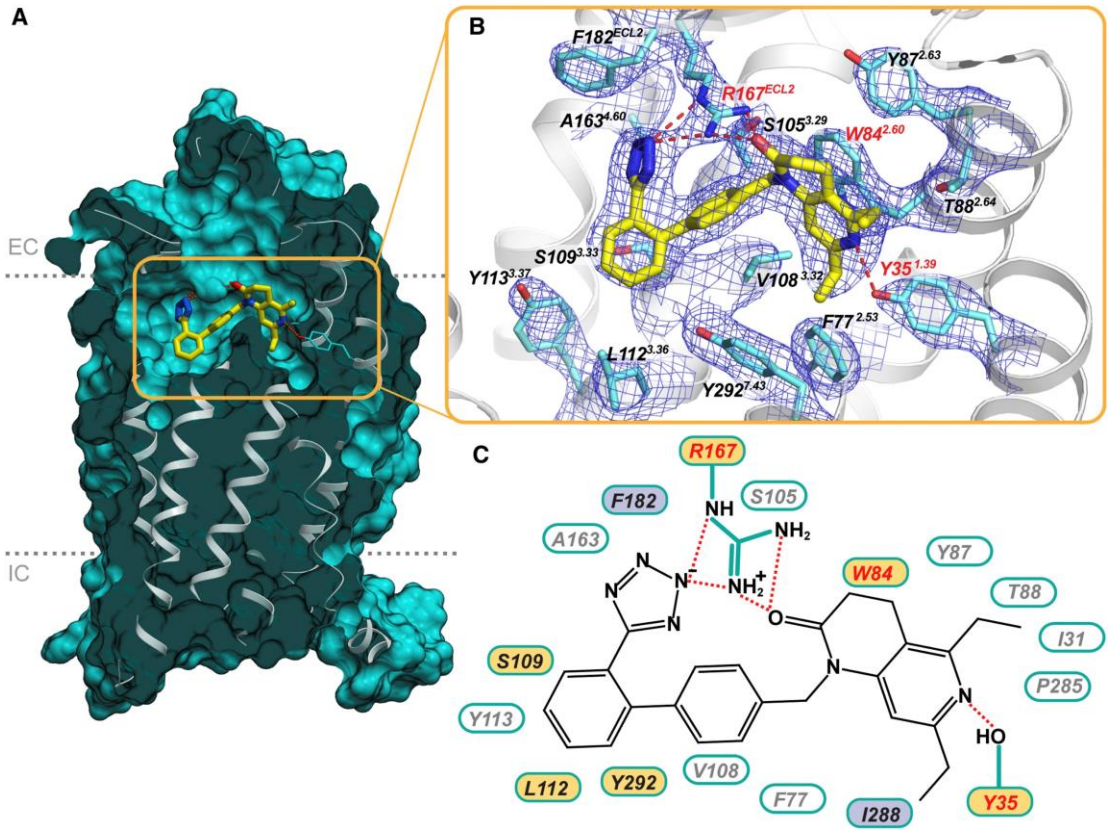

Figure 6.4 Interactions of ZD7155 with AT_1R

a) Cross-section view of AT_1R highlighting the shape of the ligand binding pocket. b) Zoomed-in view of the ligand binding pocket showing all residues within 4 Å from the ligand ZD7155, along with the 2mFo-DFc electron density (blue mesh) contoured at 1 σ level. In (A) and (B) ZD7155 is shown as sticks with yellow carbons. c) Schematic representation of interactions between AT_1R and ZD7155. Hydrogen bonds/salt bridges are shown as red dashed lines. The residues shown by mutagenesis to be critical for ligand binding are labeled red, those that are important for either peptide or non-peptide ligands binding are labeled in yellow, and the residues that discriminate between peptide and non-peptide ligands are labeled in purple.

disease and as an important drug target for treatment of hypertension (high blood pressure). This research provides the first structure of AT_1R through use of nanocrystals embedded in LCP using the method of SFX for structure determination. The structure of the AT_1R-ZD7155 complex was solved to high resolution (shown in figure 6.4) and allowed insight into the pharmacophore composition and mechanism of AT_1R that was thus far elusive. This structure, was the first structure of this important GPCR and it reveals for the first time the drug binding site with huge implications towards rational drug design. The drug binding site of the angiotensin receptor significantly differs from other GPCRs as there were three residues found (Arg167, Tyr35 and Trp84) not previously seen in binding small molecule ligands involved in the inhibitor binding. This work provided

important first insights into the structural basis of mechanistic modulation to be elucidated through multiple anti-hypertensive antagonists in combination with site-specific mutation experiments. Overall, the structural insight gained paves the way for future drug design. My contributions involved characterization of crystalline samples using both microscopy and SHG spectroscopy, sample delivery preparation and logging of SFX experimental conditions and results.

Microfluidic sorting of protein nanocrystals by size for X-ray free-electron laser diffraction

Structural Dynamics 2.4 (2015): 041719.(Abdallah, Zatsepin et al. 2015)

Bahige G. Abdallah,[1,2] Nadia A. Zatsepin,[2,3] Shatabdi Roy-Chowdhury,[1,2] **Jesse Coe**,[1,2] Chelsie E. Conrad,[1,2] Katerina Doerner,[4] Raymond G. Sierra,[5] Hilary P. Stevenson,[6] Fernanda Camacho-Alanis,[1] Thomas D. Grant,[7] Garrett Nelson,[2,3] Daniel James,[2,3] Guillermo Calero,[6] Rebekka M. Wachter,[1] John C. H. Spence,[2,3] Uwe Weierstall,[2,3], Petra Fromme,[1,2] and Alexandra Ros[1,2]

[1]Department of Chemistry and Biochemistry, Arizona State University, Tempe, Arizona 85287, USA
[2]Center for Applied Structural Discovery, The Biodesign Institute, Arizona State University,Tempe, Arizona 85287, USA
[3]Department of Physics, Arizona State University, Tempe, Arizona 85287, USA
[4]Deutsches Elektronen-Synchrotron, Hamburg, Germany
[5]Stanford PULSE Institute, SLAC National Accelerator Laboratory, Menlo Park, California 94025, USA
[6]Department of Structural Biology, University of Pittsburgh School of Medicine, Pittsburgh, Pennsylvania 15261, USA
[7]Hauptman-Woodward Medical Research Institute, University at Buffalo, Buffalo, New York 14203, USA

Abstract

The advent and application of the X-ray free-electron laser (XFEL) has uncovered the structures of proteins that could not previously be solved using traditional crystallography. While this new technology is powerful, optimization of the process is still needed to improve data quality and analysis efficiency. One area is sample heterogeneity, where variations in crystal size (among other factors) lead to the requirement of large data sets (and thus 10–100 mg of protein) for determining accurate structure factors. To decrease sample dispersity, we developed a high-throughput microfluidic sorter operating on the principle of dielectrophoresis, whereby polydisperse particles can be transported into various fluid streams for size fractionation. Using this microsorter, we isolated several milliliters of photosystem I nanocrystal fractions ranging from 200 to 600 nm in size as characterized by dynamic light scattering, nanoparticle tracking, and electron microscopy. Sorted nanocrystals were delivered in a liquid jet via the gas dynamic virtual nozzle into the path of the XFEL at the Linac Coherent Light Source. We obtained diffraction to ~4A° resolution, indicating that the small crystals were not damaged by the sorting process. We also observed the shape transforms of photosystem I nanocrystals, demonstrating that our device can optimize data collection for the shape transform-based phasing method. Using simulations, we show that narrow crystal size distributions can significantly improve merged data quality in serial crystallography. From this proof-of-concept work, we expect that the

automated size-sorting of protein crystals will become an important step for sample production by reducing the amount of protein needed for a high quality final structure and the development of novel phasing methods that exploit inter-Bragg reflection intensities or use variations in beam intensity for radiation damage-induced phasing. This method will also permit an analysis of the dependence of crystal quality on crystal size.

This article, reports on the further development and optimization of a microfluidic device for sorting nanocrystals for segregation by size using DEP with special focus on fast sorting speeds and high volume, to match the high sample consumption and flow rates required for SFX sample delivery. PSI crystals were homogenized and split before a fraction was passed through the device. Once the crystals were sorted, they were delivered to the XFEL beam. SFX data were collected at the CXI beamline at LCLS from the size homogeneous fractions as well as from the original unprocessed control group The fraction that was separated with the device showed a marked improvement in size homogeneity as seen in the histogram in figure 6.5, showing a size distribution between of between 150 and 550 nm reported with DLS and 125 to 300 nm measured with NTS compared to the unsorted size distribution of 150 nm to 10 µm measured with DLS (NTA cannot detect particles over 1 µm as they diffuse too slowly and thereby the particle tracking system is unable to determine their diffusion constant and thereby particle size

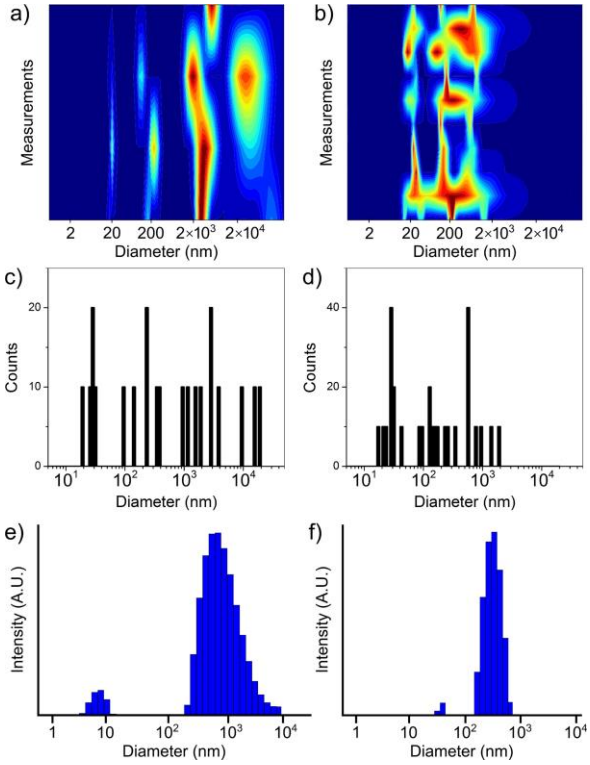

Figure 6.5 Size Distribution Before and After Sorting

DLS heat map of (a) the PSI crystal suspension prior to fractionation, indicating a wide size distribution (~200 nm to ~20 μm), and (b) a PSI crystal fraction collected from the [S] channels indicating a narrowed submicron size distribution (~200 nm to ~600 nm). Signal increases from blue (lowest) to red (highest). (c) and (d) show DLS histograms corresponding to (a) and (b), respectively. (e) and (f) show DLS histograms of the PSI suspension prior to sorting (~200 nm to ~10 μm) and an [S] channel fraction (~150 nm to ~550 nm), respectively, measured using a cuvette-based instrument for comparison with (a)–(d), confirming the differences in the size distribution. (Originally published in Abdallah, Zatsepin et al. (2015))

as well as mechanical constriction). Data sets were collected on both sorted and non-sorted fractions and evaluated to ~4 Å, indicating no significant loss of resolution due to processing through the device. My contribution to this included isolation, purification and crystallization of PSI, characterization of the crystals by DLS and NTA, data collection at LCLS as well as initial hitfinding of the data. Furthermore, I have written the PSI and sample related part of the paper, discussed the results with the team and provided edits and comments for the finalization of the manuscript.

Crystal structure of rhodopsin bound to arrestin by femtosecond X-ray laser

Nature 523.7562 (2015): 561.(Kang, Zhou et al. 2015)

Yanyong Kang[1], X. Edward Zhou[1], Xiang Gao[1], Yuanzheng He[1], Wei Liu[2], Andrii Ishchenko[3], Anton Barty[5], Thomas A. White[5], Oleksandr Yefanov[5], Gye Won Han[3], Qingping Xu[6], Parker W. de Waal[1], Jiyuan Ke[1], M. H. Eileen Tan[1,7], Chenghai Zhang[1], Arne Moeller[8], Graham M. West[9], Bruce Pascal[9], Ned Van Eps[10,11], Lydia N. Caro[11], Sergey A. Vishnivetskiy[12], Regina J. Lee[12], Kelly M. Suino-Powell[1], Xin Gu[1], Kuntal Pal[1], Jinming Ma[1], Xiaoyong Zhi[1], Sébastien Boutet[13], Garth J. Williams[13], Marc Messerschmidt[13,14], Cornelius Gati[5], Nadia A. Zatsepin[2,15], Dingjie Wang[2,15], Daniel James[2,15], Shibom Basu[2,15], Shatabdi Roy-Chowdhury[2,15], Chelsie Conrad[2], **Jesse Coe**[2], Haiguang Liu[2,16], Stella Lisova[2], Christopher Kupitz[2,17], Ingo Grotjohann[2], Raimund Fromme[2], Yi Jiang[18], Minjia Tan[18], Huaiyu Yang[18], Jun Li[7], Meitian Wang[19], Zhong Zheng[4], Dianfan Li[20], Nicole Howe[20], Yingming Zhao[14,21], Jörg Standfuss[22], Kay Diederichs[23], Yuhui Dong[24], Clinton S Potter[8], Bridget Carragher[8], Martin Caffrey[20], Hualiang Jiang[18], Henry N. Chapman[5,25], John C. H. Spence[2,15], Petra Fromme[2], Uwe Weierstall[2,15], Oliver P. Ernst[11,26], Vsevolod Katritch[4], Vsevolod V. Gurevich[12], Patrick R. Griffin[9], Wayne L. Hubbell[10], Raymond C. Stevens[3,4,27], Vadim Cherezov[3], Karsten Melcher[1], and H. Eric Xu[1,28]

1 Laboratory of Structural Sciences, Center for Structural Biology and Drug Discovery, Van Andel Research Institute, Grand Rapids, MI 49503, USA
2 Department of Chemistry and Biochemistry, and Center for Applied Structural Discovery, Biodesign Institute, Arizona State University, Tempe, AZ 85287-1604, USA
3 Department of Chemistry, Bridge Institute, University of Southern California, Los Angeles, CA 90089, USA
4 Department of Biological Sciences, Bridge Institute, University of Southern California, Los Angeles, CA 90089, USA
5 Center for Free Electron Laser Science, Deutsches Elektronen-Synchrotron DESY, 22607 Hamburg, Germany
6 Joint Center for Structural Genomics, Stanford Synchrotron Radiation Lightsource, SLAC National Accelerator Laboratory, Menlo Park, CA 94025, USA
7 Department of Obstetrics & Gynecology, Yong Loo Lin School of Medicine, National University of Singapore, Singapore
8 The National Resource for Automated Molecular Microscopy, New York Structural Biology Center, New York, NY 10027, USA
9 Department of Molecular Therapeutics, The Scripps Research Institute, Scripps Florida, Jupiter, FL 33458, USA
10 Jules Stein Eye Institute and Department of Chemistry and Biochemistry, University of California, Los Angeles, CA 90095, USA
11 Department of Biochemistry, University of Toronto, Toronto, Ontario M5S 1A8, Canada
12 Department of Pharmacology, Vanderbilt University, Nashville, TN 37232, USA
13 Linac Coherent Light Source (LCLS), SLAC National Accelerator Laboratory, Menlo Park, CA 94025, USA

14 BioXFEL, NSF Science and Technology Center, 700 Ellicott Street, Buffalo, NY 14203, USA
15 Department of Physics, Arizona State University, Tempe, AZ 85287, USA
16 Beijing Computational Science Research Center, Haidian District, Beijing 10084, China
17 Department of Physics, University of Wisconsin - Milwaukee, Milwaukee WI 53211, USA
18 State Key Laboratory of Drug Research, Shanghai Institute of Materia Medica, Chinese Academy of Sciences, Shanghai 201203, China
19 Swiss Light Source at Paul Scherrer Institute, CH-5232 Villigen, Switzerland
20 School of Medicine and School of Biochemistry and Immunology, Trinity College, Dublin, Ireland
21 Ben May Department for Cancer Research, University of Chicago, Chicago, IL 60637, USA
22 Laboratory of Biomolecular Research at Paul Scherrer Institute, CH-5232 Villigen, Switzerland
23 Department of Biology, Universität Konstanz, 78457 Konstanz, Germany
24 Beijing Synchrotron Radiation Facility, Institute of High Energy Physics, Chinese Academy of Sciences, Beijing 100049, China
25 Centre for Ultrafast Imaging, 22761 Hamburg, Germany
26 Department of Molecular Genetics, University of Toronto, Toronto, Ontario M5S 1A8, Canada
27 iHuman Institute, ShanghaiTech University, 2F Building 6, 99 Haike Road, Pudong New District, Shanghai, 201210, China
28 VARI-SIMM Center, Center for Structure and Function of Drug Targets, CAS-Key Laboratory of Receptor Research, Shanghai Institute of Materia Medica, Chinese Academy of Sciences, Shanghai 201203, China

Abstract

G protein-coupled receptors (GPCRs) signal primarily through G proteins or arrestins. Arrestin binding to GPCRs blocks G protein interaction and redirects signaling to numerous G protein-independent pathways. Here we report the crystal structure of a constitutively active form of human rhodopsin bound to a pre-activated form of the mouse visual arrestin, determined by serial femtosecond X-ray laser crystallography. Together with extensive biochemical and mutagenesis data, the structure reveals an overall architecture of the rhodopsin-arrestin assembly, in which rhodopsin uses distinct structural elements, including TM7 and Helix 8 to recruit arrestin. Correspondingly, arrestin adopts the pre-activated conformation, with a ~20° rotation between the N- and C- domains, which opens up a cleft in arrestin to accommodate a short helix formed by the second intracellular loop of rhodopsin. This structure provides a basis for understanding GPCR-mediated arrestin-biased signaling and demonstrates the power of X-ray lasers for advancing the frontiers of structural biology.

This article reports a breakthrough in structural biology of GPCRs with the rhodopsin-arrestin complex representing the first structure of any GPCR bound to arrestin (pictured in figure 6.65). This work provided the first detailed structural insights into the molecular basis behind signaling in the largest family of cell surface receptors. It has a huge impact and is also of significant pharmacological interest as currently one third of all clinical drugs are targeted to GPCRs (Kim, Hofmann et al. 2013, Shukla, Manglik et al. 2013). In addition to the first report of a structure of the GPCR-arrestin complex, the publication includes a multitude of biophysical techniques that were combined to provide proof that the structure represents the functionally active complex in a

conformation similar to the native complex in the living cell. The combination of the structure and the biophysical and functional studies provided a deep insight into intracellular signaling in arrestin pathways. Both active and inactive structures were solved in the course of this research and

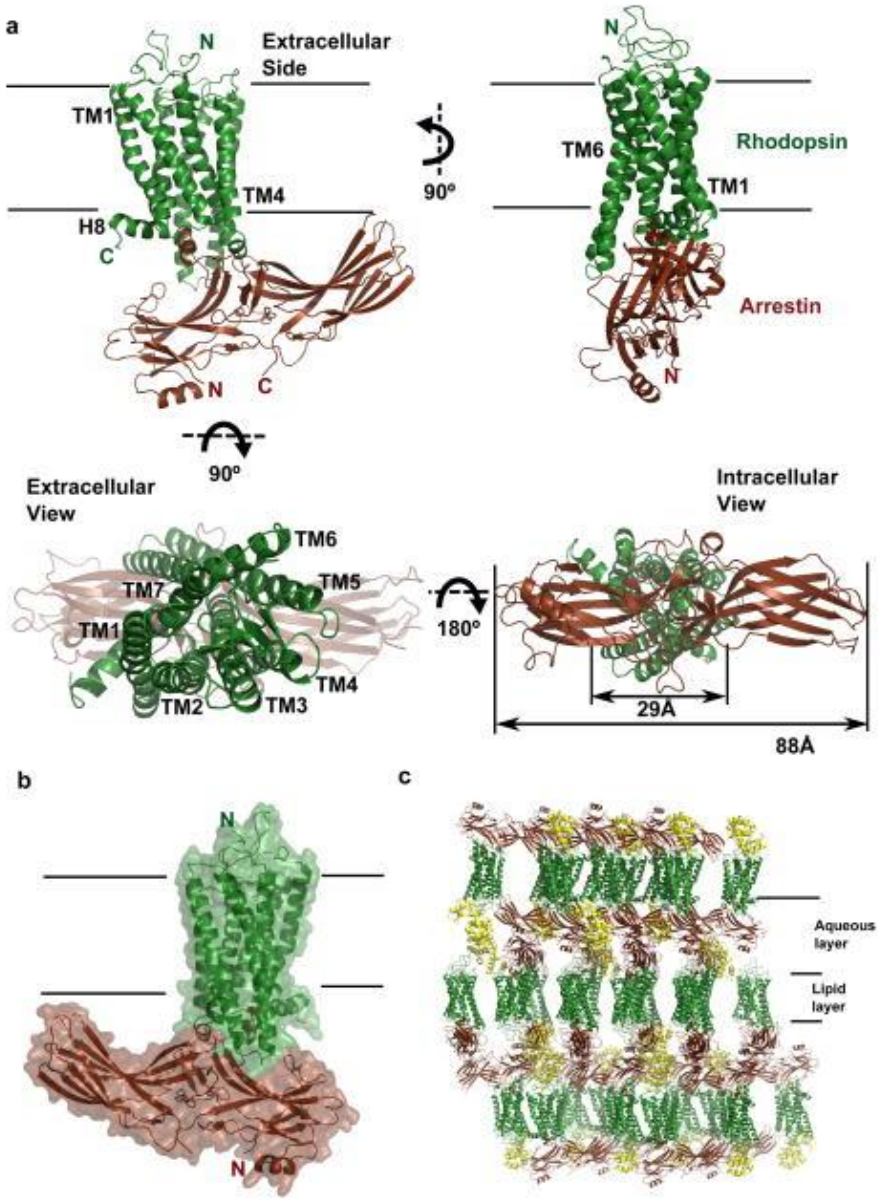

Figure 6.6 The Structure of the Rhodopsin-Arrestin Complex

a. The structure of the rhodopsin-arrestin complex in four orientations. The relative dimensions of rhodopsin and arrestin are shown in the intracellular view. TM1-TM7 indicates rhodopsin transmembrane helices 1–7; H8 is intracellular Helix 8. b. An overall view of the rhodopsin-arrestin complex shown with transparent solid surface. T4 Lysozyme (T4L) is omitted from this view. c. Crystal packing diagram of the rhodopsin-arrestin complex with T4L as yellow ribbon model. (Originally published in Kang, Zhou et al. (2015))

coupled with the previously solved rhodopsin bound to GαCT, a high affinity peptide that stimulates the active site of rhodopsin. With these combined results, evidence for the mechanisms behind both arrestin recruitment and activation was revealed. As rhodopsin serves as a model for many GPCRs, these findings represent a significant advance within the field with significant implications for the future of many pharmaceuticals. My contributions towards this project consisted of characterization of nanocrystals, including on site analysis at LCLS, data collection, testing and preparing sample delivery injectors and log keeping of the experimental runs during data collection at LCLS.

A novel inert crystal delivery medium for serial femtosecond crystallography

IUCrJ 2.4 (2015): 421-430.(Conrad, Basu et al. 2015)

Chelsie E. Conrad[1,2], Shibom Basu[1,2], Daniel James[2,3], Dingjie Wang[3], Alexander Schaffer[1,2], Shatabdi Roy-Chowdhury[1,2], Nadia A. Zatsepin[2,3], Andrew Aquila[4], **Jesse Coe**[1,2], Cornelius Gati[5], Mark S. Hunter[4], Jason E. Koglin[4], Christopher, Kupitz[2,6], Garrett Nelson[2,3], Ganesh Subramanian[2,3], Thomas A. White[5], Yun, Zhao[2,3], James Zook[1,2], Sebastien Boutet[4], Vadim Cherezov[7], John C. H. Spence[2,3], Raimund Fromme[1,2], Uwe Weierstall[2,3] and Petra Fromme[1,2]

1 Department of Chemistry and Biochemistry, Arizona State University, PO Box 871604, Tempe, AZ 85287-1604, USA
2 Center for Applied Structural Discovery, The Biodesign Institute, PO Box 875001, Tempe, AZ 85287-5001, USA
3 Department of Physics, Arizona State University, PO Box 871604, Tempe, AZ 85287-1504, USA
4 SLAC National Accelerator Laboratory, 2575 Sand Hill Road, Menlo Park, CA 94025, USA
5 Center for Free-Electron Laser Science, Deutsches Elektronen-Synchrotron DESY, Notkestrasse 85, 22607 Hamburg, Germany
6 Department of Physics,University of Wisconsin-Milwaukee, 1900 East Kenwood Boulevard, Milwaukee, WI 53211, USA
7 Bridge Institute, Department of Chemistry, University of Southern California, 3430 S. Vermont Avenue, Los Angeles, CA 90089, USA

Abstract

Serial femtosecond crystallography (SFX) has opened a new era in crystallography by permitting nearly damage-free, room-temperature structure determination of challenging proteins such as membrane proteins. In SFX, femtosecond X-ray free-electron laser pulses produce diffraction snapshots from nanocrystals and microcrystals delivered in a liquid jet, which leads to high protein consumption. A slow-moving stream of agarose has been developed as a new crystal delivery medium for SFX. It has low background scattering, is compatible with both soluble and membrane proteins, and can deliver the protein crystals at a wide range of temperatures down to 4_C. Using this crystal-laden agarose stream, the structure of a multi-subunit complex, phycocyanin, was solved to 2.5 A ° resolution using 300 mg of microcrystals embedded into the agarose medium post-crystallization. The agarose delivery method reduces

protein consumption by at least 100-fold and has the potential to be used for a diverse population of proteins, including membrane protein complexes.

This article describes the development of a novel agarose-based sample delivery medium for SFX. It expands upon a method of sample conservation for serial crystallography experiments in which crystals grown in lipidic cubic phases were delivered using a viscous sample injection system. In SFX experiments where viscous media are used, the sample necessary for collection of a data set can be significantly decreased compared to liquid jets due to high viscosity allowing for a stable sample introduction with orders of magnitude lower flow rate (Weierstall, James et al. 2014). As LCP is a membrane mimetic, it is largely available to select membrane proteins and also generally necessitates *in meso* crystallogenesis. While soluble proteins grown conventionally in solution might be mixed with LCP for sample delivery, membrane proteins grown in detergent micelles are thought to denature when mixed with LCP due to detergent depletion, leading to the need for new crystallization conditions to be found. The use of agarose as reported extends the benefits of a slow flowing jet to both membrane and soluble proteins. Furthermore, due to the process of mixing crystals with the medium post-crystallization (depicted in figure 6.7) allows pre-existing crystallogenesis conditions to be used without requiring to find completely new crystallization conditions. Multiple proteins were embedded into agarose and X-ray diffraction data collected using SFX in order to validate the agarose-based sample delivery method. Results included a full data set for phycocyanin that showed no loss in diffracting resolution for the protein as well as test data sets collected on the membrane protein crystals PSI, PSI-ferredoxin as well as Photosystem II. In addition, sample needed for the data sets was reduced by an order of magnitude as compared to a liquid jet and the medium showed minimal background, lower than that of LCP. My contributions to this project include isolation of protein and growth of the crystals (PSI, PSI-Fd), testing various compositions of the medium, experimental data collection at LCLS, including sample characterization on site, loading, collection of data as well as logging, participation in data processing and evaluation as well as edits of the manuscript. Furthermore, after the publication I helped implement this technique at multiple beamtimes, growing its use within the community, and

developed a more consistent and convenient way to prepare the medium through use of a heating block and redesign of the coupling protocol.

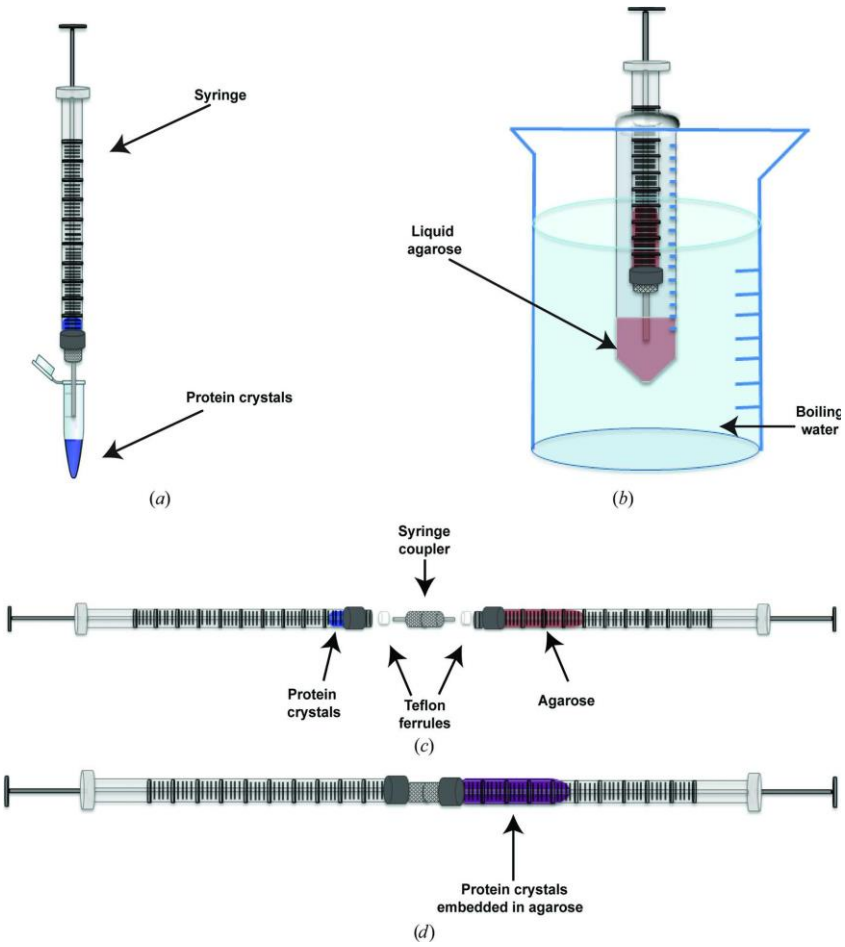

Figure 6.7 Embedding Crystals in Agarose

Diagram showing how the crystals are embedded into the agarose medium. (a) A dense pellet of crystals is drawn up into a syringe, (b) the agarose solution (contained in a 15 ml centrifuge tube) is submerged in boiling water until the agarose dissolves, the liquid agarose is drawn up into a warmed syringe and the agarose is allowed to gel and equilibrate to room temperature, (c) the protein crystals and agarose syringe are connected by a syringe coupler and (d) using the syringe coupler, the crystals are embedded throughout the agarose by moving the plungers back and forth. (Originally published in Conrad, Basu et al. (2015))

Serial femtosecond X-ray diffraction of enveloped virus microcrystals

Structural Dynamics 2.4 (2015): 041720.(Lawrence, Conrad et al. 2015)

Robert M. Lawrence,[1,2,3] Chelsie E. Conrad,[1,3,4] Nadia A. Zatsepin,[1,3,5] Thomas D. Grant,[6,7] Haiguang Liu,[5,8] Daniel James,[1,3,5] Garrett Nelson,[1,3,5] Ganesh Subramanian,[1,3,5] Andrew Aquila,[9]

Mark S. Hunter,[9] Mengning Liang,[9] Sebastien Boutet,[9] **Jesse Coe**,[1,3,4] John C. H. Spence,[1,3,5] Uwe Weierstall,[1,3,5] Wei Liu,[1,3,4] Petra Fromme,[1,3,4] Vadim Cherezov,[10] and Brenda G. Hogue[1,2,3,11]

1 Biodesign Institute, Arizona State University, Tempe, Arizona 85287, USA
2 Center for Infectious Diseases and Vaccinology, Arizona State University, Tempe, Arizona 85287, USA
3 Center for Applied Structural Discovery, Arizona State University, Tempe, Arizona 85287, USA
4 Department of Chemistry and Biochemistry, Arizona State University, Tempe, Arizona 85287, USA
5 Department of Physics, Arizona State University, Tempe, Arizona 85287, USA
6 Hauptman-Woodward Institute, State University of New York, Buffalo, New York 14203, USA
7 Department of Structural Biology, State University of New York, Buffalo, New York 14203, USA
8 Beijing Computational Science Research Center, Beijing 100084, China
9 Linac Coherent Light Source, SLAC National Accelerator Laboratory, Menlo Park, California 94025, USA
10 Department of Chemistry, Bridge Institute, University of Southern California, Los Angeles, California 90089, USA
11 School of Life Sciences, Arizona State University, Tempe, Arizona 85287, USA

Abstract

Serial femtosecond crystallography (SFX) using X-ray free-electron lasers has produced high-resolution, room temperature, time-resolved protein structures. We report preliminary SFX of Sindbis virus, an enveloped icosahedral RNA virus with ~700 A ° diameter. Microcrystals delivered in viscous agarose medium diffracted to ~40A ° resolution. Small-angle diffuse X-ray scattering overlaid Bragg peaks and analysis suggests this results from molecular transforms of individual particles. Viral proteins undergo structural changes during entry and infection, which could, in principle, be studied with SFX. This is an important step toward determining room temperature structures from virus microcrystals that may enable time-resolved studies of enveloped viruses.

In this article, microcrystals of Sindbis virus were delivered to the XFEL beam at LCLS in the medium agarose to obtain a structure of the capsid through SFX. The Sindbis virus is a highly symmetric enveloped virus and represents a model system for structural insight into this family which includes dengue, West Nile, Yellow Fever and Chikungunya (King, Lefkowitz et al. 2011). It is further useful as a model due to its exhibition of icosahedral symmetry in both its capsid and envelope (Zhang, Mukhopadhyay et al. 2002, Hernandez, Sinodis et al. 2005). Results from this study led to a 40 Å resolution structure, an important step towards using SFX to uncover structural information on viruses that could lead to new therapeutic solutions. My contributions to this research were sample preparation by embedding crystals into agarose (many test experiments at ASU as well as the final embedding at LCLS prior to sample delivery, characterization of the crystals

by DLS and SONICC as well as data collection at LCLS, which also include logging during the SFX experiment. I also gave comments and suggestions in the editing phase of the manuscript.

Serial femtosecond crystallography opens new avenues for structural biology

Protein and peptide letters 23.3 (2016): 255-272 (Coe and Fromme 2016)

Jesse Coe and Petra Fromme

Department of Chemistry and Biochemistry and Center for Applied Structural Discovery at the Biodesign Institute, Arizona State University, Tempe, AZ 85287

Abstract

Free electron lasers (FELs) provide X-ray pulses in the femtosecond time domain with up to 1012 higher photon flux than synchrotrons and open new avenues for the determination of difficult to crystallize proteins, like large complexes and human membrane proteins. While the X-ray pulses are so strong that they destroy any solid material, the crystals diffract before they are destroyed. The most successful application of FELs for biology has been the method of serial femtosecond crystallography (SFX) where nano or microcrystals are delivered to the FEL beam in a stream of their mother liquid at room temperature, which ensures the replenishment of the sample before the next X-ray pulse arrives. New injector technology allows also for the delivery of crystal in lipidic cubic phases or agarose, which reduces the sample amounts for an SFX data set by two orders of magnitude. Time-resolved SFX also allows for analysis of the dynamics of biomolecules, the proof of principle being recently shown for light-induced reactions in photosystem II and photoactive yellow protein. An SFX data sets consist of thousands of single crystal snapshots in random orientations, which can be analyzed now “on the fly” by data analysis programs specifically developed for SFX, but de-novo phasing is still a challenge, that might be overcome by two-color experiments or phasing by shape transforms.

In this review progress, methods, advantages and challenges involved in the first 6 years of SFX are presented and discussed. This includes comparisons with existing crystallographic methods, sample crystallogenesis and characterization, sample delivery, data collection and analysis, and experimental strategies. My contributions to this review are writing the bulk of the material and handling the majority of the editing and submitting process.

Femtosecond structural dynamics drives the trans/cis isomerization in photoactive yellow protein

Science 352.6286 (2016): 725-729 (Pande, Hutchinson et al. 2015)

Kanupriya Pande[1,2], Christopher D. M. Hutchison[3], Gerrit Groenhof[4], Andy Aquila[5], Josef S. Robinson[5], Jason Tenboer[1], Shibom Basu[6], Sébastien Boutet[5], Daniel P. DePonte[5], Mengning Liang[5], Thomas A. White[2], Nadia A. Zatsepin[7], Oleksandr Yefanov[2], Dmitry Morozov[4], Dominik

Oberthuer[2], Cornelius Gati[2], Ganesh Subramanian[7], Daniel James[7], Yun Zhao[7], Jake Koralek[5], Jennifer Brayshaw[1], Christopher Kupitz[1], Chelsie Conrad[6], Shatabdi Roy-Chowdhury[6], Jesse D. Coe[6], Markus Metz[2], Paulraj Lourdu Xavier[2,8], Thomas D. Grant[9], Jason E. Koglin[5], Gihan Ketawala[6], Raimund Fromme[6], Vukica Šrajer[10], Robert Henning[10], John C. H. Spence[7], Abbas Ourmazd[1], Peter Schwander[1], Uwe Weierstall[7], Matthias Frank[11], Petra Fromme[6], Anton Barty[2], Henry N. Chapman[2,12], Keith Moffat[10,13], Jasper J. van Thor[3], Marius Schmidt[1]

1Department of Physics, University of Wisconsin–Milwaukee, Milwaukee, WI 53211, USA.
2Center for Free Electron Laser Science, Deutsches Elektronen Synchrotron, Notkestrasse 85, 22607 Hamburg, Germany.
3Faculty of Natural Sciences, Department of Life Sciences, Imperial College, London SW7 2AZ, UK.
4Nanoscience Center and Department of Chemistry, University of Jyväskylä, Post Office Box 35, 40014 Jyväskylä, Finland.
5Linac Coherent Light Source, SLAC National Accelerator Laboratory, Sand Hill Road, Menlo Park, CA 94025, USA.
6School of Molecular Sciences and Biodesign Center for Applied Structural Discovery, Arizona State University, Tempe, AZ 85287, USA.
7Department of Physics, Arizona State University, Tempe, AZ 85287, USA.
8IMPRS-UFAST, Max Planck Institute for Structure and Dynamics of Matter, Luruper Chaussee 149, 22761 Hamburg, Germany.
9Hauptman-Woodward Institute, State University of New York at Buffalo, 700 Ellicott Street, Buffalo, NY 14203, USA.
10Center for Advanced Radiation Sources, University of Chicago, Chicago, IL 60637, USA.
11Lawrence Livermore National Laboratory, Livermore, CA 94550, USA.
12Center for Ultrafast Imaging, University of Hamburg, Luruper Chaussee 149, 22761 Hamburg, Germany.
13Department of Biochemistry and Molecular Biology and Institute for Biophysical Dynamics, University of Chicago, Chicago, IL 60637, USA.

Abstract

A variety of organisms have evolved mechanisms to detect and respond to light, in which the response is mediated by protein structural changes after photon absorption. The initial step is often the photoisomerization of a conjugated chromophore. Isomerization occurs on ultrafast time scales and is substantially influenced by the chromophore environment. Here we identify structural changes associated with the earliest steps in the trans-to-cis isomerization of the chromophore in photoactive yellow protein. Femtosecond hard x-ray pulses emitted by the Linac Coherent Light Source were used to conduct time-resolved serial femtosecond crystallography on photoactive yellow protein microcrystals over a time range from 100 femtoseconds to 3 picoseconds to determine the structural dynamics of the photoisomerization reaction.

This article presents further research on PYP using TR-SFX, pushing temporal limits to visualize the trans/cis isomerization occurring on the femtosecond timescale. Building off of results obtained and reported in Tenboer, Basu et al. (2014), TR-SFX was performed on PYP with time points including dark and 200 ns controls, 3 ps, and sub-ps time points spanning from 100-1000 fs. The sub-ps data sets represent the shortest and most highly resolved time points ever obtained

using crystallography. A 140 fs pump laser was used to excite crystals prior to exposure to 40 fs XFEL pulses. Due to a 280 fs jitter between the pump and probe lasers, a timing tool (Bionta, Lemke et al. 2011, Hartmann, Helml et al. 2014) was used to mark actual time delays in the fs regime. All sub ps pulses were measured using estimated 300 fs and 600 fs time delays and data were binned post collection by their time stamps. A 200 ns time delay was used as a positive control to compare with previously measured 1 µs data (Pande, Hutchinson et al. 2015) in order to quantify initiation yield from the pump laser. This successfully showed a consistent ratio of pR_1 and pR_2 states expected at this point along the reaction timeline, with a calculated reaction initiation of 12.6%. This value is lower than the previous 40% reported in Tenboer, Basu et al. (2014) due to the need for a fs pump vs. a ns pump. Whereas ns pulses allow for secondary initiations to occur to molecules that have backreacted to the ground state post initial excitation, fs pulses are faster

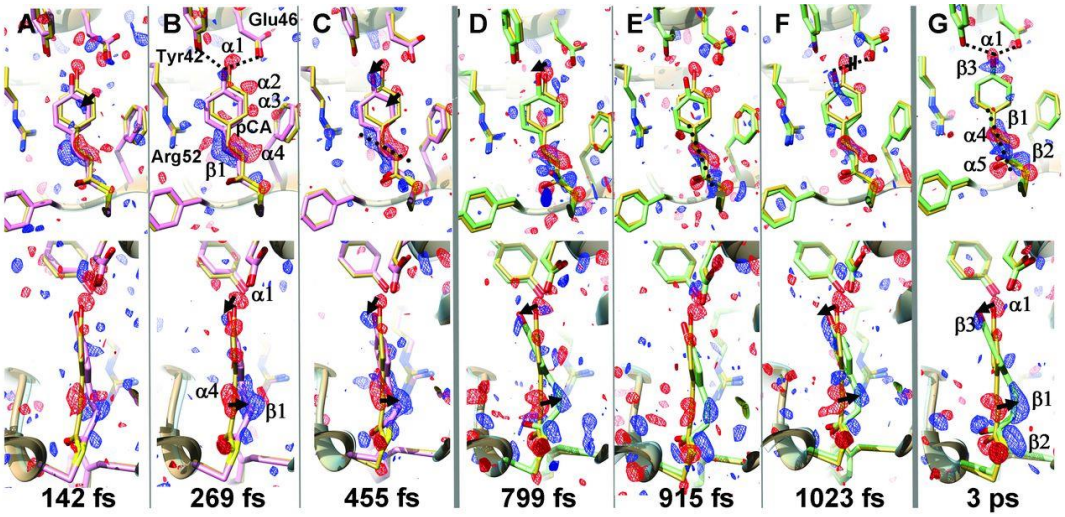

Figure 6.8 Trans-to-Cis Isomerization in PYP

Weighted DED maps in red (–3σ) and blue (3σ); front (upper) and side view (lower). Each map is prepared from about the same number of diffraction patterns, except the 3-ps map (table S1, B and C). The reference dark structure is shown in yellow throughout; structures before the transition and still in the electronic excited state PES are shown in pink; structures after the transition and in the electronic ground state PES are shown in light green. Important negative difference density features are denoted as α and positive features as β in (B) and (G). Pronounced structural changes are marked by arrows. (A to C) Time delays before the transition. (A) Twisted trans at 142 fs, ϕtail 154°. (B) Twisted trans at 269 fs, ϕtail 140°, some important residues are marked; dotted lines: hydrogen bond of the ring hydroxyl to Glu46 and Tyr42. (C) Twisted trans at 455 fs, ϕtail 144°; dotted line: direction of C2=C3 double bond. (D to G) Time delays and chromophore configuration after the+ transition. (D) Early cis at 799 fs, ϕtail 50°. (E) Early cis at 915 fs; dotted line: direction of C2 = C3 double bond. (F) Early cis at 1023 fs; for (E) and (F), ϕtail ~ 65°. (G) 3-ps delay; dashed line: direction of C2=C3 double bond, feature β1; ϕtail is 35°. Figure and caption originally published in Pande, Hutchinson et al. (2015).

than the time scale for an initially excited molecule to revert to the ground state, precluding the chance for a second excitation event.

The 3 ps and binned, sub-ps time points observed comprise a conformational dynamic progression from the trans-p-coumaric acid chromophore to the cis state over this time range as inferred from difference electron density maps. The remarkable visualization of this isomerization is highlighted in figure 6.8, showing difference electron density evolving over the course of these time delays. Through a theoretical and spectroscopically supported conical intersection of excited state and ground state potential energy surfaces, the 550 fs observed timing of the isomerization of the chromophore is in good agreement with previous studies on the photoactivated dynamics of PYP. My contributions to this project included crystallization and characterization prior to and during beamtime as well as log keeping and assistance with data reduction during the experiment.

Second harmonic generation correlation spectroscopy for characterizing translationally diffusing protein nanocrystals

Acta Crystallographica Section D: Structural Biology 72.7 (2016): 849-859.(Dow, Dettmar et al. 2016)

Ximeng Y. Dow[1], Christopher M. Dettmar[1], Emma L. DeWalt[1], Justin A. Newman[1], Alexander R. Dow[1], Shatabdi Roy-Chowdhury[2,3], **Jesse Coe**[2,3], Christopher Kupitz[2], Petra Fromme[2,3] and Garth J. Simpson[1]

1 Chemistry Department, Purdue University, West Lafayette, IN 47907, USA
2 School of Molecular Sciences, Arizona State University, Tempe, AZ 85287-1604, USA
3 Center for Applied Structural Discovery, Biodesign Institute, Arizona State University, Tempe, AZ 85287-7401, USA

Abstract

Second harmonic generation correlation spectroscopy (SHG-CS) is demonstrated as a new approach to protein nanocrystal characterization. A novel linescanning approach was performed to enable autocorrelation analysis without sample damage from the intense incident beam. An analytical model for autocorrelation was developed, which includes a correction for the optical scattering forces arising when focusing intense, infrared beams. SHG-CS was applied to the analysis of $BaTiO_3$ nanoparticles ranging from 200 to _500 nm and of photosystem I nanocrystals. A size distribution was recovered for each sample and compared with the size histogram measured by scanning electron microscopy (SEM). Good agreement was observed between the two independent measurements. The intrinsic selectivity of the second-order nonlinear optical process provides SHG-CS with the ability to distinguish well-ordered nanocrystals from conglomerates and amorphous aggregates.

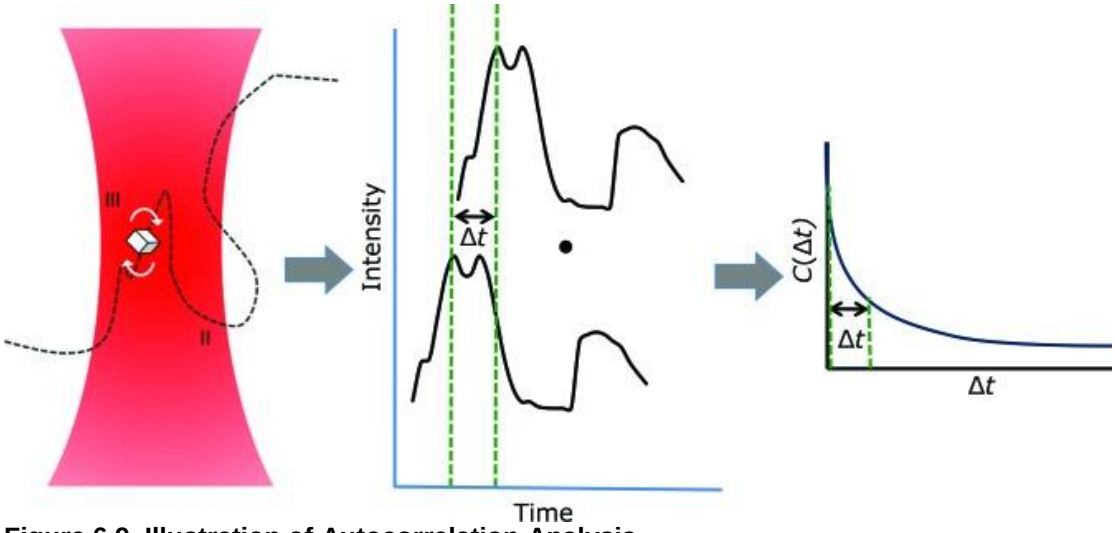

Figure 6.9 Illustration of Autocorrelation Analysis

As the nanocrystal diffuses though the focal volume, the SHG intensity will fluctuate. Multiplying the signal by itself with a time delay and integrating yields an autocorrelogram. With sufficient particles sampled, the autocorrelation decay provides a measure of diffusion. (Originally published in Dow, Dettmar et al. (2016))

> Combining the recovered distribution of particle diameters with the histogram of measured SHG intensities provides the inherent hyperpolarizability per unit volume of the SHG-active nanoparticles. Simulations suggest that the SHG activity per unit volume is likely to exhibit relatively low sensitivity to the subtle distortions within the lattice that contribute to resolution loss in X-ray diffraction, but high sensitivity to the presence of multi-domain crystals.

This article describes research done towards using SHG correlation spectroscopy to measure size and size distribution for nanocrystals by SONICC instrumental design and practical validation. This work was conducted by the group of G. Simpson who invented the SONICC method. While the original SONICC measurements were focused solely on the detection of nanocrystals this work now expands the SONICC method for the detection of size and quality of nanocrystals. It could be developed into a new tool that could be incorporated as a feature into the SONICC instrumentation in the future, possibly replacing the need for DLS or NTA analysis that are usually coupled with SHG spectroscopy for nanocrystal characterization. The autocorrelation function can be determined during SHG generation by use of light scattering fluctuations and evaluated with methods similar to the methods used for data evaluation using a DLS instrument or fluorescence correlation spectroscopy. Here data are collected as particles flow through the focal volume of a laser sufficiently powerful enough to induce SHG. The intensity fluctuations of the SHG signal are then used to determine the size of the nanocrystals. Figure 6.910 illustrates how this

autocorrelation analysis works. The pattern in these fluctuations is directly correlated to its Brownian movement through the region which is related to its size through the Stokes-Einstein equation. The benefit of using SHG is that its intensity is quadratically proportional to the crystal size and, like Bragg diffraction, is dependent upon translational order, becoming generally negligible for aggregates and free molecules (Haupert and Simpson 2011). This gives the system a huge advantage over DLS, which cannot discriminate between disordered particles (aggregates) and nanocrystals. With the new SHG-correlation based method, one can determine the size of nanocrystals even in the presence of amorphous aggregates which often co-exists with nanocrystals in crystallization experiments. As the beam must be sufficiently intense, it has an influence on the dynamics of the particles being measured. In order to deconvolute this influence, $BaTiO_3$ particles were initially used to validate and iteratively improve theoretical models of this influence. This was then tested on PSI nanocrystals for practical validation as macromolecular crystals are the intended beneficiary of this technique. With comparison of TEM and DLS data on the results, the size distribution from SHG-CS showed strong agreement and proof of concept for this technique proved successful. My contributions to this work were the isolation of PSI and the growth of an array of different sized PSI nano- and microcrystals. I also provided the PSI sample section for the paper, discussed results and read and provided comments for the manuscript.

Lipidic cubic phase injector is a viable crystal delivery system for time-resolved serial crystallography

Nature communications 7 (2016): 12314. (Nogly, Panneels et al. 2016)

Przemyslaw Nogly[1], Valerie Panneels[1], Garrett Nelson[2], Cornelius Gati[3], Tetsunari Kimura[4], Christopher Milne[5], Despina Milathianaki[6], Minoru Kubo[4,7], Wenting Wu[1], Chelsie Conrad[8], **Jesse Coe**[8], Richard Bean[3], Yun Zhao[2], Petra Båth[9], Robert Dods[9], Rajiv Harimoorthy[9], Kenneth R. Beyerlein[3], Jan Rheinberger[1], Daniel James[1], Daniel DePonte[6], Chufeng Li[2], Leonardo Sala[5], Garth J. Williams[6], Mark S. Hunter[6], Jason E. Koglin[6], Peter Berntsen[9], Eriko Nango[10], So Iwata[10,11], Henry N. Chapman[3,12,13], Petra Fromme[8], Matthias Frank[14], Rafael Abela[5], Se´bastien Boutet[6], Anton Barty[3], Thomas A. White[3], Uwe Weierstall[2], John Spence[2], Richard Neutze[9], Gebhard Schertler[1,15] & Jörg Standfuss[1]

1 Laboratory for Biomolecular Research, Paul Scherrer Institute, Villigen 5232, Switzerland.
2 Department of Physics, Arizona State University, Tempe, Arizona 85287, USA.
3 Center for Free-Electron Laser Science, Deutsches Elektronen-Synchrotron DESY, 22607 Hamburg, Germany.
4 Biometal Science Laboratory, RIKEN SPring-8 Center, Hyogo 679-5148, Japan.
5 SwissFEL, Paul Scherrer Institute, Villigen 5232, Switzerland.

[6] Linac Coherent Light Source (LCLS), SLAC National Accelerator Laboratory, Menlo Park, California 94025, USA.
[7] PRESTO, JST, Saitama 332-0012, Japan.
[8] Department of Chemistry and Biochemistry, and Center for Applied Structural Discovery, Biodesign Institute, Arizona State University, Tempe, Arizona 85287-1604, USA.
[9] Department of Chemistry and Molecular Biology, University of Gothenburg, Box 462, SE-40530 Gothenburg, Sweden.
[10] SACLA Science Research Group, RIKEN/SPring-8 Center, Hyogo 679-5148, Japan.
[11] Department of Cell Biology, Kyoto University, Kyoto 606-8501, Japan.
[12] Department of Physics, University of Hamburg, 22761 Hamburg, Germany.
[13] Centre for Ultrafast Imaging, University of Hamburg, 22761 Hamburg, Germany.
[14] Lawrence Livermore National Laboratory, Livermore 94550, USA.
[15] Department of Biology, ETH Zurich, Zürich 8093, Switzerland.

Abstract

Serial femtosecond crystallography (SFX) using X-ray free-electron laser sources is an emerging method with considerable potential for time-resolved pump-probe experiments. Here we present a lipidic cubic phase SFX structure of the light-driven proton pump bacteriorhodopsin (bR) to 2.3Å resolution and a method to investigate protein dynamics with modest sample requirement. Time-resolved SFX (TR-SFX) with a pump-probe delay of 1ms yields difference Fourier maps compatible with the dark to M state transition of bR. Importantly, the method is very sample efficient and reduces sample consumption to about 1mg per collected time point. Accumulation of M intermediate within the crystal lattice is confirmed by time-resolved visible absorption spectroscopy. This study provides an important step towards characterizing the complete photocycle dynamics of retinal proteins and demonstrates the feasibility of a sample efficient viscous medium jet for TR-SFX.

This article shows the proof of principle for TR-SFX within a viscous media. Crystals of active bacteriorhodopsin (bR) were grown in LCP and loaded in the LCP injector in the dark for delivery to the XFEL beam. The protein is the excited by short laser 75 fs pulses “on the fly in the LCP jet” during sample, which initiated the photoreaction cycle. Data were then collected with a time delay of 1 ms to progress the system into the M state. Though TR-SFX was established for sample delivery in liquid jets at this point, the use of a viscous medium was seen by many groups as a severe challenge for TR-SFX. The main concerns were the slow flow rates, the question how laser light would penetrate the 30um thick opaque LCP jet. This study provided the first experimental data on the feasibility of TR-SFX for crystals grown and delivered in viscous media. The conventional liquid sample delivery jets required tens to hundreds of mg of the valuable protein samples, which is not feasible for many difficult to crystallize proteins.

This work now extends TR-SFX to the study of proteins that can be produced only in very small amounts and are difficult and costly to provide in quantities needed for liquid jet SFX. bR is acts as a light-driven proton pump and, like rhodopsin, binds the biological chromophore retinal. The reaction is phototriggered by a laser light pulse at 530 nm and 50 fs excitation. Previous to this experiment, data had been collected on the dark state of bR using serial crystallography at a microfocus beamline (Nogly, James et al. 2015). The bR was crystallized in LCP. Along with a structure solved with cryogenic traditional crystallography, a basis for validation of the SFX structure was obtained which showed high agreement between the three, a comparison of which is shown in figure 6.10. After time resolved spectroscopy experiments on crystals diffracted at the

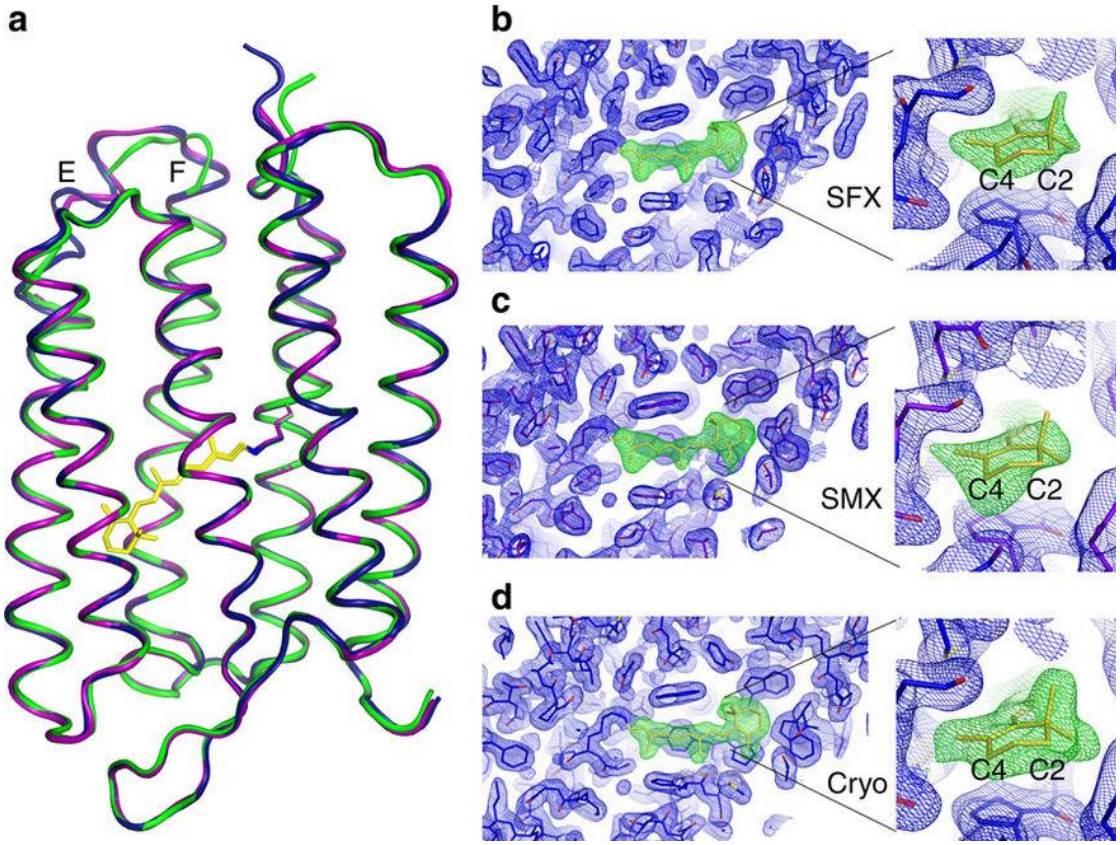

Figure 6.10 Comparison of bR Structures from SFX, SMX and Cryo

(a) Overall structures are highly similar with only minor deviations in loop regions and the termini. (b–d) Comparison of electron density maps in the retinal-binding pocket (SFX (b), SMX (c) and Cryo (d)). The electron density maps (blue, $2F_o-F_c$, 1 σ) are well defined in all three cases and strong positive density is observed when retinal (yellow sticks; left panel) is omitted during refinement (green, F_o-F_c, 2.5 σ). Flexible regions of the retinal β-ionone ring (insets), which are not part of the retinal conjugated double bond system, can be clearly identified in the two room temperature structures. Originally published in Nogly, Panneels et al. (2016).

synchrotron, a maximum of the M intermediate of bR was found to accumulate at 1 ms, therefore 1 ms was used as the delay time in the TR-SFX experiment. The electron density map and the structure determined confirmed that we have reached the M state intermediate, showing high agreement with the existing trapped M state from traditional crystallography (Sass, Büldt et al. 2000). These results pave the way for future photoactivated TR-SFX experiments in viscous media. My contributions to this project include characterization of embedded crystals, sample loading, sample introduction and logging during the experiment. I also provided comments and edits to the manuscript.

Structural Enzymology Using X-ray Free Electron Lasers

Structural Dynamics 4.4 (2017): 044003. (Kupitz, Olmos Jr et al. 2017)

Christopher Kupitz[1], Jose L. Olmos Jr.[2], Mark Holl[3], Lee Tremblay[4], Kanupriya Pande[5,6], Suraj Pandey[1], Dominik Oberthür[5,6], Mark Hunter[7], Mengning Liang[7], Andrew Aquila[7], Jason Tenboer[1], George Calvey[8], Andrea Katz[8], Yujie Chen[8], Max O. Wiedorn[5], Juraj Knoska[5], Alke Meents[6], Valerio Majriani[5,6], Tyler Norwood[1], Ishwor Poudyal[1], Thomas Grant[9], Mitchell D. Miller[2], Weijun Xu[2], Aleksandra Tolstikova[5], Andrew Morgan[5], Markus Metz[5], Jose M. Martin-Garcia[10], James D. Zook[10], Shatabdi Roy-Chowdhury[10], Jesse Coe[10], Nirupa Nagaratnam[10], Domingo Meza[10], Raimund Fromme[10], Shibom Basu[10], Matthias Frank[11], Thomas White[5], Anton Barty[5], Sasa Bajt[5], Oleksandr Yefanov[5], Henry N. Chapman[5,6], Nadia Zatsepin[3], Garrett Nelson[3], Uwe Weierstall[3], John Spence[3], Peter Schwander[1], Lois Pollack[8], Petra Fromme[10], Abbas Ourmazd[1], George N. Phillips Jr.[2], Marius Schmidt[1]

1Physics Department, University of Wisconsin-Milwaukee, 3135 N. Maryland Ave, Milwaukee, Wisconsin 53211, USA
2Department of BioSciences, Rice University, 6100 Main Street, Houston, Texas 77005, USA
3Department of Physics, Arizona State University, Tempe, Arizona 85287, USA
4Marbles Inc., 1900 Belvedere Pl, Westfield, Indiana 46074, USA
5Center for Free-Electron Laser Science, DESY, Notkestrasse 85, 22607 Hamburg, Germany
6University of Hamburg, Luruper Chaussee 149, 22761 Hamburg, Germany
7Linac Coherent Light Source, Stanford Linear Accelerator Center (SLAC) National Accelerator Laboratory, 2575 Sand Hill Road, Menlo Park, California 94025, USA
8Department of Applied and Engineering Physics, Cornell University, 254 Clark Hall, Ithaca, New York 14853, USA
9Hauptman-Woodward Institute, State University of New York at Buffalo, 700 Ellicott Street, Buffalo, New York 14203, USA
10School of Molecular Sciences and Biodesign Center for Applied Structural Discovery, Arizona State University, Tempe, Arizona 85287-1604, USA
11Lawrence Livermore National Laboratory, Livermore, California 94550, USA

Abstract

Mix-and-inject serial crystallography (MISC) is a technique designed to image enzyme catalyzed reactions in which small protein crystals are mixed with a substrate just prior to being probed by an X-ray pulse. This approach offers several advantages over flow cell studies. It provides (i) room

temperature structures at near atomic resolution, (ii) time resolution ranging from microseconds to seconds, and (iii) convenient reaction initiation. It outruns radiation damage by using femtosecond X-ray pulses allowing damage and chemistry to be separated. Here, we demonstrate that MISC is feasible at an X-ray free electron laser by studying the reaction of M. tuberculosis ß-lactamase microcrystals with ceftriaxone antibiotic solution. Electron density maps of the apo-ß-lactamase and of the ceftriaxone bound form were obtained at 2.8 Å and 2.4 Å resolution, respectively. These results pave the way to study cyclic and non-cyclic reactions and represent a new field of time-resolved structural dynamics for numerous substrate-triggered biological reactions.

This publication describes results from mix-and-inject TR-SFX on β-lactamase (BlaC) from *Mycobacterium tuberculosis* in both its apo form and in complex with the antibiotic ceftriaxone. This marks one of the first published diffusive mixing TR-SFX experiments. B-lactams are one of the largest classes of antibiotics and acts on both Gram-positive and Gram-negative pathogens. The tuberculosis causing bacteria *M. tuberculosis* is resistant to treatment with these antibiotics due to the evolution of its BlaC protein which uses a serine residue to open the β-lactam ring via nucleophilic attack, rendering the antibiotic inactive. In order to combat this medicinally, clarity on the mechanism of this inactivation is needed and so visualization of the structures along the reaction timeline are desired. A T-junction was used to mix crystals with a 2-3 µm thickness with a solution of Ceftriaxone using a 15 µL/min flow rate of crystal slurry and a 60 µL/min with a time delay of ~2 sec, leading to steady state data collection (turnover rate has been measured to be 49 +/- 17/min). Structures of the apo (2.8 Å) and substrate bound (2.4 Å) enzyme were achieved from collection of 12,853 and 22,646 indexed diffraction patterns respectively. As can be seen in figure 6.11, difference electron density maps exhibit strong evidence of successful diffusion into the binding pocket by Ceftriaxone. This allowed successful method validation by comparison to previous work with large BlaC crystals soaked with cefamandole, another β-lactam antibiotic (Tremblay, Xu et al. 2010). In addition, this provides a path forward for uncovering unknown intermediates at higher temporal resolution in the push for mechanistic understanding. My contributions to this work included initial microcrystallization trials, sample characterization and handling, logging during the experiment, and edits in the manuscript.

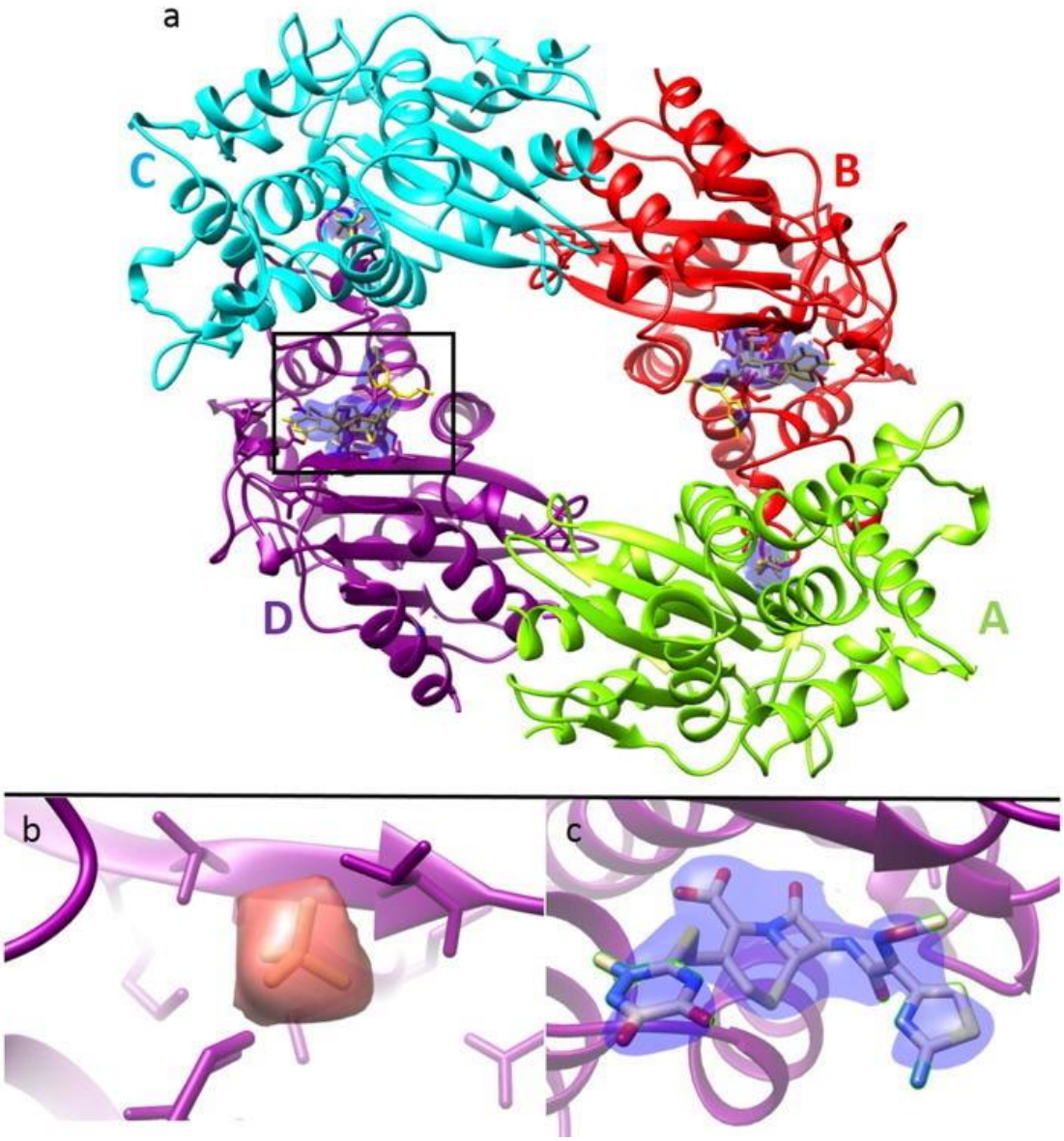

Figure 6.11 Electron Densities of Apo and Ceftriaxone Bound BlaC Catalytic Cleft

(a) Refined model of the entire tetramer (σ = 1.1) in the asymmetric unit after mixing. The mixed electron density (2Fo-Fc) is shown in blue in the binding pockets. Subunits A and C contain phosphate while subunits B and D have a bound ceftriaxone, with the electron density of D being slightly stronger. (b) Enlarged section of subunit D showing the unmixed ED, which corresponds to a bound phosphate. (c) Enlarged section of subunit D showing the mixed ED (blue electron density) with ceftriaxone modelled in. Figure and caption originally from Kupitz, Olmos Jr et al. (2017).

Serial millisecond crystallography of membrane and soluble protein microcrystals using synchrotron radiation

IUCrJ 4.4 (2017): 439-454.(Martin-Garcia, Conrad et al. 2017)

Jose M. Martin-Garcia[1], Chelsie E. Conrad[1,6], Garrett Nelson[1,2], Natasha Stander[1,2], Nadia A. Zatsepin[1,2], James Zook[1], Lan Zhu[1], James Geiger[1], Eugene Chun[1], David Kissick[4], Mark C. Hilgart[4], Craig Ogata[4], Andrii Ishchenko[3], Nirupa Nagaratnam[1], Shatabdi Roy-Chowdhury[1], **Jesse Coe**[1], Ganesh Subramanian[1,2], Alexander Schaffer[1], Daniel James[5], Gihan Ketawala[2], Nagarajan Venugopalan[4], Shenglan Xu[4], Stephen Corcoran[4], Dale Ferguson[4], Uwe Weierstall[1,2], John C. H. Spence[2], Vadim Cherezov[3], Petra Fromme[1], Robert F. Fischetti[4], Wei Liu[1]

[1]Biodesign Center for Applied Structural Discovery, Biodesign Institute, School of Molecular Sciences, Arizona State University, 727 East Tyler Street, Tempe, AZ 85287, USA
[2]Department of Physics, Arizona State University, PO Box 871504, Tempe, AZ 85287, USA
[3]Department of Chemistry, Bridge Institute, University of Southern California, 3430 South Vermont Avenue, MC 3303, Los Angeles, CA 90089, USA
[4]Advanced Photon Source, Argonne National Laboratory, 9700 South Cass Ave, Lemont, IL, USA
[5]Paul Scherrer Institute, 5232 Villigen, Switzerland
[6]Structural Biophysics Laboratory, National Cancer Institute, Frederick, MD 21702, USA

Abstract

Crystal structure determination of biological macromolecules using the novel technique of serial femtosecond crystallography (SFX) is being severely limited by the scarcity of X-ray free electron laser (XFEL) sources. However, recent and future upgrades render synchrotron radiation sources at micro-focused beamlines suitable for room temperature serial crystallography data collection as well. Due to the longer exposure times needed at synchrotrons, serial data collection is termed serial millisecond crystallography (SMX). As a result, the number of SMX experiments is rapidly growing, with a dozen experiments reported so far. Here, we present the first high-viscosity injector-based SMX experiments carried out at a U.S. synchrotron source, the Advanced Photon Source (APS). Micro-crystals (5-20 μm) of a wide variety of proteins including lysozyme, thaumatin, phycocyanin, the human A_{2A} adenosine receptor (A_{2A}AR), the soluble fragment of the membrane lipoprotein Flpp3, 3-deoxy-D-manno-2-octulosunate-8-phosphate synthase (KDO8PS), and proteinase K were screened. Crystals suspended in lipidic cubic phase (LCP) or a high molecular weight poly (ethylene oxide) (PEO) (MW=8,000,000) were delivered to the beam using a high viscosity injector. In-house data reduction (hit-finding) software developed at APS as well as SFX data-reduction and analysis software suites, Cheetah and CrystFEL, enabled efficient on-site SMX data monitoring, reduction and processing. The best diffracting crystals were from A_{2A}AR, phycocyanin, Flpp3, KDO8PS, proteinase K, thaumatin and lysozyme, with hit rates of 3.0 %, 5.0 %, 11.6 %, 1.5 %, 4.2 %, 6.0 % and 34.2 %, respectively. Complete data sets of A_{2A}AR, phycocyanin, Flpp3, proteinase K, and lysozyme were collected and their structures were determined at 3.2 Å, 3.1 Å, 3.0 Å, 2.65 Å, and 2.05 Å resolution, respectively. Our data demonstrate the feasibility of serial millisecond crystallography from 5–20 μm crystals using a high viscosity injector at APS. The resolution of the crystal structures obtained in this study was dictated by the current flux density and crystal size, but upcoming developments in beamline optics and the planned

APS-U upgrade will increase intensity by two orders of magnitude. These developments will enable structure determination from smaller and/or weakly diffracting micro-crystals.

This article reports on a series of experiments carried out at microfocus beamlines at the Advance Photo Source (APS) acting as a proof of principle for serial millisecond crystallography at synchrotron sources. This technique uses millisecond X-ray exposures at a synchrotron analogous to SFX (illustrated in figure 6.12). A suite14). Suites of proteins were used over the course of these experiments with five complete data sets being collected for A_{2A} adenosine receptor (A_{2A}AR, a membrane protein and GPCR), phycocyanin (a soluble phycobiliprotein complex), Flpp3 soluble domain, proteinase K (soluble) and lysozyme (soluble), all previously solved structures to allow for method validation. All the crystals were delivered using viscous media with A_{2A}AR being grown in LCP, lysozyme and Fllp3 being embedded in LCP with a similar protocol to that of agarose (described previously). In addition, Flpp3, phycocyanin and proteinase K were also embedded into viscous phase of 6 % poly(ethylene oxide) MW=1,000,000 (PEO). This is the first report of PEO being used as a viscous

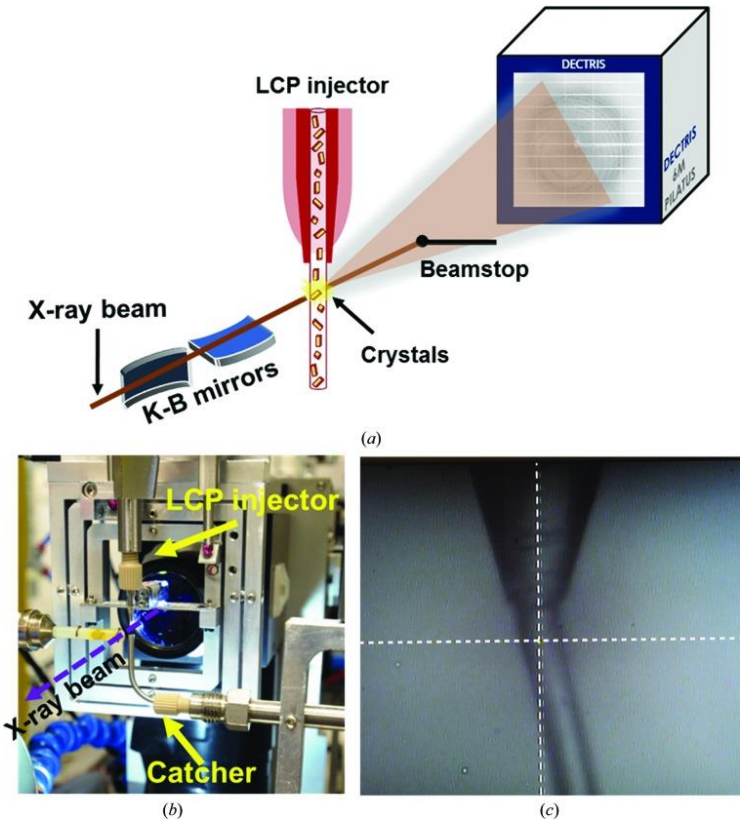

Figure 6.12 Experimental Setup at the GM/CA 23-ID-D Beamline

(*a*) Schematic diagram of the setup. (*b*) LCP injector (Weierstall, James et al. 2014) mounted on translation stages (not shown). The catcher is also shown. (*c*) View of the LCP stream extruding out of a 50 µm glass capillary nozzle. The intersection point of the two white dashed lines indicates the position of the X-ray beam. Originally published in Martin-Garcia, Conrad et al. (2017).

carrier. While the embedding procedure is analogous to the protocol for agarose, PEO behaves much better in air than agarose in forming a stable jet (the converse has been observed in vacuum) and appears to have a similar compatibility range. Data sets were collected and structures were determined to a resolution range of 2.05-3.2 Å for the various proteins. Thereby SMX achieved similar resolutions to data sets collected by cryo-crystallography and SFX in previous experiments, leading to a demonstration of feasibility for serial millisecond crystallography as a viable method and tool in structural discovery. My contributions to this publication included isolation and purification of protein, growth of crystals, preparation of and embedding of crystals in the PEO, operation of the injector, and participation in data processing and evaluation.

Structures of riboswitch RNA reaction states by mix-and-inject XFEL serial crystallography

*Nature*541.7636 (2017): 242.(Stagno, Liu et al. 2016)

J. R. Stagno[1], Y. Liu[1], Y. R. Bhandari[1], C. E. Conrad[2,3], S. Panja[4], M. Swain[1], L. Fan[5], G. Nelson[6], C. Li[6], D. R. Wendel[1], T. A. White[7], **J. D. Coe**[2,3], M. O. Wiedorn[7,8], J. Knoska[7,8], D. Oberthuer[7], R. A. Tuckey[1], P. Yu[1], M. Dyba[1], S. G. Tarasov[1], U. Weierstall[3,6], T. D. Grant[9], C. D. Schwieters[10], J. Zhang[11], A. R. Ferré-D'Amaré[12], P. Fromme[2,3], D. E. Draper[13], M. Liang[14], M. S. Hunter[14], S. Boutet[14], K. Tan[15], X. Zuo[16], X. Ji[17], A. Barty[7], N. A. Zatsepin[3,6], H. N. Chapman[7,8], J. C. H. Spence[3,6], S. A. Woodson[4] & Y.-X. Wang[1]

1 Protein-Nucleic Acid Interaction Section, Structural Biophysics Laboratory, Center for Cancer Research, National Cancer Institute, Frederick, Maryland 21702, USA.
2 Department of Biochemistry, Arizona State University, Tempe, Arizona 85287, USA.
3 Center for Applied Structural Discovery, The Biodesign Institute, Arizona State University, Tempe, Arizona 85287, USA.
4 Department of Biophysics, Johns Hopkins University, Baltimore, Maryland 21218, USA.
5 Small Angle X-ray Scattering Core Facility, Center for Cancer Research, National Cancer Institute, Frederick, Maryland 21702, USA.
6 Department of Physics, Arizona State University, Tempe, Arizona 85287, USA.
7 Center for Free-Electron Laser Science, Deutsches Elektronen-Synchrotron DESY, Notkestraße 85, 22607 Hamburg, Germany.
8 Department of Physics, University of Hamburg, Luruper Chaussee 149, 22607 Hamburg, Germany.
9 Hauptmann-Woodward Medical Research Institute, Buffalo, New York 14203, USA.
10 Center for Information Technology, National Institutes of Health, Bethesda, Maryland 20892-5624, USA.
11 Laboratory of Molecular Biology, National Institute of Diabetes and Digestive and Kidney Diseases, National Institutes of Health, Bethesda, Maryland 20892, USA.
12 Laboratory of RNA Biophysics and Cellular Physiology, National Heart Lung and Blood Institute, National Institutes of Health, Bethesda, Maryland 20892, USA.
13 Department of Chemistry, Johns Hopkins University, Baltimore, Maryland 21218, USA.
14 Linac Coherent Light Source, SLAC
National Accelerator Laboratory, Menlo Park, California 94025, USA.

15 Structural Biology Center, Biosciences Division, Advanced Photon Source, Argonne National Laboratory, Argonne, Illinois
60439, USA.
16 X-ray Science Division, Advanced Photon Source, Argonne National Laboratory, Argonne, Illinois 60439, USA.
17 Macromolecular Crystallography Laboratory, Center for Cancer
Research, National Cancer Institute, Frederick, Maryland 21702, USA.

Abstract

Riboswitches are structural RNA elements that are generally located in the 5′untranslated region of messenger RNA. During regulation of gene expression, ligand binding to the aptamer domain of a riboswitch triggers a signal to the downstream expression platform(Nahvi, Sudarsan et al. 2002, Mandal, Boese et al. 2003, Breaker 2012). A complete understanding of the structural basis of this mechanism requires the ability to study structural changes over time(Hajdu, Neutze et al. 2000). Here we use femtosecond X-ray free electron laser (XFEL) pulses(Chapman, Fromme et al. 2011, Boutet, Lomb et al. 2012) to obtain structural measurements from crystals so small that diffusion of a ligand can be timed to initiate a reaction before diffraction. We demonstrate this approach by determining four structures of the adenine riboswitch aptamer domain during the course of a reaction, involving two unbound apo structures, one ligand-bound intermediate, and the final ligand-bound conformation. These structures support a reaction mechanism model with at least four states and illustrate the structural basis of signal transmission. The three-way junction and the P1 switch helix of the two apo conformers are notably different from those in the ligand-bound conformation. Our time-resolved crystallographic measurements with a 10-second delay captured the structure of an intermediate with changes in the binding pocket that accommodate the ligand. With at least a 10-minute delay, the RNA molecules were fully converted to the ligand-bound state, in which the substantial conformational changes resulted in conversion of the space group. Such notable changes *in crystallo* highlight the important opportunities that micro- and nanocrystals may offer in these and similar time-resolved diffraction studies. Together, these results demonstrate the potential of ‘mix-and-inject’ time-resolved serial crystallography to study biochemically important interactions between biomacromolecules and ligands, including those that involve large conformational changes.

This research describes a milestone in TR-SFX research where four structures were obtained of the adenine riboswitch aptamer domain over the course of its reaction pathway after being chemically triggered. The adenine riboswitch modulates gene expression through conformational ‘switching’ upon (and in the absence of) binding adenine as a ligand in its 71-nucleotide RNA aptamer domain. In determining the ground state structure, two distinct conformers were discovered within the asymmetric unit, only one of which being ligand-binding competent. The structure of the binding pocket revealed residues key to mechanistic activity, contrary to previous suspicion of lack of order in the absence of a bound ligand (Rieder, Lang et al. 2007).

The intermediate and ligand bound states were solved at time points of 10 second and 10 minutes respectively after introduction of adenine as a ligand using a T-junction mixer as depicted in figure 6.13a. Interestingly, the space group itself changed when comparing the apo structures with the final ligand bound structure from $P2_1$ → $P2_12_12_1$. This transformation occurs *in crystallo* over the 10 minute incubation with the adenine ligand (illustrated in figure 6.13b). This polymorphic transformation was astonishing to occur in crystals, but the structure of final state reached is similar to the previously reported structure of the ligand bound state (Zhang and Ferré-D'Amaré 2014) as can be seen in figure 6.13c. In contrast, the 10 second intermediate showed $P2_1$ packing like the apo forms, indicating no large conformational change had occurred in that time frame. However, there were interesting differences in the electron density of the binding pocket and a loss of electron density in the first helix of the aptamer domain, in

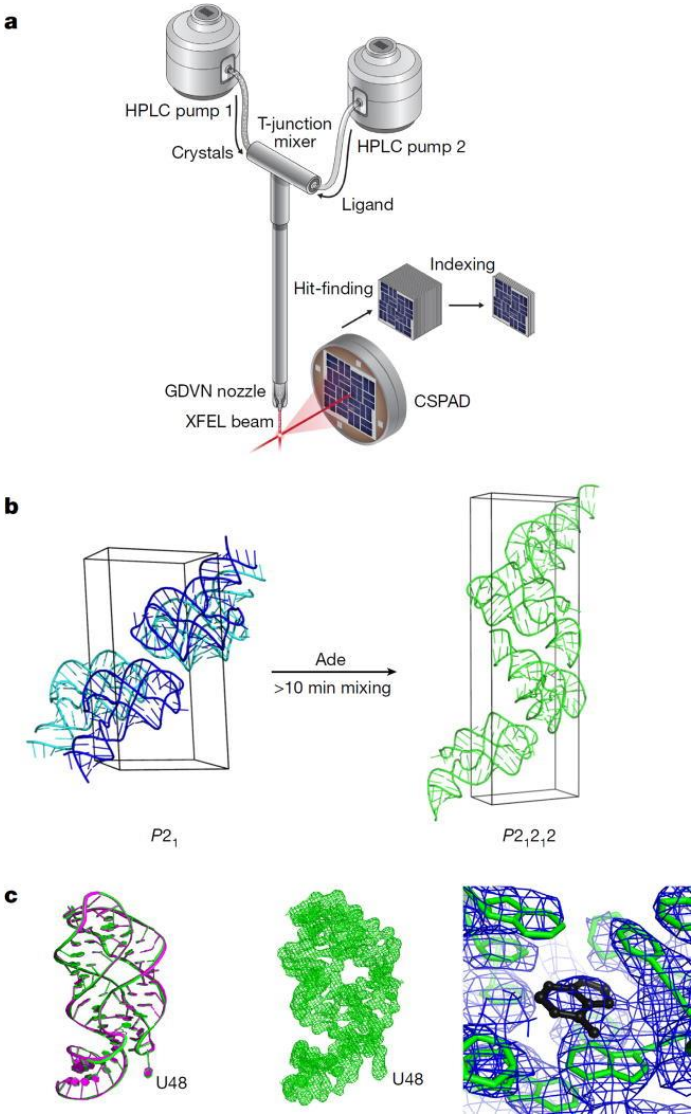

Figure 6.13 Setup of **M**ix-and-**I**nject SFX and **C**onversion of the **S**tructure and **C**rystal **L**attice

(a) Cartoon of the SFX ligand-mixing experiment. (b) The unit cells of the crystals of apo ($P2_1$) and ligand-bound ($P2_12_12$), the structure of which was generated *in crystallo* from the apo structures after at least 10 min of mixing with the adenine ligand. (c) Superimposition (left) of the ligand-bound structures of the 10-min-mix (green) and PDB code 4TZX (magenta), and 2 $F_o - F_c$ electron density maps contoured at 1σ for the whole structure of the 10-min-mix (middle) and the binding pocket (right) showing the ligand (black). Figure and caption originally published in Stagno, Liu et al. (2017).

agreement with an intermediate state predicted by the kinetics model to occur prior to the large conformational change. The results of this experiment provide a structural basis for observed kinetics and the possible mechanism for ligand binding based signaling in riboswitches. My contributions towards this project were characterization and advice on sample selection, preparation of sample for injection, sample delivery operation, participation in XFEL data collection at LCLS as well as log keeping and manuscript editing.

Crystal structure of CO-bound cytochrome c oxidase determined by serial femtosecond X-ray crystallography at room temperature

Proceedings of the National Academy of Sciences 114.30 (2017): 8011-8016.(Ishigami, Zatsepin et al. 2017)

Izumi Ishigami[1], Nadia A. Zatsepin[2,3], Masahide Hikita[1], Chelsie E. Conrad[3,4], Garrett Nelson[2], **Jesse Coe**[3,4], Shibom Basu[3,4], Thomas D. Grant[5], Matthew H. Seaberg[6], Raymond G. Sierra[6], Mark S. Hunter[6], Petra Fromme[3,4], Raimund Fromme[3,4], Syun-Ru Yeh[1], and Denis L. Rousseau[1]

1 Department of Physiology and Biophysics, Albert Einstein College of Medicine, Bronx, NY 10461
2 Department of Physics, Arizona State University, Tempe, AZ 85287;
3 Center for Applied Structural Discovery, The Biodesign Institute, Arizona State University, Tempe, AZ 85287
4 School of Molecular Sciences, Arizona State University, Tempe, AZ 85287
5 Department of Structural Biology, Hauptman-Woodward Institute, State University of New York at Buffalo,
Buffalo, NY 14203
6 SLAC National Accelerator Laboratory, Menlo Park, CA 94025

Abstract

Cytochrome c oxidase (CcO), the terminal enzyme in the electron transfer chain, translocates protons across the inner mitochondrial membrane by harnessing the free energy generated by the reduction of oxygen to water. Several redox-coupled proton translocation mechanisms have been proposed, but they lack confirmation, in part from the absence of reliable structural information due to radiation damage artifacts caused by the intense synchrotron radiation. Here we report the room temperature, neutral pH (6.8), damage-free structure of bovine CcO (bCcO) in the carbon monoxide (CO)-bound state at a resolution of 2.3 Å, obtained by serial femtosecond X-ray crystallography (SFX) with an X-ray free electron laser. As a comparison, an equivalent structure was obtained at a resolution of 1.95 Å, from data collected at a synchrotron light source. In the SFX structure, the CO is coordinated to the heme a_3 iron atom, with a bent Fe–C–O angle of ~142°. In contrast, in the synchrotron structure, the Fe–CO bond is cleaved; CO relocates to a new site near Cu_B, which, in turn, moves closer to the heme a_3 iron by ~0.38 Å. Structural comparison reveals that ligand binding to the heme a_3 iron in the SFX structure is associated with an allosteric structural transition, involving partial unwinding of the helix-X between heme a and a_3, thereby establishing a communication

linkage between the two heme groups, setting the stage for proton translocation during the ensuing redox chemistry.

This article reports and discusses results from TR-SFX upon structural studies of cytochrome *c* oxidase (CcO) and reports for the first time a CO bound state solved from data collected at an XFEL. CcO is a large membrane protein complex that is the terminal electron acceptor in the respiratory electron transfer pathway. It catalyzes the reduction of molecular oxygen to water and significantly contributes to the electrochemical gradient and membrane potential across the inner mitochondrial membrane by pumping protons across the membrane. While many structural studies have been performed in search of the mechanistic coupling between oxygen reduction and proton translocation, the exact molecular mechanism remains elusive largely due to

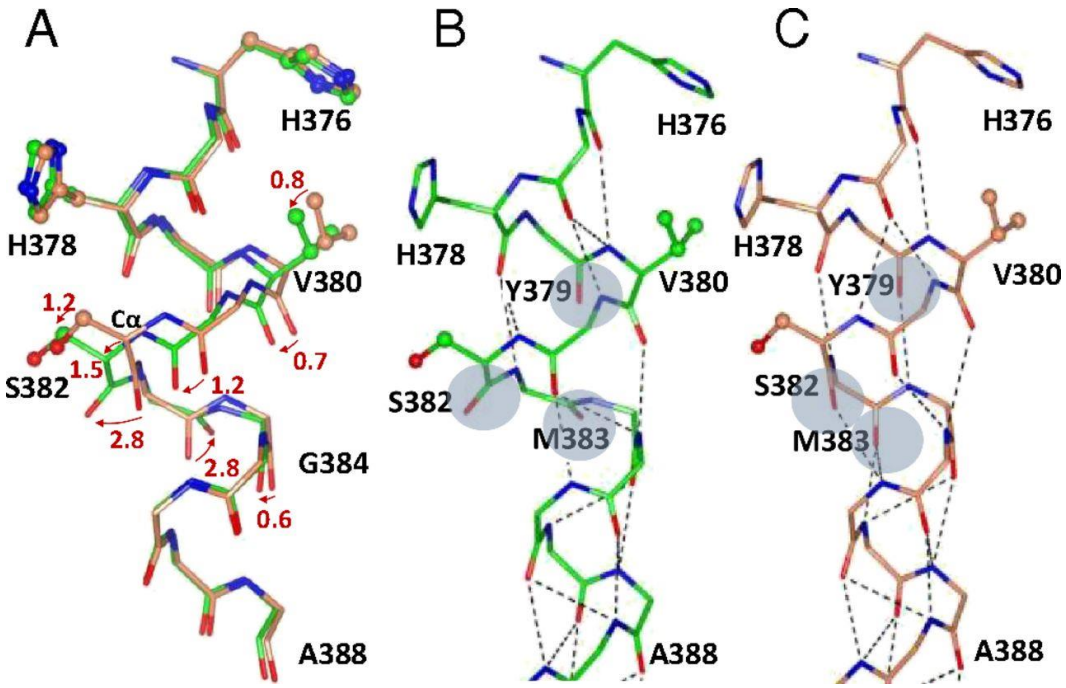

Figure 6.14 Allosteric Structural Transition in the Helix-X fragment Induced by Ligand Binding to Heme a3

(a) Superimposed structures of helix-X in CcO-CO and CcO-CO* obtained by SFX (green) and by synchrotron radiation (coral), respectively. The arrows designate the [380–384] peptide backbone movements (in Å) induced by ligand binding to heme a3. In the comparison of the two structures, the Cα carbon atoms of S382 and M383 differ by 1.5 Å, and the backbone carbonyl groups differ by 2.8 Å. Comparison of the alpha-helix hydrogen bonding in (b) the CcO-CO structure obtained by SFX and (c) the CcO-CO* structure obtained by synchrotron radiation. In C, in which the CO ligand was dissociated from the heme a3 iron atom, the normal α-helical H-bonding is established, whereas in B, the SFX structure, the α-helical H-bonding patterns of the carbonyl groups of Y379, S382, and M383 are disrupted. Figure and caption originally published in Ishigami, Zatsepin et al. (2017).

the metallocatalytic center that experiences localized radiation damage due to the high cross section of metals with X-rays. The use of an XFEL uniquely allows the X-ray damage to be bypassed due to the diffract and destroy serial nature of SFX. Furthermore, the use of a hydrated microcrystal slurry for sample delivery allows room temperature data collection at physiological pH, possibly critical in the ability to visualize the structural mechanism. These advantages were apparent when comparing the structure obtained from an XFEL and that from a synchrotron, in which the Fe-CO bond was cleaved. The results from this research uncover an allosteric conformational transition that is triggered by ligand binding to a heme, illustrated in figure 6.14. Among other insights gained, the biologically relevant structure showed visualization of a bent Fe-C-O moiety, agreeing with observed deviations in the correlation between frequencies of the Fe-CO and C-O stretching modes (Egawa, Haber et al. 2015). My contributions to this work were sample characterization, sample preparation, sample delivery, participation in SFX data collection at LCLS as well as data evaluation with special focus on hitfinding and online monitoring, and log keeping during the beamtime.

Enzyme intermediates captured "on-the-fly" by mix-and-inject serial crystallography

bioRxiv (2017): 202432 ol(Olmos, Pandey et al. 2017)

Jose Olmos[a], Suraj Pandey[b], Jose M. Martin-Garcia[c], George Calvey[d], Andrea Katz[d], Juraj Knoska[e,f], Christopher Kupitz[b], Mark S. Hunter[g], Mengning Liang[g], Dominik Oberthuer[e], Oleksandr Yefanov[e], Max Wiedorn[e,f], Michael Heyman[h], Mark Holl[c], Kanupriya Pande[i] , Anton Barty[e], Mitchell D. Miller[a], Stephan Stern[e], Shatabdi RoyChowdhury[c], Jesse Coe[c], Nirupa Nagaratnam[c], James Zook[c], Jacob Verburgt[b,j], Tyler Norwood[b], Ishwor Poudyal[b], David Xu[a], Jason Koglin[g], Matt Seaberg[g], Yun Zhao[c], Saša Bajt[k] , Thomas Grant[l] , Valerio Mariani[e], Garrett Nelson[m], Ganesh Subramanian[m], Euiyoung Bae[n], Raimund Fromme[c] , Russel Fung[b], Peter Schwander[b], Matthias Frank[o], Thomas White[e], Uwe Weierstallm, Nadia Zatsepin[m], John Spence[m], Petra Fromme[c], Henry N. Chapman[e,f,p], Lois Pollack[d], Lee Tremblay[q,r], Abbas Ourmazd[b], George N. Phillips, Jr.[a], Marius Schmidt[b]

[a] Department of BioSciences, Rice University, 6100 Main Street, Houston, Texas 77005, USA
[b] Physics Department, University of Wisconsin-Milwaukee, 3135 N. Maryland Ave, Milwaukee, Wisconsin 53211, USA
[c] School of Molecular Sciences and Biodesign Center for Applied Structural Discovery, Arizona State University, Tempe, Arizona 85287-1604, USA
[d] Department of Applied and Engineering Physics, Cornell University, 254 Clark Hall, Ithaca, New York 14853, USA
[e] Center for Free-Electron Laser Science, DESY, Notkestrasse 85, 22607 Hamburg, Germany
[f] University of Hamburg, Luruper Chaussee 149, 22761 Hamburg, Germany
[g] Linac Coherent Light Source, Stanford Linear Accelerator Center (SLAC) National Accelerator Laboratory, 2575 Sand Hill Road, Menlo Park, California 94025, USA

[h] Max Planck Institut fuer Biochemie, Am Klopferspitz 18, 82152 Planegg, Germany
[i] Lawrence Berkeley National Lab, 1 Cyclotron Road, Berkeley CA 94720
[j] Milwaukee School of Engineering, Milwaukee WI 53202-3109, USA
[k] Photon Science, DESY, Notkestrasse 85, 22607 Hamburg, Germany
[l] University of New York Buffalo, Hauptman-Woodward Institute, 700 Ellicott St, Buffalo, NY 14203, USA. [m] Department of Physics, Arizona State University, Tempe, Arizona 85287, USA
[n] Department of Agricultural Biotechnology, Seoul National University, Seoul 151-921, Korea
[o] Lawrence Livermore National Laboratory, Livermore, CA 94550, USA
[p] Centre for Ultrafast Imaging, Luruper Chaussee 149, 22761 Hamburg, Germany
[q] 4Marbles Inc., 1900 Belvedere Pl, Westfield, Indiana 46074, USA
[r] GlaxoSmithKline, Gunnels Wood Road, Stevenage, SG1 2NY, UK

Abstract

Ever since the first atomic structure of an enzyme was solved, the discovery of the mechanism and dynamics of reactions catalyzed by biomolecules has been the key goal for the understanding of the molecular processes that drive life on earth. Despite a large number of successful methods for trapping reaction intermediates, the direct observation of an ongoing reaction has been possible only in rare and exceptional cases. Here, we demonstrate a general method for capturing enzyme catalysis 'in action' by 'mix-andinject serial crystallography'. Specifically, we follow the catalytic reaction of the Mycobacterium tuberculosis β-lactamase with the 3rd generation antibiotic ceftriaxone by time-resolved serial femtosecond crystallography. The results reveal, in near atomic detail, antibiotic cleavage and inactivation on the millisecond to second time scales including the crossover from transition state kinetics to steady-state kinetics.

This article reports mix-and-inject TR-SFX of BlaC and its substrate antibiotic Ceftriaxone in the ms to s regime, following up on previously summarized experiments reported in Kupitz, Olmos Jr et al. (2017). Two different crystal morphologies were compared at time delays after initial reaction initiation of 30 ms, 100 ms, 500 ms and 2 s using in nozzle mixing as described in Calvey, Katz et al. (2016). This marked the first sub-second diffusive mixing TR-SFX to be reported. Analysis of the data showed the enzyme substrate complex (ES) occurring by the 30 ms time point and continuing to dominate through the 100 ms time point. By the 500 ms time point, an increased occupancy of a state in which BlaC and a ligand presumed to be cleaved Ceftriaxone are covalently bound is observed (E-CFO*). Interestingly, there were differences observed in the electron densities obtained from the two morphologies even though both showed highly similar overall structures and occupancy progressions. This suggests that a critical role may be played by the packing beyond whether or not the active site is accessible to a chemical trigger, particularly with the intercrystal diffusion rates and subsequent reaction initiation homogeneity. Figure 6.15 shows the calculated profile of the different states over the reaction timeline as a function of

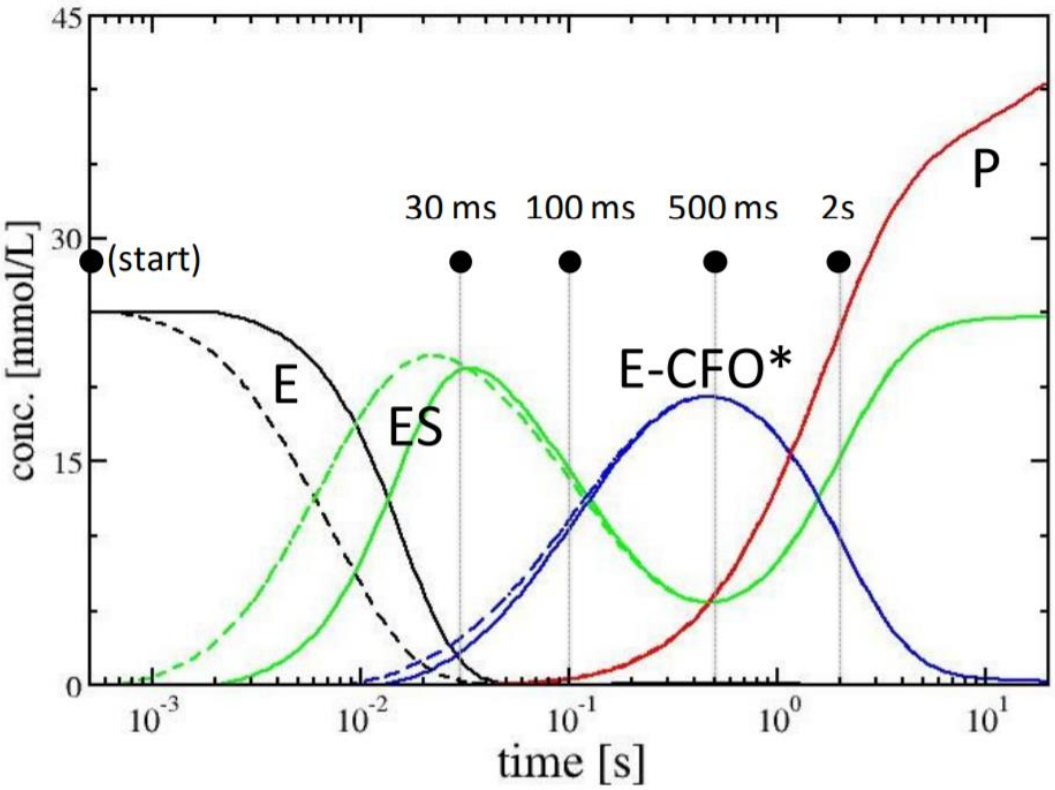

Figure 6.15 Concentration Profile of the Catalytic BlaC Reaction with Ceftriaxone

Concentration profile of the catalytic BlaC reaction with CEF as simulated with realistic parameters and a kinetic mechanism. The solid lines are calculated with τD = 15 ms, the dashed lines with τD = 1.5 ms. Black lines: free enzyme (E). Green lines: enzyme substrate complex (ES). Blue lines: enzyme acyl-intermediate complex (E-CFO*). Red lines: product P (CFO, inactive CEF without leaving group, lactam ring open), released from the enzyme. Black dots: observed time-delays. Figure and caption originally from Olmos, Pandey et al. (2017).

concentration over time, highlighting that visualization of the intermediates in this system are minimally effected by diffusion times. My contribution to this research included sample loading, sample delivery, and logging of the experiment.

Supersaturation-controlled microcrystallization and visualization analysis for serial femtosecond crystallography

Scientific Reports 8.1 (2018): 2541.(Lee, Kim et al. 2018)

Dan Bi Lee[1], Jong-Min Kim[2], Jong Hyeon Seok[1], Ji-Hye Lee[1], Jae Deok Jo[1], Ji Young Mun[3], Chelsie Conrad[4], **Jesse Coe**[4], Gerrett Nelson[5], Brenda Hogue[6], Thomas A. White[7], Nadia Zatsepin[5], Uwe Weierstall[5], Anton Barty[7], Henry Chapman[7], Petra Fromme[4], John Spence[5], Mi Sook Chung[8], Chang-Hyun Oh[2] & Kyung Hyun Kim[1]

1 Department of Biotechnology & Bioinformatics, Korea University, Sejong, Korea.
2 Department of Electronics & Information Engineering, Korea University, Sejong, Korea.

3 Department of Structure and Function of Neural Network, Korea Brain Research Institute, Daegu, Korea.
4 Department of Chemistry, Arizona State University, Tempe, Arizona, USA.
5 Department of Physics, Arizona State University, Tempe, Arizona, USA.
6 Biodesign Center for Applied Structural Discovery, Arizona State University, Tempe, Arizona, USA.
7 Center for Free-Electron Laser Science, Deutsches Elektronen-Synchrotron DESY, Hamburg, Germany.
8 Department of Food and Nutrition, Duksung Women's University, Seoul, Korea.

Abstract

Time-resolved serial femtosecond crystallography with X-ray free electron laser (XFEL) holds the potential to view fast reactions occurring at near-physiological temperature. However, production and characterization of homogeneous micron-sized protein crystals at high density remain a bottleneck, due to the lack of the necessary equipments in ordinary laboratories. We describe here supersaturationcontrolled microcrystallization and visualization and analysis tools that can be easily used in any laboratory. The microcrystallization conditions of the influenza virus hemagglutinin were initially obtained with low reproducibility, which was improved by employing a rapid evaporation of hanging drops. Supersaturation-controlled microcrystallization was then developed in a vapor diffusion mode, where supersaturation was induced by evaporation in hanging drops sequentially for durations ranging from 30 sec to 3 min, depending on the protein. It was applied successfully to the microcrystal formation of lysozyme, ferritin and hemagglutinin with high density. Moreover, visualization and analysis tools were developed to characterize the microcrystals observed by light microscopy. The size and density distributions of microcrystals analyzed by the tools were found to be consistent with the results of manual analysis, further validated by high-resolution microscopic analyses. Our supersaturation controlled microcrystallization and visualization and analysis tools will provide universal access to successful XFEL studies.

This article describes a new microcrystallization technique for creating crystals suitable for SFX studies using rapid evapo-concentration. The new method was validated using three different proteins as model systems and produced showers of microcrystals that were formed duing the evapo-concentration using vapor diffusion. The crystals were then characterized using microscopy, SONICC and DLS as well as a use of a hemocytometer for density measurement. SFX data were collected for all three proteins at an XFEL with a structural solution being obtained for lysozyme up to 1.9 Å. The hemagglutinin showed diffraction up to 3.2 Å though a structure could not be obtained due to minimal sample volume and a loss of resolution upon mixing with agarose. My contribution to this paper was crystallization of the lysozyme, preparation and embedding of the hemagglutinin with agarose, sample characterization, sample loading, sample

injection participation in SFX data collection at LCLS as well as participation in data evaluation including hitfinding, as well as comments and edits to the manuscript.

Snapshot of the Ferryl Intermediate of the Oxygen Reduction by the Cytochrome c Oxidase based on time-resolved femtosecond crystallography

Submitted and under review

Izumi Ishigami[1], Ariel Lewis-Ballester[1], Austin Echelmeier[2,3], Gerrit F. Brehm[2,3], Nadia A. Zatsepin[2,4], Thomas D. Grant[5], **Jesse Coe**[2,3], Garrett Nelson[2,4], Shangji Zhang[2,3], Zachary F. Dobson[2,3], Sebastien Boutet[6], Raymond G. Sierra[6], Alexander Batyuk[6], Petra Fromme[2,3], Raimund Fromme[2,3], John Spence[4], Alexandra Ros[2,3], Syun-Ru Yeh[1] and Denis L. Rousseau[1]

1 Department of Physiology and Biophysics, Albert Einstein College of Medicine, Bronx, NY, 10461, USA.
2 Biodesign Center for Applied Structural Discovery, The Biodesign Institute, Arizona State University, Tempe, AZ, 85287, USA.
3 School of Molecular Sciences, Arizona State University, Tempe, AZ 85287, USA.
4 Department of Physics, Arizona State University, Tempe, AZ, 85287, USA.
5 Hauptman-Woodward Institute and SUNY University of Buffalo, Buffalo, NY, 14203, USA.
6 SLAC National Accelerator Laboratory, Menlo Park. CA, 94025, USA.

Abstract

Cytochrome *c* oxidase catalyzes the reduction of dioxygen to water and harnesses the redox energy to pump protons across the inner mitochondrial membrane. How the oxygen reaction is coupled to proton translocation remains unproven. By time-resolved serial femtosecond crystallography, coupled with a mix-and-inject method, we identified the transient **F**-intermediate in the oxygen reaction, in which the heme a_3 iron atom is in a ferryl ($Fe^{4+}=O^{2-}$) configuration. The intermediate is characterized by (*i*) an allosteric transition which poises a helix-X segment to be in an open conformation, (*ii*) a 120° rotation of the farnesyl sidechain of heme *a*, and (*iii*) a large conformational change in loop-I-II. In addition, a new water molecule is identified in the catalytic site, 2.6 Å from the oxygen atom of Y244. These data offer new insights into the mechanism by which the oxygen chemistry drives unidirectional proton translocation through the protein matrix.

This manuscript reports the crystal structure of the F intermediate of bovine cytochrome *c* oxidase (bC*c*O) through a diffusive mixing TR-SFX experiment. Previously reported spectroscopic results support a sequential mechanism for the reduction of O_2 whereby a reduced heme-iron first binds an O_2 and reduces it first to a superoxide (**A**). This is followed by two distinct ferryl intermediates, first **P** by which the two electrons are acquired from a copper and a nearby tyrosine (which concurrently forms a radical) followed by **F** in which a second electron is gained from the heme and coupled with a proton to form a tyrosinate. This state then proceeds to a hydroxide

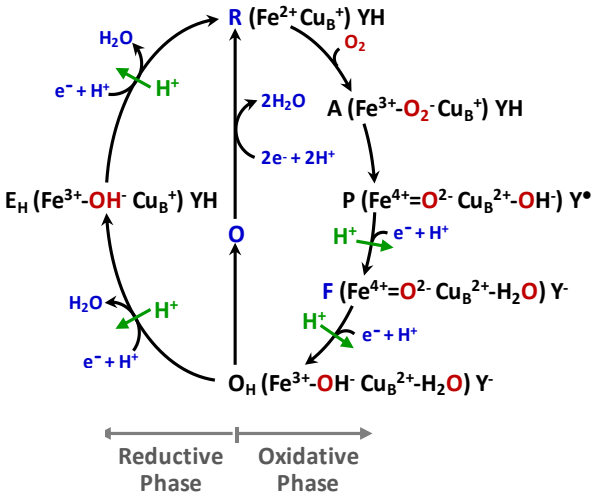

Figure 6.16 Proposed O_2 Reduction Cycle of bC*c*O

Highlighted putative intermediates of bCcO in the reduction of O2 and their oxidative and chemical composition with respect ot the copper-heme binuclear active site, ligands and the state of tyrosine Y244 which is implicated in the mechanism. Figure from Ishigami et. al (in submission).

bound state and proceeds through the cycle from there. This proposed reaction cycle is shown in figure 6.16. Previous to this work, none of the hypothesized oxygen intermediates had been identified, hindering mechanistic understanding of this process. However, spectroscopic assessment of the reaction cycle in the crystals showed that the **F** intermediate was sustained *in crystallo* for much longer than what had been observed in solution, stabilizing the F intermediate for up to 600 s.

The experiments were carried out by using a microfluidic device to mix an anoxygenic suspension of bC*c*O crystals with an oxygenated buffer solution that allowed for diffusive mixing between the two solutions to occur within 10 ms. With the mobility of O_2 as a substrate, the 20 x 20 x 4 µm bC*c*O crystals allowed for diffusive mixing into the crystal to occur within another 2 ms, giving a reaction initiation homogeneity within 12 ms. By manipulating flow rate and post-mixing path length, X-ray diffraction data were collected at multiple time points and a full TR-SFX data set was collected at 8 seconds that showed signature features of the anticipated **F** intermediate including a rotation of the farnesyl sidechain from a heme and movement of helix X, which coordinates the active site. This allowed novel insight to be gained on the mechanism of proton translocation and the oxidative phase of oxygen reduction by bC*c*O. My contributions to this project included sample characterization and preparation as well as injection, experimental setup and data collection at LCLS and real-time data monitoring and initial data evaluation.

References

Abdallah, B. G., T.-C. Chao, C. Kupitz, P. Fromme and A. Ros (2013). "Dielectrophoretic sorting of membrane protein nanocrystals." ACS nano **7**(10): 9129-9137.

Abdallah, B. G., S. Roy-Chowdhury, J. Coe, P. Fromme and A. Ros (2015). "High throughput protein nanocrystal fractionation in a microfluidic sorter." Anal Chem **87**(8): 4159-4167.

Abdallah, B. G., N. A. Zatsepin, S. Roy-Chowdhury, J. Coe, C. E. Conrad, K. Dörner, R. G. Sierra, H. P. Stevenson, F. Camacho-Alanis and T. D. Grant (2015). "Microfluidic sorting of protein nanocrystals by size for X-ray free-electron laser diffraction." Structural Dynamics **2**(4): 041719.

Abdelhamid, E. E., M. Sultana, P. Portoghese and A. Takemori (1991). "Selective blockage of delta opioid receptors prevents the development of morphine tolerance and dependence in mice." Journal of Pharmacology and Experimental Therapeutics **258**(1): 299-303.

Bionta, M. R., H. Lemke, J. Cryan, J. Glownia, C. Bostedt, M. Cammarata, J.-C. Castagna, Y. Ding, D. Fritz and A. Fry (2011). "Spectral encoding of x-ray/optical relative delay." Optics express **19**(22): 21855-21865.

Boutet, S., L. Lomb, G. J. Williams, T. R. Barends, A. Aquila, R. B. Doak, U. Weierstall, D. P. DePonte, J. Steinbrener and R. L. Shoeman (2012). "High-resolution protein structure determination by serial femtosecond crystallography." Science **337**(6092): 362-364.

Breaker, R. R. (2012). "Riboswitches and the RNA world." Cold Spring Harbor perspectives in biology **4**(2): a003566.

Calvey, G. D., A. M. Katz, C. B. Schaffer and L. Pollack (2016). "Mixing injector enables time-resolved crystallography with high hit rate at X-ray free electron lasers." Structural Dynamics **3**(5): 054301.

Chapman, H. N., P. Fromme, A. Barty, T. A. White, R. A. Kirian, A. Aquila, M. S. Hunter, J. Schulz, D. P. DePonte and U. Weierstall (2011). "Femtosecond X-ray protein nanocrystallography." Nature **470**(7332): 73-77.

Coe, J., C. Kupitz, S. Basu, C. E. Conrad, S. Roy-Chowdhury, R. Fromme and P. Fromme (2015). "Crystallization of Photosystem II for Time-Resolved Structural Studies Using an X-ray Free Electron Laser." Methods Enzymol **557**: 459-482.

Coe, J. and P. Fromme (2016). "Serial femtosecond crystallography opens new avenues for Structural Biology." Protein and peptide letters **23**(3): 255-272.

Conrad, C. E., S. Basu, D. James, D. Wang, A. Schaffer, S. Roy-Chowdhury, N. A. Zatsepin, A. Aquila, J. Coe, C. Gati, M. S. Hunter, J. E. Koglin, C. Kupitz, G. Nelson, G. Subramanian, T. A. White, Y. Zhao, J. Zook, S. Boutet, V. Cherezov, J. C. Spence, R. Fromme, U. Weierstall and P. Fromme (2015). "A novel inert crystal delivery medium for serial femtosecond crystallography." IUCrJ **2**(Pt 4): 421-430.

Conrad, C. E., S. Basu, D. James, D. Wang, A. Schaffer, S. Roy-Chowdhury, N. A. Zatsepin, A. Aquila, J. Coe, C. Gati, M. S. Hunter, J. E. Koglin, C. Kupitz, G. Nelson, G. Subramanian, T. A. White, Y. Zhao, J. Zook, S. b. Boutet, V. Cherezov, J. C. H. Spence, R. Fromme, U. Weierstall and P. Fromme (2015) "A novel inert crystal delivery medium for serial femtosecond crystallography." IUCrJ **2**.

Dow, X. Y., C. M. Dettmar, E. L. DeWalt, J. A. Newman, A. R. Dow, S. Roy-Chowdhury, J. D. Coe, C. Kupitz, P. Fromme and G. J. Simpson (2016). "Second harmonic generation correlation spectroscopy for

characterizing translationally diffusing protein nanocrystals." Acta Crystallographica Section D: Structural Biology **72**(7): 849-859.

Egawa, T., J. Haber, J. A. Fee, S.-R. Yeh and D. L. Rousseau (2015). "Interactions of CuB with Carbon Monoxide in Cytochrome c Oxidase: Origin of the Anomalous Correlation between the Fe–CO and C–O Stretching Frequencies." The Journal of Physical Chemistry B **119**(27): 8509-8520.

Fenalti, G., P. M. Giguere, V. Katritch, X.-P. Huang, A. A. Thompson, V. Cherezov, B. L. Roth and R. C. Stevens (2014). "Molecular control of δ-opioid receptor signalling." Nature **506**(7487): 191.

Fenalti, G., N. A. Zatsepin, C. Betti, P. Giguere, G. W. Han, A. Ishchenko, W. Liu, K. Guillemyn, H. Zhang, D. James, D. Wang, U. Weierstall, J. C. Spence, S. Boutet, M. Messerschmidt, G. J. Williams, C. Gati, O. M. Yefanov, T. A. White, D. Oberthuer, M. Metz, C. H. Yoon, A. Barty, H. N. Chapman, S. Basu, J. Coe, C. E. Conrad, R. Fromme, P. Fromme, D. Tourwe, P. W. Schiller, B. L. Roth, S. Ballet, V. Katritch, R. C. Stevens and V. Cherezov (2015). "Structural basis for bifunctional peptide recognition at human delta-opioid receptor." Nat Struct Mol Biol **22**(3): 265-268.

Granier, S., A. Manglik, A. C. Kruse, T. S. Kobilka, F. S. Thian, W. I. Weis and B. K. Kobilka (2012). "Structure of the δ-opioid receptor bound to naltrindole." Nature **485**(7398): 400.

Hajdu, J., R. Neutze, T. Sjögren, K. Edman, A. Szöke, R. C. Wilmouth and C. M. Wilmot (2000). "Analyzing protein functions in four dimensions." Nature Structural and Molecular Biology **7**(11): 1006.

Hartmann, N., W. Helml, A. Galler, M. Bionta, J. Grünert, S. Molodtsov, K. Ferguson, S. Schorb, M. Swiggers and S. Carron (2014). "Sub-femtosecond precision measurement of relative X-ray arrival time for free-electron lasers." Nature Photonics **8**(9): 706.

Haupert, L. M. and G. J. Simpson (2011). "Screening of protein crystallization trials by second order nonlinear optical imaging of chiral crystals (SONICC)." Methods **55**(4): 379-386.

Healy, J. R., P. Bezawada, J. Shim, J. W. Jones, M. A. Kane, A. D. MacKerell Jr, A. Coop and R. R. Matsumoto (2013). "Synthesis, modeling, and pharmacological evaluation of UMB 425, a mixed μ agonist/δ antagonist opioid analgesic with reduced tolerance liabilities." ACS chemical neuroscience **4**(9): 1256-1266.

Hernandez, R., C. Sinodis and D. T. Brown (2005). "Sindbis virus: propagation, quantification, and storage." Current protocols in microbiology: 15B. 11.11-15B. 11.41.

Ihee, H., S. Rajagopal, V. Šrajer, R. Pahl, S. Anderson, M. Schmidt, F. Schotte, P. A. Anfinrud, M. Wulff and K. Moffat (2005). "Visualizing reaction pathways in photoactive yellow protein from nanoseconds to seconds." Proceedings of the National Academy of Sciences of the United States of America **102**(20): 7145-7150.

Ishigami, I., N. A. Zatsepin, M. Hikita, C. E. Conrad, G. Nelson, J. D. Coe, S. Basu, T. D. Grant, M. H. Seaberg and R. G. Sierra (2017). "Crystal structure of CO-bound cytochrome c oxidase determined by serial femtosecond X-ray crystallography at room temperature." Proceedings of the National Academy of Sciences **114**(30): 8011-8016.

Jung, Y. O., J. H. Lee, J. Kim, M. Schmidt, K. Moffat, V. Šrajer and H. Ihee (2013). "Volume-conserving trans–cis isomerization pathways in photoactive yellow protein visualized by picosecond X-ray crystallography." Nature chemistry **5**(3): 212.

Kang, Y., X. E. Zhou, X. Gao, Y. He, W. Liu, A. Ishchenko, A. Barty, T. A. White, O. Yefanov and G. W. Han (2015). "Crystal structure of rhodopsin bound to arrestin by femtosecond X-ray laser." Nature **523**(7562): 561-567.

Kim, Y. J., K. P. Hofmann, O. P. Ernst, P. Scheerer, H.-W. Choe and M. E. Sommer (2013). "Crystal structure of pre-activated arrestin p44." Nature **497**(7447): 142.

King, A. M., E. Lefkowitz, M. J. Adams and E. B. Carstens (2011). Virus taxonomy: ninth report of the International Committee on Taxonomy of Viruses, Elsevier.

Kupitz, C., S. Basu, I. Grotjohann, R. Fromme, N. A. Zatsepin, K. N. Rendek, M. S. Hunter, R. L. Shoeman, T. A. White and D. Wang (2014). "Serial time-resolved crystallography of photosystem II using a femtosecond X-ray laser." Nature **513**(7517): 261-265.

Kupitz, C., J. L. Olmos Jr, M. Holl, L. Tremblay, K. Pande, S. Pandey, D. Oberthür, M. Hunter, M. Liang and A. Aquila (2017). "Structural enzymology using X-ray free electron lasers." Structural Dynamics **4**(4): 044003.

Lawrence, R. M., C. E. Conrad, N. A. Zatsepin, T. D. Grant, H. Liu, D. James, G. Nelson, G. Subramanian, A. Aquila and M. S. Hunter (2015). "Serial femtosecond X-ray diffraction of enveloped virus microcrystals." Structural Dynamics **2**(4): 041720.

Lee, D. B., J.-M. Kim, J. H. Seok, J.-H. Lee, J. D. Jo, J. Y. Mun, C. Conrad, J. Coe, G. Nelson and B. Hogue (2018). "Supersaturation-controlled microcrystallization and visualization analysis for serial femtosecond crystallography." Scientific Reports **8**(1): 2541.

Mandal, M., B. Boese, J. E. Barrick, W. C. Winkler and R. R. Breaker (2003). "Riboswitches control fundamental biochemical pathways in Bacillus subtilis and other bacteria." Cell **113**(5): 577-586.

Manglik, A., A. C. Kruse, T. S. Kobilka, F. S. Thian, J. M. Mathiesen, R. K. Sunahara, L. Pardo, W. I. Weis, B. K. Kobilka and S. Granier (2012). "Crystal structure of the μ-opioid receptor bound to a morphinan antagonist." Nature **485**(7398): 321.

Martin-Garcia, J. M., C. E. Conrad, G. Nelson, N. Stander, N. A. Zatsepin, J. Zook, L. Zhu, J. Geiger, E. Chun and D. Kissick (2017). "Serial millisecond crystallography of membrane and soluble protein microcrystals using synchrotron radiation." IUCrJ **4**(4).

Multiphysics, C. "2013, Version 4.4, COMSOL." Inc., Burlington, MA, USA.

Nahvi, A., N. Sudarsan, M. S. Ebert, X. Zou, K. L. Brown and R. R. Breaker (2002). "Genetic control by a metabolite binding mRNA." Chemistry & biology **9**(9): 1043-1049.

Nogly, P., D. James, D. Wang, T. A. White, N. Zatsepin, A. Shilova, G. Nelson, H. Liu, L. Johansson and M. Heymann (2015). "Lipidic cubic phase serial millisecond crystallography using synchrotron radiation." IUCrJ **2**(2): 0-0.

Nogly, P., V. Panneels, G. Nelson, C. Gati, T. Kimura, C. Milne, D. Milathianaki, M. Kubo, W. Wu and C. Conrad (2016). "Lipidic cubic phase injector is a viable crystal delivery system for time-resolved serial crystallography." Nature communications **7**: 12314.

Olmos, J., S. Pandey, J. M. Martin-Garcia, G. Calvey, A. Katz, J. Knoska, C. Kupitz, M. S. Hunter, M. Liang and D. Oberthuer (2017). "Authentic Enzyme Intermediates Captured" on-the-fly" by Mix-and-Inject Serial Crystallography." bioRxiv: 202432.

Pande, K., C. D. M. Hutchinson, G. Groenhof, A. Aquila, J. S. Robinson, J. Tenboer, S. Basu, S. Boutet, D. Deponte, M. Liang, T. White, N. Zatsepin, O. Yefanov, D. Morozov, D. Oberthuer, C. Gati, G. Subramanian, D. James, Y. Zhao, J. Koralek, J. Brayshaw, C. Kupitz, C. Conrad, S. Roy-Chowdhury, J. Coe, M. Metz, X. Paulraj Lourdu, T. Grant, J. Koglin, G. Ketawala, R. Fromme, V. Srajer, R. Henning, J. Spence, A. Ourmazd, P. Schwander, U. Weierstall, M. Frank, P. Fromme, A. Barty, H. Chapman, K. Moffat, J. J. Van Thor and M.

Schmidt (2015). "Femtosecond Structural Dynamics Drives the Trans/Cis Isomerization in Photoactive Yellow Protein." in submission.

Pasternak, G. W. (2014). "Opioids and their receptors: Are we there yet?" Neuropharmacology **76**: 198-203.

Rieder, R., K. Lang, D. Graber and R. Micura (2007). "Ligand-Induced Folding of the Adenosine Deaminase A-Riboswitch and Implications on Riboswitch Translational Control." Chembiochem **8**(8): 896-902.

Sass, H. J., G. Büldt, R. Gessenich, D. Hehn, D. Neff, R. Schlesinger, J. Berendzen and P. Ormos (2000). "Structural alterations for proton translocation in the M state of wild-type bacteriorhodopsin." Nature **406**(6796): 649.

Schiller, P. W. (2010). "Bi-or multifunctional opioid peptide drugs." Life sciences **86**(15-16): 598-603.

Schmidt, M., V. Srajer, R. Henning, H. Ihee, N. Purwar, J. Tenboer and S. Tripathi (2013). "Protein energy landscapes determined by five-dimensional crystallography." Acta Crystallographica Section D: Biological Crystallography **69**(12): 2534-2542.

Shukla, A. K., A. Manglik, A. C. Kruse, K. Xiao, R. I. Reis, W.-C. Tseng, D. P. Staus, D. Hilger, S. Uysal and L.-Y. Huang (2013). "Structure of active β-arrestin-1 bound to a G-protein-coupled receptor phosphopeptide." Nature **497**(7447): 137.

Stagno, J., Y. Liu, Y. Bhandari, C. Conrad, S. Panja, M. Swain, L. Fan, G. Nelson, C. Li and D. Wendel (2016). "Structures of riboswitch RNA reaction states by mix-and-inject XFEL serial crystallography." Nature.

Stagno, J., Y. Liu, Y. Bhandari, C. Conrad, S. Panja, M. Swain, L. Fan, G. Nelson, C. Li and D. Wendel (2017). "Structures of riboswitch RNA reaction states by mix-and-inject XFEL serial crystallography." Nature **541**(7636): 242.

Tenboer, J., S. Basu, N. Zatsepin, K. Pande, D. Milathianaki, M. Frank, M. Hunter, S. Boutet, G. J. Williams and J. E. Koglin (2014). "Time-resolved serial crystallography captures high-resolution intermediates of photoactive yellow protein." Science **346**(6214): 1242-1246.

Tremblay, L. W., H. Xu and J. S. Blanchard (2010). "Structures of the Michaelis complex (1.2 Å) and the covalent acyl intermediate (2.0 Å) of cefamandole bound in the active sites of the Mycobacterium tuberculosis β-lactamase K73A and E166A mutants." Biochemistry **49**(45): 9685-9687.

Weierstall, U., D. James, C. Wang, T. A. White, D. Wang, W. Liu, J. C. Spence, R. B. Doak, G. Nelson and P. Fromme (2014). "Lipidic cubic phase injector facilitates membrane protein serial femtosecond crystallography." Nature communications **5**.

Zhang, H., H. Unal, C. Gati, G. W. Han, W. Liu, N. A. Zatsepin, D. James, D. Wang, G. Nelson, U. Weierstall, M. R. Sawaya, Q. Xu, M. Messerschmidt, G. J. Williams, S. Boutet, O. M. Yefanov, T. A. White, C. Wang, A. Ishchenko, K. C. Tirupula, R. Desnoyer, J. Coe, C. E. Conrad, P. Fromme, R. C. Stevens, V. Katritch, S. S. Karnik and V. Cherezov (2015). "Structure of the Angiotensin receptor revealed by serial femtosecond crystallography." Cell **161**(4): 833-844.

Zhang, J. and A. R. Ferré-D'Amaré (2014). "Dramatic improvement of crystals of large RNAs by cation replacement and dehydration." Structure **22**(9): 1363-1371.

Zhang, W., S. Mukhopadhyay, S. V. Pletnev, T. S. Baker, R. J. Kuhn and M. G. Rossmann (2002). "Placement of the structural proteins in Sindbis virus." Journal of virology **76**(22): 11645-11658.

7 CONCLUDING REMARKS AND OUTLOOK

Summary of Work and Accomplishments

Both SFX and SMX are relatively young techniques and are extremely multidisciplinary, requiring large teams and collaborations with varying specialties to perform successful investigations. Over the course of my time as a graduate student, I have been involved in over 70 beamtimes, 52 of which were at LCLS alone. Among this has been work on dozens of different targets ranging from photosynthetic membrane proteins to human GPCR drug targets to virus and RNA work. I have been fortunate to have the opportunity to explore temporal boundaries of pump-probe TR-SFX, the development and first implementations of diffusive mixing TR-SFX, structural discovery of impactful medical targets, advancing techniques for minimization of sample consumption, and successful implementation of serial crystallography at synchrotron sources. Over the course of exploring this variety of scientific problems and method development, I have gained expertise in protein production and purification, microcrystallogenesis, sample characterization and handling, sample delivery with both GDVNs and viscous injectors, data reduction and processing, time-resolved consideration for both pump-probe and diffusive mixing, and general experimental design.

In particular to the aims of this dissertation, I have successfully purified and crystallized photosynthetic membrane proteins PSII and PSI, including co-crystallization with Fd, for structural and time-resolved investigation using SFX and KDO8PS in efforts to develop and perform structural enzymology using TR-SFX and SMX. In the push towards elucidating the structural characteristics of PSII as it progresses through the Kok cycle, method development including TR-SFX on fixed targets and use of diffuse scattering for higher resolution structural elucidation have been attained. Towards understanding the electron transfer process between PSI and Fd, crystallization conditions have been improved and a control over size and homogeneity achieved that paves the way for successful TR-SFX of the co-complex. In addition, ongoing research utilizing the method of resolution extension using continuous diffraction is underway towards the first structure of the co-complex in its ground state.

KDO8PS microcrystallization techniques have been improved and now size controlled, homogeneous microcrystals ranging from 2-25 µm can be achieved, critical for homogenizing reaction homogeneity in current and future diffusive mixing TR-SFX and SMX experiments with it. They have been shown to be well diffracting and practically achievable in the high quantities necessary for TR-SFX. Chemical activity *in crystallo* has been confirmed and initial time points have been identified along with the experimental design necessary to achieve them. In addition, a high-resolution structure of the apo form is likely to arise out of the recent beamtime that has the distinction of being the second SFX experiment performed at the EU-XFEL

Outlook for Biology at XFELs

With the recent commissioning's of the EU-XFEL in Germany and the PAL XFEL in South Korea, first light at the SwissFEL in Switzerland, and ongoing construction of the upgraded LCLS-II in addition to the existing LCLS in California and SACLA in Japan, it is clear that there is a commitment to using these fourth-generation light sources to further our scientific understanding of issues facing the world today. This proliferation of XFEL sources is extremely valuable in particular to biology, with dedicated beamlines for structural biology occurring at each of these sources and a growing community of scientists dedicating their time to pushing the boundaries of this field. From the efforts towards making molecular movies with ultrashort temporal resolution and enzymatic activation, to damage-free high-resolution structures of metalloproteins and nanocrystals containing just hundreds of molecules, structural biology has enjoyed a renaissance of sorts in its ability and breadth to understand life at its most fundamental level thanks to the advent of the XFEL.

Over the past five years, the field of serial crystallography has matured through its infancy to a state where the power of the technique is being realized and continuously pushing forward to its full potential. I believe the heart of this potential lies with TR-SFX, with the ability to make 'molecular movies'. By visualizing macromolecules structurally along their reaction timeline, there lies an immense potential to revolutionize our ability to understand and reverse engineer the molecular machines that evolution has created to sustain and advance life through its existence here on earth. Truly, it has been an exciting time to be part of this burgeoning community, watching

it grow with innovative ideas and clever solutions that keep pushing forward the range of our scientific arsenal and expanding our knowledge of the world around us. Even better, there is surely more breakthroughs just around the corner with XFEL sources proliferating and the efficiency of data collection and processing improving every day. I feel humbly fortunate I was able to partake in this journey, it has been an experience I will carry with me for the rest of my life.

REFERENCES

Abdallah, B. G., T.-C. Chao, C. Kupitz, P. Fromme and A. Ros (2013). "Dielectrophoretic sorting of membrane protein nanocrystals." ACS nano **7**(10): 9129-9137.

Abdallah, B. G., S. Roy-Chowdhury, J. Coe, P. Fromme and A. Ros (2015). "High Throughput Protein Nanocrystal Fractionation in a Microfluidic Sorter." Analytical chemistry **87**(8): 4159-4167.

Abdallah, B. G., N. A. Zatsepin, S. Roy-Chowdhury, J. Coe, C. E. Conrad, K. Dörner, R. G. Sierra, H. P. Stevenson, T. D. Grant, G. Nelson, D. R. James, G. Calero, R. M. Wachter, J. C. H. Spence, U. Weierstall, P. Fromme and A. Ros (2015). "Microfluidic sorting of protein nanocrystals by size for XFEL diffraction." Structural Dynamics **2**: 041719.

Abdallah, B. G., S. Roy-Chowdhury, R. Fromme, P. Fromme and A. Ros (2016). "Protein Crystallization in an Actuated Microfluidic Nanowell Device." Crystal Growth & Design **16**: 2074-2082.

Abdelhamid, E. E., M. Sultana, P. Portoghese and A. Takemori (1991). "Selective blockage of delta opioid receptors prevents the development of morphine tolerance and dependence in mice." Journal of Pharmacology and Experimental Therapeutics **258**(1): 299-303.

Ackermann, W., G. Asova, V. Ayvazyan, A. Azima, N. Baboi, J. Bähr, V. Balandin, B. Beutner, A. Brandt and A. Bolzmann (2007). "Operation of a free-electron laser from the extreme ultraviolet to the water window." Nature photonics **1**(6): 336-342.

Allahgholi, A., J. Becker, L. Bianco, A. Delfs, R. Dinapoli, P. Goettlicher, H. Graafsma, D. Greiffenberg, H. Hirsemann and S. Jack (2015). "AGIPD, a high dynamic range fast detector for the European XFEL." Journal of Instrumentation **10**(01): C01023.

Altarelli, M., R. Brinkmann, M. Chergui, W. Decking, B. Dobson, S. Düsterer, G. Grübel, W. Graeff, H. Graafsma and J. Hajdu (2006). "The European x-ray free-electron laser." Technical design report, DESY **97**: 1-26.

Altarelli, M. (2010). "From 3rd-to 4th-generation light sources: Free-electron lasers in the X-ray range." Crystallography Reports **55**(7): 1145-1151.

Altarelli, M. and A. P. Mancuso (2014). "Structural biology at the European X-ray free-electron laser facility." Philosophical Transactions of the Royal Society of London B: Biological Sciences **369**(1647): 20130311.

Antonkine, M. L., P. Jordan, P. Fromme, N. Krauß, J. H. Golbeck and D. Stehlik (2003). "Assembly of protein subunits within the stromal ridge of photosystem I. Structural changes between unbound and sequentially PS I-bound polypeptides and correlated changes of the magnetic properties of the terminal iron sulfur clusters." Journal of molecular biology **327**(3): 671-697.

Aquila, A., M. S. Hunter, R. B. Doak, R. A. Kirian, P. Fromme, T. A. White, J. Andreasson, D. Arnlund, S. Bajt and T. R. Barends (2012). "Time-resolved protein nanocrystallography using an X-ray free-electron laser." Optics express **20**(3): 2706-2716.

Aquila, A., A. Barty, C. Bostedt, S. Boutet, G. Carini, D. DePonte, P. Drell, S. Doniach, K. Downing and T. Earnest (2015). "The linac coherent light source single particle imaging road map." Structural Dynamics **2**(4): 041701.

Arnlund, D., L. C. Johansson, C. Wickstrand, A. Barty, G. J. Williams, E. Malmerberg, J. Davidsson, D. Milathianaki, D. P. DePonte and R. L. Shoeman (2014). "Visualizing a protein quake with time-resolved X-ray scattering at a free-electron laser." Nature methods **11**(9): 923-926.

Aro, E.-M., I. Virgin and B. Andersson (1993). "Photoinhibition of photosystem II. Inactivation, protein damage and turnover." Biochimica et Biophysica Acta (BBA)-Bioenergetics **1143**(2): 113-134.

Asojo, O., J. Friedman, N. Adir, V. Belakhov, Y. Shoham and T. Baasov (2001). "Crystal structures of KDOP synthase in its binary complexes with the substrate phosphoenolpyruvate and with a mechanism-based inhibitor." Biochemistry **40**(21): 6326-6334.

Ayvazyan, V., N. Baboi, J. Bähr, V. Balandin, B. Beutner, A. Brandt, I. Bohnet, A. Bolzmann, R. Brinkmann and O. Brovko (2006). "First operation of a free-electron laser generating GW power radiation at 32 nm wavelength." The European Physical Journal D-Atomic, Molecular, Optical and Plasma Physics **37**(2): 297-303.

Ayyer, K., O. Yefanov, D. Oberthuer, S. Roy-Chowdhury, L. Galli, V. Mariani, S. Basu, J. Coe, C. Conrad, R. Fromme, A. Schaffer, K. Doerner, D. James, C. Kupitz, M. Metz, G. Nelson, P. L. Xavier, K. R. Beyerlein, M. Schmidt, I. Sarrou, J. Spence, U. Weierstall, T. White, J. H. Yang, Y. Zhao, M. Liang, A. Aquila, M. Hunter, J. S. Robinson, J. Koglin, S. Boutet, P. Fromme, A. Barty and H. Chapman (2016). "Macromolecular diffractive imaging using imperfect crystals." Nature **Accepted**.

Baasov, T. and A. Kohen (1995). "Synthesis, inhibition, and acid-catalyzed hydrolysis studies of model compounds of the proposed intermediate in the KDO8P-synthase-catalyzed reaction." Journal of the American Chemical Society **117**(23): 6165-6174.

Bai, K., G. V. Barnett, S. R. Kar and T. K. Das (2017). "Interference from Proteins and Surfactants on Particle Size Distributions Measured by Nanoparticle Tracking Analysis (NTA)." Pharmaceutical Research **34**(4): 800-808.

Balbirnie, M., R. Grothe and D. S. Eisenberg (2001). "An amyloid-forming peptide from the yeast prion Sup35 reveals a dehydrated β-sheet structure for amyloid." Proceedings of the National Academy of Sciences **98**(5): 2375-2380.

Barends, T. R., L. Foucar, S. Botha, R. B. Doak, R. L. Shoeman, K. Nass, J. E. Koglin, G. J. Williams, S. Boutet and M. Messerschmidt (2014). "De novo protein crystal structure determination from X-ray free-electron laser data." Nature **505**(7482): 244-247.

Barends, T. R., L. Foucar, A. Ardevol, K. Nass, A. Aquila, S. Botha, R. B. Doak, K. Falahati, E. Hartmann and M. Hilpert (2015). "Direct observation of ultrafast collective motions in CO myoglobin upon ligand dissociation." Science **350**(6259): 445-450.

Barty, A., C. Caleman, A. Aquila, N. Timneanu, L. Lomb, T. A. White, J. Andreasson, D. Arnlund, S. Bajt and T. R. Barends (2012). "Self-terminating diffraction gates femtosecond X-ray nanocrystallography measurements." Nature Photonics **6**(1): 35-40.

Barty, A., R. A. Kirian, F. R. Maia, M. Hantke, C. H. Yoon, T. A. White and H. Chapman (2014). "Cheetah: software for high-throughput reduction and analysis of serial femtosecond X-ray diffraction data." Journal of Applied Crystallography **47**(3): 1118-1131.

Berman, H. M., J. Westbrook, Z. Feng, G. Gilliland, T. N. Bhat, H. Weissig, I. N. Shindyalov and P. E. Bourne (2006). The protein data bank, 1999–. International Tables for Crystallography Volume F: Crystallography of biological macromolecules, Springer**:** 675-684.

Berne, B. J. and R. Pecora (1976). Dynamic light scattering: with applications to chemistry, biology, and physics, Courier Corporation.

Bionta, M. R., H. Lemke, J. Cryan, J. Glownia, C. Bostedt, M. Cammarata, J.-C. Castagna, Y. Ding, D. Fritz and A. Fry (2011). "Spectral encoding of x-ray/optical relative delay." Optics express **19**(22): 21855-21865.

Blankenship, R. E. and H. Hartman (1998). "The origin and evolution of oxygenic photosynthesis." Trends in biochemical sciences **23**(3): 94-97.

Blow, D. and F. Crick (1959). "The treatment of errors in the isomorphous replacement method." Acta Crystallographica **12**(10): 794-802.

Bolduc, J. M., D. H. Dyer, W. G. Scott, P. Singer, R. M. Sweet, D. Koshland and B. L. Stoddard (1995). "Mutagenesis and Laue structures of enzyme intermediates: isocitrate dehydrogenase." Science **268**(5215): 1312-1318.

Borie, B. (1965). "X-Ray Diffraction in Crystals, Imperfect Crystals, and Amorphous Bodies." Journal of the American Chemical Society **87**(1): 140-141.

Bourgeois, D., T. Ursby, M. Wulff, C. Pradervand, A. Legrand, W. Schildkamp, S. Labouré, V. Srajer, T. Teng and M. Roth (1996). "Feasibility and realization of single-pulse Laue diffraction on macromolecular crystals at ESRF." Journal of synchrotron radiation **3**(2): 65-74.

Boutet, S., L. Lomb, G. J. Williams, T. R. Barends, A. Aquila, R. B. Doak, U. Weierstall, D. P. DePonte, J. Steinbrener and R. L. Shoeman (2012). "High-resolution protein structure determination by serial femtosecond crystallography." Science **337**(6092): 362-364.

Bragg, W. H. and W. L. Bragg (1913). The structure of the diamond. Proc. R. Soc. Lond. A, The Royal Society.

Breaker, R. R. (2012). "Riboswitches and the RNA world." Cold Spring Harbor perspectives in biology **4**(2): a003566.

Brehms, W. and K. Diederichs (2014). "Breaking the indexing ambiguity in serial crystallography." Acta Crystallographica Section D **D70**: 101-109.

Brettel, K. (1997). "Electron transfer and arrangement of the redox cofactors in photosystem I." Biochimica et Biophysica Acta (BBA)-Bioenergetics **1318**(3): 322-373.

Britt, R. D., K. A. Campbell, J. M. Peloquin, M. L. Gilchrist, C. P. Aznar, M. M. Dicus, J. Robblee and J. Messinger (2004). "Recent pulsed EPR studies of the photosystem II oxygen-evolving complex: implications as to water oxidation mechanisms." Biochimica et Biophysica Acta (BBA)-Bioenergetics **1655**: 158-171.

Brown, G., K. Halbach, J. Harris and H. Winick (1983). "Wiggler and undulator magnets—A review." Nuclear Instruments and Methods in Physics Research **208**(1-3): 65-77.

Bublitz, M., K. Nass, N. D. Drachmann, A. J. Markvardsen, M. J. Gutmann, T. R. Barends, D. Mattle, R. L. Shoeman, R. B. Doak and S. Boutet (2015). "Structural studies of P-type ATPase–ligand complexes using an X-ray free-electron laser." IUCrJ **2**(4): 409-420.

Burmeister, W. P. (2000). "Structural changes in a cryo-cooled protein crystal owing to radiation damage." Acta Crystallographica Section D: Biological Crystallography **56**(3): 328-341.

Byrdin, M., P. Jordan, N. Krauss, P. Fromme, D. Stehlik and E. Schlodder (2002). "Light harvesting in photosystem I: modeling based on the 2.5-Å structure of photosystem I from Synechococcus elongatus." Biophysical journal **83**(1): 433-457.

Caffrey, M. (2015). "A comprehensive review of the lipid cubic phase or in meso method for crystallizing membrane and soluble proteins and complexes." Acta Crystallographica Section F: Structural Biology Communications **71**(1): 3-18.

Calvey, G. D., A. M. Katz, C. B. Schaffer and L. Pollack (2016). "Mixing injector enables time-resolved crystallography with high hit rate at X-ray free electron lasers." Structural Dynamics **3**(5): 054301.

Carr, B. and A. Malloy (2006). NanoParticle Tracking Analysis–The NANOSIGHT system.

Carugo, O. and K. D. Carugo (2005). "When X-rays modify the protein structure: radiation damage at work." Trends in Biochemical Sciences **30**(4): 213-219.

Chapman, H. N., A. Barty, M. J. Bogan, S. Boutet, M. Frank, S. P. Hau-Riege, S. Marchesini, B. W. Woods, S. Bajt and W. H. Benner (2006). "Femtosecond diffractive imaging with a soft-X-ray free-electron laser." Nature Physics **2**(12): 839-843.

Chapman, H. N., A. Barty, S. Marchesini, A. Noy, S. P. Hau-Riege, C. Cui, M. R. Howells, R. Rosen, H. He, J. C. Spence, U. Weierstall, T. Beetz, C. Jacobsen and D. Shapiro (2006). "High-resolution ab initio three-dimensional x-ray diffraction microscopy." J Opt Soc Am A Opt Image Sci Vis **23**(5): 1179-1200.

Chapman, H. N., P. Fromme, A. Barty, T. A. White, R. A. Kirian, A. Aquila, M. S. Hunter, J. Schulz, D. P. DePonte and U. Weierstall (2011). "Femtosecond X-ray protein nanocrystallography." Nature **470**(7332): 73-77.

Chasman, R., G. K. Green and E. Rowe (1975). "Preliminary design of a dedicated synchrotron radiation facility." IEEE Transactions on Nuclear Science **22**(3): 1765-1767.

Chen, A. U. and O. A. Basaran (2002). "A new method for significantly reducing drop radius without reducing nozzle radius in drop-on-demand drop production." Physics of fluids **14**: L1-L4.

Cheng, A., B. Hummel, H. Qiu and M. Caffrey (1998). "A simple mechanical mixer for small viscous lipid-containing samples." Chemistry and Physics of Lipids **95**(1): 11-21.

Coe, J., C. Kupitz, S. Basu, C. E. Conrad, S. Roy-Chowdhury, R. Fromme and P. Fromme (2015). "Crystallization of Photosystem II for Time-Resolved Structural Studies Using an X-ray Free Electron Laser." Methods Enzymol **557**: 459-482.

Coe, J. and P. Fromme (2016). "Serial femtosecond crystallography opens new avenues for Structural Biology." Protein and peptide letters **23**(3): 255-272.

Cohen, A. E., S. M. Soltis, A. Gonzalez, L. Aguila, R. Alonso-Mori, C. O. Barnes, E. L. Baxter, W. Brehmer, A. S. Brewster, A. T. Brunger, G. Calero, J. F. Chang, M. Chollet, P. Ehrensberger, T. L. Eriksson, Y. Feng, J. Hattne, B. Hedman, M. Hollenbeck, J. M. Holton, S. Keable, B. K. Kobilka, E. G. Kovaleva, A. C. Kruse, H. T. Lemke, G. Lin, A. Y. Lyubimov, A. Manglik, Mathews, II, S. E. McPhillips, S. Nelson, J. W. Peters, N. K. Sauter, C. A. Smith, J. Song, H. P. Stevenson, Y. Tsai, M. Uervirojnangkoorn, V. Vinetsky, S. Wakatsuki, W. I. Weis, O. A. Zadvornyy, O. B. Zeldin, D. Zhu and K. O. Hodgson (2014). "Goniometer-based femtosecond crystallography with X-ray free electron lasers." Proc Natl Acad Sci U S A **111**(48): 17122-17127.

Conrad, C. E., S. Basu, D. James, D. Wang, A. Schaffer, S. Roy-Chowdhury, N. A. Zatsepin, A. Aquila, J. Coe, C. Gati, M. S. Hunter, J. E. Koglin, C. Kupitz, G. Nelson, G. Subramanian, T. A. White, Y. Zhao, J. Zook, S. b. Boutet, V. Cherezov, J. C. H. Spence, R. Fromme, U. Weierstall and P. Fromme (2015) "A novel inert crystal delivery medium for serial femtosecond crystallography." IUCrJ **2**.

Conrad, C. E. (2016). Overcoming Barriers in Structural Biology Through Method Development of Serial Crystallography, Arizona State University.

Coquelle, N., M. Sliwa, J. Woodhouse, G. Schirò, V. Adam, A. Aquila, T. R. Barends, S. Boutet, M. Byrdin and S. Carbajo (2018). "Chromophore twisting in the excited state of a photoswitchable fluorescent protein captured by time-resolved serial femtosecond crystallography." Nature chemistry **10**(1): 31.

Cosier, J. t. and A. Glazer (1986). "A nitrogen-gas-stream cryostat for general X-ray diffraction studies." Journal of Applied Crystallography **19**(2): 105-107.

Cox, N., M. Retegan, F. Neese, D. A. Pantazis, A. Boussac and W. Lubitz (2014). "Electronic structure of the oxygen-evolving complex in photosystem II prior to OO bond formation." Science **345**(6198): 804-808.

Cusack, S., H. Belrhali, A. Bram, M. Burghammer, A. Perrakis and C. Riekel (1998). "Small is beautiful: protein micro-crystallography." Nature Structural & Molecular Biology **5**: 634-637.

Dattoli, G. and A. Renieri (1985). Experimental and theoretical aspects of the free-electron laser. Laser handbook. Vol. 4.

Dau, H., I. Zaharieva and M. Haumann (2012). "Recent developments in research on water oxidation by photosystem II." Current opinion in chemical biology **16**(1-2): 3-10.

Dauter, Z., M. Jaskolski and A. Wlodawer (2010). "Impact of synchrotron radiation on macromolecular crystallography: a personal view." Journal of synchrotron radiation **17**(4): 433-444.

Debus, R. J., M. A. Strickler, L. M. Walker and W. Hillier (2005). "No evidence from FTIR difference spectroscopy that aspartate-170 of the D1 polypeptide ligates a manganese ion that undergoes oxidation during the S0 to S1, S1 to S2, or S2 to S3 transitions in photosystem II." Biochemistry **44**(5): 1367-1374.

Demirci, H., R. G. Sierra, H. Laksmono, R. L. Shoeman, S. Botha, T. R. M. Barends, K. Nass, I. Schlichting, R. B. Doak, C. Gati, G. J. Williams, S. Boutet, M. Messerschmidt, G. Jogl, A. E. Dahlberg, S. T. Gregory and M. J. Bogan (2013). "Serial femtosecond X-ray diffraction of 30S ribosomal subunit microcrystals in liquid suspension at ambient temperature using an X-ray free-electron laser." Acta Crystallographica Section F **69**(9): 1066-1069.

Denes, P. and B. Schmitt (2014). "Pixel detectors for diffraction-limited storage rings." Journal of synchrotron radiation **21**(5): 1006-1010.

DePonte, D. P., U. Weierstall, K. Schmidt, J. Warner, D. Starodub, J. C. H. Spence and R. B. Doak (2008). "Gas dynamic virtual nozzle for generation of microscopic droplet streams." Journal of Physics D: Applied Physics **41**(19): 195505.

Diaz-Quintana, A., W. Leibl, H. Bottin and P. Sétif (1998). "Electron transfer in photosystem I reaction centers follows a linear pathway in which iron-sulfur cluster FB is the immediate electron donor to soluble ferredoxin." Biochemistry **37**(10): 3429-3439.

Doering, D., Y.-D. Chuang, N. Andresen, K. Chow, D. Contarato, C. Cummings, E. Domning, J. Joseph, J. Pepper and B. Smith (2011). "Development of a compact fast CCD camera and resonant soft x-ray scattering endstation for time-resolved pump-probe experiments." Review of Scientific Instruments **82**(7): 073303.

Doublié, S. (2007). Macromolecular crystallography protocols, Springer.

Dow, X. Y., C. M. Dettmar, E. L. DeWalt, J. A. Newman, A. R. Dow, S. Roy-Chowdhury, J. D. Coe, C. Kupitz, P. Fromme and G. J. Simpson (2016). "Second harmonic generation correlation spectroscopy for characterizing translationally diffusing protein nanocrystals." Acta Crystallographica Section D: Structural Biology **72**(7): 849-859.

Doye, J. P. and W. C. Poon (2006). "Protein crystallization in vivo." Current opinion in colloid & interface science **11**(1): 40-46.

Drenth, J. (2007). Principles of protein X-ray crystallography, Springer Science & Business Media.

D'Souza, F. W., Y. Benenson and T. Baasov (1997). "Catalytic mechanism of KDO8P synthase: synthesis and evaluation of a putative reaction intermediate." Bioorganic & Medicinal Chemistry Letters **7**(19): 2457-2462.

Duewel, H. S., S. Radaev, J. Wang, R. W. Woodard and D. L. Gatti (2001). "Substrate and Metal Complexes of 3-Deoxy-d-manno-octulosonate-8-phosphate Synthase from Aquifex aeolicus at 1.9-Å Resolution IMPLICATIONS FOR THE CONDENSATION MECHANISM." Journal of Biological Chemistry **276**(11): 8393-8402.

Duisenberg, A. J. (1992). "Indexing in single-crystal diffractometry with an obstinate list of reflections." Journal of applied crystallography **25**(2): 92-96.

Duke, E., S. Wakatsuki, A. Hadfield and L. Johnson (1994). "Laue and monochromatic diffraction studies on catalysis in phosphorylase b crystals." Protein Science **3**(8): 1178-1196.

Eaton-Rye, J. J. and W. F. Vermaas (1991). "Oligonucleotide-directed mutagenesis of psbB, the gene encoding CP47, employing a deletion mutant strain of the cyanobacterium Synechocystis sp. PCC 6803." Plant molecular biology **17**(6): 1165-1177.

Egawa, T., J. Haber, J. A. Fee, S.-R. Yeh and D. L. Rousseau (2015). "Interactions of CuB with Carbon Monoxide in Cytochrome c Oxidase: Origin of the Anomalous Correlation between the Fe–CO and C–O Stretching Frequencies." The Journal of Physical Chemistry B **119**(27): 8509-8520.

Elser, V. (2003). "Phase retrieval by iterated projections." JOSA A **20**(1): 40-55.

Elser, V. and R. Millane (2008). "Reconstruction of an object from its symmetry-averaged diffraction pattern." Acta Crystallographica Section A: Foundations of Crystallography **64**(2): 273-279.

Emma, P., R. Akre, J. Arthur, R. Bionta, C. Bostedt, J. Bozek, A. Brachmann, P. Bucksbaum, R. Coffee and F.-J. Decker (2010). "First lasing and operation of an ångstrom-wavelength free-electron laser." nature photonics **4**(9): 641-647.

Feld, G. K., M. Heymann, W. H. Benner, T. Pardini, C.-J. Tsai, S. Boutet, M. A. Coleman, M. S. Hunter, X. Li, M. Messerschmidt, A. Opathalage, B. Pedrini, G. J. Williams, B. A. Krantz, S. Fraden, S. Hau-Riege, J. E. Evans, B. W. Segelke and M. Frank (2015). "Low-Z polymer sample supports for fixed-target serial femtosecond X-ray crystallography." Journal of Applied Crystallography **48**(4): 1072-1079.

Fenalti, G., P. M. Giguere, V. Katritch, X.-P. Huang, A. A. Thompson, V. Cherezov, B. L. Roth and R. C. Stevens (2014). "Molecular control of δ-opioid receptor signalling." Nature **506**(7487): 191.

Fenalti, G., N. A. Zatsepin, C. Betti, P. Giguere, G. W. Han, A. Ishchenko, W. Liu, K. Guillemyn, H. Zhang and D. James (2015). "Structural basis for bifunctional peptide recognition at human δ-opioid receptor." Nature structural & molecular biology.

Fiedler, E., S. Thorell, T. Sandalova, R. Golbik, S. König and G. Schneider (2002). "Snapshot of a key intermediate in enzymatic thiamin catalysis: Crystal structure of the α-carbanion of (α, β-dihydroxyethyl)-thiamin diphosphate in the active site of transketolase from Saccharomyces cerevisiae." Proceedings of the National Academy of Sciences **99**(2): 591-595.

Fienup, J. R. (1987). "Reconstruction of a complex-valued object from the modulus of its Fourier transform using a support constraint." JOSA A **4**(1): 118-123.

Filipe, V., A. Hawe and W. Jiskoot (2010). "Critical evaluation of Nanoparticle Tracking Analysis (NTA) by NanoSight for the measurement of nanoparticles and protein aggregates." Pharmaceutical research **27**(5): 796-810.

Fischer, N., M. Hippler, P. Setif, J. P. Jacquot and J. D. Rochaix (1998). "The PsaC subunit of photosystem I provides an essential lysine residue for fast electron transfer to ferredoxin." The EMBO journal **17**(4): 849-858.

Fischer, N., P. Neumann, A. L. Konevega, L. V. Bock, R. Ficner, M. V. Rodnina and H. Stark (2015). "Structure of the E. coli ribosome–EF-Tu complex at< 3 Å resolution by C s-corrected cryo-EM." Nature **520**(7548): 567.

Fisher, A., B. McKinney, J.-P. Wery and J. Johnson (1992). "Crystallization and preliminary data analysis of Flock House virus." Acta Crystallographica Section B: Structural Science **48**(4): 515-520.

Foucar, L., A. Barty, N. Coppola, R. Hartmann, P. Holl, U. Hoppe, S. Kassemeyer, N. Kimmel, J. Küpper and M. Scholz (2012). "CASS—CFEL-ASG software suite." Computer Physics Communications **183**(10): 2207-2213.

Friedrich, W., P. Knipping and M. Laue (1913). "Interferenzerscheinungen bei roentgenstrahlen." Annalen der Physik **346**(10): 971-988.

Fromme, P. and H. T. Witt (1998). "Improved isolation and crystallization of Photosystem I for structural analysis." Biochimica et Biophysica Acta (BBA)-Bioenergetics **1365**(1): 175-184.

Fromme, P., H. Bottin, N. Krauss and P. Sétif (2002). "Crystallization and electron paramagnetic resonance characterization of the complex of photosystem I with its natural electron acceptor ferredoxin." Biophysical journal **83**(4): 1760-1773.

Fromme, P., A. Melkozernov, P. Jordan and N. Krauss (2003). "Structure and function of photosystem I: interaction with its soluble electron carriers and external antenna systems." FEBS letters **555**(1): 40-44.

Fromme, P. and I. Grotjohann (2006). Structural analysis of cyanobacterial photosystem I. Photosystem I, Springer**:** 47-69.

Fromme, P. and I. Grotjohann (2008). "Overview of photosynthesis." Wiley-VCH Verlag, Weinheim, Germany.

Fromme, R., A. Ishchenko, M. Metz, S. R. Chowdhury, S. Basu, S. Boutet, P. Fromme, T. A. White, A. Barty and J. C. Spence (2015). "Serial femtosecond crystallography of soluble proteins in lipidic cubic phase." IUCrJ **2**(5): 545-551.

Gallat, F.-X., N. Matsugaki, N. P. Coussens, K. J. Yagi, M. Boudes, T. Higashi, D. Tsuji, Y. Tatano, M. Suzuki and E. Mizohata (2014). "In vivo crystallography at X-ray free-electron lasers: the next generation of structural biology?" Philosophical Transactions of the Royal Society of London B: Biological Sciences **369**(1647): 20130497.

Galli, L., S.-K. Son, T. A. White, R. Santra, H. N. Chapman and M. H. Nanao (2015). "Towards RIP using free-electron laser SFX data." Journal of synchrotron radiation **22**(2): 249-255.

Garcıa-Ruiz, J. M. (2003). "Nucleation of protein crystals." Journal of structural biology **142**(1): 22-31.

Garman, E. F. and R. L. Owen (2006). "Cryocooling and radiation damage in macromolecular crystallography." Acta Crystallographica Section D: Biological Crystallography **62**(1): 32-47.

Garman, E. F. (2010). "Radiation damage in macromolecular crystallography: what is it and why should we care?" Acta Crystallographica Section D: Biological Crystallography **66**(4): 339-351.

Geloni, G., E. Saldin, L. Samoylova, E. Schneidmiller, H. Sinn, T. Tschentscher and M. Yurkov (2010). "Coherence properties of the European XFEL." New Journal of Physics **12**(3): 035021.

Genick, U. K., G. E. Borgstahl, K. Ng, Z. Ren, C. Pradervand, P. M. Burke, V. Šrajer, T.-Y. Teng, W. Schildkamp and D. E. McRee (1997). "Structure of a protein photocycle intermediate by millisecond time-resolved crystallography." Science **275**(5305): 1471-1475.

Giacovazzo, C. (2002). Fundamentals of crystallography, Oxford university press, USA.

Giegé, R. (2013). "A historical perspective on protein crystallization from 1840 to the present day." The FEBS journal **280**(24): 6456-6497.

Ginn, H. M., A. S. Brewster, J. Hattne, G. Evans, A. Wagner, J. M. Grimes, N. K. Sauter, G. Sutton and D. Stuart (2015). "A revised partiality model and post-refinement algorithm for X-ray free-electron laser data." Acta Crystallographica Section D: Biological Crystallography **71**(6): 1400-1410.

Ginn, H. M., M. Messerschmidt, X. Ji, H. Zhang, D. Axford, R. J. Gildea, G. Winter, A. S. Brewster, J. Hattne and A. Wagner (2015). "Structure of CPV17 polyhedrin determined by the improved analysis of serial femtosecond crystallographic data." Nature communications **6**.

Golbeck, J. H. (1992). "Structure and function of photosystem I." Annual review of plant biology **43**(1): 293-324.

Golbeck, J. H. (1994). Photosystem I in cyanobacteria. The molecular biology of cyanobacteria, Springer**:** 319-360.

Golbeck, J. H. (1999). "A comparative analysis of the spin state distribution of in vitro and in vivo mutants of PsaC. A biochemical argument for the sequence of electron transfer in Photosystem I as FX→ FA→ FB→ ferredoxin/flavodoxin." Photosynthesis research **61**(2): 107-144.

Granier, S., A. Manglik, A. C. Kruse, T. S. Kobilka, F. S. Thian, W. I. Weis and B. K. Kobilka (2012). "Structure of the δ-opioid receptor bound to naltrindole." Nature **485**(7398): 400.

Green, D., V. Ingram and M. Perutz (1954). The structure of haemoglobin-IV. Sign determination by the isomorphous replacement method. Proc. R. Soc. Lond. A, The Royal Society.

Grossman, A. R., M. R. Schaefer, G. G. Chiang and J. L. Collier (1993). "The phycobilisome, a light-harvesting complex responsive to environmental conditions." Microbiological reviews **57**(3): 725-749.

Guergova-Kuras, M., B. Boudreaux, A. Joliot, P. Joliot and K. Redding (2001). "Evidence for two active branches for electron transfer in photosystem I." Proceedings of the National Academy of Sciences **98**(8): 4437-4442.

Guss, J. M., E. A. Merritt, R. P. Phizackerley, B. Hedman, M. Murata, K. O. Hodgson and H. C. Freeman (1988). "Phase determination by multiple-wavelength x-ray diffraction: crystal structure of a basic" blue" copper protein from cucumbers." Science **241**(4867): 806-811.

Hajdu, J. and L. N. Johnson (1990). "Progress with Laue diffraction studies on protein and virus crystals." Biochemistry **29**(7): 1669-1678.

Hajdu, J., R. Neutze, T. Sjögren, K. Edman, A. Szöke, R. C. Wilmouth and C. M. Wilmot (2000). "Analyzing protein functions in four dimensions." Nature Structural and Molecular Biology **7**(11): 1006.

Hammond, C. and C. Hammond (2001). The Basics of Cristallography and Diffraction, Oxford.

Hart, P., S. Boutet, G. Carini, M. Dubrovin, B. Duda, D. Fritz, G. Haller, R. Herbst, S. Herrmann and C. Kenney (2012). The CSPAD megapixel x-ray camera at LCLS. SPIE Optical Engineering+ Applications, International Society for Optics and Photonics.

Hartmann, N., W. Helml, A. Galler, M. Bionta, J. Grünert, S. Molodtsov, K. Ferguson, S. Schorb, M. Swiggers and S. Carron (2014). "Sub-femtosecond precision measurement of relative X-ray arrival time for free-electron lasers." Nature Photonics **8**(9): 706.

Hattne, J., N. Echols, R. Tran, J. Kern, R. J. Gildea, A. S. Brewster, R. Alonso-Mori, C. Glöckner, J. Hellmich and H. Laksmono (2014). "Accurate macromolecular structures using minimal measurements from X-ray free-electron lasers." Nature methods **11**(5): 545.

Haumann, M., C. Müller, P. Liebisch, L. Iuzzolino, J. Dittmer, M. Grabolle, T. Neisius, W. Meyer-Klaucke and H. Dau (2005). "Structural and oxidation state changes of the photosystem II manganese complex in four transitions of the water oxidation cycle (S0→ S1, S1→ S2, S2→ S3, and S3, 4→ S0) characterized by X-ray absorption spectroscopy at 20 K and room temperature." Biochemistry **44**(6): 1894-1908.

Haupert, L. M. and G. J. Simpson (2011). "Screening of protein crystallization trials by second order nonlinear optical imaging of chiral crystals (SONICC)." Methods **55**(4): 379-386.

Hau-Riege, S. P., R. A. London and A. Szoke (2004). "Dynamics of biological molecules irradiated by short x-ray pulses." Phys Rev E Stat Nonlin Soft Matter Phys **69**(5 Pt 1): 051906.

Healy, J. R., P. Bezawada, J. Shim, J. W. Jones, M. A. Kane, A. D. MacKerell Jr, A. Coop and R. R. Matsumoto (2013). "Synthesis, modeling, and pharmacological evaluation of UMB 425, a mixed μ agonist/δ antagonist opioid analgesic with reduced tolerance liabilities." ACS chemical neuroscience **4**(9): 1256-1266.

Helliwell, J. (1988). "Protein crystal perfection and the nature of radiation damage." Journal of Crystal Growth **90**(1-3): 259-272.

Helliwell, J. R. (1997). [14] Overview of synchrotron radiation and macromolecular crystallography. Methods in enzymology, Elsevier. **276:** 203-217.

Helliwell, J. R., Y. P. Nieh, J. Habash, P. F. Faulder, J. Raftery, M. Cianci, M. Wulff and A. Hädener (2003). "Time-resolved and static-ensemble structural chemistry of hydroxymethylbilane synthase." Faraday discussions **122**: 131-144.

Hendrickson, W. A. and M. M. Teeter (1981). "Structure of the hydrophobic protein crambin determined directly from the anomalous scattering of sulphur." Nature **290**(5802): 107.

Hernandez, R., C. Sinodis and D. T. Brown (2005). "Sindbis virus: propagation, quantification, and storage." Current protocols in microbiology: 15B. 11.11-15B. 11.41.

Hirata, K., K. Shinzawa-Itoh, N. Yano, S. Takemura, K. Kato, M. Hatanaka, K. Muramoto, T. Kawahara, T. Tsukihara and E. Yamashita (2014). "Determination of damage-free crystal structure of an X-ray-sensitive protein using an XFEL." Nature Methods **11**(7): 734-736.

Hofbauer, W., A. Zouni, R. Bittl, J. Kern, P. Orth, F. Lendzian, P. Fromme, H. Witt and W. Lubitz (2001). "Photosystem II single crystals studied by EPR spectroscopy at 94 GHz: The tyrosine radical Y." Proceedings of the National Academy of Sciences **98**(12): 6623-6628.

Holton, J. M. (2009). "A beginner's guide to radiation damage." J Synchrotron Radiat **16**(Pt 2): 133-142.

Holton, J. M. and K. A. Frankel (2010). "The minimum crystal size needed for a complete diffraction data set." Acta Crystallographica Section D: Biological Crystallography **66**(4): 393-408.

Howells, M. R., T. Beetz, H. N. Chapman, C. Cui, J. Holton, C. Jacobsen, J. Kirz, E. Lima, S. Marchesini and H. Miao (2009). "An assessment of the resolution limitation due to radiation-damage in X-ray diffraction microscopy." Journal of electron spectroscopy and related phenomena **170**(1-3): 4-12.

Huldt, G., A. Szőke and J. Hajdu (2003). "Diffraction imaging of single particles and biomolecules." Journal of structural biology **144**(1-2): 219-227.

Hunter, M. S., B. Segelke, M. Messerschmidt, G. J. Williams, N. A. Zatsepin, A. Barty, W. H. Benner, D. B. Carlson, M. Coleman and A. Graf (2014). "Fixed-target protein serial microcrystallography with an x-ray free electron laser." Scientific reports **4**.

Ibrahim, M., R. Chatterjee, J. Hellmich, R. Tran, M. Bommer, V. K. Yachandra, J. Yano, J. Kern and A. Zouni (2015). "Improvements in serial femtosecond crystallography of photosystem II by optimizing crystal uniformity using microseeding procedures." Structural Dynamics **2**(4): 041705.

Ihee, H., S. Rajagopal, V. Šrajer, R. Pahl, S. Anderson, M. Schmidt, F. Schotte, P. A. Anfinrud, M. Wulff and K. Moffat (2005). "Visualizing reaction pathways in photoactive yellow protein from nanoseconds to seconds." Proceedings of the National Academy of Sciences of the United States of America **102**(20): 7145-7150.

Ishigami, I., N. A. Zatsepin, M. Hikita, C. E. Conrad, G. Nelson, J. D. Coe, S. Basu, T. D. Grant, M. H. Seaberg and R. G. Sierra (2017). "Crystal structure of CO-bound cytochrome c oxidase determined by serial femtosecond X-ray crystallography at room temperature." Proceedings of the National Academy of Sciences **114**(30): 8011-8016.

Isobe, H., M. Shoji, S. Yamanaka, Y. Umena, K. Kawakami, N. Kamiya, J.-R. Shen and K. Yamaguchi (2012). "Theoretical illumination of water-inserted structures of the CaMn 4 O 5 cluster in the S 2 and S 3 states of oxygen-evolving complex of photosystem II: full geometry optimizations by B3LYP hybrid density functional." Dalton transactions **41**(44): 13727-13740.

Jancarik, J. and S.-H. Kim (1991). "Sparse matrix sampling: a screening method for crystallization of proteins." Journal of applied crystallography **24**(4): 409-411.

Johansson, L. C., D. Arnlund, T. A. White, G. Katona, D. P. DePonte, U. Weierstall, R. B. Doak, R. L. Shoeman, L. Lomb and E. Malmerberg (2012). "Lipidic phase membrane protein serial femtosecond crystallography." Nature Methods **9**(3): 263-265.

Johansson, L. C., D. Arnlund, G. Katona, T. A. White, A. Barty, D. P. DePonte, R. L. Shoeman, C. Wickstrand, A. Sharma and G. J. Williams (2013). "Structure of a photosynthetic reaction centre determined by serial femtosecond crystallography." Nature communications **4**.

Jordan, P., P. Fromme, H. T. Witt, O. Klukas, W. Saenger and N. Krauß (2001). "Three-dimensional structure of cyanobacterial photosystem I at 2.5 Å resolution." Nature **411**(6840): 909-917.

Jung, Y. O., J. H. Lee, J. Kim, M. Schmidt, K. Moffat, V. Šrajer and H. Ihee (2013). "Volume-conserving trans–cis isomerization pathways in photoactive yellow protein visualized by picosecond X-ray crystallography." Nature chemistry **5**(3): 212.

Kabsch, W. (2010). "Xds." Acta Crystallographica Section D: Biological Crystallography **66**(2): 125-132.

Kahn, R., R. Fourme, R. Bosshard, M. Chiadmi, J. Risler, O. Dideberg and J. Wery (1985). "Crystal structure study of Opsanus tau parvalbumin by multiwavelength anomalous diffraction." FEBS letters **179**(1): 133-137.

Kang, Y., X. E. Zhou, X. Gao, Y. He, W. Liu, A. Ishchenko, A. Barty, T. A. White, O. Yefanov and G. W. Han (2015). "Crystal structure of rhodopsin bound to arrestin by femtosecond X-ray laser." Nature **523**(7562): 561-567.

Karlsson, A., J. V. Parales, R. E. Parales, D. T. Gibson, H. Eklund and S. Ramaswamy (2003). "Crystal structure of naphthalene dioxygenase: side-on binding of dioxygen to iron." Science **299**(5609): 1039-1042.

Katona, G., U. Andreasson, E. M. Landau, L.-E. Andreasson and R. Neutze (2003). "Lipidic cubic phase crystal structure of the photosynthetic reaction centre from Rhodobacter sphaeroides at 2.35 Å resolution." Journal of molecular biology **331**(3): 681-692.

Keedy, D. A., L. R. Kenner, M. Warkentin, R. A. Woldeyes, J. B. Hopkins, M. C. Thompson, A. S. Brewster, A. H. Van Benschoten, E. L. Baxter, M. Uervirojnangkoorn, S. E. McPhillips, J. Song, R. Alonso-Mori, J. M. Holton, W. I. Weis, A. T. Brunger, S. M. Soltis, H. Lemke, A. Gonzalez, N. K. Sauter, A. E. Cohen, H. van den Bedem, R. E. Thorne and J. S. Fraser (2015). "Mapping the conformational landscape of a dynamic enzyme by multitemperature and XFEL crystallography." eLife **4**: e07574.

Kendrew, J. C., G. Bodo, H. M. Dintzis, R. Parrish, H. Wyckoff and D. C. Phillips (1958). "A three-dimensional model of the myoglobin molecule obtained by x-ray analysis." Nature **181**(4610): 662-666.

Kendrew, J., R. Dickerson, B. Strandberg, R. Hart, D. Davies, D. Phillips and V. Shore (1960). "Structure of myoglobin." Nature **185**(422): 427-1960.

Kern, J., R. Alonso-Mori, J. Hellmich, R. Tran, J. Hattne, H. Laksmono, C. Glöckner, N. Echols, R. G. Sierra, J. Sellberg, B. Lassalle-Kaiser, R. J. Gildea, P. Glatzel, R. W. Grosse-Kunstleve, M. J. Latimer, T. A. McQueen, D. DiFiore, A. R. Fry, M. Messerschmidt, A. Miahnahri, D. W. Schafer, M. M. Seibert, D. Sokaras, T.-C. Weng, P. H. Zwart, W. E. White, P. D. Adams, M. J. Bogan, S. Boutet, G. J. Williams, J. Messinger, N. K. Sauter, A. Zouni, U. Bergmann, J. Yano and V. K. Yachandra (2012). "Room temperature femtosecond X-ray diffraction of photosystem II microcrystals." Proceedings of the National Academy of Sciences of the United States of America **109**(25): 9721-9726.

Kern, J., R. Alonso-Mori, R. Tran, J. Hattne, R. J. Gildea, N. Echols, C. Glöckner, J. Hellmich, H. Laksmono and R. G. Sierra (2013). "Simultaneous femtosecond X-ray spectroscopy and diffraction of photosystem II at room temperature." Science **340**(6131): 491-495.

Kim, Y. J., K. P. Hofmann, O. P. Ernst, P. Scheerer, H.-W. Choe and M. E. Sommer (2013). "Crystal structure of pre-activated arrestin p44." Nature **497**(7447): 142.

King, A. M., E. Lefkowitz, M. J. Adams and E. B. Carstens (2011). Virus taxonomy: ninth report of the International Committee on Taxonomy of Viruses, Elsevier.

Kirian, R. A., X. Wang, U. Weierstall, K. E. Schmidt, J. C. Spence, M. Hunter, P. Fromme, T. White, H. N. Chapman and J. Holton (2010). "Femtosecond protein nanocrystallography—data analysis methods." Optics express **18**(6): 5713-5723.

Kirian, R. A., T. A. White, J. M. Holton, H. N. Chapman, P. Fromme, A. Barty, L. Lomb, A. Aquila, F. R. Maia and A. V. Martin (2011). "Structure-factor analysis of femtosecond microdiffraction patterns from protein nanocrystals." Acta Crystallographica Section A: Foundations of Crystallography **67**(2): 131-140.

Kirian, R. A., R. J. Bean, K. R. Beyerlein, O. M. Yefanov, T. A. White, A. Barty and H. N. Chapman (2014). "Phasing coherently illuminated nanocrystals bounded by partial unit cells." Philosophical Transactions of the Royal Society of London B: Biological Sciences **369**(1647): 20130331.

Kirian, R. A., R. J. Bean, K. R. Beyerlein, M. Barthelmess, C. H. Yoon, F. Wang, F. Capotondi, E. Pedersoli, A. Barty and H. N. Chapman (2015). "Direct phasing of finite crystals illuminated with a free-electron laser." Physical Review X **5**(1): 011015.

Kissick, D. J., D. Wanapun and G. J. Simpson (2011). "Second-order nonlinear optical imaging of chiral crystals." Annual review of analytical chemistry (Palo Alto, Calif.) **4**: 419.

Koerner, L. J., H. T. Philipp, M. S. Hromalik, M. W. Tate and S. M. Gruner (2009). "X-ray tests of a Pixel Array Detector for coherent x-ray imaging at the Linac Coherent Light Source." Journal of Instrumentation **4**(03): P03001.

Kona, F., X. Xu, P. Martin, P. Kuzmic and D. L. Gatti (2007). "Structural and mechanistic changes along an engineered path from metallo to nonmetallo 3-deoxy-D-manno-octulosonate 8-phosphate synthases." Biochemistry **46**(15): 4532-4544.

Koopmann, R., K. Cupelli, L. Redecke, K. Nass, D. P. DePonte, T. A. White, F. Stellato, D. Rehders, M. Liang and J. Andreasson (2012). "In vivo protein crystallization opens new routes in structural biology." Nature methods **9**(3): 259-262.

Krauß, N. (2008). "Structure and function of cyanobacterial photosystem I." Photosynthetic Protein Complexes: A Structural Approach: 23-64.

Kupitz, C., S. Basu, I. Grotjohann, R. Fromme, N. A. Zatsepin, K. N. Rendek, M. S. Hunter, R. L. Shoeman, T. A. White and D. Wang (2014). "Serial time-resolved crystallography of photosystem II using a femtosecond X-ray laser." Nature **513**(7517): 261-265.

Kupitz, C., I. Grotjohann, C. E. Conrad, S. Roy-Chowdhury, R. Fromme and P. Fromme (2014). "Microcrystallization techniques for serial femtosecond crystallography using photosystem II from Thermosynechococcus elongatus as a model system." Philosophical Transactions of the Royal Society of London B: Biological Sciences **369**(1647): 20130316.

Kupitz, C., J. L. Olmos Jr, M. Holl, L. Tremblay, K. Pande, S. Pandey, D. Oberthür, M. Hunter, M. Liang and A. Aquila (2017). "Structural enzymology using X-ray free electron lasers." Structural Dynamics **4**(4): 044003.

Laue, M. (1936). "The external shape of crystals and its influence on interference phenomena in crystalline lattices." Ann. Phys **26**: 55.

Lawrence, R. M., C. E. Conrad, N. A. Zatsepin, T. D. Grant, H. Liu, D. James, G. Nelson, G. Subramanian, A. Aquila and M. S. Hunter (2015). "Serial femtosecond X-ray diffraction of enveloped virus microcrystals." Structural Dynamics **2**(4): 041720.

Lawrence, R. M., C. E. Conrad, N. A. Zatsepin, T. D. Grant, H. Liu, D. James, G. Nelson, G. Subramanian, A. Aquila, M. S. Hunter, M. Liang, S. Boutet, J. Coe, J. C. H. Spence, U. Weierstall, W. Liu, P. Fromme, V. Cherezov and B. G. Hogue (2015). "Serial femtosecond X-ray diffraction of enveloped virus microcrystals." Structural Dynamics **2**(4): 041720.

Lee, H. H., I. Cherni, H. Yu, R. Fromme, J. D. Doran, I. Grotjohann, M. Mittman, S. Basu, A. Deb, K. Dorner, A. Aquila, A. Barty, S. Boutet, H. N. Chapman, R. B. Doak, M. S. Hunter, D. James, R. A. Kirian, C. Kupitz, R. M. Lawrence, H. Liu, K. Nass, I. Schlichting, K. E. Schmidt, M. M. Seibert, R. L. Shoeman, J. C. Spence, F. Stellato, U. Weierstall, G. J. Williams, C. Yoon, D. Wang, N. A. Zatsepin, B. G. Hogue, N. Matoba, P. Fromme and T. S. Mor (2014). "Expression, purification and crystallization of CTB-MPR, a candidate mucosal vaccine component against HIV-1." IUCrJ **1**(Pt 5): 305-317.

Lee, D. B., J.-M. Kim, J. H. Seok, J.-H. Lee, J. D. Jo, J. Y. Mun, C. Conrad, J. Coe, G. Nelson and B. Hogue (2018). "Supersaturation-controlled microcrystallization and visualization analysis for serial femtosecond crystallography." Scientific Reports **8**(1): 2541.

Leiros, I., S. McSweeney and E. Hough (2004). "The reaction mechanism of phospholipase D from Streptomyces sp. strain PMF. Snapshots along the reaction pathway reveal a pentacoordinate reaction intermediate and an unexpected final product." Journal of molecular biology **339**(4): 805-820.

Li, Z., A. K. Sau, C. M. Furdui and K. S. Anderson (2005). "Probing the role of tightly bound phosphoenolpyruvate in Escherichia coli 3-deoxy-D-manno-octulosonate 8-phosphate synthase catalysis using quantitative time-resolved electrospray ionization mass spectrometry in the millisecond time range." Analytical biochemistry **343**(1): 35-47.

Li, D., J. A. Lyons, V. E. Pye, L. Vogeley, D. Aragão, C. P. Kenyon, S. T. Shah, C. Doherty, M. Aherne and M. Caffrey (2013). "Crystal structure of the integral membrane diacylglycerol kinase." Nature **497**(7450): 521-524.

Li, M., D. A. Semchonok, E. J. Boekema and B. D. Bruce (2014). "Characterization and evolution of tetrameric photosystem I from the thermophilic cyanobacterium Chroococcidiopsis sp TS-821." The Plant Cell **26**(3): 1230-1245.

Li, D., P. J. Stansfeld, M. S. Sansom, A. Keogh, L. Vogeley, N. Howe, J. A. Lyons, D. Aragao, P. Fromme and R. Fromme (2015). "Ternary structure reveals mechanism of a membrane diacylglycerol kinase." Nature communications **6**.

Li, D., P. J. Stansfeld, M. S. Sansom, A. Keogh, L. Vogeley, N. Howe, J. A. Lyons, D. Aragao, P. Fromme, R. Fromme, S. Basu, I. Grotjohann, C. Kupitz, K. Rendek, U. Weierstall, N. A. Zatsepin, V. Cherezov, W. Liu, S. Bandaru, N. J. English, C. Gati, A. Barty, O. Yefanov, H. N. Chapman, K. Diederichs, M. Messerschmidt, S. Boutet, G. J. Williams, M. Marvin Seibert and M. Caffrey (2015). "Ternary structure reveals mechanism of a membrane diacylglycerol kinase." Nat Commun **6**: 10140.

Liang, P.-H., A. Kohen, T. Baasov and K. S. Anderson (1997). "Catalytic mechanism of Kdo8P synthase. Pre-steady-state kinetic analysis using rapid chemical quench flow methods." Bioorganic & Medicinal Chemistry Letters **7**(19): 2463-2468.

Liao, J., H. Li, W. Zeng, D. B. Sauer, R. Belmares and Y. Jiang (2012). "Structural insight into the ion-exchange mechanism of the sodium/calcium exchanger." Science **335**(6069): 686-690.

Liu, H., B. K. Poon, D. K. Saldin, J. C. Spence and P. H. Zwart (2013). "Three-dimensional single-particle imaging using angular correlations from X-ray laser data." Acta Crystallographica Section A: Foundations of Crystallography **69**(4): 365-373.

Liu, W., D. Wacker, C. Gati, G. W. Han, D. James, D. Wang, G. Nelson, U. Weierstall, V. Katritch and A. Barty (2013). "Serial femtosecond crystallography of G protein–coupled receptors." Science **342**(6165): 1521-1524.

Liu, W., D. Wacker, C. Gati, G. W. Han, D. James, D. Wang, G. Nelson, U. Weierstall, V. Katritch, A. Barty, N. A. Zatsepin, D. Li, M. Messerschmidt, S. Boutet, G. J. Williams, J. E. Koglin, M. M. Seibert, C. Wang, S. T. Shah, S. Basu, R. Fromme, C. Kupitz, K. N. Rendek, I. Grotjohann, P. Fromme, R. A. Kirian, K. R. Beyerlein, T. A. White, H. N. Chapman, M. Caffrey, J. C. Spence, R. C. Stevens and V. Cherezov (2013). "Serial femtosecond crystallography of G protein-coupled receptors." Science **342**(6165): 1521-1524.

Liu, H. and J. C. Spence (2014). "The indexing ambiguity in serial femtosecond crystallography (SFX) resolved using an expectation maximization algorithm." IUCrJ **1**(6): 393-401.

Liu, W., A. Ishchenko and V. Cherezov (2014). "Preparation of microcrystals in lipidic cubic phase for serial femtosecond crystallography." Nature protocols **9**(9): 2123-2134.

Liu, W., D. Wacker, C. Wang, E. Abola and V. Cherezov (2014). "Femtosecond crystallography of membrane proteins in the lipidic cubic phase." Philosophical Transactions of the Royal Society of London B: Biological Sciences **369**(1647): 20130314.

Loh, N.-T. D. and V. Elser (2009). "Reconstruction algorithm for single-particle diffraction imaging experiments." Physical Review E **80**(2): 026705.

Loll, B., J. Kern, W. Saenger, A. Zouni and J. Biesiadka (2005). "Towards complete cofactor arrangement in the 3.0 Å resolution structure of photosystem II." Nature **438**(7070): 1040-1044.

Lomb, L., T. R. Barends, S. Kassemeyer, A. Aquila, S. W. Epp, B. Erk, L. Foucar, R. Hartmann, B. Rudek and D. Rolles (2011). "Radiation damage in protein serial femtosecond crystallography using an x-ray free-electron laser." Physical Review B **84**(21): 214111.

Lyubimov, A. Y., T. D. Murray, A. Koehl, I. E. Araci, M. Uervirojnangkoorn, O. B. Zeldin, A. E. Cohen, S. M. Soltis, E. L. Baxter, A. S. Brewster, N. K. Sauter, A. T. Brunger and J. M. Berger (2015). "Capture and X-ray diffraction studies of protein microcrystals in a microfluidic trap array." Acta Crystallogr D Biol Crystallogr **71**(Pt 4): 928-940.

Madden, J. T., E. L. DeWalt and G. J. Simpson (2011). "Two-photon excited UV fluorescence for protein crystal detection." Acta Crystallographica Section D: Biological Crystallography **67**(10): 839-846.

Madey, J. M. (1971). "Stimulated emission of bremsstrahlung in a periodic magnetic field." Journal of Applied Physics **42**(5): 1906-1913.

Mandal, M., B. Boese, J. E. Barrick, W. C. Winkler and R. R. Breaker (2003). "Riboswitches control fundamental biochemical pathways in Bacillus subtilis and other bacteria." Cell **113**(5): 577-586.

Manglik, A., A. C. Kruse, T. S. Kobilka, F. S. Thian, J. M. Mathiesen, R. K. Sunahara, L. Pardo, W. I. Weis, B. K. Kobilka and S. Granier (2012). "Crystal structure of the μ-opioid receptor bound to a morphinan antagonist." Nature **485**(7398): 321.

Marchesini, S., H. He, H. N. Chapman, S. P. Hau-Riege, A. Noy, M. R. Howells, U. Weierstall and J. C. Spence (2003). "X-ray image reconstruction from a diffraction pattern alone." Physical Review B **68**(14): 140101.

Mariani, V., A. Morgan, C. H. Yoon, T. J. Lane, T. A. White, C. O'Grady, M. Kuhn, S. Aplin, J. Koglin and A. Barty (2016). "OnDA: online data analysis and feedback for serial X-ray imaging." Journal of applied crystallography **49**(3): 1073-1080.

Martin-Garcia, J. M., C. E. Conrad, G. Nelson, N. Stander, N. A. Zatsepin, J. Zook, L. Zhu, J. Geiger, E. Chun and D. Kissick (2017). "Serial millisecond crystallography of membrane and soluble protein microcrystals using synchrotron radiation." IUCrJ **4**(4).

Matthews, B. W. (1968). "Solvent content of protein crystals." Journal of molecular biology **33**(2): 491-497.

McNeil, B. W. and N. R. Thompson (2010). "X-ray free-electron lasers." Nature photonics **4**(12): 814.

McPherson, A. (1999). Crystallization of biological macromolecules, Cold Spring Harbor Laboratory Press.

McPherson, A. and B. Cudney (2014). "Optimization of crystallization conditions for biological macromolecules." Acta Crystallographica Section F: Structural Biology Communications **70**(11): 1445-1467.

McPherson, A. (2017). "Protein crystallization." Protein Crystallography: Methods and Protocols: 17-50.

Meents, A., S. Gutmann, A. Wagner and C. Schulze-Briese (2010). "Origin and temperature dependence of radiation damage in biological samples at cryogenic temperatures." Proceedings of the National Academy of Sciences **107**(3): 1094-1099.

Miao, J., P. Charalambous, J. Kirz and D. Sayre (1999). "Extending the methodology of X-ray crystallography to allow imaging of micrometre-sized non-crystalline specimens." Nature **400**(6742): 342.

Miao, J., H. N. Chapman, J. Kirz, D. Sayre and K. O. Hodgson (2004). "Taking X-Ray Diffraction to the Limit: Macromolecular Structures from Femtosecond X-Ray Pulses and Diffraction Microscopy of Cells with Synchrotron Radiation*." Annu. Rev. Biophys. Biomol. Struct. **33**: 157-176.

Miao, J., T. Ishikawa, I. K. Robinson and M. M. Murnane (2015). "Beyond crystallography: Diffractive imaging using coherent x-ray light sources." Science **348**(6234): 530-535.

Mikkelsen, M., M. Jørgensen and F. C. Krebs (2010). "The teraton challenge. A review of fixation and transformation of carbon dioxide." Energy & Environmental Science **3**(1): 43-81.

Moffat, K. (1998). "Time-resolved crystallography." Acta Crystallographica Section A: Foundations of Crystallography **54**(6): 833-841.

Moffat, K. (1998). "Ultrafast time-resolved crystallography." Nature Structural and Molecular Biology **5**(8s): 641.

Moffat, K. (2001). "Time-resolved biochemical crystallography: a mechanistic perspective." Chemical reviews **101**(6): 1569-1582.

Mueller, C., A. Marx, S. W. Epp, Y. Zhong, A. Kuo, A. R. Balo, J. Soman, F. Schotte, H. T. Lemke, R. L. Owen, E. F. Pai, A. R. Pearson, J. S. Olson, P. A. Anfinrud, O. P. Ernst and R. J. Dwayne Miller (2015). "Fixed target matrix for femtosecond time-resolved and in situ serial micro-crystallography." Structural Dynamics **2**(5): 054302.

Müller, M. G., C. Slavov, R. Luthra, K. E. Redding and A. R. Holzwarth (2010). "Independent initiation of primary electron transfer in the two branches of the photosystem I reaction center." Proceedings of the National Academy of Sciences **107**(9): 4123-4128.

Multiphysics, C. "2013, Version 4.4, COMSOL." Inc., Burlington, MA, USA.

Murata, N., S. Takahashi, Y. Nishiyama and S. I. Allakhverdiev (2007). "Photoinhibition of photosystem II under environmental stress." Biochimica et Biophysica Acta (BBA)-Bioenergetics **1767**(6): 414-421.

Nahvi, A., N. Sudarsan, M. S. Ebert, X. Zou, K. L. Brown and R. R. Breaker (2002). "Genetic control by a metabolite binding mRNA." Chemistry & biology **9**(9): 1043-1049.

Nave, C. and E. F. Garman (2005). "Towards an understanding of radiation damage in cryocooled macromolecular crystals." Journal of synchrotron radiation **12**(3): 257-260.

Neutze, R., R. Wouts, D. van der Spoel, E. Weckert and J. Hajdu (2000). "Potential for biomolecular imaging with femtosecond X-ray pulses." Nature **406**(6797): 752-757.

Newman, J. A., N. M. Scarborough, N. R. Pogranichniy, R. K. Shrestha, R. G. Closser, C. Das and G. J. Simpson (2015). "Intercalating dyes for enhanced contrast in second-harmonic generation imaging of protein crystals." Acta Crystallographica Section D: Biological Crystallography **71**(7): 1471-1477.

Nield, J., E. P. Morris, T. S. Bibby and J. Barber (2003). "Structural analysis of the photosystem I supercomplex of cyanobacteria induced by iron deficiency." Biochemistry **42**(11): 3180-3188.

Nogly, P., D. James, D. Wang, T. A. White, N. Zatsepin, A. Shilova, G. Nelson, H. Liu, L. Johansson and M. Heymann (2015). "Lipidic cubic phase serial millisecond crystallography using synchrotron radiation." IUCrJ **2**(2): 168-176.

Nogly, P., V. Panneels, G. Nelson, C. Gati, T. Kimura, C. Milne, D. Milathianaki, M. Kubo, W. Wu and C. Conrad (2016). "Lipidic cubic phase injector is a viable crystal delivery system for time-resolved serial crystallography." Nature communications **7**: 12314.

Oberthuer, D., J. Knoška, M. O. Wiedorn, K. R. Beyerlein, D. A. Bushnell, E. G. Kovaleva, M. Heymann, L. Gumprecht, R. A. Kirian and A. Barty (2017). "Double-flow focused liquid injector for efficient serial femtosecond crystallography." Scientific reports **7**: 44628.

Oh-oka, H., Y. Takahashi, K. Kuriyama, K. Saeki and H. Matsubara (1988). "The protein responsible for center A/B in spinach photosystem I: isolation with iron-sulfur cluster (s) and complete sequence analysis." The Journal of Biochemistry **103**(6): 962-968.

Olmos, J., S. Pandey, J. M. Martin-Garcia, G. Calvey, A. Katz, J. Knoska, C. Kupitz, M. S. Hunter, M. Liang and D. Oberthuer (2017). "Authentic Enzyme Intermediates Captured" on-the-fly" by Mix-and-Inject Serial Crystallography." bioRxiv: 202432.

Ostermeier, C. and H. Michel (1997). "Crystallization of membrane proteins." Current opinion in structural biology **7**(5): 697-701.

Owen, R. L., E. Rudiño-Piñera and E. F. Garman (2006). "Experimental determination of the radiation dose limit for cryocooled protein crystals." Proceedings of the National Academy of Sciences of the United States of America **103**(13): 4912-4917.

Pande, K., C. D. M. Hutchinson, G. Groenhof, A. Aquila, J. S. Robinson, J. Tenboer, S. Basu, S. Boutet, D. Deponte, M. Liang, T. White, N. Zatsepin, O. Yefanov, D. Morozov, D. Oberthuer, C. Gati, G. Subramanian, D. James, Y. Zhao, J. Koralek, J. Brayshaw, C. Kupitz, C. Conrad, S. Roy-Chowdhury, J. Coe, M. Metz, X. Paulraj Lourdu, T. Grant, J. Koglin, G. Ketawala, R. Fromme, V. Srajer, R. Henning, J. Spence, A. Ourmazd, P. Schwander, U. Weierstall, M. Frank, P. Fromme, A. Barty, H. Chapman, K. Moffat, J. J. Van Thor and M. Schmidt (2015). "Femtosecond Structural Dynamics Drives the Trans/Cis Isomerization in Photoactive Yellow Protein." in submission.

Pasternak, G. W. (2014). "Opioids and their receptors: Are we there yet?" Neuropharmacology **76**: 198-203.

Pecora, R. (2000). "Dynamic Light Scattering Measurement of Nanometer Particles in Liquids." Journal of Nanoparticle Research **2**(2): 123-131.

Pedrini, B., C. J. Tsai, G. Capitani, C. Padeste, M. S. Hunter, N. A. Zatsepin, A. Barty, W. H. Benner, S. Boutet, G. K. Feld, S. P. Hau-Riege, R. A. Kirian, C. Kupitz, M. Messerschmitt, J. I. Ogren, T. Pardini, B. Segelke, G. J. Williams, J. C. Spence, R. Abela, M. Coleman, J. E. Evans, G. F. Schertler, M. Frank and X. D. Li (2014). "7 A resolution in protein two-dimensional-crystal X-ray diffraction at Linac Coherent Light Source." Philos Trans R Soc Lond B Biol Sci **369**(1647): 20130500.

Pellegrini, C. and J. Stöhr (2003). "X-ray free-electron lasers—principles, properties and applications." Nuclear Instruments and Methods in Physics Research Section A: Accelerators, Spectrometers, Detectors and Associated Equipment **500**(1): 33-40.

Pellegrini, C. and S. Reiche (2004). "The development of X-ray free-electron lasers." Selected Topics in Quantum Electronics, IEEE Journal of **10**(6): 1393-1404.

Pellegrini, C. (2012). "The history of X-ray free-electron lasers." The European Physical Journal H **37**(5): 659-708.

Perry, R. H. and C. Chilton (1973). "Chemical engineering's handbook." McGraw-Hill Kogakusha, Ltd: 2-74.

Perutz, M. F., M. G. Rossmann, A. F. Cullis, H. Muirhead, G. Will and A. North (1960). "Structure of hæmoglobin: a three-dimensional Fourier synthesis at 5.5-Å. resolution, obtained by X-ray analysis." Nature **185**(4711): 416-422.

Philipp, H. T., L. J. Koerner, M. S. Hromalik, M. W. Tate and S. M. Gruner (2010). "Femtosecond radiation experiment detector for x-ray free-electron laser (XFEL) coherent x-ray imaging." Nuclear Science, IEEE Transactions on **57**(6): 3795-3799.

Philipp, H. T., M. Hromalik, M. Tate, L. Koerner and S. M. Gruner (2011). "Pixel array detector for X-ray free electron laser experiments." Nuclear Instruments and Methods in Physics Research Section A: Accelerators, Spectrometers, Detectors and Associated Equipment **649**(1): 67-69.

Phillips, J. C., A. Wlodawer, M. M. Yevitz and K. O. Hodgson (1976). "Applications of synchrotron radiation to protein crystallography: preliminary results." Proceedings of the National Academy of Sciences **73**(1): 128-132.

Porra, R., W. Thompson and P. Kriedemann (1989). "Determination of accurate extinction coefficients and simultaneous equations for assaying chlorophylls a and b extracted with four different solvents: verification of the concentration of chlorophyll standards by atomic absorption spectroscopy." Biochimica et Biophysica Acta (BBA)-Bioenergetics **975**(3): 384-394.

Powell, H. R. (1999). "The Rossmann Fourier autoindexing algorithm in MOSFLM." Acta Crystallographica Section D: Biological Crystallography **55**(10): 1690-1695.

Powell, H. R., O. Johnson and A. G. Leslie (2013). "Autoindexing diffraction images with iMosflm." Acta Crystallographica Section D: Biological Crystallography **69**(7): 1195-1203.

Prasil, O. (1992). "Dynamics of photosystem II: mechanism of photoinhibition and recovery process." Topics in Photosynthesis: The Photosystem Structure, Function and Molecular Biology.

Proteau, A., R. Shi and M. Cygler (2010). "Application of dynamic light scattering in protein crystallization." Current protocols in protein science: 17.10. 11-17.10. 19.

Pushkar, Y., J. Yano, K. Sauer, A. Boussac and V. K. Yachandra (2008). "Structural changes in the Mn4Ca cluster and the mechanism of photosynthetic water splitting." Proceedings of the National Academy of Sciences **105**(6): 1879-1884.

Raetz, C. and W. Dowhan (1990). "Biosynthesis and function of phospholipids in Escherichia coli." Journal of Biological Chemistry **265**(3): 1235-1238.

Raines, C. A. (2003). "The Calvin cycle revisited." Photosynthesis research **75**(1): 1-10.

Rappaport, F., M. Guergova-Kuras, P. J. Nixon, B. A. Diner and J. Lavergne (2002). "Kinetics and pathways of charge recombination in photosystem II." Biochemistry **41**(26): 8518-8527.

Rasband, W. (1997). ImageJ. US National Institutes of Health, Bethesda, MD.

Ravelli, R. B. and S. M. McSweeney (2000). "The 'fingerprint'that X-rays can leave on structures." Structure **8**(3): 315-328.

Ray, P. (1980). "Purification and characterization of 3-deoxy-D-manno-octulosonate 8-phosphate synthetase from Escherichia coli." Journal of bacteriology **141**(2): 635-644.

Redecke, L., K. Nass, D. P. DePonte, T. A. White, D. Rehders, A. Barty, F. Stellato, M. Liang, T. R. Barends and S. Boutet (2013). "Natively inhibited Trypanosoma brucei cathepsin B structure determined by using an X-ray laser." Science **339**(6116): 227-230.

Regtmeier, J., R. Eichhorn, T. T. Duong, D. Anselmetti and A. Ros (2007). "Dielectrophoretic Manipulation of DNA: Separation and Polarizability." Anal.Chem. **79**: 3925-3932.

Ren, Z., D. Bourgeois, J. R. Helliwell, K. Moffat, V. Srajer and B. L. Stoddard (1999). "Laue crystallography: coming of age." Journal of Synchrotron Radiation **6**(4): 891-917.

Rieder, R., K. Lang, D. Graber and R. Micura (2007). "Ligand-Induced Folding of the Adenosine Deaminase A-Riboswitch and Implications on Riboswitch Translational Control." Chembiochem **8**(8): 896-902.

Robinson, I. K., I. A. Vartanyants, G. Williams, M. Pfeifer and J. Pitney (2001). "Reconstruction of the shapes of gold nanocrystals using coherent x-ray diffraction." Physical review letters **87**(19): 195505.

Robinson, A. L. (2015). "History of synchrotron radiation." Synchrotron Radiation News **28**(4): 4-9.

Roedig, P., H. M. Ginn, T. Pakendorf, G. Sutton, K. Harlos, T. S. Walter, J. Meyer, P. Fischer, R. Duman and I. Vartiainen (2017). "High-speed fixed-target serial virus crystallography." nAture methods **14**(8): 805.

Roegner, M., D. A. Chisholm and B. A. Diner (1991). "Site-directed mutagenesis of the psbC gene of photosystem II: isolation and functional characterization of CP43-less photosystem II core complexes." Biochemistry **30**(22): 5387-5395.

Roessler, C. G., A. Kuczewski, R. Stearns, R. Ellson, J. Olechno, A. M. Orville, M. Allaire, A. S. Soares and A. Héroux (2013). "Acoustic methods for high-throughput protein crystal mounting at next-generation macromolecular crystallographic beamlines." Journal of synchrotron radiation **20**(5): 805-808.

Rosenbaum, G., K. C. Holmes and J. Witz (1971). "Synchrotron radiation as a source for X-ray diffraction." Nature **230**(5294): 434.

Rossmann, M. G. and D. M. Blow (1962). "The detection of sub-units within the crystallographic asymmetric unit." Acta Crystallographica **15**(1): 24-31.

Rossmann, M. and D. Blow (1963). "Determination of phases by the conditions of non-crystallographic symmetry." Acta Crystallographica **16**(1): 39-45.

Rossmann, M. G. (1972). The molecular replacement method: a collection of papers on the use of non-crystallographic symmetry, Routledge.

Rossmann, M. G. and C. G. van Beek (1999). "Data processing." Acta Crystallographica Section D: Biological Crystallography **55**(10): 1631-1640.

Rousseau, F., P. Setif and B. Lagoutte (1993). "Evidence for the involvement of PSI-E subunit in the reduction of ferredoxin by photosystem I." The EMBO journal **12**(5): 1755-1765.

Rupp, B. (2009). Biomolecular crystallography: principles, practice, and application to structural biology, Garland Science.

Saldin, E., E. Schneidmiller and M. V. Yurkov (2013). The physics of free electron lasers, Springer Science & Business Media.

Sass, H. J., G. Büldt, R. Gessenich, D. Hehn, D. Neff, R. Schlesinger, J. Berendzen and P. Ormos (2000). "Structural alterations for proton translocation in the M state of wild-type bacteriorhodopsin." Nature **406**(6796): 649.

Sauter, N. K., R. W. Grosse-Kunstleve and P. D. Adams (2004). "Robust indexing for automatic data collection." Journal of applied crystallography **37**(3): 399-409.

Sawaya, M. R., D. Cascio, M. Gingery, J. Rodriguez, L. Goldschmidt, J.-P. Colletier, M. M. Messerschmidt, S. Boutet, J. E. Koglin and G. J. Williams (2014). "Protein crystal structure obtained at 2.9 Å resolution from injecting bacterial cells into an X-ray free-electron laser beam." Proceedings of the National Academy of Sciences **111**(35): 12769-12774.

Sayre, D. (1952). "Some implications of a theorem due to Shannon." Acta Crystallographica **5**(6): 843-843.

Sayre, D. (1952). "The squaring method: a new method for phase determination." Acta Crystallographica **5**(1): 60-65.

Schiller, P. W. (2010). "Bi-or multifunctional opioid peptide drugs." Life sciences **86**(15-16): 598-603.

Schlichting, I., G. Rapp, J. John, A. Wittinghofer, E. F. Pai and R. S. Goody (1989). "Biochemical and crystallographic characterization of a complex of c-Ha-ras p21 and caged GTP with flash photolysis." Proceedings of the National Academy of Sciences **86**(20): 7687-7690.

Schlichting, I., J. Berendzen, K. Chu, A. M. Stock, S. A. Maves, D. E. Benson, R. M. Sweet, D. Ringe, G. A. Petsko and S. G. Sligar (2000). "The catalytic pathway of cytochrome P450cam at atomic resolution." Science **287**(5458): 1615-1622.

Schlichting, I. and J. Miao (2012). "Emerging opportunities in structural biology with X-ray free-electron lasers." Current opinion in structural biology **22**(5): 613-626.

Schlichting, I. (2015). "Serial femtosecond crystallography: the first five years." IUCrJ **2**(2): 246-255.

Schmidt, M. (2013). "Mix and inject: reaction initiation by diffusion for time-resolved macromolecular crystallography." Advances in Condensed Matter Physics **2013**.

Schmidt, M., V. Srajer, R. Henning, H. Ihee, N. Purwar, J. Tenboer and S. Tripathi (2013). "Protein energy landscapes determined by five-dimensional crystallography." Acta Crystallographica Section D: Biological Crystallography **69**(12): 2534-2542.

Schmitz, K. S. (1990). An introduction to dynamic light scattering of macromolecules. United States.

Schotte, F., M. Lim, T. A. Jackson, A. V. Smirnov, J. Soman, J. S. Olson, G. N. Phillips, M. Wulff and P. A. Anfinrud (2003). "Watching a protein as it functions with 150-ps time-resolved X-ray crystallography." Science **300**(5627): 1944-1947.

Schotte, F., H. S. Cho, V. R. Kaila, H. Kamikubo, N. Dashdorj, E. R. Henry, T. J. Graber, R. Henning, M. Wulff and G. Hummer (2012). "Watching a signaling protein function in real time via 100-ps time-resolved Laue crystallography." Proceedings of the National Academy of Sciences **109**(47): 19256-19261.

Schotte, F., H. S. Cho, J. Soman, M. Wulff, J. S. Olson and P. A. Anfinrud (2013). "Real-time tracking of CO migration and binding in the α and β subunits of human hemoglobin via 150-ps time-resolved Laue crystallography." Chemical physics **422**: 98-106.

Schubert, R., A. Meyer, K. Dierks, S. Kapis, R. Reimer, H. Einspahr, M. Perbandt and C. Betzel (2015). "Reliably distinguishing protein nanocrystals from amorphous precipitate by means of depolarized dynamic light scattering." Journal of Applied Crystallography **48**(5): 1476-1484.

Scopes, R. K. (2013). Protein purification: principles and practice, Springer Science & Business Media.

Setif, P. Q. and H. Bottin (1994). "Laser flash absorption spectroscopy study of ferredoxin reduction by photosystem I in Synechocystis sp. PCC 6803: evidence for submicrosecond and microsecond kinetics." Biochemistry **33**(28): 8495-8504.

Setif, P. Q. and H. Bottin (1995). "Laser flash absorption spectroscopy study of ferredoxin reduction by photosystem I: spectral and kinetic evidence for the existence of several photosystem I-ferredoxin complexes." Biochemistry **34**(28): 9059-9070.

Shapiro, D., P. Thibault, T. Beetz, V. Elser, M. Howells, C. Jacobsen, J. Kirz, E. Lima, H. Miao and A. M. Neiman (2005). "Biological imaging by soft x-ray diffraction microscopy." Proceedings of the National Academy of Sciences **102**(43): 15343-15346.

Shukla, A. K., A. Manglik, A. C. Kruse, K. Xiao, R. I. Reis, W.-C. Tseng, D. P. Staus, D. Hilger, S. Uysal and L.-Y. Huang (2013). "Structure of active β-arrestin-1 bound to a G-protein-coupled receptor phosphopeptide." Nature **497**(7447): 137.

Sierra, R. G., H. Laksmono, J. Kern, R. Tran, J. Hattne, R. Alonso-Mori, B. Lassalle-Kaiser, C. Glöckner, J. Hellmich and D. W. Schafer (2012). "Nanoflow electrospinning serial femtosecond crystallography." Acta Crystallographica Section D: Biological Crystallography **68**(11): 1584-1587.

Smith, J. L., R. F. Fischetti and M. Yamamoto (2012). "Micro-crystallography comes of age." Current opinion in structural biology **22**(5): 602-612.

Soares, A. S., M. A. Engel, R. Stearns, S. Datwani, J. Olechno, R. Ellson, J. M. Skinner, M. Allaire and A. M. Orville (2011). "Acoustically mounted microcrystals yield high-resolution X-ray structures." Biochemistry **50**(21): 4399-4401.

Son, S.-K., H. N. Chapman and R. Santra (2011). "Multiwavelength anomalous diffraction at high x-ray intensity." Physical review letters **107**(21): 218102.

Son, S.-K., H. N. Chapman and R. Santra (2013). "Determination of multiwavelength anomalous diffraction coefficients at high X-ray intensity." Journal of Physics B: Atomic, Molecular and Optical Physics **46**(16): 164015.

Spence, J. C., R. A. Kirian, X. Wang, U. Weierstall, K. E. Schmidt, T. White, A. Barty, H. N. Chapman, S. Marchesini and J. Holton (2011). "Phasing of coherent femtosecond X-ray diffraction from size-varying nanocrystals." Optics express **19**(4): 2866-2873.

Spence, J. C. H., U. Weierstall and H. N. Chapman (2012). "X-ray lasers for structural and dynamic biology." Reports on Progress in Physics **75**(10).

Stagno, J., Y. Liu, Y. Bhandari, C. Conrad, S. Panja, M. Swain, L. Fan, G. Nelson, C. Li and D. Wendel (2017). "Structures of riboswitch RNA reaction states by mix-and-inject XFEL serial crystallography." Nature **541**(7636): 242.

Steitz, T. A., T. J. Richmond, D. Wise and D. Engelman (1974). "The lac repressor protein: molecular shape, subunit structure, and proposed model for operator interaction based on structural studies of microcrystals." Proceedings of the National Academy of Sciences **71**(3): 593-597.

Stellato, F., D. Oberthur, M. Liang, R. Bean, C. Gati, O. Yefanov, A. Barty, A. Burkhardt, P. Fischer and L. Galli (2014). "Room-temperature macromolecular serial crystallography using synchrotron radiation." IUCrJ **1**(4): 0-0.

Stevenson, H., D. DePonte, A. Makhov, J. F. Conway, O. Zeldin, S. Boutet, G. Calero and A. Cohen (2014). "Transmission electron microscopy as a tool for nanocrystal characterization pre-and post-injector." Philosophical Transactions of the Royal Society of London B: Biological Sciences **369**(1647): 20130322.

Stevenson, H. P., A. M. Makhov, M. Calero, A. L. Edwards, O. B. Zeldin, I. I. Mathews, G. Lin, C. O. Barnes, H. Santamaria and T. M. Ross (2014). "Use of transmission electron microscopy to identify nanocrystals of challenging protein targets." Proceedings of the National Academy of Sciences **111**(23): 8470-8475.

Stevenson, H. P., G. W. Lin, C. O. Barnes, I. Sutkeviciute, T. Krzysiak, S. C. Weiss, S. Reynolds, Y. Wu, V. Nagarajan, A. M. Makhov, R. Lawrence, E. Lamm, L. Clark, T. J. Gardella, B. G. Hogue, C. M. Ogata, J.

Ahn, A. M. Gronenborn, J. F. Conway, J. P. Vilardaga, A. E. Cohen and G. Calero (2016). "Transmission electron microscopy for the evaluation and optimization of crystal growth." Acta Crystallographica Section D-Structural Biology **72**: 603-615.

Stoddard, B. L. and G. K. Farber (1995). "Direct measurement of reactivity in the protein crystal by steady-state kinetic studies." Structure **3**(10): 991-996.

Stoddard, B. L., B. E. Cohen, M. Brubaker, A. D. Mesecar and D. E. Koshland (1998). "Millisecond Laue structures of an enzyme–product complex using photocaged substrate analogs." Nature Structural & Molecular Biology **5**(10): 891-897.

Strüder, L., S. Epp, D. Rolles, R. Hartmann, P. Holl, G. Lutz, H. Soltau, R. Eckart, C. Reich and K. Heinzinger (2010). "Large-format, high-speed, X-ray pnCCDs combined with electron and ion imaging spectrometers in a multipurpose chamber for experiments at 4th generation light sources." Nuclear Instruments and Methods in Physics Research Section A: Accelerators, Spectrometers, Detectors and Associated Equipment **614**(3): 483-496.

Suga, M., F. Akita, K. Hirata, G. Ueno, H. Murakami, Y. Nakajima, T. Shimizu, K. Yamashita, M. Yamamoto and H. Ago (2015). "Native structure of photosystem II at 1.95 A resolution viewed by femtosecond X-ray pulses." Nature **517**(7532): 99-103.

Sugahara, M., E. Mizohata, E. Nango, M. Suzuki, T. Tanaka, T. Masuda, R. Tanaka, T. Shimamura, Y. Tanaka, C. Suno, K. Ihara, D. Pan, K. Kakinouchi, S. Sugiyama, M. Murata, T. Inoue, K. Tono, C. Song, J. Park, T. Kameshima, T. Hatsui, Y. Joti, M. Yabashi and S. Iwata (2015). "Grease matrix as a versatile carrier of proteins for serial crystallography." Nat Meth **12**(1): 61-63.

Tenboer, J., S. Basu, N. Zatsepin, K. Pande, D. Milathianaki, M. Frank, M. Hunter, S. Boutet, G. J. Williams and J. E. Koglin (2014). "Time-resolved serial crystallography captures high-resolution intermediates of photoactive yellow protein." Science **346**(6214): 1242-1246.

Teng, T.-Y. (1990). "Mounting of crystals for macromolecular crystallography in a free-standing thin film." Journal of Applied Crystallography **23**(5): 387-391.

Theisen, M. J., I. Misra, D. Saadat, N. Campobasso, H. M. Miziorko and D. H. Harrison (2004). "3-hydroxy-3-methylglutaryl–CoA synthase intermediate complex observed in "real-time"." Proceedings of the National Academy of Sciences of the United States of America **101**(47): 16442-16447.

Tremblay, L. W., H. Xu and J. S. Blanchard (2010). "Structures of the Michaelis complex (1.2 Å) and the covalent acyl intermediate (2.0 Å) of cefamandole bound in the active sites of the Mycobacterium tuberculosis β-lactamase K73A and E166A mutants." Biochemistry **49**(45): 9685-9687.

Uervirojnangkoorn, M., O. B. Zeldin, A. Y. Lyubimov, J. Hattne, A. S. Brewster, N. K. Sauter, A. T. Brunger and W. I. Weis (2015). "Enabling X-ray free electron laser crystallography for challenging biological systems from a limited number of crystals." Elife **4**: e05421.

Umena, Y., K. Kawakami, J.-R. Shen and N. Kamiya (2011). "Crystal structure of oxygen-evolving photosystem II at a resolution of 1.9 Å." Nature **473**(7345): 55-60.

Ursby, T., M. Weik, E. Fioravanti, M. Delarue, M. Goeldner and D. Bourgeois (2002). "Cryophotolysis of caged compounds: a technique for trapping intermediate states in protein crystals." Acta Crystallographica Section D: Biological Crystallography **58**(4): 607-614.

Vainer, R., V. Belakhov, E. Rabkin, T. Baasov and N. Adir (2005). "Crystal structures of Escherichia coli KDO8P synthase complexes reveal the source of catalytic irreversibility." Journal of molecular biology **351**(3): 641-652.

Vekilov, P. G., A. Feeling-Taylor, S.-T. Yau and D. Petsev (2002). "Solvent entropy contribution to the free energy of protein crystallization." Acta Crystallographica Section D: Biological Crystallography **58**(10): 1611-1616.

Von Dreele, R. B. (2007). "Multipattern Rietveld refinement of protein powder data: an approach to higher resolution." Journal of Applied Crystallography **40**(1): 133-143.

Wampler, R. D., D. J. Kissick, C. J. Dehen, E. J. Gualtieri, J. L. Grey, H.-F. Wang, D. H. Thompson, J.-X. Cheng and G. J. Simpson (2008). "Selective detection of protein crystals by second harmonic microscopy." Journal of the American Chemical Society **130**(43): 14076-14077.

Wang, J., H. S. Duewel, R. W. Woodard and D. L. Gatti (2001). "Structures of Aquifex aeolicus KDO8P synthase in complex with R5P and PEP, and with a bisubstrate inhibitor: role of active site water in catalysis." Biochemistry **40**(51): 15676-15683.

Wang, D., U. Weierstall, L. Pollack and J. Spence (2014). "Double-focusing mixing jet for XFEL study of chemical kinetics." Journal of synchrotron radiation **21**(6): 1364-1366.

Weierstall, U., J. Spence and R. Doak (2012). "Injector for scattering measurements on fully solvated biospecies." Review of Scientific Instruments **83**(3): 035108.

Weierstall, U. (2014). "Liquid sample delivery techniques for serial femtosecond crystallography." Philosophical Transactions of the Royal Society of London B: Biological Sciences **369**(1647): 20130337.

Weierstall, U., D. James, C. Wang, T. A. White, D. Wang, W. Liu, J. C. Spence, R. B. Doak, G. Nelson and P. Fromme (2014). "Lipidic cubic phase injector facilitates membrane protein serial femtosecond crystallography." Nature communications **5**.

Weinert, T., N. Olieric, R. Cheng, S. Brünle, D. James, D. Ozerov, D. Gashi, L. Vera, M. Marsh and K. Jaeger (2017). "Serial millisecond crystallography for routine room-temperature structure determination at synchrotrons." Nature communications **8**(1): 542.

Wen, J. G. (2014). Transmission electron microscopy. Practical Materials Characterization, Springer**:** 189-229.

White, T. A., A. Barty, F. Stellato, J. M. Holton, R. A. Kirian, N. A. Zatsepin and H. N. Chapman (2013). "Crystallographic data processing for free-electron laser sources." Acta Crystallographica Section D: Biological Crystallography **69**(7): 1231-1240.

Witt, I., H. Witt, D. Di Fiore, M. Rögner, W. Hinrichs, W. Saenger, J. Granzin, C. Betzel and Z. Dauter (1988). "X-Ray Characterization of Single Crystals of the Reaction Center I of Water Splitting Photosynthesis." Berichte der Bunsengesellschaft für physikalische Chemie **92**(12): 1503-1506.

WL Bragg, B. (1913). The structure of some crystals as indicated by their diffraction of X-rays. Proc. R. Soc. Lond. A, The Royal Society.

Wu, W., P. Nogly, J. Rheinberger, L. M. Kick, C. Gati, G. Nelson, X. Deupi, J. Standfuss, G. Schertler and V. Panneels (2015). "Batch crystallization of rhodopsin for structural dynamics using an X-ray free-electron laser." Acta Crystallographica Section F: Structural Biology Communications **71**(7): 856-860.

Xia, Z., R. W. Broadhurst, E. D. Laue, D. A. Bryant, J. H. Golbeck and D. S. Bendall (1998). "Structure and properties in solution of PsaD, an extrinsic polypeptide of photosystem I." The FEBS Journal **255**(1): 309-316.

Xu, Q., Y.-S. Jung, V. P. Chitnis, J. A. Guikema, J. H. Golbeck and P. R. Chitnis (1994). "Mutational analysis of photosystem I polypeptides in Synechocystis sp. PCC 6803. Subunit requirements for reduction of NADP+ mediated by ferredoxin and flavodoxin." Journal of Biological Chemistry **269**(34): 21512-21518.

Yamaguchi, K., S. Yamanaka, H. Isobe, T. Saito, K. Kanda, Y. Umena, K. Kawakami, J. R. Shen, N. Kamiya and M. Okumura (2013). "The nature of chemical bonds of the CaMn4O5 cluster in oxygen evolving complex of photosystem II: Jahn-Teller distortion and its suppression by Ca doping in cubane structures." International Journal of Quantum Chemistry **113**(4): 453-473.

Yamashita, K., D. Pan, T. Okuda, M. Sugahara, A. Kodan, T. Yamaguchi, T. Murai, K. Gomi, N. Kajiyama and E. Mizohata (2015). "An isomorphous replacement method for efficient de novo phasing for serial femtosecond crystallography." Scientific reports **5**.

Yano, J., J. Kern, K.-D. Irrgang, M. J. Latimer, U. Bergmann, P. Glatzel, Y. Pushkar, J. Biesiadka, B. Loll and K. Sauer (2005). "X-ray damage to the Mn4Ca complex in single crystals of photosystem II: a case study for metalloprotein crystallography." Proceedings of the National Academy of Sciences of the United States of America **102**(34): 12047-12052.

Yano, J. and V. K. Yachandra (2008). "Where water is oxidized to dioxygen: structure of the photosynthetic Mn4Ca cluster from X-ray spectroscopy." Inorganic chemistry **47**(6): 1711-1726.

Yano, J. and V. Yachandra (2014). "Mn4Ca cluster in photosynthesis: where and how water is oxidized to dioxygen." Chemical reviews **114**(8): 4175-4205.

Yeagle, G. J., M. L. Gilchrist, L. M. Walker, R. J. Debus and R. D. Britt (2008). "Multifrequency electron spin-echo envelope modulation studies of nitrogen ligation to the manganese cluster of photosystem II." Philosophical Transactions of the Royal Society B: Biological Sciences **363**(1494): 1157-1166.

Zeldin, O. B., M. Gerstel and E. F. Garman (2013). "Optimizing the spatial distribution of dose in X-ray macromolecular crystallography." Journal of synchrotron radiation **20**(1): 49-57.

Zhang, W., S. Mukhopadhyay, S. V. Pletnev, T. S. Baker, R. J. Kuhn and M. G. Rossmann (2002). "Placement of the structural proteins in Sindbis virus." Journal of virology **76**(22): 11645-11658.

Zhang, J. and A. R. Ferré-D'Amaré (2014). "Dramatic improvement of crystals of large RNAs by cation replacement and dehydration." Structure **22**(9): 1363-1371.

Zhang, H., H. Unal, C. Gati, G. W. Han, W. Liu, N. A. Zatsepin, D. James, D. Wang, G. Nelson and U. Weierstall (2015). "Structure of the angiotensin receptor revealed by serial femtosecond crystallography." Cell **161**(4): 833-844.

Zhou, Q., Y. Lai, T. Bacaj, M. Zhao, A. Y. Lyubimov, M. Uervirojnangkoorn, O. B. Zeldin, A. S. Brewster, N. K. Sauter, A. E. Cohen, S. M. Soltis, R. Alonso-Mori, M. Chollet, H. T. Lemke, R. A. Pfuetzner, U. B. Choi, W. I. Weis, J. Diao, T. C. Sudhof and A. T. Brunger (2015). "Architecture of the synaptotagmin-SNARE machinery for neuronal exocytosis." Nature **525**(7567): 62-67.

Zouni, A., H.-T. Witt, J. Kern, P. Fromme, N. Krauss, W. Saenger and P. Orth (2001). "Crystal structure of photosystem II from Synechococcus elongatus at 3.8 Å resolution." Nature **409**(6821): 739.

APPENDIX A

PERMISSIONS

Chapter 1:

Figure 1.2 reprinted from Howells, M.R., Beetz, T., Chapman, H.N., Cui, C., Holton, J.M., Jacobsen, C.J., Kirz, J., Lima, E., Marchesini, S., Miao, H. and Sayre, D., 2009. An assessment of the resolution limitation due to radiation-damage in X-ray diffraction microscopy. *Journal of electron spectroscopy and related phenomena*, *170*(1-3), pp.4-12 with permission from Elsevier.

Figure 1.3 reprinted from Miao, J., Ishikawa, T., Robinson, I.K. and Murnane, M.M., 2015. Beyond crystallography: Diffractive imaging using coherent x-ray light sources. *Science*, *348*(6234), pp.530-535. with permission from AAAS.

Figure 1.5 reprinted from McNeil, B.W. and Thompson, N.R., 2010. X-ray free-electron lasers. *Nature photonics*, *4*(12), p.814.with permission from Springer Nature.

Figure 1.6 reprinted from Neutze, R., Wouts, R., van der Spoel, D., Weckert, E. and Hajdu, J., 2000. Potential for biomolecular imaging with femtosecond X-ray pulses. *Nature*, *406*(6797), p.752. with permission from Springer Nature.

Figure 1.7 reprinted from Chapman, H.N., Barty, A., Bogan, M.J., Boutet, S., Frank, M., Hau-Riege, S.P., Marchesini, S., Woods, B.W., Bajt, S., Benner, W.H. and London, R.A., 2006. Femtosecond diffractive imaging with a soft-X-ray free-electron laser. *Nature Physics*, *2*(12), p.839.with permission from Springer Nature.

Chapter 3:

Figures 3.1, 3.4 reprinted from Fromme, P. and Grotjohann, I., 2008. Overview of photosynthesis. *Wiley-VCH Verlag, Weinheim, Germany*.with permission from Wiley.

Figure 3.2 reprinted from Govindjee and Wilber Veit, 'Z-scheme of Electron Transport in Photosynthesis', 2010 http://www.life.illinois.edu/govindjee/Z-Scheme.html with written permission from Govindjee.

Figures 3.3, 3.5 reprinted from Jordan, P., Fromme, P., Witt, H.T., Klukas, O., Saenger, W. and Krauß, N., 2001. Three-dimensional structure of cyanobacterial photosystem I at 2.5 Å resolution. *Nature*, *411*(6840), p.909.with permission from Springer Nature.

Figures 3.6, 3.7b reprinted from Umena, Y., Kawakami, K., Shen, J.R. and Kamiya, N., 2011. Crystal structure of oxygen-evolving photosystem II at a resolution of 1.9 Å. *Nature*, *473*(7345), p.55.with permission from Springer Nature.

Figure 3.7a reprinted from Loll, B., Kern, J., Saenger, W., Zouni, A. and Biesiadka, J., 2005. Towards complete cofactor arrangement in the 3.0 Å resolution structure of photosystem II. *Nature*, *438*(7070), p.1040.with permission from Springer Nature.

Figure 3.8 reprinted from Kupitz, C., Basu, S., Grotjohann, I., Fromme, R., Zatsepin, N.A., Rendek, K.N., Hunter, M.S., Shoeman, R.L., White, T.A., Wang, D. and James, D., 2014. Serial time-resolved crystallography of photosystem II using a femtosecond X-ray laser. *Nature*, *513*(7517), p.261..with permission from Springer Nature.

Figure 3.13 reprinted from Li, Z., Sau, A.K., Shen, S., Whitehouse, C., Baasov, T. and Anderson, K.S., 2003. A snapshot of enzyme catalysis using electrospray ionization mass spectrometry. *Journal of the American Chemical Society*, *125*(33), pp.9938-9939.with permission from the American Chemical Society.

Chapter 5:

Figure 5.2 reprinted from Chapman, H.N., Fromme, P., Barty, A., White, T.A., Kirian, R.A., Aquila, A., Hunter, M.S., Schulz, J., DePonte, D.P., Weierstall, U. and Doak, R.B., 2011. Femtosecond X-ray protein nanocrystallography. *Nature*, *470*(7332), p.73.with permission from Springer Nature.

Chapter 6:

Figure 6.1 reprinted from Tenboer, J., Basu, S., Zatsepin, N., Pande, K., Milathianaki, D., Frank, M., Hunter, M., Boutet, S., Williams, G.J., Koglin, J.E. and Oberthuer, D., 2014. Time-resolved serial crystallography captures high-resolution intermediates of photoactive yellow protein. *Science*, *346*(6214), pp.1242-1246.with permission from AAAS.

Figure 6.3 reprinted from Abdallah, B.G., Roy-Chowdhury, S., Coe, J., Fromme, P. and Ros, A., 2015. High throughput protein nanocrystal fractionation in a microfluidic sorter. *Analytical chemistry*, *87*(8), pp.4159-4167.with permission from the American Chemical Society.

Figure 6.8 reprinted from Pande, K., Hutchison, C.D., Groenhof, G., Aquila, A., Robinson, J.S., Tenboer, J., Basu, S., Boutet, S., DePonte, D.P., Liang, M. and White, T.A., 2016. Femtosecond structural dynamics drives the trans/cis isomerization in photoactive yellow protein. *Science*, *352*(6286), pp.725-729.with permission from AAAS.